A Fourth Generation ^{192}Ir Source-Based CT Scanner for Brachytherapy

by

Anita Glenda Berndt

A Thesis

Submitted to the Faculty of Graduate Studies

In Partial Fulfillment of the Requirements

For the Degree of

Doctor of Philosophy

Department of Physics and Astronomy
University of Manitoba
Winnipeg, Manitoba

THE UNIVERSITY OF MANITOBA

FACULTY OF GRADUATE STUDIES

*****

COPYRIGHT PERMISSION PAGE

A FOURTH GENERATION ^{192}IR SOURCE-BASED CT SCANNER FOR BRACHYTHERAPY

BY

Anita Glenda Berndt

A Thesis/Practicum submitted to the Faculty of Graduate Studies of The University of Manitoba in partial fulfillment of the requirements of the degree of

Doctor of Philosophy

Abstract

This thesis describes and characterizes the sub-systems (source, detectors, data acquisition system and collimator) of a prototype fourth generation computed tomography scanner consisting of a ring of 96 8-channel photodiode scintillator ($CdWO_4$) detectors. The ^{192}Ir brachytherapy source and transport mechanism of a commercial high-dose-rate treatment unit provides the photons for measuring projections of the scanned object. It is envisioned that the tomographic images generated with this scanner will be used to plan high-dose-rate brachytherapy treatments.

Prototype detectors responded linearly to an incident γ-ray fluence over a wide dynamic range (2.6 decades). The noise analysis of the prototype detectors indicated that the detector noise is dominated by quantum noise for incident γ-ray intensities expected when imaging patients up to about 45 cm in diameter. A pair of lead rings collimates both the source and the detectors to provide a maximum scan field of view 50 cm in diameter. The full-widths at half-maximum of the radiation sensitivity and image (slice) sensitivity profiles in the longitudinal direction are 2.7 cm and 0.4 cm respectively.

High contrast resolution, image noise and radiation dose were investigated using a combination of measurements and computer simulations. Computer simulations were performed to assess the effect of varying detector number, source size and number of source positions. The high contrast resolution was examined by modeling wire phantoms, and images of uniform Plexiglas disks were used to quantify the scanner noise. The full-width at half-maximum of the point spread function was found to be 0.21 cm using source and detector dimensions of 0.36 cm and 0.275 cm respectively (768 detectors, 864 source positions). This configuration resulted in a standard deviation of 23 Hounsfield units at the center of a 25 cm diameter Plexiglas phantom for a 7.5 Ci ^{192}Ir source. The multiple-scan average dose for a 100 second scan (1.0 cm slice spacing, 2.7 cm slice thickness) measured using prototype collimators is 1.1 cGy. The high contrast resolution and image noise are adequate for visualizing brachytherapy implants and contrast filled

critical organs for planning brachytherapy treatments. Preliminary images clearly show streak free visualization of objects containing high Z materials.

To Dietmar and Trudy

Acknowledgements

I thank my supervisor Dr. Bews for his advice and encouragement throughout my graduate work. Special thanks to Dr. Rickey and Dr. Rathee for their technical expertise and support, without which this project would not have been possible. Thanks also to my committee, Dr. Holdsworth, Dr. McLeod, Dr. Jones and Dr. Tabisz for their advice.

I thank the Medical Devices Section of CancerCare Manitoba for engineering the mechanical hardware. Thanks especially to Bob Miller for the countless hours spent constructing the scanner and many times he accommodated our rush requests. Thanks also to Chad for construction of the LED support stand.

I thank Jeff Sandemann for assistance with the light meter. Thanks also to Marsha for use of the spectrophotometer.

I acknowledge the expert assistance of the Nuclear Electronics Section of CancerCare Manitoba and thank K. Kundu for the circuit board layout.

Major funding for this project provided by the Manitoba Health Research Council.

Finally thanks to my husband Marvin, and my parents for their patience, understanding and support throughout this project.

Table of Contents

Chapter 1

Introduction

Modern medicine has provided us with a number of imaging modalities that allow visualization of patient anatomy without resorting to exploratory surgery. Of these, computed tomography (CT) has become a widespread imaging technique, proven to be useful for both diagnosis and as a tool in radiation treatment planning. Computed tomography provides cross-sectional images of the body using *x*-ray transmission data collected at various angles around the patient. This data provides adequate information regarding the internal structure of the object that a mathematical algorithm can be used to reconstruct a cross-sectional view. Although CT images generally do not have the exquisite spatial resolution afforded by planar radiographs, they provide true three-dimensional anatomical information not available in conventional radiographs, as shown in Figure 1.1. More specifically, cross-sectional CT images are not cluttered by "structural noise" (Hanson, 1981) as is the case for planar radiographs where all structures are superimposed onto a single plane. An example of this is shown in Figure 1.1a where the ribs obscure the fine details of the lung. Therefore, cross-sectional images provide superior visualization of structures with small differences in attenuation coefficients (Hanson, 1981). As such, CT scanners have revolutionized both radiologic and oncologic imaging and, in general, our ability to non-invasively obtain anatomical information.

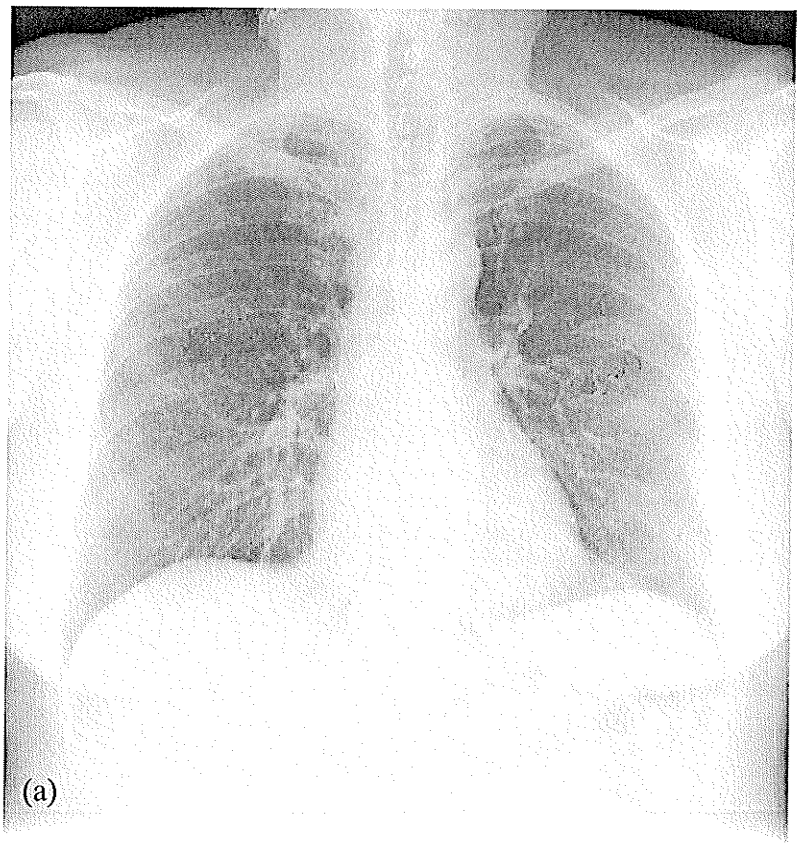

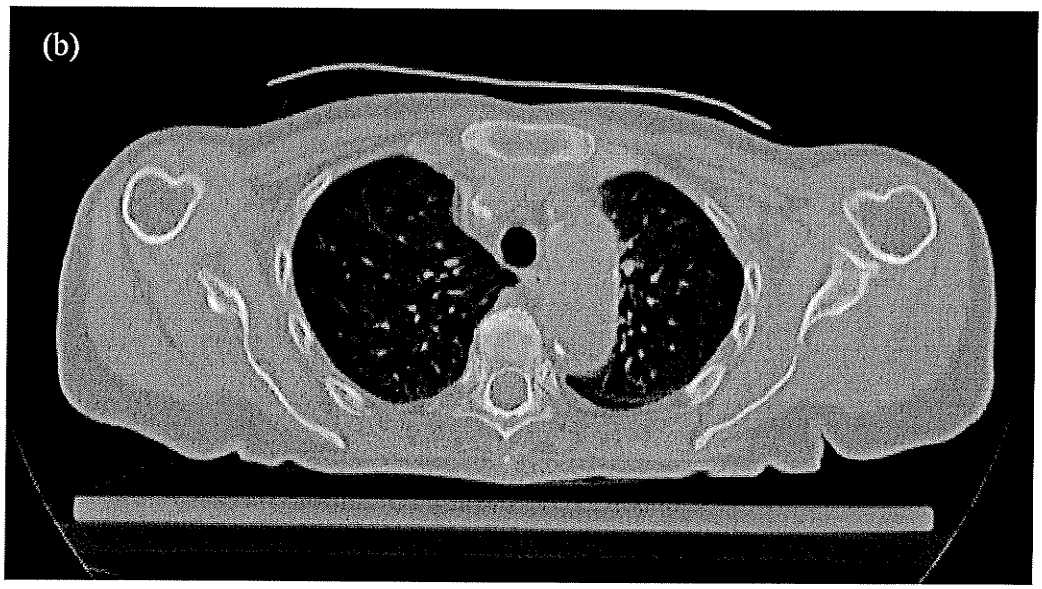

Figure 1.1 Images of an adult chest given by (a) a postero-anterior radiograph and (b) a cross-sectional CT image. Note the superior contrast of the CT image. Structures that attenuate more *x*-rays are indicated by an increase in brightness. For example, bones appear nearly white and the air-filled lungs are nearly black.

1.1 History of CT

The mathematical foundation for CT was established in 1917 by J. Radon when he demonstrated that the interior of any object could be reconstructed using an infinite number of projections of the object (Radon, 1917). Besides requiring an infinite number of projections, Radon's reconstruction expression is very susceptible to the noise in experimentally measured data, and as such is not used in practice (Joseph, 1995). A further attempt at image reconstruction from projections was presented by Bracewell (Bracewell, 1956), who used a microwave antenna to measure solar activity. The measurements provided projections of the solar activity, which were reconstructed into maps of solar activity (Brooks and DiChiro, 1976).

The very first experimental set-up to measure radiological projections of an object was built in 1961 by Oldendorf (Oldendorf, 1961). In this set-up, an ^{131}I radioisotope source was facing a detector consisting of a NaI scintillation crystal and a photomultiplier tube. The radiological projections of a plastic phantom containing nails of different densities were measured and studied from various angles using a translate-rotate system[1]. A tomographic image of the phantom was however not reconstructed due to the lack of computer resources. Kuhl and Edwards (Kuhl and Edwards, 1963) employed a similar translate-rotate system and a scintillation detector to collect emission data. A simple backprojection was used to obtain blurred cross-sectional images of the radioisotope uptake.

In 1963 Cormack presented a prototype CT scanner using a ^{60}Co source and a Geiger-Mueller counter. In his first paper, Cormack (Cormack, 1963) developed an alternative solution to the one presented by Radon for reconstructing an object from projection data (Joseph, 1995). Since this method was derived only for circularly symmetrical objects, his experiments used an aluminum cylinder surrounded by a wooden annulus and a simple translation stage (Cormack, 1980). Measurements were

[1] A translate-rotate system refers to a data collection geometry in which the source and the detector are translated linearly past the stationary object to obtain a projection at a particular angle. After each transverse pass, the source and the detector are rotated with respect to the object to obtain projection data from a different angle. Alternatively, the source and the detector may be held stationary, and the object translated and rotated. Both collection schemes yield the same projection data.

performed at only one projection angle. Cormack's second paper (Cormack, 1964) provided a generalization of the reconstruction algorithm to allow for objects that are not circularly symmetrical. It was tested using a translate-rotate system to image a Lucite phantom containing two aluminum cylinders surrounded by an aluminum annulus.

Hounsfield was credited with building the first clinically viable CT scanner (Hounsfield, 1973). Hounsfield and Cormack shared the 1979 Nobel Prize for Medicine and Physiology for their respective contributions to CT. Hounsfield had previously built a prototype scanner that used an ^{241}Am source and a NaI/PMT detector (Bull, 1981). The weak source strength resulted in excessively long scan times (9 days). As such, an *x*-ray tube with much higher photon fluence rates was employed in the first clinical CT scanner (EMI Ltd.) that was installed in the Atkinson Morley Hospital in 1971 (Hendee, 1980). This translate-rotate scanner could perform only head scans, but provided the first non-invasive technique for imaging the anatomy within the skull (Bull, 1981).

1.2 Scanner Generations

X-ray transmission data must be measured at a large number of different angles through an object in order to generate a cross-sectional image. A number of mathematical algorithms such as algebraic reconstruction, Radon transform method, Fourier transform method and filtered back-projection can then be used to generate a cross-sectional image (Macovski, 1981; Herman, 1981). Of these, filtered back-projection is the most common reconstruction technique. Briefly, the transmission data are spatially filtered and then back-projected to generate a map of the *x*-ray attenuation coefficients present in the scanned object. This technique is discussed in more detail in Chapter 6. The data required to generate an image can be collected using a variety of scanner geometries, as discussed below.

All of the translate-rotate scanners mentioned in §1.1, including Hounsfield's EMI scanner, are known as first generation scanners. In a clinical first generation scanner, shown schematically in Figure 1.2a, the source and the detector synchronously translate linearly past the stationary patient. The black lines in Figure 1.2a represent positions at which the detector makes measurements, referred to as ray-sums or line

integrals. The source and detector combination then rotates by a small amount, e.g. 1° and translates across the patient again. Each set of ray-sums acquired at a particular angle is referred to as a view or a projection, three of which are shown in Figure 1.2a. This procedure is repeated until the source and detector combination has rotated through 180°. The views in the EMI scanner were collected over 180° using 1° increments, with 160 ray-sums per view (Hendee, 1980), resulting in a scan time of about 4.5 minutes, with an additional 20 minutes required for reconstruction of the image. This long scan time was impractical, especially if a large number of sections were to be imaged. Furthermore, patient motion during the long scans resulted in artifacts.

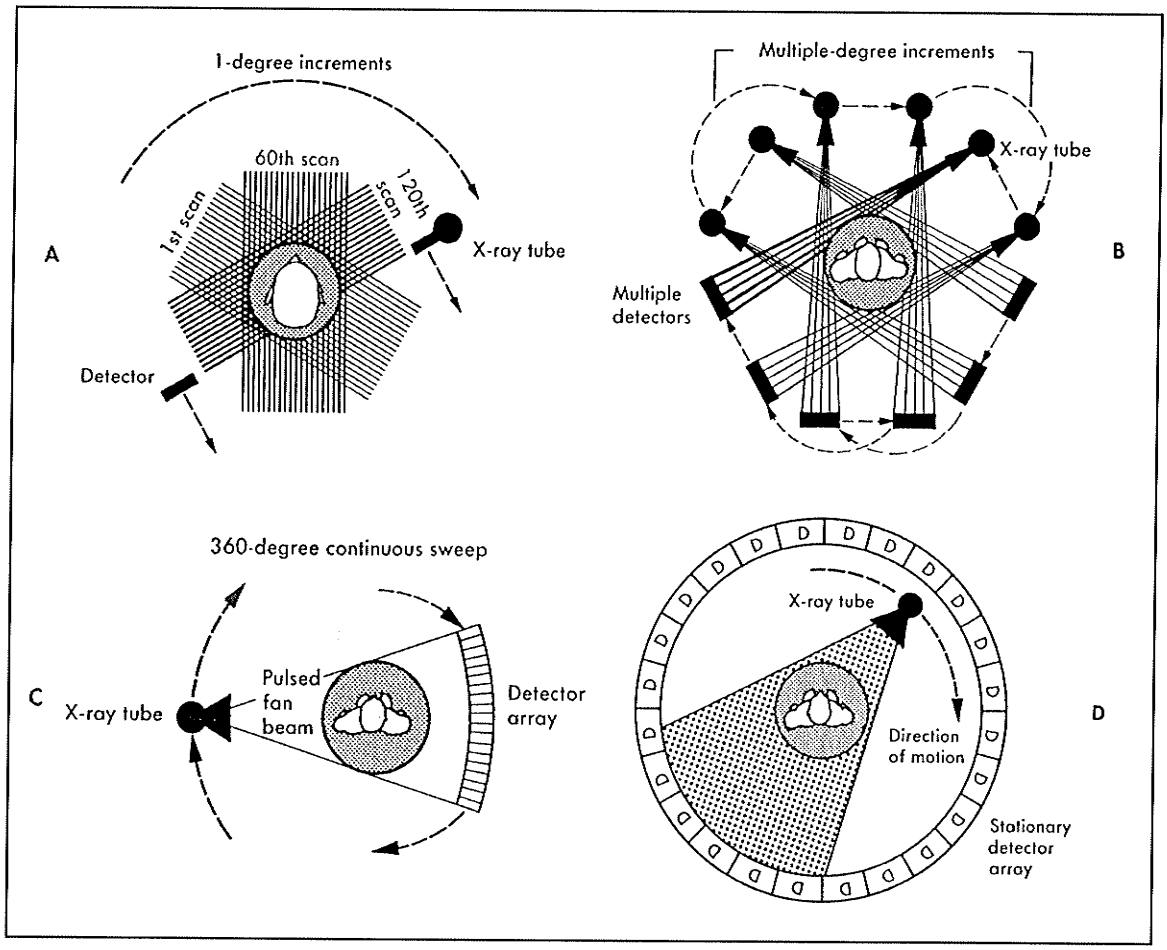

Figure 1.2 Schematic of a (a) first generation scanner geometry; (b) second generation geometry; (c) third generation geometry; and (d) fourth generation geometry. (Figure from Zatz, 1981)

An obvious approach to reducing the scan time was facilitated by adding more detectors to the existing scanner geometry. In the second generation scanner, the detectors were arranged in a small arc as shown in Figure 1.2b. The x-ray or γ-ray source and the detectors were mounted on a gantry that allowed simultaneous translation and rotation of the source and the detectors around the object. For a given translation, each detector provided a projection of the object at a different orientation. Therefore, fewer angular increments were required to acquire projections of a patient over 180° than for the first generation system. This resulted in a reduction in scan time. The first commercial second generation scanner, introduced in 1973 by the Ohio Nuclear Delta Scanner used three detectors, resulting in a 2.5 minute scan time (Zatz, 1981). Later models incorporating 30 detectors could complete a scan within 20 seconds.

The translation motion of the second generation scanner still resulted in fairly long scan times, and CT imaging remained limited to the skull because of motion artifacts. Third generation scanners were built primarily to further reduce scan times. In these scanners, the x-ray beam was collimated in the form of a fan and a large number of radiation detectors (120 to 500 detectors) arranged within this fan (Zatz, 1981). The number of detectors and the width of the fan-beam at the center of the scanner was large enough to encompass the entire patient such that only rotational motion of the x-ray tube and detector assembly was required (Figure 1.2c). The third generation scanner, achieving a 2 second scan time was first produced in 1975 by General Electric. This scanner geometry is still being commercially produced with typical scan times of 1 second.

Although third generation scanners are capable of providing scan times of less than a second, they present a number of other problems (Brooks, 1980). First, the absence of translational motion prevents the detectors from being calibrated between views, thus requiring more stable detectors than was necessary for the previous two generations. An unstable detector results in an objectionable circular artifact in the image because the source-to-detector ray provides a ray-sum at a constant distance from the center of rotation. In addition, the rotate-only motion provides limited radial sampling (i.e. a

limited number of ray sums per projection), whereas adjustable radial sampling was possible with the first and second generation scanners.

The solution to these shortcomings was provided by the fourth generation geometry shown in Figure 1.2d. In this geometry, a stationary ring of detectors surrounds the patient: only the *x*-ray tube rotates about the patient with a fan angle large enough to encompass the entire patient. The first clinical fourth generation scanner, consisting of a ring of 620 detectors was introduced in 1976 by the American Science and Engineering Company (Hendee, 1980). This arrangement allows adjustable radial sampling and detector calibration, but results in sub-optimal scatter rejection as the orientation of the *x*-ray source with respect to the detectors is continually changing, unlike in third generation scanners where the detector collimation was "focussed" on the *x*-ray tube (Brooks, 1980). This scanner generation is also commercially available.

Fifth generation scanners provided a huge reduction in scan time (scan time $\approx$ 50 ms) by eliminating all moving parts. This scanner geometry consists of a detector ring and an anode ring. Note that these are both only partial rings, not completely surrounding the patient (McCollough, 1995). An electromagnetically steered electron beam impinges on the anode ring in a circular motion to mimic a rotating *x*-ray tube. These scanners are primarily considered research scanners and are used in only a small number of hospitals.

A further advance in CT scanning technology was introduced by Siemens in 1990, when they marketed the first spiral scanner. Spiral scanners are essentially third or fourth generation scanners that move the patient couch continuously during scanning, resulting in a spiral scan, as shown in Figure 1.3, rather than collecting only one slice at a time. A number of algorithms allow the reconstruction of any transverse, sagittal, or coronal section. Although this configuration was not widely used until 1992 (Kalender, 1995), nearly all scanners commercially available today are classified as spiral scanners. The primary advantage of spiral CT scanners over conventional third or fourth generation scanners is that slices can be reconstructed anywhere along the scanned volume (Kalender, 1995).

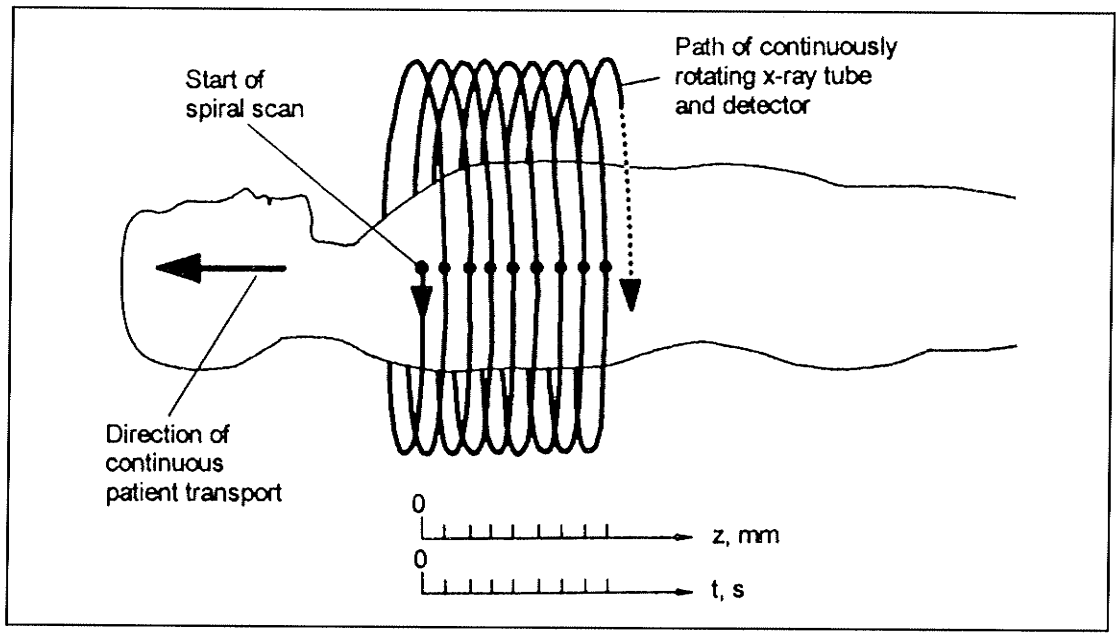

Figure 1.3 Scan path followed by a spiral CT scanner (Figure from Kalender et al., 1990).

1.3 CT Applied to Brachytherapy

The main objective of all radiation treatments is to provide a tumoricidal dose to the treatment volume, while minimizing the radiation damage inflicted on nearby critical (normal radiosensitive) structures. Brachytherapy (BT), meaning "short distance therapy" is a cancer treatment modality whereby radioactive sources are placed within or adjacent to the tumor by means of source holders. In particular, high-dose-rate brachytherapy (HDR BT) utilizes sources with a high activity, such that a treatment lasts only a few minutes. Conversely, low-dose-rate brachytherapy (LDR BT) employs sources with a lower activity resulting in treatments several days in duration. In either case, the source holders are surgically implanted, or inserted into naturally occurring cavities, depending upon the site being treated. The source holders inserted into naturally occurring orifices are referred to as applicators, while inserting needles into the tumor treats less easily accessed tumor sites. Unlike the more common external beam treatments, radiation delivered using brachytherapy is not required to first travel through overlaying normal tissues in order to reach the tumor. In addition, because of the close proximity of the sources to the tumor, the effect of the inverse square law is severe and the radiation dose

falls off very rapidly outside of the target volume, providing superior sparing of critical structures. Both of these characteristics improve the probability of cure.

At present, the planning and assessment of BT treatments at most institutions is performed on the basis of the information contained in two orthogonal radiographs of the implant and patient anatomy, as illustrated in Figure 1.4 for a cervix treatment. Corresponding dummy marker[2] positions in the two images are digitized into a BT treatment planning computer and used to build a patient model, allowing a treatment plan to be generated[3]. For some radiograph orientations, such as the LAT radiograph in Figure 1.4, the overlap of the applicators requires additional guesswork in order to locate the dummy markers, adding to the treatment planning time. Although the planar radiographs generally provide good visualization of the implant, they provide minimal information regarding the surrounding tumor site and nearby critical structures. For that matter, contrast agents are generally required to visualize any soft tissue organs, e.g. the bladder and the rectum. In the images shown in Figure 1.4, a Foley catheter containing iodine contrast has been inserted into the bladder, and barium injected into the rectum. The Foley catheter and portions of the rectum are visible on both the AP and the LAT films. It should be noted that only one or two points are chosen on each radiograph to identify each critical structure, i.e., a single point, indicated by a "B" on the films represents the bladder, while an estimate of the rectum location is indicated by an "R". Poor visualization of organ boundaries prevents the incorporation of additional critical structure points (Kapp et al., 1992). The diseased tissue can not be distinguished in the radiographs. The inability to generate a complete three-dimensional representation of the patient anatomy hinders assessment of the tumor coverage and the dose received by the critical structures. It must be noted that the dose delivered per fraction is extremely high (on the order of 800 cGy), with a steep dose gradient. This means that critical structures near the implant can receive a prohibitively large dose. Conversely, diseased tissue even 1 cm beyond the prescription point can receive inadequate dose. As such, the inability to

[2] Dummy markers, consisting of tantalum beads clipped to a wire are inserted into the applicator so that corresponding positions in the applicators can be identified on the two radiographs.

[3] An optimization program determines the optimal dwell times for each source position based upon a user-defined treatment volume. The resulting treatment plan is then assessed on the basis of the target dose and the dose to critical structures.

assess the dose to all target and critical structure points presents a significant limitation of planar radiographs. Imaging techniques that identify the critical structures and diseased tissue are therefore essential to ensure adequate tumor coverage without overdosing normal structures.

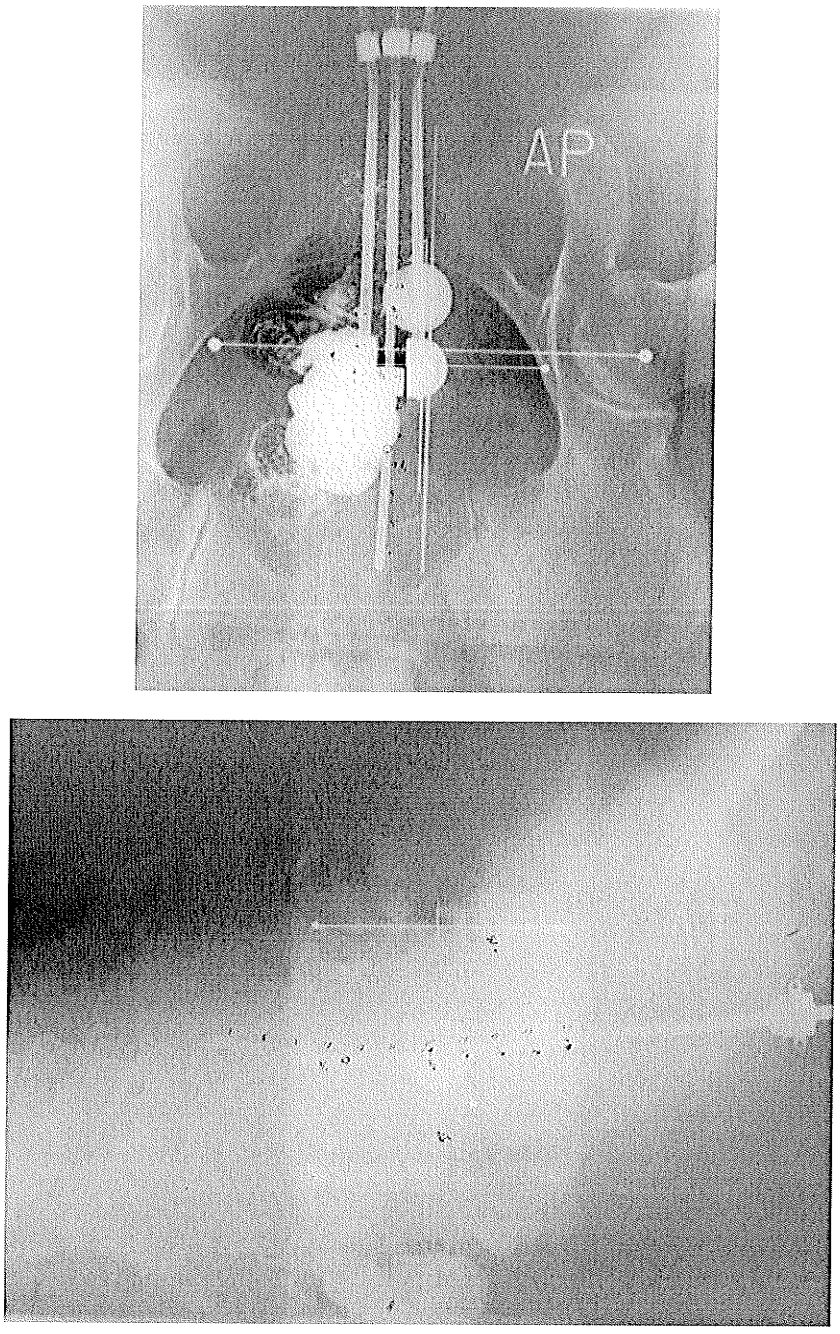

Figure 1.4 Planning anterior-posterior (AP) radiograph (top) and lateral (LAT) radiograph (bottom) of an HDR BT cervix treatment using a Henschke applicator.

In addition, the absence of three-dimensional information in planar radiographs prevents the calculation of dose volume histograms (DVH), normal tissue complication probabilities (NTCP) and tumor control probabilities (TCP) (Munzenrider et al., 1991). These parameters provide additional information for evaluating and comparing treatment plans.

1.3.1 Clinical Justification for CT Scanning

An effective BT treatment requires localization of the diseased tissue and critical structures, followed by adequate irradiation of the diseased tissue without causing excessive damage to the surrounding normal tissue. Incorrect localization of the tumor would result in a geometric miss, greatly reducing the probability of a cure. The consequences of incorrect critical structure localization can be just as devastating. If these structures receive excessive dose, unacceptable patient morbidity, or even mortality may result. As described above, localization is especially important in BT treatments, which are highly conformal, as opposed to external beam treatments, where margins allowing for uncertainties such as organ motion are incorporated. The three-dimensional nature of CT and its associated ability to generate cross-sectional images provides a vastly superiour visualization of soft tissue structures, including the tumor and critical structures, than is afforded by planar radiographs.

Computed tomography scanning has been shown to be useful in overcoming the difficulties in planning (Fontanesi et al., 1995; Grimm et al., 1994; Koutrouvelis, 1998; La Vigne et al., 1991; Perera et al., 1995; Roy et al., 1991; Scharfen et al., 1992; Teo and Chung, 1987; Wallner et al., 1991; Zamorano et al., 1987), performing (Brach et al., 1994; Griffen et al., 1994), and assessing the quality of brachytherapy treatments (Brinkmann and Kline, 1998; Cionini and Santoni, 1990; Kapp et al., 1992; Ling et al., 1987; Palmer et al., 1990; Roy et al., 1993; Stuecklschweiger et al., 1991). Because of its three-dimensional nature and inherent soft tissue contrast, CT provides accurate visualization of the relative location of the source holders with respect to the treatment volume and critical structures. Using this information, a three-dimensional distribution of the radiation dose delivered to the treatment volume can be visualized on a treatment

planning computer system to ensure adequate target coverage. Accurate knowledge of the three-dimensional dose distribution within the critical structures is equally important, as critical structure tolerance doses often influence the dose prescription (Ling et al., 1987). In addition, the amount of radiation required for local control is often nearly equal to critical structure tolerances (Cionini and Santoni, 1990). The implications are that a lower tumor dose to ensure that critical structures are spared could result in a recurrence, while a larger tumor dose that would completely eradicate the tumor could result in unacceptable normal tissue damage. It is also possible to use the three-dimensional dose distributions and anatomical information to generate DVH, NTCP, and TCP for further assessment of the treatment plan.

Consider now some examples demonstrating the utility of CT scanning in planning, performing and assessing the quality of brachytherapy implants.

1.3.2 Treatment Planning

CT scanning has been shown to be useful for planning BT implants for sites such as base-of-tongue, breast (Perera et al., 1995; Teo and Chung, 1987), brain (Fontanesi et al., 1995; Scharfen et al., 1992; Zamorano et al., 1987), prostate (Grimm et al., 1994, Roy et al., 1991; Wallner et al., 1991; Koutrouvelis, 1998) and cervix (La Vigne et al., 1991).

At CancerCare Manitoba, CT scanning is used to determine the implant location for base-of-tongue treatments. For this treatment site the tumor is not visible in conventional *x*-ray films where all structures are superimposed. This can be seen in Figure 1.5a, which shows the left-anterior oblique radiograph of a patient with the source catheters inserted for an HDR treatment. As soft tissue is poorly visualized in this image, it is impossible to determine the tumor volume from the radiograph. However, CT scans eliminate this clutter, as shown in Figures 1.5b and 1.5c, allowing identification of the tumor location with respect to the patient anatomy, as outlined in black. The physician uses this information to determine the BT implantation volume. Clearly, such information could not possibly be found from the planar radiographs.

Another application of CT-planned BT treatments is in the irradiation of lumpectomy sites for the treatment of breast cancer (Perera et al., 1995; Teo and Chung,

1987). Surgical clips placed at the boundaries of the lumpectomy site identify the target volume in the CT images, allowing the optimal number and orientation of the implant planes to be determined more accurately than is possible with conventional radiographs.

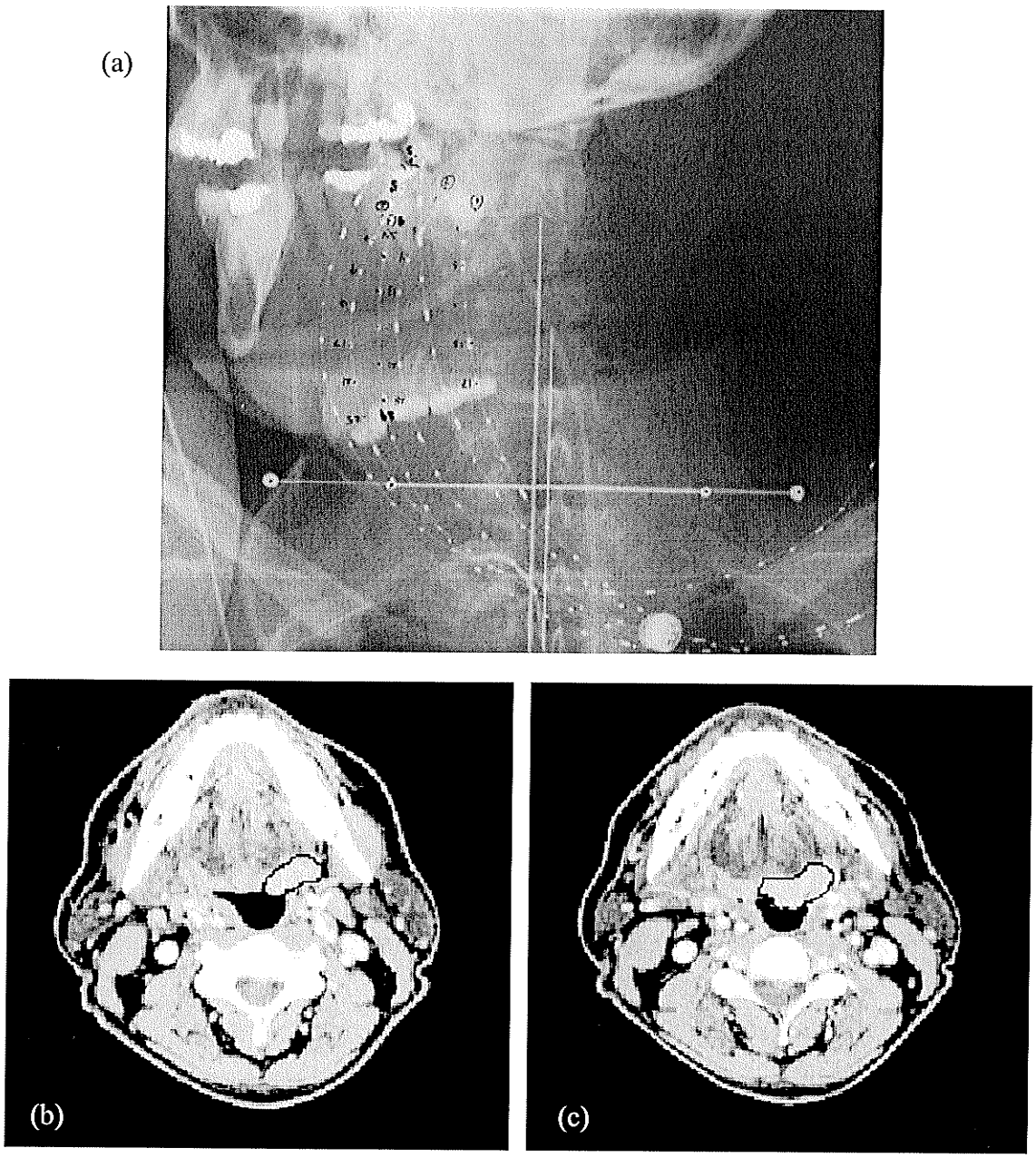

Figure 1.5 (a) Left-anterior oblique radiograph of a patient with source catheters inserted for a base-of-tongue treatment. Dummy markers inserted into the catheters identify the source dwell positions. (b) and (c) are pre-implantation CT scans of the same patient showing the tumor outlined in black. The radiograph shows only bony anatomy, while the CT scans show soft-tissue structures.

CT scanning has also been used to decide the implant volume and catheter location in the interstitial irradiation of brain tumors (Fontanesi et al., 1995; Scharfen et al., 1992; Zamorano et al., 1987). For this site it is particularly important to localize the tumor accurately in order to avoid treating the surrounding healthy brain tissue. In this type of study, a reference coordinate axis is defined by a stereotactic frame fixed to the patient's skull and a series of CT images is collected. Catheter and source positions are then selected on the basis of isodose lines overlaying the image series as generated using a treatment planning computer. In some instances (Zamorano et al., 1987), a CT scan is taken after implantation to verify the implanted needle trajectory. Importantly, the geometric fidelity and reasonable soft-tissue contrast provided by CT scans is necessary for this treatment technique.

Permanent implantation of low dose rate seeds in the prostate is an increasingly popular treatment technique for early stage prostate cancer. The location of the pubic bones is important for transperineal implants, as they may block portions of the prostate, preventing complete target coverage (Roy et al., 1991; Wallner et al., 1991). The group at Memorial Sloan Kettering Cancer Center has developed a planning technique whereby the needles are angled to maneuver around the pubic bones in order to place seeds in the entire prostate (Roy et al., 1991; Wallner et al., 1991). Although transrectal ultrasound (TRUS) is generally used to plan and perform the insertion, TRUS has a limited field of view and the spatial information is affected by geometrical distortions. Thus, the large field of view and geometric fidelity of CT scans are required to perform this angled needle technique.

At another center (Koutrouvelis, 1998), prostate implants are performed by inserting needles through the ischiorectal region, rather than placing them through the perineal region. Grimm et al. (1994) claim that this needle insertion technique can be used regardless of prostate size and pubic arch location. For this insertion configuration TRUS is not an option, as needles are inserted through the ischiorectal region, leaving no room for the ultrasound probe. Here CT is the only imaging modality that can be used to obtain 3D images of the prostate and critical structures.

La Vigne et al. (1991) describe a technique whereby CT images are used to plan the treatment of gynecologic cancers. Implants parallel to the long axis of the patient may not allow for adequate tumor coverage if the tumor is blocked by the bladder or the pelvic bones. A three-dimensional view of the patient's anatomy, achieved by contouring[4] a CT scan of the patient can however be rotated such that the critical structures are avoided. Implantation parallel to this rotation angle, rather than parallel to the long axis of the patient then results in superior tumor coverage. The information necessary to construct such a 3D model could not possibly be found from orthogonal radiographs.

1.3.3 Performing BT Treatments

CT scanning has also been useful during catheter placement for sites such as lung cancer (Brach et al., 1994) and metastasis to the pelvis (Griffen et al., 1994). In both instances CT scanning the patient found the location and size of the tumor. This 3D information is necessary to accurately determine the insertion location and assess the needle trajectory with respect to the tumor and any nearby critical structures.

The paper by Griffen et al. (1994) is worthy of additional discussion because a large number of scans were performed to carry out a single treatment. CT-guided catheter insertion was chosen to avert the morbidity associated with inserting the catheters using open surgery. Numerous (about seven) CT scans of the patient were performed. These enabled the authors to (i) localize the tumor and critical structures, and determine the number and trajectory of the catheters; (ii) re-locate the tumor after planning and place metal markers on the patient's skin to indicate the needle insertion location; (iii) verify the position of the markers; (iv) monitor the needle orientation and position during insertion (catheters were then placed inside of the needles, and the needles removed); (v) confirm that the catheter positions agreed with the planned positions; and, (vi) acquire simulation images with dummy markers placed in the catheters. This ensured that the actual needle positioning agreed with the planned needle positioning. Clearly the number of CT scans performed should be less than described here. This could have easily been

[4] Contouring involves outlining structures of interest such as the tumor volume and any nearby critical structures.

achieved by placing reference marks on the patient's skin at the time of scan (i). Using their position, it should have been possible to calculate the location of the needle insertion markers, thereby eliminating scans (ii) and (iii). Scan (v) could have also been eliminated, as the catheter positions were verified in scan (iv). Although the exact technique used here was flawed, it showed the potential of using CT to ensure the accurate placement of BT needles. By way of its overuse, this example helps illustrate how reliant one can become upon the abilities and usefulness of CT.

1.3.4 Assessing BT Treatments

Before a BT treatment is delivered, it must be assessed to ensure that the clinical goals of the plan are achieved, namely, that a tumoricidal dose is delivered to the diseased tissue without exceeding the normal structure tolerances. This allows the plan to be modified if these objectives are not met.

Planar radiographs are often used to assess brachytherapy treatments, in particular to determine the dose received by critical structures in gynecological treatments. At present, most centers simply estimate the dose to critical structures at a small number of points. This technique suffers from two major shortcomings. First, the points identified on the radiographs are different at different centers (Kapp et al., 1992), and second, the identified points may not indicate the maximum dose received by the organ (Cionini and Santoni, 1990; Palmer et al., 1990; Stuecklschweiger et al., 1991), resulting in an underestimation of the critical structure dose. Portions of the critical structure receiving a dose in excess of the tolerance dose for that organ may be damaged. Thus, an underestimation of the critical structure dose may result in an unexpected patient morbidity.

1.3.4.1 Impact of CT on determining Critical Structure Dose

Several studies have examined the benefits of CT scanning in gynecological BT treatments. In particular, the dose delivered to critical structures as found from CT scans has been compared to the dose determined from orthogonal radiographs. Others have

quantified the shortcomings of assessing a treatment based on the dose at a single point, as opposed to considering the target coverage on the basis of CT scans.

Kapp et al. (1992) and Stuecklschweiger et al. (1991) describe a retrospective analysis of bladder and rectum doses in 15 patients who underwent BT treatment for cervical or endometrial cancer. Specifically, they compared the dose to these critical structures found using orthogonal *x*-rays and CT scans. In this study, a number of patients were CT scanned with the applicator, rectal markers and bladder markers still in place after a gynecological treatment. Four rectal points were defined using a 12 cm long, 2 cm diameter tube with four metal rings. The bladder base was marked by a metal chain inserted into the bladder, while the position of the bladder neck was identified using a Foley catheter filled with contrast medium. The maximum doses to the critical structures were determined using both CT and orthogonal radiographs. The ratio of orthogonal radiograph doses to CT doses given to the rectum, bladder neck and bladder base ranged from 1.1-2.7, 1.0-1.7 and 1.0-5.4 respectively, where the larger dose was always found from the CT scan (Kapp et al., 1992). Comparable results were found in a similar study performed by Ling et al. (1987). The large variation in the dose ratios is due to variations in patient anatomy, packing and applicator positioning.

A prospective study by Cionini and Santoni (1990) involving 65 patients found a ratio of 1.5-2.5 between the dose received by the bladder point identified on radiographs, and the maximum bladder dose determined from CT scans, i.e. using radiographs led to a severe underestimation of the dose. No significant difference was found between the rectal dose calculated using the reference point on the orthogonal radiographs and the maximum rectal dose from CT scans. However, the sigmoid colon received a substantial dose when the most superior tandem dwell position was loaded. Because the comparison was made before treatment, the dose distribution was modified by adjusting the dwell positions to prevent overdosing of critical structures.

These authors (Ling et al., 1987; Cionini and Santoni, 1990; Stuecklschweiger et al., 1991, Kapp et al., 1992) have concluded that a single point localization of critical structures from orthogonal radiographs provides inadequate and misleading dose information. This deficiency is clearly demonstrated when comparing the dose to the

bladder neck as opposed to the bladder base (Stuecklschweiger et al., 1991). It was found that the bladder base dose was on average 1.5 times larger than the bladder neck dose. Stuecklschweiger et al. (1991) and Kapp et al. (1992) stated that employing more critical structure dose calculation points on plane film radiographs is not an option due to the inherent poor visualization of organ boundaries. The estimation of critical structure location is further complicated by large inter-patient anatomical variations (Cionini and Santoni, 1990), which is especially true in the case of hysterectomy patients (Kapp et al., 1992), and variations in bladder anterior wall and small bowel position as a function of bladder filling (Cionini and Santoni, 1990). Consequently, a CT scan and organ contouring are required for an accurate estimate of organ dose in order to ensure that critical structures are not overdosed during treatment (Ling et al., 1987; Cionini and Santoni, 1990; Stuecklschweiger et al., 1991, Kapp et al., 1992).

1.3.4.2 Impact of CT on determining Tumor Coverage

Besides considering the dose to critical structures, the information contained in CT scans can also be used to assess the dose to the target volume. Knowledge of the dose at only one point, such as the Manchester Point A (Tod and Meredith, 1953), is just as inadequate because assessing the dose received by critical structures using only one calculation point as it results in an incomplete picture of the actual volume being treated (Cionini and Santoni, 1990). In the study described by Cionini and Santoni (1990), a CT study of the patient was performed just after insertion of the applicators with a Foley catheter in the bladder and dilute contrast agent in the rectum. The CT images were examined to determine the target volume and the location of the critical structures with respect to the applicator. Cionini found that treatments planned using Point A as the prescription point[5] resulted in unacceptable treatment volume coverage in 30% of the cases, requiring the treatment plan to be modified. In other words, about one in three

[5] It is not clear from the paper whether the source dwell times were optimized, or whether standard Manchester loading (Khan, 1994) was used. It is believed that treatments planned using point A refer to non-optimized plans that did not take into consideration the shape of the target. It is important to note that the shortcoming described here does not refer to choosing Point A as a prescription point, but pertains to evaluating the dose at *only* point A, rather than considering the shape of the entire isodose curve in relation to the target.

treatments were deemed to have a geographical miss of the treatment volume, suggesting that CT scans are needed to properly assess target coverage, just as they are needed to determine the volumetric critical structure doses.

A number of other authors (Kapp et al., 1992; Ling et al., 1987) have also registered the source positions found from the orthogonal radiographs with the anatomical structures localized in CT scans. Isodose lines superimposed on the CT images allow the physician to clearly and easily assess the treatment volume coverage, and also determine the dose being received by critical structures. Note that the longitudinal spatial resolution in CT depends on the slice thickness with a practical limit of 2 to 3 mm. Therefore conventional radiographs can not be abandoned completely as their exquisite spatial resolution is required to localize the dummy source position markers within the catheters.

CT studies are regularly used to assess the post-implant dosimetry of prostate BT treatments (Brinkmann and Kline, 1998; Koutrouvelis, 1998; Roy et al., 1993; Wallner et al., 1991). This capability has been incorporated into all commercial prostate planning systems. Various computer algorithms (Roy et al., 1993; Brinkmann and Kline, 1998) enable semi-automated seed localization after implantation. The seed position information combined with the anatomical information contained in the images allows graphic presentation of isodose surfaces and 3D volumes representing the target and critical structures. Dose volume histograms can also be generated to further assess the target coverage and normal tissue dose. Formerly, planar radiographs were used; although this allowed visualization of the sources, it provided no information regarding target coverage.

1.3.5 Inadequacy of Conventional CT Scanners

The advantages of applying the information in CT scans to BT treatments have been clearly demonstrated. However, CT scanning suffers from the logistical drawbacks of transporting the patient from the CT scanner to the brachytherapy treatment room, including increased treatment planning times. Importantly, the source holder may be displaced during transport, thereby invalidating the geometrical information in the CT

scan and possibly injuring the patient. Stuecklschweiger et al. (1991) also recognized the shortcomings of using an off-site CT scanner and stated that every effort was made to ensure that the patient position during the CT scan was identical to that during the brachytherapy treatment. They however acknowledged that exact positioning was virtually impossible and commented that "the time interval between insertion of the applicator and performance of the CT examination may result in a change in the spatial relationship of the implant to the adjacent structures because of movement" (Stuecklschweiger et al., 1991).

In addition, the purchase of a CT scanner is a substantial capital investment, requiring a dedicated room, and a large number of staff, including therapists and maintenance personnel. The costs associated with service contracts and tube replacement must also be taken into consideration.

1.4 ^{192}Ir source-based CT Solution

To overcome the drawbacks discussed above, we are developing a cost-effective, compact novel fourth-generation CT scanner which uses the source from a commercially available HDR BT treatment unit instead of an *x*-ray tube to provide the photons needed to form a CT image of the patient and the source holders.

This project makes a number of contributions to both the fields of CT and BT:

(i) The concept of building a clinically useful fourth generation CT scanner designed specifically for BT imaging is novel concept. Although a diagnostic CT scanner could be used to image the BT implant, a conventional CT scanner has the disadvantages that it is expensive, large and images at energies that would cause substantial streaking due to the beam hardening produced by the metal applicators. The scanner described in this thesis overcomes all three of these limitations. The reduced cost and compact size would allow a larger number of centres to incorporate CT imaging into the BT treatment planning process, and the high energy of the ^{192}Ir source allows streak free images to be generated.

(ii) Using a BT source to image a patient is a novel concept. To date, BT sources have been used solely to treat patients. This is the first instance in which a BT treatment source

has also been proposed to provide the images necessary for the treatment planning process.

(iii) The concept of transporting the source at the end of a wire, driven by a computer controlled stepper motor is also a new concept. This source transportation mechanism is quite different from that of a conventional CT scanner (Kalender, 1995); incorporating the source transportation mechanism of the BT treatment unit is responsible for a huge cost saving in that a separate source transportation mechanism is not required.

(iv) The detectors are novel in that they have been customized for the high average γ-ray energy of the ^{192}Ir source (355 keV) and low γ-ray fluence.

1.5 Radioisotope Based Scanners

Although most CT scanners use an x-ray source, a number of radioisotope based scanners have been built for applications such as bone density measurements, single-photon emission computed tomography (SPECT) attenuation corrections, and imaging for radiotherapy planning. In the following sections, some of the advantages and disadvantages of using a radioisotope rather than an x-ray tube are presented, along with an overview of some existing radioisotope based CT scanners.

1.5.1 Advantages and Disadvantages

Radioisotopes have a number of advantages over x-ray tubes in CT applications (Boyd, 1977). First, their emission rate is free of fluctuations, thus eliminating the hardware used to monitor beam instabilities. Second, radioisotopes are mechanically simpler and smaller than x-ray tubes, which require a high voltage power supply and the associated control system electronics. In addition, if the source is monoenergetic, beam hardening artifacts are eliminated (Boyd, 1977). Even the filtered Bremstrahlung spectrum of an x-ray tube is quite broad, which leads to beam hardening artifacts. This is manifested as cupping and streak artifacts (Joseph, 1981). Conversely, γ-ray sources emit photons at a few discrete energies, which may result in reduced beam hardening artifacts or simpler correction methods.

Dual energy isotopes are used in bone densitometry to eliminate the effect of fat on bone density measurements (Wilson, 1980). For instance, ^{153}Gd has been used to provide twin CT images: one at 100 keV and the other at 42 keV. These two images are then used to separately estimate the mineral and non-mineral (marrow) content of trabecular bone (Boyd et al., 1979).

Isotope sources also have a number of disadvantages in CT imaging applications, most importantly, their low specific activity. As isotope sources emit photons isotropically, a significant fraction of emitted photons is not used for CT imaging. Therefore, isotope CT images tend to be noisier and low-contrast resolution is compromised. A high source activity may only be realized when using large physical source sizes, which will decrease the spatial resolution in the CT images (Blumfield and Glover, 1981). The γ-ray spectrum of isotope sources is fixed and can not be adapted to imaging site or patient size as is the case for an x-ray tube. In addition, the number of suitable isotopes, and their corresponding γ-ray energies is limited. The sources with the desired energy spectrum and specific activity may have a shorter half-life, and would therefore have to be replaced more frequently, increasing the cost of maintaining the scanner. Note however, that replacement of an x-ray tube is also associated with considerable cost and acceptance testing.

1.5.2 Radioisotope Sources

Possible candidates for a radioisotope-based scanner include ^{169}Yb, ^{153}Gd, ^{57}Co, ^{155}Eu and ^{192}Ir (Boyd, 1977), ^{60}Co (Salomons et al., 1999), ^{137}Cs (Leach et al., 1982) and ^{125}I (Hangartner, 1993). The half-life and energy characteristics of these sources are listed in Table 1.1. Note that the total yields can exceed 100%, as several photons can be emitted for each disintegration.

The source type has a strong effect on the scanner design and performance. Several factors including the energy spectrum, the specific activity, and the half-life determine the suitability of an isotope source for CT applications. An isotope that emits low energy γ-rays results in large differences in attenuation from one tissue type to the next, but image noise is increased due to the lower number of transmitted photons; this in

turn reduces the low contrast resolution. The specific activity of the isotope determines the physical size and hence the inherent spatial resolution. The half-life of the source determines the replacement frequency. Note that a large specific activity, which would allow for a smaller physical source size is associated with a shorter half-life. Thus a compromise must be made between a long half-life and a high specific activity.

Table 1.1 Possible Sources for a Radioisotope Based CT Scanner

Source	Energy (keV)	Yield %$^{\nabla}$
$^{169}Yb^{\#}$	50	185
$t_{1/2}$ = 30 days	63	45
	110	18
	131	11
	177	22
	198	35
$^{153}Gd^{\#}$	41.5	60
$t_{1/2}$ = 241 days	97	30
	103	22
$^{57}Co^{\#}$	122	89
$t_{1/2}$ = 270 days	138	9
$^{155}Eu^{\#}$	140	43
$t_{1/2}$ = 1.8 years	158	32
	187	10
	247	15
$^{192}Ir^{\#}$	308	140
$t_{1/2}$ = 74 days	468	50
	608	13
$^{60}Co^{*}$	1170	100
$t_{1/2}$ = 5.26 years	1330	100
$^{137}Cs^{*}$	660	95
$t_{1/2}$ = 30.0 years		
$^{125}I^{*}$	27.3	115
$t_{1/2}$ = 60.2 days	30.9	21
	31.8	4
	35.4	7

$^{\#}$(Boyd, 1977 – note that some of the source spectra have been simplified)
*(Attix, 1986)
$^{\nabla}$Normalized to the mean number of photons emitted per disintegration

1.5.3 CT Scanners for Bone Densitometry

A number of radioisotope-based CT scanners have been built for bone density measurements. Their purpose is to noninvasively determine the density of trabecular bone independent of the surrounding cortical bone, as any reduction in trabecular bone density is a more sensitive indicator of demineralization i.e., osteoporosis (Rüegsegger et al., 1976). Although the scanners listed below have shortcomings that prevent their use as a scanner for BT treatment planning, they provide an interesting overview of existing radioisotope scanner technology.

Isotope sources such as ^{125}I (27 keV to 35 keV) exist with energies in the range of 30 to 40 keV, which provide the best sensitivity and precision for trabecular bone density measurements (Hangartner, 1993). An example of an ^{125}I based scanner is given by Rüegsegger (Rüegsegger et al., 1976). A 0.5 mm thick NaI crystal and a photomultiplier tube detect individual transmitted photons in a first generation acquisition geometry. Refinements to the scanner (Hangartner and Overton, 1982; Hangartner, 1993) resulted in a second generation scanner utilizing 16 detectors to reduce the scan time from five minutes to 90 seconds. It should be noted that these scanners are not suitable for generating images for BT treatment planning. The low energy of ^{125}I and the small scan field diameters of the scanners are only suitable for imaging the extremities (Horsman et al., 1987), whereas BT at CancerCare Manitoba is primarily used to treat pelvic tumors.

Horsman (Horsman et al., 1987) proposed a completely new and different isotope CT scanner for imaging the radius, ulna and femur. This multi-slice cone beam third generation scanner would incorporate a multiwire proportional counter comprising 128 x 128 detectors. This scanner presents the interesting feature of generating volume scans, which eliminates the need to scan several slices, but is unsuitable for generating images for BT treatment planning because of a severe count rate limitation on the detector.

An elaborate fourth generation scanner using ^{153}Gd sources was proposed by Boyd (Boyd et al., 1979; Boyd, 1981). This scanner would incorporate three 12 Ci ^{153}Gd sources each with an active area of 0.5 cm^2, spaced 120° apart, which rotate about the patient and 900 stationary solid state germanium detectors cooled with liquid N_2. The design of this scanner is similar to that of the scanner proposed in this thesis, as they both

utilize a fourth generation geometry. The spectrum of ^{153}Gd is closer to the Bremstrahlung spectrum of conventional CT than the energy spectrum of ^{192}Ir is. Boyd's scanner however suffers from the complexities of having to provide a source rotation mechanism for multiple sources and liquid N_2 cooling for the detectors.

1.5.4 CT Scanners for SPECT Attenuation Corrections

Radioisotope based CT scanning has also been incorporated into SPECT imaging in order to perform attenuation corrections (Araujo et al., 2000; Wang et al., 1994; Garrard et al.). SPECT uses emission data from Tl-201 or Tc-99m injected into the patient's blood stream to image the function of organs such as the heart. However, structures overlaying the heart, such as breast tissue and bone attenuate the emitted photons, mimicking the effect of reduced perfusion, resulting in false test results. This effect is particularly pronounced in large patients. In order to correct this problem, companies such as ADAC and Picker International Inc. have incorporated a Gd-153 line source into their SPECT detector assembly. The line source provides photons for transmission images of the torso that are detected by the SPECT camera. The source moves along the long axis of the patient, and rotates around the patient along with the detectors, allowing CT images of the patient to be generated. These are used to determine the amount of tissue overlaying the heart, which is in turn used to correct the emission data for attenuation.

1.5.5 CT Scanners for Treatment Planning

A number of radioisotope-based scanners have also been built for obtaining CT images for radiotherapy planning and treatment verification. An early isotope scanner described by Grindrod (1979) consisted of a modified double-headed isotope scanner with a ^{137}Cs source. The purpose of this scanner was to obtain attenuation coefficients useful for megavoltage radiotherapy treatment planning. The ^{137}Cs was a reasonable isotope choice with its energy of 660 keV (conventional CT scanners have a mean energy of approximately 60 keV), as attenuation coefficients have minimal energy dependence for energies greater than about 150 keV (Monohan, 1977). Although the energy of this scanner is suitable for generating the pelvis images required for BT treatment planning,

its long scan times and low signal-to-noise ratio (SNR) render it impractical. The long scan time and low SNR are a consequence of the low source activity (100 mCi) and first generation scanner geometry. Note that this example does not invalidate the use of ^{137}Cs as a possible isotope in a radioisotope based CT scanner.

Like Grinrod, Leach and Webb (Webb and Leach, 1981; Leach et al., 1982) modified an existing SPECT scanner (J & P Engineering Multipoise scanner, Mk III – double headed isotope scanner) by replacing one of the two NaI(Tl) detector heads with a ^{137}Cs source to allow CT projection data to be collected. This scanner was also built to collect data for radiotherapy treatment planning. Based on a first generation geometry, data collection employed 65 projections over 180° with scan times varying from 36 to 145 minutes, depending upon the translation speed of the source-detector assembly. As was the case for Grinrod's scanner, this scanner would be unsuitable for BT applications due to the long data collection times.

More recently, a prototype first generation scanner was built using a ^{60}Co source (Salomons, et al., 1999). Its purpose was to generate images for confirming patient set up in tomotherapy treatments. The scanner is a modified first generation system in which the object is rotated and translated while the source/detector combination remains stationary. A total of 16 views are collected using an ISORAD solid-state detector (Sun Nuclear Corporation, Melbourne, FL), where each view consists of 25 ray-sums with a 1 cm spacing. The small number of views and ray-sums present a limitation on the image quality achievable with this scanner.

1.6 Thesis Overview

Film screen radiographs provide limited information for BT planning, performance and assessment. CT imaging is an ideal adjunct to the plane films and offers the potential for designing treatment plans that exhibit improved tumor coverage and reduced dose to healthy tissue. However, BT requires a dedicated scanner for best results. Because of the high cost and large size of a diagnostic-quality scanner we propose building a scanner that uses the BT source in place of an *x*-ray tube. Since previous designs are not suitable for this application, we have developed our own design.

This thesis describes and characterizes a fourth generation scanner, which uses an ^{192}Ir brachytherapy source to provide the photons necessary to form an image. The design constraints of the detector used in this scanner are different from those for a diagnostic *x*-ray CT scanner because of the relatively low fluence rate of the ^{192}Ir treatment source (7.5 Ci). The organization of this thesis somewhat reflects the progression of the scanner development from its early prototype stage to a (nearly) completed instrument.

1.6.1 Chapter 2: Instrumentation

Chapter 2 of this thesis provides an overview of the CT scanner. The scanner is based on a commercial HDR BT instrument, which can not be modified because it is routinely used to treat patients. The impact of this constraint on the design of the CT scanner is substantial, in particular, the dimensions and energy spectrum of the ^{192}Ir source. The most important component of this scanner is the γ-ray detector boards. These are discussed, starting with a description of a prototype single-channel detector and its components. The associated data acquisition control circuit is described for both single and eight-channel detectors. An overview of available scintillating crystals is then given, along with reasons for utilizing $CdWO_4$ in the final design. The various aspects of scintillating crystal array design are then presented and evaluated including the incorporation of an array mask, crystal thickness and length. To conclude, various crystal coating materials are examined and a final array design is described.

1.6.2 Chapter 3: Single-Channel Measurements

For initial development and testing, a single-channel γ-ray detector was constructed. Although the final scanner design employs a collection of eight-channel detector assemblies, the single-channel detector allowed development and characterization of the detector without the complication of seven additional channels. In Chapter 3[6], measurements characterizing various aspects of the detector are described, perhaps the most important aspect being its noise and associated SNR. A theoretical calculation was

[6] Chapters 3 and 4 form the basis of a paper that has been published in IEEE Trans. N.S. (Berndt et al., 2000a). For this work, I performed experiments, collected, and analyzed the data. The design of the detector boards and electronics was a group effort.

performed to determine the noise contribution from the individual electronic components. The actual noise output of the detector along with the noise power spectrum was measured. Because CT algorithms are very sensitive to non-linearities, the linearity of the detector output both with and without a scintillating crystal in place was measured. Measurements were carried out using collimation similar to that of the final scanner as well as under "narrow beam" conditions. The detector response in the absence of optical or ^{192}Ir photons was measured as a function of temperature to determine the influence of temperature on the detector output. Finally, the single-channel detector described in this chapter was used in a first-generation geometry to generate three images.

1.6.3 Chapter 4: Eight-channel Measurements

The scanner requires 96 compact eight-channel γ-ray detector assemblies. To evaluate and characterize the design, a large prototype 8-channel detector board was fabricated using wire-wrap techniques. Expected problem areas of the eight-channel detector including channel-to-channel variations in sensitivity and inter-channel cross-talk were examined. Chapter 4 describes measurements of the total inter-channel variability, as well as the variability due to the electronic gain alone. Inter-channel cross-talk was examined using two different measurement and analysis techniques. First, cross-talk was assessed using the cross-covariance technique, which involved mathematically analyzing the output of simultaneously irradiated channels. The second technique involved direct experimental measurements, whereby the detector was translated past a highly collimated (slit) source. In this technique, output registered in a particular detector when neighboring detectors were irradiated is a consequence of cross-talk between the detectors.

1.6.4 Chapter 5: Scanner Design

Our CT scanner is based on a clinical (commercial) HDR BT instrument and its performance depends in part on the characteristics of that instrument. The high contrast spatial resolution depends on the source size and reproducibility of the dwell positions. Although the manufacturer of the HDR instrument provided source dimensions, an

independent verification of source size and uniformity was made[7]. Reproducibility of the ^{192}Ir source dwell positions, as investigated in Chapter 5 is also very important[7]. A discussion of collimator design and the associated design constraints is then presented, along with measurements of the dose profile along the scanner axis for several collimator prototypes.

1.6.5 Chapter 6: Image Quality

Many parameters of the CT scanner are determined by limitations of the HDR BT instrument. It is therefore desirable to study their impact. Since modifications to the HDR BT instrument are not possible, the scanner was modeled in a computer for this investigation. Chapter 6 examines the high contrast resolution by determining the impact of varying detector size, detector spacing, source size, source spacing and reconstruction filter on the scanner point-spread function (PSF) and modulation transfer function (MTF). The noise characteristics of the scanner are determined by calculating the standard deviation at the center of a uniform object as a function of source strength, number of projections, sample spacing, reconstruction filter and interpolation scheme. The noise power spectrum (NPS) was also determined for a number of selected cases. Lastly, the dose was determined by measuring the computed tomography dose index (CTDI).

1.6.6 Chapter 7: Conclusion

Chapter 7 summarizes the results of the experiments carried out in this thesis and draws conclusions regarding the scanner design parameters. Future work required for clinical implementation is also outlined.

---

[7] These sections forms the basis of a paper that has been published in Medical Physics (Berndt et al., 2000b). For this work, I performed experiments, collected, and analyzed the data.

Chapter 2

Instrumentation

This chapter describes the major components of the ^{192}Ir source-based CT scanner, namely the photon source, the detector electronics and the scintillating crystals. The characteristics of the ^{192}Ir BT source that provides the photons necessary to form the image are summarized. The discussion of the detector electronics starts with a detailed description of the individual components of a single-channel detector. The data acquisition circuits for the single-channel and eight-channel detector are then outlined. Finally, an overview of scintillating crystals is provided, including the justification for choosing $CdWO_4$ for the ^{192}Ir source-based CT scanner. The effect of crystal size and array design on the detector output is examined experimentally.

2.1 Scanner Overview

Figure 2.1 shows a photograph of the fourth generation scanner along with the BT treatment unit. A total of 96 stationary photodiode $CdWO_4$ scintillator detector assemblies, each consisting of 8 detectors are mounted on a 77.6 cm diameter ring collimator surrounding the patient. Eighteen flexible 6F catheters inside of a plastic guide form a source-guide ring 68.8 cm in diameter. These catheters are connected to the HDR BT treatment unit to provide a path for the HDR BT source to travel around the patient.

The source moves under computer control at the end of a 150 cm long steel cable and can be programmed to stop at a total of 48 dwell positions per catheter, spaced 0.25 cm or 0.50 cm apart. The 0.25 cm spacing was chosen for the ^{192}Ir source-based scanner. Thus, the scanner has a total of 768 detectors and 864 source positions. The lead collimator plates are 0.6 cm thick and extend radially inward beyond the source ring by 9.4 cm such that the scanner inner bore diameter is 50 cm.

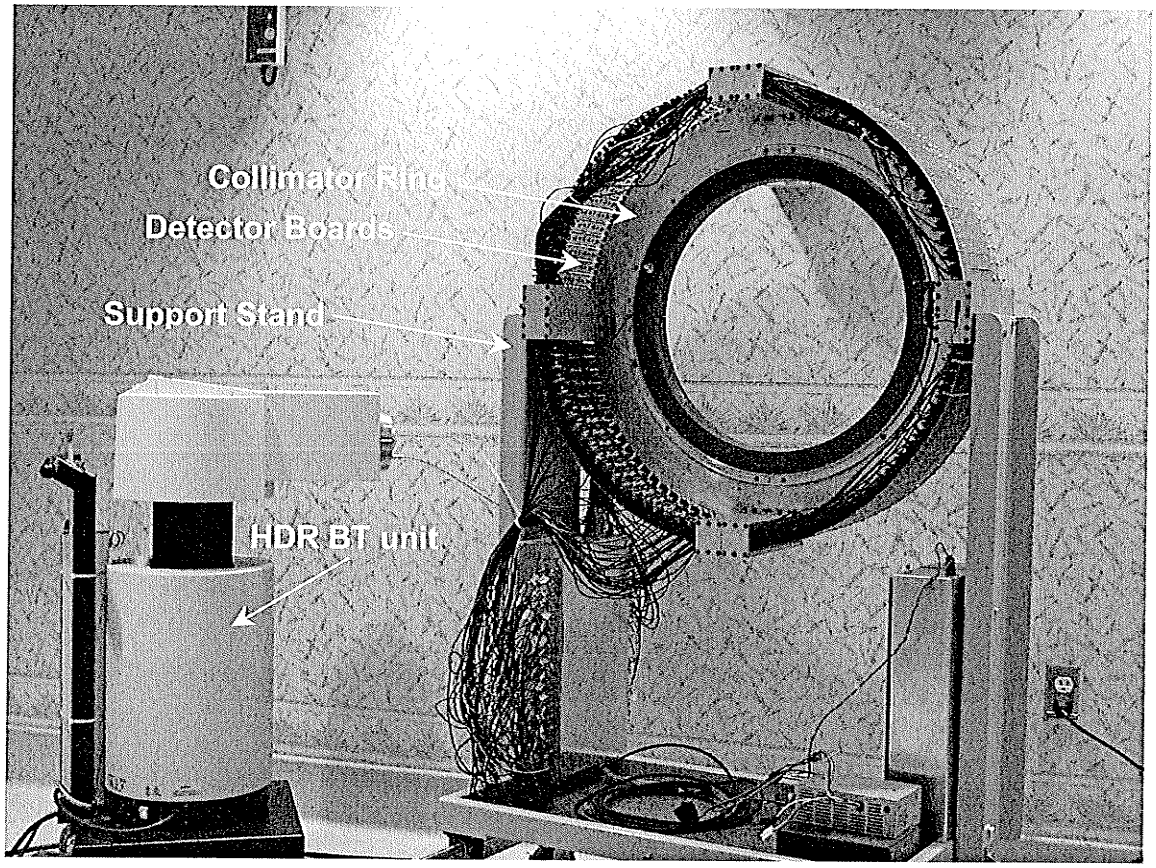

Figure 2.1 Fourth generation ^{192}Ir source-based CT scanner showing the collimator ring, support stand, detector boards and the HDR BT unit.

2.2 Radioactive source

The scanner uses the ^{192}Ir source of a Microselectron HDR BT treatment unit (Nucletron Oldeft Corporation). The nominal activity of a newly installed source is 10 Ci. With a half-life of 74.02 days, the ^{192}Ir source is replaced quarterly so as to ensure that treatment times remain practical. The source has a diameter of 0.06 cm, is 0.35 cm long, and moves

under the control of the Microselectron HDR BT Computer at the end of a 150 cm long steel cable. Source dwell times must be chosen in increments of 100 ms.

The γ-ray spectrum of this source is considerably different from that of a conventional x-ray tube. First, an x-ray tube emits a continuous spectrum of energies, whereas the ^{192}Ir source emits photons at the discrete energies listed in Table 2.1. Second, the mean photon energy of ^{192}Ir, found using a weighted average, is 355 keV, whereas the average energy for a conventional CT scanner x-ray tube is about 60 keV. The average photon energy influences the total number of interactions within the patient and the detectors, as well as the proportion of Compton scattering and photoelectric effect, as can be seen in Figure 2.2a. Figure 2.2a shows the spectral peaks of ^{192}Ir (Kocher, 1981), where the heights of the peaks reflect their relative intensity, and the mass attenuation coefficients for Compton scattering, the photoelectric effect and coherent scattering in water (ICRU 44, 1989). For the 60 keV photons produced by a conventional CT scanner x-ray tube, Compton and coherent scattering account for 92.7% of the interactions in water, while the remaining 7.3% are due to the photoelectric effect. The weighted average of the total, Compton and photoelectric attenuation coefficients can be calculated to determine the Compton scattering and photoelectric effect fractions in a particular material for ^{192}Ir. The weighted average of the total attenuation coefficient $\overline{\mu}$ is found using the expression (Attix, 1986)

$$\overline{\mu} = \frac{\sum_{i=1}^{n} A_i \mu_i}{\sum_{i=1}^{n} A_i} \tag{2.1a}$$

where A_i is the relative amplitude of the i^{th} peak in the ^{192}Ir spectrum, and μ_i is the total attenuation coefficient at the energy of the i^{th} peak. The weighted average of the Compton attenuation coefficient $\overline{\mu}_C$ and the photoelectric attenuation coefficient $\overline{\mu}_{PE}$ is found using

$$\overline{\mu}_C = \frac{\sum_{i=1}^{n} A_i \mu_{C\,i}}{\sum_{i=1}^{n} A_i} \tag{2.1b}$$

and

$$\overline{\mu}_{PE} = \frac{\sum_{i=1}^{n} A_i \mu_{PE\,i}}{\sum_{i=1}^{n} A_i} \tag{2.1c}$$

where $\mu_{C\,i}$ is the Compton attenuation coefficient and $\mu_{PE\,i}$ is the photoelectric attenuation coefficient at the energy of the i^{th} peak. It was found that for ^{192}Ir 99.37% of the interactions in water can be attributed to Compton and coherent scattering, with only 0.63% being due to the photoelectric effect. This will result in a decreased low contrast resolution, compared to a conventional CT scanner because there are smaller differences between the attenuation coefficients of different materials at 355 keV than at 60 keV (Zatz, 1981).

Table 2.1 ^{192}Ir Spectrum (Kocher, 1981)

Energy	Relative Fluence
61.4867	1.363
63.0005	2.366
65.1220	3.174
66.8320	5.456
71.4	1.014
75.7	2.378
136.346	0.218
201.306	0.564
205.79549	3.971
283.257	0.315
295.9582	35.027
308.45689	35.824
316.50789	100.000
374.476	0.881
416.460	0.801
468.0715	58.057
484.578	3.814
489.06	0.480
588.5845	5.516
604.4142	9.897
612.465	6.445
884.514	0.365

Table 2.2 Effective mass attenuation coefficients and densities for various materials, calculated using the ^{192}Ir spectrum

Material	$\overline{\mu}/\rho$ (cm^2 / g)	ρ (g/cm^3)
Lead*	0.538	11.4
Water*	0.116	1.00
Plexiglas*	0.112	1.19
Muscle*	0.115	1.04
$CdWO_4$†	0.525	7.90
Copper*	0.171	8.96

*(Attix, 1986) †(Derenzo and Moses, 1992; Bicron Brochure, 1990)

By substituting the mass attenuation coefficient μ/ρ for the attenuation coefficient μ in (2.1a), the effective mass attenuation coefficient for various materials can be found. The mass attenuation coefficient is plotted in Figure 2.2b as a function of energy for lead, $CdWO_4$ and muscle. The effective mass attenuation coefficients for these materials are listed in Table 2.2. It can be seen that the scintillator material chosen for the ^{192}Ir source-based CT scanner is highly attenuating, leading to a high absorption efficiency.

2.3 Detector Electronics

The measurements in this thesis characterize the behavior of a single- and an eight-channel detector. The components constituting a single-channel detector assembly are identical to those in the eight-channel detector assembly because the single-channel detector assembly was designed taking into consideration the expansion to eight channels. Although the following discussion refers primarily to an eight-channel detector assembly, much of what is written also pertains to a single-channel detector assembly.

The detector electronics for both the single- and the eight-channel detector consist of three distinct circuit boards: a detector assembly, a data acquisition control circuit and an analogue-to-digital (A-to-D) converter board. A schematic showing these three circuits is depicted in Figure 2.3. The detector assembly for an eight-channel detector consists of the front-end electronics for a set of eight detectors, where the time-multiplexed output of the detector assembly is a voltage proportional to the γ-ray

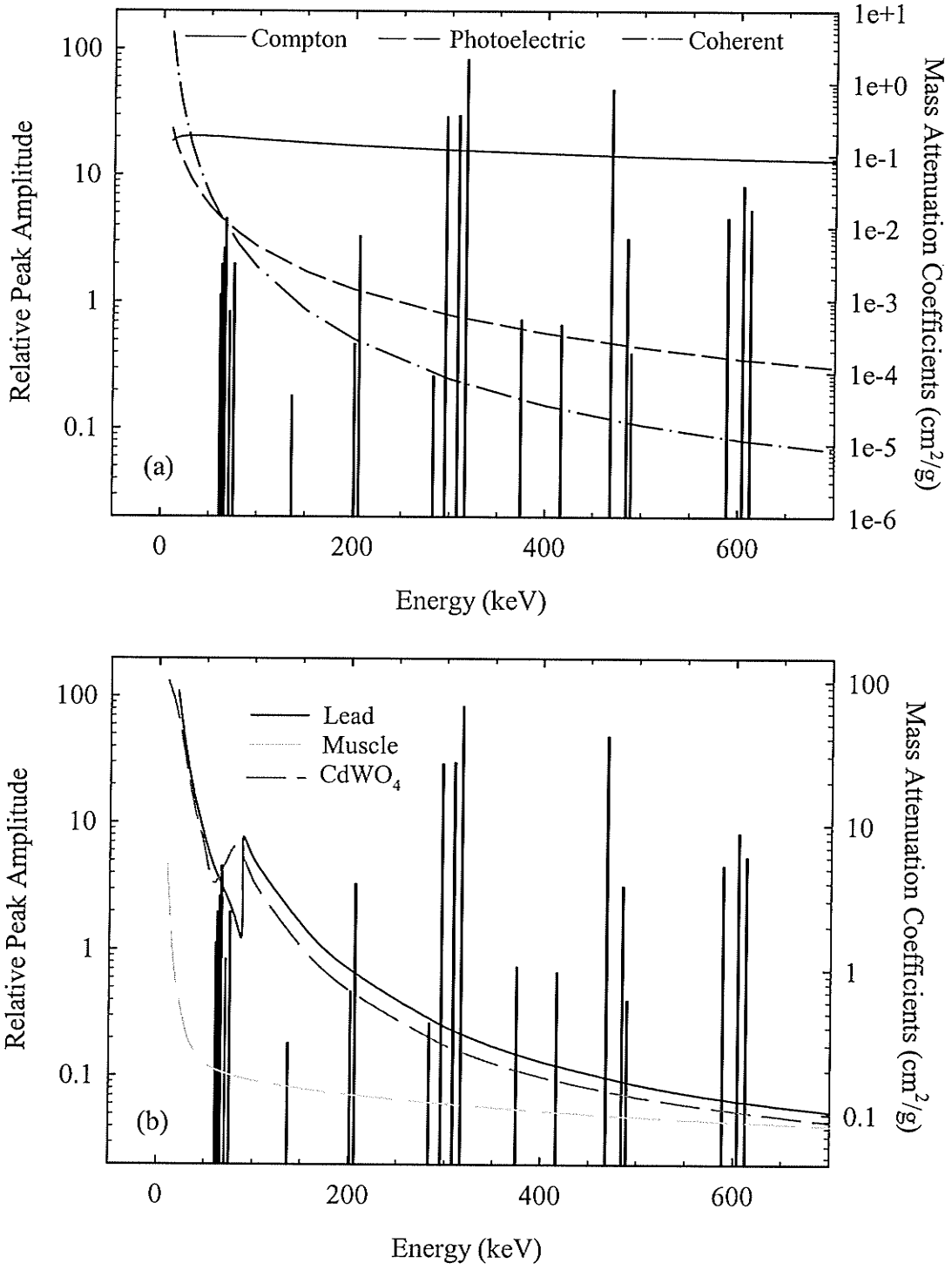

Figure 2.2 ^{192}Ir spectrum (Kocher, 1981) and (a) Compton, photoelectric and coherent interaction cross sections in water (ICRU 44, 1989) and (b) mass attenuation coefficients as a function of energy for lead, muscle and $CdWO_4$ (Attix, 1986; Bicron Brochure, 1990). The heights of the peaks in the ^{192}Ir spectrum reflect their relative intensity.

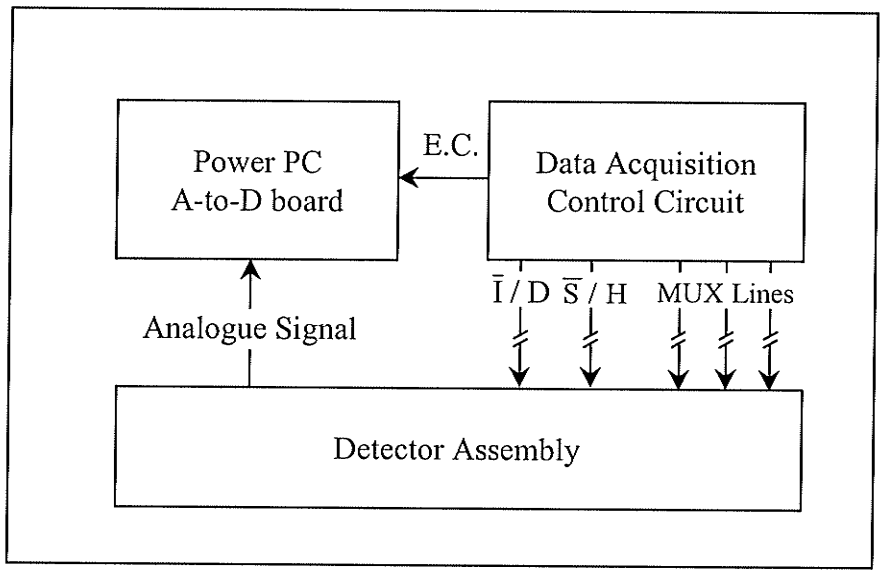

Figure 2.3 Detector electronics schematic showing the detector assembly, the control circuit and the A-to-D converter board. The breaks in the $\overline{I}$/D, $\overline{S}$/H and MUX control lines indicate the presence of opto-isolators.

fluence incident on the scintillating crystals. There are four electronic control signals that regulate the various functions performed by the detector assembly and the A-to-D converter board. An integrate-discharge ($\overline{I}$/D) signal controls the acquisition cycle of the detector assembly and the sample-and-hold ($\overline{S}$/H) indicates when the output from the detector assembly is stable and ready to be read. The multiplexer (MUX) lines control which of the eight detector channels are to be read, and an external convert (E.C.) clock pulse dictates when the A-to-D converter board reads a channel. All of these components are discussed in more detail below.

2.3.1 Detector Assembly Components

The electronics of a detector assembly constitute eight parallel analogue signal processing channels, one for each individual detector. Each channel, as shown in Figure 2.4, consists of two photodiodes (Hamamatsu S5668-02), a gated integrator (Texas Instruments TL074C op-amp; Temic DG442 Analogue Switch) followed by a gain-and-filter stage (gain = 47, f_c = 339 Hz). The photodiode produces a current i_{photo} proportional to the incident γ-ray fluence rate. The gated integrator accumulates this current for a

predetermined time interval ΔT to produce a voltage signal, which is linearly proportional to the photocurrent in the photodiodes and the integration time. The voltage signal is amplified and low-pass filtered by the gain-and-filter stage. A sample-and-hold circuit (Analog Devices SMP-04) holds the output of each channel before being routed to an 8-to-1 analogue multiplexer (MUX) (Motorola MC14051B). A sample-and-hold circuit is needed since the A-to-D converter is shared among all 8 detector channels. This circuit follows its input voltage until it is instructed to hold the voltage for a predetermined period within each sampling interval. During this hold period, the timing circuit cycles the output voltages of the eight sample-and-hold circuits to the A-to-D converter via an 8-to-1 MUX. Voltage signals from the detector assembly are digitized to a precision of 16-bits by an A-to-D converter (National Instruments PCI-MIO-16XE-50) located in a Macintosh G3 PowerPC. The acquisition software was written in LabView (National Instruments). The analogue signal processing electronics for the detector assembly receive timing signals from the data acquisition control circuit via opto-isolators (Motorola H11L1) to provide electric isolation from interference noise.

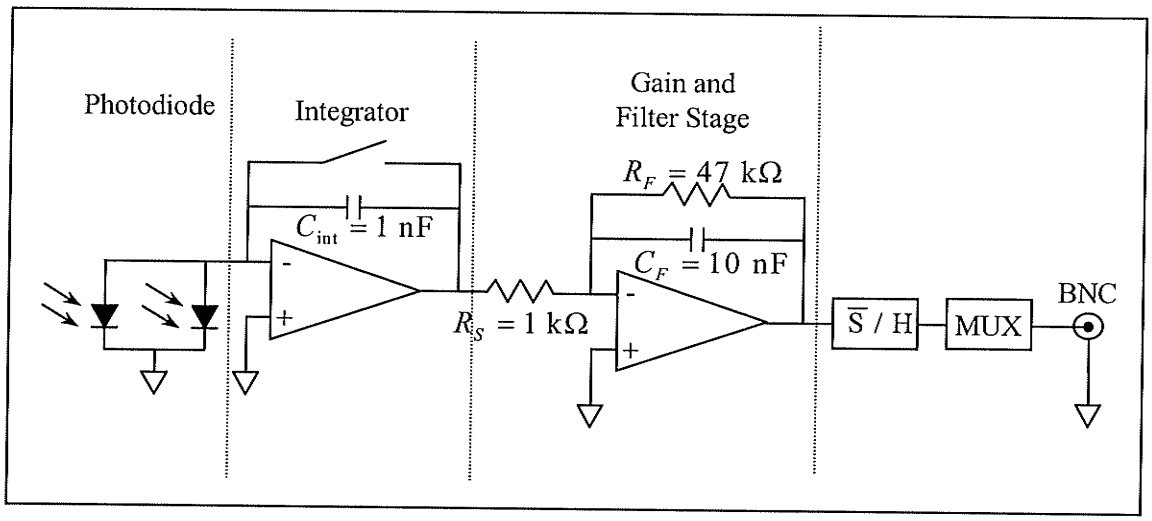

Figure 2.4 Circuit diagram showing the electronic components of one channel of the detector assembly: photodiodes, integrator, gain-and-filter stage, sample-and-hold ($\overline{S}$/H) chip, MUX and the BNC connection to the A-to-D converter board.

2.3.1.1 Photodiode

To detect the light emitted by the scintillators, we used the 16 element photodiode array (Hamamatsu S5668-02) shown in Figure 2.5. Adjacent elements were joined in parallel to give a total of 8 channels per array. Each $CdWO_4$ crystal has dimensions of 10.0 x 8.0 x 2.75 mm^3 (thickness x length x width), while each photodiode element is 1.175 mm wide and 2.0 mm long with a 0.4 mm gap between consecutive elements. Therefore, each $CdWO_4$ crystal covers exactly two photodiode elements with a space of 0.4 mm between adjacent crystals, as shown in Figure 2.5c.

Photodiodes are semiconductor light sensors that produce a voltage or current by means of the photovoltaic effect when the P-N junction is illuminated by light. As shown in Figure 2.6, a photodiode may be thought of as a conventional diode with an internal current source producing a photocurrent i_{photo} proportional to the light level present. The

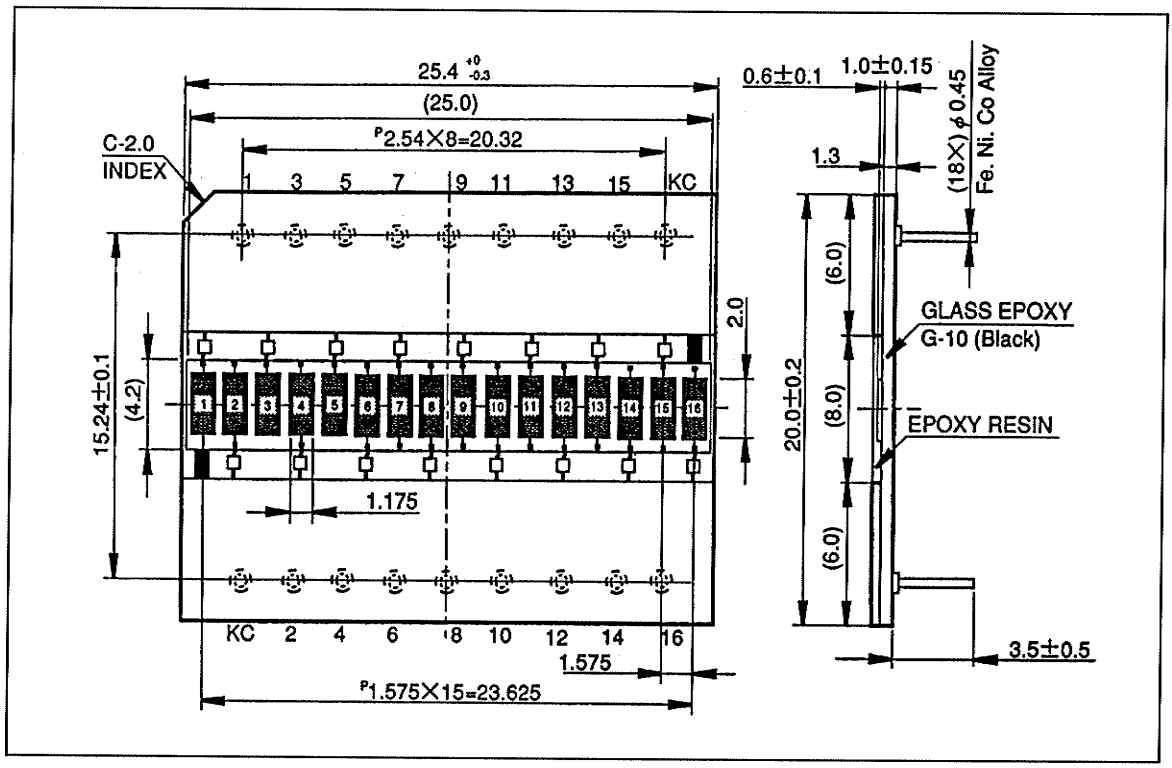

Figure 2.5a Schematic of the photodiode array showing the dimensions of the active elements. The horizontal strip of height 4.2 mm is metallic (i.e. shiny) silver in color, while the remainder of the photodiode array, including the active elements are black (see Figure 2.5b). Dimensions are in mm. (From Hamamtsu, 1994)

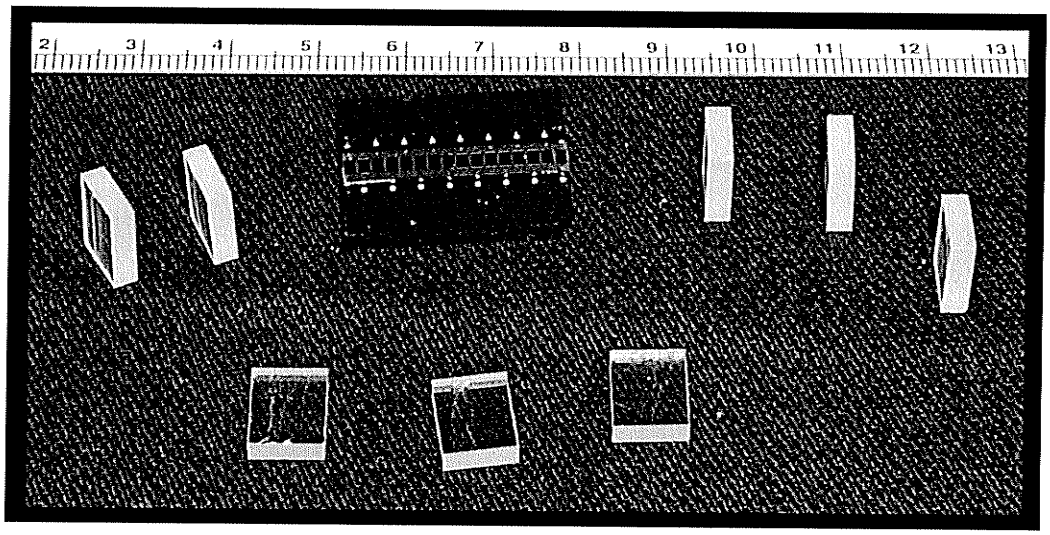

Figure 2.5b Photograph of the photodiode array and the $CdWO_4$ crystals.

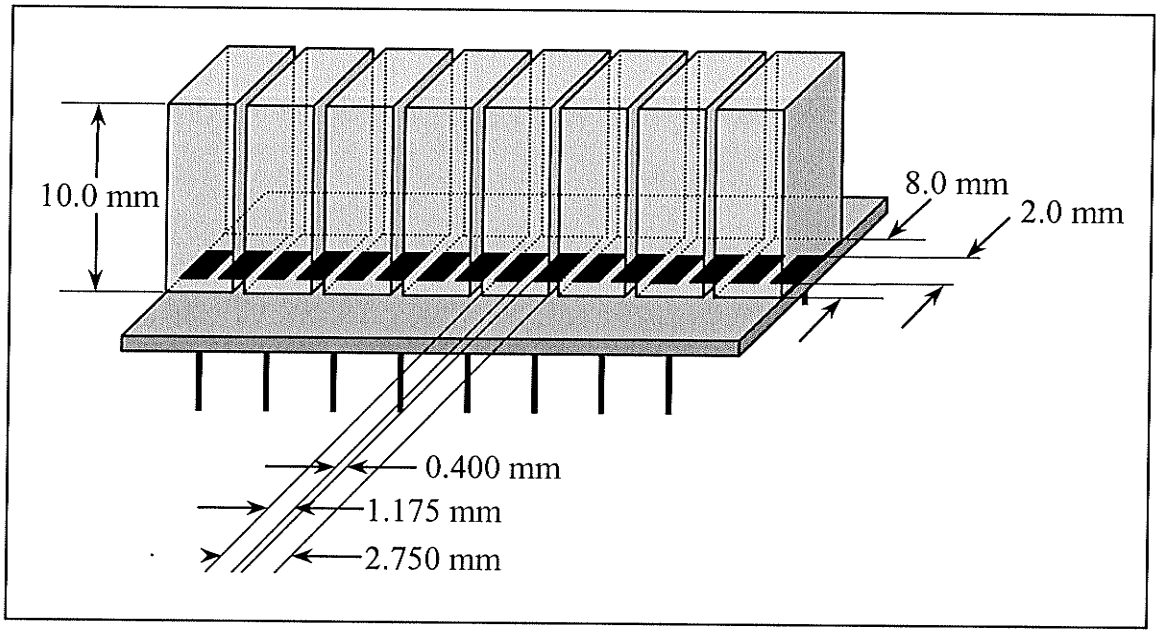

Figure 2.5c Diagram showing the position of the scintillating crystals (large gray blocks 10.0 mm x 8.0 mm x 2.75 mm) with respect to the individual photodiode elements (black rectangles 2.0 mm x 1.175 mm). Note that the width of one scintillating crystal is exactly equal to the sum of the widths of two photodiode elements and the space between them, i.e. 2.75 mm. Thus one scintillating crystal covers exactly two photodiode elements. The space between scintillating crystals is equal to the space between the photodiode elements, namely 0.4 mm.

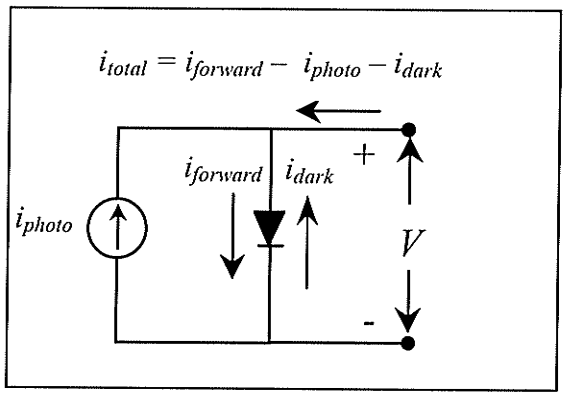

Figure 2.6 Schematic of a photodiode, which can be thought of as a current source in parallel with a conventional diode. (Graeme, 1996)

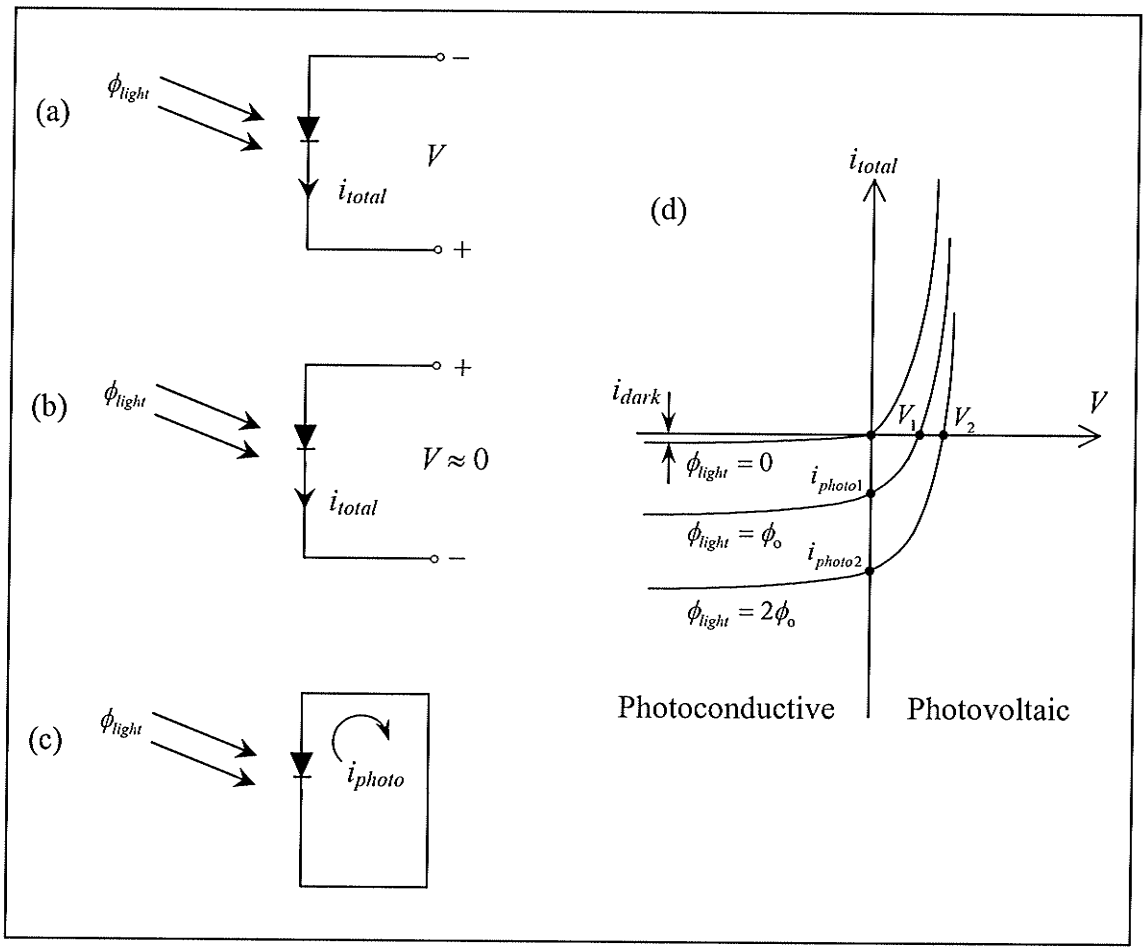

Figure 2.7 Photodiode operating in (a) photoconductive mode, (b) photovoltaic mode and (c) short-circuited. (d) Plot showing the photodiode current plotted as a function of voltage for different incident light intensities. (Hamamatsu Catalogue, 1995; Saleh and Teich, 1991)

total current i_{total} measured by an external ammeter is equal to the current flowing through the photodiode, namely, $i_{total} = i_{forward} - i_{dark} - i_{photo}$, where $i_{forward}$ is the current forced through the photodiode by the external positive voltage and i_{dark} is the current flowing through the photodiode in the reverse bias condition (negative applied voltage) in the absence of light.

Photodiodes can be operated in two modes, namely photoconductive (PC) mode where a reverse bias voltage is applied, and photovoltaic (PV) mode where no external bias voltage or a positive bias voltage is applied. The mode of operation depends upon the application; PC mode is used for high frequency (e.g. up to 1 GHz) applications, whereas PV mode is most suitable for low frequency (e.g. below 1 kHz) applications, as is the case here. The advantage of using PV mode is an increase in signal-to-noise performance of the photodiode (EG&G Catalogue, 1992). The latter is a consequence of the reduced shot noise (noise due to the discrete nature of current; Simpson, 1987) due to the absence of a dark current in PV mode (UDT Sensors, Inc. Catalogue).

For conventional diodes, only a small leakage or dark current i_{dark} is detected when a reverse voltage V is applied. However, for photodiodes the magnitude of the reverse current i_{photo} increases with increasing light levels. When operating in PC mode, as illustrated in Figure 2.7a, the bias voltage V is negative and consequently $i_{forward} = 0$, so that $i_{total} = -i_{photo} - i_{dark}$. This means that the measured current will be directly proportional to the intensity of the light illuminating the photodiode.

In photovoltaic mode, shown in Figure 2.7b, a positive bias voltage V applied across the photodiode results in $i_{forward}$ 0 and $i_{dark} = 0$ so that $i_{total} = i_{forward} - i_{photo}$. If no external bias voltage V is applied, the photocurrent provides the total photodiode current so that $i_{total} = -i_{photo}$ as shown in Figure 2.7c.

2.3.1.2 Integrator

An integrator is used to collect the charge produced by the photodiode. This portion of the circuit consists of a low noise JFET operational amplifier, a 1 nF capacitor and an analogue reset switch, as illustrated in Figure 2.4. While the switch is open, charge

collects on the capacitor, whereas closing the switch discharges the capacitor. In the case of an ideal integrator, the output voltage of the detector ΔV_{total} is given by

$$\Delta V_{total} = \frac{G}{C_{\text{int}}} \int_{1.925\,\text{ms}}^{T_o - 0.3\,\text{ms}} (i_{photo} + i_D)dt\,. \tag{2.2}$$

where i_{photo} is the photocurrent, C_{int} is the capacitance in the feedback loop, G is the gain of the gain-and-filter stage and T_o is the sample period. The choice of integration limits in (2.2) is discussed in §2.3.1.4. Here $i_{forward} = 0$ and $i_{dark} = 0$ because no bias voltage is applied. The parameter i_D is the sum of the op-amp input bias current and the switch leakage current, and can be thought of as a "dark current" (not to be confused with the photodiode dark current i_{dark}) in the sense that it flows even in the absence of light, i.e., in the absence of radiation, leading to a non-zero signal of magnitude

$$\begin{aligned} \Delta V_D &= i_D G(T_o - 2.225\,\text{ms})/C_{\text{int}} \\ &= i_D G \Delta T / C_{\text{int}}\,. \end{aligned} \tag{2.3}$$

where ΔT is the integration time. The voltage ΔV_D produced by the dark current will always be subtracted from the measurements performed in subsequent chapters. Assuming the photocurrent to be constant over the integration time, the corrected detector output is given by

$$\begin{aligned} \Delta V &= i_{photo} G(T_o - 2.225\,\text{ms})/C_{\text{int}} \\ &= i_{photo} G \Delta T / C_{\text{int}}\,. \end{aligned} \tag{2.4}$$

2.3.1.3 Analogue Switch

The purpose of the analogue switch is to discharge the capacitor so that it is ready for integration during the next measuring cycle. An ideal switch has zero current flowing through it when it is open, and zero voltage across it when it is closed. However, real switches allow a small leakage current to flow when they are open. This is not a serious problem in this application because the leakage current produces a constant offset voltage that is simply subtracted, as described in §2.3.1.2. The contribution of the leakage current to the shot noise is discussed in §3.1.1.4.

A major shortcoming of electronically controlled analogue switches is the injection of charge from the digital control inputs into the analogue outputs as a consequence of stray capacitance. The switch being used (Temic DG442) injects a charge

of approximately 1 pC RMS at the common point of the integrating capacitor, photodiode and operational amplifier when it is opened. The effect of this is to introduce a relatively large random offset that is added to ΔV_{total} in (2.2). Further details regarding this noise source, as well as measures to eliminate it are outlined in §3.1.1.3.

2.3.1.4 Gain-and-Filter Stage

The purpose of the gain-and-filter stage is to remove the high frequency noise from the output of the integration stage, and to amplify the voltage. The bandwidth of the low-pass filter is a very important design parameter. If the bandwidth is too high, the circuit provides amplification to noise at high frequencies, while too low of a bandwidth can result in slower measuring cycles or loss of information if fast measuring cycles are used. More specifically, the output of a low-pass filter is given by

$$v_{out} = V_o(1 - e^{-t/\tau}) \tag{2.5}$$

where $\tau = R_F C_F$ is the time constant required for the output voltage v_{out} to reach $1/e$ of the applied input voltage V_o. As can be seen from (2.5), several time constants must pass for the voltage to reach V_o, e.g., $v_{out} = 0.98V_o$ in 4τ. The time constant is inversely proportional to the bandwidth of the low-pass filter, thus imposing a lower limit on the measuring cycle period. In this application, the smallest dwell time for the radiation source at a particular position is equal to 100 ms. Thus the smallest sampling interval is also 100 ms. Abrupt changes in voltage at the input of the gain-and-filter stage are only expected at the beginning of a measuring cycle when the capacitor is discharged. However, due to the time constant of the gain-and-filter stage, the output voltage is delayed by several time constants. This delay in response must be kept small compared to the total measuring cycle time.

The choice of bandwidth is a compromise between two competing factors: the bandwidth should be as small as possible to provide optimal noise reduction, but yet must be large enough to allow reasonably fast measuring cycles. In keeping with this trade-off, the resistors and capacitors in the gain-and-filter stage were chosen such that the cut-off frequency of the filter is

$$f_c = \frac{1}{2\pi R_F C_F} = \frac{1}{2\pi(47\text{k}\Omega)(10\text{nF})} = 339\text{ Hz}. \tag{2.6}$$

For this choice of cut-off frequency, the delay of four time constants (4 $R_F C_F$) amounts to 1.9 ms and is a small fraction of the smallest sampling interval, i.e. 100 ms. In the interest of keeping scans times under 2 minutes/slice it was decided to use a 100 ms source dwell time, resulting in a 100 ms sampling interval.

The complex gain of the gain-and-filter stage is given by

$$F(i\omega) = \frac{R_F / R_S}{1 + i2\pi f C_F R_F} = \frac{47\text{k}\Omega/1\text{k}\Omega}{1 + \text{i}2\pi f(10\text{nF})(47\text{k}\Omega)} = \frac{47}{1 + 4.7\times10^{-4} i2\pi f}. \quad (2.7)$$

2.3.1.5 Sample-and-Hold Stage

The photocurrent and the integration time determine the output voltage of the gain-and-filter stage for each channel, as described by (2.4). The integration period must be the same for all channels. This is achieved by the sample-and-hold circuit. Since a single $\overline{\text{S}}$/H control signal is used for all sample-and-hold circuits, the outputs of all channels are held at the same instant in time during the measuring cycle. The held output of each channel is multiplexed to a single coaxial cable by an 8-to-1 analogue MUX (the detector assembly provides a single coaxial connection to the A-to-D converter board), digitized into a 16-bit binary number, and stored in computer memory.

2.3.1.6 Opto-isolators

The data acquisition control circuit is used to generate the necessary control signals for the detector assembly and the A-to-D converter board. However, switching of the control lines introduces glitches into the DC power supply. Consequently, the power supply and ground lines in the digital circuits will always contain low-amplitude, high frequency glitches. Although this has no adverse effect on the digital control signal, significant electronic noise will be introduced into the detector output voltage if the detector assembly and digital control circuit share the same DC power and ground connections. To solve this problem, the digital control signals are optically (as opposed to electrically) coupled to the detector circuit by means of Schmitt trigger opto-isolators (Motorola H11L1). In other words, the opto-isolators electrically isolate the digital from the analogue portion of the circuit, and thus prevent the noise in the digital portion of the circuit from affecting the analogue signal.

2.3.2 Data Acquisition Control Circuits and Acquisition Sequences

The purpose of the data acquisition control circuit is to generate the control signals shown in Figures 2.8 and 2.9 for the gated integrator, the sample-and-hold, the MUX, and the A-to-D converter. A stand-alone 1 MHz clock is used to generate these control signals. The sampling frequency is obtained by dividing the 1 MHz clock by a 20-bit binary counter, realized by cascading five synchronous 4-bit counters (Texas Instruments 74LS161). The higher 16 bits of this counter can be set via dip switches and provide an easy means of changing the sampling frequency. The output of this counter is a trigger signal that initiates the generation of the other control signals. The remainder of the circuit produces six additional control signals, namely:

(i) an external control signal for the A-to-D converter (external convert signal);

(ii) an integrate/discharge ($\overline{\text{I}}$/D) signal;

(iii) a sample-and-hold ($\overline{\text{S}}$/H) signal; and,

(iv) three binary control lines for the 8-to-1 analogue MUX.

2.3.2.1 Single-Channel Data Acquisition Sequence

In the single-channel data acquisition control circuit the trigger signal derived from the 1 MHz clock is used as an external convert signal, as shown in Figure 2.8. An additional external convert pulse is generated in each measuring cycle, which is delayed from the trigger signal by 2.15 ms. The integrate discharge signal is a 0.150 ms wide pulse delayed by 0.150 ms from the trigger signal. The sample-and-hold signal is a 0.150 ms wide pulse occurring at the same time as the trigger pulse.

To understand how the control lines manipulate the behavior of the various components, consider the pulse sequence illustrated in Figure 2.8. At the start of an acquisition sequence (indicated by line labeled "t = 0") the current generated by the photodiode is integrated, and the sample-and-hold circuit is in sample mode[1]. After 1.925

[1] The bar over the "S" in $\overline{\text{S}}$/H indicates that the sample-and-hold circuit samples when the control signal is low, and holds when the control signal is high.

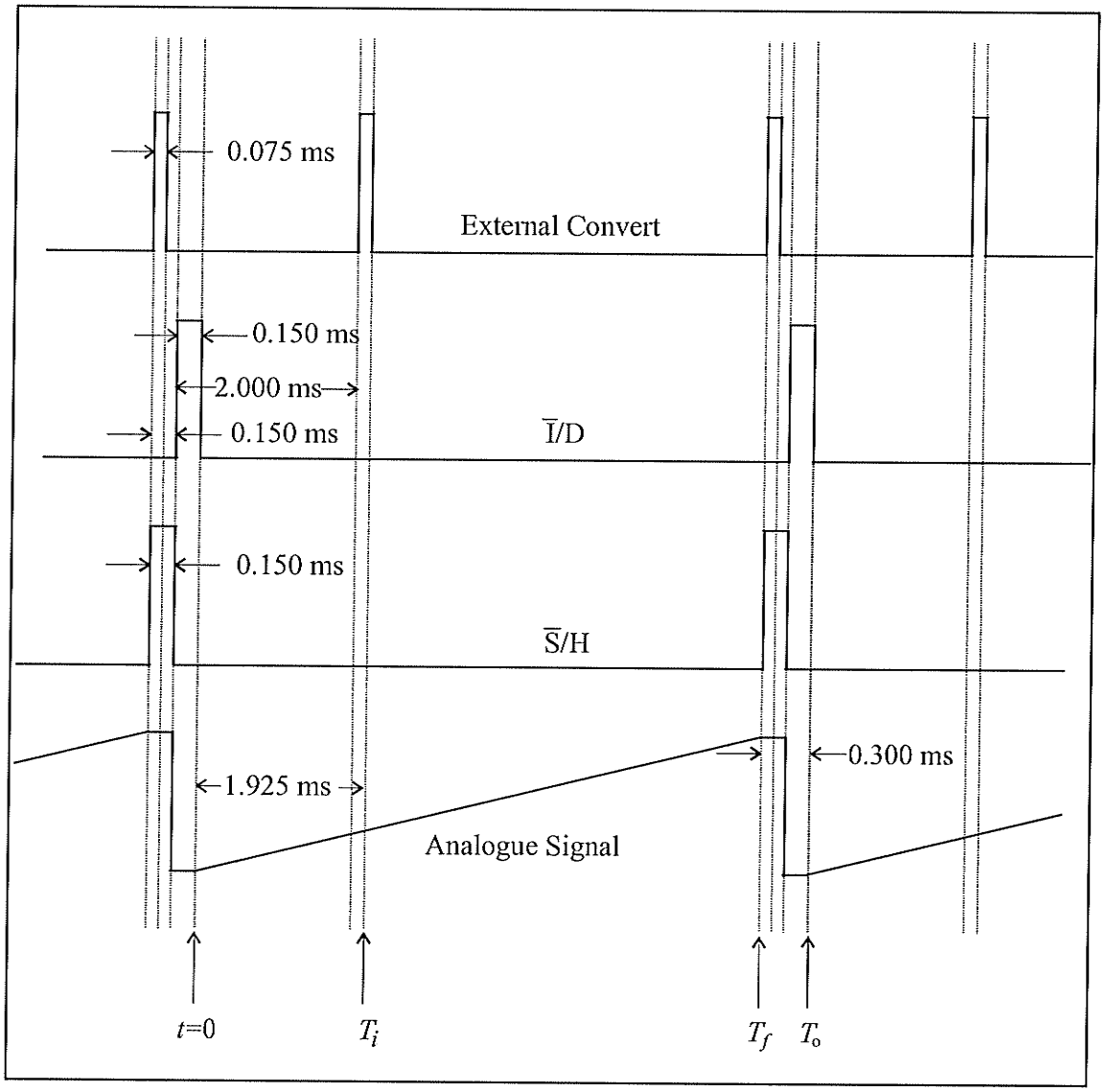

Figure 2.8 Data acquisition timing sequence for a single-channel detector. The point labeled T_i denotes the time when the initial voltage acquisition V_i takes place, and T_f indicates when V_f is read. The two voltages V_i and V_f are then subtracted to yield the voltage difference $\Delta V = V_f - V_i$.

ms, at time T_i an initial signal value V_i is acquired. This is triggered by the falling edge of the second pulse on the external convert control line. The current continues to be integrated, and after the desired time interval has elapsed, at time $T_f = T_o - 0.3$ ms, the sample-and-hold circuit is placed in hold mode, and a final signal value V_f is acquired.

Immediately following this, the capacitor is discharged[2], and the cycle is repeated again. Both V_i and V_f are read by the computer and subtracted to find $\Delta V = V_f - V_i$. The purpose of this subtraction is discussed below.

The sawtooth waveform constituting the bottom line in Figure 2.8 represents the output of the sample-and-hold chip, which is also the signal being sent to the A-to-D converter. Note that the smoothing effects of the gain-and-filter stage upon the saw-tooth wave have been neglected; these will be discussed in more detail in Chapter 3.

It is important to understand how the $\overline{\text{I}}$/D and $\overline{\text{S}}$/H signals dictate the shape of the analogue signal. While the $\overline{\text{I}}$/D signal is low, the capacitor is integrating charge and the output of the gain-and-filter stage increases. A high $\overline{\text{I}}$/D signal eliminates the charge buildup on the capacitor and the output of the integrator is zero. Note that the discharge time causes a narrow zero portion at the bottom of the saw-tooth wave. The effect of the $\overline{\text{S}}$/H signal can be understood by realizing that while the sample-and-hold chip is sampling, it is continually monitoring the output of the gain-and-filter stage. The charge on the capacitor in the integrator stage increases during sampling, resulting in a "ramping-up" of the analogue signal. When the $\overline{\text{S}}$/H signal is high, the output of the gain-and-filter stage is no longer being monitored, but rather, the last sampled value is being held, as evidenced by the narrow flat portion at the top of the saw-tooth.

2.3.2.2 Eight-Channel Data Acquisition Sequence

The shapes of the control signals for the eight-channel detector are shown in Figure 2.9. For the eight-channel detector, the first group of eight external convert pulses (one for each channel) is initiated by the trigger signal. A delay of 2.048 ms from the trigger signal is provided by two 4-bit counters cascaded from the lower 4-bits of the 20-bit counter. After the delay, a second group of eight external convert pulses is generated. The

[2] The bar over the "I" in $\overline{\text{I}}$/D indicates that the integrate-and-discharge circuit integrates when the control signal is low, and discharges the capacitor when the control signal is high.

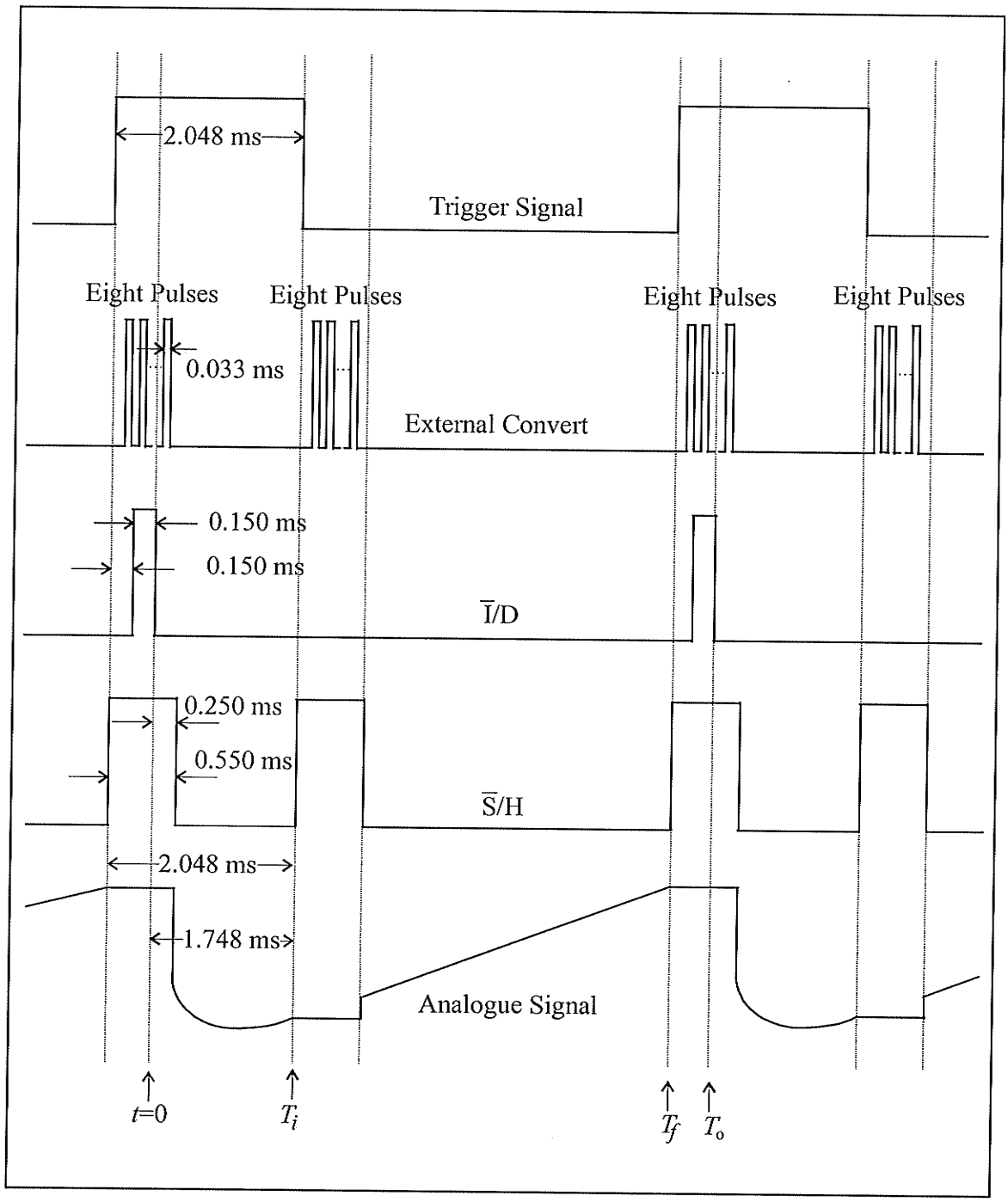

Figure 2.9 Data acquisition timing sequence for the eight-channel detector assembly. Only one of the eight analogue channels is shown. Of the eight pulses in the external convert signal, only the first, second and eighth pulses are shown.

$\overline{\text{I}}$/D signal remains unchanged from the single-channel detector. The $\overline{\text{S}}$/H signal has a width of 0.550 ms and is toggled twice during each integration cycle. The three MUX control lines (not shown in Figure 2.9) generate a 3 bit number between 0 and 7 that determines which channel is read during each external convert pulse.

The eight-channel data acquisition sequence shown in Figure 2.9 is very similar to the single-channel data acquisition sequence. At the beginning of an acquisition sequence (indicated by the vertical line labeled "t = 0") the integration capacitors have been discharged. The sample-and-hold circuits start sampling the output of the gain-and-filter stage 0.250 ms later. After a delay of 1.748 ms (determined by the filter bandwidth), at time T_i, initial voltages V_i for each channel are measured by the A-to-D converter. This is accomplished by holding the output of the gain-and-filter stage for a duration of 0.550 ms and sending eight external convert pulses to the A-to-D converter. The three binary control lines to the 8-to-1 MUX are pulsed synchronously with the external convert pulses. This allows the output of all channels in turn to be acquired by the A-to-D converter. It should be noted that the photocurrent continues being integrated during this time. The gain-and-filter stage output is again sampled until the end of the desired integration time at $T_f = T_o - 0.3\,\text{ms}$, where T_o is the sample period. At this time the output of the gain-and-filter stage is held and the integrating capacitors are discharged. The A-to-D converter measures the held output voltage V_f in the same manner as the initial voltage. The difference ΔV between the initial voltage reading and final voltage reading $\Delta V = V_f - V_i$ is then found for each channel.

The waveform constituting the bottom line in Figure 2.9 represents the output of the sample-and-hold chip, which is also the signal being sent to the A-to-D converter via the coaxial cable. Note that the smoothing effects of the gain-and-filter stage upon the saw-tooth wave have been taken into consideration here.

2.4 Choice of Scintillator

There are several scintillating materials currently available for γ-ray detection, some of which are listed in Table 2.3. Of note is the wide range of characteristic properties. The following properties are important for CT imaging applications (Derenzo and Moses, 1992; Grabmaier, 1984).

(i) *Optical spectral output:* The optical spectrum produced by the scintillator should be closely matched with the spectral response of the light detector. The spectral response of silicon photodiodes ranges from 320 nm to 1100 nm with a peak sensitivity occurring at 960 mm, as shown in Figure 2.10, so that a scintillator emitting optical photons with a long wavelength is desired.

(ii) *Chemical stability:* Susceptibility to contamination must be minimal to avoid the need for bulky, cumbersome packaging. Of the materials listed in Table 2.3, those which are hygroscopic can immediately be eliminated as possible candidates, as it would be highly impractical to hermetically seal the crystals in an array as required for the photodiode detector.

(iii) *γ-ray absorption efficiency:* The γ-ray absorption efficiency is defined as the probability that an incident photon will deposit all of its energy in the scintillating crystal, i.e., (energy absorbed)/(incident energy). The γ-ray absorption efficiency is largest in scintillators with a large density and a high atomic number. As the mean photon energy of the ^{192}Ir source (355 keV) is much larger than that of diagnostic x-ray tubes (60 keV), it is essential that the density of the scintillator be large enough that an appreciable amount of energy is deposited in the crystal.

(iv) *Photon output, or luminous efficiency (in photons/MeV):* The (optical) photon output characterizes the efficiency with which the scintillator converts the absorbed γ–ray energy into optical photons. This parameter determines the minimum detectable radiation. This characteristic can also be described in terms of the average scintillation efficiency (Holl et al., 1988), which is the percentage of incident absorbed γ–ray energy that is converted into optical photon energy. Considering, for example, the specifications listed for $CdWO_4$ in Table 2.3, 15,000 optical photons are produced for every MeV of γ-ray energy deposited in the crystal. Assuming all of

these optical photons have a wavelength λ equal to the peak wavelength of 470 nm, this corresponds to $(4.23 \times 10^{-19}$ J/photon)·(15,000 photons) = 0.0397 MeV of optical photons produced for every 1 MeV of γ–ray energy deposited in the crystal. The average scintillation efficiency is therefore about 3.97%.

It is worthwhile to consider the relative importance of γ–ray absorption efficiency versus luminous efficiency. Two factors must be taken into consideration, namely, the measurement uncertainty and the overall detection efficiency. The discrete nature of γ–ray photon interactions produces a relative measurement uncertainty that is inversely proportional to the square root of the number of γ–ray photons interacting. Similarly, the discrete nature of optical photon production within the scintillating crystal results in a relative measurement uncertainty that decreases inversely with the square root of the number of optical photons produced. However, a very large number of optical photons are produced for every 1 MeV of γ–ray energy deposited in the crystal. For instance, a single 355 keV photon produces 5325 optical photons if it deposits all of its energy in a $CdWO_4$ crystal. Even a material with a low luminous efficiency will produce a relatively large number of optical photons for each incoming γ–ray. Thus the noise associated with a low luminous efficiency will always be less than the noise associated with a low γ–ray absorption efficiency.

Although γ–ray absorption efficiency has a greater impact on noise than luminous efficiency, the effect of the latter on the overall detector efficiency can not be neglected. The overall detector efficiency (taking into account only the influence of the scintillating crystal) can be thought of as the product of the γ–ray absorption efficiency and the luminous efficiency. Clearly, a small luminous efficiency will result in a small overall efficiency. As patient radiation doses during imaging procedures must be kept to a minimum, a large overall efficiency is desired.

(v) *Susceptibility to radiation damage:* The characteristics of the scintillating crystal must not be affected by large doses of radiation. Each crystal in the fourth generation scanner receives about 0.2 Gy/scan. The transmission of $CdWO_4$ decreases by about 15% for doses on the order of 10^4 Gy (Bicron, 1990). This indicates that 50 000

scans could be performed before these crystals would suffer any substantial radiation damage.

(vi) *Afterglow:* This term describes the continued emission of optical photons after the exciting γ-ray radiation has been removed, i.e. phosphorescence (Farukhi, 1978). Large afterglow results in incorrect signals being recorded for the different projections because readings are influenced by the previous detector signals. The afterglow of CsI 100 ms after excitation is about an order of magnitude larger than that of $CdWO_4$ (Grabmeier, 1984).

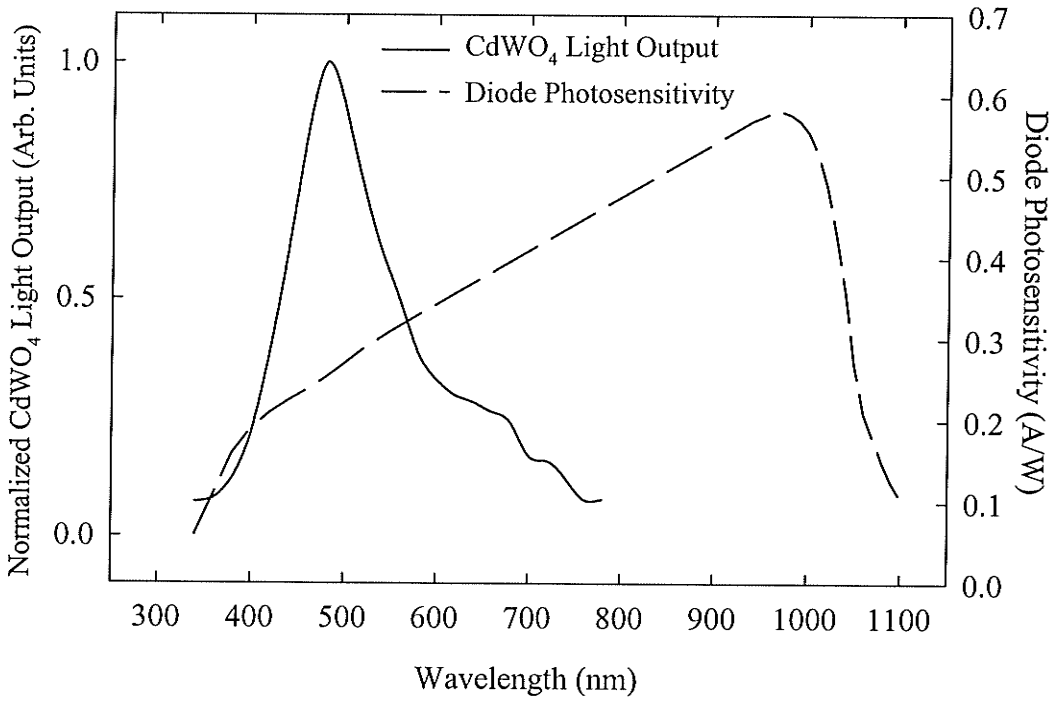

Figure 2.10 Plot of the normalized $CdWO_4$ light output (solid line) (Kinloch et al., 1994) and the photodiode photosensitivity (dashed line) in A/W (Hamamatsu, 1994, 1995) as a function of wavelength.

Of the scintillators listed in Table 2.3, four suitable candidates for the CT scanner are BGO, $CdWO_4$, LSO and $ZnWO_4$. CsI can not be used because of its large afterglow and low attenuation coefficient. The afterglow characteristics of LSO and $ZnWO_4$ are not known. The other characteristics of the four scintillators are actually quite similar. Their

Table 2.3 Properties of γ-ray detecting scintillators (Derenzo and Moses, 1992; Farukhi, 1978)

Scintillator	Density (g/cm^3)	μ (cm^{-1})*	Hygro-scopic	λ_{peak} (nm)	ξ (Photons/ MeV)	Afterglow (% at 3 ms)	Shortcomings
$Bi_4Ge_3O_{12}$ (BGO)	7.13	0.90	no	480 480	700 7500	< 0.005	low light output
CaF_2(Eu)	3.19	0.27	no	435	19000	≤0.3	low absorption efficiency
$CaWO_4$	6.1	0.67	no	430	6000	1 – 5	low light output
$CdWO_4$	7.90	0.83	no	470	15000	≤ 0.005	
CsI(Na)	4.51	0.41	yes	420	39000		hygroscopic
CsI(Tl)	4.51	0.41	no	540	64400	0.5 – 5	long afterglow
Gd_2SiO_5(Ce) (GSO)	6.71	0.67	no	440	10000		
LiI(Eu)	4.08	0.37	very	470	11000		hygroscopic, low absorption efficiency
Lu_2SiO_5(Ce) (LSO)	7.4	0.82	no	420	30000		
NaI(Tl)	3.67	0.33	yes	415	3800	0.5 – 5	hygroscopic, low absorption efficiency
$ZnWO_4$	7.87	0.84	no	480	10000		

*value for 511 keV photons

attenuation coefficients are nearly equal, as are their peak emission wavelengths (although LSO is somewhat inferior to the others in this area). LSO has the highest luminous efficiency, followed by $CdWO_4$, $ZnWO_4$ and BGO. It would appear that LSO is the optimal scintillator. However, it is not readily available (Derenzo and Moses, 1992), eliminating the possibility that it could be used in the proposed scanner. Considering the other three options, $CdWO_4$ has the largest luminous efficiency, making it the scintillator of choice for this project.

2.5 Crystal Array Design

Several parameters must be taken into consideration when designing a crystal array. These include the crystal dimensions and crystal coating material. The crystal thickness and length are variable, whereas the crystal width is fixed by the spacing of the active elements in the photodiode array. The crystal size must be chosen to compromise between absorption efficiency and cost, which is approximately proportional to the crystal volume. The crystal coating material encases all sides of each crystal except for the face in contact with the photodiode array. Its purpose is to prevent optical photons from leaving a crystal and reaching the adjacent crystals. The ideal material is adequately opaque to prevent light produced in one crystal from reaching the adjacent crystal, but is also reflective, so that the maximum number of optical photons reach the active area of the photodiode.

2.5.1 Array Mask

The active areas of the photodiodes in the array are represented by the black rectangles in Figures 2.5a and 2.5b. As all of the crystals being studied are larger than the photodiode elements, light impinging on the outer black region of the photodiode array, i.e., beyond the silver region, will not be detected. In an attempt to reflect this light back into the crystal, where it may fall on the active detecting region, a strip of reflective material, referred to as an array mask, was placed on either side of the active detecting region. Two

reflectors, Bare Metal Foil[3] (BMF) and 3M 850 tape were considered. Also examined was the effect of the separation of the strips of reflective material, which is referred to as "gap width" (Figure 2.11a) in the subsequent discussion.

2.5.1.1 Method

To evaluate the effect of the reflective array mask, strips of BMF were fixed to the photodiode array on both sides of the active detecting elements with various gap widths. The gap width was measured using a comparator (magnifier with a reticule). A 1.0 cm x 0.8 cm x 0.275 cm (thickness x length x width) crystal with ground faces was wrapped in a 10 cm long piece of Teflon tape such that only the face in contact with the photodiode array was exposed. The detector was placed 68 cm from an uncollimated 4.0576 Ci ^{192}Ir source and the crystal position was adjusted to ensure an optimal signal. The detector output was sampled using a 0.1 s sampling interval, corrected for dark current, and the average of 100 data points calculated. These measurements were repeated for the 850 tape. All of the measurements performed in §2.5 use a coupling grease (Dow Corning Q2-3067) to achieve optical coupling between the crystals and the photodiode array.

2.5.1.2 Results

The detector output is plotted in Figure 2.11b as a function of gap width for the two reflective materials. The vertical lines indicate the width of the photodiode elements, the width of the photodiode array silver region, and the length of the crystal. A gap width of 8 mm or larger is equivalent to using no reflective tape. For the BMF, the detector output increases slightly with increasing gap width until the BMF is placed beyond the silver region. This is in agreement with the visual assessment that the silver region is more reflective than the BMF. The trend is similar for the 850 tape, but the data are noisier. The decrease in detector output for gap widths greater than 4.2 mm is clearly because some of the optical photons are being absorbed by the black region of the photodiode array.

---

[3] Bare Metal Foil is a reflective foil with an adhesive backing, designed to provide a shiny finish on plastic model parts.

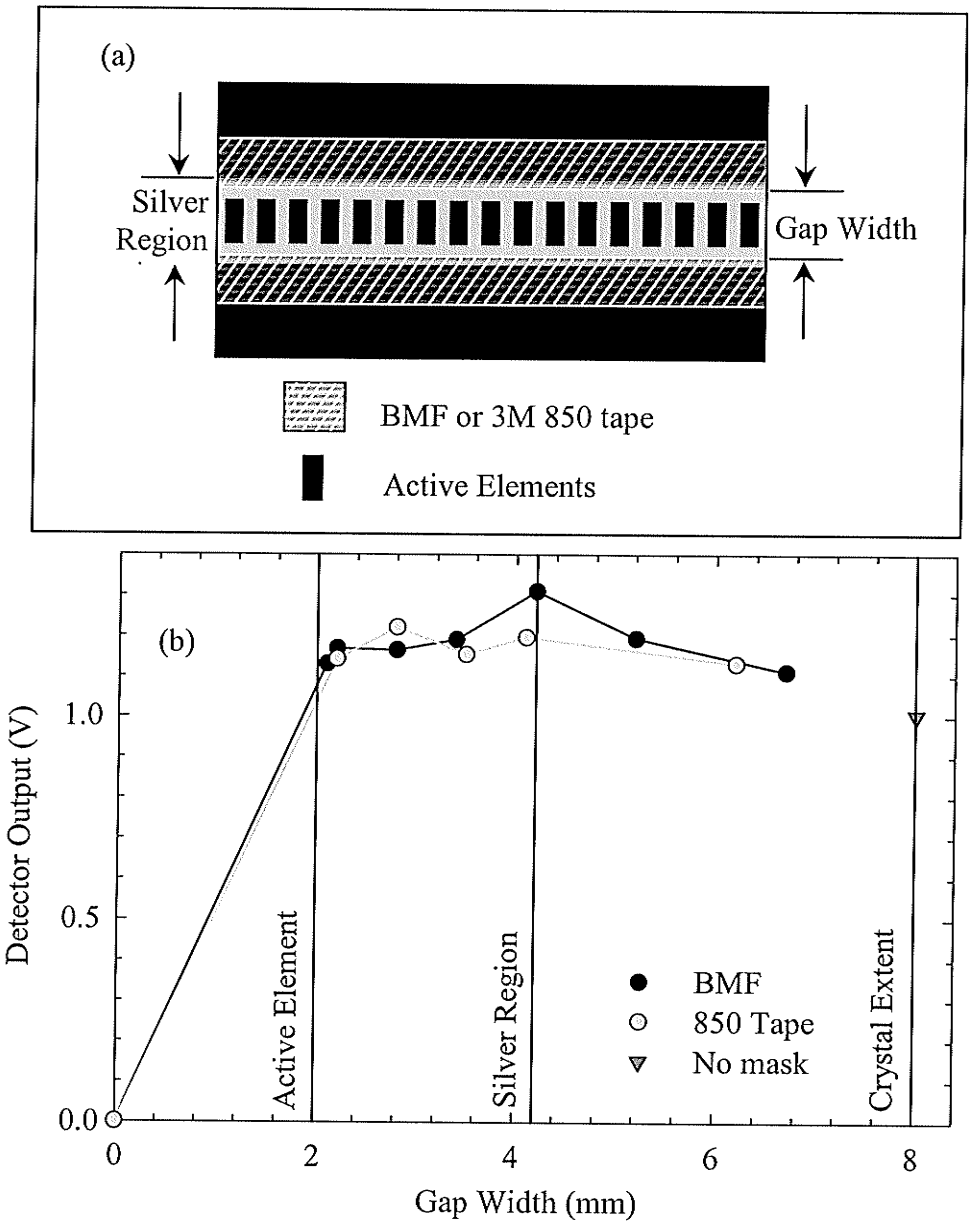

Figure 2.11 (a) Diagram showing the placement of the reflective material (drawn translucent to show the extent of the silver region) on the photodiode array. (b) Plot of the detector output as a function of gap width.

Figure 2.11b demonstrates that the application of a reflector increases the detector output by approximately 30%. Although the data are noisy, BMF seems to provide the largest detector output voltage. This could be because it is thinner (thickness = 0.0020 cm) than the 850 tape (thickness = 0.0051 cm), thus allowing for better contact between the scintillating crystal and the photodiode array.

2.5.2 Crystal Thickness

Crystals of dimensions (0.8 cm x 0.275 cm x 0.4, 0.8, 1.0, 1.2, 1.6 and 2.0 cm – length x width x thickness) were studied. These could be placed with the 0.8 cm x 0.275 cm surface in contact with the photodiode array to provide crystals of constant length with various thicknesses, as described in this section, or could be turned on their side to provide crystals of constant thickness and variable length, as discussed in §2.5.3.

2.5.2.1 Method

The detector output is dependent upon the thickness of the $CdWO_4$ crystals because shorter crystals will attenuate fewer γ-rays, resulting in less energy being absorbed in the crystal. However, increasing the crystal thickness beyond a certain limit will also result in a decrease in detector output, as more of the optical photons produced near the front of the crystal will be absorbed in the crystal and not reach the photodiode. The detector output was measured for crystal of thickness 0.4 cm, 0.8 cm, 1.0 cm, 1.2 cm, 1.6 cm and 2.0 cm. Two crystals of each thickness were used. The length and width of all crystals were 0.8 cm and 0.275 cm respectively.

The crystals were wrapped in Teflon tape on all sides (except for the side in contact with the photodiode) to provide a non-permanent reflective crystal coating material. Dow Corning Q2-3067 optical couplant was used to provide optical coupling between the crystals and the photodiodes. The detector was placed at a distance of 68 cm from a 4.6258 Ci ^{192}Ir source and 100 output voltage readings were collected for each of the two crystals. Crystal positioning was adjusted to ensure a maximum signal. All measurements were corrected for dark current.

2.5.2.2 Results

The detector output is plotted as a function of crystal thickness in Figure 2.12. The average output for the two crystals is plotted as a solid line. The detector response increases with increasing scintillator thickness up to a crystal thickness of 1.2 cm. The decrease in detector output beyond a thickness of 1.6 cm is likely due to light absorption in the crystal coating and self-absorption of the optical photons in the crystal (Mosleh-

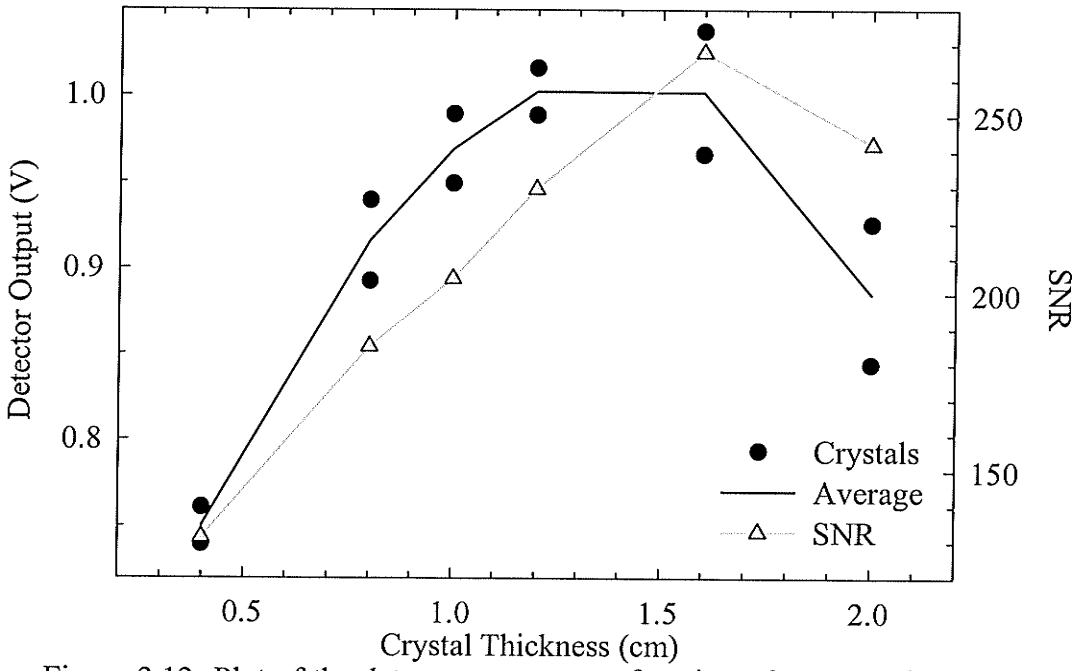

Figure 2.12 Plot of the detector output as a function of crystal thickness. The detector output was measured for two crystals of each thickness. The maximum output for each crystal is shown, along with the average for the two crystals. The SNR was found by dividing the detector output by the standard deviation in the detector output.

Shirazi et al., 1998; Vittori et al., 2000). The optimal crystal thickness in terms of detector output is thus 1.2 cm. The 3% increase in detector output, and 12% increase in signal-to-noise ratio (SNR) found when increasing the crystal size from 1.0 to 1.2 cm is accompanied by an approximate 20% increase in crystal cost. It was therefore decided to use 1.0 cm thick crystals in the final scanner.

2.5.3 Crystal Length

2.5.3.1 Method

To test the effect of crystal length, the 0.4 cm, 0.8 cm, 1.0 cm and 1.2 cm thick crystals used in the previous experiment were turned on their side to provide a constant thickness, i.e., 0.8 cm, and a variable length. The crystals were wrapped in Teflon tape to provide a non-permanent crystal coating material as previously discussed. The detector was placed at a distance of 68 cm from a 4.5831 Ci ^{192}Ir source and 100 output voltage readings collected. Once again, measurements were made on two crystals of each length. Crystal

positioning was adjusted to ensure maximum signal. The average reading for each crystal was found and corrected for dark current. These measurements were repeated after placing a strip of BMF on either side of the active elements with a gap width of 3.5 mm.

2.5.3.2 Results

The individual and average crystal results are plotted in Figure 2.13. As can be seen, there is an increase in detector output between the 0.4 cm and the 0.8 cm long crystals for the measurements made in the absence of an array mask. Increasing the crystal length beyond 0.8 cm offers no increase in detector output because photons impinging on the black portion of the photodiode array are not detected. For the measurements made with the array mask in place, the detector output increases with increasing crystal length. The most dramatic increase in signal however occurs when increasing the crystal length from 0.4 cm to 0.8 cm. When using an array mask, photons impinging outside of the active detecting region of the photodiode array are reflected back into the crystal, whereupon they may be detected. This is the reason for the increased detector output seen in Figure 2.13. Although the 1.2 cm long crystals provide an 8% increase in detector output and 10% increase in SNR over the 0.8 cm crystals, the increase in crystal size is accompanied by an approximate 50% increase in crystal cost. It was therefore decided to use the 0.8 cm crystals in the final scanner.

2.5.4 Crystal Coatings

An ideal crystal coating must be both opaque and reflective. The measurements described below examine a number of different crystal coating and crystal surface preparations in order to find the optimal material to be used in the scanner. These measurements also provide an opportunity to assess the variability in crystal sensitivity due to manufacturing among crystals of similar dimensions. To this end, a series of measurements was carried out using three different crystals. Measurements were also performed to assess the variation in detector output for crystals produced by different manufacturers. A final set of measurements examines two of the crystal coating materials more closely by measuring their optical density as a function of wavelength. This measurement aids in a

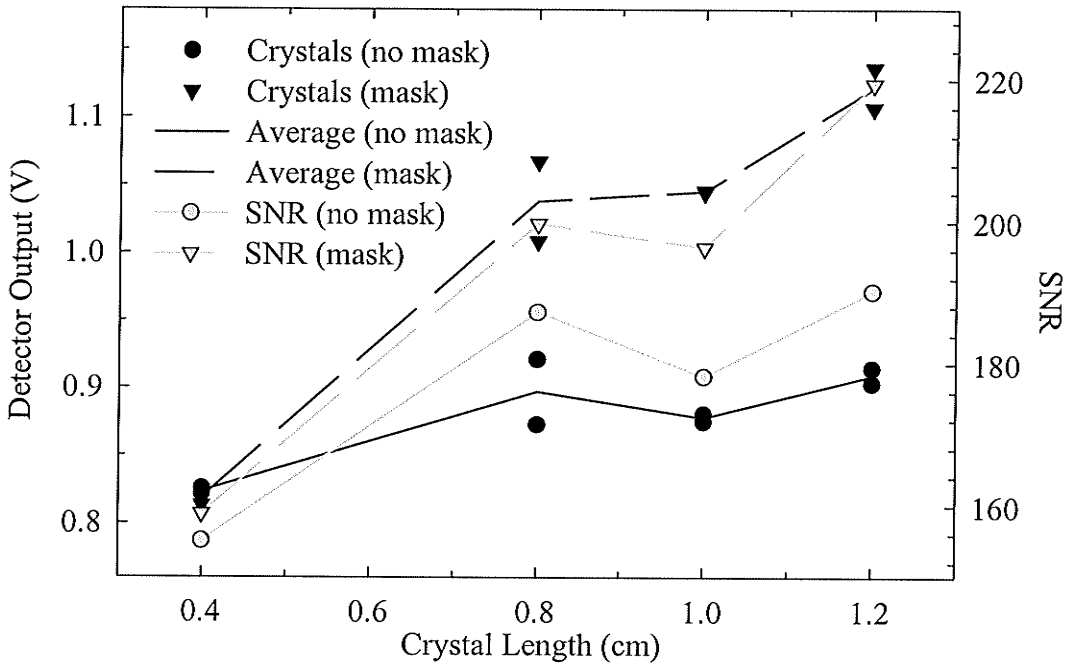

Figure 2.13 Plot of the detector output as a function of crystal length with and without a BMF mask in place. The detector output was measured for two crystals of each length. The output for each crystal is shown, along with the average for the two crystals. The SNR was found by dividing the detector output by the standard deviation in the detector output.

selecting crystal coating material that minimizes the cross-talk between adjacent channels and improves the light collection efficiency from the crystals. Once again, crystal position was adjusted until a maximum signal was obtained, and all readings were corrected for dark current

2.5.4.1 Intercrystal Variability

Method

The first set of measurements examines the intercrystal variability using three crystals of the same size (1.0 cm x 0.8 cm x 0.275 cm; thickness x length x width). All permutations of crystal and coating material were tested to separate the effects of coating material and intracrystal variations in sensitivity. A 9.0814 Ci ^{192}Ir source was placed about 72.5 cm from the detector assembly and a total of 250 detector output voltage readings collected and averaged. Measurements were repeated six times with each crystal/coating combination (the crystals were repositioned between trials). Five trials were also carried

out in the absence of a crystal to measure the signal produced by γ-rays interacting directly with the photodiode itself.

Results

The average detector output voltage readings for the various crystals and coating materials are plotted in Figure 2.14. It can be seen that the inter-crystal and inter-trial variations are much smaller than the effects of the coating material. The averages of the six trials are listed in Table 2.4. The reproducibility of one crystal and one coating material is characterized by the standard deviation in the "Average Reading" column. The scatter in the points for a particular crystal is primarily due to crystal placement variations on the photodiode array. As can be seen from the "Combined Average" values, the intercrystal variability is much smaller than the differences in detector output found for the various crystal coatings. Note that the measurements made with no crystal result in a non-negligible detector output, indicating that direct interaction of the γ-rays with the photodiode array contributes to the detector output. Note that irradiation of the photodiode array with large doses using a therapeutic radiation beam found no change in array performance, indicating that the photodiode array is not readily damaged by radiation (Private Communication, S. Rathee). In practice, the photodiode array will receive only a small amount of radiation, as most of the γ-rays are absorbed by the scintillating crystals.

2.5.4.2 Permanent Coating Materials

Besides assessing intercrystal variability, the results shown in Figure 2.14 and listed in Table 2.4 examine Teflon tape and BMF as possible crystal coating materials. Teflon tape is a well-established scintillator coating. The BMF was examined in an attempt to improve upon Teflon tape. This material is highly reflective on one side, but is somewhat duller on the adhesive side. The shiny side is unfortunately on the outside of the crystal. The electrical tape was not examined as a possible crystal coating, but rather was used to assess the amount of light reaching the photodiode when using a very inadequate reflective coating.

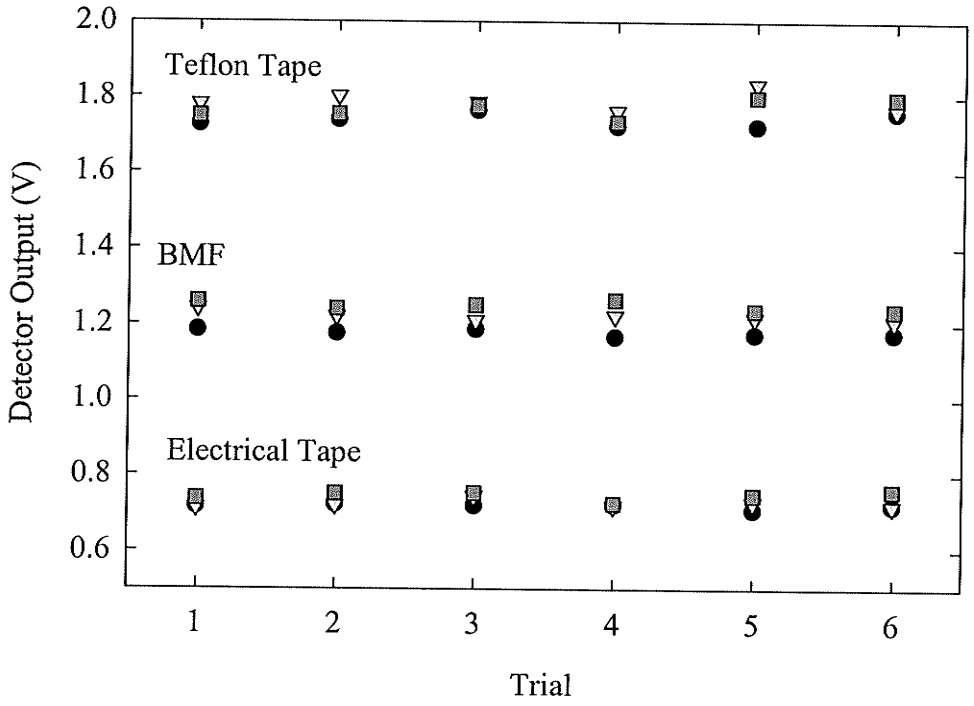

Figure 2.14 Plot of the detector output for the crystal coatings electrical tape, BMF and Teflon tape. The circles represent measurements done with Crystal 1, the triangles measurements done with Crystal 2 and the squares measurements done with Crystal 3.

Table 2.4 Detector output for various crystal coatings

Crystal Covering	Crystal Number	Average Reading (V)	Combined Average (V)
Electrical Tape	1	0.717 ± 0.006	
	2	0.72 ± 0.01	0.73 ± 0.01
	3	0.74 ± 0.01	
Teflon Tape	1	1.74 ± 0.02	
	2	1.78 ± 0.02	1.76 ± 0.02
	3	1.76 ± 0.02	
Metal Foil	1	1.179 ± 0.006	
	2	1.22 ± 0.01	1.21 ± 0.03
	3	1.24 ± 0.01	
No Crystal	-	0.278 ± 0.005	0.278 ± 0.005

The detector output is largest with Teflon tape, emphasizing the importance of a reflective crystal coating. Although Teflon tape yields superior results, it would be impractical to wrap the crystals in Teflon tape and then bundle them into arrays. (The Teflon tape is somewhat bulky, making a precision 0.4 mm intercrystal spacing difficult to achieve.) Moreover, it was found that the detector output decreased as a function of time when using crystals wrapped in Teflon tape. This is most likely because the Teflon tape became translucent near the base of the crystal as the Teflon tape "absorbed" the optical coupling gel.

To this end, a number of alternative coating materials were examined. The first coating material investigated involved mixing a two-part clear epoxy resin (Loctite Durabond 530CL) that cures within about 24 hours with Al_2O_3 (Aldrich, 26,549-7), a fine (diameter < 10 μm) white powder. Different Al_2O_3 concentrations were produced by varying the % by weight of Al_2O_3. Increasing the Al_2O_3 concentration resulted in an increasingly opaque paste that solidified into a rigid material encasing the crystal. The Al_2O_3 concentration was limited by the requirement that the mixture remain adequately viscous to flow between adjacent crystals in a crystal array. The second coating material investigated was a white gelcoat (Ashland Chemical Type 1 polyester gelcoat). This polyester resin epoxy is used as the outer coat for Fiberglas boats, and cures within 3 to 4 hours using a catalyst. Both of these coating materials are inexpensive, easy to prepare, and are adequately viscous and durable for manufacturing crystal arrays. Characteristics such reflectivity and opacity will be used to determine the most appropriate coating material.

Measurements were performed on crystals from the two different manufacturers Bicron (Bicron, Saint-Gobain/Norton Industrial Ceramics Corporation, 6801 Cochran Road, Solon, Ohio 44139) and Rexon Components, Inc. (24500 Highpoint Road, Beachwood, Ohio, 44122).

The detector outputs for the various scintillator configurations are plotted in Figure 2.15. As can be seen, a Bicron crystal wrapped in Teflon tape gives the largest signal. The decrease in signal from Crystal Configuration (CC) 1 to CC 4 could be due to the fact that CC 1 has cleaved sides, whereas CC 4 has ground sides. Correspondence

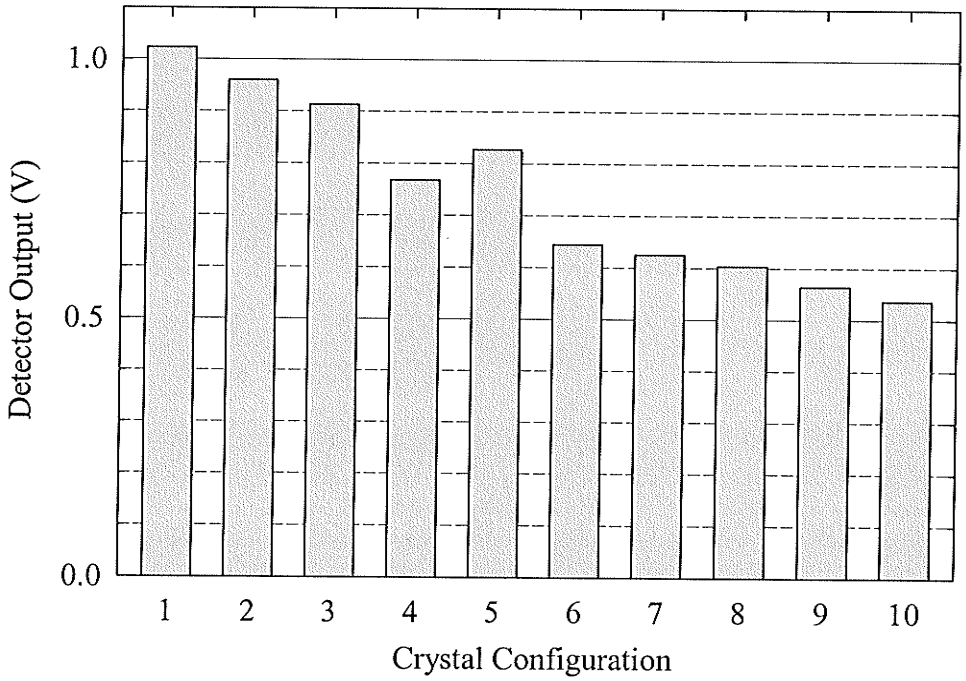

Figure 2.15 Plot of the detector output for various crystal coating materials and configurations.

Coating	Configuration
10 cm Teflon tape	1. single Bicron crystal with cleaved sides, source and detector side faces ground 2. single Bicron crystal with cleaved sides, source side face ground and detector side face polished 3. single Bicron crystal with cleaved sides, source side face polished and detector side face ground 4. single Rexon crystal with all faces ground
Gelcoat	5. single Bicron crystal with cleaved sides, source side face ground and detector side face polished 6. single Rexon crystal with all faces ground
Al_2O_3 Epoxy Mixture	7. single Bicron crystal with cleaved sides, source side and detector side face ground 8. eight element Bicron crystal array (construction described in §2.5.5.1) using crystals with cleaved sides, source side face ground and detector side face polished
BMF	9. single Bicron crystal with cleaved sides, source side face ground and detector side face polished
3M 850 Tape	10. single Rexon crystal, all faces ground

with Rexon indicated a typical 10% inter-batch variability, which could also account in part for the reduced output of the Rexon crystals. Comparison of CC 4 and CC 6 indicates that gelcoat is not as reflective a crystal coating material as Teflon tape. However, for the reasons discussed above, Teflon tape is not a practical crystal coating material for this application. CC 7 and CC 8 suggest that Al_2O_3 is inferior to gelcoat as a crystal coating material, even though the Bicron, as opposed to the Rexon crystals were used. Finally, BMF and 3M 850 tape are not suitable coating materials. Although both are opaque, an important consideration in minimizing optical cross-talk, they yield the lowest detector outputs. Thus, gelcoat was chosen as the crystal coating material. It is not clear whether the difference in output between the Rexon and Bicron crystals is due to a difference in manufacturing techniques, or is a result of normal batch-to-batch variations. For the final scanner, Rexon supplied the crystals because they were less expensive and easier to acquire.

2.5.4.3 Spacer Optical Density

To further investigate the properties of the different Al_2O_3 Loctite combinations and the gelcoat, their optical densities were measured as a function of wavelength. This allows comparison of the spectral response of the various materials, taking into consideration the output of $CdWO_4$ as shown in Figure 2.10. For instance, $CdWO_4$ emits light between 400 and 700 nm. Opacity in this wavelength range would therefore eliminate optical cross-talk.

Method

The optical density of the various crystal coating materials was measured using a spectrophotometer (Varian CARY1 UV-Visible Spectrophotometer). A mould consisting of two acrylic plates, one with a 0.4 mm slot (equal to the crystal spacing) machined into it, was used to control the sample height. After placing a small amount of coating material on the plate with the slot, the second plate was aligned on top and the two plates screwed together, forcing the crystal coating material to harden into a 0.4 mm thick slab.

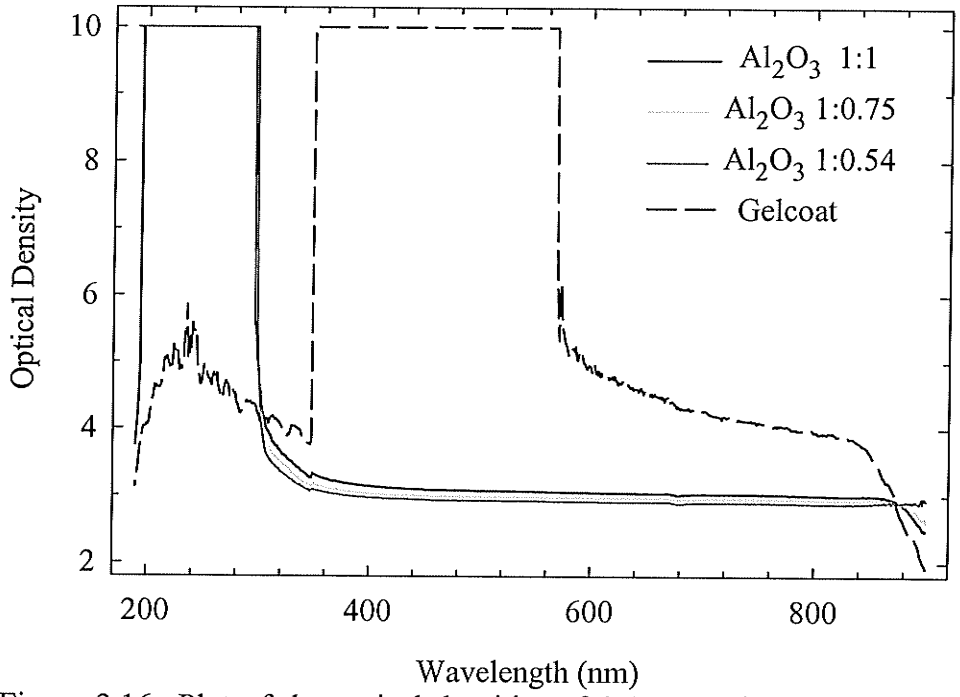

Figure 2.16 Plot of the optical densities of 0.4 mm thick samples as a function of wavelength.

Three samples containing Al_2O_3 were produced, with ratios of 1:0.54, 1:0.75 and 1:1 of epoxy to Al_2O_3 by weight. The 1:0.54 sample was used to construct the crystal array assessed in Figure 2.15 (CC 8). The optical density of white gelcoat was also measured.

Results

The spectrophotometer output as a function of wavelength is shown in Figure 2.16. The sharp discontinuity in the gelcoat optical density at about 350 nm is not a characteristic of the gelcoat, but is due to a calibration error in the spectrophotometer. This wavelength corresponds to a change in the light source and detector combination used by the spectrophotometer, i.e., the change to a visible light source and detector from an ultra-violet light source and detector. Note that this does not pose a serious problem, as all materials with an optical density above about 4.0 can be considered to be opaque. Recalling Figure 2.10, the $CdWO_4$ light output falls primarily between 400 nm and 700 nm, which is effectively blocked by the gelcoat. This reinforces the decision made in

§2.5.4.2 to use gelcoat as the crystal coating material. In addition, it shows that 0.4 mm of gelcoat should eliminate optical cross-talk between the crystals.

2.5.5 Array Preparation

In the fourth generation scanner the crystals must be accurately placed on the photodiode array, with an inter-crystal spacing equal to the spacing between the photodiode array elements. As a large number (96) of photodiode arrays will be used, the technique developed must be practical, as well as accurate. Coating single crystals and individually placing them on the photodiode array would be very inefficient, and would result in large positioning errors. The solution was to combine a group of eight crystals into a single unit, held together at the correct spacing with a crystal coating material, and then mount this unit onto the photodiode array.

Evaluation of the eight-channel detector board as described in subsequent chapters was performed using two different crystal arrays: 1) an array coated in epoxy resin and Al_2O_3 powder; and, 2) an array coated in white gelcoat. The construction of both arrays is described in the following sections.

2.5.5.1 Al_2O_3 Coated Array

The Al_2O_3 coated array was constructed by covering eight Bicron $CdWO_4$ crystals (sides cleaved, faces ground) with a mixture of Al_2O_3 powder and clear epoxy resin. The Al_2O_3 powder was added to the clear epoxy to prevent the light generated in one crystal from reaching the neighboring crystal. The Al_2O_3 also provides a reflective coating for the crystals, which allows more light to reach the photodiodes, as discussed previously.

Before applying the epoxy, the crystals were placed in a precision metal spacer, and then in a polyethylene mould, as shown in Figure 2.17. A 1:0.54 mixture of epoxy to Al_2O_3 by weight was placed into the mould and allowed to harden around the crystals. The crystals, now set in place with respect to one another, were covered in the epoxy and Al_2O_3 mixture. Special care was taken to ensure that the mixture flowed between the crystals. This procedure was repeated again to ensure that the crystals were completely covered. Excess epoxy was sanded down and the faces of the crystals polished using jeweler's rouge (Enkay) and a polishing tool (Dremel).

The crystal array was mounted on the photodiode array using clear GE Silicone. Optical coupling between the crystals and the photodiode array was achieved using an optical couplant (Dow Corning Q2-3067).

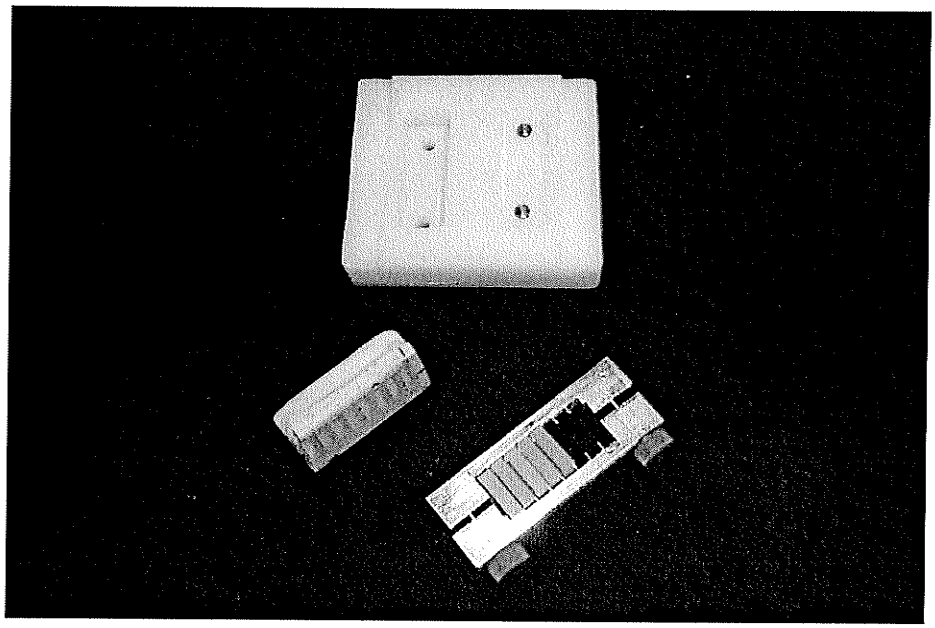

Figure 2.17 Photograph of the precision metal spacer, polyethylene mould and completed crystal array.

2.5.5.2 Gelcoat Coated Array

The gelcoat coated array was manufactured using a technique similar to that described in §2.5.5.1. Three strips of tape (3M 850) were fixed to the polyethylene slab as shown in Figure 2.18a to protect the slab from the gelcoat. A strip of double-sided tape was placed on top of the 3M 850 tape, followed by the precision metal spacer, as shown in Figure 2.18b. Eight Rexon crystals (all faces ground) were placed in the precision metal spacer, and the latter gently removed so that the crystals remained fixed to the double sided tape. Polyethylene moulds were then placed around the crystals, using the positioning pegs on the base, as can be seen in Figure 2.18c. Note that the base was made of high-density polyethylene, which chemically reacts with gelcoat, whereas the moulds were made of low-density polyethylene, which is unaffected by the gelcoat. A mould release was used

to aid removal of the arrays. Finally, gelcoat mixed with hardener was injected into the mould using a 30-gauge needle to fill the spaces between the crystals, and a 23-gauge needle to fill the space surrounding the crystals. The entire assembly, including the base-plate and the moulds was then placed inside a 50° C oven to speed the curing process. The gelcoat hardened after several hours, allowing the crystal arrays to be removed from the moulds. Any remaining gaps between the crystals were filled with gelcoat using a 30-gauge needle.

Measurements using the crystal arrays described in §2.5.5.1 and §2.5.5.2 are carried out in Chapter 4.

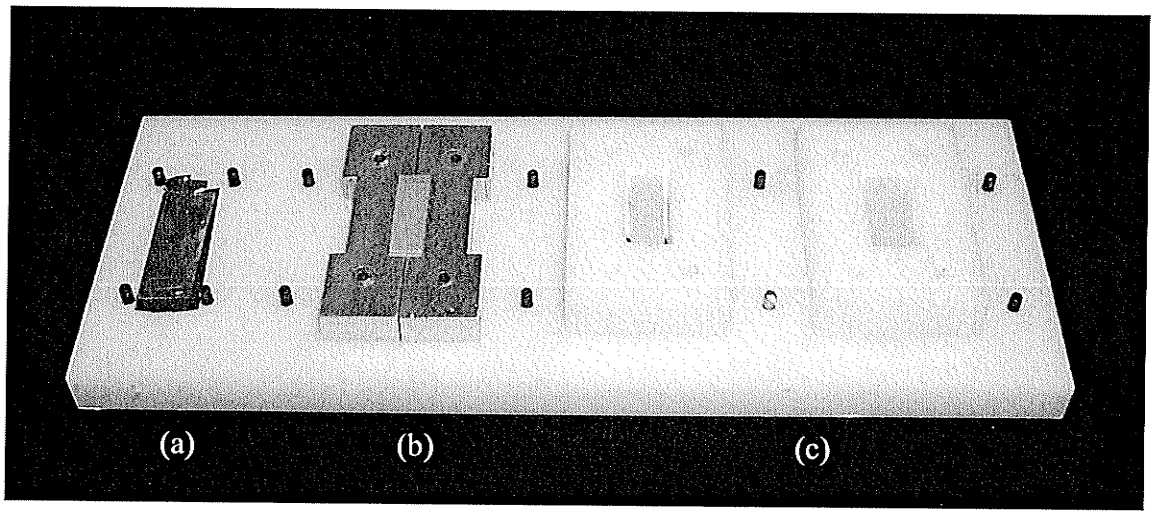

Figure 2.18 Photograph of the assembly used to construct the gelcoat arrays showing (a) the 3M 850 tape covered by the double sided tape, (b) the precision metal spacer with the crystals in place, and (c) the moulds placed around the crystals using the positioning pegs.

Chapter 3

System Characterization: Single-Channel Measurements

Any γ-ray detector used in imaging must have a signal-to-noise ratio that is limited by fundamental photon statistics and not by the electronic noise of the detector. In addition, the detector's response to radiation must be understood so that any non-linearities can be corrected. Lastly, a thorough understanding of the detector allows for optimization of the scanner design. This chapter describes a series of measurements carried out using a single-channel detector assembly. A theoretical estimate of the electronic noise was found by combining the noise produced by the various electronic components constituting the detector. Noise characteristics of the detector were measured both in the presence and absence of γ-radiation. Measurements were also performed to determine the detector's response to light and integration time. For these measurements, an external light source, namely a light-emitting diode, rather than the output from a scintillating crystal, was used to illuminate the photodiode array. This light source provided a controlled and known illumination to characterize the photodiode response to light. The detector output voltage as a function of γ-ray intensity was also measured using an ^{192}Ir brachytherapy source, thereby quantifying the detection efficiency of the scintillating crystal/photodiode combination. The temperature dependence of the detector was measured in the absence of optical photons or γ-rays. Finally, images collected using the single-channel detector in a first generation geometry are presented.

3.1 Noise Analysis

The smallest light intensity that can be detected by the detector assembly depends on the noise in the photodiode and the associated electronic circuitry. There are several sources of noise, which contribute to the electronic noise in the detected signal. These include:

(i) the current noise in the photodiode and the integrating operational amplifier;

(ii) the input noise voltage of the operational amplifiers;

(iii) cycle-to-cycle variation of the charge injected onto the integration capacitor from the digital control inputs;

(iv) cycle-to-cycle variation of retained charge after capacitor discharge;

(v) shot noise due to leakage current when the discharge switch is in its open state; and,

(vi) A-to-D board noise.

A detailed analysis[1] of the various noise sources is provided in the following sections.

3.1.1 Current Noise Sources

3.1.1.1 Photodiode

The current noise from a photodiode operating in photovoltaic mode is determined by its shunt resistance R_{sh}, which is defined as the ratio of the voltage to the current near 0 V. As the V-I curve (Figure 2.7d) is approximately linear near 0 V, the shunt resistance is given by the reciprocal of the slope near 0 V. More specifically, the manufacturers of the photodiode array (Hamamatsu) define $R_{sh} = 10\,\text{mV}/i_{dark}$, where i_{dark} is the dark current at 10 mV. The shunt resistance produces a thermal (Johnson) noise current with density i_j that is frequency independent (i.e. white) from DC to approximately the photodiode cutoff frequency, and is given by the Schottkey formula (EG&G Catalogue, 1992; Simpson, 1987)

$$i_j = \sqrt{\frac{4\text{k}T}{R_{sh}}}\,\text{A}/\sqrt{\text{Hz}} \qquad (3.1)$$

where k is Boltzmann's constant, and T is the absolute temperature of the photodiode.

---

[1] Based on an analysis developed by S. Rathee.

In the presence of light, the shot noise current density i_{sp} from the photocurrent i_{photo} is given by

$$i_{sp} = \sqrt{2qi_{photo}} \ \text{A}/\sqrt{\text{Hz}} \tag{3.2}$$

where q is the electron charge. The total photodiode noise i_n is found by adding (3.1) and (3.2) in quadrature.

Manufacturers specify the noise in a photodiode in terms of the noise equivalent power (NEP), defined as the minimum light required to produce a photocurrent i_{photo} equal to the photodiode noise current i_n (EG&G Catalogue, 1992). Alternatively, the NEP may be described as the light power necessary to produce a signal-to-noise ratio (SNR) of 1. Mathematically, this is defined as

$$\text{NEP}(\text{W}/\sqrt{\text{Hz}}) = \frac{i_n \ (\text{A}/\sqrt{\text{Hz}})}{S_p \ (\text{A/W})} \tag{3.3}$$

where the photosensitivity S_p is defined as the photocurrent per unit incident light power (in Watts). The photosensitivity at $\lambda =$ 540 nm is $S_{p\,\lambda=540\,\text{nm}} = 0.31$ A/W (Hamamatsu, 1994). Using the data in Table 3.1, and the expression $i_n = S_p \cdot \text{NEP}$ the photodiode noise current density can be calculated to be $i_n = (0.31\,\text{A/W}) \cdot (9.3\times10^{-15}\,\text{W}/\sqrt{\text{Hz}}) = 2.883 \times 10^{-15}\,\text{A}/\sqrt{\text{Hz}}$.

Table 3.1 Noise Sources (Hamamatsu, 1994; Texas Instruments, 1996; Temic, 1997)

Noise Source	Magnitude
S5668-02 Photodiode NEP (λ_p = 540 nm)	9.3×10^{-15} W/$\sqrt{\text{Hz}}$ at V_R = 10 mV
TL074C Input Noise Current, i_{TL704C}	0.01 pA/$\sqrt{\text{Hz}}$ at 1 kHz
TL074C Input Noise Voltage	18 nV/$\sqrt{\text{Hz}}$ at 1 kHz
DG442 Leakage Current, i_s	0.01 nA

3.1.1.2 Op-Amp Noise Current

The input noise current density of the TL074C op amp is stated in the manufacturer's specification sheet as being $0.01\,\text{pA}/\sqrt{\text{Hz}}$. The input noise current is the result of thermal noise and shot noise as discussed above.

3.1.1.3 Charge Injection Noise

At the beginning of each current integration cycle, the analogue switch is opened using its digital control input. Due to a small stray capacitance between the digital control input and the analogue switch, a small amount of charge is injected onto the integrating capacitor. This, in itself, does not produce noise. However, the amount of charge injected varies significantly from cycle to cycle as the stray capacitance varies from cycle to cycle. This variation results in a random noise voltage at the output of the integrator. The root means square (rms) noise voltage is proportional to the mean charge injected, which in the case of the switch being used is 1 pC.

In order to remove this noise, the output voltage of the integrator is sampled twice, as shown in Figure 2.8; it is sampled at $T_i = 1.925$ ms to give V_i, and again at $T_f = T_0 - 0.3$ ms to give V_f. The two voltages are then subtracted to give $\Delta V = V_f - V_i$. Charge is only injected onto the capacitor when the switch is opened. As this does not occur between T_i and T_f, both voltages V_i and V_f will be affected equally by the initial charge injection. By subtracting these two values, the effect of the injected charge is removed, completely eliminating this noise source. The voltage resulting from any charge retained by the capacitor after discharge will also be removed using this subtraction procedure. Although this discussion refers to the single-channel circuit, exactly the same comments apply to the eight-channel detector assembly.

3.1.1.4 Switch Leakage Current

The shot noise from the switch leakage current can be determined using

$$i_{switch} = \sqrt{2qi_s} \ \text{A}/\sqrt{\text{Hz}} \qquad (3.4)$$

where $i_s = 0.01$ nA is the leakage current. In this case the noise from the switch is $i_{swich} = 1.79\times10^{-15}\ \text{A}/\sqrt{\text{Hz}}$.

3.1.1.5 Voltage Noise due to Current Noise

Given the noise power spectrum of the current noise, one can utilize linear systems theory to calculate the noise voltage at the output of the detector circuit. Recall that the circuit contains an integrator followed by a gain-and-filter stage. The output of the gain-

and-filter stage is sampled at T_i to give V_i, and then again at T_f to give V_f. These two voltages are then subtracted to give $\Delta V = V_f - V_i$. The noise in both V_i and V_f must be calculated separately and then added in quadrature to determine the total voltage noise due to the current noise.

The transfer functions $H_{1i}(\omega)$ and $H_{1f}(\omega)$ of the integrator, relating the output voltages $V_i(\omega)$ and $V_f(\omega)$ to the input current amplitude $|i_{in}(\omega)|$ are defined as

$$H_{1i}(\omega) = \frac{V_i(\omega)}{|i_{in}(\omega)|} \tag{3.5a}$$

and

$$H_{1f}(\omega) = \frac{V_f(\omega)}{|i_{in}(\omega)|} \tag{3.5b}$$

respectively. If the input current is a DC current, $H_{1i}(\omega)$ and $H_{1f}(\omega)$ become

$$H_{1i}(0) = \frac{T_i}{C_{\text{int}}} \tag{3.6a}$$

$$H_{1f}(0) = \frac{T_f}{C_{\text{int}}}. \tag{3.6b}$$

However, in the case of a time varying current, as would be the case when the photodiode thermal noise current is taken into consideration, the noise current at frequency ω may be modeled as $i_{in}(\omega) = I(\omega)\cos(\omega t)$. Using this expression, it can be shown that

$$\begin{aligned} V_i(\omega) &= \frac{1}{C}\int_0^{T_i} i_{in}(\omega)dt \\ &= \frac{1}{C}\int_0^{T_i} I(\omega)\cos(\omega t)dt \\ &= \frac{1}{C} I(\omega)\frac{\sin(\omega T_i)}{\omega} \end{aligned} \tag{3.7a}$$

and

$$\begin{aligned} V_f(\omega) &= \frac{1}{C}\int_0^{T_f} i_{in}(\omega)dt \\ &= \frac{1}{C}\int_0^{T_f} I(\omega)\cos(\omega t)dt \\ &= \frac{1}{C} I(\omega)\frac{\sin(\omega T_f)}{\omega}. \end{aligned} \tag{3.7b}$$

The corresponding transfer functions are then

$$H_{1i}(\omega) = \frac{V_i(\omega)}{I(\omega)} = \left(\frac{\sin(\omega T_i)}{\omega T_i}\right)\cdot\left(\frac{T_i}{C_{\text{int}}}\right) \tag{3.8a}$$

$$H_{1f}(\omega) = \frac{V_f(\omega)}{I(\omega)} = \left(\frac{\sin(\omega T_f)}{\omega T_f}\right)\cdot\left(\frac{T_f}{C_{\text{int}}}\right) \tag{3.8b}$$

which reduce to (3.6a) and (3.6b) when $\omega \to 0$, as expected.

The transfer function $H_2(\omega)$ of the gain-and-filter stage must also be taken into account. The transfer function of a low-pass filter amplifier is given by the function

$$H_2(\omega) = \frac{G}{\sqrt{1+(\omega/\omega_c)^2}} \tag{3.9}$$

where $G = 47$ is the gain of this stage (see §2.3.1.4), $\omega_c = 2\pi f_c$, and $f_c = 339$ Hz is the cut-off frequency of the filter. As can be seen in Figure 3.1, $H_{1f}^2(\omega)$ (solid black line) decays to near zero before $H_2^2(\omega)$ (solid grey line) drops appreciably. However $H_{1i}^2(\omega)$ (dashed black line) is still appreciable when $H_2^2(\omega)$ starts to decrease.

The transfer function for the initial voltage measurement V_i is the product of $H_{1i}(\omega)$ and $H_2(\omega)$, namely,

$$H_i(\omega) = H_{1i}(\omega)H_2(\omega) = \left(\frac{T_i}{C_{\text{int}}}\right)\cdot\left(\frac{\sin(\omega T_i)}{\omega T_i}\right)\cdot\frac{G}{\sqrt{1+(\omega/\omega_c)^2}} \tag{3.10a}$$

while that of the final voltage measurement V_f is

$$H_f(\omega) = H_{1f}(\omega)H_2(\omega) = \left(\frac{T_f}{C_{\text{int}}}\right)\cdot\left(\frac{\sin(\omega T_f)}{\omega T_f}\right)\cdot\frac{G}{\sqrt{1+(\omega/\omega_c)^2}}. \tag{3.10b}$$

The quantity of interest is the variance in the output voltage σ_V^2, which can be related to the input noise by means of the transfer functions (3.10a) and (3.10b). As will be discussed in more detail in §3.2.1, the variance is given by the integral of the output voltage power spectrum, namely,

$$\sigma_{V\,current\,i}^2 = \frac{1}{2\pi}\int_{-\infty}^{\infty} P_{Vi}(\omega)d\omega \tag{3.11a}$$

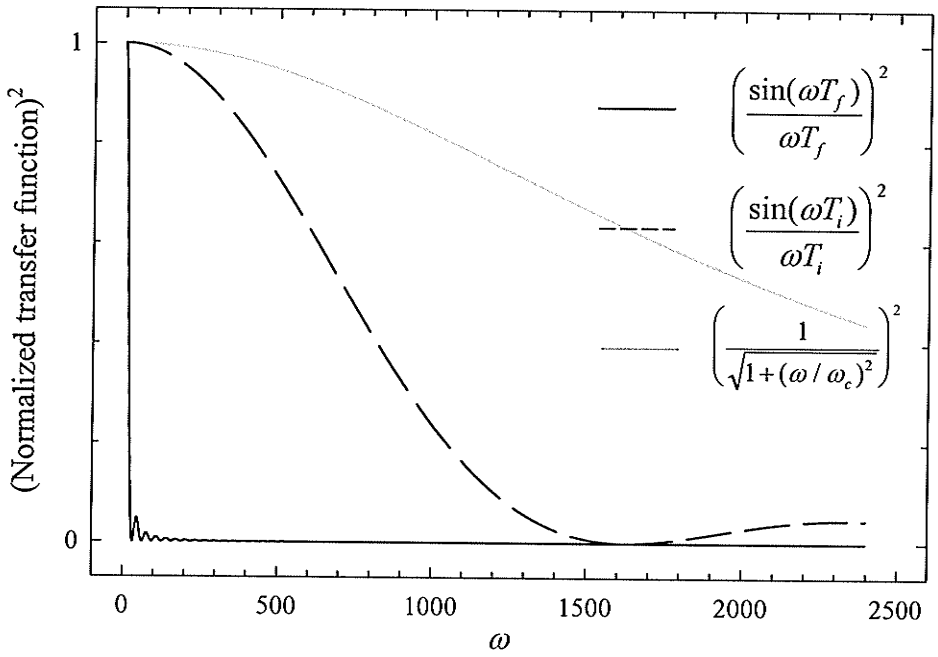

Figure 3.1 Plot showing the square of the normalized transfer functions $H_{1i}(\omega)$, $H_{1f}(\omega)$ and $H_2(\omega)$, using T_i = 0.001925 seconds and T_f = 0.0997 seconds (i.e. T_o = 0.1 seconds, f = 10 Hz).

and

$$\sigma^2_{V\,current\,f} = \frac{1}{2\pi}\int_{-\infty}^{\infty} P_{Vf}(\omega)d\omega \tag{3.11b}$$

where $P_{Vi}(\omega)$ is the output voltage power spectrum for the V_i measurements, $P_{Vf}(\omega)$ is the output voltage power spectrum for the V_f measurements, and $\sigma^2_{V\,current\,i}$ and $\sigma^2_{V\,current\,f}$ are the variances in V_i and V_f, respectively, due to current noise. The power spectra can be written as

$$P_{Vi}(\omega) = H_i^2(\omega)P_{current}(\omega) \tag{3.12a}$$

$$P_{Vf}(\omega) = H_f^2(\omega)P_{current}(\omega) \tag{3.12b}$$

where $P_{current}(\omega)$ is the noise current spectral density. Combining (3.10) with (3.11) and (3.12) gives

$$\begin{aligned}\sigma^2_{V\,current\,i} &= \frac{1}{2\pi}\int_{-\infty}^{\infty} H_i^2(\omega)P_{current}(\omega)d\omega \\ &= \frac{1}{2\pi}\left(\frac{T_i}{C_{\text{int}}}\right)^2\int_{-\infty}^{\infty}\left(\frac{\sin(\omega T_i)}{\omega T_i}\right)^2\left(\frac{G}{\sqrt{1+(\omega/\omega_c)^2}}\right)^2 P_{current}(\omega)d\omega\end{aligned} \tag{3.13a}$$

$$\sigma^2_{V\,current\,f} = \frac{1}{2\pi}\int_{-\infty}^{\infty} H_f^2(\omega) P_{current}(\omega)\,d\omega$$

$$= \frac{1}{2\pi}\left(\frac{T_f}{C_{\text{int}}}\right)^2 \int_{-\infty}^{\infty}\left(\frac{\sin(\omega T_f)}{\omega T_f}\right)^2\left(\frac{G}{\sqrt{1+(\omega/\omega_c)^2}}\right)^2 P_{current}(\omega)\,d\omega. \qquad (3.13b)$$

Assuming all of the above noise sources to be white, the noise current spectral density is independent of frequency, i.e., $P_{current}(\omega) = P_{current}$, where

$$\begin{aligned} P_{current} &= i_n^2 + i_{TL704C}^2 + i_{switch}^2 \\ &= [(2.883\times10^{-15})^2 + (0.01\times10^{-12})^2 + (1.79\times10^{-15})^2]\ \text{A}^2/\text{Hz} \\ &= 1.12\times10^{-28}\ \text{A}^2/\text{Hz}. \end{aligned} \qquad (3.14)$$

Equations (3.13a) and (3.13b) can be simplified respectively to

$$\sigma^2_{V\,current\,i} = \frac{1}{2\pi}\left(\frac{T_i}{C_{\text{int}}}\right)^2 P_{current}\int_{-\infty}^{\infty}\left(\frac{\sin(\omega T_i)}{\omega T_i}\right)^2\left(\frac{G^2}{1+(\omega/\omega_c)^2}\right)d\omega \qquad (3.15a)$$

$$\sigma^2_{V\,current\,f} = \frac{1}{2\pi}\left(\frac{T_f}{C_{\text{int}}}\right)^2 P_{current}\int_{-\infty}^{\infty}\left(\frac{\sin(\omega T_f)}{\omega T_f}\right)^2\left(\frac{G^2}{1+(\omega/\omega_c)^2}\right)d\omega. \qquad (3.15b)$$

If the frequency $f = 1/T$ satisfies the inequality $f << f_c$ then $H_2(\omega) \approx G$. As can be seen in Figure 3.1, this approximation holds for T_f when $f = 10$ Hz, but does not hold nearly as well for T_i. Taking $H_2(\omega) \approx G$ to be valid (it will be shown in §3.2.3.1 that the error introduced by this assumption is small), (3.15a) and (3.15b) can be written as

$$\begin{aligned} \sigma^2_{V\,current\,i} &\approx \frac{1}{2\pi}\left(\frac{GT_i}{C_{\text{int}}}\right)^2 P_{current}\int_{-\infty}^{\infty}\left(\frac{\sin(\omega T_i)}{\omega T_i}\right)^2 d\omega \\ &= \frac{1}{2\pi}\left(\frac{GT_i}{C_{\text{int}}}\right)^2 \frac{P_{current}\pi}{T_i} \\ &= \frac{G^2 T_i P_{current}}{2C_{\text{int}}^2} \end{aligned} \qquad (3.16a)$$

$$\begin{aligned} \sigma^2_{V\,current\,f} &\approx \frac{1}{2\pi}\left(\frac{GT_f}{C_{\text{int}}}\right)^2 P_{current}\int_{-\infty}^{\infty}\left(\frac{\sin(\omega T_f)}{\omega T_f}\right)^2 d\omega \\ &= \frac{1}{2\pi}\left(\frac{GT_f}{C_{\text{int}}}\right)^2 \frac{P_{current}\pi}{T_f} \\ &= \frac{G^2 T_f P_{current}}{2C_{\text{int}}^2}. \end{aligned} \qquad (3.16b)$$

The standard deviation $\sigma_{V\,current\,i}$ in V_i due to the current noise is

$$\sigma_{V\ current\ i} = \frac{G}{C_{\text{int}}}\sqrt{\frac{T_i P_{current}}{2}}$$
$$= \frac{47}{1\,\text{nF}}\sqrt{\frac{(0.001925)(1.12\times10^{-28})}{2}} \qquad (3.17a)$$
$$= 15.4\,\mu\text{V}$$

and the standard deviation $\sigma_{V\ current\ f}$ in V_f due to the current noise is

$$\sigma_{V\ current\ f} = \frac{G}{C_{\text{int}}}\sqrt{\frac{T_f P_{current}}{2}}$$
$$= \frac{47}{1\,\text{nF}}\sqrt{\frac{(0.0997)(1.12\times10^{-28})}{2}} \qquad (3.17b)$$
$$= 111.1\,\mu\text{V}.$$

Adding these two noise sources in quadrature gives $\sigma_{V\ current\ total} = 112.2\ \mu\text{V}$.

3.1.2 Voltage Noise Sources

The voltage noise sources are the input noise voltages of the two op-amps. Both of these have an equivalent input noise voltage of 18 nV / $\sqrt{\text{Hz}}$. Considering first the op-amp in the integration stage, the gain for the input noise voltage is given by (Burr-Brown Application Bulletin AB-057A)

$$G_1 = 1 + \frac{C_1}{C_2} \qquad (3.18)$$

where C_1 is the sum of the capacitance of the two photodiodes C_D (recall, adjacent elements of the photodiode array are wired together in parallel to form a single detector), and C_2 is the sum of the capacitance of the integration capacitor C_{int} and the switch C_s. The capacitance of the photodiode, the integration capacitor and the switch are 28 pF, 1000 pF and 16 pF, respectively. Inserting these values into (3.18) gives

$$G_1 = 1 + \frac{C_D + C_D}{C_{\text{int}} + C_s}$$
$$= 1 + \frac{28\,\text{pF} + 28\ \text{pF}}{1000\,\text{pF} + 16\,\text{pF}} \qquad (3.19)$$
$$= 1.06\ .$$

The total gain for the noise from the first op-amp is the product of the gain from the first stage G_1 and the second stage G_2, where the latter was found to equal 47 in §2.3.1.4. The

total gain is therefore $G = G_1 \cdot G_2 = (1.06) \cdot (47) = 49.6$. The standard deviation in the output voltage due to this noise source is then equal to

$$\sigma_{V1} = (18\,\text{nV}/\sqrt{\text{Hz}}) \cdot G \cdot \sqrt{B} \tag{3.20}$$

where B is the noise bandwidth. The noise generated by the first stage must pass through the second stage. As the noise bandwidth of the second stage is much less than that of the first stage, it is valid to simply use the noise bandwidth of the second stage. The noise bandwidth of a low-pass filter is given by

$$B = \frac{\pi}{2} f_c \tag{3.21}$$

where f_c =339 is the cutoff frequency found in §2.3.1.4. Using these values, σ_{V1} is equal to 20.6 μV.

The noise in the output voltage due to the input noise voltage of the second op-amp is found in a similar manner. In this case however, the noise is affected by only the second gain stage. Assuming that the input noise voltage source is connected to the non-inverting input (recall that the output noise voltage from the first gain stage enters the inverting input), the gain is given by

$$G' = 1 + \frac{R_F}{R_s} \tag{3.22}$$

where R_F and R_S are defined in Figure 2.4. The total gain is then equal to $G' = 48$, giving an output noise voltage σ_{V2} due to this noise source of

$$\begin{aligned} \sigma_{V2} &= (18\,\text{nV}/\sqrt{\text{Hz}}) \cdot G' \cdot \sqrt{B} \\ &= 19.9\,\mu\text{V}. \end{aligned} \tag{3.23}$$

3.1.3 A-to-D Board Noise

The voltage noise contributed by the A-to-D board may be found using the following expression (Pratt, 1984)

$$\sigma_{V\,A\text{-}to\text{-}D} = \frac{\text{Range}}{2^{\text{No. of bits}} \times 12}. \tag{3.24}$$

When a gain of 10 is used, the range is 2 V (-1 V to 1 V) and the number of bits is 16. Inserting these values in (3.24) gives $\sigma_{V\,A\text{-}to\text{-}D} = 2.5\,\mu\text{V}$.

3.1.4 Total Noise

The total noise is found by adding the current and voltage noise sources in quadrature according to the expression

$$\sigma^2_{total} = \sigma^2_{V\,current\ total} + 2(\sigma^2_{V1} + \sigma^2_{V2}) + \sigma^2_{V\,A\text{-}to\text{-}D} \qquad (3.25)$$

where the factor of 2 preceding the voltage noise is to account for the subtraction process. This gives a total noise of 119.3 μV at a sampling frequency of 10 Hz.

The theoretical noise analysis performed in this section provides a foundation for the experimental measurements performed in the next section. It further demonstrates that the electronic noise is dominated by the current noise, in particular, the op-amp input noise current. If the electronic noise is found to be too large, efforts should be focussed on reducing the input noise current of the op-amp. Further discussion of the consequences of the results found in this section, as well as the results of the following sections is given in Chapter 7.

3.2 Electronic Noise Measurements

3.2.1 Theory

3.2.1.1 Autocovariance Function

Although the variance σ^2 is often used to characterize the noise of a detector system, this is generally inadequate, as it depends upon factors such as the aperture size used for sampling the data (Giger et al., 1984), and provides no information regarding the texture of the noise. A more complete description of the noise in a system is provided by the autocovariance function (ACVF)[2], which for a stationary process[3] is defined as (Oppenheim and Schafer, 1975; Barrett and Swindell, 1981)

$$\gamma_{VV}(\tau) = \left\langle \left[\tilde{V}(t) - \bar{V}\right]\left[\tilde{V}(t+\tau) - \bar{V}\right]^* \right\rangle \qquad (3.26)$$

---

[2] Many authors use the term autocorrelation function to describe (3.26), although the autocorrelation function, by definition, does not include the subtraction of the mean from the data. In practice, the distinction between the autocorrelation and autocovariance function is somewhat artificial in that the autocorrelation function is meaningless unless zero mean data is used (Bracewell, 1986).

[3] A process is defined as being *stationary* if the mean, variance, and higher order moments are not affected by a shift in the origin, i.e., the ACVF depends only on the difference between the two time arguments, and not on the time arguments themselves. (Barrett and Swindell, 1981; Dainty and Shaw, 1974)

where the * represents complex conjugation and $\overline{V}$ denotes the mean of the random process $\{\widetilde{V}(t)\}\ -\infty < t < \infty$[4].

In practice however, we must deal with finite length samples to give an approximation of the ACVF. Taking $V(n) = \widetilde{V}(n) - \overline{V}$, where $\overline{V}$ denotes the mean of the random process $\{\widetilde{V}(n)\}$, an estimate of the population ACVF $c_{VV}(l)$ can be found using (Oppenheim and Schafer, 1975)

$$c_{VV}(l) = \frac{1}{N}\sum_{n=0}^{N-l-1} V(n)V^*(n+l) \qquad l = 0,1,2,\ldots,N-1 \tag{3.27}$$

where N is the number of sample values, l is the lag, and $V(n)$ represents the sampled detector output corrected for its mean. As the ACVF is an ergodic process[5], a "sample" ACVF over some finite interval will converge to the "population" ACVF as the length of the sample increases (Wagner and Sandrik, 1979). More specifically, the variance in the ACVF for any lag value l decreases as $1/N$ with increasing sample length N (Jenkins and Watts, 1968).

3.2.1.2 Power Spectrum

The Fourier transform of the ACVF, referred to as the power spectrum $\Gamma_{VV}(f)$ is a more common method of characterizing the noise in a system. The power spectrum describes the distribution of noise power as a function of frequency and allows the variance to be expressed in terms of its spatial frequency components, thereby describing both the magnitude and the texture of the noise.

For a stochastic process, the population power spectrum may be found using (Jenkins and Watts, 1968)

$$\Gamma_{VV}(f) = \int_{-\infty}^{\infty} \gamma_{VV}(\tau) e^{-2\pi i f \tau} d\tau\,. \tag{3.28}$$

---

[4] The notation in this section, adopted from Jenkins and Watts (1968) is such that the lower case Greek letters represent the *ensemble average* of a quantity in the spatial domain (e.g. population autocovariance function: γ_{VV}), whereas the lower case Roman letters represent an *estimate* of the quantity in the spatial domain (e.g. autocovariance estimate: c_{VV}). Upper case Greek letter represent the ensemble average of the quantity in the frequency domain (e.g. population noise power spectrum – Fourier transform of the population autocovariance function: Γ_{VV}) and the upper case Roman letters represent the estimate of that quantity in the frequency domain (e.g. noise power spectrum estimate: C_{VV}).

[5] A process is defined as being *ergodic* if the ensemble average may be replaced by a temporal (or spatial) average (Barrett and Swindell, 1981).

According to the Wiener-Khintchin theorem, the population ACVF, and the population power spectrum are Fourier transform pairs, so that

$$\gamma_{VV}(\tau) = \int_{-\infty}^{\infty} \Gamma_{VV}(f) e^{2\pi i f \tau} df \tag{3.29}$$

also holds. Evaluating the above equation at $\tau = 0$ and recognizing that $\gamma_{VV}(0) = \sigma^2$, demonstrates that the variance is equal to the integral of the power spectrum over frequency (Jenkins and Watts, 1968).

If $X(f)$ and $Y(f)$ are the Fourier transforms of $x(t)$ and $y(t)$ respectively, then the following are Fourier transform pairs (Gonzalez and Wintz, 1977)

$$x(t) \circ y(t) \Leftrightarrow X(f) Y^*(f) \tag{3.30}$$

where "$\circ$" and "$*$" indicate correlation and complex conjugate respectively. Using (3.30), it can be seen that $\Gamma_{VV}(f)$ may alternatively be written as (Jenkins and Watts, 1968)

$$\Gamma_{VV}(f) = \lim_{t \to \infty} \left\langle \left| \int_{-t/2}^{t/2} V(t') e^{-2\pi i f t'} dt' \right|^2 \right\rangle \tag{3.31}$$

where the braces indicate an ensemble average.

As was the case for ACVF, finite length samples can be used to calculate an estimate $C_{VV}(f)$ of the population power spectrum $\Gamma_{VV}(f)$. For discrete signals, this estimate may be found using (Jenkins and Watts, 1968)

$$C_{VV}(f_k) = \left\langle \left| \frac{1}{N} \sum_{j=0}^{N-1} V(j) e^{-2\pi i f_k j / N} \right|^2 \right\rangle \qquad k = 0, 1, \ldots, N-1 \tag{3.32}$$

where N is the number of data points in the sample. If Δt is the time between data points then

$$f_k = \frac{k}{N \Delta t}. \tag{3.33}$$

Unlike the ACVF, which is statistically "well-behaved" in the sense that it converges to the population ACVF with increasing record length N, the sample power spectrum is not ergodic, and therefore does not converge to the population power spectrum with increasing record length, i.e., the variance of a particular component of the power spectrum is independent of the number of sample points used (Jenkins and Watts, 1968). Jenkins and Watts (1968) provide the following intuitive explanation. If the record length is increased, $c_{VV}(l)$ for a fixed lag value l contains increased information. Thus

$c_{VV}(l)$ approaches $\gamma_{VV}(l)$ with increasing record length N. However, the only advantage of using a larger number of data points to create the power spectrum is that the points in the power spectrum will be more closely spaced. More specifically, the spacing between the points in the frequency domain is given by

$$\Delta f = \frac{1}{N\Delta t}. \tag{3.34}$$

The maximum frequency that is not aliased is given by the Nyquist frequency,

$$f_N = \frac{1}{2\Delta t} \tag{3.35}$$

meaning that the estimate of the population power spectrum $C_{VV}(f)$ will contain data points with spacing Δf up to a maximum frequency of $f_{\max} = f_N$. As can be seen from the above expressions, Δf decreases as the record length increases while f_N remains unchanged. In other words, the only effect of increasing the sample length is to decrease the spacing between the points within the power spectrum. The accuracy of the values in the power spectrum does not improve (Jenkins and Watts, 1968).

A rigorous proof of the above statement demonstrates that the variance of the estimate of the power spectrum $\sigma^2_{C_{VV}(f)}$ for zero mean Gaussian white noise is equal to (Percival and Walden, 1993, Wagner and Sandrik, 1979; Jenkins and Watts, 1968)

$$\sigma^2_{C_{VV}(f)} = \begin{cases} \Gamma^2_{VV}(f) & \text{for } f \neq 0, f_N \\ 2\Gamma^2_{VV}(f) & \text{for } f = 0, f_N. \end{cases} \tag{3.36}$$

where $C_{VV}(f)$ is the estimate of the power spectrum, and $\Gamma_{VV}(f)$ is the population power spectrum. The above expression holds approximately for any normal stochastic (nonwhite) process, providing a large enough sample is used.

To deal with the non-ergodic nature of the power spectrum, an approach referred to as Bartlett's procedure is used. This involves collecting a long record of length N and sectioning it into M segments with $n = N / M$ data values in each segment. The power spectrum is found for each segment of length n; this is referred to as a periodogram. The resulting M periodograms are averaged as follows

$$\overline{C}_{VV}(f_k) = \frac{1}{M}\sum_{m=0}^{M-1}\left|\frac{1}{n}\sum_{j=0}^{n-1} V_m(j) e^{-2\pi i f_k j/n}\right|^2 \tag{3.37}$$

to find a smoothed estimate of the power spectrum $\overline{C}_{VV}(f_k)$. This method of finding a smoothed spectrum is valid if $c_{VV}(l)$ is small for $l > n$ (Oppenheim and Schafer, 1975),

meaning that the periodograms are independent[6]. As this procedure is required to smooth the power spectrum, a large number of data points (>10,000) is required (Wagner, 1977). The spacing between samples in the estimated power spectrum is

$$\Delta f' = \frac{M}{N\Delta t} = M\Delta f \tag{3.38}$$

when the power spectra of the M segments are averaged (Dainty and Shaw, 1974). The ensemble averaged power spectrum $\overline{C}_{VV}(f)$ may be further smoothed by using a running average. However, unless the power spectrum changes linearly with frequency, this will bias the spectrum (Wagner and Sandrik, 1979).

For white noise, the periodograms are independent so that the variance in the power spectrum estimate is equal to that given in (3.36), divided by the number of periodograms M, namely (Jenkins and Watts, 1968)

$$\sigma^2_{\overline{C}_{VV}(f)} = \begin{cases} \Gamma^2_{VV}(f)/M & \text{for } f \neq 0, f_N \\ 2\Gamma^2_{VV} f(f)/M & \text{for } f = 0, f_N. \end{cases} \tag{3.39}$$

Dividing a long sample into M periodograms and then averaging these periodograms to obtain a power spectrum will therefore produce a smoother spectrum, but will also result in a decrease in frequency resolution and a possible bias in the estimate.

3.2.1.3 Relationship between the ACVF and the Power Spectrum

To demonstrate that the variance is equal to the integral of the power spectrum over frequency, recall (3.29). Evaluated at $\tau = 0$, this expression becomes

$$\gamma_{VV}(0) = \int_{-\infty}^{\infty} \Gamma_{VV}(f)\,df \tag{3.40}$$

which means that the area under the power spectrum equals the ACVF evaluated at zero lag. This is in turn equal to the variance. In the discrete case, the area under the power spectrum, expressed using the definition given in (3.37) is

$$\sum_{k=0}^{n-1} \overline{C}_{VV}(k) = \sum_{k=0}^{n-1} \frac{1}{M} \sum_{m=0}^{M-1} \frac{1}{n^2} \sum_{j'=0}^{n-1} V_m^*(j') e^{2\pi i j' k/n} \sum_{j=0}^{n-1} V_m(j) e^{-2\pi i j k/n} \tag{3.41}$$

[6] If the samples are correlated, a bias will likely be introduced in the power spectrum.

where the substitution $f_k \rightarrow k$ was made. Note that the power in the first exponential of (3.41) (i.e. $e^{2\pi ij'k/n}$) is positive because of the absolute value sign in (3.37). As summation is a linear operation, the order of the summations can be interchanged to give

$$\sum_{k=0}^{n-1} \overline{C}_{VV}(k) = \frac{1}{M} \sum_{m=0}^{M-1} \frac{1}{n^2} \sum_{j'=0}^{n-1} V_m(j') \sum_{j=0}^{n-1} V_m(j) \sum_{k=0}^{n-1} e^{-2\pi i(j-j')k/n} . \tag{3.42}$$

Using the identity

$$\sum_{k=0}^{n-1} e^{-2\pi i(j-j')k/n} = n\delta(j-j') \tag{3.43}$$

(3.42) can be rewritten as

$$\sum_{k=0}^{n-1} \overline{C}_{VV}(k) = \frac{1}{M} \sum_{m=0}^{M-1} \frac{1}{n^2} \sum_{j'=0}^{n-1} \sum_{j=0}^{n-1} V_m(j') V_m(j)\ n\,\delta(j-j') . \tag{3.44}$$

The double summation is reduced to a single sum, such that

$$\begin{aligned} \sum_{k=0}^{n-1} \overline{C}_{VV}(k) &= \frac{1}{nM} \sum_{m=0}^{M-1} \sum_{j=0}^{n-1} V_m^2(j) \\ &= \frac{1}{N} \sum_{m=0}^{M-1} \sum_{j=0}^{n-1} V_m^2(j) \\ &= \sigma_{VV}^2 \end{aligned} \tag{3.45}$$

verifying that the area under the power spectrum is equal to the ACVF evaluated at zero lag, which is also the variance. Note that the zero mean data is assumed.

3.2.2 Method

The purpose of this section is to analyze the electronic noise of the detector. Consequently, the measurements were performed in the absence of light or radiation, without a scintillator placed on the diode. In order to experimentally determine the power spectrum, the output of the detector was digitized at sampling frequencies of 10 Hz, 50 Hz, 100 Hz and 200 Hz. A large number (N = 50,000) of data points were collected at each frequency. The measured standard deviation was compared to the values calculated theoretically in §3.1, prior to performing a detailed noise analysis. The detector output was first converted to zero mean data $V(j)$ by dividing the data into subsets, and then subtracting the mean of each subset from that particular subset. It was necessary to subtract the mean of each subset from that particular subset, rather than subtracting the mean of all 50,000 data points in order to remove the long term drift found in the data

collected at slower sampling frequencies (especially 10 Hz). This will be discussed in more detail below.

The ACVF was found at each sampling frequency using (3.27) before finding the power spectrum to ensure that $c_{VV}(l)$ is small for large lag values. The data were first converted to zero mean data using subsets 64 data points in length. Using relatively short subsets most effectively removes the long-term drift in the 10 Hz data.

Having confirmed that it is valid to use Bartlett's procedure, estimates of the power spectrum $\overline{C}_{VV}(f_k)$ were found using (3.37). Each sampled sequence of length N was divided into M segments of length n = 128, 512, 1024 and 4096, and converted to zero mean data sets $V_m(j)$, $m = 0, 1, 2, \ldots, M$, as described above. The M periodograms generated by finding the magnitude of the Fourier transform of the signal $V_m(j)$ were averaged to yield the final power spectrum $\overline{C}_{VV}(f_k)$. To further smooth the power spectrum estimate, the results of (3.37) were smoothed using a three point running average.

To ensure that the power spectra satisfied (3.45), the areas under the experimentally calculated power spectra were found and compared with values calculated for the right-hand side of this expression.

3.2.3 Results

3.2.3.1 Experimentally Measured Noise as a Function of Sampling Frequency

Before finding any power spectra, it is important to compare the measured standard deviation at the various sampling frequencies with that calculated in §3.1. The sampling frequency dependence of the noise voltage at the detector output arises mainly due to the current noise sources at the input of the integrator. Equations (3.15a) and (3.15b) were evaluated (Maple v.3.5) to determine the noise in the detector output due to these sources. The results found using these expressions are listed in Table 3.2. The total current noise $\sigma_{V\,current\,total}$ listed in Table 3.3 was found by adding $\sigma_{V\,current\,i}$ and $\sigma_{V\,current\,f}$ in quadrature. When comparing the estimated current noise at 10 Hz sampling frequency calculated in §3.1.1.5 ($\sigma_{V\,current\,total}$ = 112.2 μV) with the exact value listed in Table 3.2, it can be seen

that the approximation made in §3.1 introduces only a small error. The total noise is found using (3.25). The values of the various noise sources are listed in Table 3.3.

The experimentally measured standard deviation at each sampling frequency for various subset lengths n is listed in Table 3.4. For data collected at 50 Hz, 100 Hz and 200 Hz, the standard deviation is nearly independent of the subset length. However, the standard deviation of the 10 Hz data increases dramatically with increasing subset length. This occurs because of a long-term drift present in this data (most likely due to a variation in the circuit temperature during data collection as discussed below).

A plot of the measured (n = 64) and calculated standard deviation is shown in Figure 3.2. The discrepancy between the measured and calculated values can be attributed to differences between the actual and typical characteristics quoted by the electronic component manufacturers. It must also be noted that some approximations were made when calculating the theoretical standard deviation. For instance, the equivalent input noise current has a frequency dependence that is not accounted for simply because the manufacturer does not supply the required data. It should however be noted that the experimental data follows the trend of the theoretical calculations, suggesting that the latter are at least a good estimate of the expected standard deviation.

Table 3.2 Current Noise as a function of Sampling Frequency

Sampling Frequency (Hz)	T_o (s)	T_i (s)	$\sigma_{V\,current\,i}$ (μV)	T_f (s)	$\sigma_{V\,current\,f}$ (μV)
10	0.1			0.0997	110.9
50	0.02	0.001925	14.5	0.0197	49.1
100	0.01			0.0097	34.2
200	0.005			0.0047	23.5

Table 3.3 Total Noise (μV) as a function of Sampling Frequency

Sampling Frequency (Hz)	$\sigma_{V\,current\,total}$	$\sigma_{V\,1}$	$\sigma_{V\,2}$	$\sigma_{V\,A-to-D}$	σ_{total}
10	111.8				118.9
50	51.2	20.6	19.9	2.5	65.3
100	37.1				55.0
200	27.6				49.1

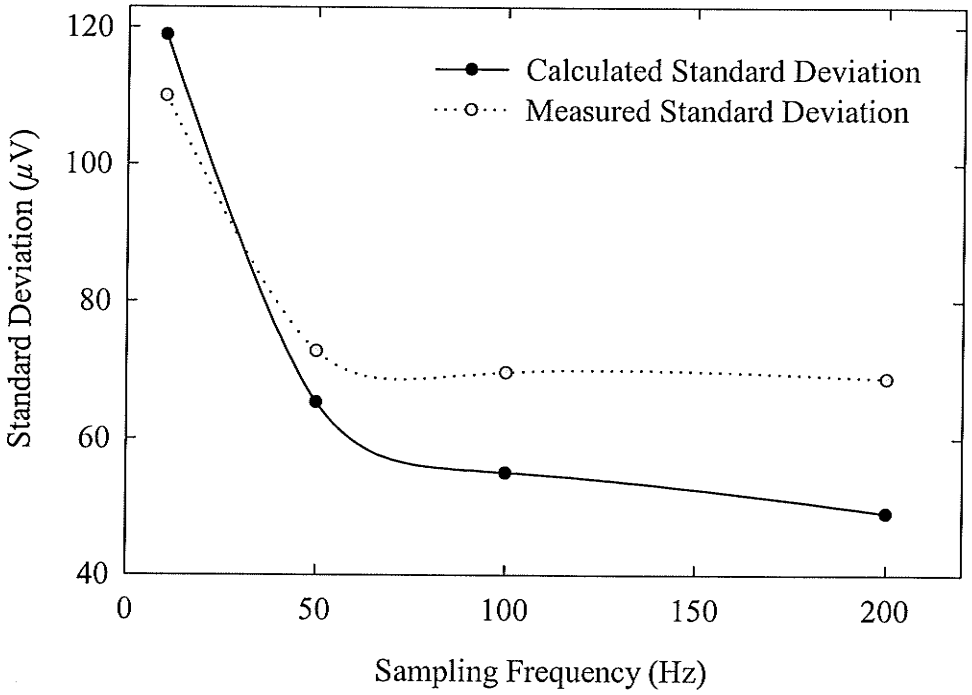

Figure 3.2 Measured and theoretically calculated standard deviation as a function of sampling frequency.

Table 3.4 Experimental Standard Deviation

Sampling Frequency (Hz)	n	Standard Deviation (μV)
10	64	109.977
	128	113.757
	256	118.679
	512	125.032
50	64	72.756
	256	73.203
	1024	72.517
	4096	70.311
100	64	69.695
	256	70.052
	1024	69.488
	4096	67.390
200	64	68.795
	256	69.166
	1024	68.665
	4096	66.738

The standard deviation in the detector output decreases with increasing sampling frequency because the noise power decreases. This is a consequence of the decrease with sampling rate in the area under the product of the integrator transfer function and the gain-and-filter stage transfer function (see Figure 3.1). As the standard deviation is the integral of the power spectrum over frequency, a decrease in the area under the power spectrum results in a decrease in the standard deviation (Berndt et al., 2000a).

3.2.3.2 Autocovariance Function

The ACVF for data collected at 10 Hz, 50 Hz, 100 Hz and 200 Hz was calculated using (3.27). Figure 3.3 shows the ACVF for the 10 Hz data. Since the ACVFs of the 50 Hz, 100 Hz, and 200 Hz data are similar to the ACVF of the 10 Hz data, these are not shown in Figure 3.3. As can be seen, $c_{VV}(l)$ is small (with respect to the zero lag value) for large values of l, meaning the Bartlett's smoothing procedure can be used.

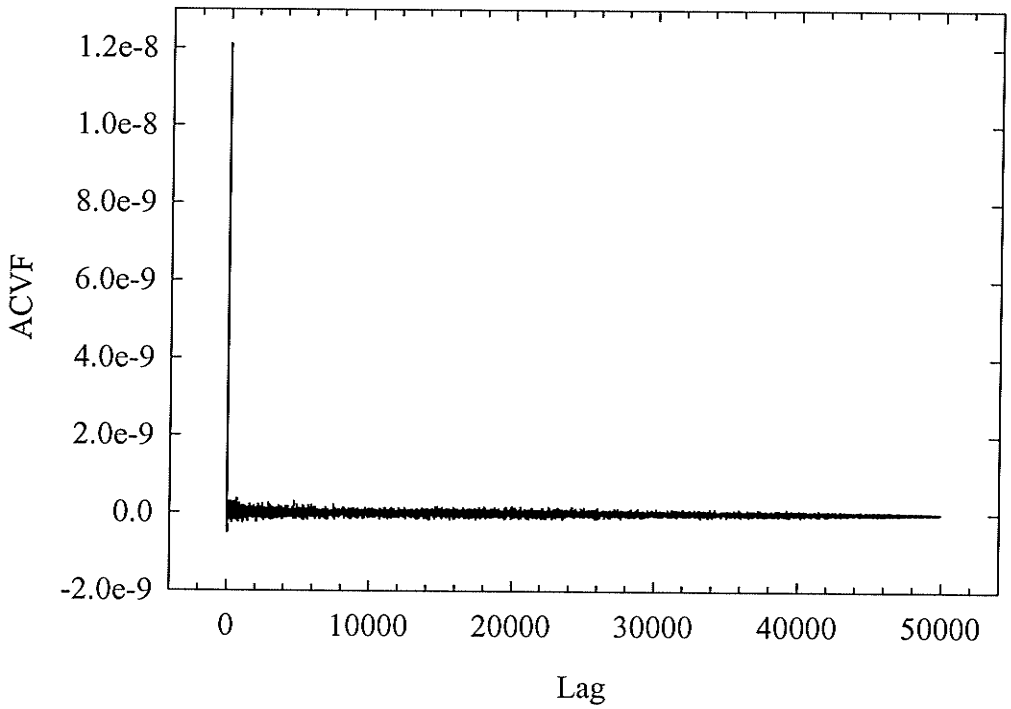

Figure 3.3 ACVF for 10 Hz data found using (3.27) for lag values $0 \leq l \leq 49900$. Only data for every fifth lag value, i.e., $l = 0, 5, 10, \ldots$ is shown.

3.2.3.3 Power Spectrum

Several estimates of the power spectrum using different periodogram lengths were found for each data set collected. For the 200 Hz data, the set of 50,000 points was divided into periodograms of length n as listed in Table 3.5. The corresponding power spectra are shown in Figures 3.4 and 3.8. As stated in §3.2.1.2, the power spectrum becomes less smooth but displays a greater frequency resolution as the periodogram length increases.

Table 3.5 n (periodogram length) and M (number of periodograms) used when analyzing a data set $N = 50{,}000$ data points in length

	n	M	
increasing bias of estimate ↑	128	390	↓ increasing variance of estimate
	512	97	
	1024	48	
	8192	6	

Recalling (3.35), the Nyquist, or folding frequency f_N for the 200 Hz data is 100 Hz. This means that the power spectrum calculated between 100 Hz and 200 Hz is simply a mirror image of the values below 100 Hz. More specifically, the power spectrum will repeat itself every 200 Hz. The discrete nature of the data collection also implies that noise power at frequencies greater than 100 Hz will be aliased to appear at frequencies less than 100 Hz. In particular, we are interested in noise at frequencies equal to the power line harmonics, i.e. noise at 60 Hz, 120 Hz and 180 Hz. A noise source at 60 Hz would be correctly displayed without aliasing. Noise at 120 Hz would be aliased to 80 Hz, and noise at 180 Hz would be aliased to 20 Hz. Thus the peaks at 60 Hz and 20 Hz in Figure 3.4 are likely due to power line interference. The other peaks are likely due to high frequency sources, aliased to lower frequencies.

The estimated power spectra using $n = 4096$ and $M = 12$ were also found for data sampled at 100 Hz, 50 Hz and 10 Hz, as shown in Figures 3.5 to 3.7 respectively. Figure 3.8 summarizes the results at all frequencies. Table 3.6 lists the frequencies to which the power line harmonics are aliased. For instance, for the data collected at 50 Hz, 60 Hz

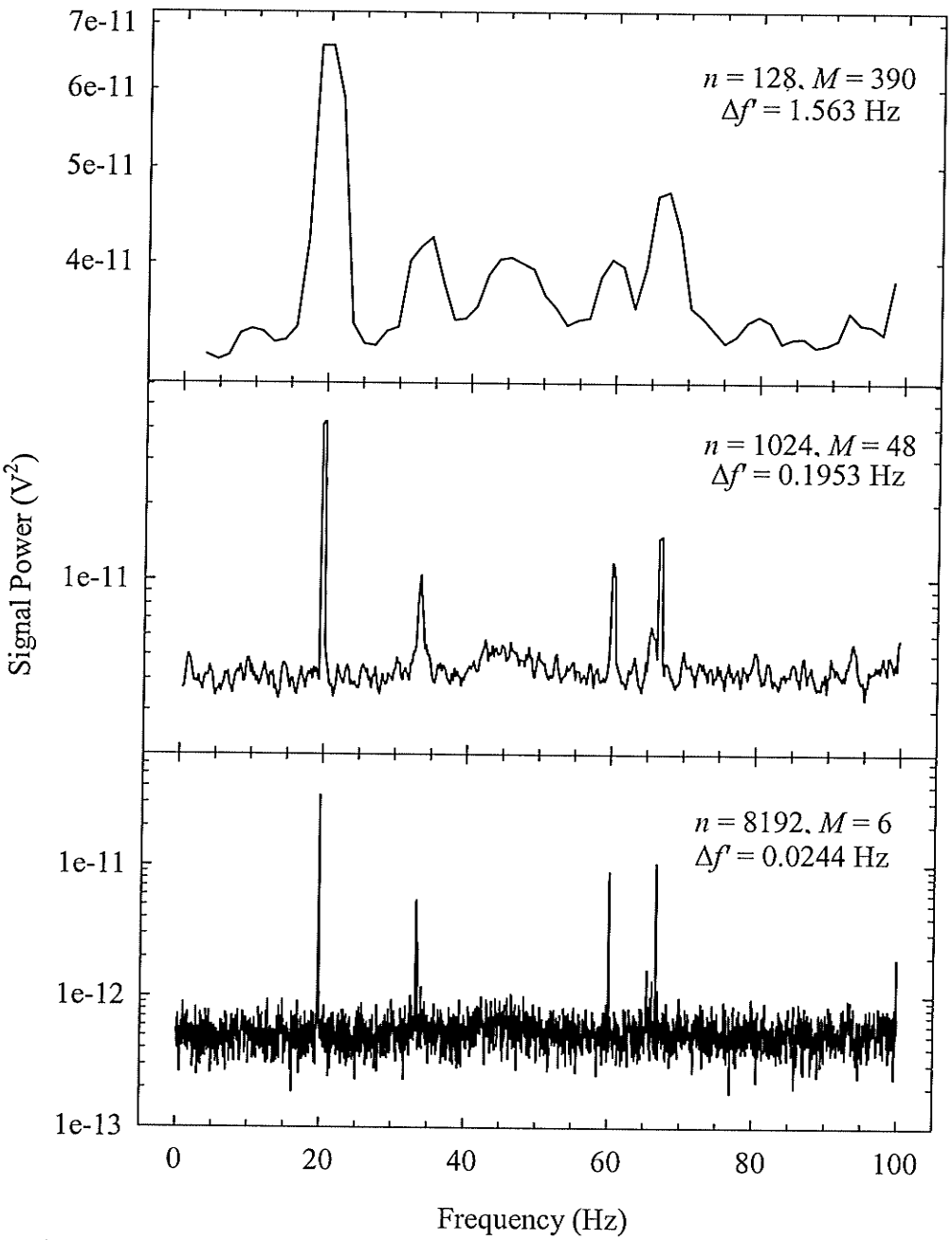

Figure 3.4 Estimated power spectra for data collected at a sampling frequency of 200 Hz. A running average of three points was used to smooth the spectra.

power line interference would alias to 10 Hz, and 120 Hz and 180 Hz noise would both be aliased to 20 Hz.

At 10 Hz (and to a lesser degree 50 Hz) there is a large DC component. This occurs because there is a long-term drift in the data that is not corrected for by the zero

mean process. This long-term drift occurs because of slight variations in the circuit temperature, which affect its response, as discussed in §3.7. This effect is not observed for the data collected using higher sampling frequencies because the 50,000 data points are collected much more quickly at 100 Hz or 200 Hz than at a sampling frequency of 10 Hz. Furthermore, for the 10 Hz data, power line harmonics are aliased to 0 Hz. Any interference near the power line frequencies would thus be aliased to frequencies near zero, also resulting in a low frequency contribution to the signal, and consequently a long term drift. To test this hypothesis, measurements were made using sampling frequencies of 11 Hz and 13 Hz and the corresponding power spectrum estimates generated. Not shown is the 13 Hz power spectrum, which is very similar to the 11 Hz power spectrum plotted in Figure 3.9. Comparing Figure 3.9 with Figure 3.7, it can be seen that the signal power near 0 Hz is greatly reduced for the 11 Hz data, suggesting that a portion of the low frequency signal power appearing in the 10 Hz plot is due to power line noise aliased to frequencies near 0 Hz. There is however still a spike near 0 Hz for both the 11 Hz and 13 Hz power spectra, which is likely the result of a temperature drift.

The standard deviation measurements perfomed in this section validate the calculations of §3.1. The results of this section are used to determine the contribution of the electronic noise to the total noise in §3.3.

Table 3.6 Frequency to which power line harmonics are aliased

Sampling Frequency	Interference Frequency		
	60 Hz	120 Hz	180 Hz
10 Hz	0 Hz	0 Hz	0 Hz
11 Hz	5 Hz	1 Hz	4 Hz
50 Hz	10 Hz	20 Hz	20 Hz
100 Hz	40 Hz	20 Hz	20 Hz
200 Hz	60 Hz	80 Hz	20 Hz

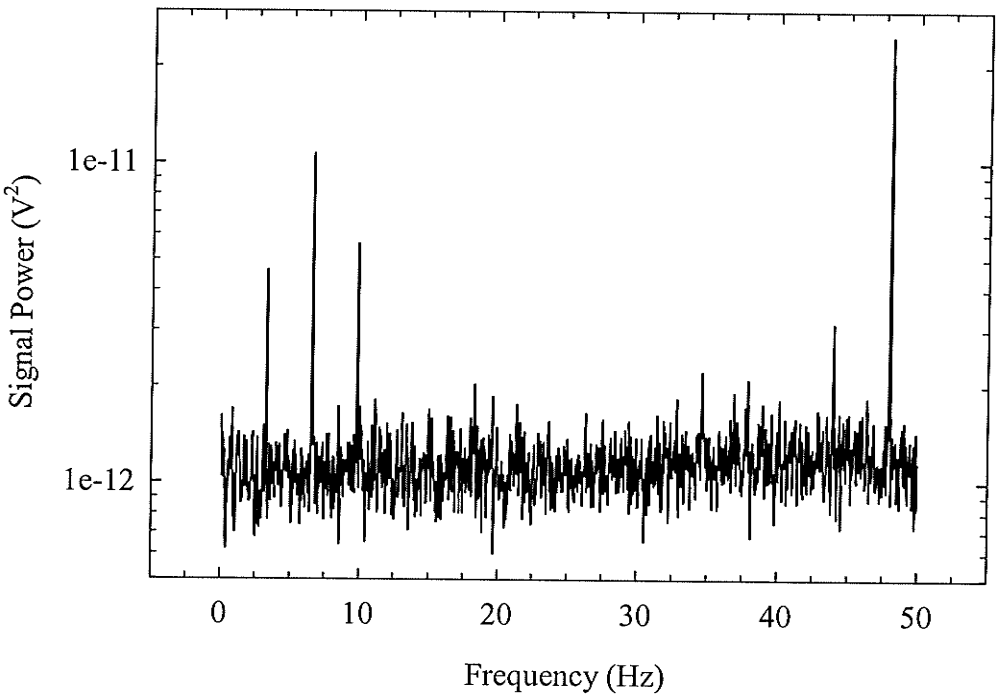

Figure 3.5 Estimated power spectrum for data collected at a sampling frequency of 100 Hz, found using $n = 4096$ and $M = 12$ ($\Delta f' = 0.0244$ Hz). A three point running average was used to smooth the power spectrum.

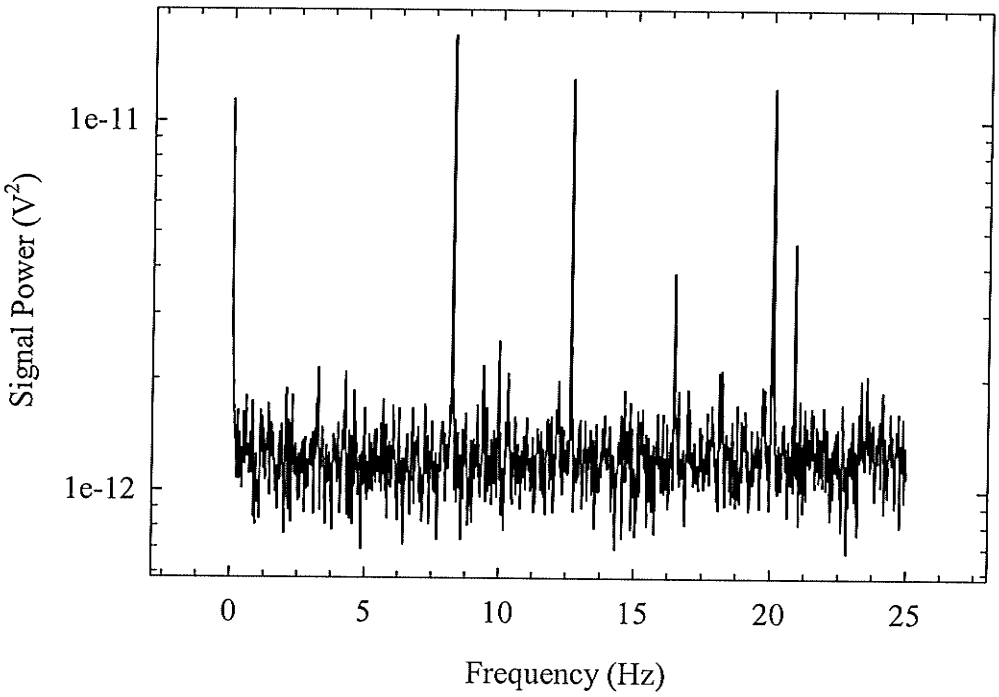

Figure 3.6 Estimated power spectrum for data collected at a sampling frequency of 50 Hz, found using $n = 4096$ and $M = 12$ ($\Delta f' = 0.0122$ Hz). A three point running average was used to smooth the power spectrum.

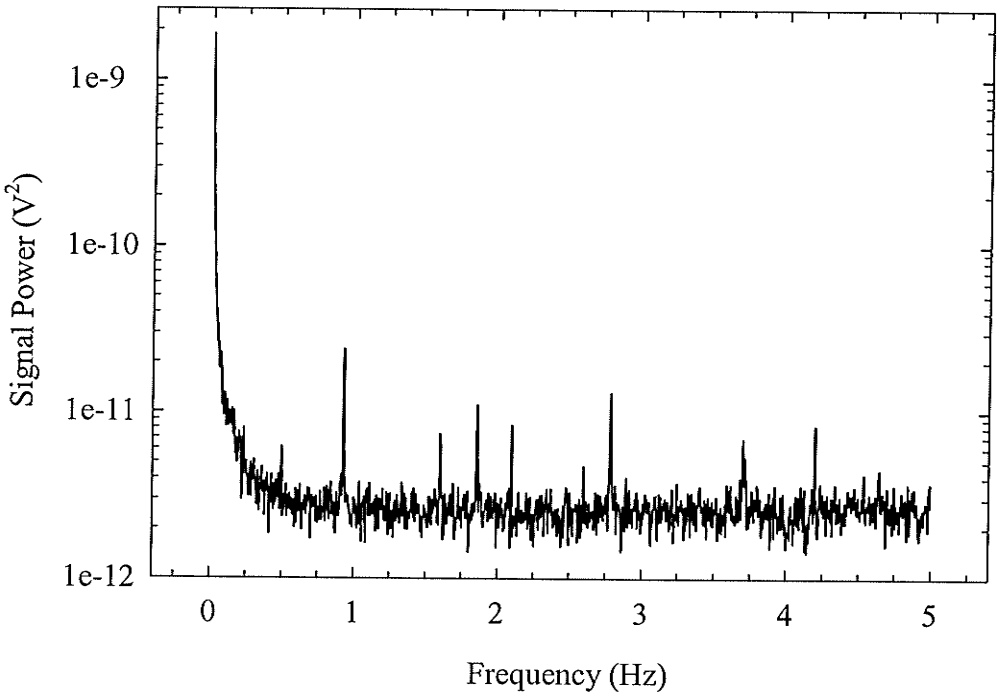

Figure 3.7 Estimated power spectrum for data collected at a sampling frequency of 10 Hz, found using $n = 4096$ and $M = 12$ ($\Delta f' = 0.00244$ Hz). A three point running average was used to smooth the power spectrum.

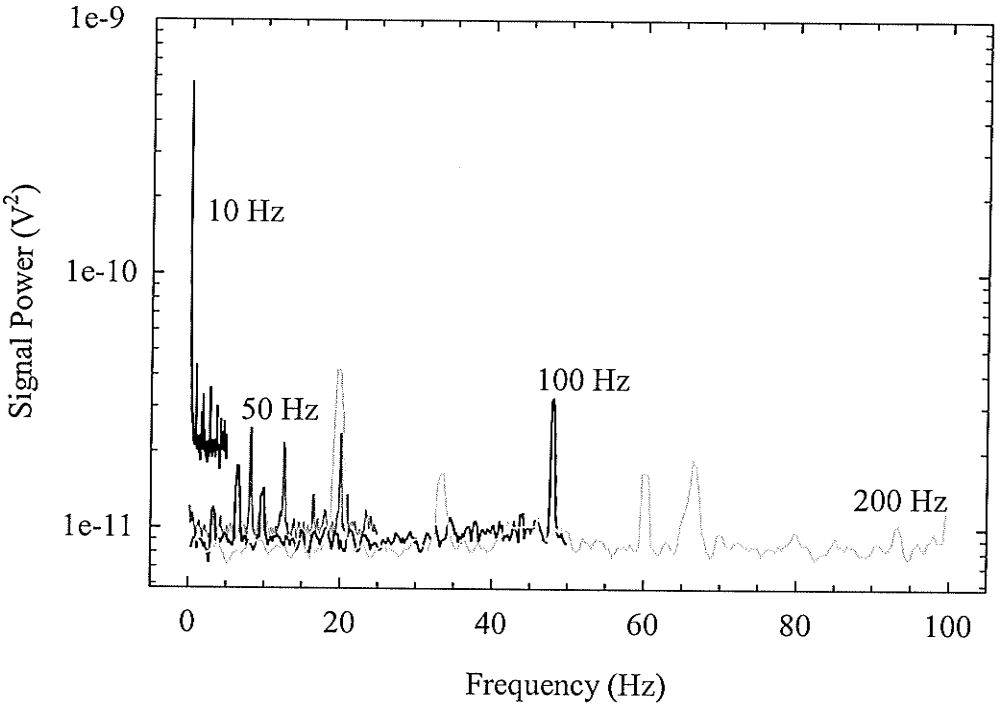

Figure 3.8 Estimated power spectra for (i) 10 Hz data ($\Delta f' = 0.0195$ Hz); (ii) 50 Hz data ($\Delta f' = 0.0977$ Hz); (iii) 100 Hz data ($\Delta f' = 0.1953$ Hz); and (iv) 200 Hz data ($\Delta f' = 0.3906$ Hz), found using $n = 512$ and $M = 97$.

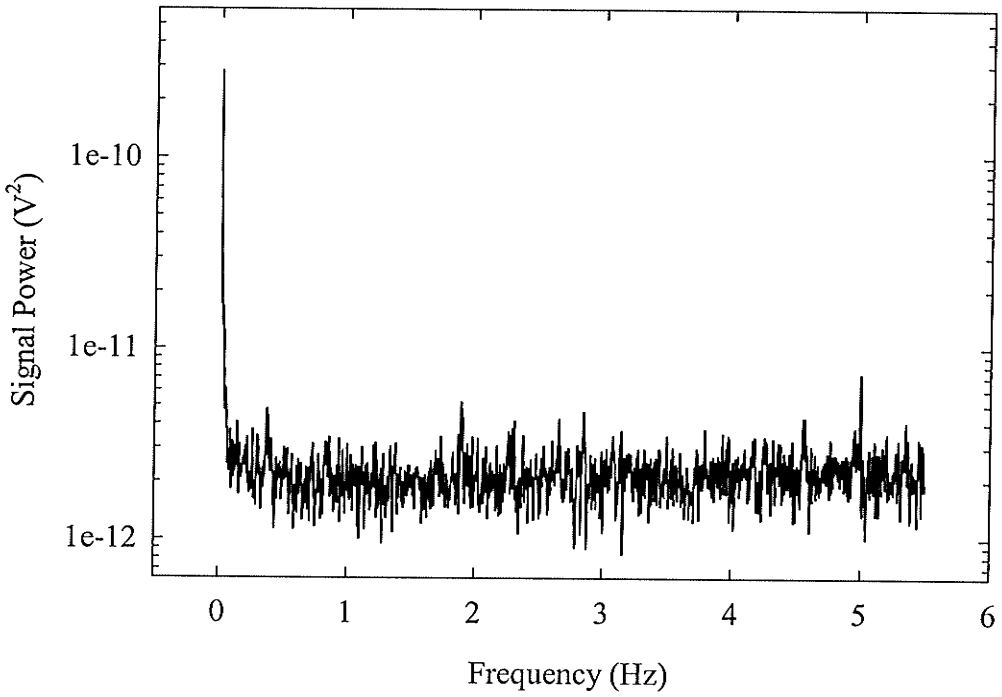

Figure 3.9 Estimated power spectrum for data collected at a sampling frequency of 11 Hz, found using $n = 4096$ and $M = 6$ ($\Delta f' = 0.00269$ Hz). A three point running average was used to smooth the power spectrum.

3.2.3.4 Relationship between the ACVF and the Power Spectrum

To validate (3.45) derived in §3.2.1.3, the area under the power spectrum (LHS) was found and compared to the summation of the square of the detector output (RHS). The results for all sampling frequencies and $n = 512$, $M = 97$ are listed in Table 3.7. Other combinations of n and M yielded comparable results. As can be seen, the agreement between $\sum_{k=0}^{n-1} \overline{C}_{VV}(k)$ and $\frac{1}{N}\sum_{m=0}^{M-1}\sum_{j=0}^{n-1} V_m^2(j)$ is excellent.

Table 3.7 Verification of (3.45)

Sampling Frequency (Hz)	n	$\sum_{k=0}^{n-1} \overline{C}_{VV}(k)$	$\frac{1}{N}\sum_{m=0}^{M-1}\sum_{j=0}^{n-1} V_m^2(j)$
10	512	15.6328×10^{-9}	15.6328×10^{-9}
50	512	5.37626×10^{-9}	5.37626×10^{-9}
100	512	4.91300×10^{-9}	4.91300×10^{-9}
200	512	4.79447×10^{-9}	4.79447×10^{-9}

3.3 Quantum Noise Measurements

The noise in the detector output when measuring radiation includes both photon quantum noise and electronic noise. Quantum noise is a consequence of the discrete number of photons N recorded by the detector. Measurements were carried out to determine the standard deviation and the signal-to-noise ratio (SNR) in the detector output as a function of measured fluence transmitted through a variable attenuator. Although the noise given by $\sqrt{N}$ decreases with increasing attenuator thickness due the decrease in the number of transmitted photons, the SNR = signal/noise = $N/\sqrt{N} = \sqrt{N}$ also decreases. The goal of this section is to demonstrate that the electronic noise is less than the quantum noise for the range of expected attenuation provided by the patient in the clinical operation of the scanner. Additional measurements were performed at three source-to-detector distances (SDD) to determine the power spectrum for three different signal levels.

3.3.1 Method

3.3.1.1 Plexiglas Attenuator Measurements

The noise in the detector output was measured using the experimental set-up shown in Figure 3.10. The detector was placed 82.5 cm from the 5.31 Ci ^{192}Ir source. Lead plates with dimensions 1x14x14 cm^3 were placed above and below both the detector and the source with a 1.1 cm spacing to provide collimation. The γ-ray intensity incident on the detector was varied by placing different thicknesses of Plexiglas in the beam path. A total of 250 readings (sampling rate of 10 Hz) were taken for each Plexiglas thickness. These were averaged and corrected for dark current. The noise was taken to be the standard deviation in these measurements.

3.3.1.2 Power Spectrum Measurements

The power spectrum data was collected using an uncollimated 8.56 Ci source, minimal detector collimation (two widely spaced 5 cm thick lead blocks to protect the electronics) and a sampling frequency of 100 Hz. The SDD was varied from 34 cm to 74 cm in 20 cm increments. Power spectra were found by applying (3.37) to zero mean data.

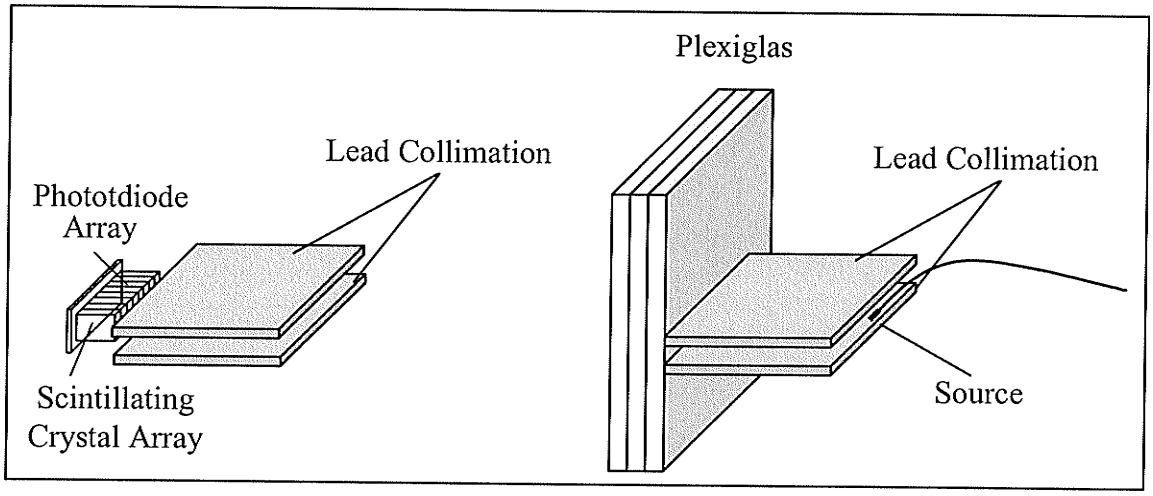

Figure 3.10 Experimental set-up used to measure the total detector noise. The geometry of the source and detector collimators is similar to that of the final scanner.

3.3.2 Results

3.3.2.1 Plexiglas Attenuator Measurements

For the measurements collected as a function of attenuator thickness, the noise is presented in form of the total SNR defined as

$$\mathrm{SNR}_{\mathrm{total}} = \frac{\mathrm{Signal}}{\mathrm{Noise}} \tag{3.46a}$$

where "Signal" is the average measured detector output and "Noise" is the standard deviation in the measured detector output. The error in the SNR was determined using the expression (Peebles, 1980; Bevington and Robinson, 1992)

$$\sigma_{\mathrm{SNR\ total}} = \left[\left(\frac{\sigma_{\mathrm{Signal}}}{\mathrm{Noise}}\right)^2 + \left(\frac{\sigma_{\mathrm{Noise}} \cdot \mathrm{Signal}}{\mathrm{Noise}^2}\right)^2\right]^{1/2}. \tag{3.46b}$$

where $\sigma_{\mathrm{Noise}} = \left(\sqrt{2}\mathrm{Noise}^2\right)/\sqrt{n}$, $\sigma_{\mathrm{Signal}} = \mathrm{Noise}/\sqrt{n}$ and n is the number of readings per data point (i.e. 250). Combining these expressions yields

$$\sigma_{\mathrm{SNR\ total}} = \left[\frac{1}{n} + \frac{2\,\mathrm{Signal}^2}{n}\right]^{1/2}. \tag{3.46c}$$

The electronic SNR is given by

$$\mathrm{SNR}_{\mathrm{electronic}} = \frac{\mathrm{Signal}}{115\mu\mathrm{V}} \tag{3.47a}$$

where 115 μV represents the standard deviation of the electronic noise.

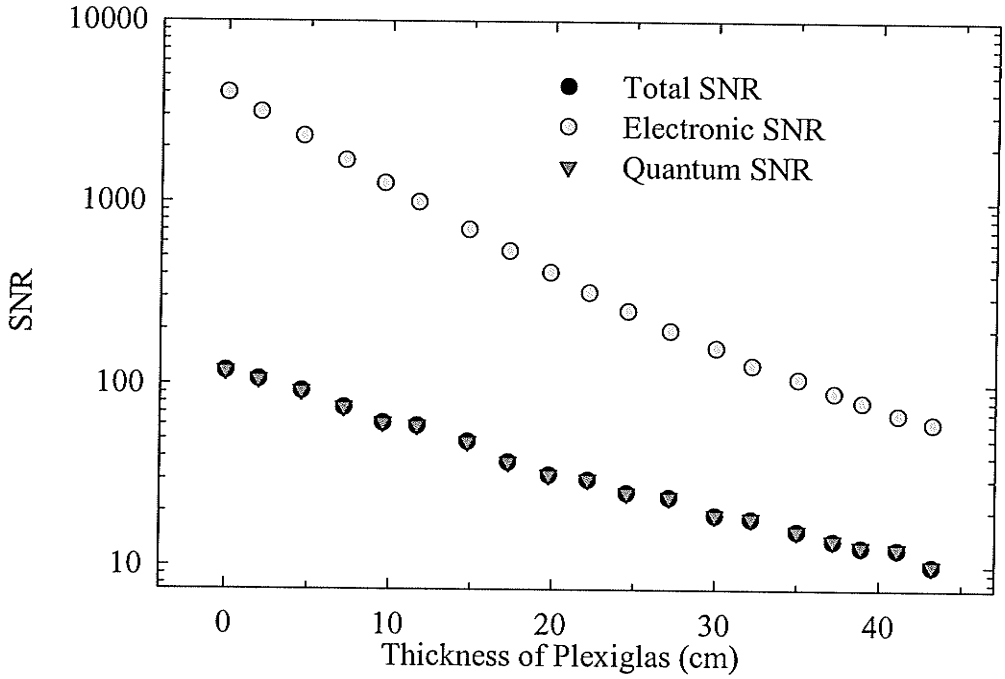

Figure 3.11a Plot of the total, electronic and quantum SNR as a function of Plexiglas attenuator thickness. The error in the SNR is smaller than the data points.

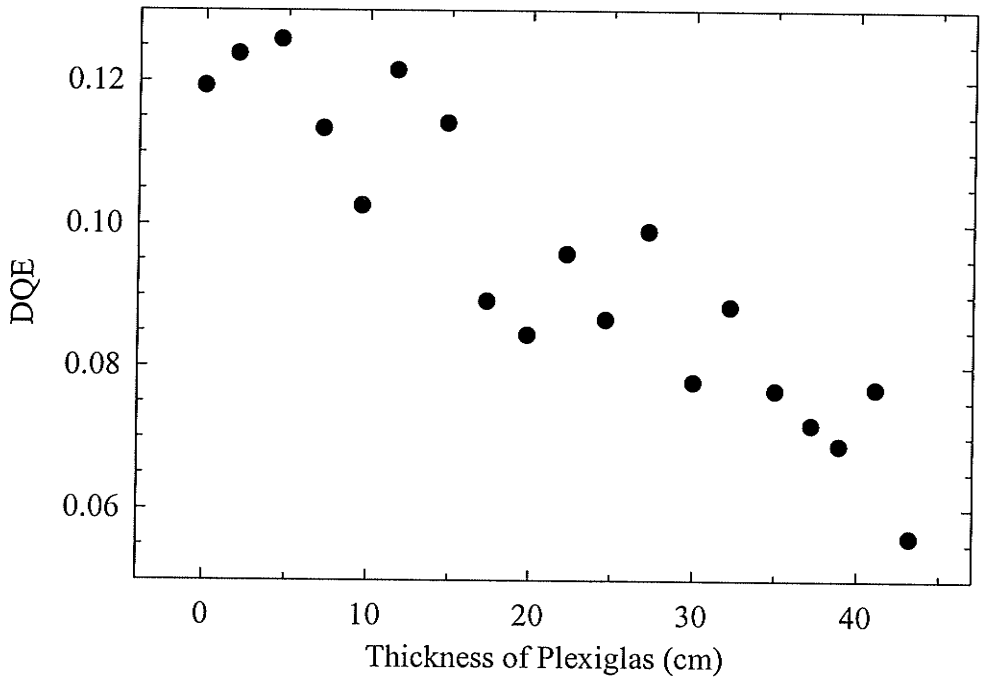

Figure 3.11b Plot of the DQE as a function of Plexiglas attenuator thickness.

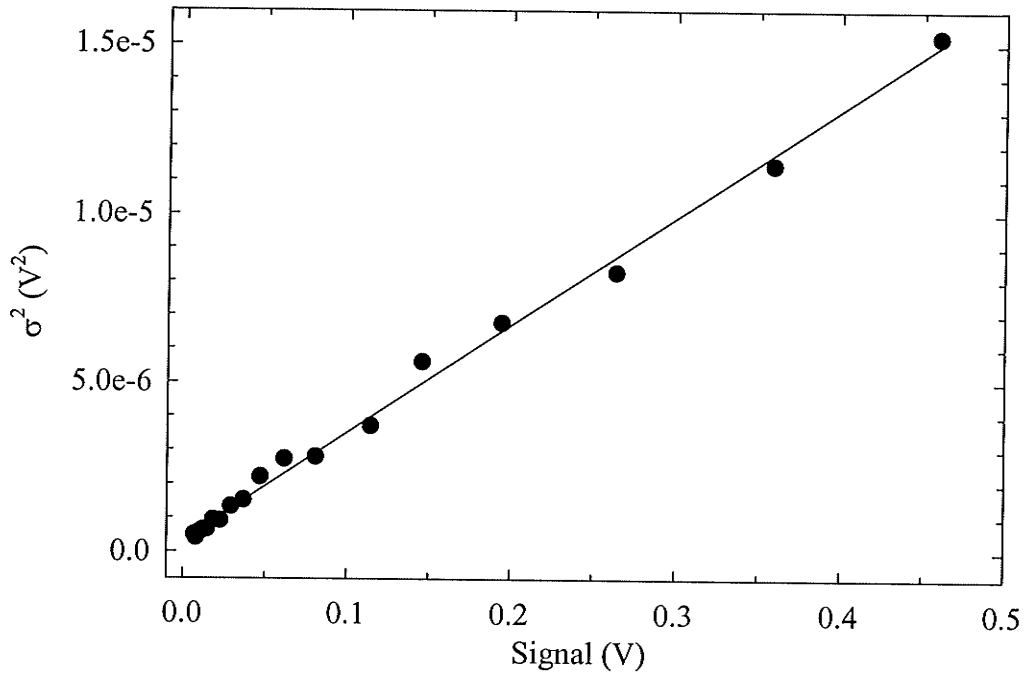

Figure 3.11c Plot of the variance in the detector signal as a function of signal. The line represents a linear regression fit to the data.

The error in the electronic SNR is

$$\sigma_{SNR_{electronic}} = \frac{\sigma_{Signal}}{115\mu V} = \frac{Noise}{\sqrt{N}\cdot 115\mu V}. \qquad (3.47b)$$

The quantum SNR, which is calculated using the quantum, rather than the total noise is given by

$$SNR_{quantum} = \frac{Signal}{\sqrt{Noise^2 - (115\mu V)^2}}. \qquad (3.48)$$

The total, electronic and quantum SNR are plotted in Figure 3.11a. As can be seen, $SNR_{electronic}$ is greater than SNR_{total} for all Plexiglas thicknesses up to 43.2 cm, indicating that the detector is not limited by electronic noise. The close agreement between the total and quantum SNR further reinforces that the electronic noise is negligible with respect to the quantum noise.

Alternatively, the detector can be characterized in terms of its detective quantum efficiency (DQE), which is defined as (Barrett and Swindell, 1981)

$$DQE = \frac{(SNR_{out})^2}{(SNR_{in})^2} \qquad (3.49)$$

where SNR_{out} is given by (3.46a) and $SNR_{in} = N/\sqrt{N} = \sqrt{N}$ where N is the number of photons incident on the detector. The number of photons in the absence of an attenuator N_o, was calculated using (6.38). The number of incident photons as a function of Plexiglas thickness was found by scaling N_o by the data in Figure 3.39, i.e., the average detector output as a function of Plexiglas thickness. The DQE found using (3.49) is plotted in Figure 3.11b. The average DQE of 0.094 indicates that our detector detects the equivalent of 9.4% of the incident photons (Barrett and Swindell, 1981). If the electronic noise is negligible, as demonstrated above, the photon statistics and DQE limit the scanner's SNR.

Mean-variance analysis (Holdsworth et al., 1990) can also be applied to the detector noise, whereby the variance in the detector output voltage σ_V^2 is expressed as

$$\sigma_V^2 = gV + \sigma_{read}^2 \tag{3.50}$$

where g is the system gain relating the number of detected γ-rays to the detector output voltage V (not to be confused with the gain of the gain-and-filter stage $G = 47$) and σ_{read} is the read noise. A plot of σ_V^2 as a function of V (Figure 3.11c) results in a graph with a slope of $g = 3.2 \times 10^{-5}$ V/γ-ray and an intercept of 3.3×10^{-7} V^2 ($\sigma_{read} = 574\ \mu$V).

The results of this section are of great importance as they demonstrate that the detector output is dominated by quantum noise, rather than electronic noise. Because photon statistics limit the scanner's SNR, further reduction of the electronic noise will not improve the SNR, indicating that the noise characteristics of the detector are acceptable.

3.3.2.2 Power Spectrum Measurements

The power spectra for SDD of 34 cm, 54 cm and 74 cm are shown in Figure 3.12. For the SDD of 34 cm, $n = 2048$ and $M = 24$ were used, while for the SDD of 54 cm and 74 cm, $n = 2048$ and $M = 18$ were used. The noise power increases with decreasing SDD because the signal, and therefore the standard deviation in the signal increases with decreasing SDD.

When comparing Figure 3.12 with Figure 3.5, it can be seen that the power line interference and other peaks have been completely obscured by the quantum noise. In

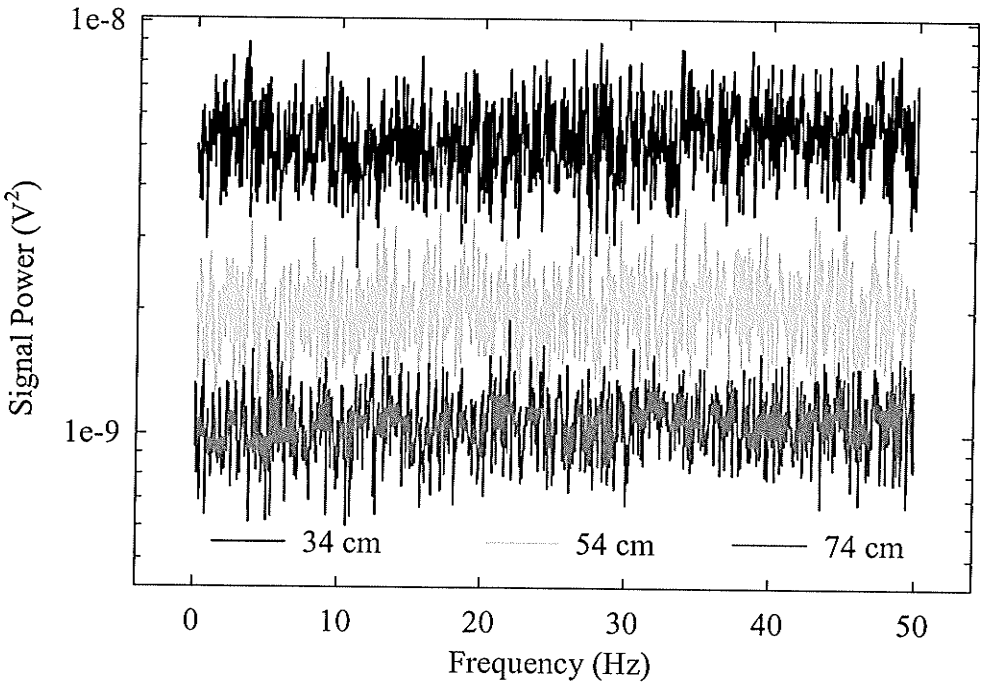

Figure 3.12 Noise power as a function of frequency for source-to-detector separations of 34 cm, 54 cm and 74 cm. A three point running average was used to further smooth the data.

addition, the total noise power at all frequencies is much larger than in Figure 3.5 because of the quantum noise.

3.4 Detector Response as a Function of Light Intensity

The first step in characterizing the output voltage of the detector assembly was to assess the photodiode response to optical photons. The purpose of these measurements was to assess the linearity of the photodiode and associated electronics as a function of luminous intensity. Measurement of the photodiode response to various light levels related the detector output voltage to the incident light intensity, from which the photosensitivity could be found.

The apparatus shown in Figure 3.13 was used to measure the light response of the detector. A 150 mCandela, green light-emitting diode (LED) ($\lambda_{\text{peak-LED}}$ = 560 nm, 535 nm $\leq \lambda_{\text{LED}} \leq$ 605 nm), which very approximately resembles the spectral output of the scintillating crystal ($\lambda_{\text{peak-CdWO}_4}$ = 470 nm, 400 nm $\leq \lambda_{\text{CdWO}_4} \leq$ 600 nm), was used to illuminate the photodiode array. The LED was powered using a 10 V DC power supply,

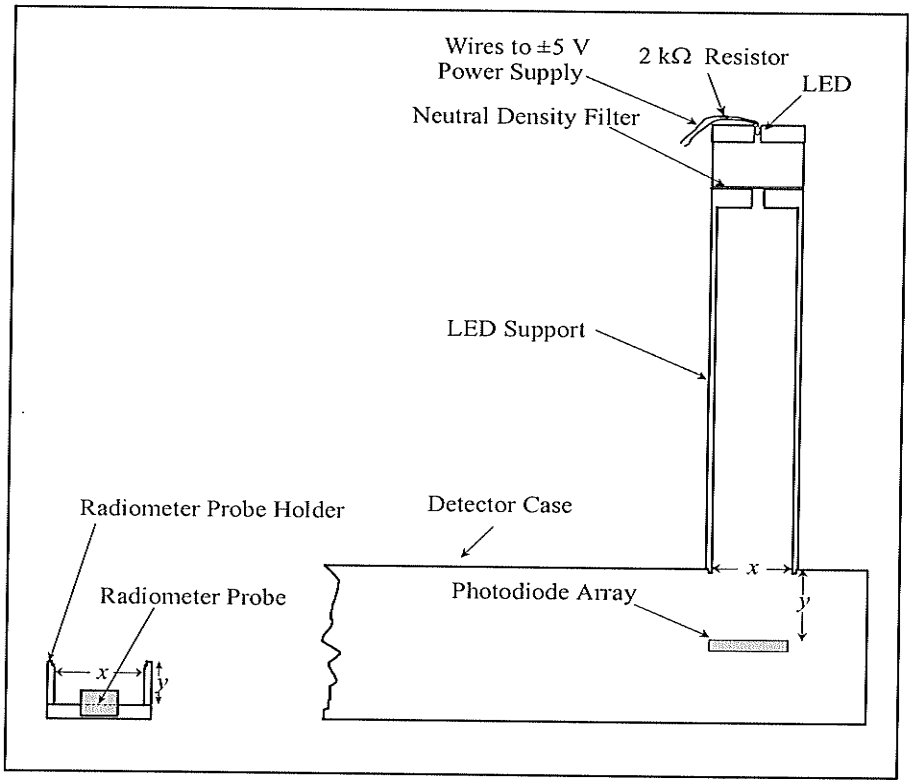

Figure 3.13 Schematic of the light source and detector holder used for the light response measurements. The distances x and y are identical in both detector (radiometer probe and photodiode array) holders, and are equal to 4.40 cm and 1.65 cm respectively. This arrangement allowed for the reproducible interchange of the radiometer probe and photodiode array so that the two detectors could be irradiated at identical light levels.

and connected in series with a 2 kΩ resistor to limit the current flowing through the LED. The LED was mounted at one end of a tube 4.4 cm in diameter and approximately 11 cm long. The purpose of the setup illustrated in Figure 3.13 was to allow interchange of the photodiode array with a radiometer probe (International Light 730A U.V. Actinic Radiometer; Model SEE 100 Detector with a CA 224 #11579 aperture and an F #11433 filter), where the latter device provided an absolute measurement of the light intensity in W/cm^2.

3.4.1 Neutral Density Filter Calibration

3.4.1.1 Method

A series of neutral density filters (Melles Griot) were placed in front of the light source to vary the light intensity incident on the photodiode array or radiometer probe. The

transmission of the neutral density filters was measured at 500 nm using a spectrophotometer (Pharmacia Biotech Ultrospec 2000 Spectrophotometer). The transmission was also measured as a function of wavelength with a scanning spectrophotometer (Varian CARY1 UV-Visible Spectrophotometer) to investigate their spectral response.

3.4.1.2 Results

The manufacturer's and measured optical density (O.D.) values for the filters are listed in Table 3.8. As can be seen, the measured values differ from the manufacturer's values by up to 20%. This is likely due to deterioration of the coating on the filters with age, which is about 15 years. The measured O.D. values were used for all ensuing calculations. Figure 3.14 plots O.D. versus wavelength for the neutral density filters listed in Table 3.8. The O.D. is relatively constant with wavelength for $\lambda > 350$ nm. The variation in O.D. for $\lambda < 350$ nm will not affect the outcome of the measurements described below, as the photodiode is not sensitive to wavelengths in this range. Similarly, the radiometer response drops to 50% of its maximum value at 360 nm, and reaches 0 at 320 nm.

Table 3.8 O.D. of the neutral density filters at 500 nm.

Nominal O.D.	Manufacturer's O.D.	Measured O.D.
0.1	0.098	0.095
0.2	0.205	0.172
0.3	0.298	0.296
0.4	0.380	0.361
0.5	0.475	0.460
0.6	0.612	0.608
0.7	0.720	0.708
0.8	0.750	0.757
0.9	0.900	0.817
1.0	1.000	0.993
1.5	1.540	1.517
2.0	1.880	1.835
2.5	2.605	2.568
3.0	2.965	2.932
4.0	3.950	Not Available

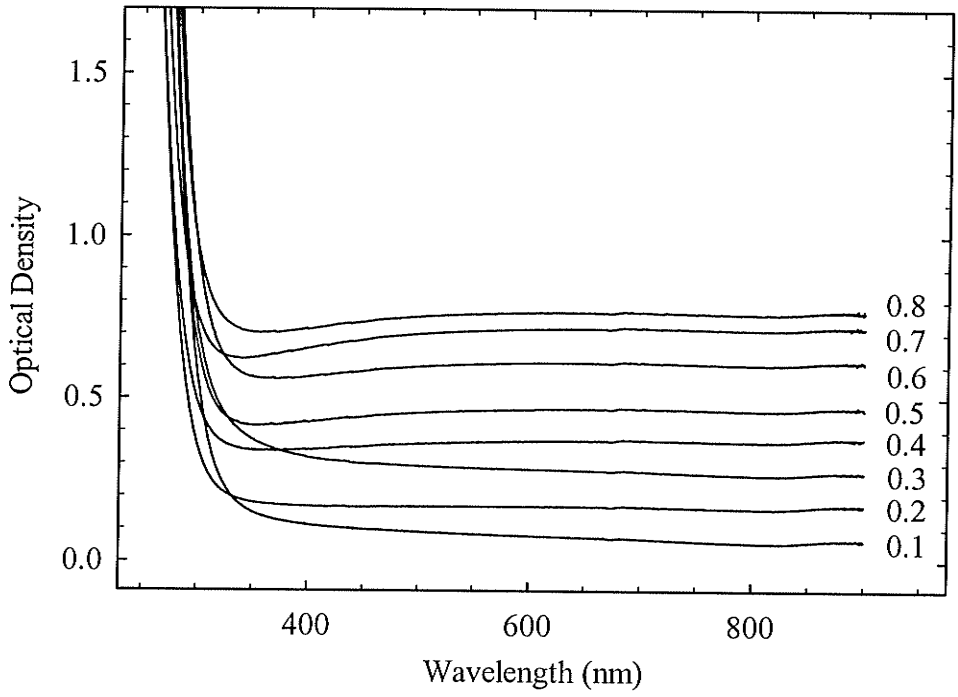

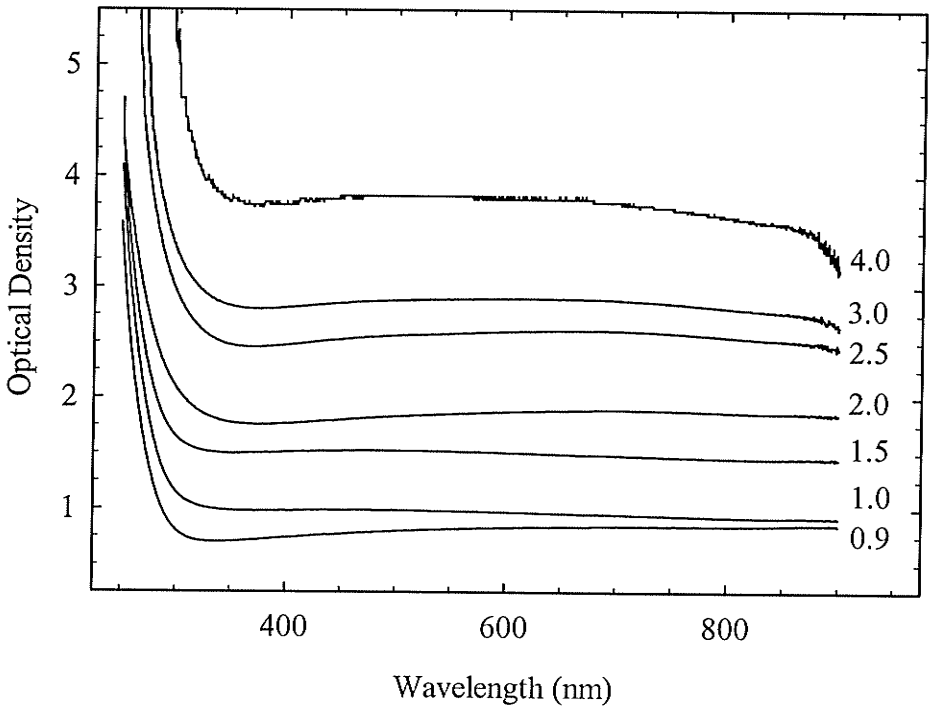

Figure 3.14 O.D. plotted as a function of wavelength for the neutral density filters listed in Table 3.8. The values listed beside the curves are the nominal optical densities.

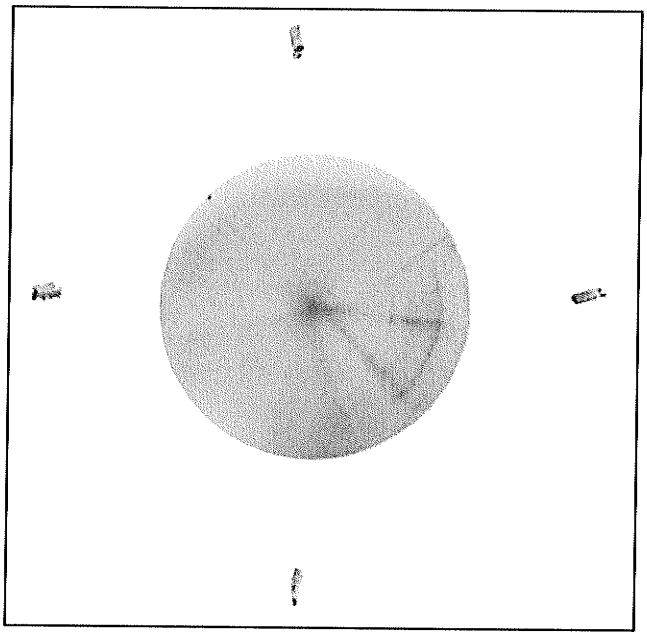

Figure 3.15 Negative image of the light source. The four ticks coincide with corresponding markers on the LED support. Note the large non-uniformity in the light source illumination, especially near the centre of the image.

3.4.2 Light Source Uniformity and Intensity Correction

The radiometer provides an absolute measurement of the light intensity incident on the photodiode array. If the light source provided a spatially uniform light intensity, the light intensity measured by the radiometer would be identical to that incident on the photodiode array. However, a photographic film exposed to the light of the LED at the base of the LED support (Figure 3.15) shows substantial spatial non-uniformities in the light intensity. Because the light source intensity is spatially varying, the light intensity incident on each of the photodiodes in the array is not the same. The purpose of this section is to find conversion factors relating the average light intensity incident on the radiometer aperture to the average light intensity incident on each of the individual photodiode array elements. These allow determination of the absolute light intensity incident on the photodiode array elements, from which the photodiode sensitivity can be found, as described in §3.4.5. The steps performed to find conversion factors are as follows:

(i) reduce the light source intensity variations to minimize the errors associated with the spatial registration of the radiometer probe and the photodiode array elements;

(ii) illuminate a film with the light source to assess residual intensity variations;
(iii) convert the grey-scale values in the film (digitized using a film scanner) to O.D., as O.D. can be related to the incident light levels;
(iv) register the radiometer probe and the photodiode array elements with respect to the film created in step (iii); and,
(v) determine the conversion factors relating the average light intensity incident on the radiometer aperture to that incident on the photodiode array elements, using the O.D. of the regions in the film corresponding to these detectors.

Reduction of the Light Source Intensity Variations

Determination of the conversion factors requires accurate geometric registration of the photodiode array elements and radiometer probe with respect to the light source. The inherent large non-uniformity in the light intensity complicates this procedure since even a small registration error will result in sizable variations in the light intensity calculated to fall on the photodiode array elements and the radiometer probe.

To reduce the intensity variations, a diffuser (created by sanding an overhead transparency with fine sandpaper to render it translucent) was placed directly below the neutral density filter shown in Figure 3.13. A second film shown in Figure 3.16 was illuminated using the light source. It can be seen that although the illumination was much more uniform, significant intensity variations were still present. To remove these, a mask was created using the film shown in Figure 3.16. The position of the LED support was carefully marked on the film. More specifically, four notches at 0°, 90°, 180° and 270°, respectively, etched into the LED support were traced onto the film with a marker, just before the film was illuminated. The image of the light source was then cut out of the developed film, and taped to the inside of the LED support at the end closest to the detector, taking care to align the four tick marks on the film with the notches etched into the LED support. The resulting mask compensated for the non-uniformities in the light source illumination; wherever the light source illumination was bright, a dark region resulted on the developed film, while regions on the film that were not as brightly illuminated by the light source remained undarkened. Thus the dark areas in the film

filtered the regions of bright illumination produced by the light source, while the regions of less illumination passed through the less dense areas of the film.

A third film taken to test the effectiveness of the mask is shown in Figure 3.17. As can be seen, the light source output was much more uniform than in Figure 3.16. However, some residual non-uniformity remained, meaning that the light intensity measured by the radiometer could still not be exactly related to that incident on each photodiode array element.

Conversion of Grey Scale Value to Optical Density

The film of the light source with the diffuser and mask in place (Figure 3.17) was digitized to a precision of 12 bits using a film scanner (Lumiscan 50, Lumisys, Inc.). To quantitatively compare the light intensity incident on the photodiode array elements and the radiometer probe, the O.D. of the regions of the film corresponding to the photodiode array elements and radiometer probe are required. To convert the grey scale value produced by the film scanner into an O.D., the lower corner of the film was illuminated with a sensitometer step wedge (X-rite 333 Dual Color Sensitometer). The O.D. within each different region of the stepwedge image was found using a densitometer (Sargent-Welch model PDD). Results were then mapped to the corresponding average grey scale values found using image processing software (IPLab 3.2.2 Eval Scanalytics Inc.). A plot of the O.D. as a function of grey scale value is shown in Figure 3.18. As the maximum O.D. in Figure 3.17 is less than 1.0, only the linear portion of the data in Figure 3.18 is of interest. A straight line fit to the data with grey scale value (GSV) $\leq$ 1538 found the relationship

$$\text{O.D.} = 0.0007525\ \text{GSV} - 0.11764. \tag{3.51}$$

The variation about the regression line may be characterized by the standard error of estimate with respect to the mean S_m (Crow et al., 1960) given by

$$S_m = \frac{\sum (y_i - y_i')^2}{(n-2)y_m} \tag{3.52}$$

where y_i indicates the experimentally collected data points, y_i' represents the corresponding points along the regression line, y_m is the midpoint of the range of all y_i values, and n is the number of data points used to form the regression line. The $n-2$ in

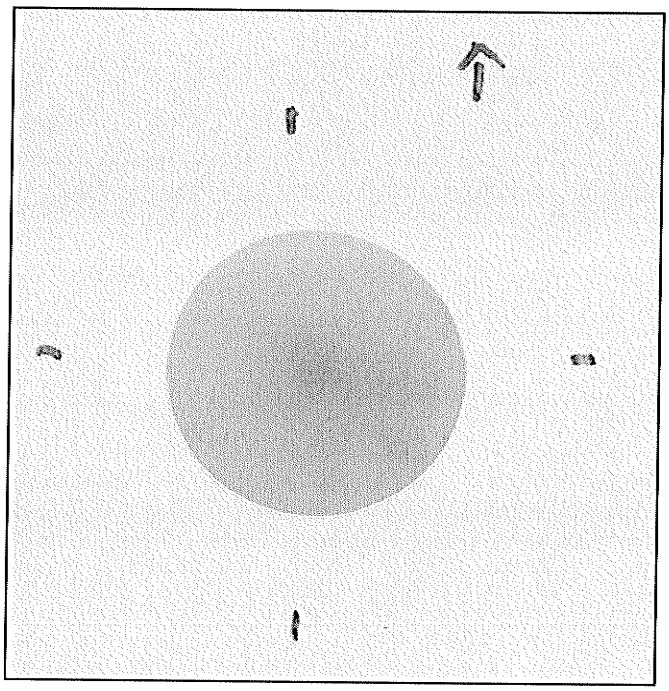

Figure 3.16 Negative image of the light source with the diffuser in place. The four ticks coincide with corresponding markers on the LED support, while the arrow indicates the orientation of the LED support. Note that the non-uniformity present in Figure 3.15 is now much more diffused.

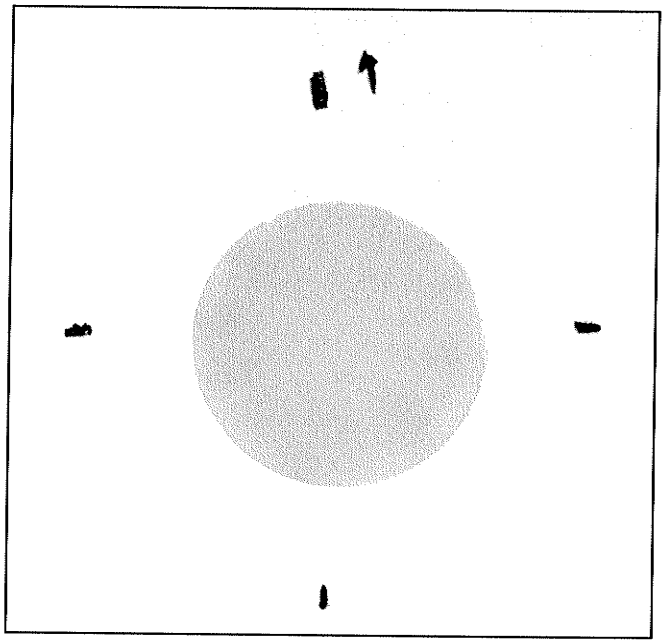

Figure 3.17 Image of the film used to assess the light source uniformity. The four ticks coincide with corresponding markers on the LED support, while the arrow indicates the orientation of the LED support.

the denominator represents the degrees of freedom of the fit, where the two has been subtracted to account for the two degrees of freedom (the slope m and the intercept b) incorporated by the line. The standard error of estimate with respect to the mean for the fit in Figure 3.18 is 0.18%, indicating that on average, the data follow a straight line to within 0.18%.

Geometrical Registration

The relative light intensity incident on each detector can be determined from the O.D. of the regions in the film (Figure 3.17) corresponding to the positions of the photodiode array elements and the active area of the radiometer probe. This requires registering both detectors with respect to the film. The was achieved by registering the film with respect to the LED holder (ticks coinciding with notches on the LED support were drawn onto the film), and then registering the LED holder with respect to both detectors using corresponding reference marks drawn onto the detector case and radiometer probe holder. Thus, the orientation of the film with respect to both detectors was established.

Because the radiometer was centered directly below the LED holder, the active detecting region of the radiometer (diameter 0.7 cm) corresponded to the centre of the image in Figure 3.17. The size of the detector aperture on the film image was found and image processing software (IPLab 3.2.2 Eval Scanalytics Inc.) used to determine the average grey scale value associated with that region. The O.D. found using (3.51) is listed in Table 3.9.

The orthogonal laser system of a CT simulator was used to register the photodiode pairs to the reference marks on the detector case. Using the reference marks on the film and the detector case, the area of the film corresponding to each photodiode element pair was found, and the average grey scale value determined. The resulting O.D. values found using (3.51) are listed in Table 3.9. Figure 3.19 shows the O.D. profile through Figure 3.17 at the level of the photodiode array. The grey bars represent the average O.D. of the film over each photodiode element pair. The centre of each bar coincides with the centre of each channel. Note that the inactive regions between the photodiode elements were ignored when averaging.

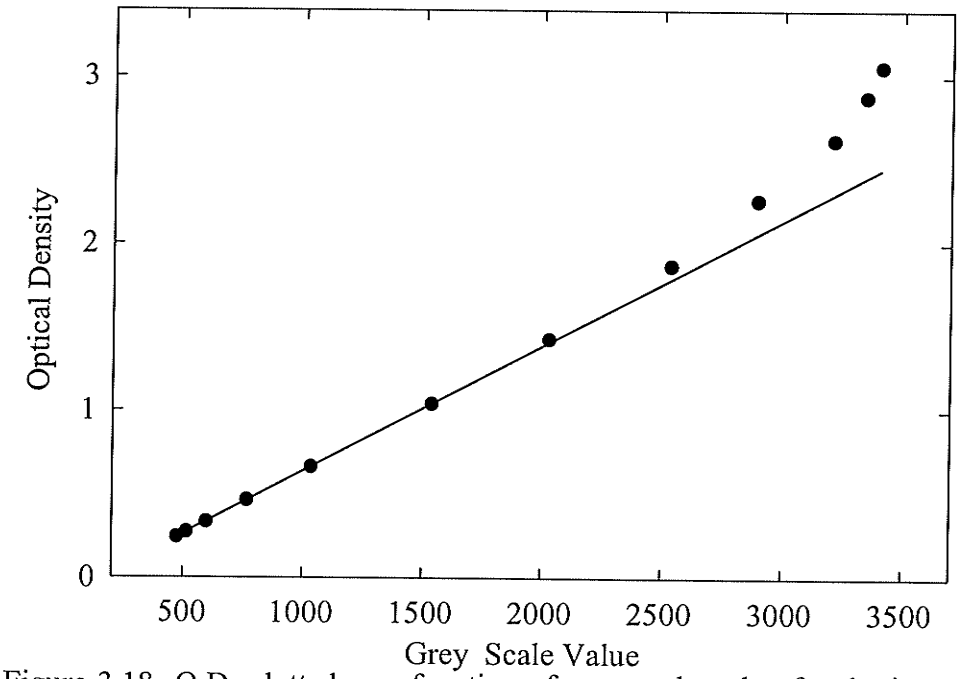

Figure 3.18 O.D. plotted as a function of grey scale value for the image shown in Figure 3.17.

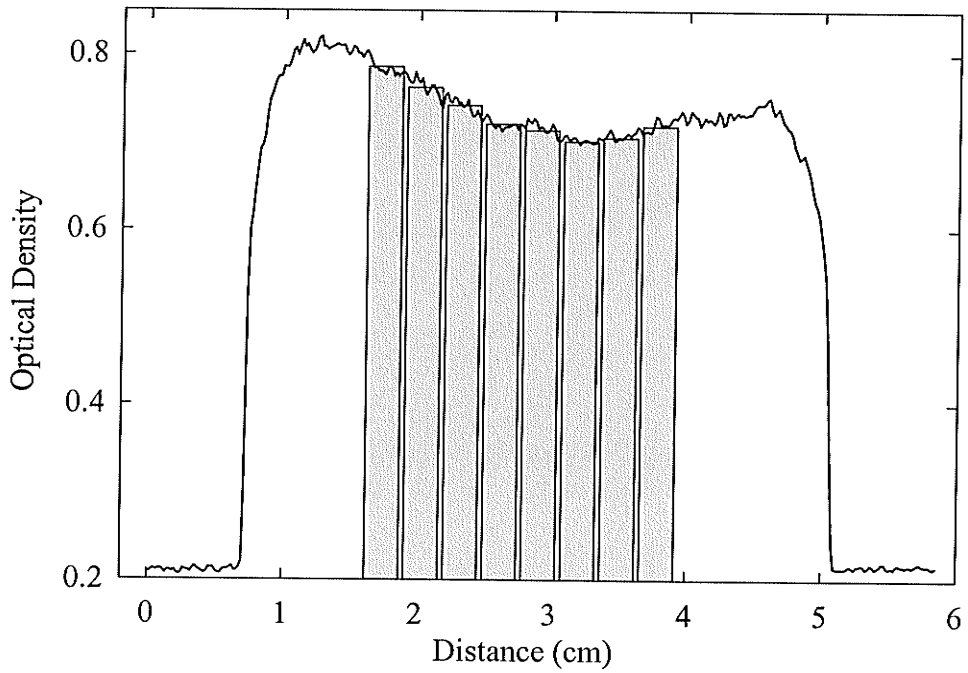

Figure 3.19 O.D. profile through Figure 3.17 at the level of the photodiode array. The bars indicate the light intensity averaged over each photodiode element pair. The positioning of the bars coincides with the actual locations of the channels, where the channels are numbered from 1 to 8, going from right to left, and the width of the bars is equal to the width of the photodiode element pairs.

Table 3.9 Incident light intensity

Film Region	Grey Scale Value	O.D.
Channel 1	1109.4 ± 7.5	0.719 ± 0.006
2	1092.9 ± 5.6	0.705 ± 0.004
3	1088.2 ± 6.6	0.701 ± 0.005
4	1105.0 ± 7.1	0.713 ± 0.005
5	1114.5 ± 5.9	0.721 ± 0.004
6	1143.7 ± 10.6	0.742 ± 0.008
7	1170.2 ± 11.4	0.762 ± 0.009
8	1200.9 ± 10.2	0.785 ± 0.008
Radiometer	1103.5 ± 9.5	0.713 ± 0.007

Conversion of Optical Density to Relative Incident Light Intensity

The relationship between the O.D. and the incident light intensity is determined by the H & D curve, which is a plot of film O.D. as a function of log(exposure) (Barrett and Swindell, 1981). For small variations in exposure (i.e., light intensity) ΔE, the resulting variation in optical density ΔO.D. is given by (Barrett and Swindell, 1981)

$$\Delta \text{O.D.} = 0.434\gamma(\Delta E / E) \tag{3.53}$$

where γ is the slope of the H & D curve at exposure E. The relative exposure incident on two areas of the film with different densities can then be found, providing γ is known.

In order to determine γ, the H & D curve was found for the film (Kodak T-MAT G/RA) and processor (Kodak RP X-OMAT Processor) used to generate all of the above images. A strip of film was illuminated using the green setting (peak wavelength = 510 nm) of a sensitometer step wedge (X-rite 333 Dual Color Sensitometer). The log relative exposure between steps is 0.15. The resulting H & D curve is shown in Figure 3.20.

The variation between the optical densities listed in Table 3.9 is small, validating the use of (3.53). The H & D curve (Figure 3.20) was found to have a slope of γ = 1.9 between O.D. = 0.7 and O.D. = 0.8. The difference in O.D. between Channel 4 (channel used for all subsequent measurements in this section) and the radiometer is ΔO.D. = 0.0, resulting in ΔE = 0. Thus, the average light intensity incident on the Channel 4 photodiode array elements equals the average light intensity incident on the radiometer.

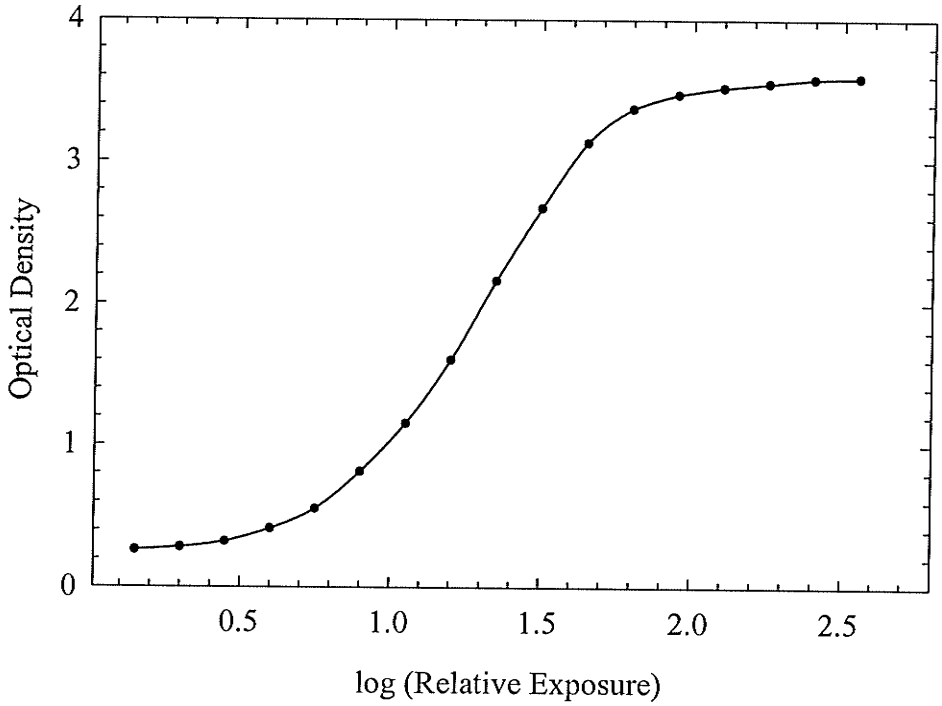

Figure 3.20 Plot of O.D. as a function of log(relative exposure), generated by illuminating a Kodak T-MAT G/RA film using the green setting of an X-rite 333 Dual Color Sensitometer step wedge, and then processing the film using a Kodak RP X-OMAT Processor.

3.4.3 Light Source Calibration

3.4.3.1 Method

The light source output was calibrated by measuring its intensity (W/cm^2) with various neutral density filters placed in the beam. These measurements were made using a radiometer (International Light 730A U.V. Actinic Radiometer) and an associated probe (Model SEE 100 Detector with a CA 224 #11579 aperture and an F #11433 filter). The output of the light source was measured five times for each of the neutral density filters.

3.4.3.2 Results

Optical density is defined as

$$\text{O.D.} = \log\frac{\phi_o}{\phi} \tag{3.54}$$

where ϕ and ϕ_o are the transmitted and incident light intensities respectively. This equation can be rearranged to give

$$\log(\phi) = -\text{O.D.} + \log(\phi_o)$$
$$y = mx + b. \tag{3.55}$$

Equation (3.55) is a linear relationship between logarithmic exposure and O.D. with a slope $m = -1$ and an intercept $b = \log(\phi_o)$.

Figure 3.21 shows the measured intensity (W/cm^2) of the light source as a function of optical density. The slope of the straight line fit shown in Figure 3.21 found using the data with $0 \leq$ O.D. < 2.6 is -1.002 ± 0.005, which is in agreement with the expected value of –1.000. Figure 3.22 shows the residuals between the linear regression line and the average light intensity. It can be seen that the largest deviations are less than 1.2×10^{-9} W/cm^2 and occur primarily for O.D. < 1.0. Evaluating (3.52) for the data and least-squares fit line in Figure 3.21 gives a standard error of estimate with respect to the mean of 0.16%, which means that, on average, the data follow a straight line to within 0.16%. It can therefore be concluded that the radiometer response is linear for the light intensities transmitted by the neutral density filters in the range $0 \leq$ O.D. < 2.6.

3.4.4 Detector Linearity

3.4.4.1 Method

To determine the linearity of the detector response to visible light, the photodiode array was illuminated directly using the light source. The detector output voltage was measured using a 10.0 Hz sampling frequency with various neutral density filters placed in the path of the light source. O.D. values greater than 3.95 were achieved by stacking two filters together, and summing their optical densities. A total of 50 data points were collected for each measurement. These were averaged and corrected for dark current. Five trials were performed for each neutral density filter combination.

Recalling the discussion in §2.3.1.2, the output voltage of the photodiode detector is proportional to the photocurrent. The latter is, in turn, proportional to the light intensity incident on the photodiode array. Therefore (3.54) and (3.55) are also valid if the light intensity ϕ is replaced by the output voltage V of the detector. The expression relating the detector output V to the O.D. is then

$$\log(V) = -\text{O.D.} + \log(V_o) \tag{3.56}$$

where V_o is the voltage in the absence of a neutral density filter. As was the case in

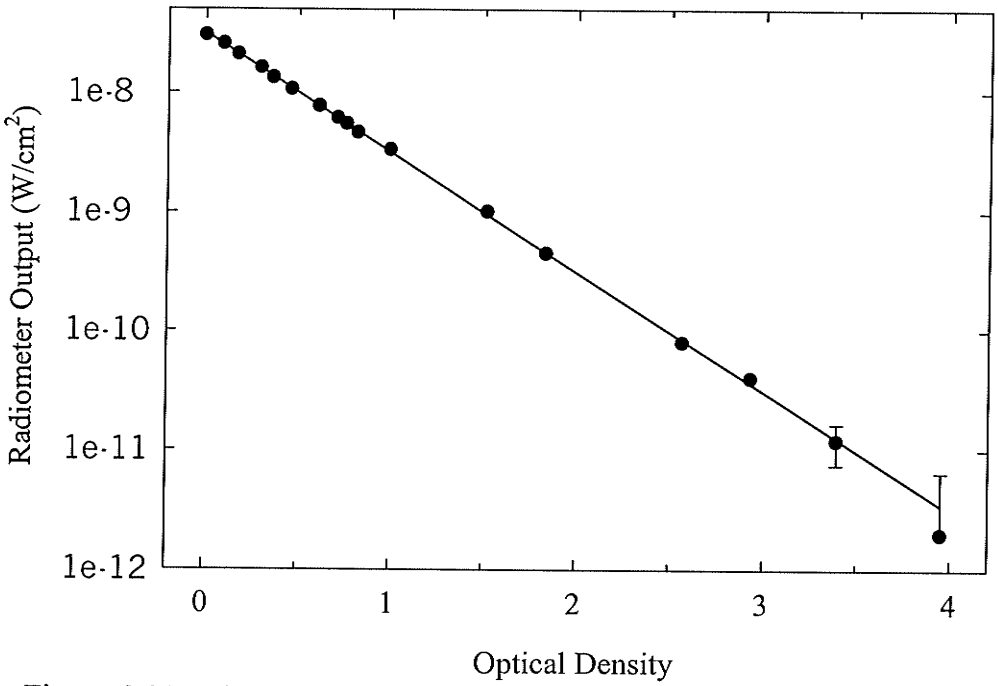

Figure 3.21 Plot showing the light source calibration data plotted as a function of the O.D. of the filters used to modulate the light intensity. Shown is the average of five trials where the error bars represent one standard deviation. The least-squares fit was found using the data for $0 \leq$ O.D. < 2.6.

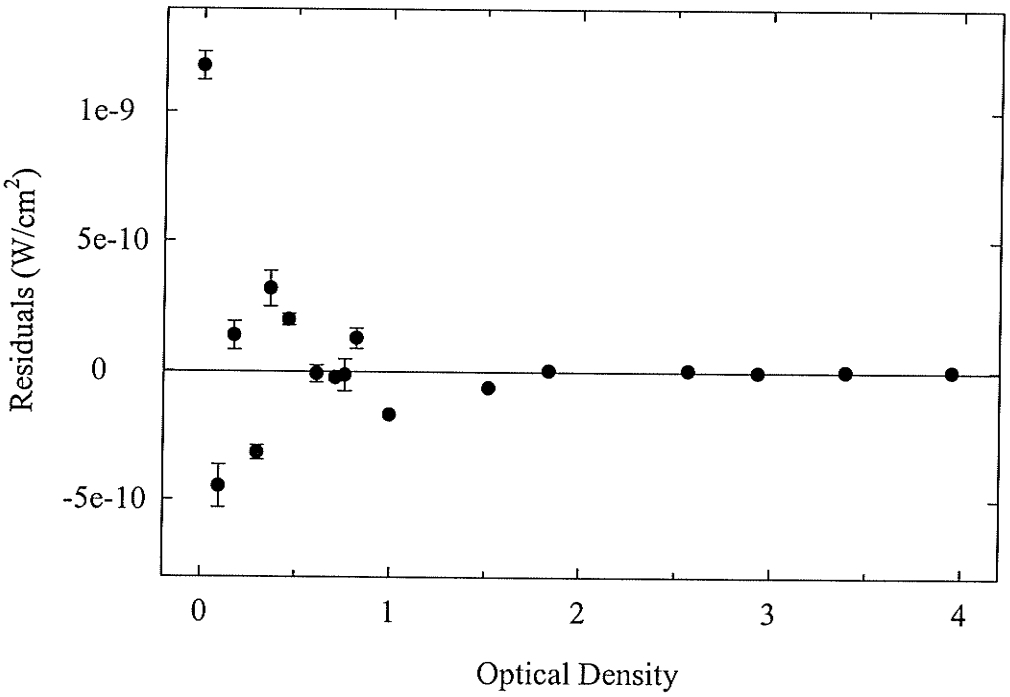

Figure 3.22 Residuals for the light source calibration data and the least-squares fit line shown in Figure 3.21.

§3.4.3.2, the slope of a plot of log(V) versus O.D. is expected to equal –1 if the detector response is linear.

3.4.4.2 Results

The detector output is plotted as a function O.D. in Figure 3.23. The reproducibility of the voltage measurements was fairly good for O.D. < 4. For the lower light intensities associated with larger O.D. values, the electronic noise of the detector circuit, as discussed in §3.1, becomes comparable to the signal level. The slope of the least-squares fit line in Figure 3.23, found for data corresponding to optical densities in the range 0 ≤ O.D. < 2.6, is –0.996 ± 0.005, which is in agreement with the expected value of –1.000.

The residuals found by subtracting the measured voltage from the least-squares fit line are shown in Figure 3.24. The largest deviations are less than 0.1 V, and occur primarily for O.D. < 1.0. The standard error of estimate about the mean was found to be 1.1%. This means that on average, the data satisfies a straight line to within 1.1%, from which it can be concluded that the luminous response of the photodiode and associated electronics is linear for the light intensities transmitted by the neutral density filters in the range 0 ≤ O.D. < 2.6.

3.4.5 Photodiode Calibration

Figure 3.25 combines the data of Figures 3.21 and 3.23 to produce a plot of detector output voltage as a function of incident light intensity. The relationship between the detector voltage V and incident light intensity ϕ can be found by recognizing that both $\log(V/V_o)$ and $\log(\phi/\phi_o)$ equal –O.D., where V_o and ϕ_o are the voltage and light intensity in the absence of a neutral density filter. Consequently,

$$\log\left(\frac{V}{V_o}\right) = \log\left(\frac{\phi}{\phi_o}\right)$$

$$\log(V) = \log(\phi) + (\log(V_o) - \log(\phi_o)) \qquad (3.57)$$

$$y = mx + b$$

which indicates that the detector output voltage varies linearly with the incident light intensity with a slope of m = 1.000. The least-squares fit line in Figure 3.25a was found to have m = 0.994 ± 0.002 for data points corresponding to a light intensity $\phi \geq$

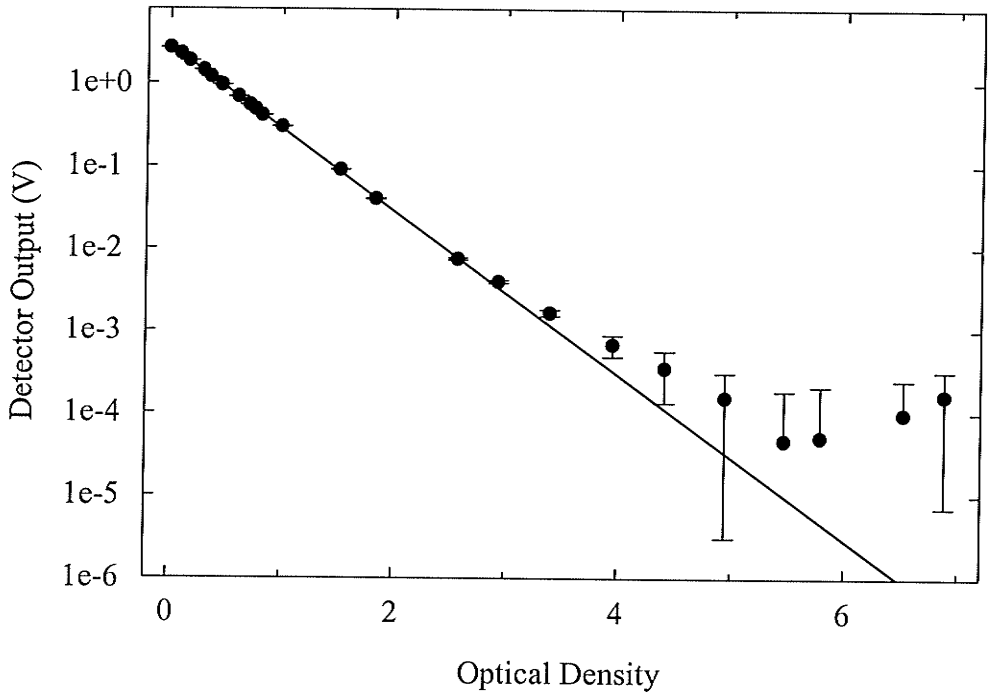

Figure 3.23 Plot showing the detector output as a function of the O.D. of the filters used to modulate the light source intensity. Shown is the average of five trials, where the error bars represent one standard deviation. The least-squares fit was found using the data for $0 \leq$ O.D. < 2.6.

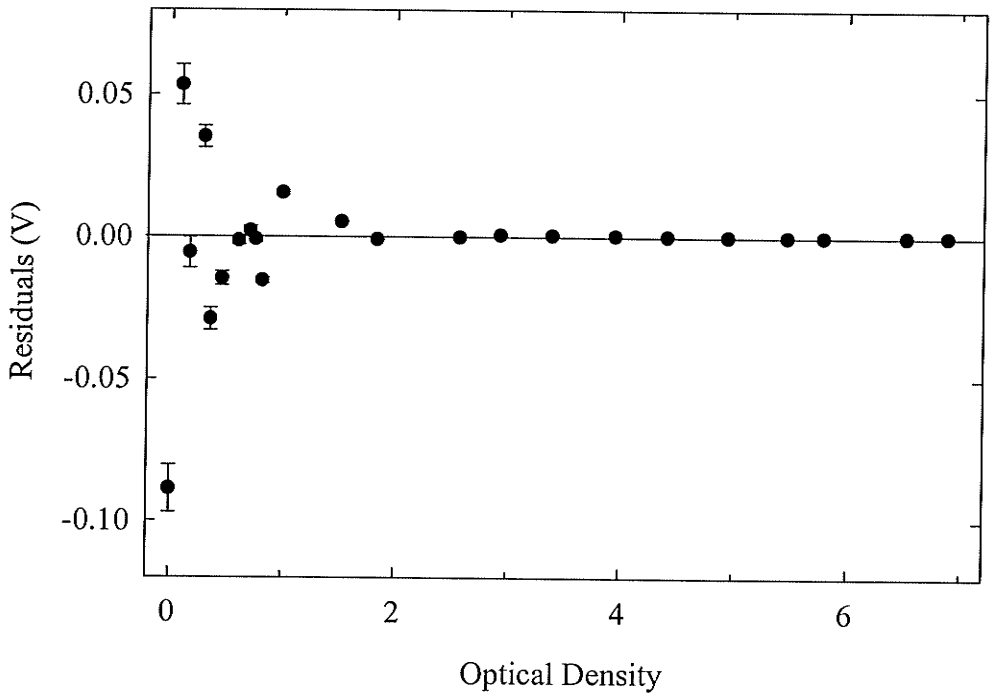

Figure 3.24 Residuals for the detector linearity measurements and the least-squares fit line shown in Figure 3.23.

8×10^{-11} W/cm^2. The standard error of estimate about the mean was found to be 0.3%. Figure 3.26a shows the residuals of the photodiode calibration measurements, which further confirm the excellent agreement between the straight line fit and the data.

For analysis pertaining to Figure 3.25b, Eqn. (3.57) may be rewritten as

$$V = \frac{V_o}{\phi_o}\phi \qquad (3.58)$$
$$y = mx + b$$

where $m = V_o / \phi_o$ and $b = 0$. The least squares fit line in Figure 3.25b has $m = (88.56 \pm 0.06) \times 10^6$ V·cm^2/W and $b = 0.0008 \pm 0.0009$ V for data points corresponding to a light intensity $\geq 8 \times 10^{-11}$ W/cm^2. The standard error of estimate about the mean was found to be 0.16%. The residuals corresponding to the least squares fit shown in Figure 3.26b clearly demonstrate the excellent agreement between the data and the least square fit.

The slope of the line in Figure 3.25b can be used to determine the photodiode sensitivity as follows. Recalling the discussion in §2.3.1.2, the output of the detector[7] V for a time-invariant luminous exposure is given by

$$V = i_{photo} \Delta T G / C_{\text{int}} \qquad (3.59)$$

where i_{photo} is the photocurrent, ΔT is the integration time, G is the gain of the gain-and-filter stage and C_{int} is the capacitor in the integrator. The photocurrent can be determined as a function of the incident light intensity ϕ using

$$i_{photo}[\text{A}] = (S_p[\text{A/W}]) \cdot (\phi[\text{W/cm}^2]) \cdot (A[\text{cm}^2]) \qquad (3.60)$$

where S_p is the photodiode sensitivity and A is the area of the photodiode. Substituting this expression into (3.59) yields

$$V = S_p \phi A \Delta T G / C_{\text{int}} . \qquad (3.61)$$

Recognizing that the slope m of Figure 3.25b is simply V/ϕ, (3.61) can be solved for S_p to yield

$$S_p = \frac{m C_{\text{int}}}{A \Delta T G} = 0.41 \text{ A/W} \qquad (3.62)$$

where $m = 88.56 \times 10^6$ V·cm^2/W, $C_{\text{int}} = 1$ nF, $A = 2$ x 0.1175 x 0.2 = 0.047cm^2, $\Delta T =$ 0.097775 s and $G = 47$.

[7]Note that V in (3.59) is equivalent to ΔV in (2.4); the "Δ" has been dropped in this section for simplicity.

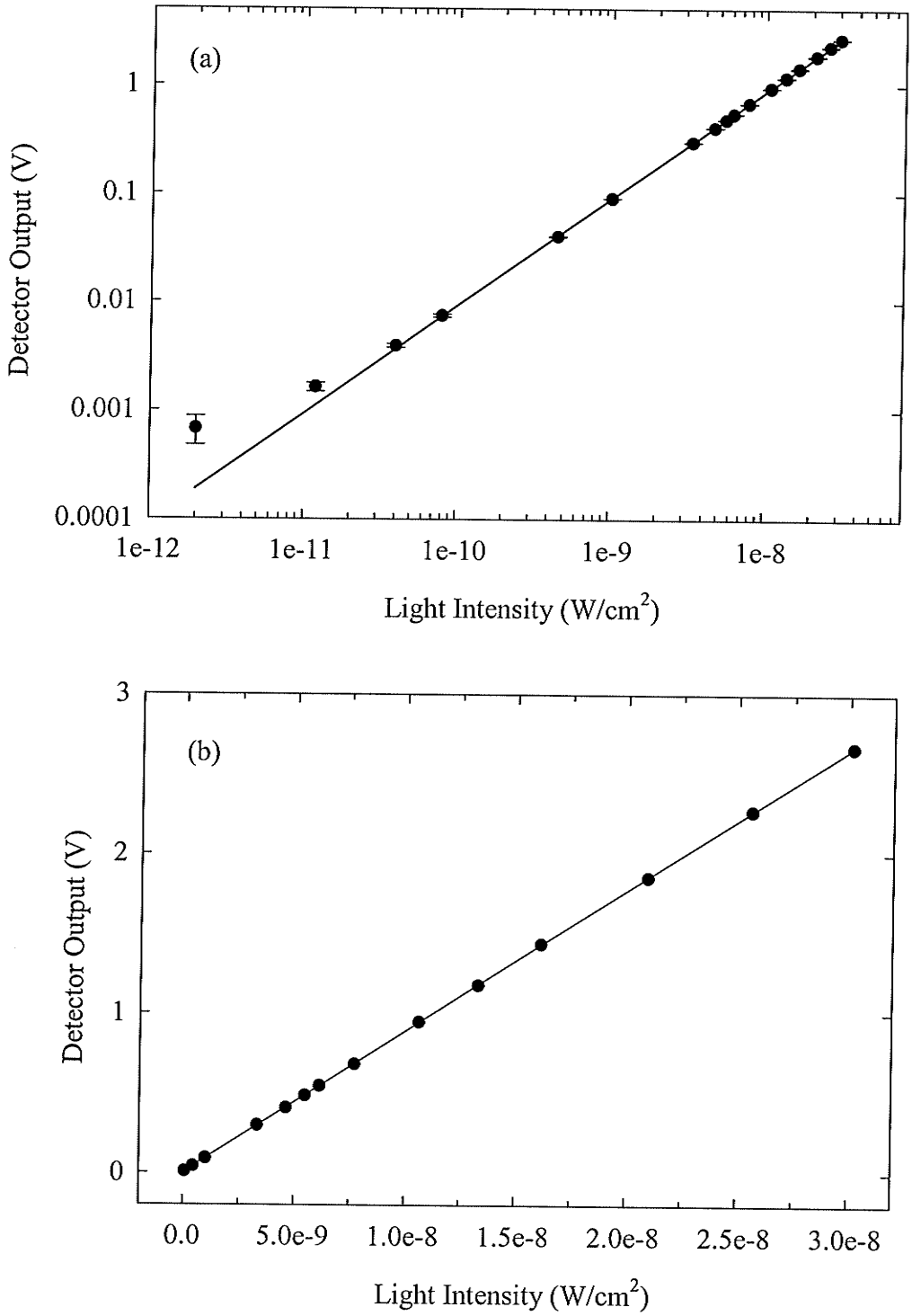

Figure 3.25 Plot showing the relationship between the detector output voltage and the incident light intensity plotted using (a) a log-log and (b) a linear scale. The solid line is a least-squares fit for light intensities $\geq 8 \times 10^{-11}$ W/cm^2.

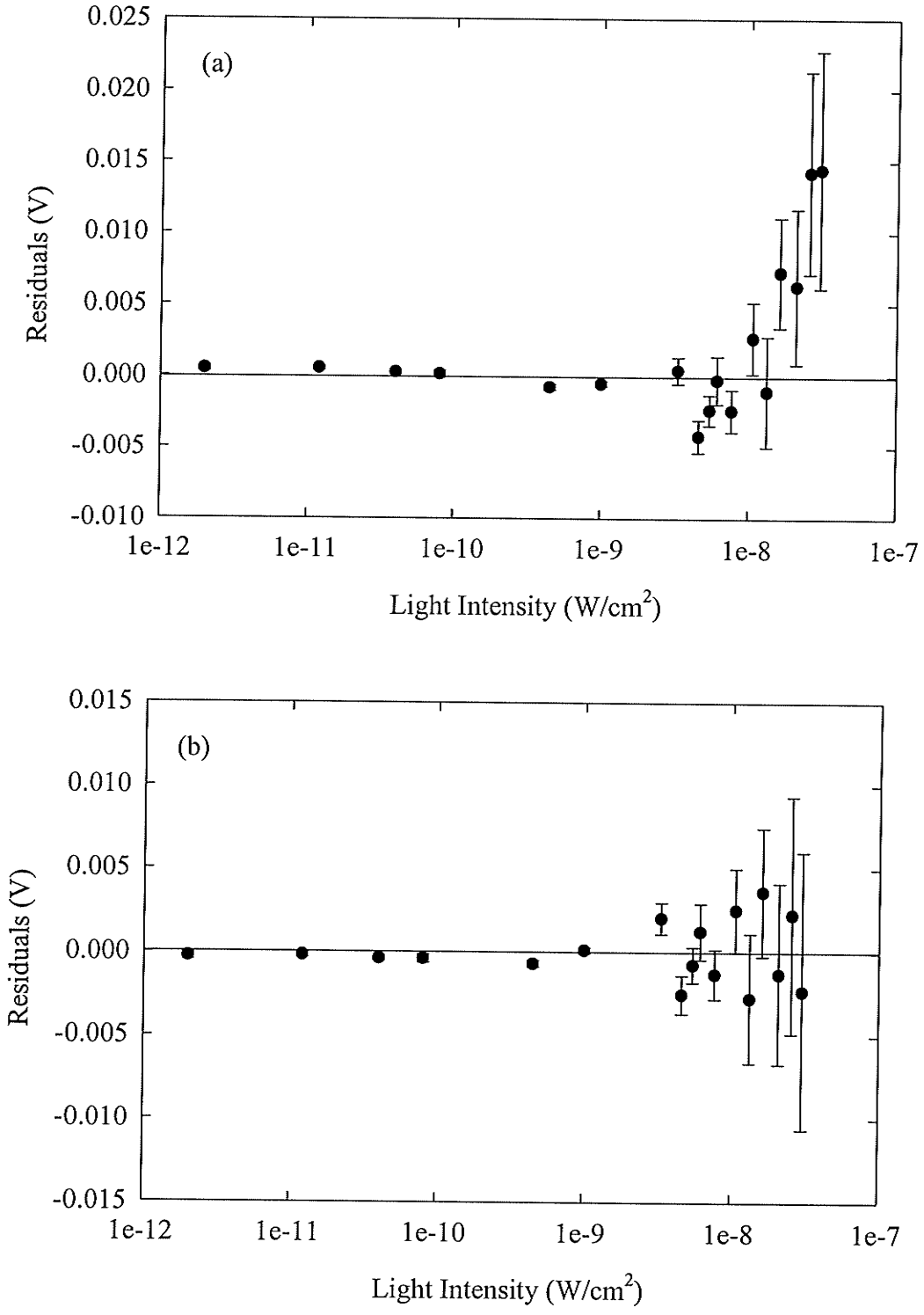

Figure 3.26 Residuals for the photodiode calibration data and best-fit lines shown in (a) Figures 3.25a and (b) 3.25b.

3.4.6 Spectral Correction

Both the radiometer and the photodiode array exhibit a spectral variation in sensitivity, i.e., their response is a function of wavelength. As the spectral responses of the photodiode array and the radiometer differ, their response to a polychromatic light source will not be identical. A radiometer calibration factor valid only for monochromatic illumination at 600 nm was assumed in the previous analysis. However, in practice, the green LED used in the previous measurements emitted a broad spectrum of optical photons. This section finds the sensitivity of the photodiode array as a function of wavelength, for comparison with the manufacturer's values shown in Figure 2.10.

3.4.6.1 Theory

The photodiode array sensitivity is a function of wavelength; consequently, the detector output V (expressed in volts) depends on the differential spectrum $\phi'(\lambda)$ of the incident illumination and can be expressed as

$$V = \frac{A\,\Delta T\,G}{C_{\text{int}}} \int_{\lambda} \phi'(\lambda) S_p(\lambda)\, d\lambda \tag{3.63}$$

where $A = 0.047$ cm^2 is the detector area, $\Delta T = 0.097775$ s is the integration time, $G = 47$ is the gain, $C_{\text{int}} = 1$ nF is the value of the integration capacitor, $\phi'(\lambda)$ is the differential illumination spectrum (W/cm^2/nm), and $S_p(\lambda)$ is the photodiode array sensitivity (A/W) as a function of wavelength. Similarly, the relative radiometer response R (W/cm^2) also depends on its spectral sensitivity according to

$$R = \int_{\lambda} \phi'(\lambda) S_r(\lambda)\, d\lambda \tag{3.64}$$

where $S_r(\lambda)$ is the radiometer sensitivity (dimensionless) as a function of wavelength. In the presence of an optical bandpass filter with spectral response $f(\lambda)$, the response of the photodiode array and associated electronics is

$$V_b = \frac{A\,\Delta T\,G}{C_{\text{int}}} \int_{\lambda} \phi'(\lambda) S_p(\lambda) f(\lambda)\, d\lambda \tag{3.65}$$

while that of the radiometer is

$$R_b = \int_{\lambda} \phi'(\lambda) S_r(\lambda) f(\lambda)\, d\lambda\,. \tag{3.66}$$

Dividing (3.65) by (3.66) yields

$$\frac{V_b}{R_b} = \frac{\dfrac{A\,\Delta T\,G}{C_{\text{int}}}\displaystyle\int_{\lambda}\phi'(\lambda)S_p(\lambda)f(\lambda)\,d\lambda}{\displaystyle\int_{\lambda}\phi'(\lambda)S_r(\lambda)f(\lambda)\,d\lambda}. \tag{3.67}$$

Assuming that the response for the i^{th} optical bandpass filter peaks at λ_{p-i} and falls to zero for wavelengths outside of the range $\lambda_{p-i} - \Delta\lambda_i/2 < \lambda < \lambda_{p-i} + \Delta\lambda_i/2$, (3.67) becomes

$$\frac{V_{b-i}}{R_{b-i}} = \frac{\dfrac{A\,\Delta T\,G}{C_{\text{int}}}\displaystyle\int_{\lambda_{p-i}-\Delta\lambda_i/2}^{\lambda_{p-i}+\Delta\lambda_i/2}\phi'(\lambda)S_p(\lambda)f_i(\lambda)\,d\lambda}{\displaystyle\int_{\lambda_{p-i}-\Delta\lambda_i/2}^{\lambda_{p-i}+\Delta\lambda_i/2}\phi'(\lambda)S_r(\lambda)f_i(\lambda)\,d\lambda}. \tag{3.68}$$

Figure 2.10 shows that $S_p(\lambda)$ varies approximately linearly as a function of wavelength for wavelengths between 450 nm and 950 nm, i.e.,

$$S_p(\lambda) = m_s\lambda + b_s, \tag{3.69}$$

where m_s is the slope of the line and b_s is the intercept. Equation (3.68) can then be written as

$$\begin{aligned}\frac{V_{b-i}}{R_{b-i}} &= \frac{\dfrac{A\,\Delta T\,G}{C_{\text{int}}}\displaystyle\int_{\lambda_{p-i}-\Delta\lambda_i/2}^{\lambda_{p-i}+\Delta\lambda_i/2}(m_s\lambda + b_s)\phi'(\lambda)f_i(\lambda)\,d\lambda}{\displaystyle\int_{\lambda_{p-i}-\Delta\lambda_i/2}^{\lambda_{p-i}+\Delta\lambda_i/2}\phi'(\lambda)S_r(\lambda)f_i(\lambda)\,d\lambda} \\ &= \frac{m_s\dfrac{A\,\Delta T\,G}{C_{\text{int}}}\displaystyle\int_{\lambda_{p-i}-\Delta\lambda_i/2}^{\lambda_{p-i}+\Delta\lambda_i/2}\lambda\phi'(\lambda)f_i(\lambda)\,d\lambda + b_s\dfrac{A\,\Delta T\,G}{C_{\text{int}}}\displaystyle\int_{\lambda_{p-i}-\Delta\lambda_i/2}^{\lambda_{p-i}+\Delta\lambda_i/2}\phi'(\lambda)f_i(\lambda)\,d\lambda}{\displaystyle\int_{\lambda_{p-i}-\Delta\lambda_i/2}^{\lambda_{p-i}+\Delta\lambda_i/2}\phi'(\lambda)S_r(\lambda)f_i(\lambda)\,d\lambda}\end{aligned} \tag{3.70a}$$

$$\frac{\dfrac{V_{b-i}}{R_{b-i}}\displaystyle\int_{\lambda_{p-i}-\Delta\lambda_i/2}^{\lambda_{p-i}+\Delta\lambda_i/2}\phi'(\lambda)S_r(\lambda)f_i(\lambda)\,d\lambda}{\dfrac{A\,\Delta T\,G}{C_{\text{int}}}} = m_s\displaystyle\int_{\lambda_{p-i}-\Delta\lambda_i/2}^{\lambda_{p-i}+\Delta\lambda_i/2}\lambda\phi'(\lambda)f_i(\lambda)\,d\lambda + b_s\displaystyle\int_{\lambda_{p-i}-\Delta\lambda_i/2}^{\lambda_{p-i}+\Delta\lambda_i/2}\phi'(\lambda)f_i(\lambda)\,d\lambda. \tag{3.70b}$$

The integrals in (3.70b) can be evaluated using an estimate of $S_r(\lambda)$ provided by the radiometer manufacturer, and measured $f_i(\lambda)$ and $\phi'(\lambda)$ values. The measurements

described in §3.4.6.2 yield V_{b-i}/R_{b-i} values for four optical bandpass filters. This allows m_s and b_s to be found, from which the functional form of $S_p(\lambda)$ can be established.

3.4.6.2 Method

The configuration shown in Figure 3.13 was used to make the radiometer and photodiode response measurements described in this section, except that the optical bandpass filters replaced the neutral density filter shown in Figure 3.13. The relative responses for the radiometer $R_{b\text{-}i}$ and the photodiode $V_{b\text{-}i}$ were measured in the presence of the 550 nm, 600 nm, 650 nm and 700 nm bandpass filters. For the photodiode measurements, a total of 250 readings were taken with each bandpass filter using a 10 Hz sampling frequency, averaged and corrected for dark current. The spectral response $f_i(\lambda)$ of the bandpass filters was measured using a spectrophotometer (Varian CARY1 UV-Visible Spectrophotometer). The LED emission spectrum $\phi'(\lambda)$ was measured using a monochromator (Beckman Model 2400 DU) and the radiometer. This measurement was corrected for dark current and the radiometer response.

3.4.6.3 Results

The detector response $V_{b\text{-}i}$ and radiometer response $R_{b\text{-}i}$ for the various optical bandpass filters are listed in Table 3.10. To evaluate the integrals in (3.70b), $f_i(\lambda)$, $S_r(\lambda)$ and $\phi'(\lambda)$ are required. The spectral responses of the optical bandpass filters $f_i(\lambda)$ are shown in Figure 3.27. The spectral response $S_r(\lambda)$ of a radiometer probe similar to that used for the measurements described in this section is shown in Figure 3.28. The emission spectrum $\phi'(\lambda)$ of the LED measured using the radiometer is plotted in Figure 3.29. Because the data are quite noisy, and are essentially flat beyond 630 nm, the data in Figure 3.29 will be used only when finding $S_p(\lambda)$ for λ = 550 nm and 600 nm. For wavelengths greater than 600 nm, the spectral output of the LED will be assumed to be constant over the width of a bandpass filters. The $\phi'(\lambda)$ term can therefore be taken outside of the integrals in (3.70b) for the 650 nm and 700 nm bandpass filters, where it cancels out, giving

$$\frac{\dfrac{V_{b-i}}{R_{b-i}}\displaystyle\int_{\lambda_{p-i}-\Delta\lambda_i/2}^{\lambda_{p-i}+\Delta\lambda_i/2} S_r(\lambda) f_i(\lambda)\, d\lambda}{\dfrac{A\,\Delta T\, G}{C_{\text{int}}}} = m_s \int_{\lambda_{p-i}-\Delta\lambda_i/2}^{\lambda_{p-i}+\Delta\lambda_i/2} \lambda f_i(\lambda)\, d\lambda + b_s \int_{\lambda_{p-i}-\Delta\lambda_i/2}^{\lambda_{p-i}+\Delta\lambda_i/2} f_i(\lambda)\, d\lambda. \qquad (3.71)$$

The integrals in (3.70b) were evaluated using the following expression

$$\frac{\dfrac{V_{b-i}}{R_{b-i}}\displaystyle\sum_k \phi'(\lambda_k) S_r(\lambda_k) f_i(\lambda_k)\,\Delta k}{\dfrac{A\,\Delta T\, G}{C_{\text{int}}}} = m_s \sum_k \lambda \phi'(\lambda_k) f_i(\lambda_k)\,\Delta k + b_s \sum_k \phi'(\lambda_k) f_i(\lambda_k)\,\Delta k \qquad (3.72)$$

Table 3.10 Spectral Response Measurements

Wavelength (nm)	$V_{b\text{-}i}$ (V)	$R_{b\text{-}i}$ (x10^{-9} W/cm^2)
550	1.292	13.72
600	0.304	3.03
650	0.0336	0.30
700	0.0766	0.69

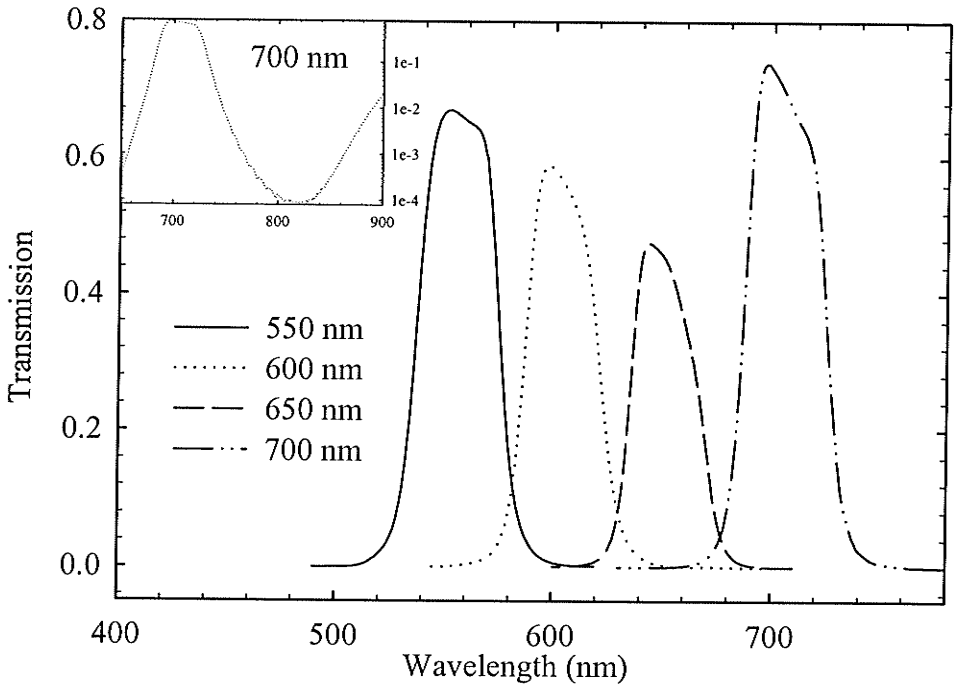

Figure 3.27 Plot of the spectral response $f_i(\lambda)$ of the 550 nm, 600 nm, 650 nm and 700 nm bandpass filters. The inset showing the 700 nm filter illustrates the transmission in the infrared region demonstrated by all of the filters.

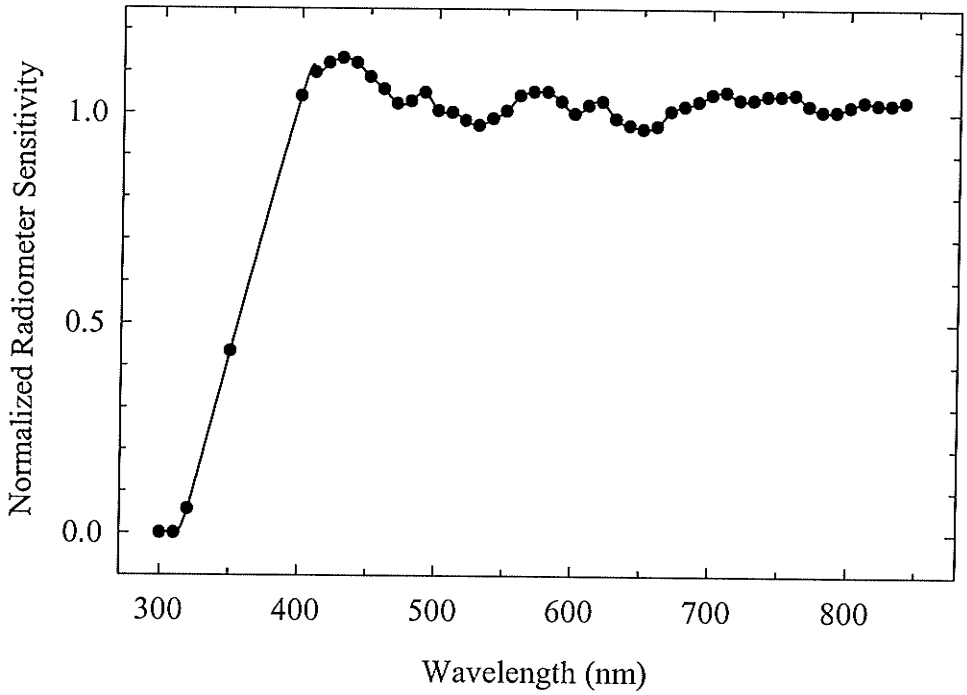

Figure 3.28 Plot of the radiometer sensitivity $S_r(\lambda)$ as a function of wavelength, normalized to its response at 600 nm (International Light Inc.).

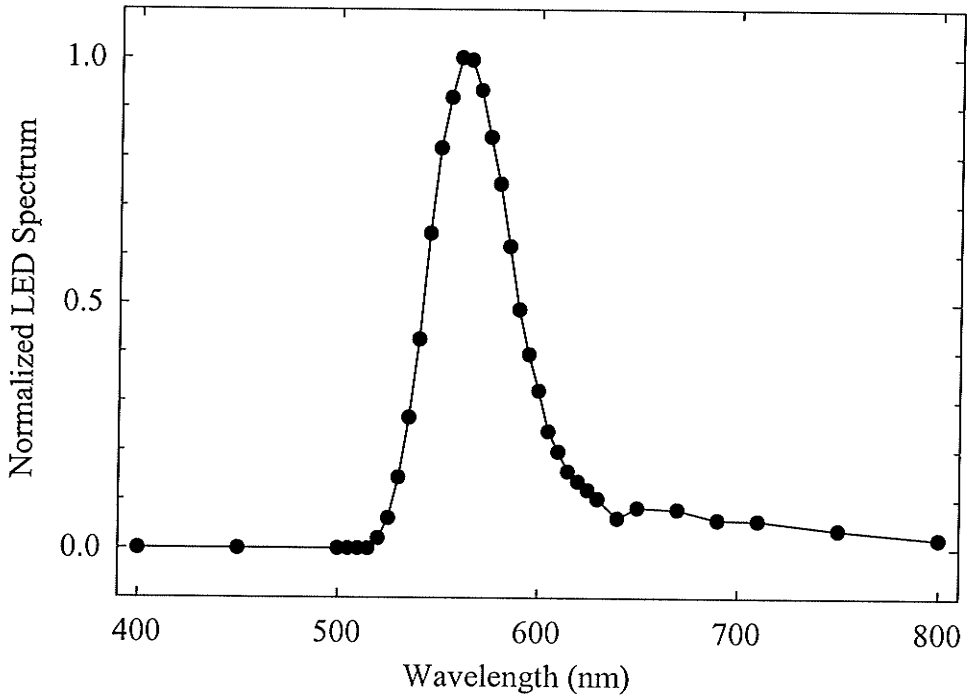

Figure 3.29 Plot of the normalized green LED output $\phi'(\lambda)$ as a function of wavelength.

where $\phi'(\lambda_k)$, $S_r(\lambda_k)$ and $f_i(\lambda_k)$ were evaluated at $\Delta k = 0.5$ nm intervals. The values for $S_r(\lambda_k)$ and $\phi'(\lambda_k)$ were found by interpolating the data shown in Figures 3.28 and 3.29. The integrals in (3.71) were calculated using

$$\frac{\dfrac{V_{b-i}}{R_{b-i}}\sum_k S_r(\lambda_k) f_i(\lambda_k)\,\Delta k}{\dfrac{A\,\Delta T\,G}{C_{\text{int}}}} = m_s \sum_k \lambda_k f_i(\lambda_k)\,\Delta k + b_s \sum_k f_i(\lambda_k)\,\Delta k. \qquad (3.73)$$

The equations (3.72) and (3.73) are of the form $C_{1\lambda_i} = m_s C_{2\lambda_i} + b_s C_{3\lambda_i}$, where $C_{1\lambda_i}$, $C_{2\lambda_i}$ and $C_{3\lambda_i}$ are constants that can be evaluated for each bandpass filter. This results in a series of equations as follows,

$$\begin{aligned} C_{1\lambda=550\text{nm}} &= m_s C_{2\lambda=550\text{nm}} + b_s C_{3\lambda=550\text{nm}}, \\ C_{1\lambda=600\text{nm}} &= m_s C_{2\lambda=600\text{nm}} + b_s C_{3\lambda=600\text{nm}}, \\ C_{1\lambda=650\text{nm}} &= m_s C_{2\lambda=650\text{nm}} + b_s C_{3\lambda=650\text{nm}}, \\ C_{1\lambda=700\text{nm}} &= m_s C_{2\lambda=700\text{nm}} + b_s C_{3\lambda=700\text{nm}}. \end{aligned} \qquad (3.74)$$

Although only two of the above expressions are required to solve for m_s and b_s, the experimental data yields an expression for each of the four optical bandpass filters. In order to incorporate all of the experimental data, the above expressions were solved for all possible combinations, as listed in Table 3.11. The variations in the data are due in part to the uncertainties in the data of Table 3.10, which were qualitatively assessed.

The photodiode sensitivity $S_{p\ measured}(\lambda)$ listed in Table 3.12 was found using (3.69) and the average m_s and b_s values from Table 3.11. The expected sensitivity $S_{p\ expected}(\lambda)$ given in Table 3.12 was found from the manufacturer's values (Figure 2.10; Hamamatsu, 1994) using linear interpolation. It can be seen that the measured sensitivity is about 30% higher than the expected sensitivity. The photodiode manufacturer specifies a maximum error of about 10% in the sensitivity values it provides (Private communication, Hamamatsu). Note that the experimentally determined slope m_s = (5.9 ± 0.6) x10^{-4} A /(W·nm) agrees well with the slope of the straight region of Figure 2.10 (≅ 7 x 10^{-4} A /(W·nm)). This indicates that the difference between the measured and the manufacturer's values is due to an incorrect assumption regarding the detector gain or the radiometer light output. The resistor values used to calculate the gain G (see §2.3.1.4) in the above expressions each have an error of 5%, so that the maximum error in G is about

10%. The radiometer was calibrated using a light intensity about four orders of magnitude larger than that encountered for the spectral response measurements. No uncertainty was provided in the calibration factor. It is reasonable to expect some uncertainty in the radiometer calibration at the light intensities encountered. With this in mind, agreement between the measured and expected values is quite good.

Note that the measurements of §3.4 would have been greatly simplified had an integrating sphere containing a white light source been used. A spatially uniform light source would have eliminated the light source uniformity and intensity correction of §3.4.2. §3.4.6 would also have been simplified as $\phi'(\lambda) = 1$ could have been used.

The measurements of this section demonstrate that the detector response is linear over 2.6 orders of magnitude. Because nonlinearities in the detector output produce image artifacts (Joseph, 1981), this is an important result. The dynamic range of the γ-ray fluence is expected to span no more than 2.4 orders of magnitude (see §3.6), indicating that the detector is linear over a range that is adequate for imaging BT patients.

Table 3.11 m_s and b_s values

Data for bandpass filters	m_s (x10^{-4}A /(W·nm))	b_s (A/W)
550 nm & 600 nm	6.74	0.0705
550 nm & 650 nm	6.28	0.0964
550 nm & 700 nm	5.82	0.1221
600 nm & 650 nm	5.95	0.1178
600 nm & 700 nm	5.50	0.1449
650 nm & 700 nm	5.05	0.1765
Average ± SD	5.9 ± 0.6	0.12 ± 0.04
Average ± Standard Error	5.9 ± 0.2	0.12 ±0.02

Table 3.12 Photodiode Sensitivity

Wavelength (nm)	$S_{p\ measured}(\lambda)$ (A/W)	$S_{p\ expected}(\lambda)$ (A/W)
550	0.44 ± 0.05	0.318
600	0.47 ± 0.05	0.355
650	0.50 ± 0.05	0.391
700	0.53 ± 0.06	0.423

3.5 Detector Response as a Function of Integration Time

3.5.1 Theory

The time-dependent output voltage of the gated integrator is a saw-tooth waveform at the sampling frequency when the photodiode array is illuminated by a constant light intensity. The effect of the gain-and-filter stage is to amplify and smooth this sawtooth wave, as described by Eqn. (2.7). Since the functional forms of both the saw-tooth waveform and the transfer function of the gain-and-filter stage are known, the shape of the resulting output waveform of the gain-and-filter stage $h(t)$ can be calculated. This is easily achieved by convolving the filter response $f(t)$ with the saw-tooth input $g(t)$.

The frequency response of a low-pass filter is given by the expression

$$F(i\omega) = \frac{G}{1 + i\omega/\omega_c} \tag{3.75}$$

where $\omega_c = 1/R_F C_F = 1/(47\text{k}\Omega)(10\text{nF}) = 2.128\times10^3$ radians/second is the cut-off frequency and G = 47 is the gain of the gain-and-filter stage. Transforming the above equation into the time domain yields

$$f(t) = \mathcal{F}^{-1}\left\{\frac{G}{1+i\omega/\omega_c}\right\} = \begin{cases} G\omega_c e^{-\omega_c t} & t \geq 0 \\ 0 & t < 0. \end{cases} \tag{3.76}$$

The functional form of the saw-tooth wave is

$$g(t) = \sum_{n=-N'}^{N'} \frac{V_o}{T_o}(t + nT_o)\cdot rect\left(\frac{t+nT_o}{T_o}\right) \tag{3.77}$$

where

$$rect\left(\frac{t+nT_o}{T_o}\right) = \begin{cases} 1 & 0 \leq \dfrac{t+nT_o}{T_o} < 1 \\ 0 & \text{otherwise} \end{cases} \tag{3.78}$$

V_o is the height of the unfiltered wave, T_o is the waveform period and N' is some large number (i.e., to simulate an "infinite" wave train). Inserting (3.76) and (3.77) into the convolution equation

$$h(t) = f(t) * g(t) = \int_{-\infty}^{\infty} f(\alpha)g(t-\alpha)\,d\alpha \tag{3.79}$$

yields

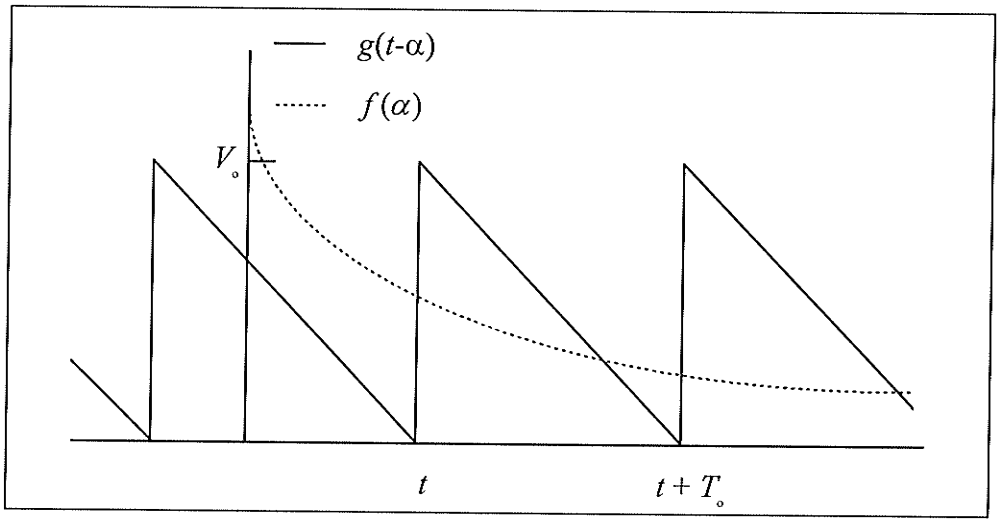

Figure 3.30 Illustration of the functions $g(t-\alpha)$ and $f(\alpha)$ used to perform the convolution.

$$h(t)=\sum_{n=-N'}^{N'}\left[\int_{-\infty}^{0}0\cdot\frac{V_o}{T_o}(t-\alpha+nT)rect\left(\frac{t-\alpha+nT_o}{T_o}\right)d\alpha + \int_{0}^{\infty}G\omega_c e^{-\omega_c\alpha}\frac{V_o}{T_o}(t-\alpha+nT)rect\left(\frac{t-\alpha+nT_o}{T_o}\right)d\alpha\right]. \tag{3.80}$$

Figure 3.30 shows that (3.80) can be simplified as follows

$$h(t)=\int_{0}^{t}G\omega_c e^{-\omega_c\alpha}\frac{V_o}{T_o}(t-\alpha)d\alpha+\sum_{n=1}^{N'}\int_{(n-1)T_o+t}^{nT_o+t}G\omega_c e^{-\omega_c\alpha}\frac{V_o}{T_o}(t-\alpha+nT_o)d\alpha\,. \tag{3.81}$$

The rect function appearing in (3.80) is incorporated into the integration limits in (3.81). In practice it was found that the exponential decays quickly enough that $N' = 2$ or 3 is adequate. Evaluating the integrals in (3.81) yields

$$\begin{aligned}h(t)&=-\frac{GV_o t}{T_o}(e^{-\omega_c t}-1)+\frac{GV_o}{T_o\omega_c}\left[e^{-\omega_c t}(\omega_c t+1)-1\right]-\sum_{n=1}^{N'}\left\{\frac{GV_o(t+nT_o)}{T_o}\left[e^{-\omega_c(nT_o+t)}-e^{-\omega_c[(n-1)T_o+t]}\right]\right.\\&\left.+\frac{GV_o}{T_o\omega_c}\left[e^{-\omega_c(nT_o+t)}[-\omega_c(nT_o+t)-1]-e^{-\omega_c[(n-1)T_o+t]}(-\omega_c[(n-1)T_o+t]-1\right]\right\}\\&=\frac{GV_o}{T_o\omega_c}\left\{(\omega_c t-1)+e^{-\omega_c t}+(\omega_c T_o-1+e^{-\omega_c t})\sum_{n=1}^{N'}e^{-\omega_c nT_o}\right\}.\end{aligned} \tag{3.82}$$

Figure 3.31 illustrates the functional form of $h(t)$ for selected periods T_o assuming $GV_o / T_o\omega_c = 1$ (this factor will be discussed in more detail below). As T_o decreases, the filter affects a larger percentage of the waveform.

3.5.2 Method

The effects of the low-pass filter were experimentally characterized by digitizing the output of the gain-and-filter stage to a precision of 16 bits (PCI-MIO-16XE-50 I/O Board, National Instruments) when the detector was illuminated with a constant intensity from the LED light source. Measurements taken with sampling times T_0 of 0.1 s, 0.01 s and 0.005 s, corresponding to integration times of ΔT = 0.097775 s, 0.007775 s and 0.002775 s were digitized at A-to-D conversion rates of 2 kHz, 20 kHz and 20 kHz respectively.

To verify the validity of (3.82), the output of the detector (as opposed to the output of the gain-and-filter stage, as was the case for the first set of measurements) was measured as a function of integration time. For these measurements, a constant light intensity was again provided by the LED light source. An O.D. = 1.0 (nominal value) filter was placed in front of the LED to prevent saturation of the detector for long integration times. A total of 100 readings of $\Delta V = V_f - V_i$ were taken in the presence of light at each integration time and averaged. These data were corrected for dark current by subtracting the average voltage measured at each integration frequency in the absence of light.

3.5.3 Results

Figure 3.31 shows the calculated output of the gain-and-filter stage at the sampling frequencies of 10 Hz, 100 Hz, and 200 Hz. It can be seen that at 10 Hz, the output very closely resembles an ideal saw-tooth wave, which becomes progressively more "distorted" with increasing sampling frequency as a consequence of the low-pass filtering. This is confirmed by the experimentally measured output of the gain-and-filter stage shown in Figure 3.32.

The detector voltage as a function of sampling frequency for a constant incident light intensity is affected by low-pass filtering of the "ideal" saw-tooth wave. In addition, the lag times in measuring V_i and V_f (shown in Figure 2.8) also affect the results. The waveform is sampled at T_i = 1.925 ms and T_f = T_0 - 0.3 ms, where T_0 is the period of the waveform. Figure 3.31 shows that the time period between T_i and T_f encompasses nearly

the entire period of the waveform for T_o = 0.1 sec (i.e., f = 10 Hz), but includes a much smaller portion of the waveform at the higher frequencies.

The detector output measurements are plotted as a function of sampling frequency in Figure 3.33 along with a linear regression fit to the low sampling frequency data. As

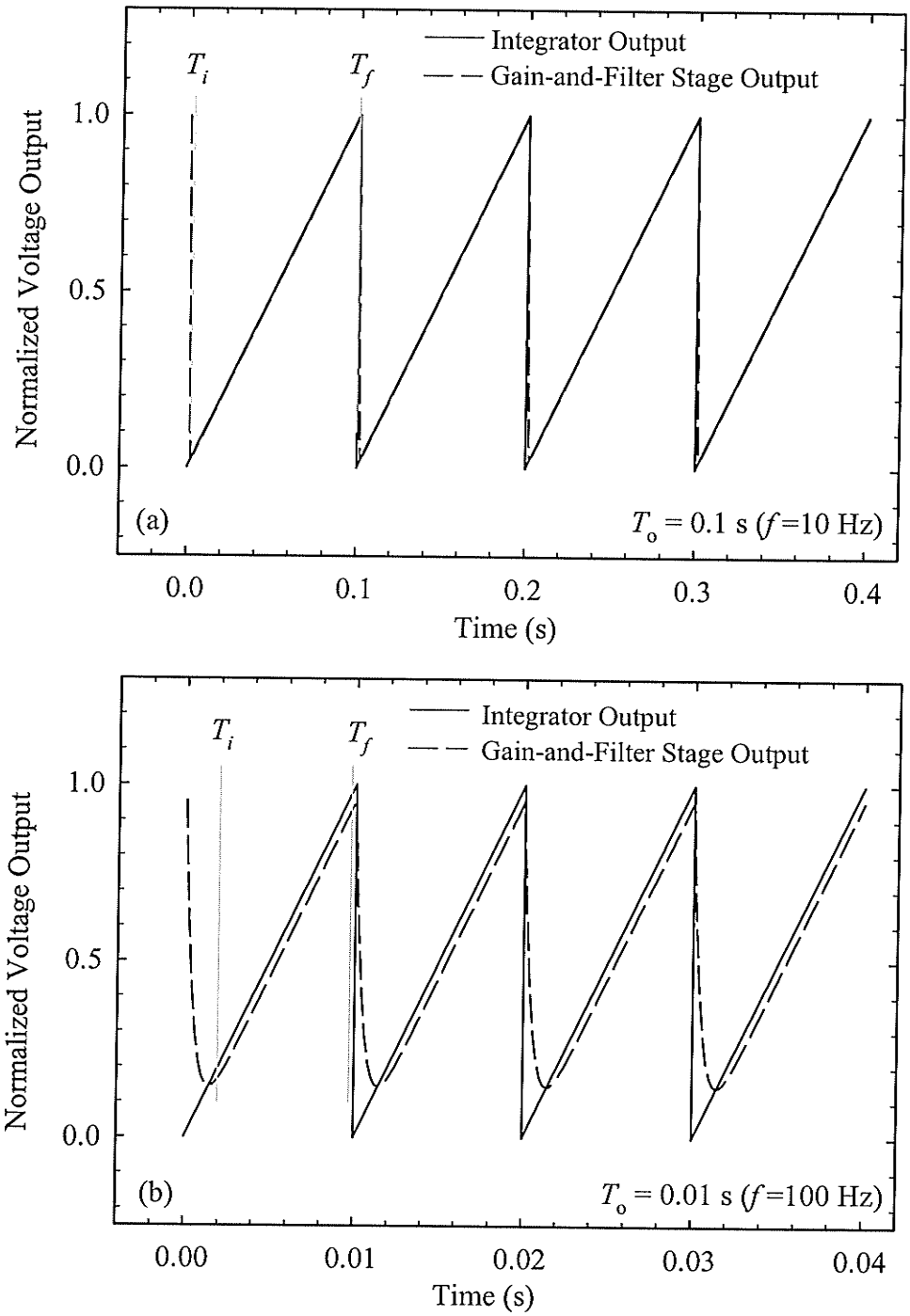

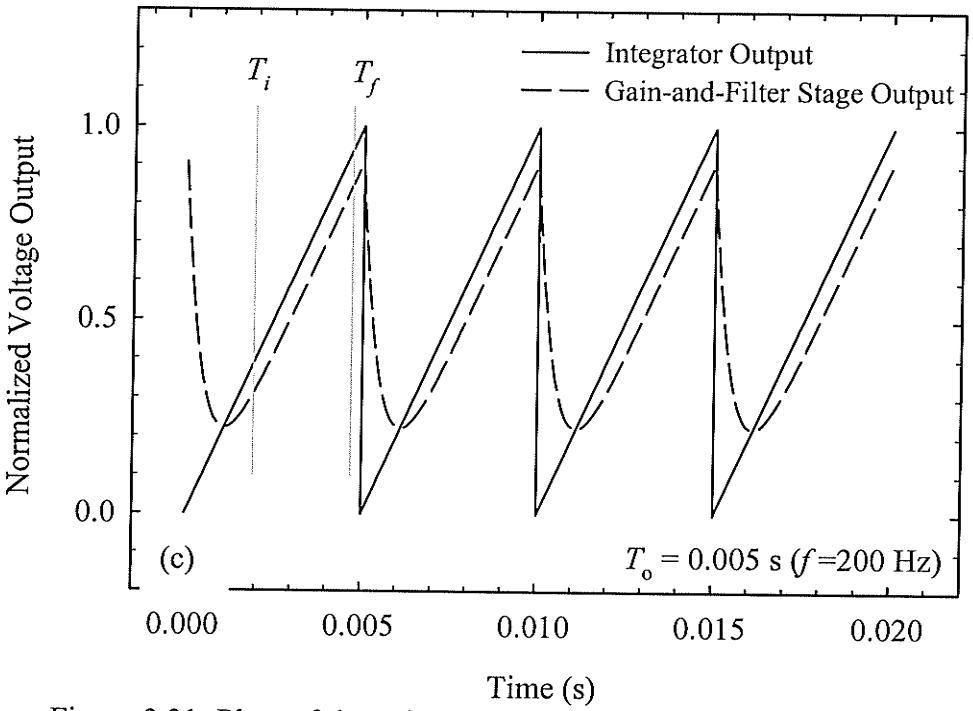

Figure 3.31 Plots of the gain-and-filter stage output $h(t)$ calculated using (3.82) and a sampling period of (a) $T_o = 0.1$ s, (b) $T_o = 0.01$ s and (c) $T_o = 0.005$ s. The solid line represents the output of the integrator (see Figure 2.4) and the dashed line represents the output of the gain-and-filter stage.

can be seen in Figure 3.33 and the corresponding residuals shown in Figure 3.34, the data curve away from the least-squares fit lines at higher sampling frequencies due to the modification in the wave shape resulting from the low-pass filtering, and the non-linear decrease in integration time.

The expected detector output $\Delta V_{theor}(T_o)$ can be calculated by rewriting (3.82) as

$$h(t) = mV_{theor}^{unscaled}(t) \tag{3.83}$$

where $m = GV_o/T_o\omega_c$ and $V_{theor}^{unscaled}(t)$ is the quantity in braces, to yield

$$\begin{aligned}\Delta V_{theor}(T_o) &= V_f - V_i \\ &= m\left[V_{theor}^{unscaled}(T_o - 0.3\text{ ms}) - V_{theor}^{unscaled}(1.925\text{ ms})\right] \\ &= m\Delta V_{theor}^{unscaled}(T_o).\end{aligned} \tag{3.84}$$

Because V_o is proportional to T_o, and G and ω_c are constants, the factor m is a constant. If the functional form of $\Delta V_{theor}^{unscaled}(T_o)$ is the same as that of the measured detector output, a plot of the detector output versus $\Delta V_{theor}^{unscaled}(T_o)$ as shown in Figure 3.35 will yield a straight line with a slope equal to m. A linear regression fit through the data in

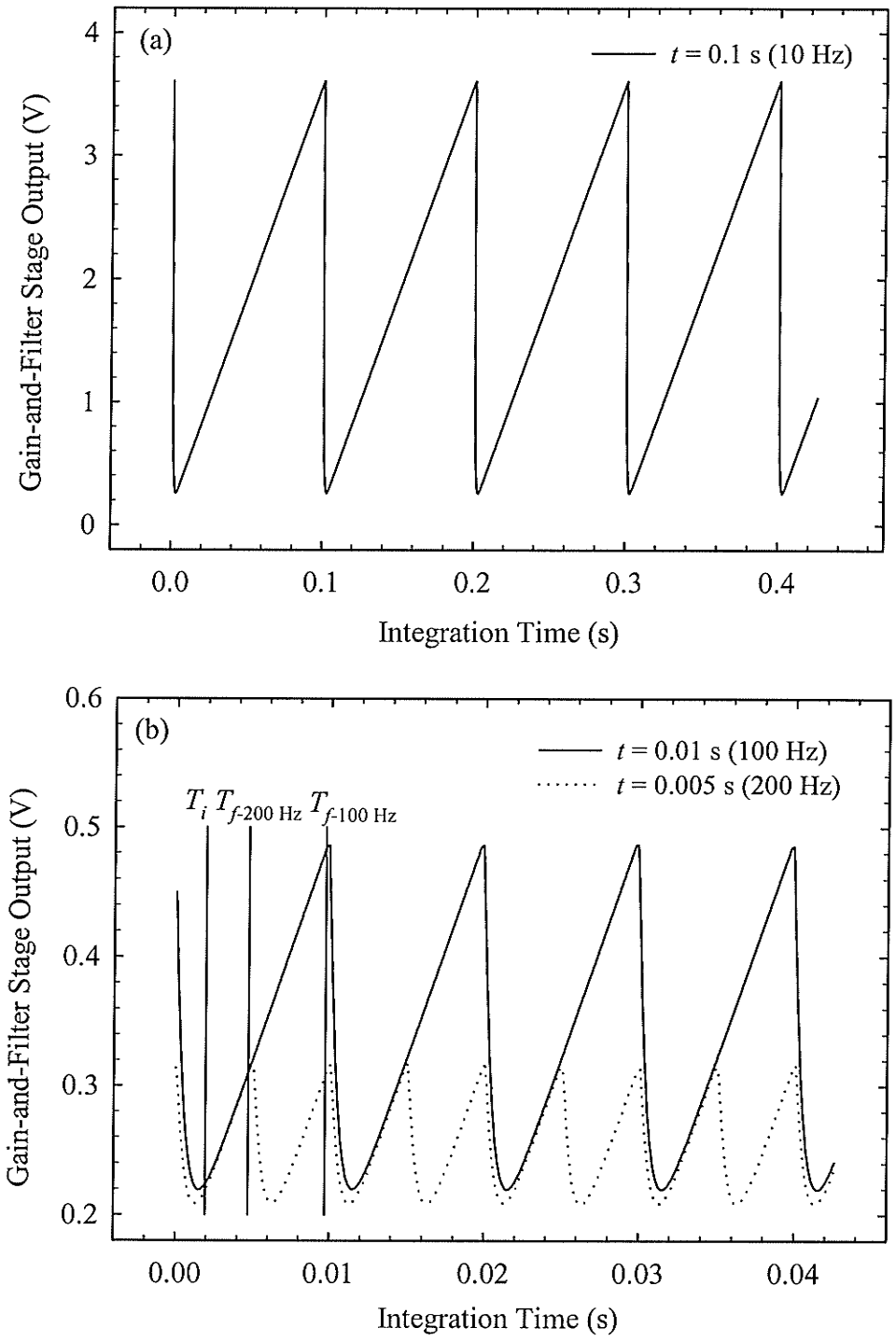

Figure 3.32 Experimentally measured gain-and-filter stage output. Measurements taken with a sampling period of (a) $T_o = 0.1$ s, and, (b) $T_o = 0.01$ s and $T_o = 0.005$ s.

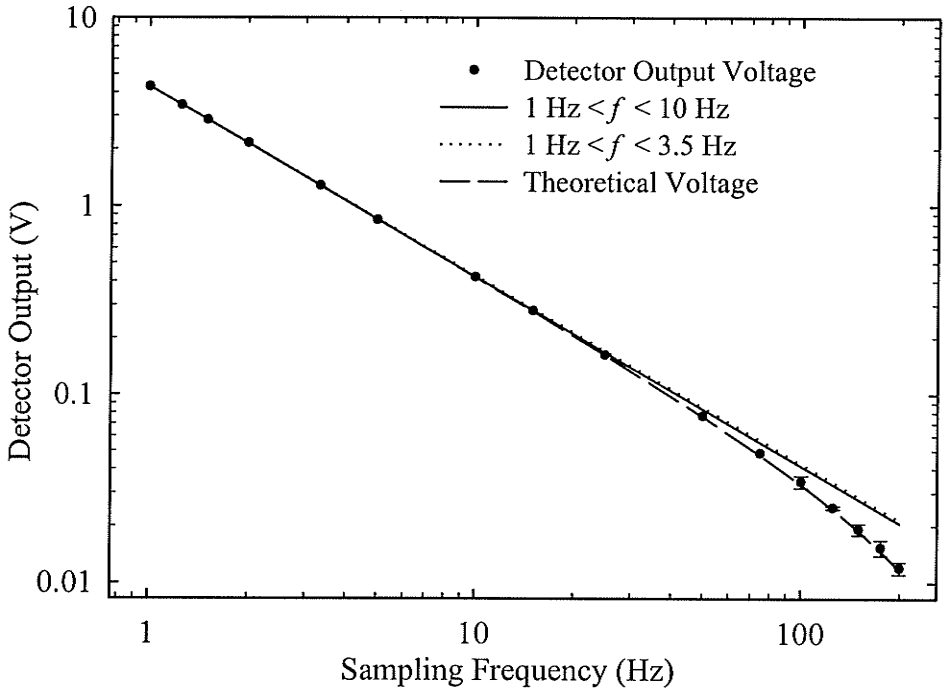

Figure 3.33 Shown is the detector output voltage versus sampling frequency. The error bars represent plus and minus one standard deviation. The least square fit lines assume a straight line fit to the data in the range indicated. The theoretical voltage was calculated taking into account the effects of the low-pass filter in the amplifier and the non-linear decrease in integration time with increasing sampling frequency.

Figure 3.35 found $m = 4.36$, with a standard error of estimate with respect to the mean of 1.03%. This indicates that, on average, the data follow a straight line to within 1.03%, thereby validating the analysis in §3.5.1.

The theoretical voltage $\Delta V_{theor}(T_o)$ calculated using $\Delta V_{theor}(T_o) = 4.36\,\Delta V_{theor}^{unscaled}(T_o)$ is plotted in Figure 3.33. The excellent agreement between the theoretically calculated values and the experimentally measured data is confirmed by a standard error of estimate with respect to the mean of 0.79%. The residuals corresponding to the theoretically predicted curve are plotted in Figure 3.36. These also demonstrate the excellent agreement between theory and experiment.

The measurements and calculations of this section demonstrate that the gain-and-filter stage only affects signals at sampling frequencies greater than 20 Hz, and thus does not introduce any errors at the 10 Hz sampling frequency proposed for the final scanner. This validates the gain-and-filter stage bandwidth chosen in §2.3.1.4.

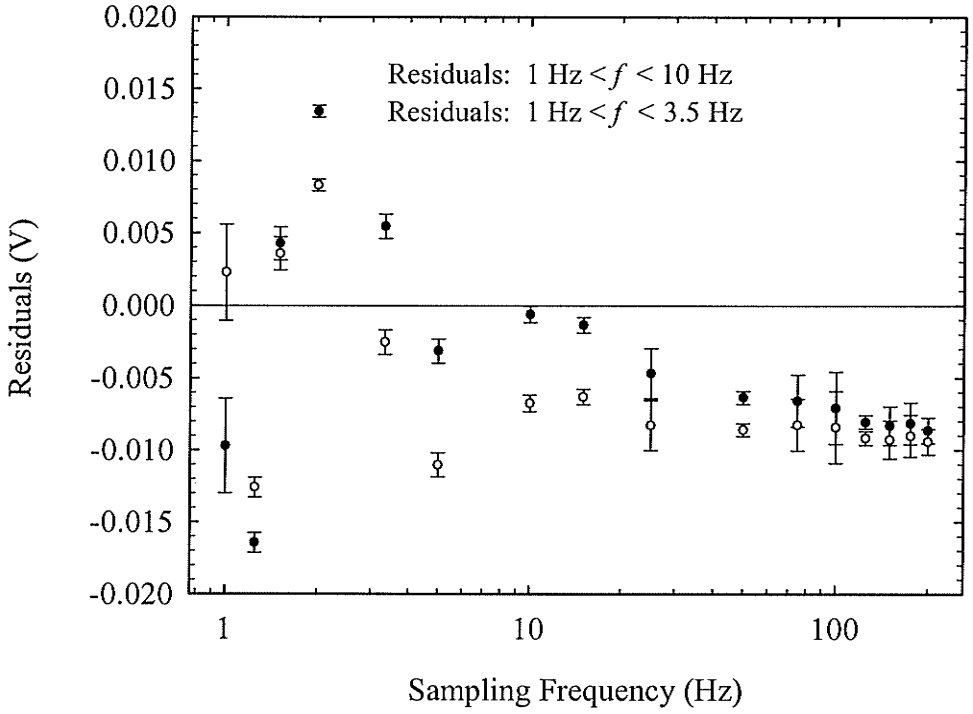

Figure 3.34 Residuals corresponding to the least-squares fit lines in Figure 3.33. The error bars represent plus and minus one standard deviation in the experimentally measured voltages.

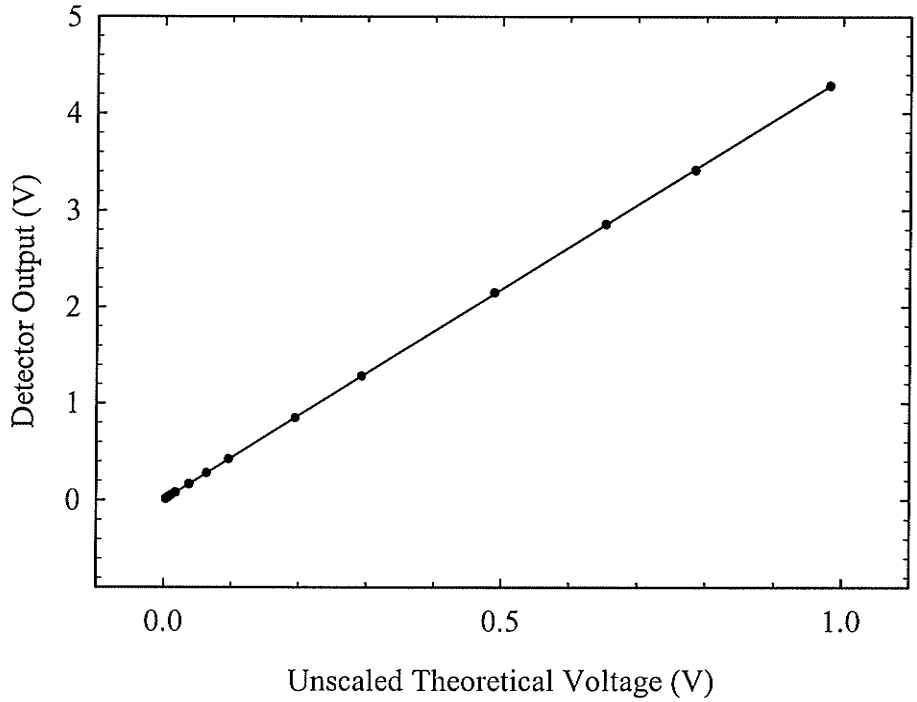

Figure 3.35 Plot of the detector output versus the unscaled theoretical voltage $\Delta V_{theor}^{unscaled}(T_o)$ for determination of the theoretical scaling factor m.

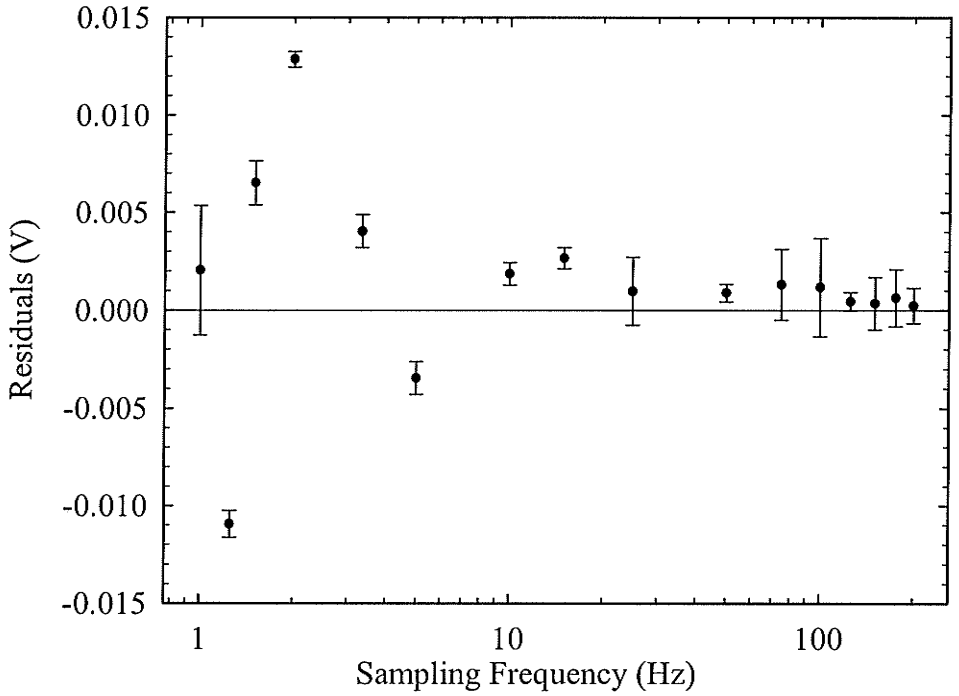

Figure 3.36 Residuals for the theoretically calculated detector output. The error bars represent plus and minus one standard deviation in the experimentally measured voltages.

3.6 Detector Response as a Function of γ-ray Intensity

3.6.1 Theory

To verify that the detector is functioning properly, it is important to estimate its output when irradiated by γ-rays. The expected voltage $\Delta V_{\text{expected}}$ of the detector irradiated by the ^{192}Ir brachytherapy source can be theoretically estimated using the exposure rate constant Γ of ^{192}Ir (Glasgow and Dillman, 1979), namely,

$$\Gamma_{^{192}\text{Ir}} = 4.69\frac{\text{R}\cdot\text{cm}^2}{\text{mCi}\cdot\text{hr}} = 1.30\times10^{-7}\frac{\text{R}\cdot\text{m}^2}{\text{mCi}\cdot\text{s}} = 3.36\times10^{-11}\frac{\text{C/kg}\cdot\text{m}^2}{\text{mCi}\cdot\text{s}}. \qquad (3.85)$$

Using this value, the exposure rate $\dot{X}$ can be found

$$\dot{X} = \Gamma_{^{192}\text{Ir}}\cdot\frac{A_c}{d^2} \qquad \left[\frac{\text{C}}{\text{kg}\cdot\text{s}}\right]. \qquad (3.86)$$

where A_c is the activity of the source in mCi, and d is the source-to-detector distance in meters. The exposure rate can be used to find the γ-ray energy fluence rate $\dot{\Psi}$ by means of the expression (Attix, 1986)

$$\dot{X} = \left(\frac{e}{\overline{W}}\right)_{air}\sum_i\left(\frac{\mu_{en}}{\rho}\right)_{E_i,air}\dot{\Psi}_{E_i} \qquad \left[\frac{\text{C}}{\text{kg}\cdot\text{s}}\right] \qquad (3.87)$$

where $(\mu_{en}/\rho)_{E_i,air}$ is the mass energy absorption coefficient of air at the i^{th} peak of energy E_i in the ^{192}Ir spectrum, $\dot{\Psi}_{E_i}$ is the γ-ray energy fluence rate at the i^{th} peak and $(e/\overline{W})_{air}$ = 1/33.97 C/J. Combining (3.86) and (3.87) gives

$$\frac{\Gamma_{^{192}\mathrm{Ir}} A_c}{d^2} = \left(\frac{e}{\overline{W}}\right)_{air} \sum_i \left(\frac{\mu_{en}}{\rho}\right)_{E_i,air} \dot{\Psi}_{E_i} \qquad \left[\frac{\mathrm{C}}{\mathrm{kg}\cdot\mathrm{s}}\right]. \tag{3.88}$$

The mass energy absorption coefficient of air is relatively constant between 300 and 600 keV where ^{192}Ir emits most of its photons, and can therefore be approximated by its average $(\overline{\mu}_{en}/\rho)_{air} = 2.90 \times 10^{-3}$ m^2/kg, resulting in

$$\begin{aligned} \frac{\Gamma_{^{192}\mathrm{Ir}} A_c}{d^2} &\cong \left(\frac{e}{\overline{W}}\right)_{air} \left(\frac{\overline{\mu}_{en}}{\rho}\right)_{air} \sum_i \dot{\Psi}_{E_i} \\ &\cong \left(\frac{e}{\overline{W}}\right)_{air} \left(\frac{\overline{\mu}_{en}}{\rho}\right)_{air} \dot{\Psi} \qquad \left[\frac{\mathrm{C}}{\mathrm{kg}\cdot\mathrm{s}}\right] \end{aligned} \tag{3.89}$$

Solving for $\dot{\Psi}$ yields

$$\dot{\Psi} \cong \left(\frac{\Gamma_{^{192}\mathrm{Ir}} A_c}{d^2}\right) \Bigg/ \left(\frac{\overline{\mu}_{en}}{\rho}\right)_{air} \left(\frac{e}{\overline{W}}\right)_{air} \qquad \left[\frac{\mathrm{J}}{\mathrm{m}^2\cdot\mathrm{s}}\right]. \tag{3.90}$$

The area A of the crystal exposed to the γ–ray photons is 2.2×10^{-5} m^2 so that the rate of energy incident on the crystal $\dot{E}_{incident}$ is

$$\begin{aligned} \dot{E}_{incident} &\cong \dot{\Psi} \cdot A \\ &\cong \left(\frac{\Gamma_{^{192}\mathrm{Ir}} A\ A_c}{d^2}\right) \Bigg/ \left(\frac{\overline{\mu}_{en}}{\rho}\right)_{air} \left(\frac{e}{\overline{W}}\right)_{air} \quad \left[\frac{\mathrm{J}}{\mathrm{s}}\right]. \end{aligned} \tag{3.91}$$

In order to account for the complex spectrum of ^{192}Ir listed in Table 2.1, the contribution of each peak to the energy absorbed in the scintillating crystal must be determined. The fraction of the incident energy absorbed depends on the thickness of the crystal and its attenuation coefficient. To incorporate the energy dependence of the absorption coefficient, the fraction of energy deposited by the peaks in the ^{192}Ir spectrum was expressed as

$$\dot{E}_{absorbed} \cong \frac{\sum_i A_i E_i (1 - e^{-\sigma_i h})}{\sum_i A_i E_i} \left(\frac{\Gamma_{^{192}\mathrm{Ir}} A\ A_c}{d^2}\right) \Bigg/ \left(\frac{\overline{\mu}_{en}}{\rho}\right)_{air} \left(\frac{e}{\overline{W}}\right)_{air} \quad \left[\frac{\mathrm{J}}{\mathrm{s}}\right] \tag{3.92}$$

where A_i is the amplitude of the i^{th} peak of energy E_i in the ^{192}Ir spectrum, σ_i is the attenuation coefficient of $CdWO_4$ at the i^{th} peak, and h is the thickness of the $CdWO_4$

crystal (1.0 cm). Note that (3.92) assumes that a photon deposits all of its energy in the crystal when it interacts. Although this is approximately valid for the photoelectric effect, this is not valid for Compton scattering, where the scattered photon may escape the crystal without interacting. Recalling Figure 2.2a, it can be seen that most of the ^{192}Ir photons will undergo Compton interactions. The mean fraction $f_{i\,Compton}$ of the incident photon energy deposited by the Compton scattering process is given by

$$f_{i\,Compton} = \left(\frac{\mu_{i\,en}/\rho}{\mu_i/\rho} \right)_{CdWO_4} \tag{3.93}$$

where $(\mu_{i\,en}/\rho)_{CdWO_4}$ is the mass energy absorption coefficient and $(\mu_i/\rho)_{CdWO_4}$ is the mass attenuation coefficient of $CdWO_4$ at the i^{th} peak. This factor is 0.38 for $CdWO_4$ at 355 keV (Private Communication, S. Rathee; http://physics.nist.gov/lab.html). Although this factor could be incorporated into (3.92), this is not entirely correct either, as (3.93) incorrectly assumes that *all* of the Compton photons escape the crystal. As some of the Compton photons will interact in the crystal, an intermediate factor between $f_{i\,Compton}$ and 1.0 would be correct. An exact value could be found using Monte Carlo calculations (Bielajew). This factor will not be explicitly incorporated into the detector output equation, but will instead contribute to the other approximations discussed below.

The luminous efficiency ξ of $CdWO_4$ (Table 2.3) indicates that 15,000 optical photons are emitted for every MeV of energy deposited in the scintillating crystal. Incorporating this into (3.92) yields the number of optical photons $N_{optical}$ emitted by the crystal

$$N_{optical} \cong \dot{E}_{absorbed} \cdot \left(\frac{1}{1.6\times10^{-13}} \frac{\text{MeV}}{\text{J}} \right) \cdot \xi \qquad \left[\frac{\text{photons}}{\text{s}} \right]. \tag{3.94}$$

To obtain the optical power P incident on each photodiode pair (recall that two adjacent photodiodes are wired together to form a single detector) assume that all of the emitted photons have a wavelength equal to the peak wavelength $\lambda_{peak} = 470$ nm (Table 2.3). This corresponds to an energy of $E_{photon} = hc/\lambda = 4.23\times10^{-19}$ J/photon, where h is Plank's constant and c is the speed of light. The optical power is then

$$\begin{aligned} P &\cong N_{optical} \cdot E_{photon} \\ &\cong \left(\frac{\dot{E}_{absorbed}\,\xi}{1.6\times10^{-13}\ \text{J/MeV}} \right) \cdot E_{photon} \qquad [\text{W}]. \end{aligned} \tag{3.95}$$

The photosensitivity S_p of the photodiode at 470 nm is approximately 0.26 A/W, so that the expected current i_{photo} from a pair of photodiodes is

$$\begin{aligned} i_{photo} &\cong P \cdot S_p \\ &\cong \left(\frac{\dot{E}_{absorbed}\, E_{photon}\, \xi}{1.6\times10^{-13}\ \text{J/MeV}} \right) \cdot S_p \qquad [\text{A}]. \end{aligned} \tag{3.96}$$

The detector output voltage $\Delta V_{\text{expected}}$ for constant irradiation can now be calculated using (2.4)

$$\Delta V_{\text{expected}} \cong \frac{G}{C_{\text{int}}} i_{photo} \Delta T; \qquad \Delta T = T_{\text{o}} - 2.225\ \text{ms} \tag{3.97}$$

where $G = 47$ is the gain of the gain-and-filter stage and $C_{\text{int}} = 1$ nF. Combining (3.92), (3.96) and (3.97) the expected detector voltage output $\Delta V_{\text{expected}}$ is

$$\Delta V_{\text{expected}} \cong \frac{G}{C_{\text{int}}} \frac{\sum_i A_i E_i (1-e^{-\sigma_i h})}{\sum_i A_i E_i} \left(\frac{\Gamma_{^{192}\text{Ir}}\, A\ A_c}{d^2} \right) \left(\frac{E_{photon}\, \xi\, S_p}{1.6\times10^{-13}\ \text{J/MeV}} \right) \Delta T \Big/ \left(\frac{\overline{\mu}_{en}}{\rho} \right)_{air} \left(\frac{e}{\overline{W}} \right)_{air} \tag{3.98}$$

where the summations can be evaluated to equal

$$\frac{\sum_i A_i E_i (1-e^{-\sigma_i h})}{\sum_i A_i E_i} = 0.791. \tag{3.99}$$

Inserting numeric values into (3.98) yields

$$\begin{aligned} \Delta V_{\text{expected}} \cong & \frac{\frac{47}{1\,\text{nF}} \cdot 0.791 \cdot \left(3.36\times10^{-11} \frac{\text{C/kg}\cdot\text{m}^2}{\text{mCi}\cdot\text{s}} \cdot\ 2.2\times10^{-5}\ \text{m}^2 \frac{A_c}{d^2} \right)}{\left(2.90\times10^{-3} \frac{\text{m}^2}{\text{kg}} \right) \cdot \left(\frac{1}{33.97} \frac{\text{C}}{\text{J}} \right)} \\ & \times \left(\frac{4.23\times10^{-19} \frac{\text{J}}{\text{photon}} \cdot 15000 \frac{\text{photons}}{\text{MeV}} \cdot 0.26 \frac{\text{A}}{\text{W}}}{1.6\times10^{-13} \frac{\text{J}}{\text{MeV}}} \right) (0.097775\text{s}) \\ \cong & \left(0.325\times10^{-3} \frac{\text{V}\cdot\text{m}^2}{\text{mCi}} \right) \cdot \frac{A_c}{d^2} \qquad [\text{V}]. \end{aligned} \tag{3.100}$$

The above analysis can be modified to incorporate the effect of a Plexiglas attenuator in the path of the beam. For a slab of Plexiglas of thickness x between the source and the detector, the incident energy on the detector $\dot{E}_{incident}$ is given by

$$\dot{E}_{incident} \cong \frac{\sum_i A_i E_i e^{-\mu_i x}}{\sum_i A_i E_i} \left(\frac{\Gamma_{^{192}\mathrm{Ir}}\, A\, A_c}{d^2} \right) \Bigg/ \left(\frac{\overline{\mu}_{en}}{\rho} \right)_{air} \left(\frac{e}{\overline{W}} \right)_{air} \quad \left[\frac{\mathrm{J}}{\mathrm{s}} \right] \tag{3.101}$$

where μ_i is the attenuation of Plexiglas at energy E_i. The absorbed energy then becomes

$$\dot{E}_{absorbed} \cong \frac{\sum_i A_i E_i e^{-\mu_i x}(1-e^{-\sigma_i h})}{\sum_i A_i E_i} \left(\frac{\Gamma_{^{192}\mathrm{Ir}}\, A\, A_c}{d^2} \right) \Bigg/ \left(\frac{\overline{\mu}_{en}}{\rho} \right)_{air} \left(\frac{e}{\overline{W}} \right)_{air} \quad \left[\frac{\mathrm{J}}{\mathrm{s}} \right], \tag{3.102}$$

resulting in an output voltage of

$$\begin{aligned}
\Delta V_{\text{expected}} &\cong \frac{G}{C_{\text{int}}} \frac{\sum_i A_i E_i e^{-\mu_i x}(1-e^{-\sigma_i h})}{\sum_i A_i E_i} \left(\frac{\Gamma_{^{192}\mathrm{Ir}} A\, A_c}{\mathrm{d}^2} \right) \left(\frac{E_{photon} \xi\, S_p}{1.6\times10^{-13}\,\mathrm{J/MeV}} \right) \Delta T \Bigg/ \left(\frac{\overline{\mu}_{en}}{\rho} \right)_{air} \left(\frac{e}{\overline{W}} \right)_{air} \\
&\cong \frac{47}{1\,\mathrm{nF}} \frac{\sum_i A_i E_i e^{-\mu_i x}(1-e^{-\sigma_i h})}{\sum_i A_i E_i} \left(\frac{3.36\times10^{-11}\,\mathrm{C\cdot m^2/(kg\cdot mCi\cdot s)} \cdot 2.2\times10^{-5}\,\mathrm{m^2} \cdot A_c}{d^2} \right) \\
&\quad \times \frac{\left(\dfrac{4.23\times10^{-19}\,\mathrm{J/photon \cdot 15000 photons/MeV \cdot 0.26\,A/W}}{1.6\times10^{-13}\,\mathrm{J/MeV}} \right) (0.097775\,\mathrm{s})}{\left(2.90\times10^{-3}\,\mathrm{m^2/kg}\right)\cdot\left(1/33.97\,\mathrm{C/J}\right)} \\
&\cong \left(0.411\times10^{-3}\,\frac{\mathrm{V\cdot m^2}}{\mathrm{mCi}} \right) \cdot \frac{\sum_i A_i E_i e^{-\mu_i x}(1-e^{-\sigma_i h})}{\sum_i A_i E_i} \cdot \frac{A_c}{d^2} \quad [\mathrm{V}].
\end{aligned} \tag{3.103}$$

Note that (3.103) does not account for the detection of scattered photons and therefore holds only under narrow beam collimation conditions.

A number of approximations were made in the above derivation regarding the efficiency of the light collection. These include the following (Holl et al., 1988).

(i) A fraction of the optical photons produced will escape the scintillating crystal and not reach the photodiode. Encasing the crystals in a reflective coating material minimizes this effect. In addition, some photons will remain trapped in the crystal due to reflection from the crystal surfaces at angles beyond the critical angle (Mosleh-Shirazi et al., 1998;Vittori et al., 2000). These photons will undergo many internal reflections and are eventually absorbed in the crystal or the crystal coating.

(ii) Most γ-ray photons will undergo Compton scattering, and not deposit all of their energy in the crystal, as discussed above.

(iii) Some optical photons are lost due to reflection from the interfaces between the scintillating crystal and the photodiode. The index of refraction of the scintillator is $2.1 < n_{CdWO_4} < 2.3$ (Kinloch et al., 1994), that of the couplant is $n_C = 1.47$ at 25°C, while the index of refraction of the resin protecting the photodiodes is $n_R = 1.54$. To estimate the reflection losses, assume normal incidence for which the reflection coefficient R is

$$R = \left(\frac{n'-n}{n'+n}\right)^2 . \tag{3.104}$$

The parameters n and n' are the index of refraction in the incident and transmitting medium respectively. Using (3.104), the reflection coefficients R_1 and R_2 at the two interfaces shown in Figure 3.37 are $R_1 = 0.0402$ and $R_2 = 0.0006$. Therefore, it is expected that 4% of the luminous power will go undetected.

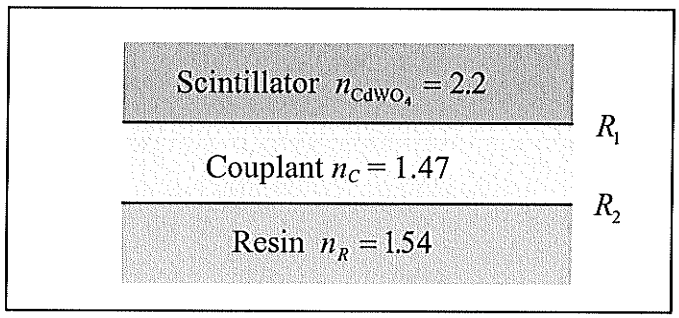

Figure 3.37 Diagram showing the index of refraction of the materials through which the optical photons must travel before reaching the photodiode.

(iv) Some optical photons are absorbed in the optical coupling grease and in the resin protecting the photodiode array. Light transmission through the couplant is provided by Dow Corning for various couplant thicknesses: at 0.4 microns the transmission is 70%, which increases to 94% at 0.8 microns, and then falls off again to 31% at 1.20 microns. Depending upon the thickness of optical coupling grease applied, considerable light may be lost in the couplant. Note that a two-part silicon optical coupling compound (Rexon Components, Inc. RX-22P) will be used in the final fourth generation scanner.

(v) Photons can be absorbed in the photodiode array without producing a photocurrent.

(vi) Light is absorbed in the region surrounding the active area of the photodiode: the active area of two photodiode elements is only 2.7 mm^2, whereas the area of the crystal is 22 mm^2. This means that optical photons impinging on regions outside of the active area are not detected. Using an array mask as described in §2.5.1 minimizes this effect. Note however that the measurements described below did not use a mask, resulting in a substantial loss of signal. Furthermore, the width of the crystal (2.75 mm) is such that it *exactly* fits over the photodiode elements (photodiode element width x 2 = 1.175 mm x 2 = 2.35 mm, inactive space = 0.40 mm) with no overlap on either side. If the crystal is not accurately positioned over the photodiode elements, further light will be lost.

As a consequence of the above factors, the actual measured voltage will be less than that calculated using (3.100) and (3.103).

3.6.2 Method

The output voltage of the detector and scintillator combination as a function of incident γ-ray intensity was determined for two different measurement conditions. The goal of the first experiment was to verify the validity of (3.103) under conditions similar to those envisioned for the final scanner. The purpose of the second experiment was to measure the detector output under narrow-beam irradiation conditions.

3.6.2.1 Detector Output for "Scanner Collimation"

The experimental set-up shown in Figure 3.10 was used for the first experiment. As described in §3.3.1.1, the detector was placed at a distance of 82.5 cm from the ^{192}Ir source (5.31 Ci) and the γ-ray intensity varied by altering the thickness of Plexiglas in the path of the beam. A total of 250 readings were taken for each Plexiglas thickness, which were averaged and corrected for dark current.

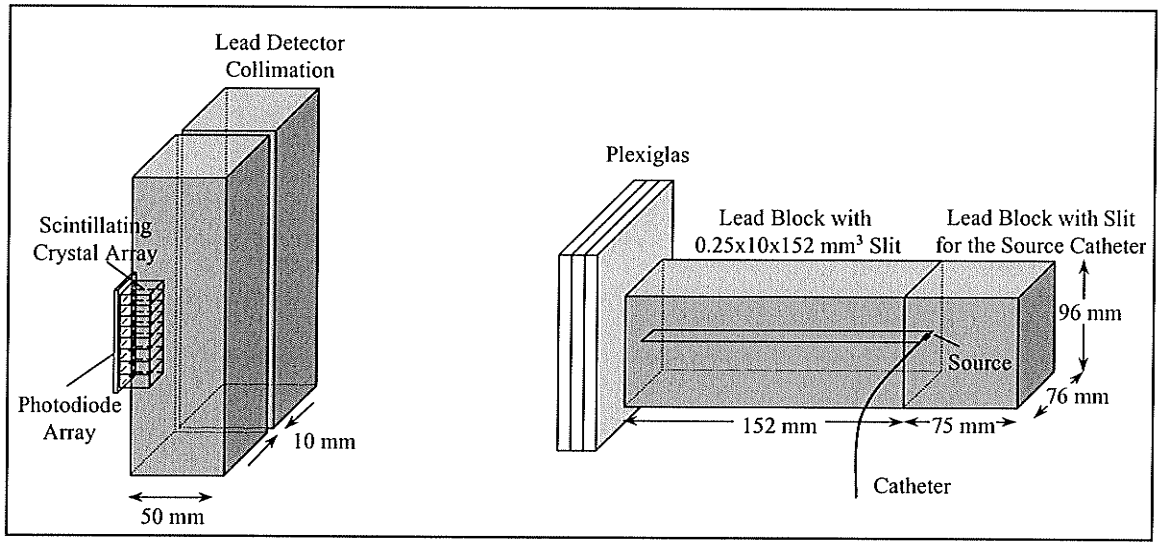

Figure 3.38 Configuration used when assessing the detector output voltage under narrow-beam irradiation conditions.

3.6.2.2 Detector Output for Narrow-Beam Collimation

The second experiment involved placing the highly collimated source (6.17 Ci) 63.3 cm from the detector, as shown in Figure 3.38 to approximate narrow-beam irradiation conditions. Collimation was accomplished using two 48 x 76 x 152 mm^3 lead blocks, one of which had a 0.25 x 10 x 152 mm^3 slit milled into it. A catheter containing the source was placed in a slit along one side of a third lead block, which served to reduce the amount of scattered radiation reaching the detector. Placing various thicknesses of Plexiglas in the path of the beam varied the γ-ray intensity. A total of 250 readings were taken for each Plexiglas thickness, averaged and corrected for dark current.

3.6.3 Results

3.6.3.1 Detector Output for "Scanner Collimation"

Figure 3.39 shows the detector output plotted as a function of Plexiglas thickness. The expected voltage $\Delta V_{expected}$ (solid line) was calculated using (3.103) and normalized to the detector output in the absence of an attenuator. Because these measurements were not carried out under narrow beam conditions, (3.103) is not expected to hold for measurements taken with more than a few centimeters of Plexiglas. In addition to attenuating the beam, the Plexiglas will produce scattered radiation, which causes a

deviation from the trend predicted by (3.103). However, good agreement is obtained between the trend predicted by (3.103) and the trend displayed by the experimentally measured data for Plexiglas thicknesses less than about 10 cm, that is, before scatter starts to become important. The measured voltage in the absence of Plexiglas is a factor of 5.5 times lower than the expected voltage ($\Delta V_{meas} = 0.459$ V and $\Delta V_{expected} = 2.537$ V). This is not unreasonable considering the magnitude of the effects discussed in §3.6.1.

The detector response measurements under scanner collimation conditions are valuable because they provide an estimate of the detector quantum efficiency QE, which represents the fraction of detected photons (Barrett and Swindell, 1981), namely, QE = 1/5.5 = 0.18. The theoretical analysis suggests that the primary loss of signal is due to Compton scattering of the incident γ-rays. As the QE provides an upper limit for the DQE (DQE $\leq$ QE $\leq$ 1; Barrett and Swindell, 1981), future improvements in detector performance should focus on this effect. Figure 3.39 also provides an estimate of the scatter contribution to the detected signal. As the latter is substantial for larger Plexiglas thicknesses, the collimator designed in Chapter 5 should attempt to minimize the detection of scattered photons.

3.6.3.2 Detector Output for Narrow-Beam Collimation

Figure 3.40 shows the detector output plotted as a function of γ–ray intensity for various Plexiglas thicknesses, measured under narrow-beam irradiation conditions. The results from (3.103) were not used directly as the collimator slit width (approximately 0.25 mm) was less than the width of the source (0.6 mm) making it very difficult to calculate the absolute expected voltage, because an unknown fraction of γ–rays are attenuated. Thus, the expected voltage was normalized to the first experimentally measured data point. The agreement between the normalized theoretical and experimental values is much improved over that in Figure 3.39 (standard error of estimate with respect to the mean of 3.8%) because the amount of scatter produced in the Plexiglas and subsequently detected, has been greatly reduced.

It is worthwhile to note that the signal measured in Figure 3.40 is smaller than expected in practice because a portion of the source was blocked by the collimator

(source diameter = 0.6 mm, collimator slit width = 0.25 mm). The results of this measurement reinforce the earlier conclusion that the detector response is linear over a range adequate for BT imaging.

3.7 Detector Response as a Function of Circuit Temperature

The electronic components used to construct the detector described in Chapter 2 exhibit a temperature dependence that influences the output voltage of the detector. To assess this temperature dependence, the output voltage was recorded in the absence of optical photons or γ-rays while the circuit temperature was changed under controlled conditions. These values were then compared with those theoretically calculated from the specification sheets of the electronic components.

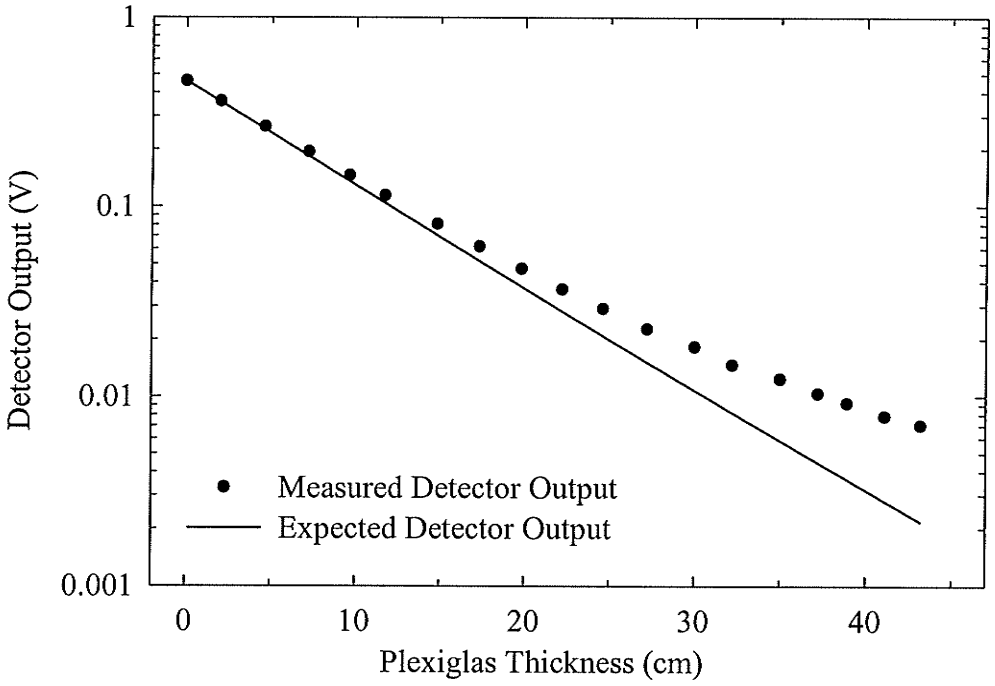

Figure 3.39 Plot of the measured detector output (points) as a function of Plexiglas thickness under "scanner collimation" condition. Error bars, taken to be the standard error in the mean, are smaller than the dots. Also shown (line) is the normalized expected detector output under narrow beam collimation conditions.

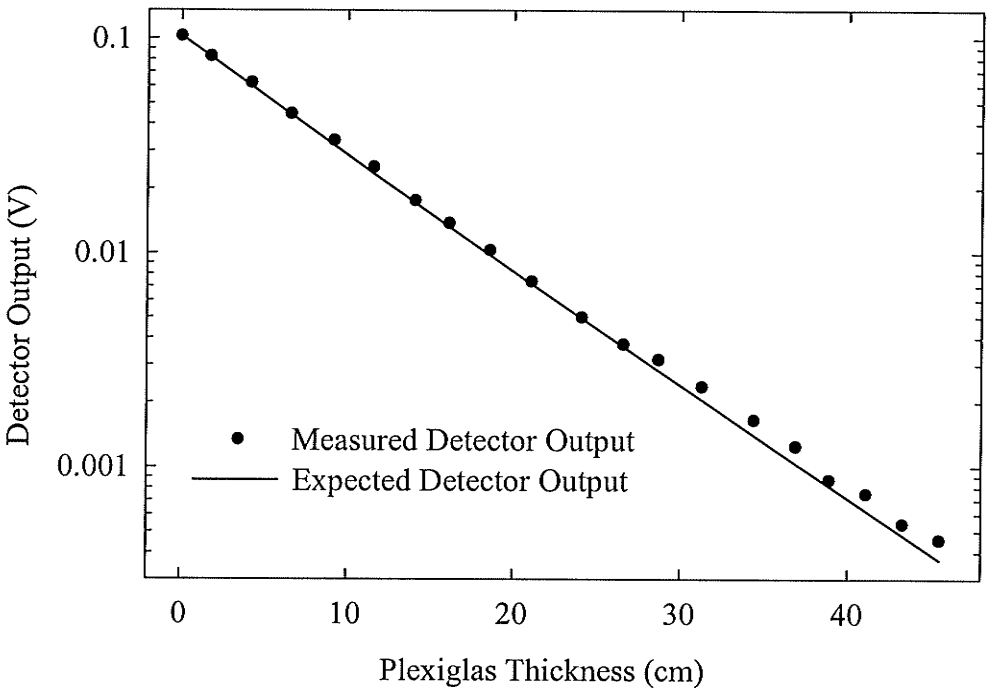

Figure 3.40 Plot of the measured detector output as a function of Plexiglas thickness (points) under narrow-beam collimation conditions. Error bars, taken to be the standard error in the mean, are smaller than the dots. Also shown (line) is the expected detector output normalized to the measured detector output in the absence of Plexiglas.

3.7.1 Theory

The output voltage of the circuit in the absence of light depends upon the sum of the op-amp input bias current i_b, the switch leakage current i_s and the photodiode dark current i_{dark}. The photodiode dark current and the op-amp input bias current both vary as a function of temperature, which in turn introduces a temperature dependence in the output voltage. The temperature dependence of the switch leakage current is not known. The light output of $CdWO_4$ also has a very slight temperature dependence (Bicron, 1990). The temperature dependence of the input offset voltage of the op-amp can be neglected as the two point subtraction $\Delta V = V_f - V_i$ used to remove the charge injection introduced by the switch also cancels out this effect. The temperature dependence of the circuit can be estimated from the data provided in the op-amp and the photodiode specification sheets.

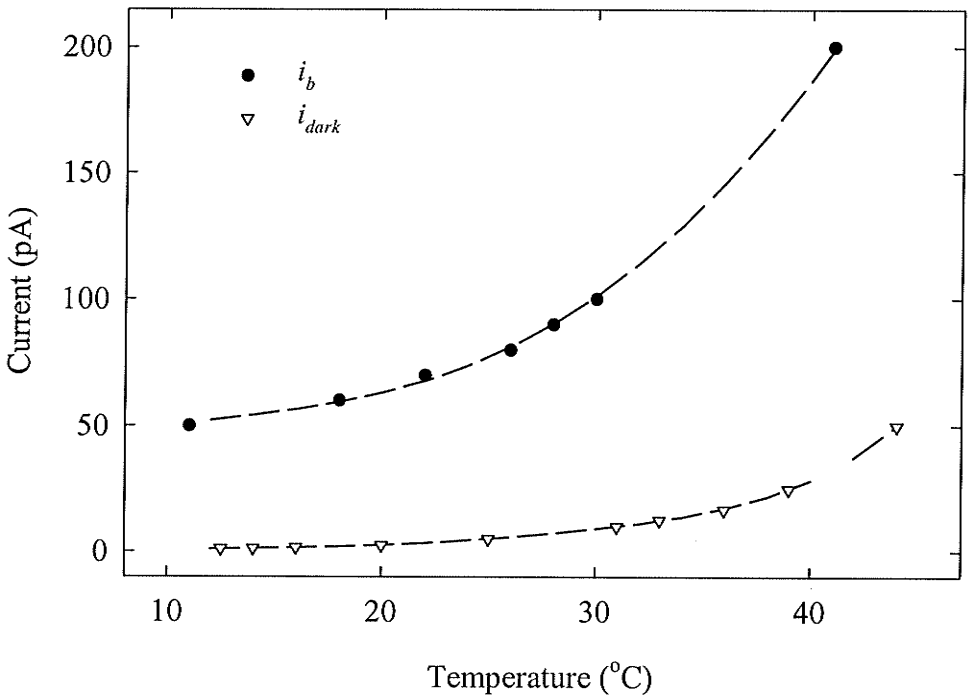

Figure 3.41 Temperature dependence of the op-amp input bias current i_b and the photodiode dark current i_{dark}. The dashed lines represent the curves fit to the data. (Texas Instruments, 1996; Hamamatsu, 1994, 1995)

The input bias current i_b flows into the inverting input of the integrator op-amp shown in Figure 2.4. A plot of the typical input bias current versus temperature is shown in Figure 3.41 (Texas Instruments, 1996). It should be noted that the actual input bias current might be significantly different from the typical value. For instance, the maximum possible input bias current in tabular data at 25°C is 200 pA (Texas Instruments, 1996), which is much larger than the 65 pA shown in Figure 3.41.

The switch leakage current at room temperature $i_s = \pm 10$ pA (Temic, 1997) is much smaller than the op-amp input bias current. In addition, its temperature dependence is not known. The effect of the switch leakage current is therefore not included in the theoretical calculations.

Special care must be taken when considering the photodiode dark current i_{dark}. As was the case for the op-amp, the actual dark current can be much larger than the typical value, i.e., as large as 30 pA at 25 °C (Hamamatsu, 1994). To further complicate matters, the typical values quoted in the Hamamatsu specification sheet (Hamamatsu, 1994, 1995) and plotted in Figure 3.41 assume that the photodiode is reverse biased with 10 mV,

which is most likely not the case here; the biasing of the photodiode depends upon the magnitude and sign of the input offset voltage of the op-amp, which can be between ±9 mV (Texas Instruments, 1996).

The total current i_D flowing through the integrating capacitor in the absence of light is

$$i_D = i_{b\text{-}s} + 2i_{dark} \tag{3.105}$$

where $i_{b\text{-}s}$ is the combined op-amp input bias current and switch leakage current. The factor of two in front of the diode dark current is necessary since two diodes are wired together in parallel. Recalling (2.3), the output voltage of the detector in the absence of light is given by

$$\Delta V_D = \frac{G\,\Delta T}{C_{\text{int}}} i_D \tag{3.106}$$

where $G = 47$ is the gain of the gain-and-filter stage, $C_{\text{int}} = 1$ nF is the capacitance of the capacitor in the integration stage, and ΔT is the integration time. For the gain-and-filter stage, the effects of both the input offset voltage and the input bias current are constant over an integration period and thus cancel out during subtraction of the initial and final readings.

3.7.2 Method

The detector assembly output voltage was measured in the absence of light as a function of circuit temperature. The circuit, a heat source, and a fan to circulate the air were placed inside of a Styrofoam box with 8 cm thick walls. The temperature inside the box was initially raised to 55°C. Detector output voltage readings were collected as a function of temperature inside the Styrofoam box while the circuit cooled to room temperature. A total of five voltage measurements were made every ten seconds, using a sampling frequency of 10 Hz. The circuit was then cooled to 14 °C. Measurements were collected while the circuit warmed to room temperature.

The temperature was measured using a thermistor placed adjacent to the photodiode, inside of the aluminum case containing the detector assembly. A data acquisition/control unit (HP 3497A) supplied a 100 μA current and measured the voltage across the thermistor. The thermistor was calibrated by fixing it to a Fisher Scientific

Digital Thermometer probe, immersing both in a water bath, and recording the thermistor voltage as a function of temperature, as determined by the thermometer.

Because the bias voltage applied to the photodiode was not known, measurements were made to estimate the magnitude of i_{dark}[8]. This was achieved indirectly by measuring i_D and $i_{b\text{-}s}$ and using (3.105) to solve for i_{dark}. The current i_D was found from measurements of ΔV_D, using (3.106). The current $i_{b\text{-}s}$ was determined from measurements of ΔV_{b-s} using

$$\begin{aligned} \Delta V_{b-s} &= \frac{G\ \Delta T}{C_{\text{int}}} i_{b-s} \\ &= \left(4.604\times 10^{9}\ \frac{\text{V}}{\text{A}}\right)\cdot i_{b-s} \qquad [\text{V}] \end{aligned} \tag{3.107}$$

where ΔV_{b-s} was found by measuring the detector output voltage with the photodiode removed (note that the contribution of i_b and i_s can not be individually found).

3.7.3 Results

The thermistor calibration data relating the thermistor voltage V_{th} to temperature is plotted in Figure 3.42. This curve was fit using a fifth order polynomial, namely,

$$\text{Temperature} = a + bV_{th} + cV_{th}^2 + dV_{th}^3 + eV_{th}^4 + fV_{th}^5 \tag{3.108}$$

where V_{th} is the thermistor voltage, a = 91.7416413, b = -389.863699, c = 1099.954549, d = -1860.53054, e =1651.545187 and f = -592.662398.

As described above, a number of measurements were carried out to find i_{dark}. The detector output voltage at 22.7°C, with and without the photodiode in the circuit was measured to find the currents i_D and $i_{b\text{-}s}$. These were subtracted to find $2i_{dark}$ = 2.47 pA. This is considerably smaller than the manufacturer's typical value of 2 x 3.72 pA = 7.44 pA, which is not surprising because it is unlikely that the photodiode bias voltage is 10 mV (typical value = 3 mV, Texas Instruments, 1996). This contribution to the current is negligible compared to the input bias current plotted in Figure 3.41, and will therefore be ignored.

---

[8] Note that these measurements were made some time after the actual temperature measurements were completed, and used the 8-channel detector described in the next chapter, rather than the single-channel detector. The measurement of i_{dark} is therefore just an estimate. It is however expected that the results are comparable to those that would have been found using the single-channel detector.

The measured and calculated (3.106) detector circuit response as a function of temperature is plotted in Figure 3.43. As can be seen, there is reasonable agreement between the predicted and measured trends for temperatures below about 38° C, although the actual values do not agree. Above 38° C, the behavior of the circuit changes dramatically from that predicted. Because the ambient room temperature is not expected to approach this temperature, and the scanner consists of low power components that are not expected to significantly raise the temperature inside of the scanner covers (a fan could be incorporated if necessary), this is not a matter of concern.

It must be noted that a large number of approximations were made when calculating the expected voltage. These are summarized below.

(i) The typical input bias current provided by the manufacturer was used, which may have been quite different from the actual current.

(ii) The temperature dependence of the photodiode dark current was ignored, as the 10 mV bias on the photodiode required for the manufacturer's values to be valid, was most likely not present. The actual bias voltage was not measured. However, the indirect measurements described above suggest that the dark current is quite small compared to the input bias current.

(iii) The temperature dependence of the switch leakage current was not available. Its value at room temperature is small compared to the input bias current and its effect was therefore ignored in the theoretical calculation.

The purpose of the theoretical calculations performed above was to provide an estimate of the temperature dependence trend. In this sense, satisfactory results were found.

Because the dark current must be subtracted from the detector output, the temperature dependence of the dark current presented in Figure 3.43 can clearly have an impact on the images. However, the temperature is not expected to vary dramatically during a single CT exam. It would be simple to perform a dark current measurement at the beginning and end of each exam, and use these values to correct the detector outputs for that particular exam. The temperature dependence of the dark current is thus unlikely to affect the image quality.

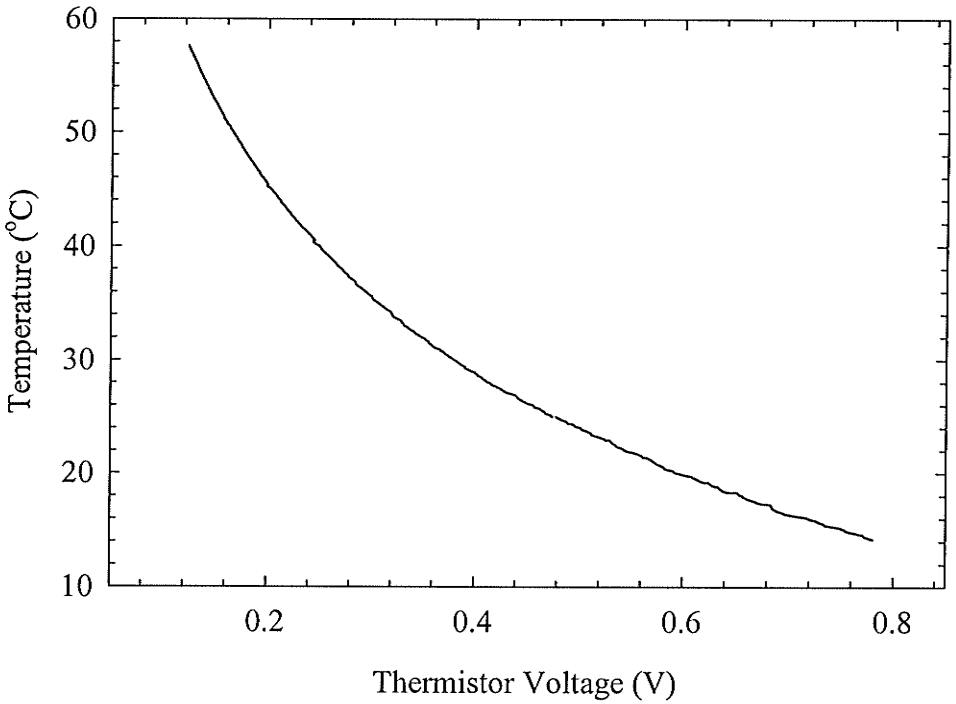

Figure 3.42 Thermistor calibration plot showing the relationship between the thermistor voltage and the temperature (°C).

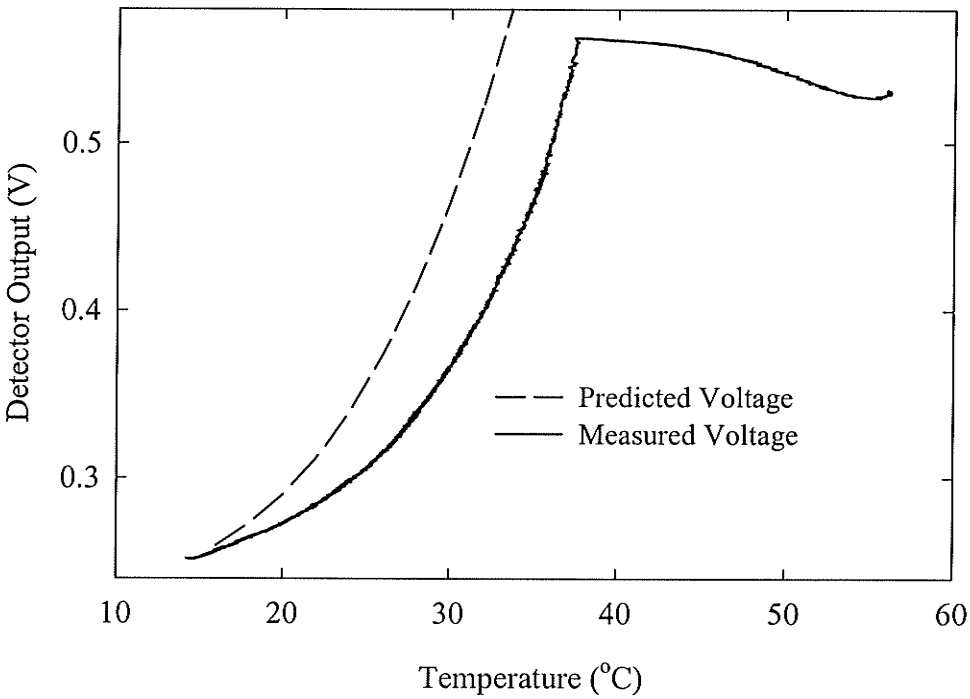

Figure 3.43 Detector output as a function of temperature in the absence of light. The solid curve represents the experimental data, and dashed curve represents the theoretically expected temperature dependence.

3.8 Scanner Images

Three images were generated using the single-channel detector described in this chapter and the first generation scanner geometry shown in Figure 3.44. The object to be scanned was placed on a turntable that was rotated and translated under computer control, while the detector and source were held stationary. Both the ^{192}Ir source and the detector were collimated with 1 cm thick by 14 cm long lead blocks to form a 1 cm thick slice. No collimation was used in the imaging plane. The source-to-detector distance was 74 cm. Translation sample spacing, number of projections and source strength are listed in the figure captions. Each measured ray-sum was the average of six detector output voltage readings, corrected for dark current. The projection data were reconstructed using a filtered backprojection technique that will be described in §6.1 (Barrett and Swindell, 1981). Shown in Figures 3.45 to 3.47 are images of a non-eviscerated chicken, and two phantoms.

Figure 3.45 clearly reveals the heart, lung and bones of the chicken. These structures can also be seen in the photograph, taken at the same level as the CT scan. Figures 3.46a and 3.47a show images of phantoms containing BT needles and inserts of different densities, taken with the single-channel detector described in this chapter. Corresponding images collected with a conventional CT scanner (Siemens Somatom Plus 4, Siemens Medical Systems) are also shown. Figure 3.46a clearly demonstrates the ability to produce an artifact free visualization of clinical BT needles, while dark streak artifacts are present in the image obtained using the diagnostic CT scanner (Figure 3.46b). The images in Figure 3.47 demonstrate that the low contrast resolution of the ^{192}Ir source-based CT scanner may be inferior to a conventional CT scanner due to the higher photon energy of ^{192}Ir and reduced number of photons reaching the detector. The image noise for the ^{192}Ir source-based CT scanner images is significantly larger than for the conventional CT scanner due to the low photon fluence of the ^{192}Ir source. It is expected that the dose delivered will be less than that associated with a conventional CT scan for the same reason.

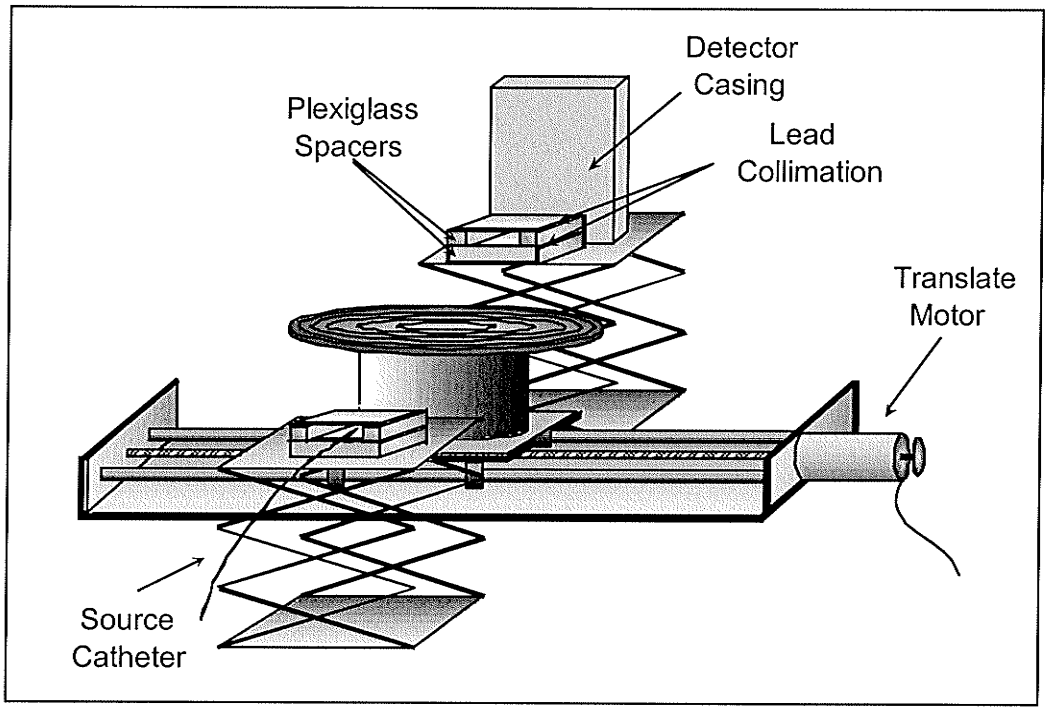

Figure 3.44 Schematic of the source detector geometry used to generate first generation images

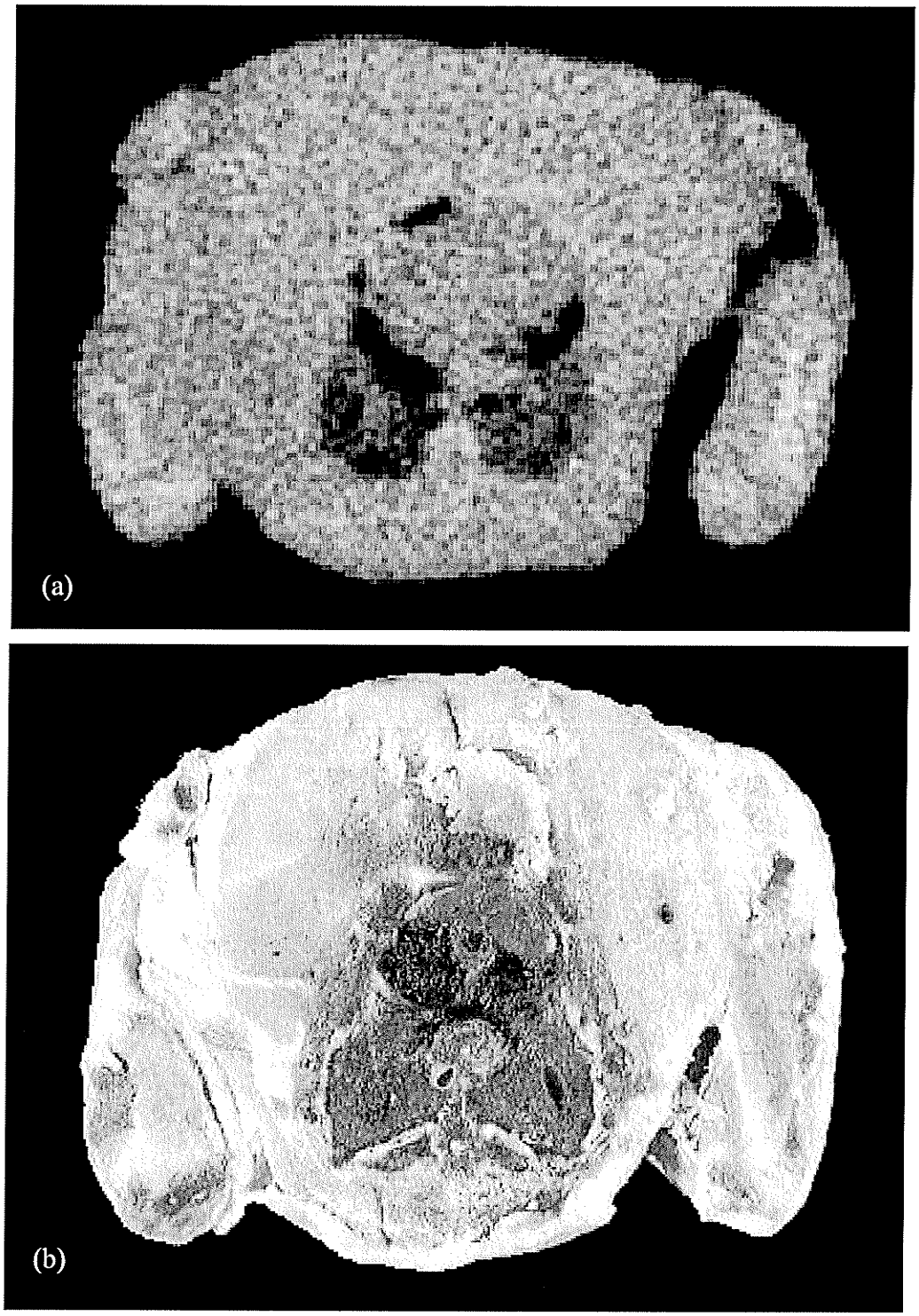

Figure 3.45 (a) CT image of a non-eviscerated chicken at the heart and lung level, generated using the first generation scanner shown in Figure 3.44. The translation sample spacing was 1.40 mm and a total of 99 projections were acquired from 0° to 178.2° using a source strength of 8.30 Ci. (b) Photograph of the chicken at the same level.

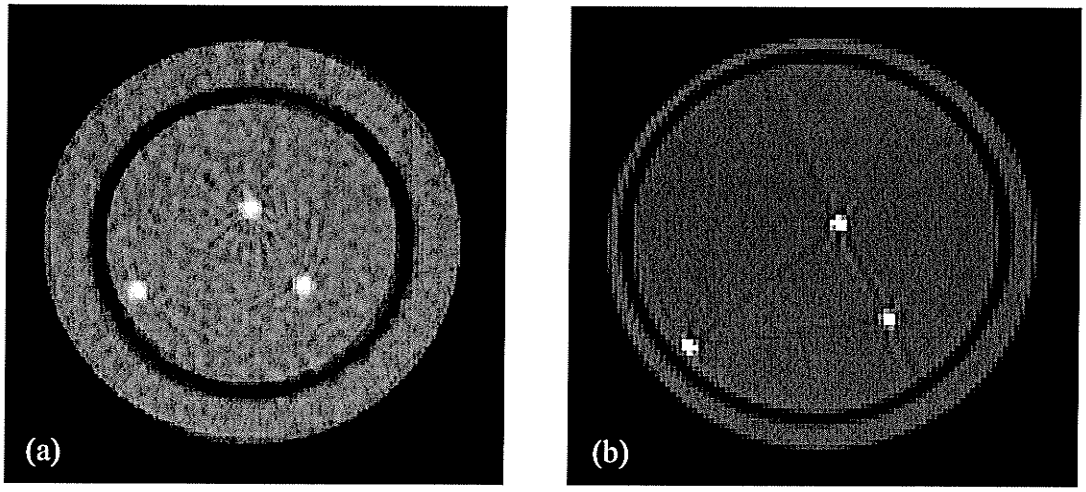

Figure 3.46 (a) CT image of a phantom consisting of a Styrofoam cup placed inside of a larger plastic beaker, both filled with water, generated using the first generation scanner shown in Figure 3.44. Three BT needles are placed inside of the Styrofoam cup and appear as three bright spots; the Styrofoam cup is the dark ring surrounding the needles; and the water appears as a fairly homogeneous gray. The translation sample spacing was 0.67 mm and a total of 49 projections were acquired from 0° to 176.4° using a source strength of 3.96 Ci. (b) Image of a similar phantom obtained using a conventional CT scanner (Somatom Plus 4, Siemens Medical Systems). Technique: 120 kVp and 50 mAs.

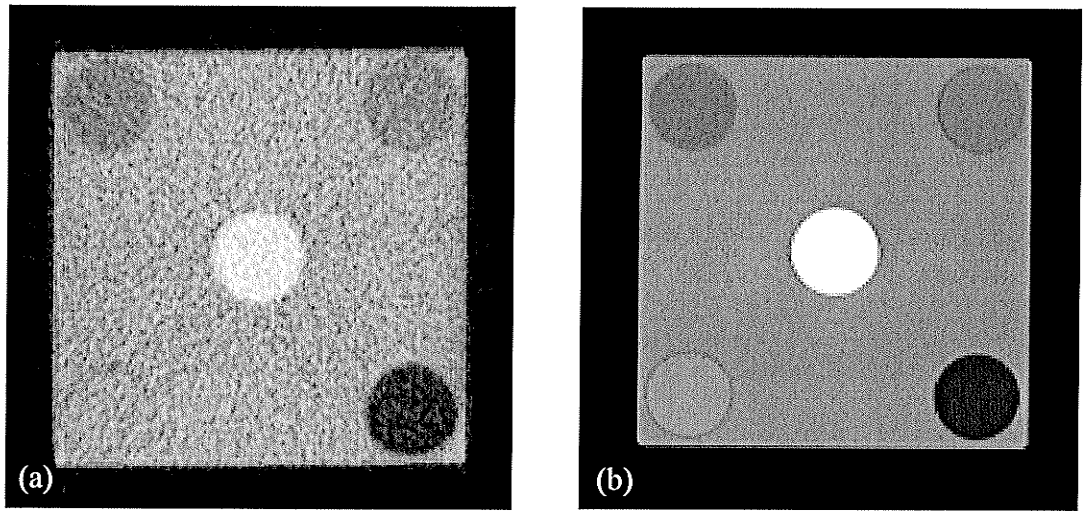

Figure 3.47 (a) CT image of a phantom consisting of cylinders of different densities inserted into a Plexiglas block, generated using the first generation scanner shown in Figure 3.44. The cylinders are AP6 adipose simulating material ρ_e^w = 0.895 (top left), solid water ρ_e^w = 1.000 (top right), $CaCO_3$ ρ_e^w = 1.142 (bottom left), LN-450 lung simulating material ρ_e^w=0.438 (bottom right), and SB3 cortical bone simulating material ρ_e^w=1.707 (center). The translation sample spacing was 1.40 mm and a total of 99 projections were acquired from 0° to 178.2° using a source strength of 8.95 Ci. (b) Image of the same phantom obtained using a conventional CT scanner (Somatom Plus 4, Siemens Medical Systems). Technique: 140 kVp and 189 mAs.

Chapter 4

System Characterization: Eight-Channel Measurements

As discussed in Chapter 2, the detector ring for the fourth generation scanner uses 96 eight-channel detectors. This chapter describes a series of measurements carried out to characterize a complete eight-channel detector assembly. The first set of measurements examines the inter-channel variability and sensitivity of the detectors. Measurements are then presented that assess the linearity of all eight channels as a function of x-ray intensity incident on the detector. Finally, cross-talk is quantified directly and via a cross-covariance technique involving mathematical analysis of the output of simultaneously irradiated channels.

4.1 Inter-channel Variability

Measurement of the inter-channel variability was the first step in a series of measurements to characterize the behavior of the eight-channel detector assembly. The inter-channel variability measurements were divided into two parts. The first examined the inter-channel variability due to differences in the electronic gains, which are a consequence of the variations in the gains of the integrators and the gain-and-filter stages. The second part measured the total inter-channel variability of the detector response for the same γ-ray fluence with the scintillating crystal array in place. This measurement

included the effects of the photodiode array sensitivity, the crystal array and its coupling to the photodiode array, as well as the effect of the differences in the electronic gain. In terms of the performance of the final scanner, the quantity of interest is the total inter-channel variability[1]. However, looking at the response of the electronics alone, enables a separation of the responses of the electronics and the detecting elements, and identifies the components that should become the focus of future efforts to minimize inter-channel variability. Measurements were also carried out using a radiotherapy simulator to irradiate the detector array at various x-ray fluence rates. The purpose of these measurements was to demonstrate that the inter-channel variability is independent of the fluence rate incident on the detector array.

4.1.1 Electronic Gain Inter-channel Variability

4.1.1.1 Method

The inter-channel variability due to differences in electronic gain was measured by modifying the 8-channel detector circuit such that a single photodiode pair (corresponding to Channel 4) was wired to the input of an 8-bit DIP switch. Each of the switch outputs was wired to one of the eight gated integrator op-amps. This is illustrated in Figure 4.1, where the term "electronics" refers to the integrator, the gain-and-filter stage, and the sample-and-hold of a particular channel. The photodiode pair connected to the DIP switch was illuminated using the same light source as in the detector response measurement of §3.4. Note that the photodiode pairs corresponding to the other channels (i.e., Channels 1, 2, 3, 5, 6, 7 and 8) were disconnected and not used.

The single photodiode pair was sequentially coupled to each of the channel electronics using the DIP switch, and the detector output voltage recorded. As an example, Figure 4.1 shows the photodiode pair connected to the Channel 6 electronics. A total of 150 detector output voltage measurements were collected for each channel using a sampling frequency of 10 Hz. These were averaged and corrected for dark current.

---

[1] In practice, the total inter-channel variability is automatically corrected for because the detector signal V is divided by the air scan data V_0 when calculating the projection data $P = -\ln(V/V_0)$. It is worth noting that images generated using fourth generation scanners are relatively insensitive to variations in detector sensitivity; a simulated fourth-generation water phantom image generated using detectors with a 1% variation in sensitivity (Joseph, 1981) displayed only a slight cupping artifact.

4.1.1.2 Results

Table 4.1 lists the detector output voltage when optical photons illuminated the single photodiode pair, and the DIP switch was cycled through the electronics of all eight channels. The normalized electronic gain $\widetilde{G}_{electonic}$ was found by dividing the measured voltage for each channel by the maximum measured voltage. As can be seen, the inter-channel variability due to differences in electronic gain is quite small. Further efforts to reduce the electronic variability are therefore not warranted.

4.1.2 Total Inter-channel Variability

The total inter-channel variability was determined after fixing the scintillating crystals to the photodiode array. Measurements were carried out for the crystal arrays coated with Al_2O_3 and gelcoat (§2.5.5). Note that the unmodified circuit described in §2.3 was used for these measurements.

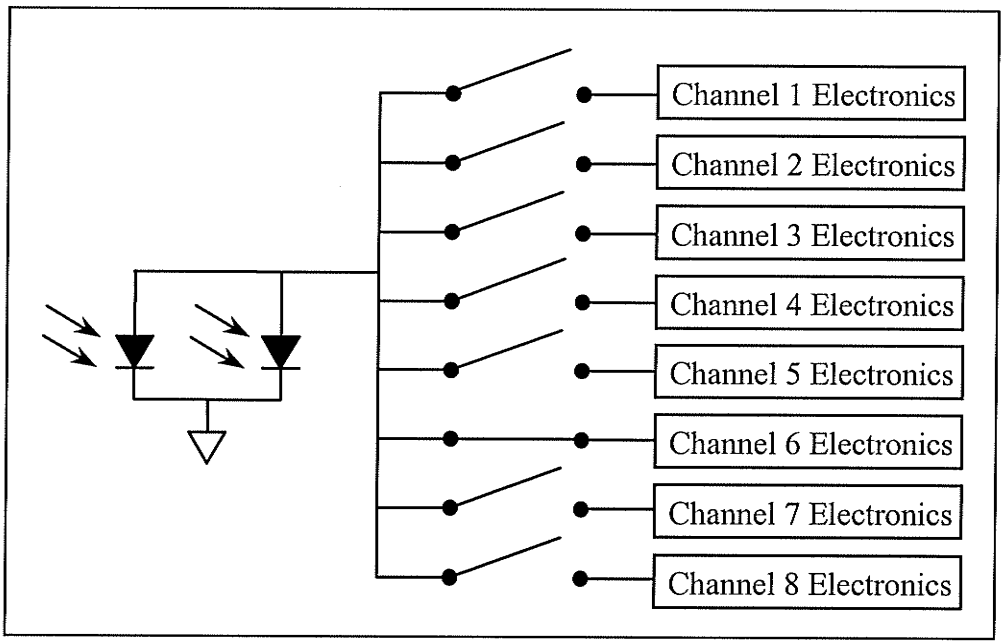

Figure 4.1 Block diagram showing the 8-channel circuit configuration used to measure the inter-channel variability due to differences in electronic gain. The photodiode pair formerly associated with Channel 4 was wired to the input of the DIP switch, while the electronics associated with the different channels were wired to the output. The designation "electronics" refers to the integrator, the gain-and-filter stage and the sample-and-hold. Here the photodiode pair is connected to the Channel 6 electronics.

Table 4.1 Inter-Channel Variability due to Differences in Electronic Gain

Channel	Detector Output (V)	Normalized Electronic Gain $\widetilde{G}_{electonic}$
1	2.9401 ± 0.0004	0.937
2	3.0958 ± 0.0007	0.987
3	3.0926 ± 0.0008	0.986
4	3.0977 ± 0.0006	0.988
5	3.0408 ± 0.0008	0.970
6	3.1365 ± 0.0006	1.000
7	3.1179 ± 0.0006	0.994
8	3.0010 ± 0.0007	0.957
Mean	3.07	0.977
SD	0.067	0.021
Electronic Gain Variability*	2.17%	2.17%

*SD/Mean x 100

4.1.2.1 Method

The detector was irradiated using the ^{192}Ir brachytherapy source (A_c = 7.4920 Ci for the gelcoat coated array; A_c = 7.4564 Ci for the Al_2O_3 coated array) placed at a large distance (74 cm) from the detector so that differences in the source-to-detector distance between the eight channels were negligible over the 2.5 cm long detector array. A total of 250 readings were collected for each channel at a sampling frequency of 10 Hz. These were averaged and corrected for dark current. The total inter-channel variability is of greater importance than the inter-channel variability due to differences in electronic gain because the detector output recorded during CT data acquisition must be corrected for this variation.

4.1.2.2 Results

The results of measurements using the Al_2O_3 and gelcoat coated arrays are listed in Table 4.2. The normalized total sensitivity $\widetilde{G}_{total}$ is the measured voltage normalized to its

maximum value. $\widetilde{G}_{total}$ reflects the variation in sensitivity of the detector channels in the collection of γ-rays. Note that in the fourth generation scanner, inter-channel variability will be corrected for by acquiring an air scan and then using those detector output voltages to determine the projection data $P = \ln(V/V_0)$, where V is the detector output for the transmission measurements and V_0 is the detector output for the air scan. This automatically normalizes the output of each detector.

4.1.3 Crystal/Photodiode Array Inter-channel Variability

The total and electronic gain inter-channel variability measurements can be used to extract the contribution arising from variations in the crystal and the photodiode array. If the variations due to the latter are much larger than the variations in the electronic gain, future endeavors can be directed at reducing the variability produced by the crystal and the photodiode array. More importantly, a large inter-channel variability could be used to detect a problem with the detector design, or the presence of a faulty component.

The detector output voltage V_{1-i} of the i^{th} channel for the measurements carried out in §4.1.1 (Table 4.1) can be described by

$$V_{1-i} = g_{electronic-i} \cdot i_{photo} \qquad \text{(light only)} \qquad (4.1)$$

where $g_{electronic-i}$ is the electronic gain of the i^{th} channel and i_{photo} is the photocurrent produced by illumination of the photodiode pair by the light source. Note that the same photodiode element pair was connected to the electronics of each channel in turn, thus i_{photo} is the same for all channels. For these measurements, neither $g_{electronic-i}$ or i_{photo} are known; only their product V_{1-i} was measured. The normalized electronic gain $\widetilde{G}_{electonic}$ is given by

$$\widetilde{G}_{electonic} = \frac{V_{1-i}}{(V_1)_{\max}} = \frac{g_{electronic-i} \cdot i_{photo}}{(g_{electronic})_{\max} \cdot i_{photo}} = \frac{g_{electronic-i}}{(g_{electronic})_{\max}}. \qquad (4.2)$$

where $(V_1)_{\max} = \max(V_{1-i})$ is the detector output voltage of the channel with the largest response (Channel 6, Table 4.1). As the photocurrent is the same for all of the channels, the channel with the largest response also has the largest electronic gain $(g_{electronic})_{\max}$. Equation (4.2) demonstrates that normalizing the detector output (light measurements) to its maximum value yields the normalized electronic gain $\widetilde{G}_{electonic}$, as listed in the right hand column of Table 4.1.

Table 4.2 Total Inter-Channel Variability (Measurements with Crystal Arrays)

Channel	Al_2O_3 Coated Array		Gelcoat Coated Array	
	Detector Output (V)	Normalized Total Sensitivity $\widetilde{G}_{total}$	Detector Output (V)	Normalized Total Sensitivity $\widetilde{G}_{total}$
1	0.815 ± 0.004	0.806	1.059 ± 0.003	0.937
2	0.959 ± 0.005	0.947	1.160 ± 0.004	0.987
3	0.967 ± 0.005	0.956	1.127 ± 0.004	0.986
4	0.980 ± 0.005	0.969	1.152 ± 0.004	0.988
5	0.905 ± 0.005	0.895	1.070 ± 0.004	0.970
6	1.011 ± 0.005	1.000	1.189 ± 0.004	1.000
7	0.925 ± 0.005	0.915	1.171 ± 0.004	0.994
8	0.696 ± 0.005	0.688	1.084 ± 0.003	0.957
Mean	0.907	0.897	1.126	0.948
SD	0.104	0.103	0.049	0.042
Total Variability*	11.5%	11.5%	4.39%	4.39%

*SD/Mean x 100

Similarly, the detector output voltage V_{2-i} of the i^{th} channel for the measurements carried out in §4.1.2 (Table 4.2) can be described by

$$V_{2-i} = g_{electronic-i} \cdot i_{photo-i} \qquad (\gamma\text{-rays}) \qquad (4.3)$$

where $g_{electronic-i}$ is the electronic gain of the i^{th} channel and $i_{photo-i}$ is the channel dependent photocurrent. The photocurrent $i_{photo-i}$ can in turn be expressed in terms of the crystal and photodiode array sensitivity s_{cp-i} and the channel independent γ-ray fluence ϕ incident on each crystal

$$i_{p-i} = s_{cp-i} \cdot \phi \,. \qquad (4.4)$$

Combining (4.3) and (4.4) yields

$$V_{2-i} = g_{electronic-i} \cdot s_{cp-i} \cdot \phi \,. \qquad (4.5)$$

Dividing by the maximum detector output yields

$$\widetilde{G}_{total} = \frac{V_{2-i}}{(V_2)_{\max}} = \frac{g_{electronic-i} \cdot s_{cp-i} \cdot \phi}{(g_{electronic-i} \cdot s_{cp-i})_{\max} \cdot \phi} = \frac{g_{electronic-i} \cdot s_{cp-i}}{(g_{electronic-i} \cdot s_{cp-i})_{\max}} \qquad (4.6)$$

where $(V_2)_{\max}$ is the detector output voltage of the channel with the largest response

(Channel 6, Table 4.2). Because ϕ is the same for all of the channels, the channel with the largest response also has the largest overall gain $\left(g_{electronic-i} \cdot s_{cp-i}\right)_{\max}$. Equation (4.6) demonstrates that normalizing the detector output (γ-ray measurements) to its maximum value yields the total normalized sensitivity $\widetilde{G}_{total}$ listed in Table 4.2, a parameter which takes into account both the variations in the electronic gain, and the variations in the crystal and photodiode array sensitivity.

The crystal and photodiode array sensitivity can be extracted from the above measurements by dividing (4.5) by (4.1) to yield

$$\frac{V_{2-i}}{V_{1-i}} = \frac{g_{electronic-i} \cdot s_{cp-i} \cdot \phi}{g_{electronic-i} \cdot i_{photo}} = s_{cp-i} \cdot \frac{\phi}{i_{photo}} \tag{4.7}$$

which cancels out the channel dependent electronic gain (assumed to be signal independent, as will be demonstrated in §4.1.4), leaving only the channel dependent crystal and photodiode array sensitivity s_{cp-i} and the channel independent term ϕ / i_{photo}. The normalized crystal and photodiode array sensitivity $\widetilde{G}_{CP}$ can therefore be found using

$$\widetilde{G}_{CP} = \frac{\left(\frac{V_{2-i}}{V_{1-i}}\right)}{\left(\frac{V_{2-i}}{V_{1-i}}\right)_{\max}} = \frac{s_{cp-i} \cdot \frac{\phi}{i_{photo}}}{\left(s_{cp-i}\right)_{\max} \cdot \frac{\phi}{i_{photo}}} = \frac{s_{cp-i}}{\left(s_{cp-i}\right)_{\max}} \tag{4.8}$$

where $\left(V_{2-i} / V_{1-i}\right)_{\max}$ is the maximum value of (4.7) (Channel 6, Table 4.3). As ϕ / i_{photo} is the same for all of the channels, Channel 6 also has the largest crystal and photodiode array sensitivity $\left(s_{cp-i}\right)_{\max}$. Equation (4.8) demonstrates that normalizing the output of (4.7) to its maximum value yields the normalized crystal and photodiode array sensitivity $\widetilde{G}_{CP}$. Results are listed in Table 4.3 for both scintillating crystal arrays.

Plotted in Figure 4.2 are $\widetilde{G}_{electronic}$, $\widetilde{G}_{total}$ and $\widetilde{G}_{CP}$ for both arrays. In the case of the gelcoat coated array, the crystal and photodiode array variability of 2.55% is only slightly larger than the electronic gain variability of 2.17%, resulting in a total variability of 4.39%. The small inter-channel variability for the gelcoat coated array is evident in Figure 4.2b. Conversely, the total variability of 11.5% for the Al_2O_3 coated array is primarily a consequence of the 9.94% crystal and photodiode array variability. The large inter-channel variability is evident in Figure 4.2a, where it can be seen that the largest

variation in the normalized total sensitivity exists for the outer two channels. This is most likely due to cross-talk, which will be characterized in §4.4. It is suspected that the reduced response of the outer channels is because the optical photons escaping from the outer scintillating crystals are not replaced by photons from a neighboring channel, as is the case for the inner channels. If the effect of Channels 1 and 8 are excluded, the crystal and photodiode array variability is only 3.3% and the total variability is reduced to 4.0%, which is comparable to the results found for the gelcoat coated array. It is interesting to note that the crystal manufacturer Bicron claims a variability of 10% if they package and mount the crystals on the photodiode array. This shows that an inter-channel variability superior to a commercially assembled photodiode/crystal array has been achieved.

Table 4.3 Inter-Channel Variability of the Crystal and Photodiode Array

Channel	Al_2O_3 Coated Array		Gelcoat Coated Array	
	Crystal and Photodiode Array Sensitivity	Normalized Crystal and Photodiode Array Sensitivity $\widetilde{G}_{CP}$	Crystal and Photodiode Array Sensitivity	Normalized Crystal and Photodiode Array Sensitivity $\widetilde{G}_{CP}$
1	0.277	0.860	0.360	0.951
2	0.310	0.960	0.375	0.988
3	0.313	0.970	0.364	0.962
4	0.316	0.981	0.372	0.981
5	0.298	0.923	0.352	0.928
6	0.322	1.000	0.379	1.000
7	0.297	0.920	0.375	0.991
8	0.232	0.719	0.361	0.953
Mean	0.296	0.917	0.367	0.969
SD	0.029	0.091	0.0094	0.025
Crystal and Photodiode Array Variability*	9.94%	9.94%	2.55%	2.55%

*SD/Mean x 100

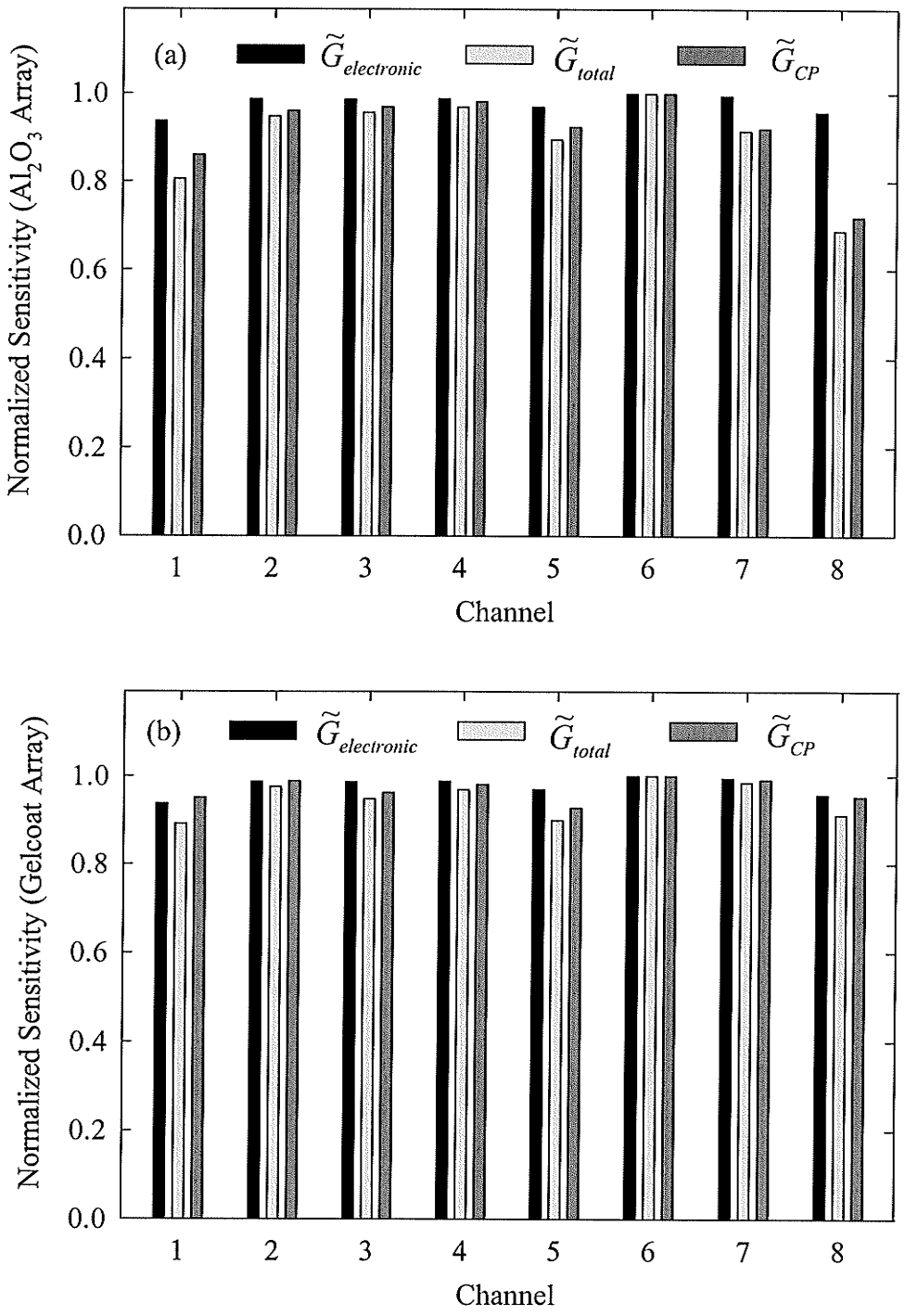

Figure 4.2 Plot of the normalized electronic gain $\tilde{G}_{electronic}$, normalized total sensitivity $\tilde{G}_{total}$ and the normalized crystal and photodiode array sensitivity $\tilde{G}_{CP}$ for (a) the Al_2O_3 coated array and (b) the gelcoat coated array.

4.1.4 RT Simulator (Al_2O_3 Array)

4.1.4.1 Method

The total inter-channel variability of the detector (Al_2O_3 coated array) in the presence of radiation was also assessed using the fluoroscopy unit of a radiotherapy simulator (Varian Ximatron Series RT). The detector response was recorded for 15 *x*-ray fluence rates ranging from 1 mA to 15 mA in 1 mA increments. A total of 100 data points were collected at each fluence rate using a 10 Hz sampling frequency. These measurements were repeated five times and the results averaged. The data corrected for dark current were normalized to the channel with the largest detector response for each mA setting.

4.1.4.2 Results

The normalized total sensitivity is illustrated as a function of the nominal *x*-ray tube current in Figure 4.3. It was necessary to normalize the detector output to the channel with the maximum response in order to allow comparison of the sensitivity with increasing mA. As there is little variation in sensitivity with increasing mA, and correspondingly, increasing detector output, these results confirm that the sensitivity is independent of incident fluence rate. The mean and standard deviation of the points shown in Figure 4.3 are listed in Table 4.4. The standard deviation is quite small for all channels, establishing numerically that the sensitivity is independent of the incident fluence rate. Note that the standard deviation for Channel 4 is zero because this channel always had the largest response, so that the normalized response for this channel was always identically 1.0. Note also that the normalized sensitivity values listed in Table 4.4 are not identical to those listed in the Al_2O_3 section of Table 4.2 as the crystal array was removed and replaced between these two experiments. The more uniform sensitivity values listed in Table 4.2 suggest that the crystal array was more accurately aligned with the photodiode array for those measurements. Nevertheless, the measurements performed in this section verify that the sensitivity is independent of incident fluence rate. This is as expected considering that the detector response is linear (§3.4 and §3.6).

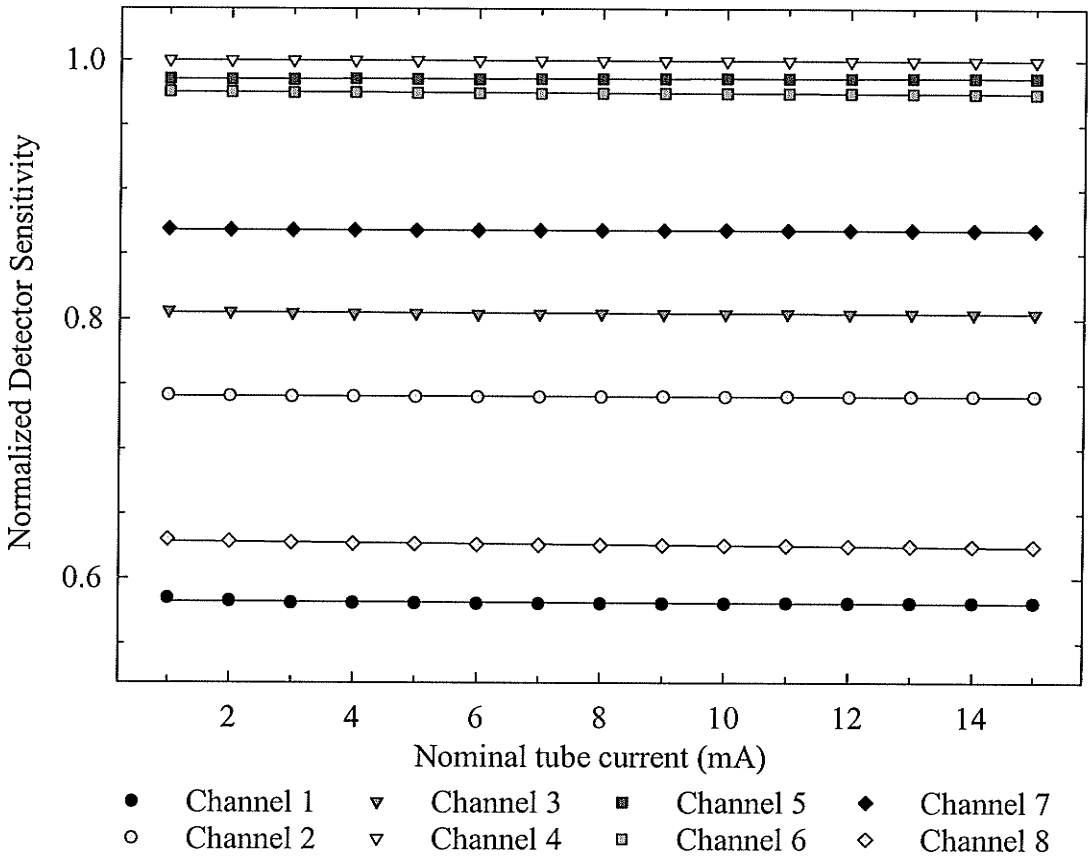

Figure 4.3 Plot of the normalized detector response as a function of nominal mA. The lines shown were found using linear regression.

Table 4.4 Total Inter-channel Variability (Al_2O_3 coated array)

Channel	Normalized Sensitivity	Standard Deviation
1	0.5812	0.0010
2	0.7406	0.0003
3	0.8046	0.0005
4	1.0000	0.0000
5	0.9861	0.0005
6	0.9749	0.0004
7	0.8685	0.0002
8	0.6263	0.0016

4.2 Linearity (Radiation Measurements – Al_2O_3 Array)

4.2.1 Method

4.2.1.1 RT Simulator Output Linearity

The linearity of the detector response as a function of incident *x*-ray fluence was assessed by irradiating the detector (Al_2O_3 coated crystal array) using the fluoroscopy unit of a radiotherapy simulator (Varian Ximatron Series RT). The output of the simulator in fluoroscopy mode was controlled by increasing the tube output in 1 mA increments from 1 mA to 15 mA. To verify that tube output varied linearly with nominal mA, a dosimeter (Model 3036 Radcal Corporation) was used to measure the output of the *x*-ray tube. Measurements were made while reducing the tube current from 15 mA to 1 mA, and then again while increasing the tube current from 1 mA to 15 mA.

4.2.1.2 Detector Output Linearity

As was the case for the inter-channel variability measurements, the detector response was measured for 15 fluence rates. A total of 100 data points were collected at each fluence rate using a 10 Hz sampling frequency. Five trials were performed and corrected for dark current.

4.2.2 Results

4.2.2.1 RT Simulator Output Linearity

The average output of the *x*-ray tube measured by the dosimeter as a function of nominal mA setting is shown in Figure 4.4. The linear regression line was found to have a slope of 0.071 C/(kg·min·mA) and an intercept of –0.009 C/(kg·min). The standard error of estimate with respect to the mean is 0.24%. This indicates that the *x*-ray tube output is linear with respect to the nominal tube output.

4.2.2.2 Detector Output Linearity

The detector response averaged over five trials and corrected for dark current is shown in Figure 4.5. The error bars, taken to be the standard deviation of the five trials are smaller than the dots. The lines shown were found using linear regression (standard error of

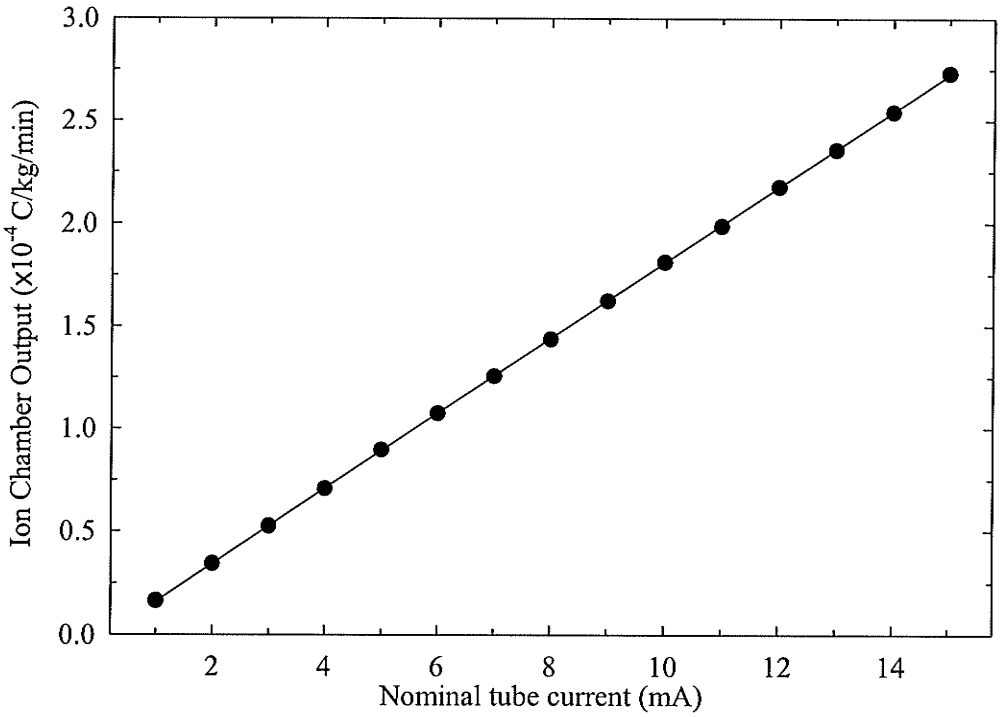

Figure 4.4 Plot showing the average dosimeter output as function of nominal fluoroscopy mA setting. The line shown was found using linear regression.

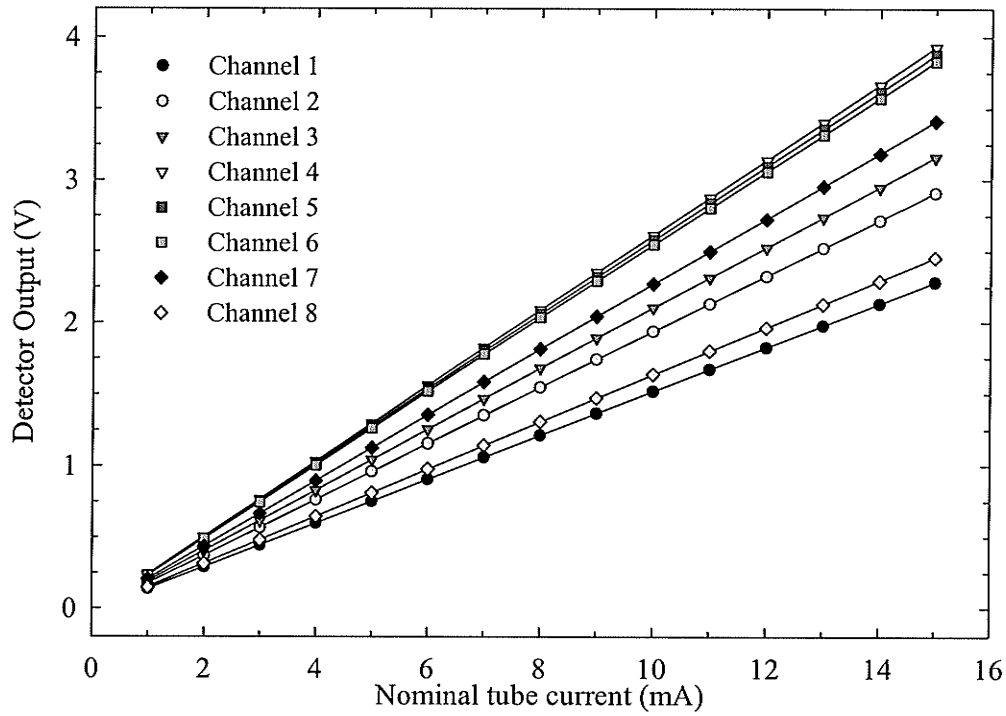

Figure 4.5 Plot showing the detector output averaged over five trials as a function of incident *x*-ray intensity. The lines shown were found using linear regression. The error bars, taken to be the standard deviation of the five trials are smaller than the dots.

estimate with respect to the mean < 0.2%). In conjunction with the results of §4.2.2.1, this indicates that the detector output is linear as a function of x-ray fluence. The different slopes of the lines in Figure 4.5 are a direct consequence of the variation in sensitivity between the various channels.

4.3 Cross-talk (Cross-Covariance Technique)

An important characteristic of the eight-channel detector assembly is the cross-talk between channels, defined as the signal detected by a channel when one or more of its neighboring channels are irradiated.

In the multi-element detectors used in CT scanners, cross-talk can often be attributed to light leakage between the crystals (optical cross-talk) and scattered radiation (radiation cross-talk) (Haque and Stanley, 1981). Of these two effects, radiation cross talk, namely Compton scattered γ-rays generated in one scintillating crystal and then interacting in an adjacent crystal, is the major source of cross-talk. Haque and Stanley (1981) suggest placing lead or tantalum spacers between the scintillating crystals. These materials would however be less reflective to optical photons than the gelcoat chosen here, resulting in a lower detector signal. Note also that the Compton scatter of ^{192}Ir γ-rays is much more forward peaked than the scatter produced in a conventional CT scanner (average energy of primary radiation is about 60 keV), reducing the prevalence of radiation cross-talk in this prototype. Dark-colored opaque spacers would eliminate optical cross-talk, but these would result in a lower detector signal. Effort has however been made (see §2.5.4.3) to use a crystal spacing material that is both reflective and opaque.

Cross-talk between detectors may cause inconsistencies in the detector outputs between projections, resulting in streak and ring artifacts (Haque and Stanley, 1981) and a reduced spatial resolution. These effects are most prevalent if there are large variations in the transmitted photon fluence. Conversely, if the photon fluence incident on adjacent detectors is similar, the optical photons or γ-rays escaping from a particular scintillating

crystal will be compensated for by incoming optical photons and γ-rays from the surrounding crystals (Haque and Stanley, 1981).

This section quantifies the cross-talk between neighboring and more distal channels by calculating the cross-covariance between the channels. Measurements were carried out both in the absence of radiation, and in the presence of radiation using the Al_2O_3 coated array. Measurements in the absence of radiation are influenced only by the detector electronics, and are used to detect the presence of electronic cross-talk. Data collected in the presence of radiation are affected by both the detector electronics and the scintillating crystal array. These measurements determine the magnitude of the total cross-talk including electronic cross-talk, optical cross-talk and radiation cross-talk.

4.3.1 Theory

4.3.1.1 Cross-Covariance

The cross-talk between channels was assessed by taking a large number of readings of the detector output and finding the cross-covariance between adjacent channels. For stationary processes, the general expression for the cross-covariance function is given by (Oppenheim and Schafer, 1975)

$$\gamma_{ij}(\tau) = \left\langle \left[\tilde{V}_i(t) - \overline{V}_i\right]\left[\tilde{V}_j(t+\tau) - \overline{V}_j\right]^* \right\rangle \qquad (4.9)$$

where the * represents complex conjugation and $\overline{V}_i$ and $\overline{V}_j$ denote the mean of the random processes $\left\{\tilde{V}_i(t)\right\}$ and $\left\{\tilde{V}_j(t)\right\}$ $-\infty < t < \infty$, respectively[2]. For discrete samples of finite length, the cross-covariance may be found using (IDL 5.3.1, Research Systems, Inc.)

$$c_{ij}(l) = \frac{1}{N}\sum_{n=0}^{N-l-1}\left(\tilde{V}_i(n) - \overline{V}_i\right)\left(\tilde{V}_j(n+l) - \overline{V}_j\right)^* \qquad \text{for } l = 0, \ldots, N-1 \quad (4.10)$$

where $\overline{V}_i$ and $\overline{V}_j$ denote the mean of random processes $\left\{\tilde{V}_i(n)\right\}$ and $\left\{\tilde{V}_j(n)\right\}$, $n = 0, 1, \ldots, N-1$, respectively, and l is the lag.

---

[2] The notation in this section follows the same convention as that in §3.2.

4.3.1.2 Cross Power Spectrum

The spectral properties of the cross-covariance can be examined using the cross power spectrum. For a stochastic process, the population cross-power spectrum may be found using (Jenkins and Watts, 1968)

$$\Gamma_{ij}(f) = \int_{-\infty}^{\infty} \gamma_{ij}(\tau) e^{-2\pi i f \tau} d\tau \,. \tag{4.11}$$

The relationship between the cross power spectrum and the cross-covariance is identical to the relationship between the power spectrum and the autocovariance function presented in Chapter 3. As was the case for the power spectrum and the autocovariance function, the cross power spectrum and the cross-covariance are Fourier transform pairs so that

$$\gamma_{ij}(\tau) = \int_{-\infty}^{\infty} \Gamma_{ij}(f) e^{2\pi i f \tau} df \tag{4.12}$$

also holds. Following the arguments associated with (3.30), the population cross-power spectrum may also be found using

$$\Gamma_{ij}(f) = \lim_{t\to\infty} \left\langle \left(\int_{-t/2}^{t/2} V_i(t') e^{-2\pi i f t'} dt' \right) \left(\int_{-t/2}^{t/2} V_j(t') e^{-2\pi i f t'} dt' \right)^* \right\rangle \tag{4.13}$$

where $V_i(t)$ and $V_j(t)$ are zero mean functions and the * indicates complex conjugation. Because the cross-covariance is not symmetrical about zero, the cross power spectrum has both a real and an imaginary component.

For discrete samples of finite length, the cross power spectrum estimate is given by

$$C_{ij}(f_k) = \left[\left(\frac{1}{N} \sum_{n=0}^{N-1} V_i(n) e^{-2\pi i n f_k / N} \right)^* \left(\frac{1}{N} \sum_{n'=0}^{N-1} V_j(n') e^{-2\pi i n' f_k / N} \right) \right] \tag{4.14}$$

where $V_i(n)$ and $V_j(n)$ are zero mean functions, N is the number of data points in the sample, Δt is the time between data points and

$$f_k = \frac{k}{N\Delta t}. \tag{4.15}$$

4.3.1.3 Relationship between the Cross-Covariance and the Cross Power Spectrum

As was the case for the power spectrum and the autocovariance function, the area under the cross power spectrum can be shown to equal the cross-covariance evaluated at zero lag. To verify this, (4.12) was evaluated at $\tau = 0$, namely,

$$\gamma_{ij}(0) = \int_{-\infty}^{\infty} \Gamma_{ij}(f)df\,, \tag{4.16}$$

which demonstrates that the area under the cross power spectrum equals the cross-covariance function evaluated at zero lag. This is also valid in the discrete case; the area under the cross power spectrum, expressed using the definition given in (4.14) is

$$\sum_{k=0}^{N-1} C_{ij}(k) = \sum_{k=0}^{N-1} \frac{1}{N^2} \sum_{n=0}^{N-1} V_i(n) e^{2\pi i n k/N} \sum_{n'=0}^{N-1} V_j(n') e^{-2\pi i n' k/N} \tag{4.17}$$

where the substitution $f_k \to k$ was made. As summation is a linear operation, the order of the summations can be interchanged to give

$$\sum_{k=0}^{N-1} C_{ij}(k) = \frac{1}{N^2} \sum_{n=0}^{N-1} V_i(n) \sum_{n'=0}^{N-1} V_j(n') \sum_{k=0}^{N-1} e^{-2\pi i (n'-n) k/N}\,. \tag{4.18}$$

Using the identity

$$\sum_{k=0}^{N-1} e^{-2\pi i (n'-n) k/N} = N\,\delta(n'-n) \tag{4.19}$$

(4.18) can be rewritten as

$$\sum_{k=0}^{N-1} C_{ij}(k) = \frac{1}{N^2} \sum_{n=0}^{N-1} V_i(n) \sum_{n'=0}^{N-1} V_j(n')\; N\,\delta(n'-n)\,. \tag{4.20}$$

The double summation is reduced to a single sum, such that

$$\sum_{k=0}^{N-1} C_{ij}(k) = \frac{1}{N} \sum_{n=0}^{N-1} V_i(n) \cdot V_j(n)\,. \tag{4.21}$$

As mentioned in §4.3.1.2, the cross power spectrum has both a real and an imaginary component. Since the data being Fourier transformed are real, the real component of $C_{ij}(k)$ is even about f_N, and the imaginary component of $C_{ij}(k)$ is odd about f_N, where f_N is given by

$$f_N = \frac{1}{2\Delta t}. \tag{4.22}$$

It must be noted that the real component and imaginary component of $C_{ij}(k)$ must be summed separately, rather than taking the absolute value of $C_{ij}(k)$ and then performing the summation. The sum of the real components will equal the right-hand side of (4.21), and the sum of the imaginary components will simply equal zero. (The latter is obvious from (4.21); as the right-hand side is real, the left-hand side must also be real.)

4.3.2 Method

In order to experimentally determine the cross-covariance, the 8-channel detector assembly was placed in a light-tight box and 5,000 readings were acquired for each channel using a sampling frequency of 100 Hz. These measurements were repeated in the presence of radiation using the Al_2O_3 array. To assess the effect of signal amplitude on cross-talk, data were acquired with a source-to-detector distance of 74 cm and 34 cm. A total of 5,000 readings were acquired at each distance using a sampling frequency of 100 Hz.

Before the cross-covariances or cross power spectra were found, the data were converted into zero mean data V_1, V_2, V_3, . . . , V_8 (the subscript denotes the channel number) by subtracting the average of all of the readings for a particular channel from the data collected for that channel. The notation used is as follows: the cross-covariance between channels i and j in the absence of light will be denoted as $c_{ij-dark}$, and the cross power spectrum will be written as $C_{ij-dark}$; measurements made with the source 34 cm or 74 cm from the detector will have a "*34 cm*" or "*74 cm*" subscript rather than a "*dark*" subscript.

4.3.3 Results

4.3.3.1 Cross-Covariance and Cross Power Spectrum

A plot of the cross-covariance between Channels 1 and 2 collected using a sampling frequency of 100 Hz in the absence of light is shown in Figure 4.6[3]. Not shown are the plots of cross-covariance between other consecutive channels, which are very similar to the plot shown in Figure 4.6. A very regular periodic structure can be seen in Figure 4.6. To examine this phenomenon more closely, the cross power spectrum shown in Figure 4.7 was found using (4.14). The cross power spectrum plots between other consecutive channels are very similar to the plot shown in Figure 4.7. It can be seen that the power spectrum is generally flat, except for a few well defined peaks at 20 Hz and 40 Hz. These are most likely due to power line interference, as explained in §3.2.3.3, and are responsible for the structure shown in Figure 4.6. For the "dark" measurements, the

[3] The decrease in cross-covariance with increasing frequency is due to the $1/N$ term in (4.10).

cross-covariance at all lag values is small and is primarily due to power-line interference that affects all channels. This indicates that there is no cross-talk between channels in the absence of radiation.

Plots of the cross-covariance between Channels 1 and 2 for source separations of 74 cm and 34 cm are shown in Figures 4.8 and 4.10, respectively. Not shown are the cross-covariance plots between the other consecutive channels, which are very similar to those shown in Figures 4.8 and 4.10. The cross-covariance plots in the presence of radiation show a spike at zero lag and are relatively smooth for larger lag values. Plots of the cross power spectra between Channels 1 and 2 for source separations of 74 cm and 34 cm are shown in Figures 4.9 and 4.11 respectively. Not shown are the cross power spectra for the other consecutive channels, which are very similar. These plots show the cross power spectrum to be relatively uniform over all frequencies.

Cross-talk between adjacent channels is indicated by the cross-covariance having a spike at zero lag and by a uniform non-zero cross power spectrum. The cross-covariances at zero lag are listed in Table 4.5 for all channels and measurement conditions.

Table 4.5 Zero Lag Values: $c_{ij-dark}(0)$, $c_{ij\text{-}74\ cm}(0)$ and $c_{ij\text{-}\ 34\ cm}(0)$

Channels		Dark	74 cm	34 cm
i	j			
1	2	4.23×10^{-10}	2.23×10^{-7}	1.06×10^{-6}
2	3	5.38×10^{-10}	2.47×10^{-7}	1.26×10^{-6}
3	4	5.22×10^{-10}	2.76×10^{-7}	1.48×10^{-6}
4	5	4.00×10^{-10}	1.96×10^{-7}	0.93×10^{-6}
5	6	4.79×10^{-10}	1.92×10^{-7}	1.32×10^{-6}
6	7	5.04×10^{-10}	2.97×10^{-7}	1.49×10^{-6}
7	8	4.49×10^{-10}	2.19×10^{-7}	0.78×10^{-6}

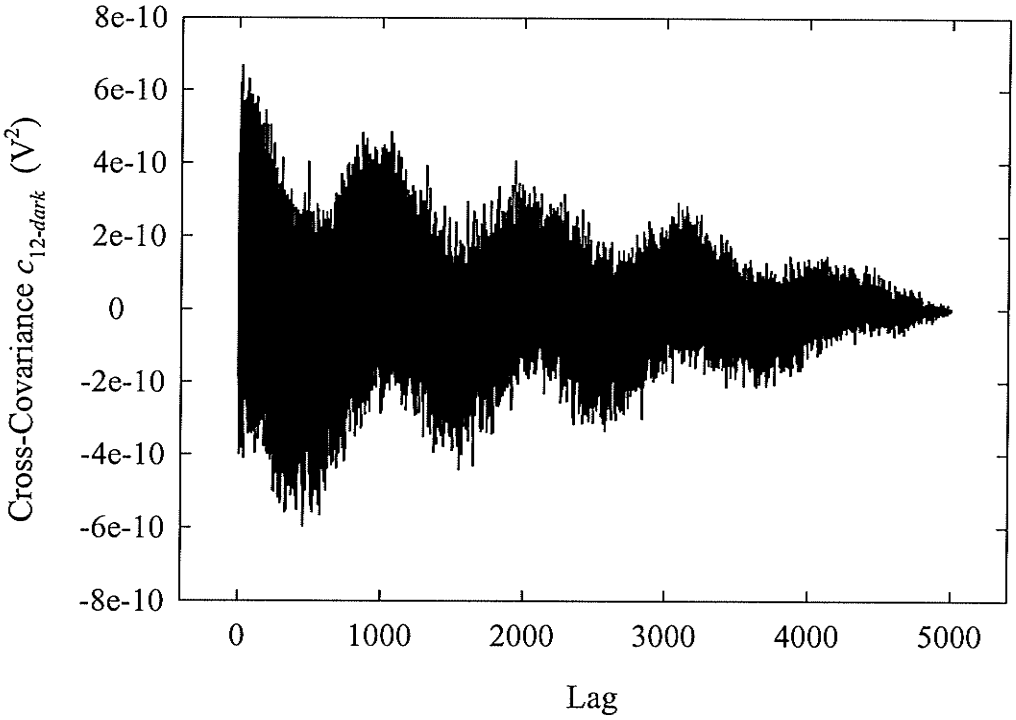

Figure 4.6 Cross-covariance between Channels 1 and 2 $c_{12\text{-}dark}$ found using a sampling frequency of 100 Hz in the absence of light, and calculated using (4.10).

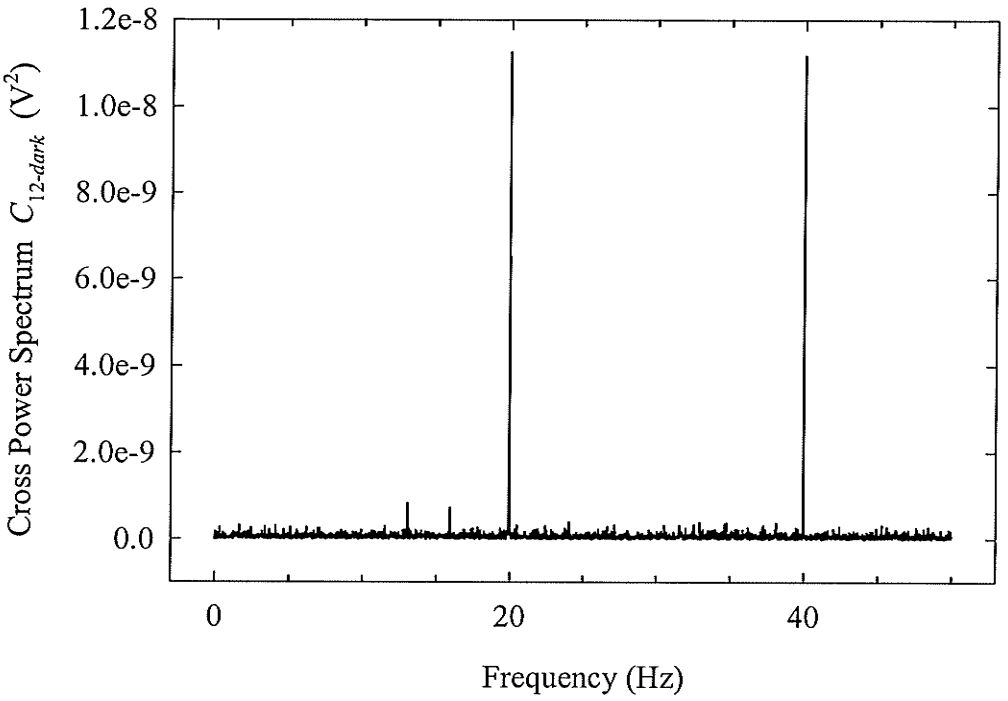

Figure 4.7 Cross power spectrum (absolute value) calculated using (4.14) for data collected at 100 Hz in the absence of light.

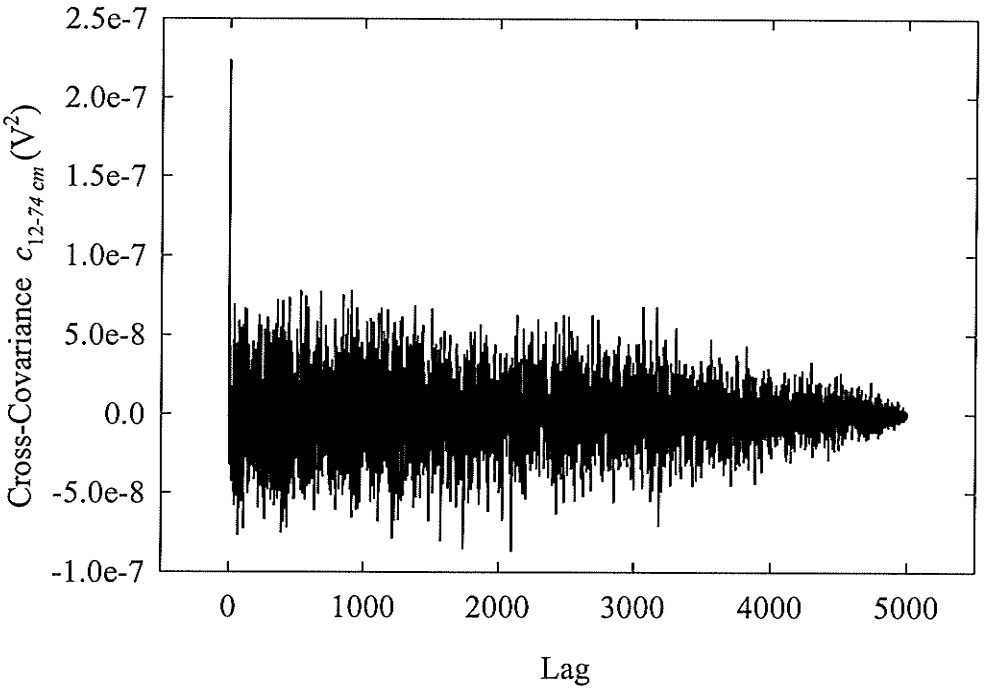

Figure 4.8 Cross-covariance between Channels 1 and 2 $c_{12\text{-}74\ cm}$ found using a sampling frequency of 100 Hz, and calculated using (4.10). The source was located a distance of 74 cm from the detector and had a strength of 8.6793 Ci.

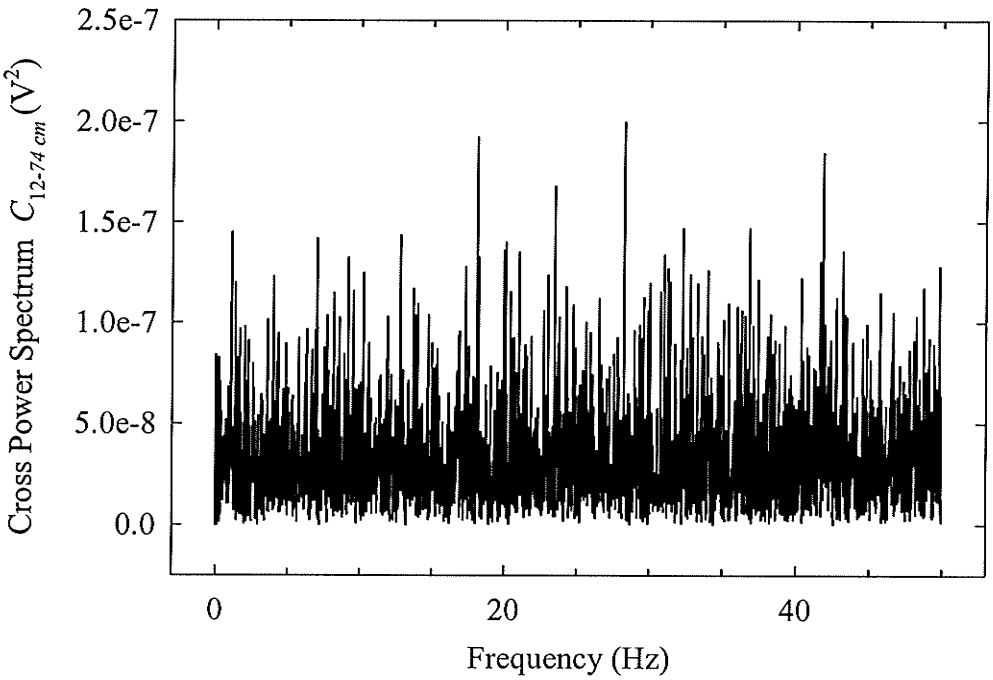

Figure 4.9 Cross power spectrum (absolute value) between Channels 1 and 2 $C_{12\text{-}74\ cm}$ calculated using (4.14) for data collected at 100 Hz. The source was located a distance of 74 cm from the detector and had a strength of 8.6793 Ci.

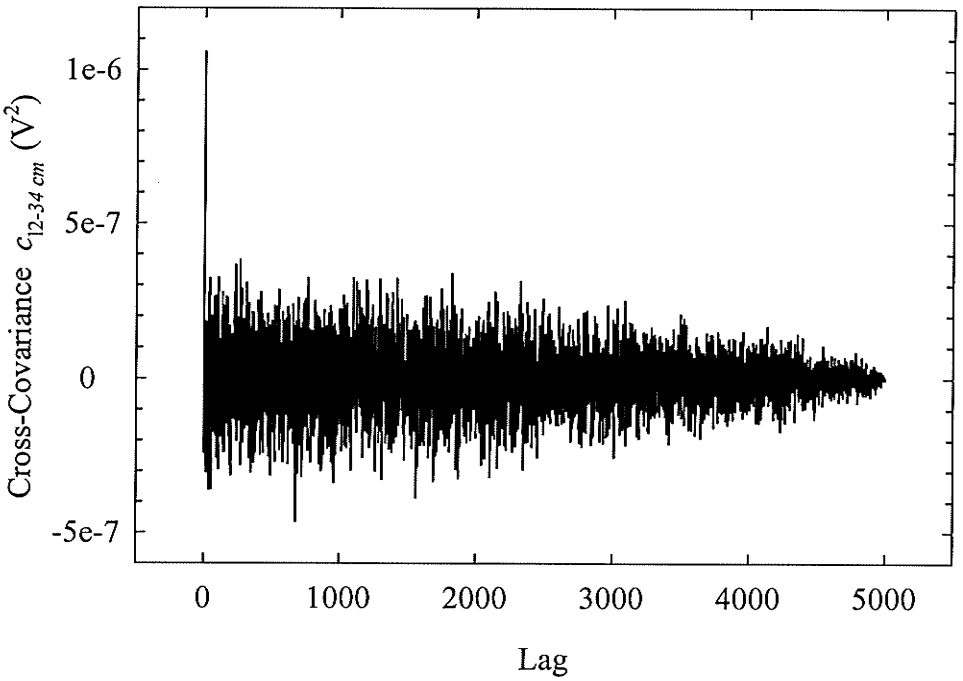

Figure 4.10 Cross-covariance between Channels 1 and 2 $c_{12\text{-}34\ cm}$ found using a sampling frequency of 100 Hz and calculated using (4.10). The source was located a distance of 34 cm from the detector and had a strength of 8.5982 Ci.

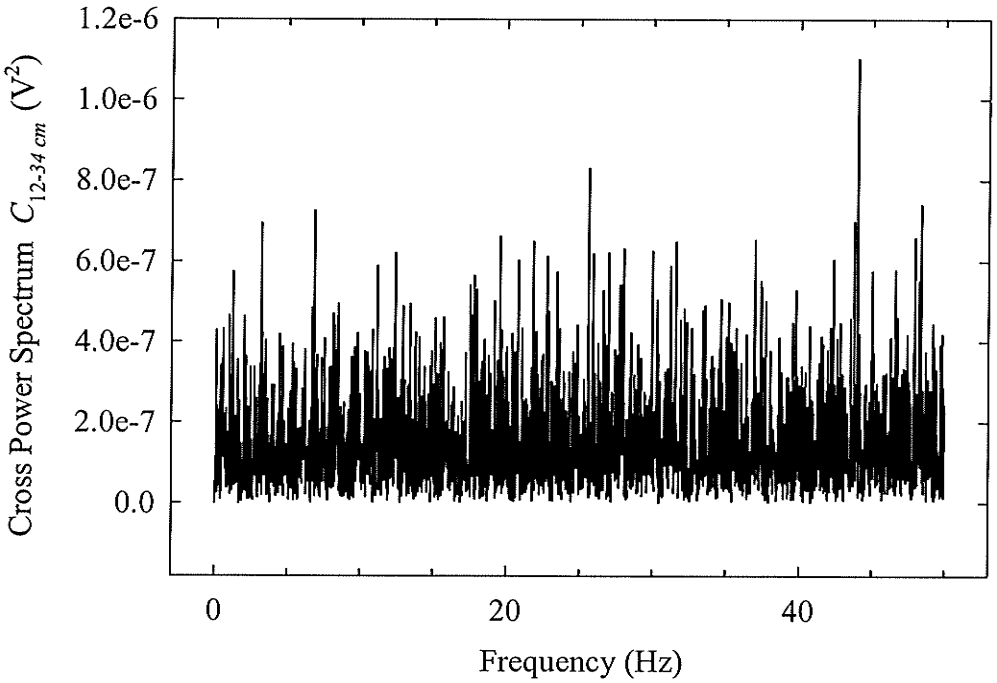

Figure 4.11 Cross power spectrum (absolute value) between Channels 1 and 2 $C_{12\text{-}34\ cm}$ calculated using (4.14) for data collected at 100 Hz. The source was located a distance of 34 cm from the detector and had a strength of 8.5982 Ci.

4.3.3.2 Cross Power Spectrum and Total Signal

The previous discussion pertains to the cross-talk between adjacent channels. It would be useful to also consider the cross-talk between non-adjacent channels. As an example, the cross-covariance plots between Channel 4 and all other channels are shown in Figure 4.12. Also shown is the cross-covariance plot between Channel 4 and itself, which is simply the autocovariance. The height of $c_{44\text{-}74\ cm}(0)$ is the largest, followed by $c_{34\text{-}74\ cm}(0)$ and $c_{54\text{-}74\ cm}(0)$. The zero lag component of $c_{14\text{-}74\ cm}$, $c_{24\text{-}74\ cm}$, $c_{64\text{-}74\ cm}$, $c_{74\text{-}74\ cm}$ and $c_{84\text{-}74\ cm}$ (not shown) is the same order of magnitude as the background cross-covariance, i.e., the noise level. This indicates that cross-talk occurs primarily between adjacent crystals.

The zero-lag cross-covariance for all channels is summarized in Figure 4.13. Figure 4.13a presents the results for measurements made with a source-to-detector distance of 74 cm, and Figure 4.13b shows the results of the dark measurements. Not shown are the results for a source-to-detector distance of 34 cm, which are very similar to Figure 4.13a.

The cross-covariance at zero lag between adjacent channels (Figure 4.13a) is about 0.1 of the autocovariance, meaning that the amplitude of the cross-talk between adjacent channels is about $\sqrt{0.1}$ x 100 = 32%. The cross-covariance at zero lag for detectors farther away than the adjacent detector is negligible with respect to the background cross-covariance. This suggests that cross-talk occurs primarily between adjacent crystals.

The plots in Figure 4.13b all have a peak coinciding with the autocovariance point, but unlike the plots shown in Figure 4.13a, the cross-covariance of adjacent channels is comparable in size to the cross-covariance from further channels. Recalling the previous analysis, this confirms that there is no cross-talk between channels in the absence of radiation.

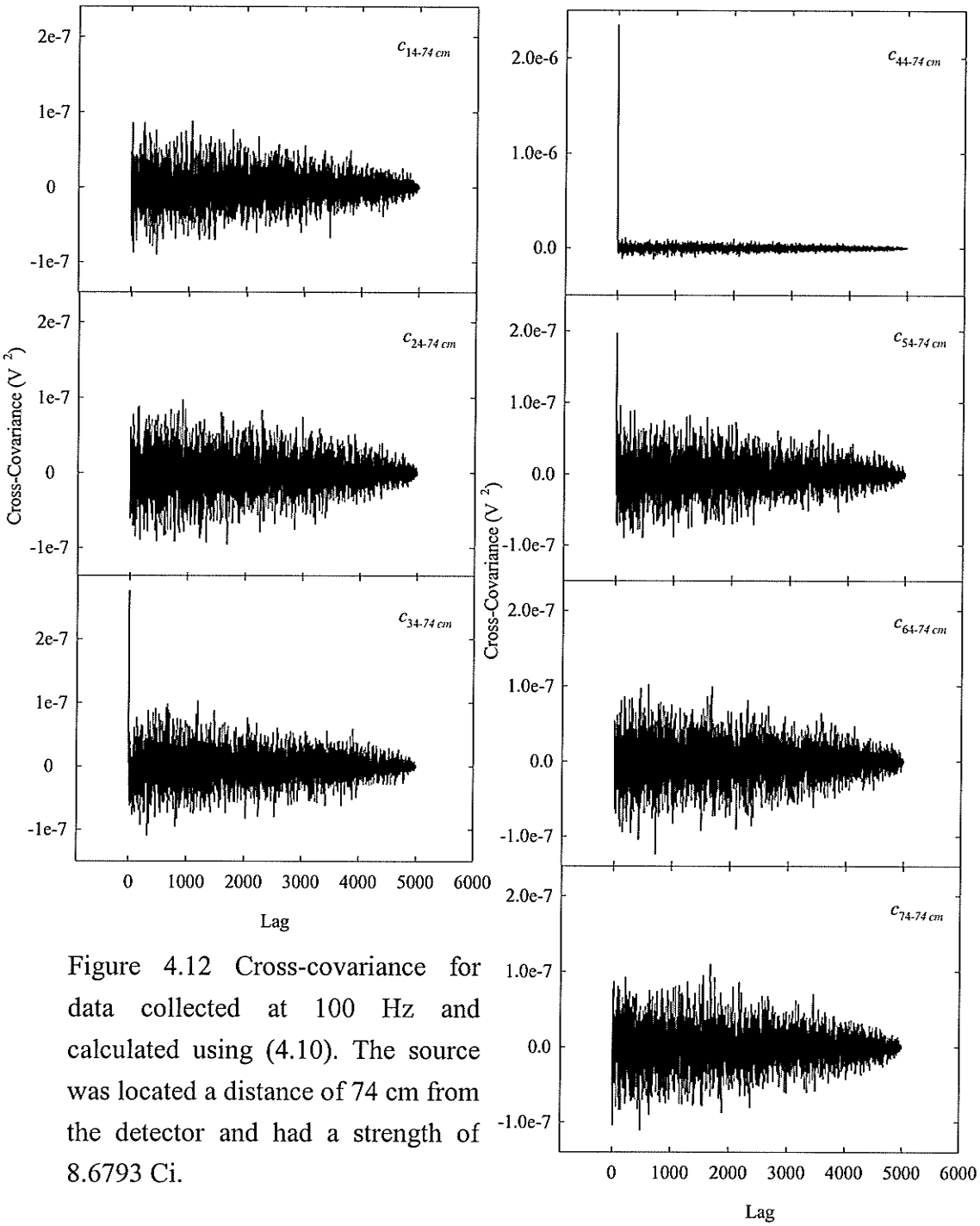

Figure 4.12 Cross-covariance for data collected at 100 Hz and calculated using (4.10). The source was located a distance of 74 cm from the detector and had a strength of 8.6793 Ci.

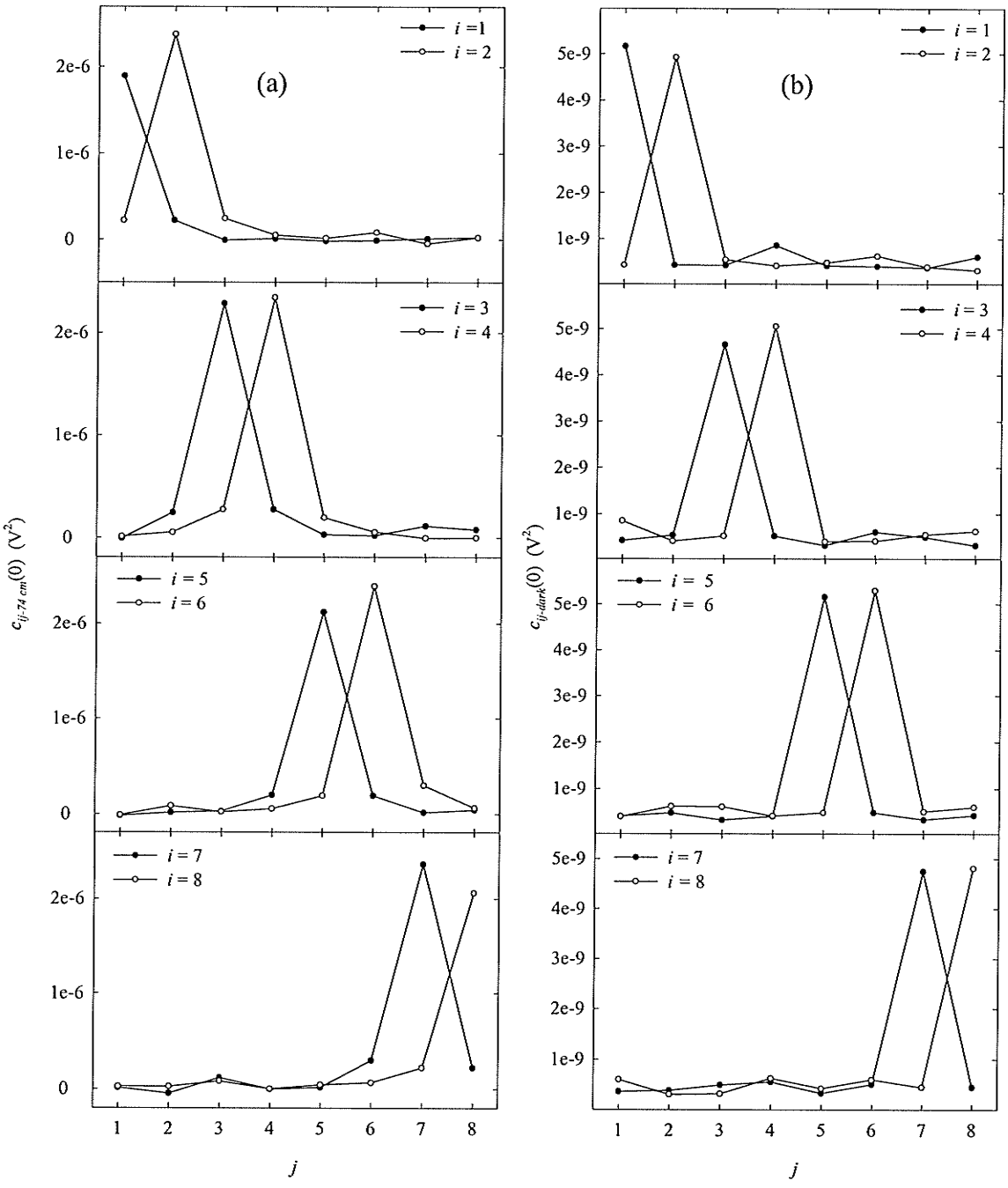

Figure 4.13 Zero lag cross-covariance plots (a) $c_{ij\text{-}74\ cm}(0)$ and (b) $c_{ij\text{-}dark}(0)$, where i is indicated in the legend, and j is labeled along the horizontal axis.

4.4 Cross-Talk (Direct Experimental Measurement)

A second more straight-forward technique for determining the cross-talk between channels is to irradiate the individual detectors using a collimated source and measure the signal output of the neighboring channels. The output voltage of the shielded channels (i.e. those not being directly irradiated) is then the result of cross-talk with the irradiated channel. Measurements were carried out using the Al_2O_3 and the gelcoat coated arrays described in §2.5.5. The cross-talk was also measured with the crystal arrays removed, using a source of collimated optical photons. The purpose of the optical photon measurements was to confirm the absence of electronic cross-talk between the channels.

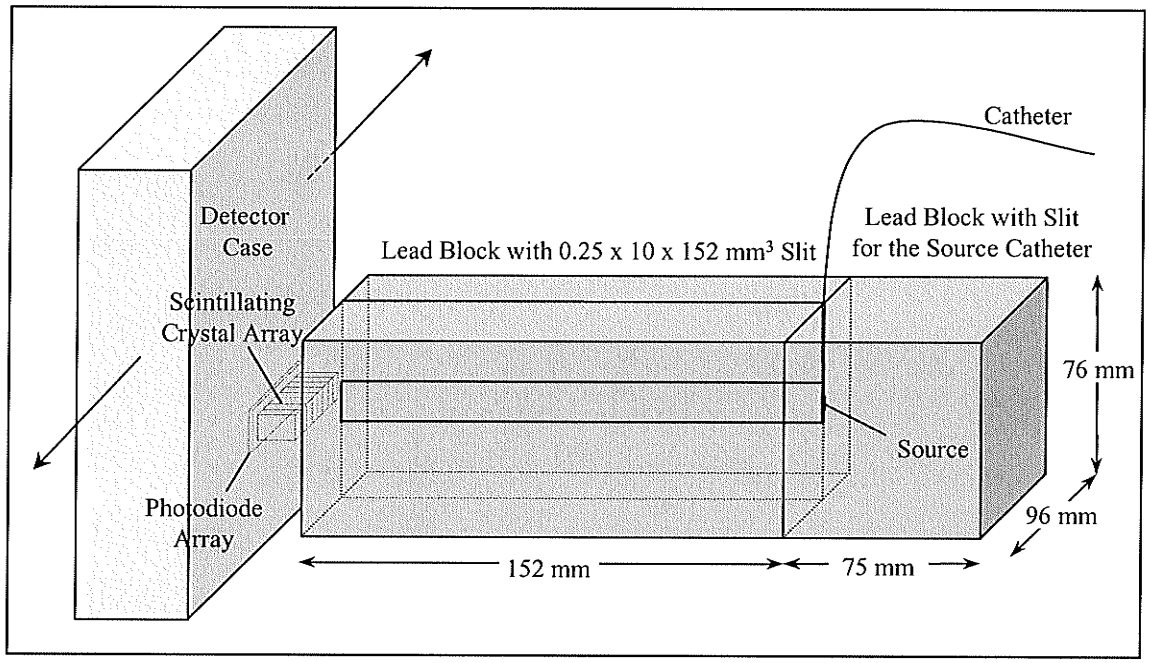

Figure 4.14 Experimental set-up used to make the radiation cross-talk measurements. Two lead blocks, one of which had a 0.25 x 10 x 152 mm^3 slit milled into it were held stationary, while the detector was translated past the source using a stepper motor. Note that the source size in the figure has been exaggerated to make it visible. The optical photon cross-talk measurements were made using a similar set-up, except that the lead block with the slit for the source catheter, along with the source catheter, were replaced by a flashlight.

4.4.1 Radiation Measurements

4.4.1.1 Method

The experimental set-up used to measure the cross-talk between the detector channels for the Al_2O_3 and gelcoat coated crystal arrays is illustrated in Figure 4.14. Collimation was accomplished using two 48 x 76 x 152 mm^3 lead blocks, one of which had a 0.25 x 10 x 152 mm^3 slit milled into it. A catheter containing the source was placed in a slit along one side of a third lead block, which served to reduce the amount of scattered radiation reaching the detector. The source catheter and the collimator blocks were held stationary, while the detector was translated horizontally in increments of 0.125 mm using a linear stage (Series A2500 Unislide, Velmex, Inc.) and a computer controlled stepper motor. A total of 100 readings were taken at each detector position for the Al_2O_3 array. These were averaged, and corrected for dark current. Measurements for the gelcoat coated array were carried out in a similar manner, except that 75, rather than 100 readings were taken at each detector postion.

4.4.1.2 Results

Al_2O_3 Coated Crystal Array

The output voltage of each channel measured using the Al_2O_3 coated array is illustrated in Figure 4.15. The largest signal for a channel naturally occurs when that particular channel is directly irradiated. The cross-talk reaching neighboring channels appears as smaller and smaller peaks. The dips between peaks are due to the inactive regions between the photodiode elements not covered by a scintillating crystal, as shown in Figure 2.5c. Since the collimator slit width is narrower than the gap between the individual photodiode elements, there are some stage positions for which none of the scintillating crystals are irradiated.

To quantify the cross-talk, it is useful to compare the area under each of the peaks shown in Figure 4.15. The "beginning" and "end" of each peak was determined by plotting the translation stage position coinciding with the dips in Figure 4.15 as a function of gap number (i.e. the gap between the first pair of detectors is denoted as "1", the gap between the next pair denoted as "2", and so forth). A linear regression fit through this

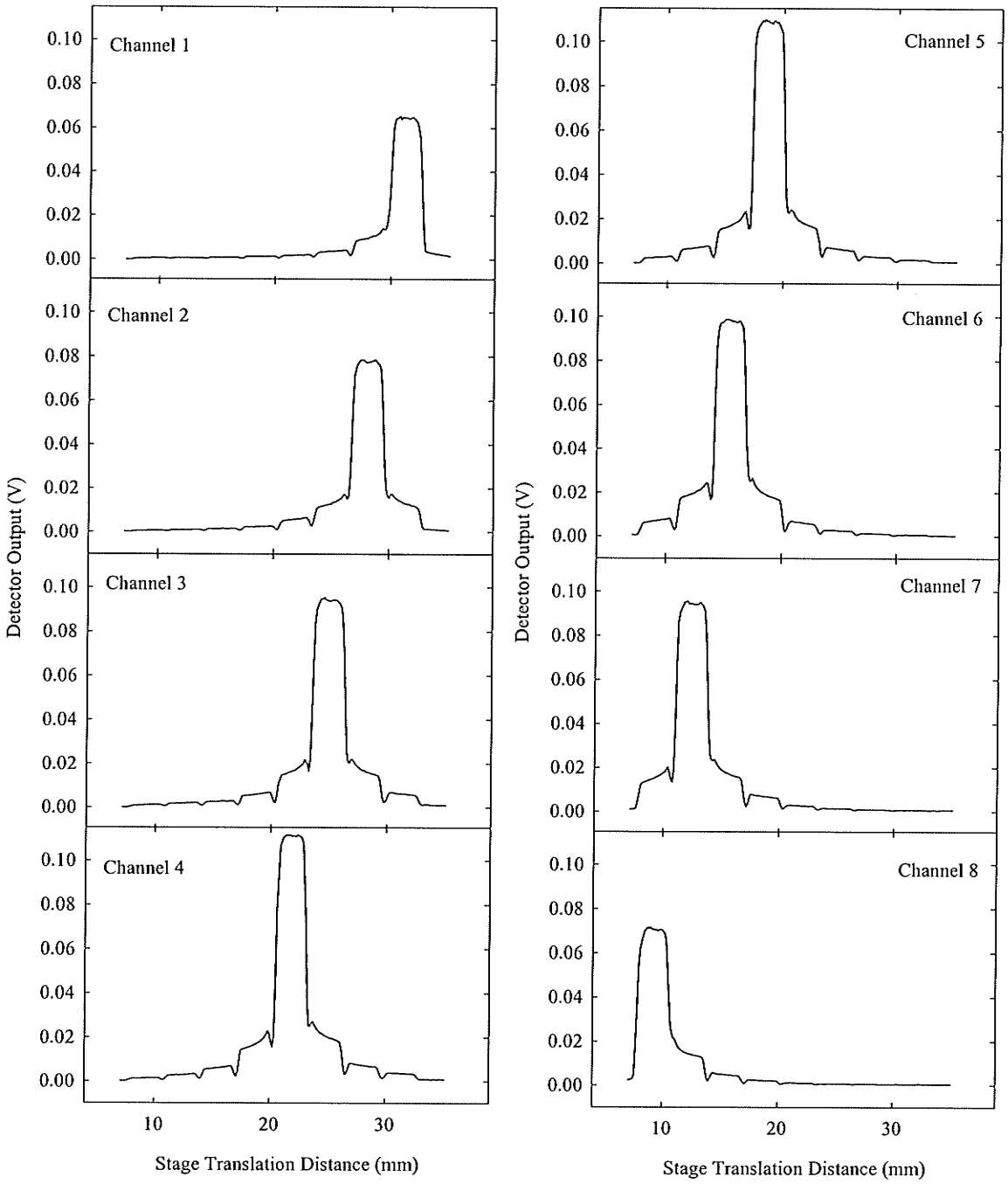

Figure 4.15 Plots showing the detector output (Al_2O_3 coated array) as the detector array is translated past the collimated ^{192}Ir source. Note that the detectors are numbered 1 through 8, starting from the right.

data, shown in Figure 4.16, has a slope of –3.075 mm/gap. Using this value, the outer edges of the first and last detector were also found, as it would have been difficult to estimate these from the plots in Figure 4.15. The area under each peak was then calculated using the translation stage position for the beginning and end of each detector. The response for each channel, expressed as percentage is listed in Table 4.6. As can be seen, there is a substantial amount of cross-talk between the channels; for the nearest neighbors of the detector being irradiated, the cross-talk is about 20%, while for the next nearest neighbors it is about 7%. Returning to Figure 4.13a, a similar trend is observed, although the background noise level masks the cross-talk from next nearest neighbors and farther detectors.

As described in §4.3, cross-talk can result in ring and streak artifacts. Clearly the prevalence of the artifacts will depend upon the magnitude of the cross-talk, which is substantial for the Al_2O_3 coated array.

Gelcoat Coated Crystal Array

Analysis for the gelcoat coated crystal array was carried out in a similar manner to that for the Al_2O_3 coated crystal array. The output voltage for each channel of the gelcoat coated array is plotted in Figure 4.17. Comparison of Figures 4.15 and 4.17 demonstrates the reduced cross-talk associated with the gelcoat coated array, as expected from the measurements in §2.5.4.3. The "beginning" and "end" of the peaks in Figure 4.17 was found by plotting the translation stage position coinciding with the dips in Figure 4.17 as a function of gap number, as was done for the Al_2O_3 coated array. A linear regression fit through the data found a slope of 3.063 mm/gap. The area under each peak is listed in Table 4.7, expressed as a percentage. As can be seen, there is a substantial decrease in the cross-talk for the gelcoat coated array, as compared to the Al_2O_3 coated array; for the nearest neighbors of the detector being irradiated, the cross-talk is about 13%, as opposed to 20%, while that for next nearest neighbors is only 2%. This confirms the results found in §2.5.4.3 regarding the optical densities of the gelcoat and Al_2O_3. This reduction in cross-talk decreases the possibility of image artifacts.

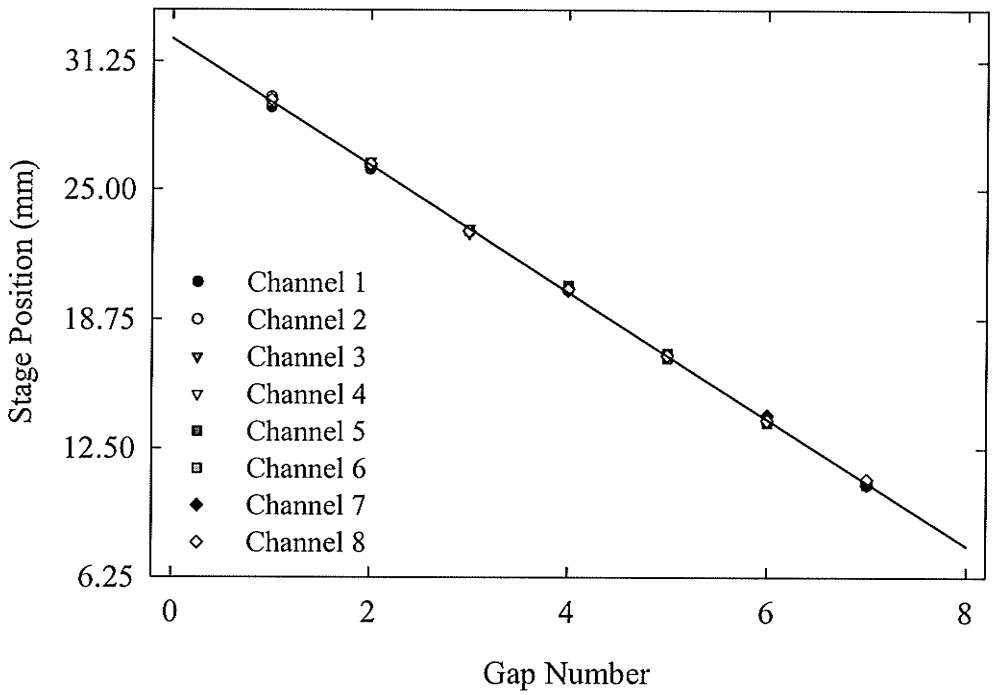

Figure 4.16 Plot showing the translation stage position coinciding with the signal dips in Figure 4.15 for all channels. The regression line was found using all of the data in the plot.

Table 4.6 Normalized Channel Response (Al_2O_3 Coated Array)

Irradiated Detector	Channel 1	Channel 2	Channel 3	Channel 4	Channel 5	Channel 6	Channel 7	Channel 8
1	100	19.7	6.7	3.7	1.7	0.8	0.8	0.9
2	19.3	100	19.0	7.3	2.8	1.3	1.1	1.0
3	6.2	19.5	100	22.2	6.1	2.8	1.6	1.2
4	3.0	7.3	18.8	100	18.2	5.9	2.8	1.6
5	2.1	3.3	6.5	18.1	100	22.5	7.7	3.6
6	1.4	2.0	3.0	6.4	17.3	100	20.8	7.4
7	1.1	1.3	2.1	3.0	6.4	21.5	100	24.3
8	1.0	0.8	1.1	1.4	2.5	7.3	17.7	100

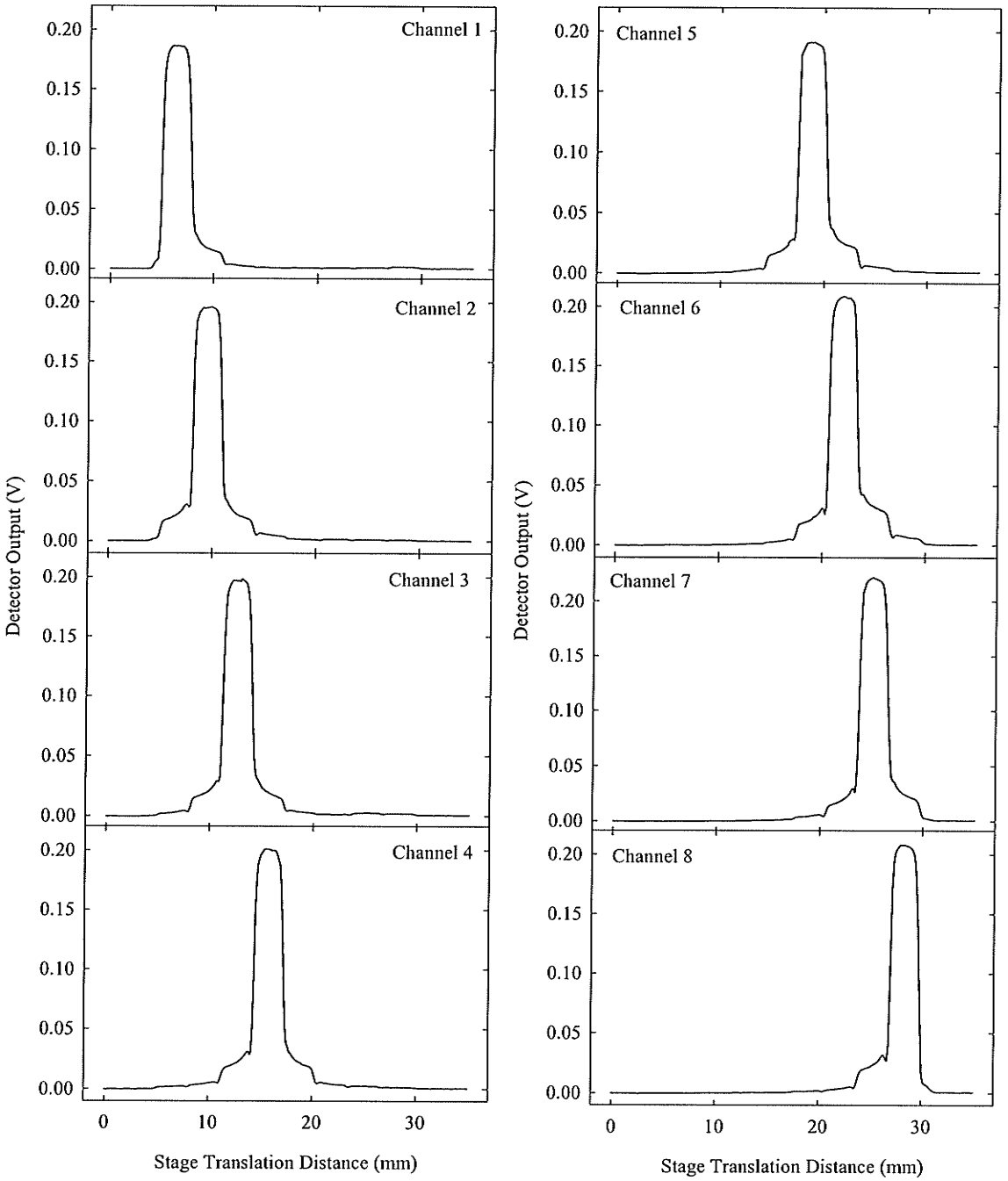

Figure 4.17 Plots showing the detector output (gelcoat coated array) as the detector array is translated past the collimated ^{192}Ir source. Note that the detectors are numbered 1 through 8, starting from the left.

Table 4.7 Normalized Channel Response (Gelcoat Coated Array)

Irradiated Detector	Channel 1	Channel 2	Channel 3	Channel 4	Channel 5	Channel 6	Channel 7	Channel 8
1	100	12.3	1.6	1.1	0.0	0.2	0.0	0.0
2	12.2	100	10.9	2.4	0.4	0.3	0.0	0.1
3	1.9	14.9	100	12.3	1.6	0.6	0.2	0.2
4	0.7	3.1	14.4	100	11.4	1.8	0.6	0.4
5	0.7	1.0	1.9	14.1	100	12.5	2.3	0.9
6	0.6	0.9	0.9	2.3	15.5	100	10.6	2.1
7	0.8	0.8	1.4	1.4	3.3	17.4	100	12.6
8	1.0	0.6	1.2	0.8	1.2	3.8	13.6	100

4.4.2 Light Measurements

Cross-talk measurements were also made using collimated optical photons (crystal array removed). The absence of cross-talk in these measurements would indicate that the cross-talk found in the previous section is due to cross-talk in the crystal array, as opposed to cross-talk in the photodiode array, electronic cross-talk, or inadequate collimation of the source.

4.4.2.1 Method

The experimental setup shown in Figure 4.14 was also used for the optical photon based cross-talk measurements. The lead block with the slit for the source catheter was removed and a flashlight put in its place. Several sheets of paper were taped over the face of the flashlight to dim its illumination, thereby preventing detector saturation. The lead collimation blocks and the flashlight were held stationary while the detector case was translated horizontally across the slit in increments of 0.125 mm using a linear stage (Series A2500 Unislide, Velmex, Inc.) and a computer controlled stepper motor. A total of 20 readings were taken at each detector position. These were averaged and corrected for dark current. Note that a smaller number of measurements were taken for the light measurements than for the radiation measurements because the light measurements

resulted in a larger detector signal than those using the the ^{192}Ir source. It was therefore acceptable to average fewer readings.

4.4.2.2 Results

The detector output when illuminated with a collimated source of optical photons is shown in Figure 4.18. The output reduction in the centers of the peaks corresponds to the space between the two photodiodes constituting a detector channel. The absence of signal in channels other than the one being illuminated indicates that the cross-talk appearing in the radiation measurements is solely due to optical or radiation cross-talk between the crystal arrays, rather than inadequate collimation of the source. The results shown in Figure 4.18 also demonstrate the absence of electronic cross-talk.

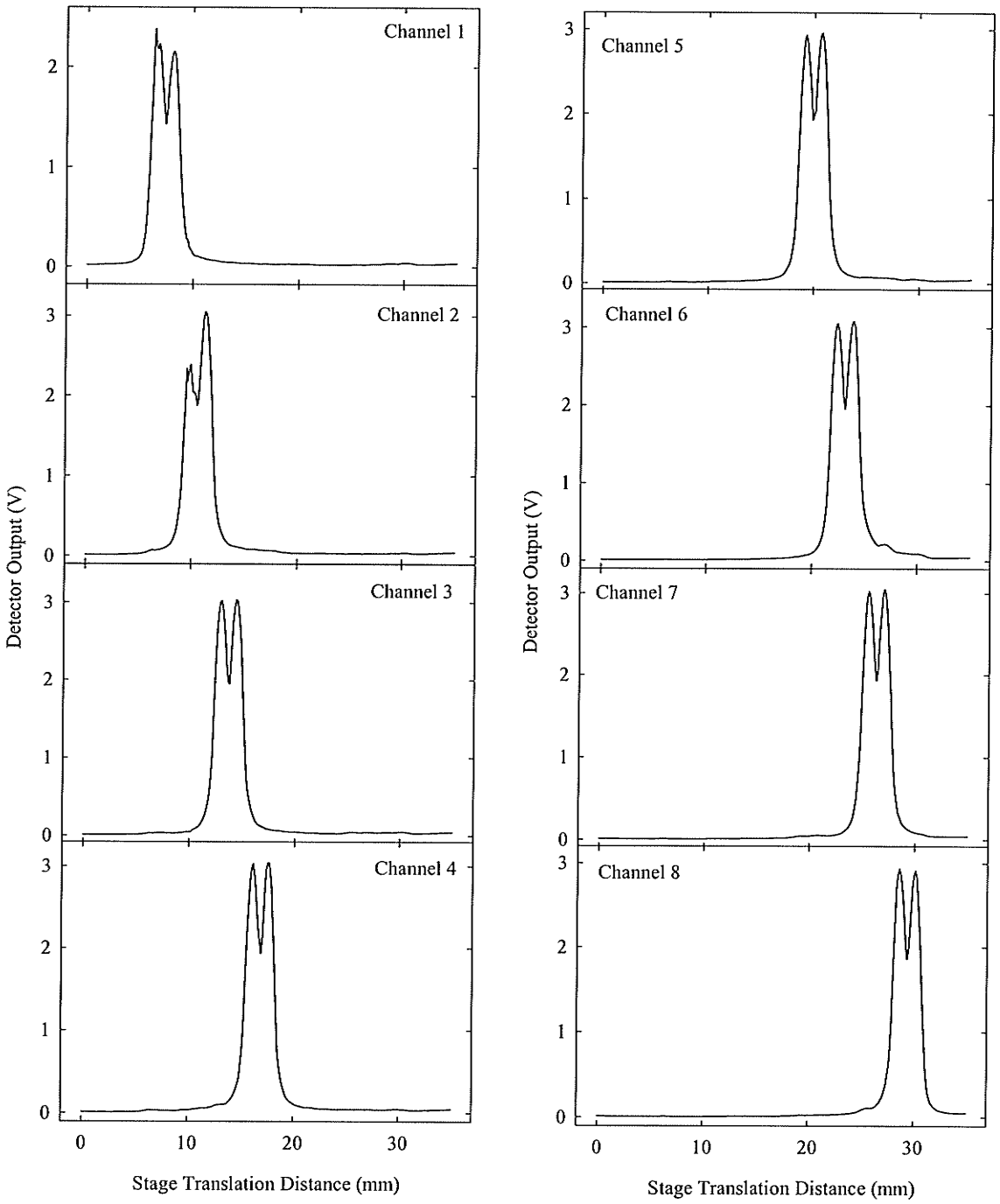

Figure 4.18 Plots showing the detector output (photodiodes only) as the detector array is translated past a source of collimated optical photons. Note that the detectors are numbered 1 through 8, starting from the left.

Chapter 5

Scanner Design

This chapter describes a series of measurements pertaining to the design of the fourth generation scanner. The first set of measurements examines the source position reproducibility, while the next set of measurements determines the width and length of an ^{192}Ir brachytherapy source. Theoretical calculations and experimental measurements were also made to investigate the collimator design. In particular, the collimator thickness, spacing and annulus size were examined. The effect of scatter and slice thickness, and design constraints such as the maximum allowable source travel distance and the low γ-ray fluence emitted by the ^{192}Ir source were taken into consideration.

5.1 Source Position Reproducibility

In the fourth generation scanner, the source stops at 864 predetermined locations. Because CT reconstruction algorithms are very sensitive to inaccuracies in projection angles, it is essential that these positions be highly reproducible from scan to scan, and accurately known in order to reconstruct an artifact free tomographic image.

Sections 5.1 and 5.2 form the basis for the paper "Size and positioning reproducibility of an ^{192}Ir brachytherapy stepping source" published in Med. Physics (Berndt et al., 2000b). The idea for these measurements is credited to D. W. Rickey. D. W. Rickey and A. Berndt developed the software, while A. Berndt performed the measurements and analysis. S. Rathee and J. Bews offered helpful suggestions that contributed to the analysis and understanding of this work.

5.1.1 Method

The collimators, detector and source geometry used for these measurements are shown in Figure 5.1. A single detector was collimated using two 48 x 76 x 152 mm^3 lead blocks, one of which had a 0.25 x 10 x 152 mm^3 slit milled into it. The detector and collimator were held stationary, while the source was translated linearly past the slit. This enabled the location of the source's tip to be accurately established, thereby allowing its positioning reproducibility to be assessed. Data were acquired by sending the ^{192}Ir source to a predetermined position in a flexible catheter, which was attached to a linear stage (Series A2500 Unislide, Velmex, Inc.). The catheter was translated past the stationary collimated detector in increments of 0.025 mm using a computer-controlled stepping motor. Several detector output readings were taken at each catheter position using a sampling frequency of 10 Hz. These readings were averaged to reduce noise, and then corrected for dark current.

5.1.1.1 Stage Position Reproducibility Measurements

The reproducibility of the stage position was characterized by translating the leading edge of the source past the collimator slit five times without retracting the source into the treatment unit. As the leading edge of the source is well defined, any positioning inaccuracies of the stage will be readily apparent. Detector output voltage measurements were obtained at 27 different stage positions, where each detector output voltage measurement was the average of 45 readings. The translation stage was returned to its home position between each of the five trials. To remove backlash in the translation stage when homed, it was translated beyond the home position, and then returned. The stage

position reproducibility measurements, consisting of 5 trials (stage translations) each were repeated three times, with the source retracted after each of the three measurement series. It was not possible to simply perform 15 trials, as the brachytherapy source could only be programmed to remain at a particular position for a maximum duration of 999.9 seconds. The analysis used to assess the stage position reproducibility is discussed below.

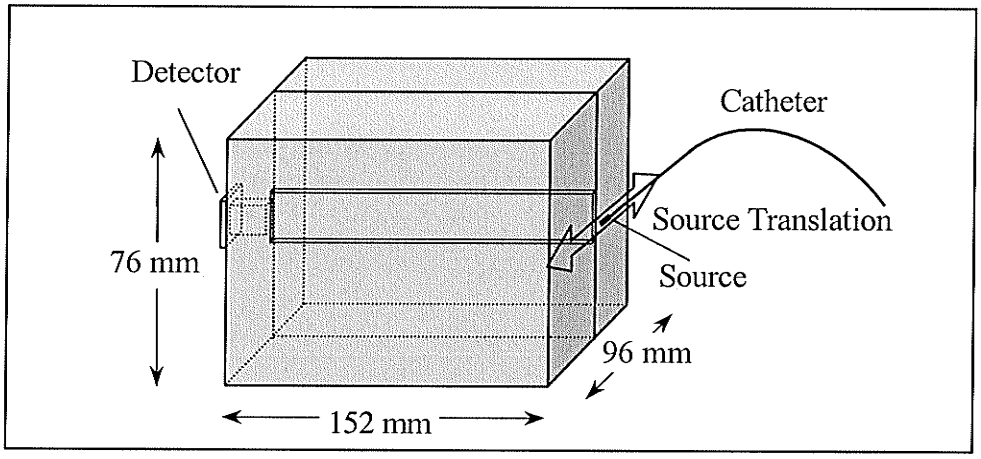

Figure 5.1 Schematic showing the detector, the source, and the lead blocks used to collimate the source. The dimensions of the slit are 0.25x10x152 mm^3. The detector and the collimator are held stationary, while the source is translated past the slit.

5.1.1.2 Source Position Reproducibility Measurements

Source position reproducibility was measured using a technique similar to that described above, except that the source was retracted after every stage translation. Three series of source position reproducibility measurements were performed. The first two series used the "interrupt" and "resume" features to retract the source and return it to the predetermined location. As this did not constitute reprogramming a treatment, the source could only be sent out for a duration of 999.9 seconds, thereby limiting the number of trials that could constitute a measurement series. For the third series of source position reproducibility measurements, each trial was initiated by reprogramming the source to the same predetermined position. The number of trials restriction therefore did not exist for this measurement series. For the first two measurement series, each data point is the

average of 40 readings, while for the third measurement series, each data point is the average of 45 readings.

5.1.2 Results

5.1.2.1 Stage Position Reproducibility Measurements

The detector output voltage from the first stage position reproducibility measurement series is plotted in Figure 5.2. Not shown are the data for the second and third measurement series, which are similar to Figure 5.2. It can be seen that the data for the five trials overlap, indicating a highly reproducible stage position. The data were analyzed by fitting a straight line to the rising portion of the curve in each of the trials. This served to further reduce the effect of noise in the detector output voltage. The position at which the fitted line crossed 0.05 V (approximately halfway up the curves in Figure 5.2) was found for each trial. The standard deviation (SD) in this position was calculated for each measurement series and is summarized in Table 5.1. As can be seen, the translation stage position is very reproducible with a maximum imprecision of 0.003 mm.

5.1.2.2 Source Position Reproducibility Measurements

The detector output voltages for the source position reproducibility measurement series are plotted in Figure 5.3 as a function of translation stage position. As can be seen, the data for the different trials do not overlap as they did for the stage position reproducibility measurements. The source position reproducibility was assessed using the techniques described in §5.1.2.1. The results of the three stage position reproducibility measurement series are summarized in Table 5.2. It can be seen from the data in Table 5.1 that the error introduced by the translation stage is negligible compared to the source position reproducibility error. Thus the SD values listed in Table 5.2 represent the source positioning error. Because the imprecision in the source position is small (0.12 mm or less), no corrections are required in the fourth generation scanner reconstruction algorithms to account for the small errors in the source position reproducibility.

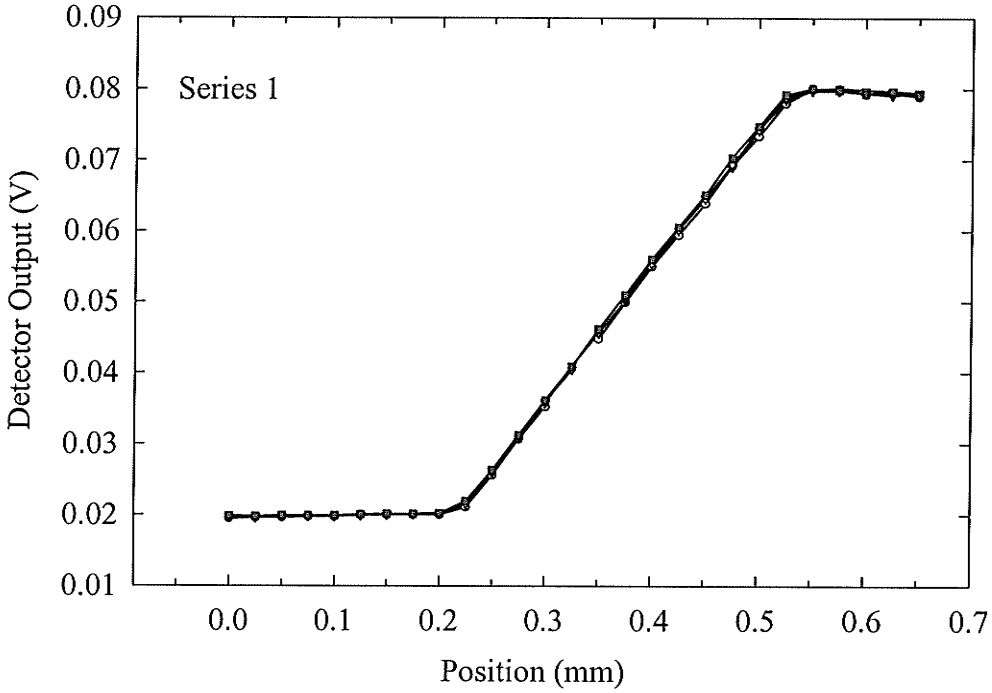

Figure 5.2 Detector output voltage for five trials plotted as a function of translation stage position for the first stage position reproducibility measurement series. The source was not retracted into the treatment unit between trials. The vertical offset is due to scattered radiation reaching the detector prior to the source reaching the slit. The error in the measurements is smaller than the plotted points.

Table 5.1 Translation Stage Reproducibility Measurements

Stage Position Reproducibility Series	Number of Trials	SD (mm)
1	5	0.0023
2	5	0.00091
3	5	0.0031

Table 5.2 Source Position Reproducibility Measurements

Source Position Reproducibility Series	Number of Trials	SD (mm)	Source Retraction
1	6	0.12	interrupt & resume
2	7	0.030	interrupt & resume
3	15	0.097	new treatment

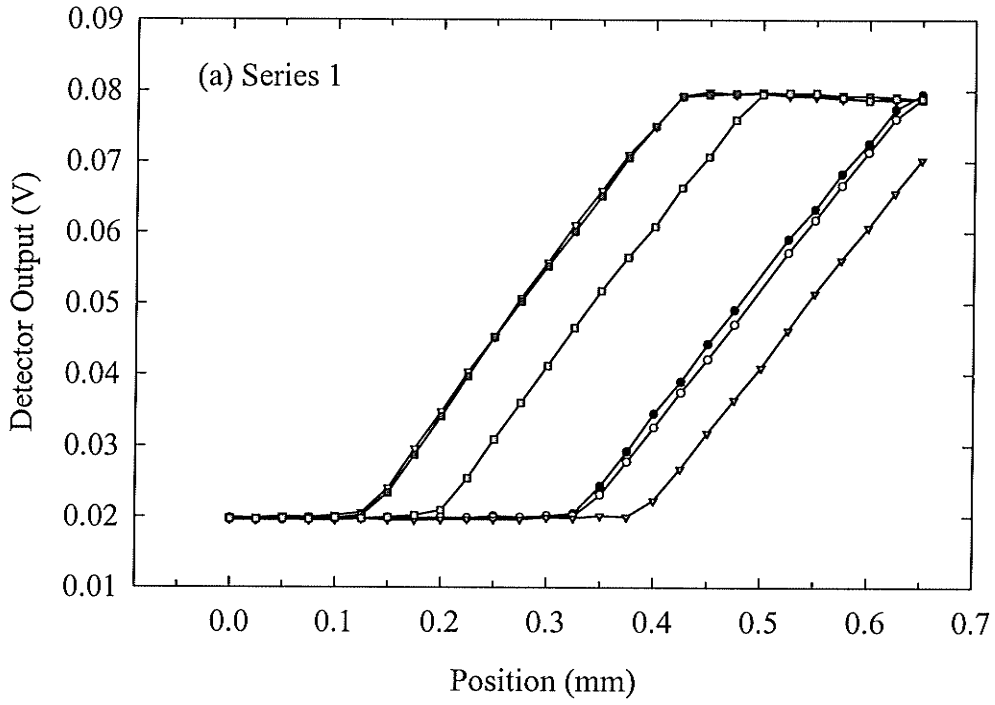
(a) Series 1
Detector Output (V)
0.09
0.08
0.07
0.06
0.05
0.04
0.03
0.02
0.01
0.0
0.1
0.2
0.3
0.4
0.5
0.6
0.7
Position (mm)

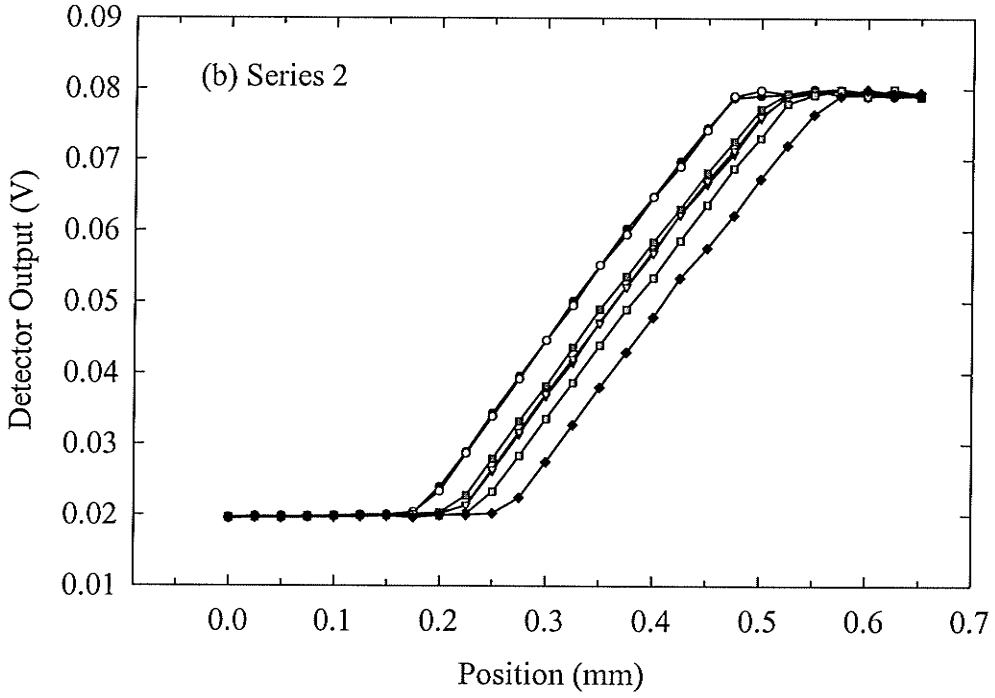
(b) Series 2
Detector Output (V)
0.09
0.08
0.07
0.06
0.05
0.04
0.03
0.02
0.01
0.0
0.1
0.2
0.3
0.4
0.5
0.6
0.7
Position (mm)

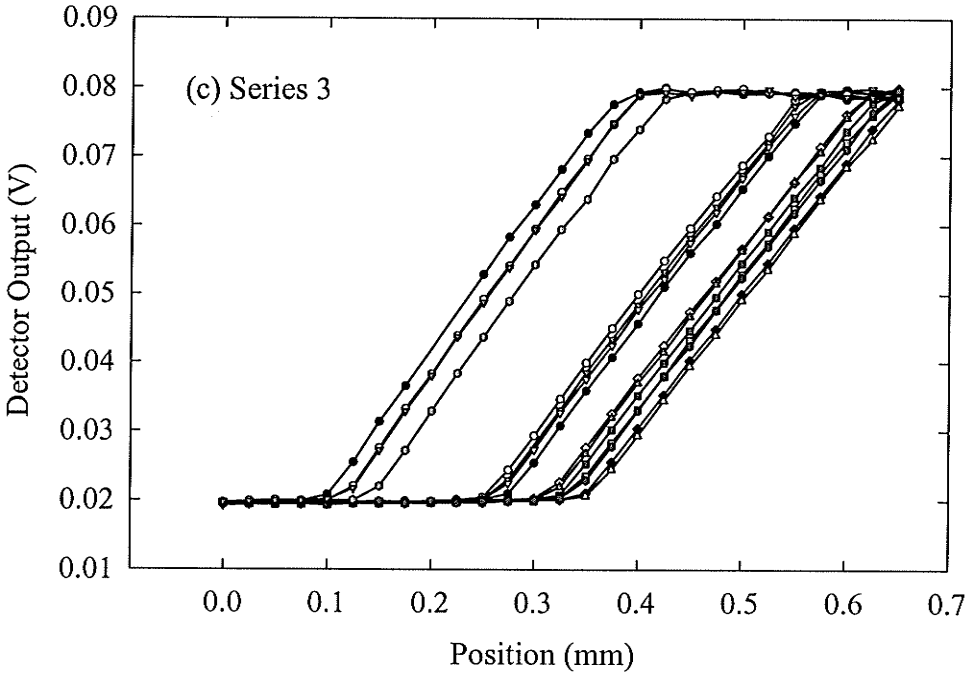

Figure 5.3 Detector output voltage plotted as a function of the translation stage position for the three source position reproducibility measurement series. Plots (a) and (b) consist of 6 and 7 trials respectively. For these measurements the source was retracted and extended using the "interrupt" and "resume" features. Plot (c) consists of 15 trials where the source was retracted using the interrupt feature and sent out again by programming a new treatment. The vertical offset is due to scattered radiation reaching the detector prior to the source reaching the slit. The error in the measurements is smaller than the plotted points.

5.2 Source Size Measurements

When imaging an object using a CT scanner, the detector and source size provide an inherent limit to the achievable in-plane spatial resolution in the reconstructed image. Although the HDR BT manufacturer provides the ^{192}Ir source dimensions, they must be experimentally verified. The source movement in the fourth generation scanner requires that the source length dimension be aligned with the tomographic slice plane, and that the source width dimension be perpendicular to the slice plane. Therefore, the source length will determine the in-plane beam profile, while the source width will affect the slice thickness. The length dimension is particularly important because no additional in-plane collimation of either the source or the detectors is used in the fourth generation scanner, as this would greatly complicate the mechanical design. The only collimation is that used to define the slice width, as described in the next section.

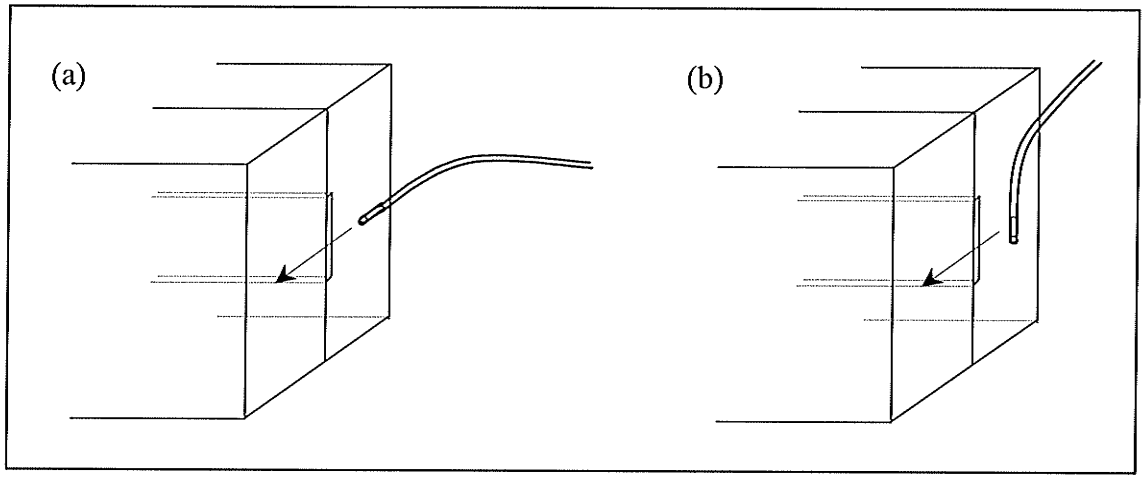

Figure 5.4 Diagram showing the translation of the catheter and the source with respect to the collimator slit for the (a) source length measurements and (b) source width measurements.

5.2.1 Theory

The source length and width were measured as shown in Figure 5.4, by translating the source lengthwise and widthwise, respectively, past the same collimator used for the source position reproducibility measurements. Detector output was recorded as a function of source position.

The effect of the collimator dimensions, as defined by the lead blocks used in these experiments must be accounted for when analyzing the measured data. The detector output as a function of source position can be described as a convolution between the collimated detector sensitivity and the source intensity distribution function along its dimensions. As the detector is collimated using a long narrow slit, its sensitivity distribution is easily modeled as a rect function $c(x)$ of width 0.25 mm. Assuming that the ^{192}Ir source is uniformly activated within its capsule, the source intensity distribution can be modeled as a rect function $l(x)$ of length s_l for the source length measurements, and as a disc $w(x)$ of radius s_w for the source width measurements.

Considering first the source length measurements, the detector output $V_l(x)$ can be written as

$$V_l(x) = l(x) * c(x) \tag{5.1}$$

where x denotes the source position. It can be shown that the above convolution results in a trapezoid with full-width at half-maximum (FWHM) of s_l. Thus the effect of the

collimator slit width is inherently cancelled out in the FWHM measurement, assuming that both the slit and the source can be modeled as rect functions.

Similarly, the detector output for the source width measurements $V_w(x)$ can be expressed as

$$V_w(x) = w(x) * c(x). \tag{5.2}$$

Written explicitly, this becomes

$$V_w(x) = \int_{-\infty}^{\infty} w(\alpha)c(x-\alpha)d\alpha \tag{5.3}$$

where

$$w(x) = \begin{cases} 2\sqrt{s_w^2 - x^2} & -s_w \le x \le s_w \\ 0 & \text{otherwise} \end{cases} \tag{5.4}$$

and

$$\begin{aligned} c(x) &= rect(x) \\ &= \begin{cases} 1 & -0.125 \le x \le 0.125 \\ 0 & \text{otherwise.} \end{cases} \end{aligned} \tag{5.5}$$

The integral in (5.3) can be expanded as follows

$$V_w(x) = \begin{cases} 0 & -\infty < x \le -s_w - 0.125 \\ \int_{-s_w}^{x+0.125} 2\sqrt{s_w^2 - \alpha^2}\, d\alpha & -s_w - 0.125 < x \le -s_w + 0.125 \\ \int_{x-0.125}^{x+0.125} 2\sqrt{s_w^2 - \alpha^2}\, d\alpha & -s_w + 0.125 < x \le s_w - 0.125 \\ \int_{-x+0.125}^{s_w} 2\sqrt{s_w^2 - \alpha^2}\, d\alpha & s_w + 0.125 < x \le s_w \\ 0 & s_w + 0.125 < x \le \infty. \end{cases} \tag{5.6}$$

The manufacturer specifies a source radius of 0.3 mm. As the measured source radius is expected to approximately equal this value, (5.6) was evaluated for s_w = 0.25, 0.30 and 0.35 mm. The results of these calculations are shown in Figure 5.5. The FWHM found for each curve is listed in Table 5.3 along with the source radius. To relate the source radius to the FWHM of the resulting detector output curve, the equation

$$s_w = \kappa \times \text{FWHM} \tag{5.7}$$

was solved for κ for each of the s_w values. The κ values listed in Table 5.3 can then be used to determine the source radius from the FWHM of the measured detector output.

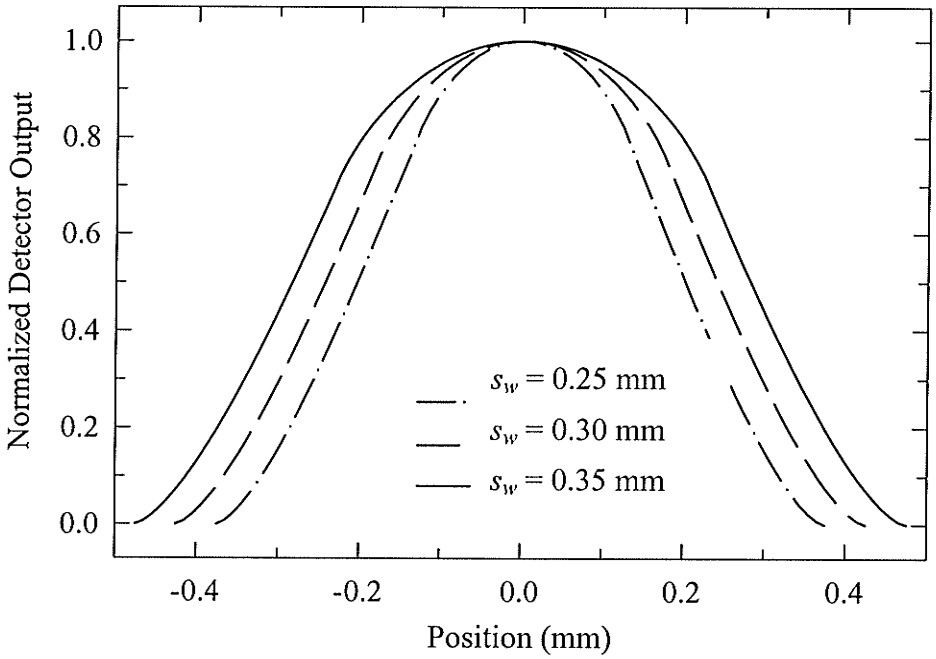

Figure 5.5 Plot of the calculated normalized detector output as a function of source position assuming a rectangular collimator slit and cylindrical sources with radii of 0.25 mm, 0.30 mm, and 0.35 mm.

Table 5.3 Source width assessment

Source Radius s_w (mm)	FWHM (mm)	κ
0.25	0.406	0.616
0.30	0.485	0.619
0.35	0.566	0.618

This empirical technique for finding the source radius is necessary because determining the source radius by deconvolving the measured data with a rect function representing the slit is inherently error prone.

5.2.2 Method

The length of the source was measured by translating the source lengthwise past the collimator slit, as shown in Figure 5.4a. The source width was measured by translating the source widthwise past the collimator slit, as illustrated in Figure 5.4b. As was the case for the source position reproducibility measurements, the collimator and the detector were held stationary, while the source was moved past the collimator by means of a translating stage. Each data point in the source length measurement is the average of 45

readings, while 100 readings were averaged for each data point in the source width measurement. The source width is smaller than the source length, thus a larger number of readings were collected at each translation stage position without exceeding the maximum source dwell time of 999.9 s. All measurements were corrected for dark current.

5.2.3 Results

Figure 5.6a shows the detector output voltage plotted as a function of stage position for the source length measurement. Taking the FWHM to be the source dimension, the length of the source is 3.58 mm. This agrees well with the length of 3.5 mm specified by the manufacturer. The solid line in Figure 5.6a is the convolution of two rect functions of width 0.25 and 3.58 mm, representing the collimated detector sensitivity distribution and the source length intensity distribution, respectively. The excellent agreement between the measured data and the convolved rect functions indicates that the rect function modeling is valid.

Similarly, the detector output for the source width measurements is plotted in Figure 5.6b. As described above, the effect of the collimator slit width is not inherently cancelled out in the FWHM measurement and the source width must be determined empirically. The FWHM of Figure 5.6b is 0.562 mm, which corresponds to a source radius of 0.35 mm (diameter = 0.69 mm), found using the data in Table 5.3 and (5.7). This agrees reasonably well with the diameter of 0.6 mm specified by the manufacturer. The convolution arguments used to extract source dimensions from the measured data assume that the detector does not record photons prior to the leading edge of the ^{192}Ir source reaching the collimator slit. Transmission through the edges of the collimator, in addition to the angular response of the collimator, are two effects that weaken this assumption. Although the length of the collimator (152 mm) minimized these effects, neither could be completely eliminated, and as such constitute the main sources of error in these measurements.

The techniques described here can be used to accurately measure the dimensions of an ^{192}Ir source. The source length and width were found to be 2% and 15% larger than those specified by the manufacturer. Only the source length is important in terms of

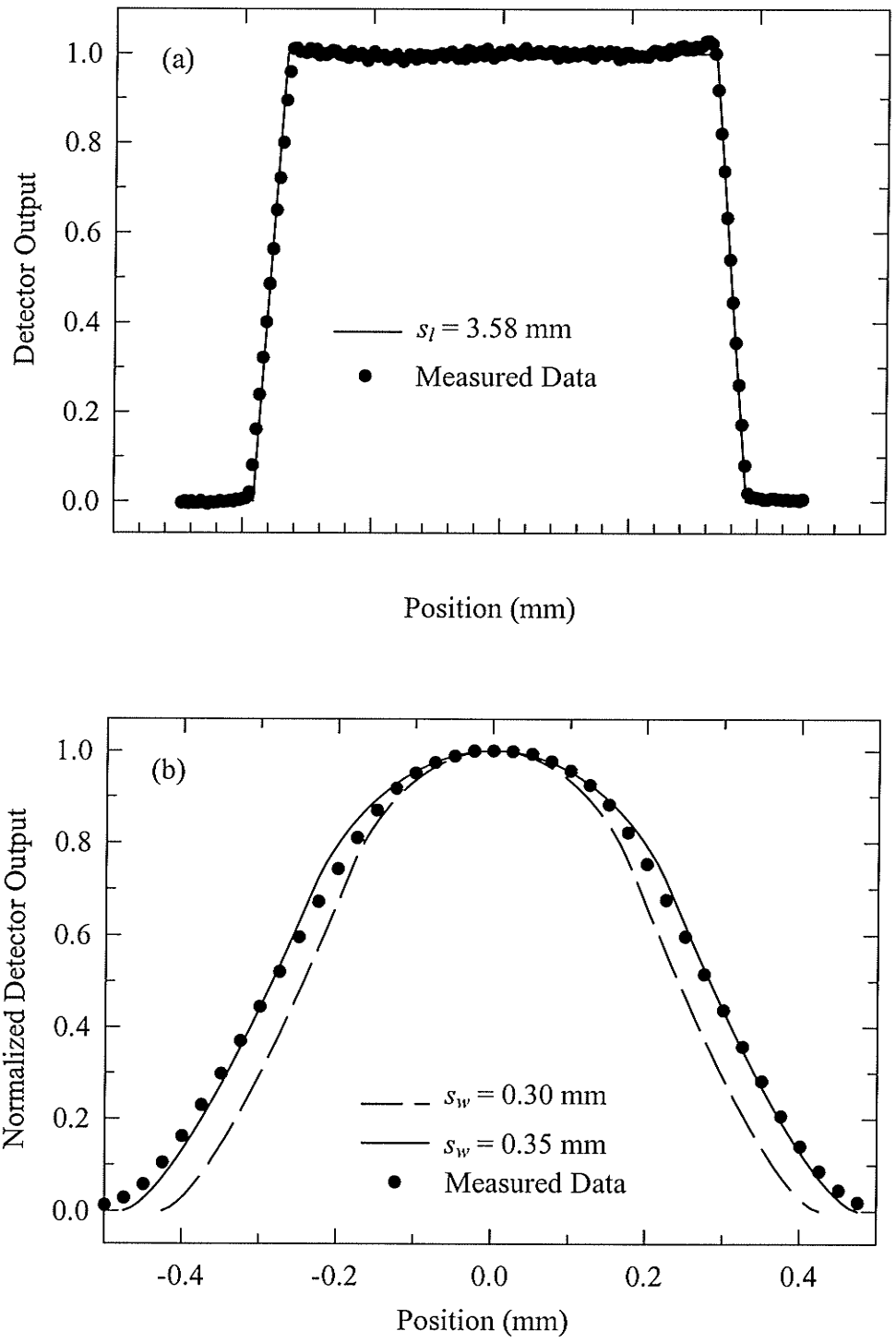

Figure 5.6 Plot of the normalized detector output voltage as a function of stage position for the (a) source length and (b) source width measurements. A vertical offset due to scattered radiation reaching the detector has been subtracted to allow comparison of the measured data (points) with the calculated convolutions (lines). The errors in the measurements are smaller than the plotted points.

the fourth generation scanner, as discussed in the next chapter. The small discrepancy in source length is not expected to have a significant impact on image quality. The source length measured here is used in §6.2 to determine the high contrast resolution of the scanner.

5.3 Collimator Design

Collimator design plays an important role in the overall scanner image quality, influencing factors such as the slice thickness, patient dose, scatter rejection and the geometric efficiency of the detectors. Thus, careful consideration must be given to the collimator design parameters, namely, their thickness, spacing and annulus size, while taking into account constraints such as the maximum source travel distance and the low γ-ray fluence emitted by the ^{192}Ir source. This section uses calculations and measurements to design the collimator for the ^{192}Ir source-based fourth generation scanner.

5.3.1 Design Considerations

Several important and often conflicting factors must be considered when designing the ring collimator. In the case of a conventional fourth generation CT scanner, factors that influence the design include the maximum scan field radius, patient dose and scattered radiation. In the case of the ^{192}Ir source-based CT scanner, the low γ-ray fluence, high γ-ray energy and maximum source ring radius must also be taken into consideration.

The four primary design parameters that can be varied in the collimator are the outer radius R_o and width w of the annular region, the collimator thickness t and the collimator spacing s, as shown in Figure 5.7. Each of these parameters and their accompanying restrictions will now be considered.

An important restriction affecting the collimator design is the limitation on source travel provided by the HDR BT treatment unit. The stepping source can be moved in steps of 0.25 or 0.5 cm. Clearly, there would be twice the number of radial sampling positions for 0.25 cm steps compared to 0.5 cm steps for any given source ring radius. The number of radial sampling positions has a direct impact on the achievable spatial resolution, as will be discussed in the following two chapters, suggesting that the 0.25 cm

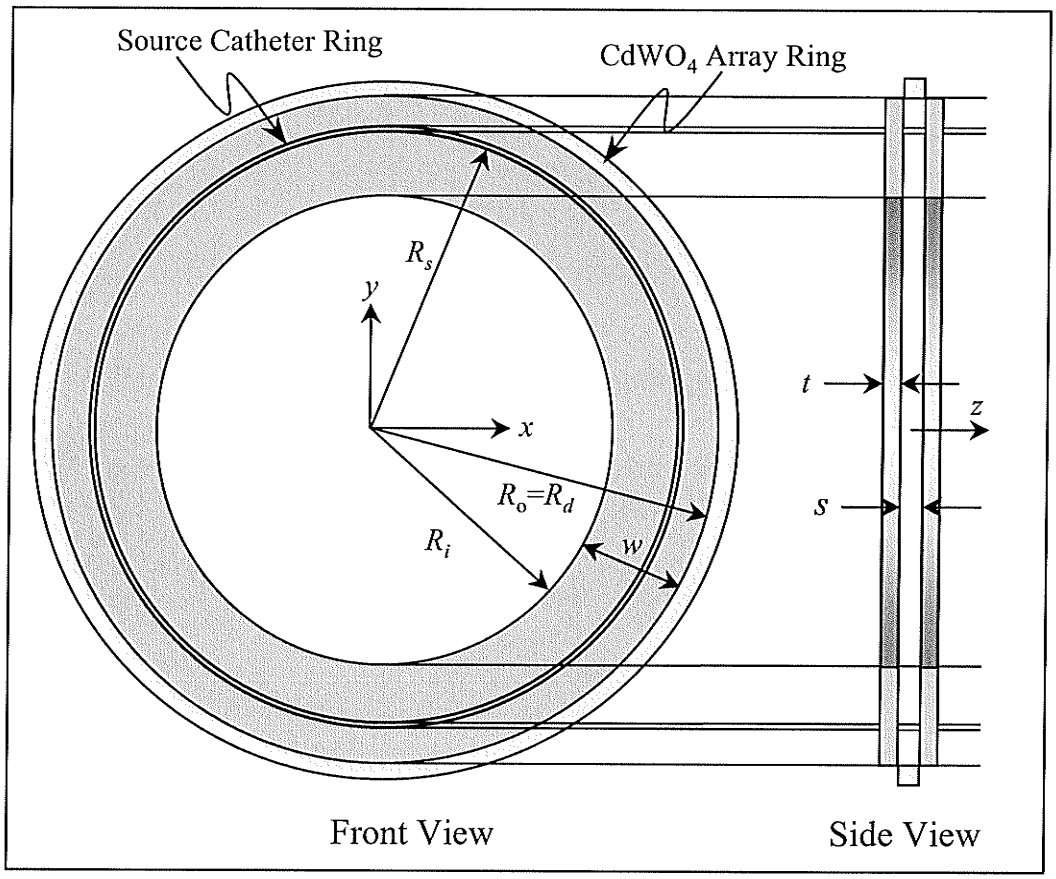

Figure 5.7 Schematic of the collimator ring (dark grey) showing the relative position of the source catheter ring and the $CdWO_4$ crystal array ring. The central axis of the scanner coincides with the z-axis.

step size would provide superior resolution. However, the HDR BT treatment unit can only position the source at a maximum of 48 dwell positions per catheter without reprogramming, which limits the arc travel provided by each channel to 12 cm when the 0.25 cm step size is used. A total of 18 catheters can be attached to the HDR BT treatment unit giving a length of 216 cm along which the source can travel. In designing the scanner it was important to maximize the bore size in order to accommodate large patients. Thus all of the available dwell positions and catheter channels were used to yield a source catheter ring of radius R_s = (216 cm)/2π = 34.38 cm.

A second design constraint is that the detectors must be placed outside of the source catheter ring, as shown in Figure 5.7. Otherwise, the γ-ray photon fluence would be greatly attenuated by the detector ring. Consequently $R_d > R_s$ is required. This influences the choice of the outer collimator radius R_o as discussed below.

5.3.1.1 Outer Collimator Radius R_o and Annular Region Width w

The inner collimator radius R_i, outer collimator radius R_o and annulus width w are related via the expression $w = R_o - R_i$. Note that the parameters R_i and R_o are constrained by the source ring radius R_s according to $R_i < R_s < R_o$.

The outer radius of the collimator ring R_o equals the detector ring radius R_d, which in turn determines the number of detectors used. As the solid angle subtended by a detector element is inversely proportional to the square of the source-to-detector distance, a larger R_o would entail a smaller γ-ray fluence impinging on a detector, thereby increasing the quantum noise. Figures 3.45a, 3.46a and 3.47a, showing images collected using our detector are quite noisy. It would not be desirable to use a source-to-detector distance much larger than the 74 cm used to generate those images. The circumference of the detector ring must furthermore be chosen in integral multiples of 2.54 cm, as this is the width of the detector arrays. In terms of electronic implementation, it would also be convenient for the number of detectors to be a multiple of eight since components such as the MUX can accommodate eight channels per integrated circuit. It was decided (somewhat arbitrarily) to use 96 detector arrays, resulting in a detector ring radius of R_d = 38.81 cm. The collimator ring outer radius was therefore chosen to be $R_d = R_o = 38.81$ cm, resulting in a source-to-detector distance of $R_s + R_d = 73.19$ cm.

The collimator width influences the amount of scattered radiation, the amount of out-of-plane patient radiation and the maximum scan field radius. To achieve the best collimation, the annular region should be as wide as possible. A large value of w will reduce both the extraneous patient irradiation, as well as the amount of scattered radiation reaching the detectors. Although it is desirable to have w as large as possible, a large collimator width will reduce the maximum scan field radius. To this end, the inner bore radius R_i must be large enough to accommodate the more corpulent patients. A review of the brachytherapy records at CancerCare Manitoba found 45 cm to be the largest lateral patient separation recorded to date. Of less significance, it would also be convenient if the scanner bore were large enough to accommodate an existing patient couch, which is 45.7 cm wide and 8.5 cm thick in the center, tapering to 1.9 cm thickness at the edges. Calculations evaluating the effects of varying collimator widths are carried out below.

5.3.1.2 Collimator Spacing *s*

The collimator spacing *s* determines the tomographic slice thickness. Generally speaking, a smaller slice thickness will result in greater resolution in the axial direction, while a larger slice thickness will result in a smaller dose being delivered to the scanned volume of the patient, assuming that the same number of photons are used for imaging. In actuality, the collimator spacing was established by the decision to use 0.8 cm long crystals (§2.5.3.2). Blocking a portion of their width by using a collimator spacing less than 0.8 cm is not advisable, because this would reduce the detector output. Increasing the collimator spacing beyond 0.8 cm does not provide any advantage in terms of patient dose or image quality, but rather increases the amount of scatter detected, and is therefore also not recommended. Consequently, $s = 0.8$ cm was used.

5.3.1.3 Collimator Thickness *t*

The collimator thickness *t* determines the attenuation of obliquely incident primary and scattered photons. Enough lead must be used to minimize the primary radiation reaching the patient outside of the slice thickness because this radiation contributes to the dose received by the patient, but does not contribute useful information to the image. However, excess lead would result in a heavier collimator, and the design challenges associated with supporting such a scanner. Calculations determining the effect of different collimator thicknesses are carried out below.

5.3.1.4 Collimator Modeling

Figure 5.8 shows a schematic of the most simple collimator design possible, namely, parallel annuli. As discussed above, the outer radius of the collimator ring was fixed by the decision to use 96 photodiode arrays, while the source catheter ring radius was selected on the basis of the maximum allowed source travel distance. In the following discussion, relative primary radiation intensity profiles are calculated along a line centered in the scan field and perpendicular to the scan plane (i.e., along the scanner *z*-axis) using various collimator widths and thicknesses.

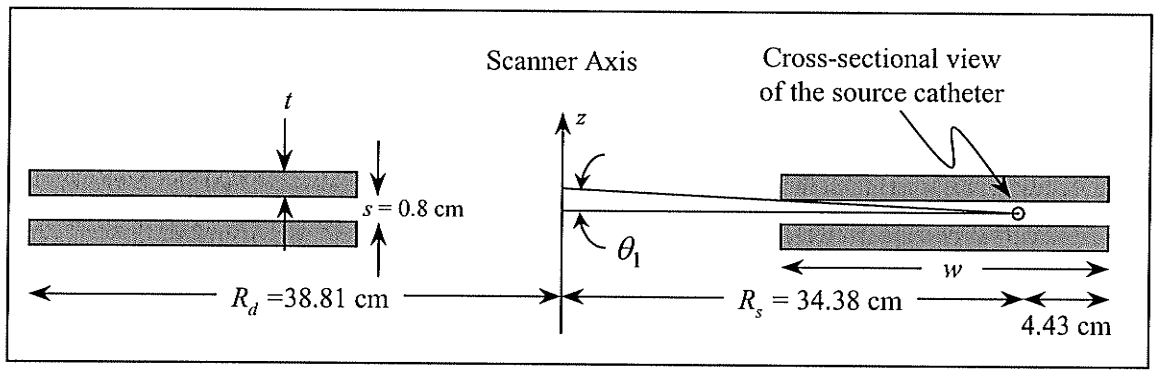

Figure 5.8 Schematic of simple parallel plate collimator design.

The radiation intensity along the scanner z-axis was found assuming a point source and the geometry shown in Figure 5.8. For γ-rays incident at angles $0° < \theta < \theta_1 = \tan^{-1}\left(\frac{s/2}{w-4.43}\right)$ where the rays do not intercept the collimators, the γ-ray intensity $I(\theta)$ is

$$I(\theta) \propto \frac{\cos^2\theta}{R_s^2}. \tag{5.8}$$

For γ-rays incident at angles $\theta > \theta_1$ the attenuation of the ray by the lead collimators must be accounted for. In this case, the γ-ray intensity was found using

$$I(\theta) \propto \frac{\cos^2\theta}{R_s^2} \cdot \frac{\sum_i A_i e^{-\mu_i d}}{\sum_i A_i}. \tag{5.9}$$

where A_i represents the relative amplitude of the i^{th} peak in the ^{192}Ir spectrum with energy E_i, μ_i is the attenuation coefficient of lead at energy E_i, and d is the thickness of lead through which the incident γ-rays must travel. In all instances, the beam profile was normalized to its maximum value, eliminating the proportionality constant implicit in (5.8) and (5.9). The angle θ was converted to a distance along the z-axis using $z = R_s \tan(\theta)$.

The effect of varying the collimator thickness t is shown in Figure 5.9. The calculations were performed using $s = 0.8$ cm, as decided above, and an arbitrarily chosen width of $w = 13.8$ cm. As can be seen, there is little reduction in the out-of-plane radiation for collimator thicknesses greater than 0.4 cm. A collimator thickness of 0.4 cm or 0.6 cm is therefore recommended.

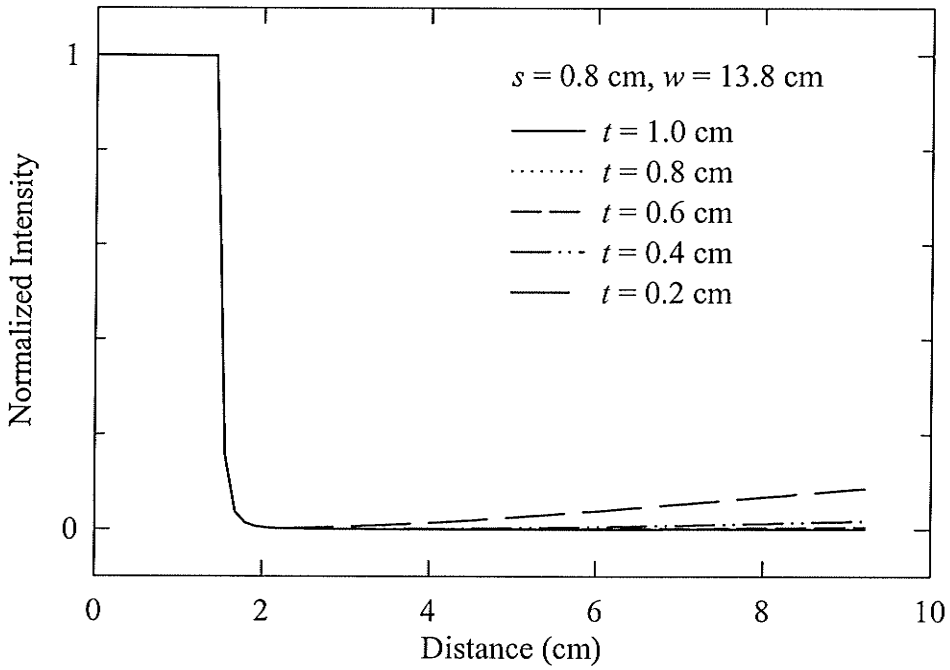

Figure 5.9 Plot of the calculated relative γ-ray intensity at the scan field center as a function of the axial distance from the tomographic plane for various lead collimator thicknesses. Note that the t = 1.0 cm and t = 0.8 cm lines are superimposed.

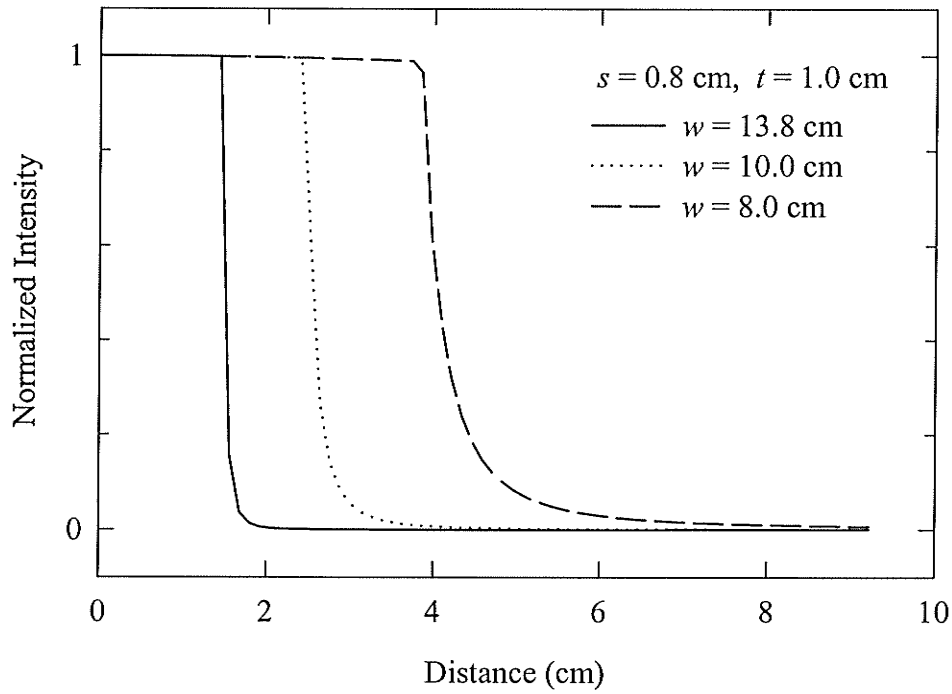

Figure 5.10 Plot of the calculated relative γ-ray intensity at the scan field center as a function of the axial distance from the tomographic plane for various collimator widths.

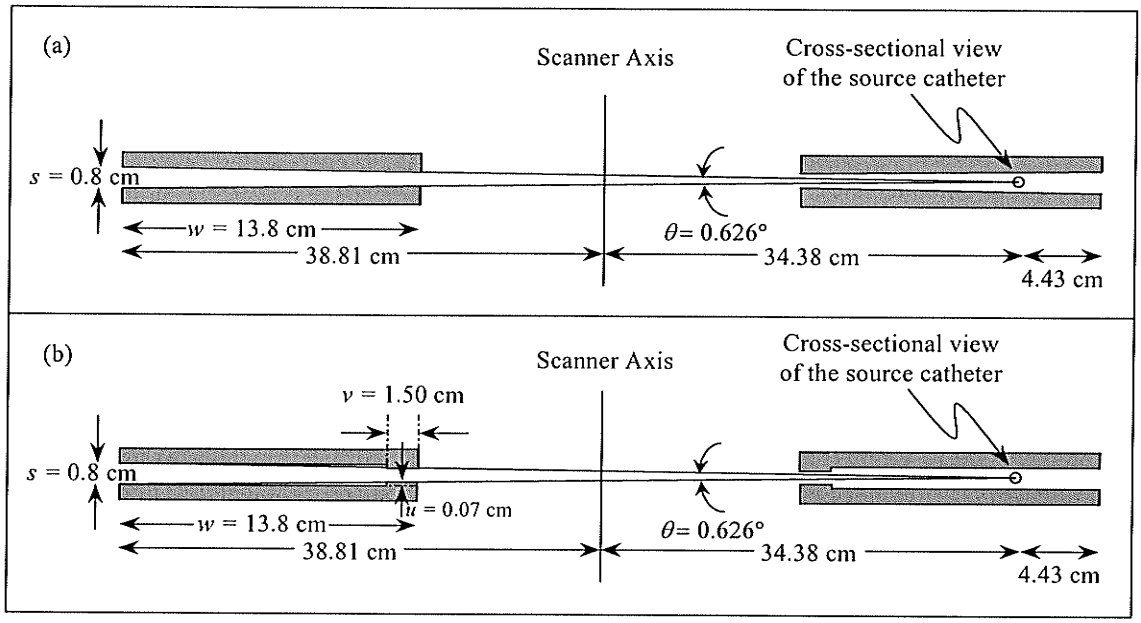

Figure 5.11 Schematic of (a) the divergent collimator and (b) the "simplified" collimator. Both compensate for beam divergence.

The effect of varying the annular region width w is shown in Figure 5.10. The calculations were performed using $s = 0.8$ cm, as decided above, and an arbitrarily chosen thickness of $t = 1.0$ cm. As can be seen, the greater the width of the annular region, the narrower the γ-ray intensity profile along the scanner axis. However, increasing the collimator width beyond 13.8 cm ($R_i = 25$ cm), would prohibit larger patients from being imaged. It is therefore recommended that a collimator width of $w = 13.8$ cm be used.

The collimator shown in Figure 5.8 has the shortcoming that an unnecessarily large portion of the patient is irradiated, as described in more detail below, which increases the amount of scatter and the patient dose. A collimator design that takes the beam divergence into account and reduces the amount of irradiated tissue is shown in Figure 5.11a. Machining the lead into a wedge shape is however a considerable challenge. The design in Figure 5.11b is thus proposed as an alternative, where a small "ledge" at the end of the collimator is used to reduce the slice thickness. The ledge thickness $u = 0.07$ cm was chosen to be approximately equal to the additional lead thickness in Figure 5.11a at 0.75 cm (half the width v of the ledge) from the front of the collimator. This ledge thickness results in a collimator separation of 0.66 cm at the collimator face. Further increasing the ledge thickness would attenuate photons that would otherwise reach the detector, resulting in a reduced detector output. The effect of

the divergent collimator on the γ-ray intensity profile is more clearly shown in Figure 5.12. The solid black lines show the region irradiated by primary photons that will reach the detector. The distance of 0.38 cm is approximately equal to the image slice thickness[1]. The solid grey lines show the volume irradiated when using the collimator design of Figure 5.11a, while the dashed grey lines show the volume irradiated when using the collimator design of Figure 5.8. It can be seen that the volume irradiated is considerably less for the collimator design of Figure 5.11a. This is important not only for reducing patient dose (the dose delivered to tissue outside of the solid black lines in Figure 5.12 is wasted dose), but also for reducing scatter, which is directly proportional to the irradiated slice thickness (Johns and Yaffe, 1982). Plots of the expected radiation intensity profiles along the scanner axis, calculated using (5.8), (5.9) and the collimator designs of Figure 5.8 and Figure 5.11b are shown in Figure 5.13.

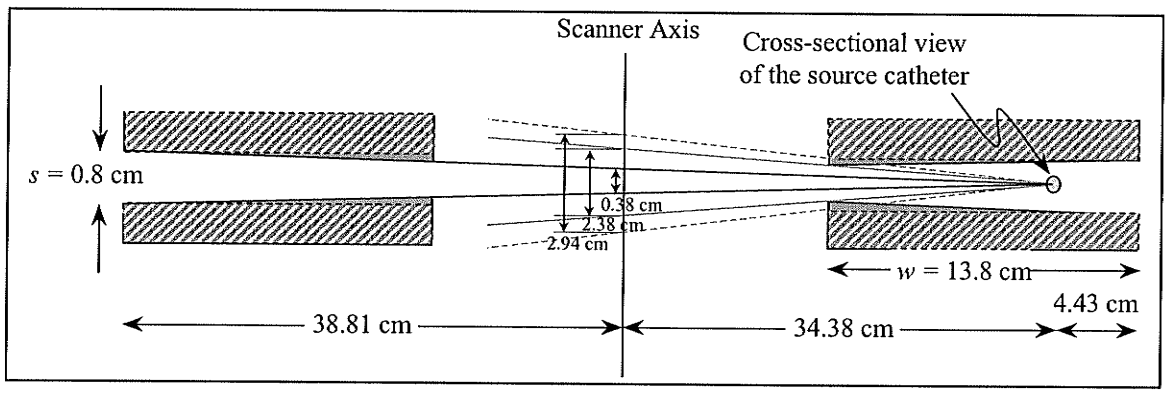

Figure 5.12 Schematic of the divergent and parallel plate (cross-hatched grey) collimator design. The additional collimation provided by the divergent collimator is shown in solid grey. Shown is the volume irradiated by (i) the primary photons that impinge on the detector (region between the solid black lines); (ii) the photons collimated using the divergent collimator (region between the solid grey lines); and, (iii) the photons collimated by the parallel plate collimator (region between the dashed grey lines). Also shown are the thicknesses of these various sections at the scanner axis. Note that transmission of photons through the collimators has not been taken into consideration in this figure.

[1] Note that the efficacy of source collimator for restricting patient irradiation to a narrow, well defined slice (radiation slice thickness) should only be measured with a film (McCollough and Zink, 1995). The efficacy of the collimator to image (as opposed to just irradiate) a narrow, well-defined slice (image slice thickness) is measured using a slice thickness phantom (McCollough and Zink, 1995). The measurements in this section only prove that the collimator design of Figure 5.11b will provide a narrower radiation profile than the collimator design of Figure 5.8. The absolute value of the FWHM is too erroneous to be called the radiation slice thickness.

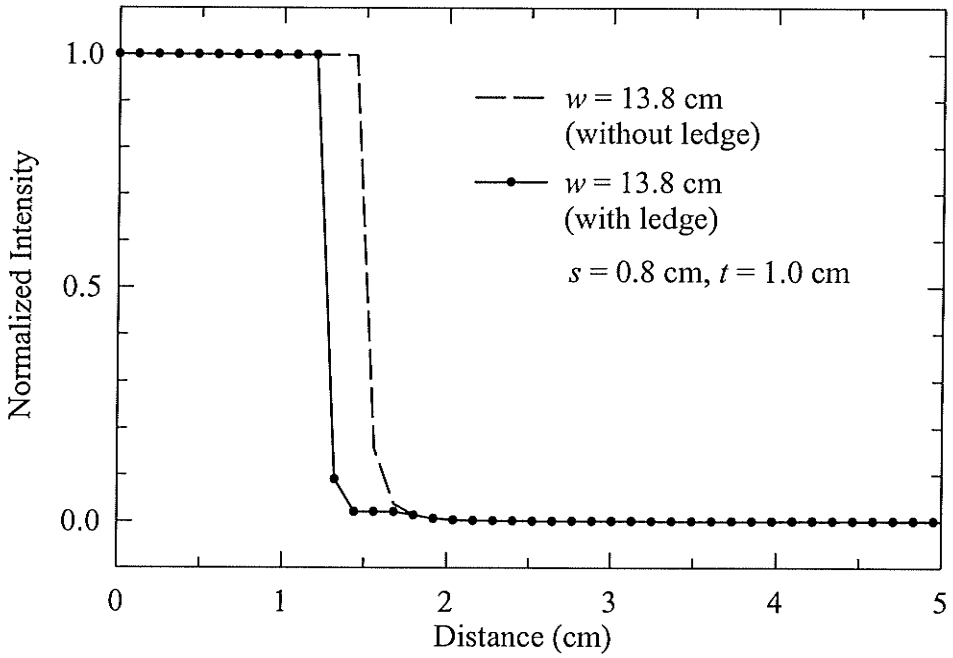

Figure 5.13 Plot of the calculated relative γ-ray intensity along the scanner axis as a function of the axial distance from the tomographic plane for the collimator designs in Figures 5.8 and 5.11b.

5.3.1.5 Required Collimator Separation as a Function of Ray Angle

A further consideration is the effect of collimator design on angled rays, as shown in Figure 5.14. The goal of this section is to ensure that the collimator does not prevent any of the primary radiation from reaching the detectors for arbitrary detector and source position pairing. The discussion of collimator separation outlined above assumes that the source and the detector were directly opposite each other. In practice, most detectors are not directly opposite the source for a particular source position. Thus, the angle θ subtended by the detector (see Figure 5.14; note that θ lies out of the plane) varies as a function of ϕ, where ϕ is the angle between the ray connecting diametrically opposite source and detector positions and the ray connecting the source with an arbitrary detector position, as shown in Figure 5.14. The calculations performed here verify that the collimator separation chosen above is adequate for all values of ϕ. More specifically, the minimum collimator separation is determined for angled rays such that the entire length of the scintillating crystal (0.8 cm) is still irradiated.

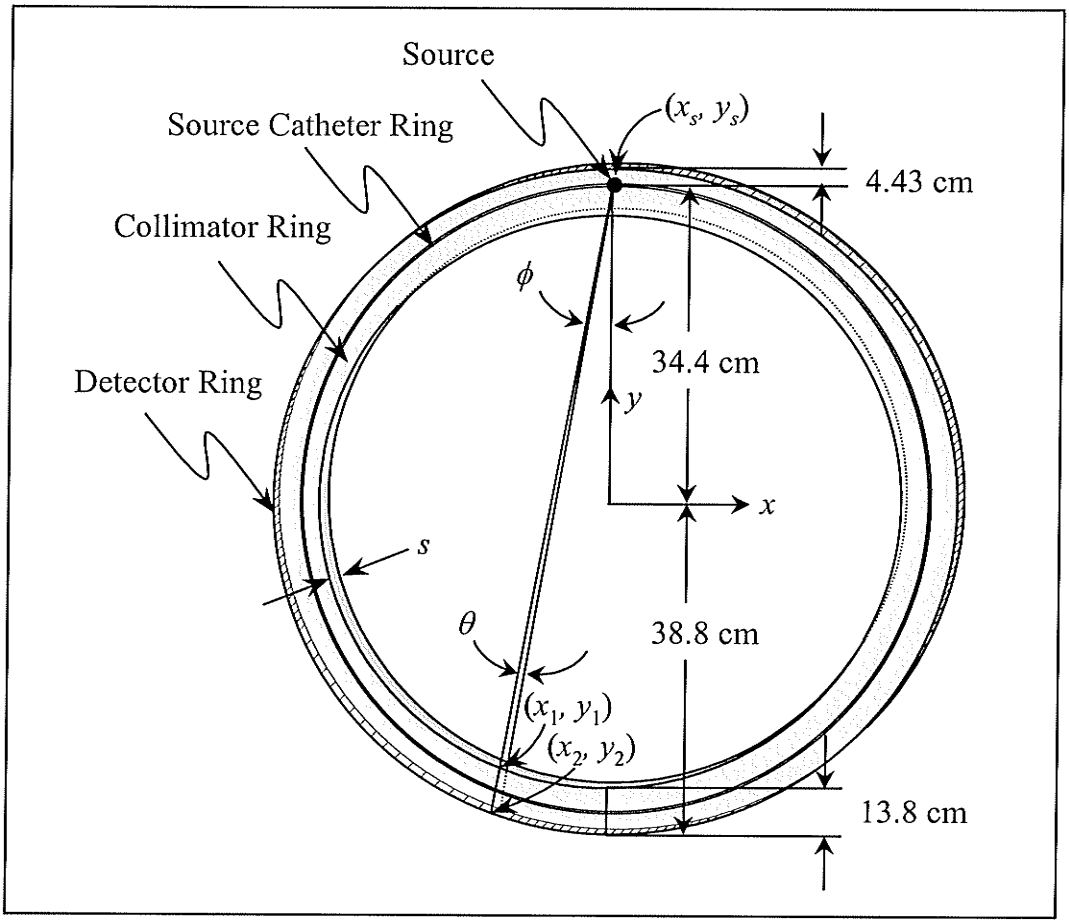

Figure 5.14 Schematic of the collimator ring showing the dimensions of the collimator. Also shown is a ray at angle ϕ, where ϕ is the angle between the ray connecting diametrically opposite source and detector positions and the ray connecting the source and a detector.

The locii of points lying along the circular paths at the collimator bore radius, source catheter ring, and the detector ring are given by

$$\text{Collimator Bore:} \quad x^2 + y^2 = (25.0\,\text{cm})^2 \tag{5.10a}$$

$$\text{Source Catheter Ring:} \quad x^2 + y^2 = (34.38\,\text{cm})^2 \tag{5.10b}$$

$$\text{Detector Ring:} \quad x^2 + y^2 = (38.81\,\text{cm})^2 \tag{5.10c}$$

respectively, where the x and y axes are as shown in Figure 5.14. The source-to-inner collimator face (SCD) and source-to-detector distances (SDD) along the angled rays can be calculated from (5.10a), (5.10b) and (5.10c) as follows. The ray emanating from the source position (x_s, y_s) at an angle ϕ intersects the collimator face at a point (x_1, y_1) and the detectector ring at (x_2, y_2), as illustrated in Figure 5.14. The SCD and SDD can then be found using the expressions

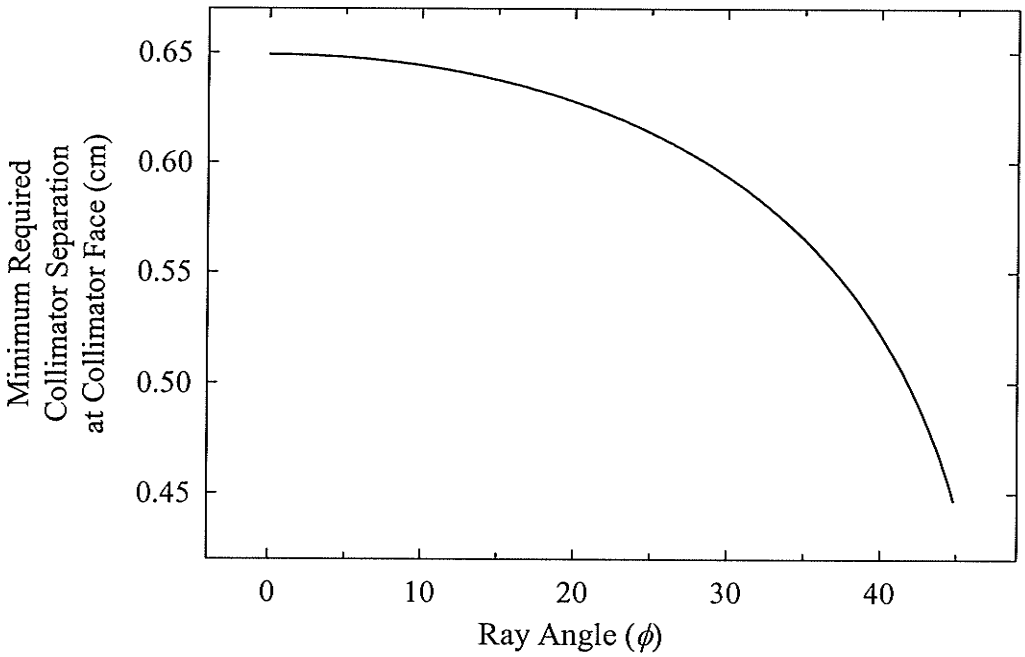

Figure 5.15 Plot of the minimum collimator separation as a function of ray angle.

$$\mathrm{SCD} = \sqrt{(x_1 - x_s)^2 + (y_1 - y_s)^2} \tag{5.11}$$

and

$$\mathrm{SDD} = \sqrt{(x_2 - x_s)^2 + (y_2 - y_s)^2}\,. \tag{5.12}$$

The angle subtended by the detector is then simply

$$\theta = (0.8\,\mathrm{cm})/\mathrm{SDD}\,. \tag{5.13}$$

The minimum required collimator separation at the collimator face $\tilde{s}$ is given by

$$\tilde{s} = \mathrm{SCD} \cdot \theta \tag{5.14}$$

and is plotted in Figure 5.15 as a function of ray angle ϕ. As can be seen, the minumim required collimator separation decreases as a function of ϕ. Thus, the collimator separation chosen above assuming that the source and the detector are directly opposite each other ($\phi = 0$) is valid for all values of ϕ.

5.3.2 Methods

Equations (5.8) and (5.9) do not incorporate the effects of scatter or the finite source size. Several measurements were performed using the experimental set-up shown in Figure 5.16 to ensure that these effects do not have a large impact on the results predicted by (5.8) and (5.9). A detector assembly configured to operate with a single crystal coated

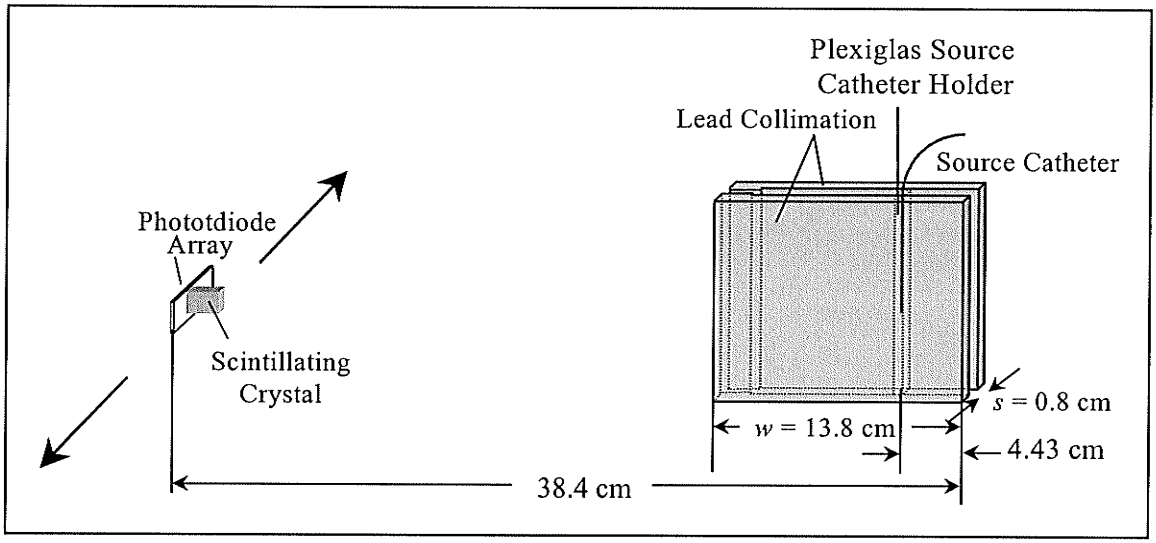

Figure 5.16 Schematic of the experimental set-up used to measure the effect of different collimator configurations.

with Gelcoat was fixed to a translating stage, and stepped in increments of 1.0 mm past a prototype collimator at a distance of 38.4 cm ($\approx R_d$ for the final scanner), to mimic the collection of a radiation intensity profile along the scanner axis. A total of 50 readings were taken at each position, which were then averaged and corrected for dark current. Four different collimator configurations were investigated. These included the collimator illustrated in Figure 5.11b; Figure 5.8 using s = 0.8 cm, t = 0.6 cm, w = 13.8 cm; Figure 5.8 using s = 0.8 cm, t = 0.6 cm, w = 11.8 cm; and, Figure 5.8 using s = 0.8 cm, t = 0.4 cm, w = 13.8 cm.

5.3.3 Results

The profile along the scanner axis for the collimator design illustrated in Figure 5.11b is shown in Figure 5.17, along with the expected profile, as calculated using (5.8) and (5.9). The discrepancy between the expected and measured results is due to the detection of γ-rays scattered from the collimators, and the finite size of the source and the detector, which were assumed to be infinitesimally narrow in the above calculations. The results for the remaining collimator configurations are plotted in Figures 5.18 through 5.20. The tilt in the measured data appearing in Figures 5.19 and 5.20 could be because the path traversed by the detector was not perfectly perpendicular to the collimators, i.e., the

source-to-detector position varied as a function of translation stage position, or because of a change in circuit temperature during the course of the measurements.

The measured full-width at half-maximum (FWHM) for all of the plots is listed in Table 5.4. The collimator configuration of Figure 5.11b yields the best results (narrowest radiation profile) and will therefore be used in the actual scanner. Comparison of Figure 5.18 with Figure 5.20 demonstrates that an increase in collimator thickness from $t = 0.4$ cm to 0.6 cm has a small influence on the intensity profile. Either thickness could therefore be used.

Table 5.4 FWHM for various collimator configurations

Collimator Configuration	Measured FWHM (cm)
Figure 5.11b	2.66
Figure 5.8: $s = 0.8$ cm, $t = 0.6$ cm, $w = 13.8$ cm	3.16
Figure 5.8: $s = 0.8$ cm, $t = 0.6$ cm, $w = 11.8$ cm	4.18
Figure 5.8: $s = 0.8$ cm, $t = 0.4$ cm, $w = 13.8$ cm	3.22

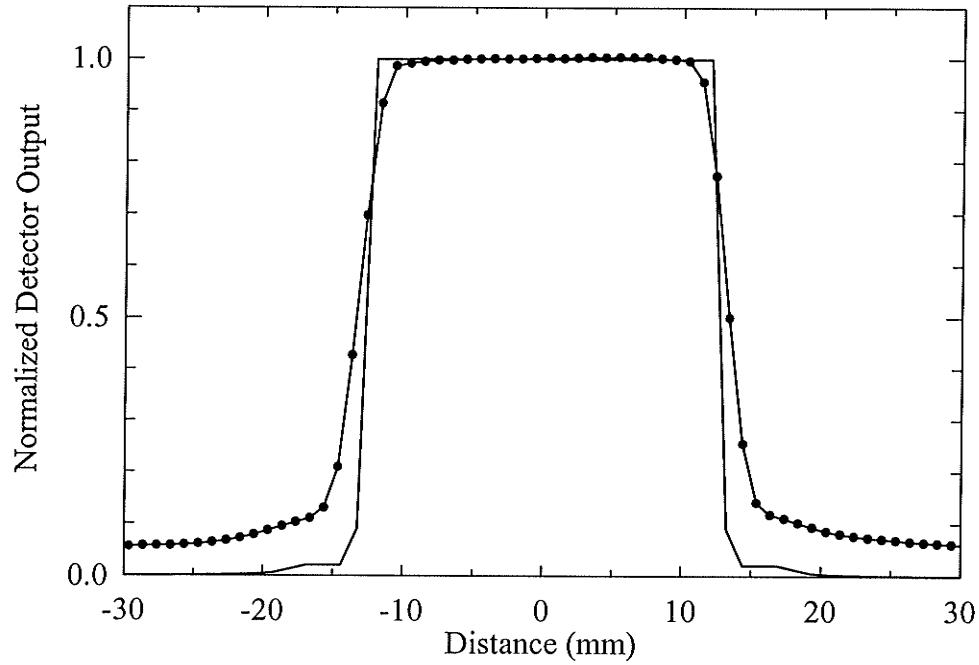

Figure 5.17 Plot of the normalized measured detector output (points) for the collimator design illustrated in Figure 5.11b and the calculated detector output (line) along the scanner axis as a function of the axial distance from the tomographic plane.

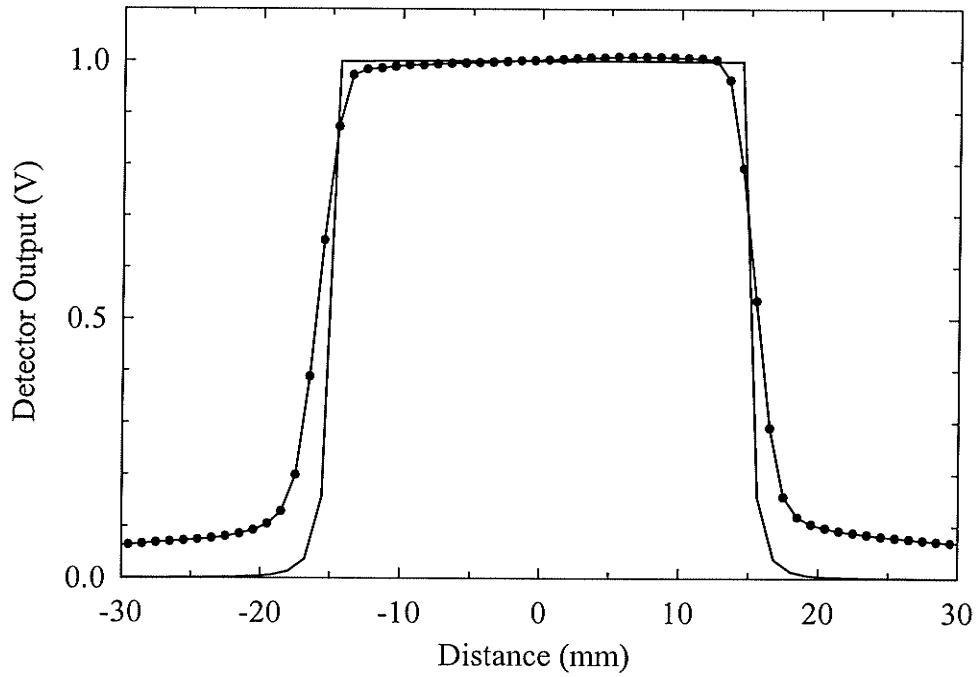

Figure 5.18 Plot of the normalized measured detector output (points) for the collimator design illustrated in Figure 5.8 (s = 0.8 cm, t = 0.6 cm, w = 13.8 cm) and the calculated detector output (line) along the scanner axis as a function of the axial distance from the tomographic plane.

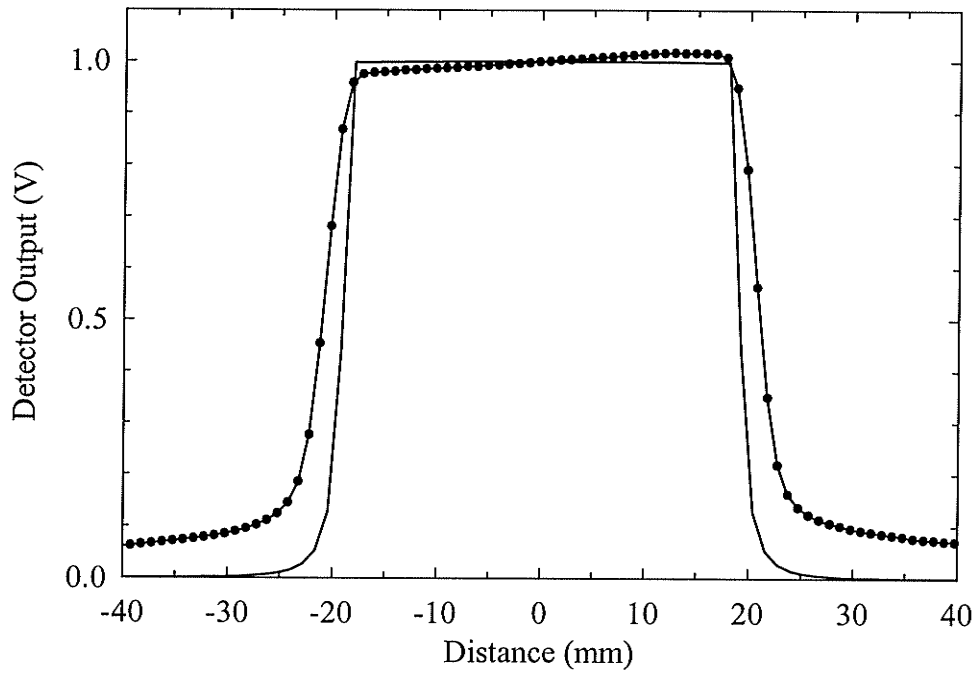

Figure 5.19 Plot of the normalized measured detector output (points) for the collimator design illustrated in Figure 5.8 (s = 0.8 cm, t = 0.6 cm, w = 11.8 cm) and the calculated detector output (line) along the scanner axis as a function of the axial distance from the tomographic plane.

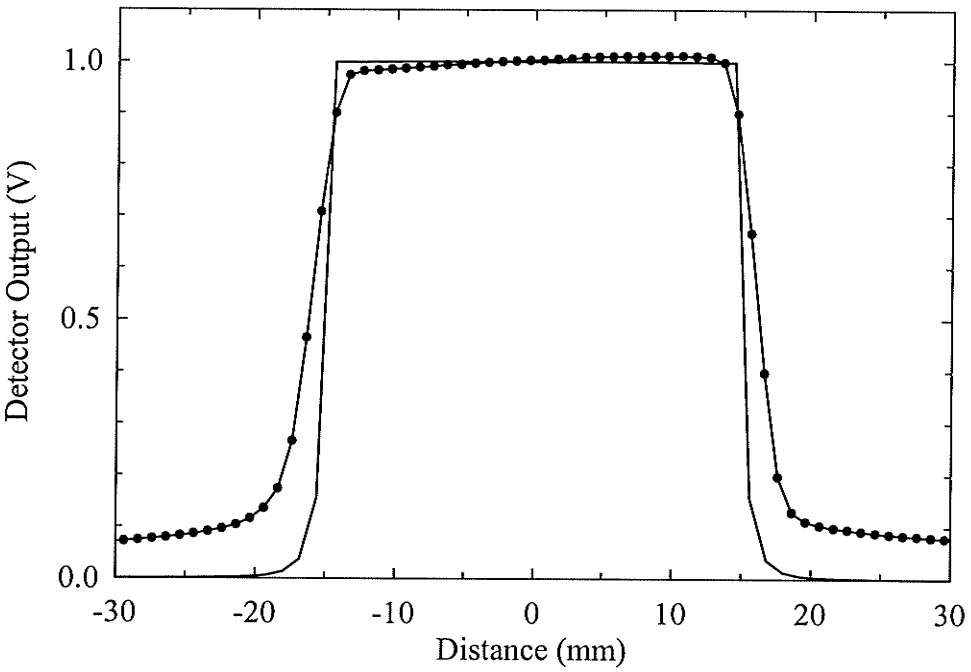

Figure 5.20 Plot of the measured normalized detector output (points) for the collimator design illustrated in Figure 5.8 (s = 0.8 cm, t = 0.4 cm, w = 13.8 cm) and the calculated detector output (line) along the scanner axis as a function of the axial distance from the tomographic plane.

Chapter 6

Image Quality

Image quality is based on a complex relationship between noise, dose and high-contrast spatial resolution. In general, none of these parameters can be individually improved without influencing the others. In this scanner design, many parameters defining image quality are determined by limitations of the HDR BT treatment unit. It is therefore important to understand how these limitations affect the image quality. In addition, future improvements or modifications to the HDR BT treatment unit may be available. The effect of these modifications on image quality must be understood.

In this chapter, the scanner geometry and data acquisition are modeled in software. The first image quality parameter examined is the high contrast resolution, as characterized by a point spread function (PSF) or modulation transfer function (MTF). High contrast resolution is the ability of the imaging device to spatially distinguish small closely spaced high contrast objects in the reconstructed image. The effects of scanner design, i.e., detector size and spacing, source length and spacing, as well as reconstruction filter function are examined. The noise characteristics of the scanner are analyzed by determining the standard deviation (SD) at the centre of uniform Plexiglas disk images as a function of source strength, number of projections, number of source

positions, filter function and interpolation scheme, and by using the concept of noise power spectrum (NPS). The dose is characterized by means of the computed tomography dose index (CTDI), which is the radiation dose received by the patient within the scanned volume of interest (Shope et al., 1981). The CTDI is measured using the prototype collimators shown in Figure 5.11b.

6.1 Simulation Program

Geometric parameters such as the source ring radius, detector ring radius, source locations and detector locations for the fourth generation ^{192}Ir source-based CT design were established in previous sections. The data gathering process associated with this geometry can be modeled easily in a computer[1]. This approach provides not only an estimate of scanner performance, but also an indication of the effect of modifying the basic design parameters. Parameters such as the source size, detector size, and spacing between consecutive source locations and detector elements can easily be modified to determine their impact on image quality. An optimal scanner design, which is not constrained by the HDR BT treatment unit, can be obtained using this procedure.

The computer simulation provides projection data (i.e. transmission measurements) in a fourth generation CT geometry. The projection data are then rebinned to an equivalent first generation geometry in order to reconstruct images using a filtered backprojection method (Barrett and Swindell, 1981). Simulated images of wire phantoms are used to assess the high contrast resolution, and images of uniform Plexiglas disks are used to quantify the image noise.

6.1.1 Detector Output

Projection data were calculated for cylindrical Plexiglas phantoms of various diameters aligned with the scanner central axis, as shown in Figure 6.1. The thickness of Plexiglas traversed T_{plexi} is determined by calculating the distance

$$T_{plexi} = \sqrt{(x_2 - x_1)^2 + (y_2 - y_1)^2} \qquad (6.1)$$

[1] The scanner is modeled using a commercial high level programming language software package (IDL 5.3.1, Research Systems, Inc.)

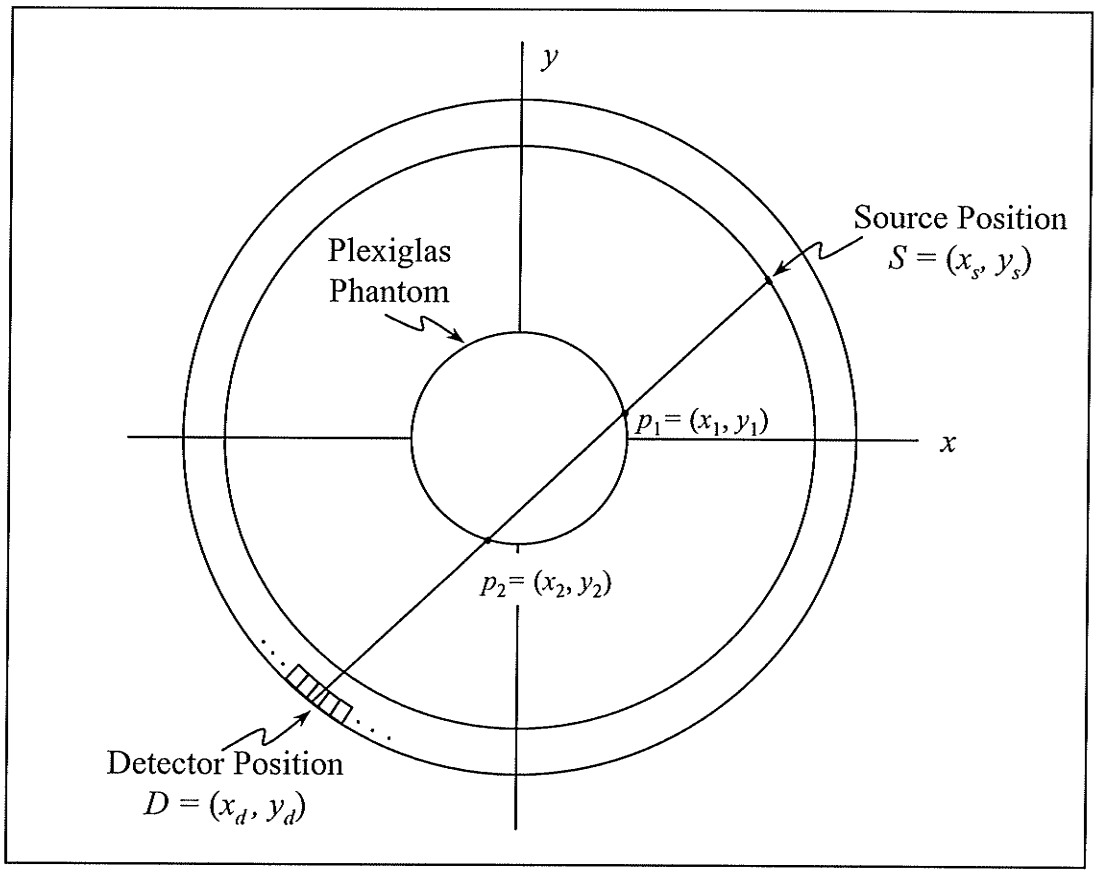

Figure 6.1 Schematic of the fourth generation scanner showing the geometry used to determine the detector output.

where $p_1 = (x_1, y_1)$ and $p_2 = (x_2, y_2)$ are the intersection points of ray SD with the outer edge of the phantom (Figure 6.1).

When testing the simulation program, the detector output V was found by evaluating (3.103) for Plexiglas thicknesses T_{plexi} = 0.0, 0.5, 1.0, . . ., 39.5 cm. These values are stored in an array, and the detector output for arbitrary Plexiglas thicknesses found by interpolating between the precalculated values. This avoids calculation of the summation in (3.103) for each ray in the projection, thereby reducing the simulation time. The errors introduced by this approximation are small. The detector output in the absence of an attenuator V_o is equal to (3.103) evaluated for T_{plexi} = 0.0 cm. The projection data P is then generated using

$$P = - \ln(V / V_o) . \qquad (6.2)$$

Note that (3.103) accounts for spectral hardening, but not for scattered radiation or the finite dimensions of the source and the detectors. Scatter is discussed in Chapter 7, and

the effect of the finite source and detector size is investigated in §6.2. Further details regarding the detector output for the high contrast resolution simulations and noise simulations are provided in §6.2.1 and §6.3.1.

6.1.2 Calculation of 4th Generation Geometry Projection Data

Projection data are generated using the fourth generation geometry shown in Figure 6.2a. The source locations are determined using

$$x_s(i_s) = R_s \cos(i_s \Delta\phi_s) \quad y_s(i_s) = R_s \sin(i_s \Delta\phi_s) \qquad i_s = 0, 1, 2, \ldots, n_s \tag{6.3}$$

and the detector positions are determined using

$$x_d(i_d) = R_d \cos(i_d \Delta\phi_d) \quad y_d(i_d) = R_d \sin(i_d \Delta\phi_d) \qquad i_d = 0, 1, 2, \ldots, n_d \tag{6.4}$$

where

$$\Delta\phi_s = \frac{2\pi}{n_s} \qquad \Delta\phi_d = \frac{2\pi}{n_d} \tag{6.5}$$

$R_s = 34.38$ cm is the source ring radius, $R_d = 38.81$ cm is the detector ring radius, n_s is the number of equally spaced source positions and n_d is the number of equally spaced detectors in the ring. (Note that it would have also been possible to vary R_s and R_d; however, this option was not investigated.) For each detector location, a predetermined number of rays joining to source positions on the opposite side were sampled to form a fan-beam projection. This was repeated for all detector positions to yield n_d fan-beam projections.

A parallel beam filtered-back projection method was used to reconstruct images from the projection data. This requires rebinning of the fourth generation fan-beam projection data into a first generation parallel beam format as follows.

The fourth generation projection data is described in terms of x_r and ϕ, as shown in Figure 6.2a. The parameter x_r is the perpendicular distance from the center of the detector and source ring to the ray SD connecting the source and a detector, and ϕ is the angle between SD and the x-axis. These parameters are given by

$$\phi = \tan^{-1}\left(\frac{y_s(i_s) - y_d(i_d)}{x_s(i_s) - x_d(i_d)}\right) \tag{6.6}$$

and

$$x_r = R_d \sin\theta \tag{6.7}$$

where

$$\theta = \phi - \phi_f \tag{6.8}$$

and

$$\phi_f = i_d \Delta\phi_d \,. \tag{6.9}$$

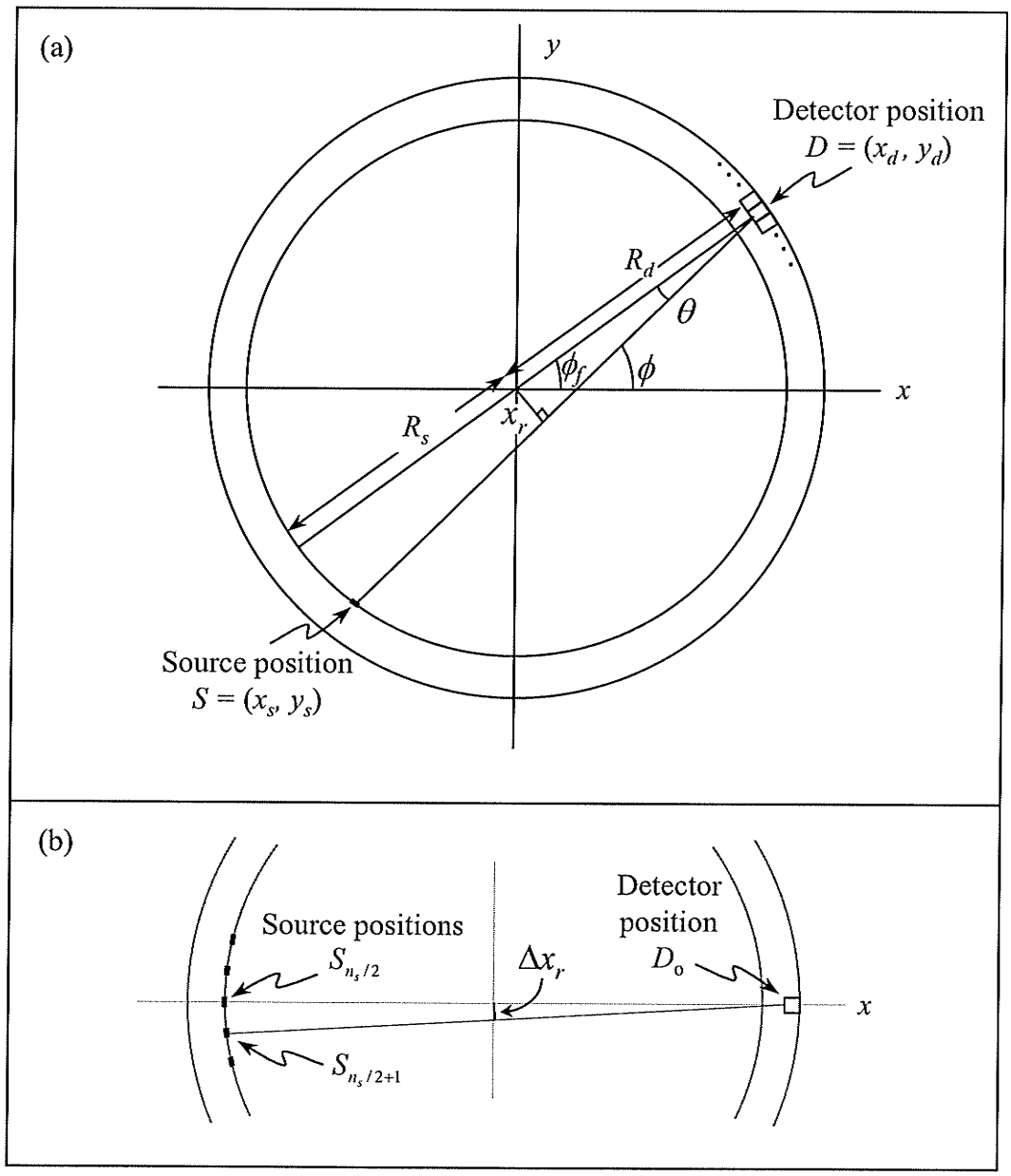

Figure 6.2 (a) Schematic of the fourth generation scanner showing the definition of x_r and ϕ. (b) Schematic showing the definition of the sample spacing Δx_r, which is the perpendicular distance from the center of the detector and source ring to the ray $S_{n_s/2+1} D_o$. Note that the spacing between the source positions has been exaggerated for illustration purposes.

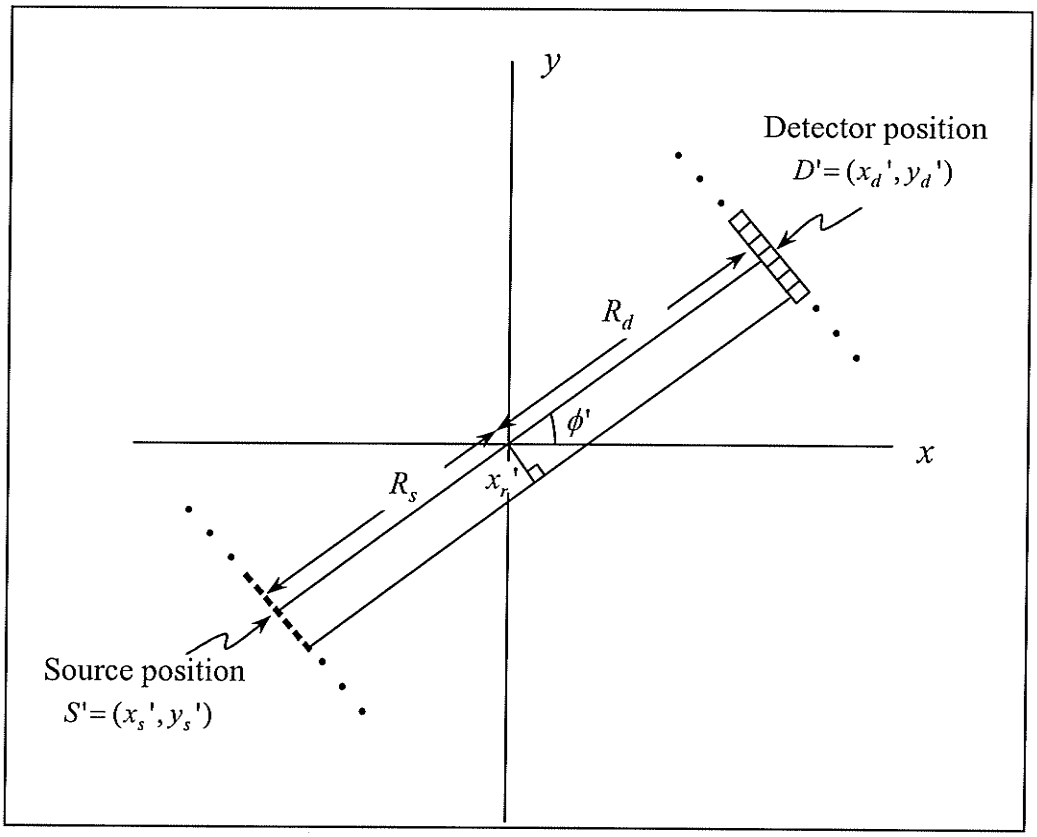

Figure 6.3 Schematic of the first generation scanner showing the definition of x_r' and ϕ'.

The first generation projection data is described in terms of x_r' and ϕ', as shown in Figure 6.3. The parameter x_r' is the perpendicular distance between the scanner centre and the ray $S'D'$ connecting the source and the detector, and ϕ' is the angle between $S'D'$ and the x-axis. These parameters are described by

$$x_r' = i_x \Delta x_r' \qquad i_x = \ldots, -2, -1, 0, 1, 2, \ldots \tag{6.10}$$

and

$$\phi' = i_\phi \Delta \phi' \qquad i_\phi = 0, 1, 2, \ldots, n_{\phi'} \tag{6.11}$$

where $\Delta x_r'$ is the spacing of the source and detector positions for the first generation scanner geometry, i_x has a range such that the object is completely encompassed for all projection angles, $n_{\phi'}$ is the number of projections in the first generation scanner geometry and $\Delta\phi' = 2\pi / n_{\phi'}$ is their angular spacing.

The rebinning process involves interpolating the fourth generation projection data $P(x_r,\phi)$ to find the first generation projection values $P(x_r',\phi')$ (Barrett and Swindell, 1981). The rebinning process was achieved by first calculating x_r for each ray in the fourth generation geometry using (6.7). Interpolation was then performed in the x_r direction for all rays within a projection (Figure 6.4a) to yield an intermediate array $P(x_r',\tilde{\phi})$ with projection data at the desired first generation x_r' values, and intermediate $\tilde{\phi}$ values, where $\tilde{\phi}$ (found using (6.7) and (6.8)) is the angle of the ray associated with each x_r' value. A second linear interpolation (Figure 6.4b) was performed in the $\tilde{\phi}$ direction to determine the projection values for the first generation ϕ' values. The number of rebinned parallel projections $n_{\phi'}$ was chosen equal to the number of detectors in the ring n_d, i.e., the number of projections in the first generation geometry was selected to equal the number of projections in the fourth generation geometry. The sample spacing $\Delta x_r'$ was chosen to equal Δx_r (Figure 6.2b), unless otherwise stated. This choice was made because coarser interpolation "throws away" data, and finer interpolation does not add new data, i.e., it simply generates redundant data.

6.1.3 Image Reconstruction

The filtered backprojection technique requires convolution of the projection data with a filter function, followed by interpolated backprojection of the data onto an image grid (Barrett and Swindell, 1981). It is necessary to filter the projection data prior to backprojection in order to prevent the blurring inherent in the backprojection process (Herman, 1981). The rebinned projection data are filtered using a Ram-Lak (Bracewell and Riddle, 1967; Ramachandran and Lakshminarayanan, 1971; Barrett and Swindell, 1981) or a Shepp-Logan (Shepp and Logan, 1974; Barrett and Swindell, 1981) filter. The Ram-Lak (RL) filter is given by

$$q_{RL}(x_r') = 2\pi f_N^2 \frac{\sin(2\pi f_N x_r')}{2\pi f_N x_r'} - \pi f_N^2 \frac{\sin^2(\pi f_N x_r')}{(\pi f_N x_r')^2} \qquad (6.12)$$

where x_r' is the perpendicular distance from the projection ray to the origin (Figure 6.3), $f_N = 1/2\Delta x_r'$ and $\Delta x_r'$ is the spacing between adjacent parallel rays. The Shepp-Logan (SL) filter is given by

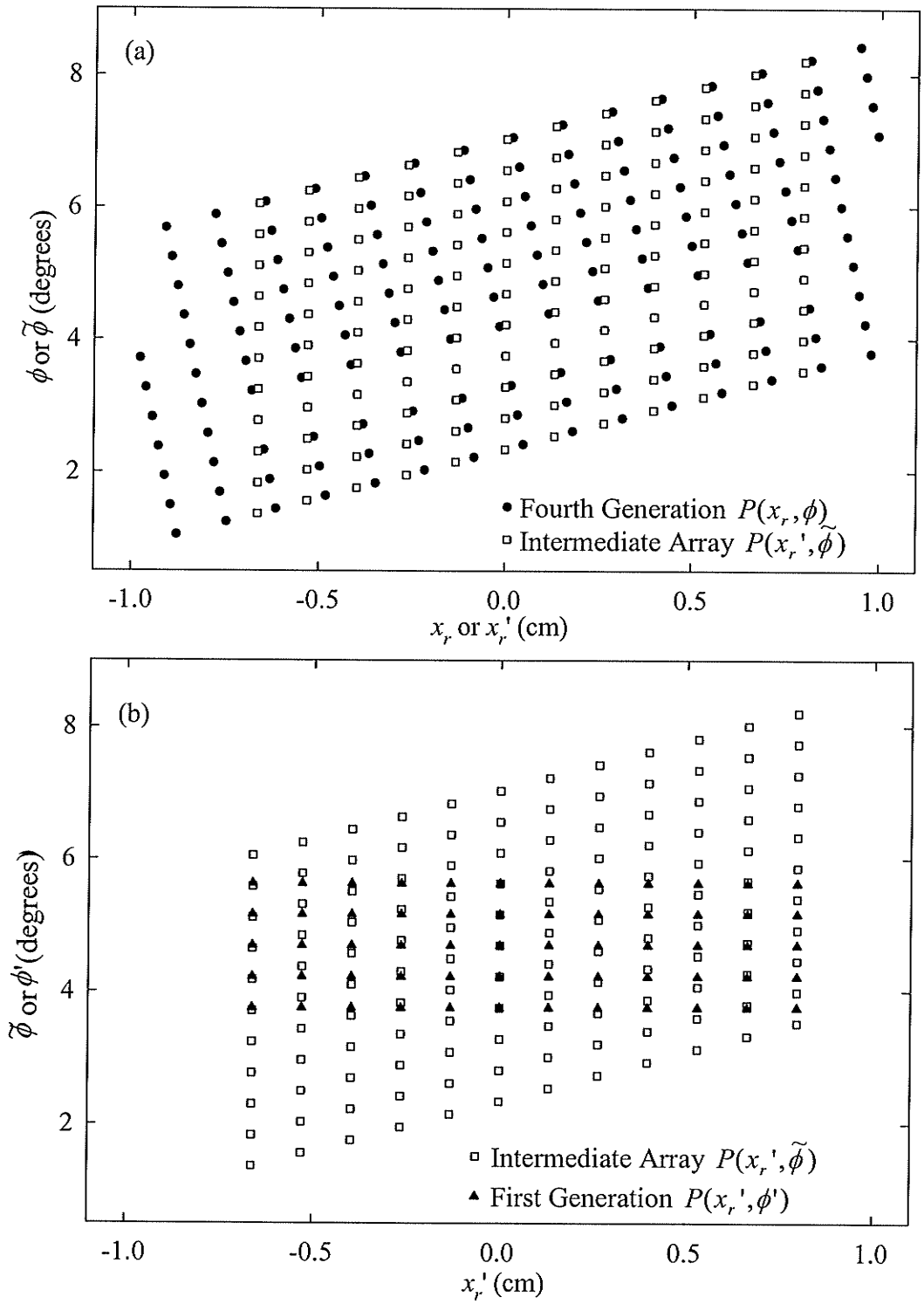

Figure 6.4 Sinogram space representation of the projection data showing (a) rebinning of the fourth generation projection data $P(x_r,\phi)$ in the x_r direction to an intermediate data set $P(x_r',\tilde{\phi})$ with first generation x_r' values; and, (b) rebinning of the intermediate data set $P(x_r',\tilde{\phi})$ in the $\tilde{\phi}$ direction to a data set with first generation x_r' and ϕ' values $P(x_r',\phi')$. Note that only a small sample of the projection data is shown. (Barrett and Swindell, 1981)

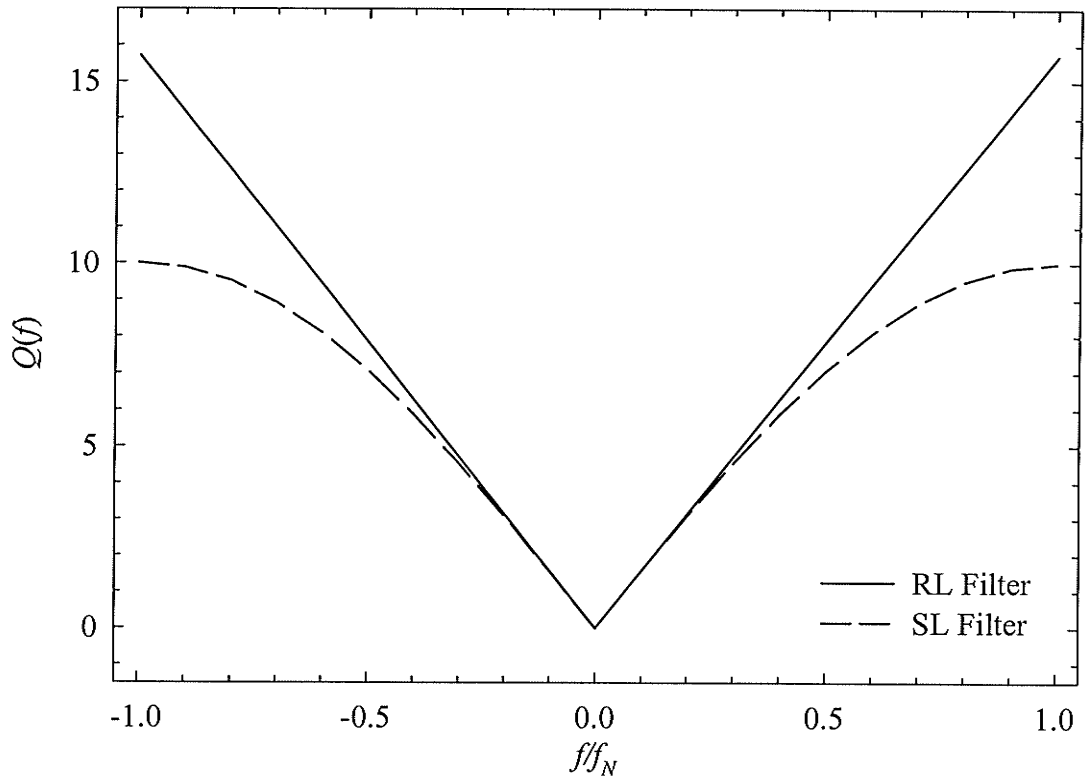

Figure 6.5 Plot of the RL and SL filter in the frequency domain as a function of normalized frequency (Barrett and Swindell, 1981).

$$q_{SL}(x_r') = \frac{-8f_N^2}{\pi}\left[\frac{1-4f_N x_r'\sin(2\pi f_N x_r')}{16f_N^2 x_r'^2-1}\right]. \tag{6.13}$$

Assuming a bandlimited reconstruction where $f_N = 1/2\Delta x_r'$, and recalling that $x_r' = i_x \Delta x_r'$, the above expressions reduce to

$$q_{RL-discrete}(i_x) = \begin{cases} \pi f_N^2 & i_x = 0 \\ -\dfrac{4f_N^2}{\pi i_x^2} & i_x = \pm 1, \pm 3, \pm 5, \ldots \\ 0 & i_x = \pm 2, \pm 4, \pm 6, .. \end{cases} \tag{6.14}$$

and

$$q_{SL-discrete}(i_x) = -\frac{8f_N^2}{\pi}\left[\frac{1}{4i_x^2-1}\right] \qquad i_x = 0, \pm 1, \pm 2, \ldots \ . \tag{6.15}$$

When viewed in the frequency domain, as shown in Figure 6.5, the RL filter can be thought of as a ramp filter in the sense that it is simply described by

$$Q_{RL}(f) = \begin{cases} \pi|f| & |f_r| \le f_N \\ 0 & |f_r| > f_N. \end{cases} \tag{6.16}$$

The SL filter given by

$$Q_{SL}(f) = Q_{RL}(f)\,\mathrm{sinc}(f/2f_N) \tag{6.17}$$

provides greater smoothing of the image than the RL filter because the high frequency components in the projection data are reduced by the additional sinc term. This smoothing is important, especially in images with sharp discontinuities, where use of the SL filter prevents ringing artifacts from appearing in the images. After filtering, the projection data are backprojected onto a grid to generate an image as described by Barrett and Swindell (1981).

6.1.4 Simulated Images

Two different phantoms were modeled to test the scanner simulation program. Shown in Figures 6.6 to 6.9 are sinograms (plots of the unfiltered projection data as a function of x_r' and ϕ') and images of a Plexiglas cylinder aligned with the scanner axis and a Plexiglas annulus offset from the scanner axis by (x_o, y_o) = (1.5 cm, 0.75 cm). The sinograms served as a valuable verification tool because they identified errors in the projection data that were not obvious in the final images. The images shown below, along with careful checks of each stage in the scanner simulation program verify that the program is performing the required calculations.

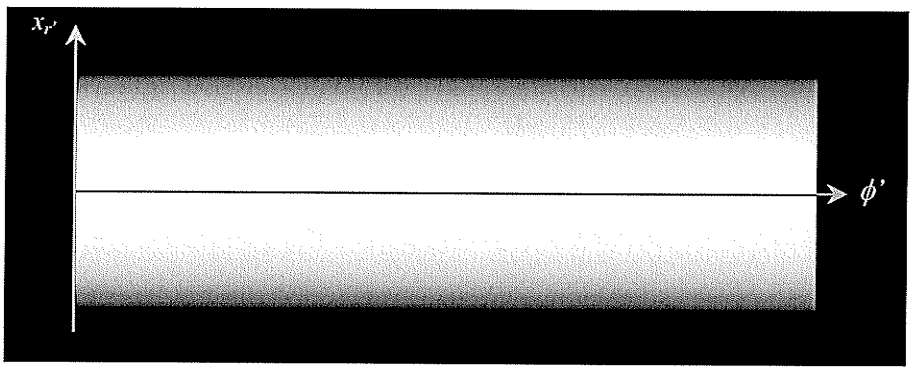

Figure 6.6 Sinogram of an 8.0 cm radius Plexiglas phantom aligned with the scanner axis. This sinogram shows the unfiltered projection data, rebinned to first generation geometry.

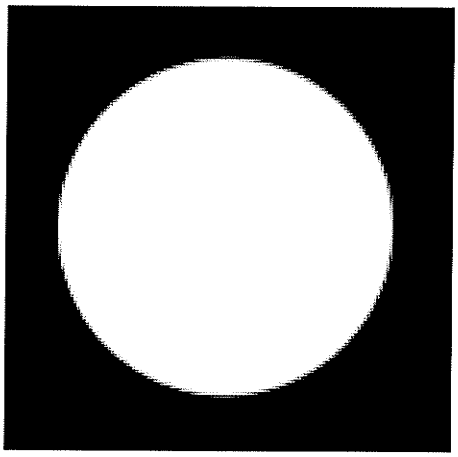

Figure 6.7 Image of an 8.0 cm radius Plexiglas phantom aligned with the scanner axis.

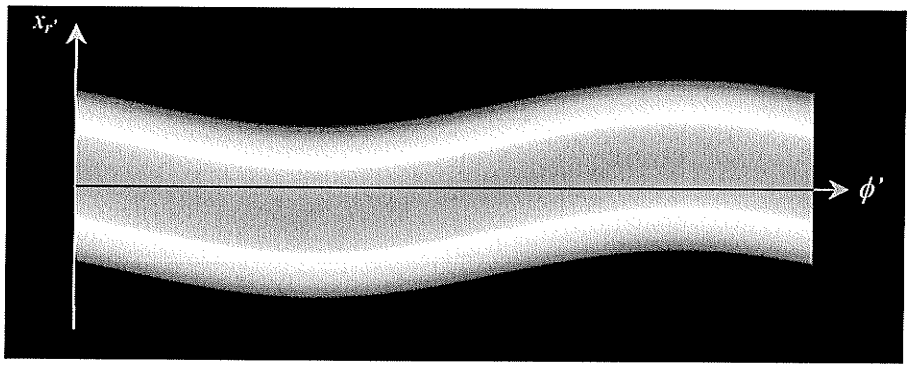

Figure 6.8 Sinogram of a 6.0 cm radius Plexiglas phantom with a concentric 3.0 cm air core, offset from the scanner axis by (x_o, y_o) = (1.5 cm, 0.75 cm). This sinogram shows the unfiltered projection data, rebinned to first generation geometry.

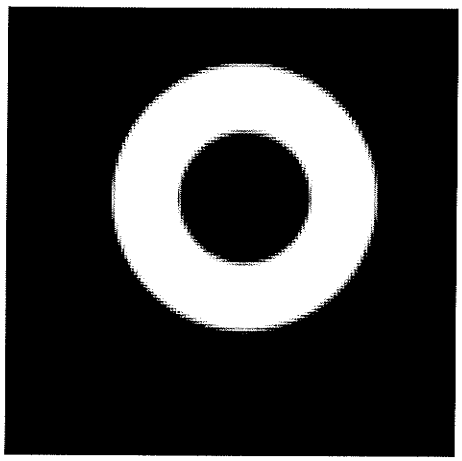

Figure 6.9 Image of a 6.0 cm radius Plexiglas phantom with a concentric 3.0 cm air core, offset from the scanner axis by (x_o, y_o) = (1.5 cm, 0.75 cm).

6.2 High Contrast Resolution

The high contrast resolution of an imaging system characterizes its ability to resolve closely spaced high contrast objects in the image. It is described by the PSF in the spatial domain and by the MTF in the frequency domain. The high contrast resolution of a CT scanner is dependent upon several factors including the source size, number of source positions, detector size, number of detectors and the filter function.

6.2.1 Detector Output for High Contrast Resolution Measurements

The scanner high contrast resolution was assessed by simulating images of a thin dense wire aligned with the center of the detector ring (i.e., along the scanner axis). In this simulation, the detector output incorporated the finite size of the source and the detectors. Both the γ-ray intensity of the source over its length s_l and the sensitivity of the detectors over their width d_w were assumed to be uniform. Since the wire being imaged is located at the center of the scan plane, the projected dimensions of the source and the detector at the location of wire are minified as follows,

$$\begin{aligned} s_{l-sc} &= \frac{R_d}{R_d + R_s} s_l \\ d_{w-sc} &= \frac{R_s}{R_d + R_s} d_w \end{aligned} \tag{6.18}$$

where R_s and R_d are as shown in Figure 6.2. The beam profile at the center of the detector ring is given by the convolution of the scaled source intensity distribution of length $s_{l\text{-}sc}$ and the scaled detector sensitivity distribution of width $d_{w\text{-}sc}$ (Barret and Swindell, 1981; Rathee et al., 1992) to yield the trapezoid

$$w(x_p) = \begin{cases} 1 & 0 \le |x_p| \le \left| \frac{s_{l-sc} - d_{w-sc}}{2} \right| \\ -\frac{|x_p|}{d_{w-sc}} + \frac{s_{l-sc} + d_{w-sc}}{2d_{w-sc}} & \left| \frac{s_{l-sc} - d_{w-sc}}{2} \right| < |x_p| < \frac{s_{l-sc} + d_{w-sc}}{2} \quad \text{if } s_{l-sc} \ge d_{w-sc} \\ -\frac{|x_p|}{s_{l-sc}} + \frac{s_{l-sc} + d_{w-sc}}{2s_{l-sc}} & \left| \frac{s_{l-sc} - d_{w-sc}}{2} \right| < |x_p| < \frac{s_{l-sc} + d_{w-sc}}{2} \quad \text{if } s_{l-sc} < d_{w-sc} \\ 0 & \frac{s_{l-sc} + d_{w-sc}}{2} < |x_p| \end{cases} \tag{6.19}$$

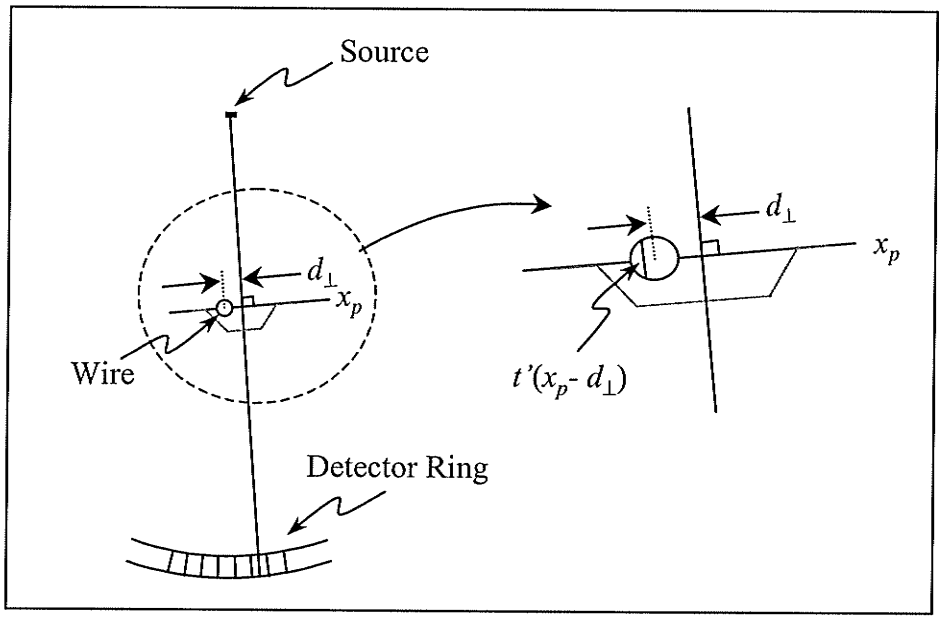

Figure 6.10 Schematic of the fourth generation scanner showing the geometry used to determine the detector output when incorporating the effect of the finite source and detector size. The grey trapezoid represents the beam profile $w(x_p)$.

where x_p is the distance along the beam profile perpendicular to the ray connecting the source and the detector (Figure 6.10).

The output for each detector[2] depends on the attenuation provided by a wire located a distance $d_\perp$ from the beam profile center

$$d_\perp = \frac{Ax_w + By_w + C}{\sqrt{A^2 + B^2}} \tag{6.20}$$

which is the perpendicular distance from a point to a line, where the line $(Ax + By + C = 0)$ connects the source and the detector, and the point (x, y) coincides with the wire centre, i.e., $(x_w = 0, y_w = 0)$. The sign of (6.20) indicates whether the line connecting the source and the detector is located to the right or the left of the wire.

The wire is modeled as a disk object of radius R_p,

$$x^2 + y^2 = R_p^2 \tag{6.21}$$

where the attenuation provided by the wire is related to its transverse thickness $t'(x)$ (Figure 6.10) at a distance x from the wire centre

$$t'(x) = 2\sqrt{R_p^2 - x^2}\,. \tag{6.22}$$

---

[2] The following analysis is based on Rathee's thesis (Rathee, 1992; Rathee et al., 1992).

The detector output is then calculated using

$$V(d_\perp) = \int_{-L/2}^{L/2} w(x_p) e^{-\mu t'(x_p - d_\perp)} dx_p \tag{6.23}$$

where $\pm L/2 = \pm\left(s_{l-sc} + d_{w-sc}\right)/2$ defines the edge of the beam profile. The projection data for a particular detector are given by

$$\begin{aligned} P &= -\ln\left(\frac{V(d_\perp)}{V_o}\right) \\ &= -\ln\left(\frac{\int_{-L/2}^{L/2} w(x_p) e^{-\mu t'(x_p - d_\perp)} dx_p}{\int_{-L/2}^{L/2} w(x_p) dx_p}\right). \end{aligned} \tag{6.24}$$

which is evaluated using

$$P = -\ln\left(\frac{\sum_{i=0}^{N-1} w(x_{p-i}) e^{-\mu t'(x_{p-i} - d_\perp)} \Delta x_p}{\sum_{i=0}^{N-1} w(x_{p-i}) \Delta x_p}\right) \tag{6.25}$$

where $x_{p-i} = i\Delta x_p$ such that $-L/2 \le x_{p-i} \le L/2$. The projection data are filtered, rebinned to a first generation geometry and backprojected to form an image, as described in §6.1.

6.2.2 Wire Size

The PSF is defined as the response of an imaging system to a delta function input (Barrett and Swindell, 1981). To this end, the wire used for PSF simulations should be infinitesimally thin. In practice, however, the wire must be large enough such that it provides a measurable attenuation. For instance, the wire in the phantom specified by AAPM has a diameter of 0.2 mm (Purtill, 2001). The purpose of this section is to determine the width of the wire image as a function of wire diameter. It is anticipated that the FWHM of the wire image will decrease with decreasing wire diameter until some lower limit is reached, after which any further decrease in the wire width will have a negligible impact on the image FWHM.

6.2.2.1 Method

Projection data for all of the PSF images in §6.2 were generated using (6.25) and N = 2000. Using a larger number of data points in the summation had a negligible effect on the width of the PSF. A 51 x 51 pixel image was generated from the projections using a pixel size of Δp = 0.265 mm. The pixel size was chosen to equal $\Delta x_r / 5$, where Δx_r is defined in Figure 6.2b. This was done somewhat arbitrarily, in the belief that smoother PSF images would result. In fact, the PSF width is equal to that found using a pixel size of Δx_r, as expected. The image dimensions of 51x51 pixels were chosen to encompass the entire wire.

For §6.2.2 a total of 768 detector positions and 864 source positions (§2.1) were simulated using an unscaled detector width of d_w = 2.75 mm (Figure 2.5c) and a source length of s_l = 3.6 mm (§5.2.3). The discrete SL filter (f_N = $1/2\,\Delta x_r'$ = 0.38 lp/mm; $\Delta x_r'$=1.326 mm) described by (6.15) was used to filter the rebinned projection data.

6.2.2.2 Results

Shaded surface and greyscale PSF images are shown in Figure 6.11 for wires of radii 0.05, 2.0 and 4.0 mm. The PSFs for the two smaller wires have sharp central maxima because the projection spacing is such that the wire is intersected by only a small number of rays for each projection. It is often adequate to show a line profile of the PSF since the PSFs are very nearly circularly symmetric. Horizontal line profiles obtained from the images of wires of radii 0.05, 0.10, 0.20, 0.50, 1.0, 2.0, 3.0, 4.0 and 5.0 mm are plotted in Figure 6.12. Their increasing width with increasing wire size is evident. The effect of wire diameter is more easily visualized in Figure 6.13 where the FWHM values of the PSFs are plotted as a function of wire diameter. Figures 6.12 and 6.13 demonstrate that the change in PSF width with decreasing wire radius becomes negligible for wire radii $\leq$ 0.5 mm. A wire of radius 0.2 mm was used in all subsequent calculations.

The MTFs corresponding to the PSFs shown in Figure 6.12 are illustrated in Figure 6.14. These were found by taking the absolute value of the Fourier transform of the PSFs. The frequencies corresponding to 50% and 10% of the maximum MTF value are shown in Figure 6.15.

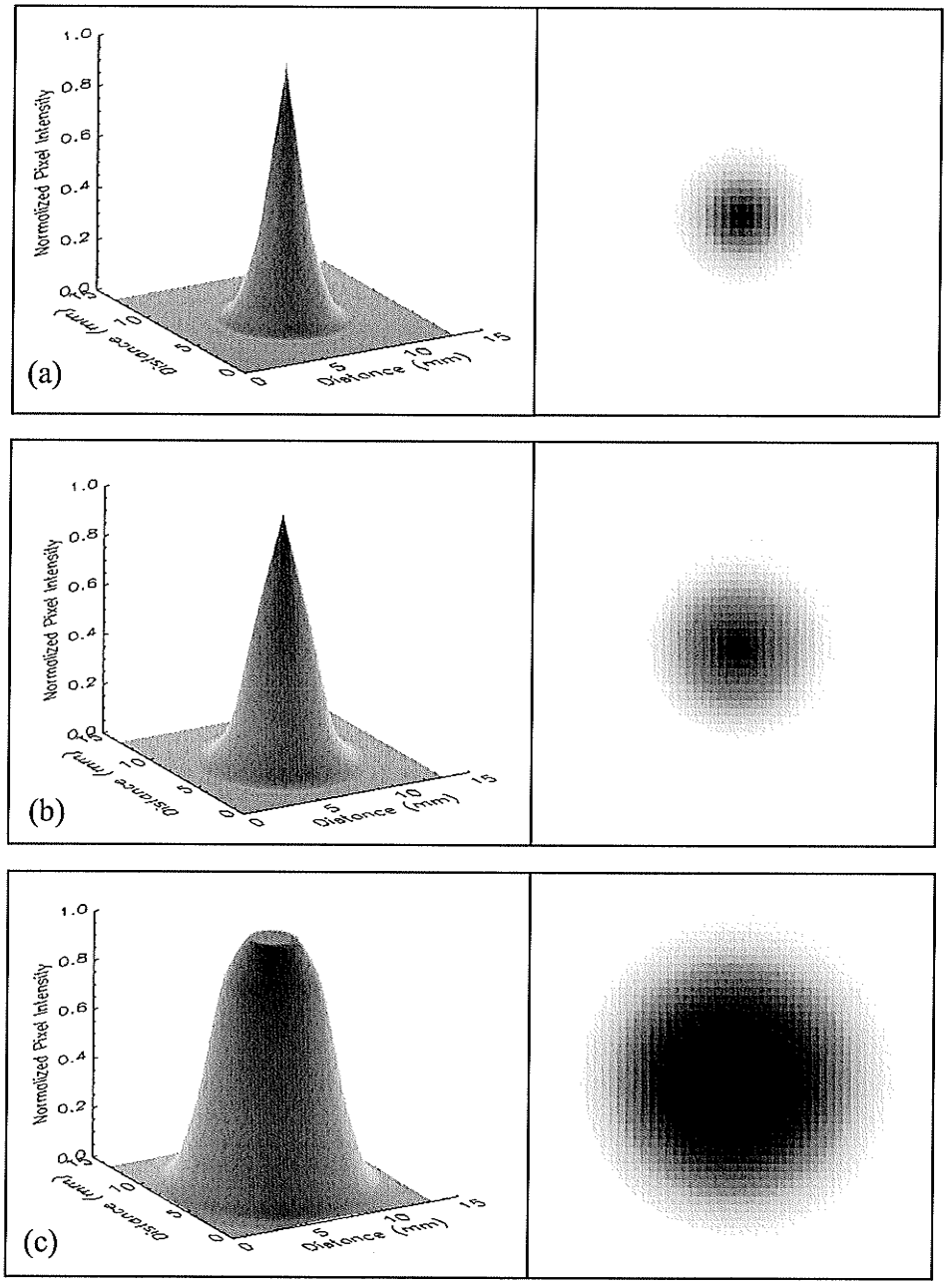

Figure 6.11 Shaded surface (left) and greyscale representations (right) of the PSFs generated using wires of radii (a) 0.05 mm, (b) 2.0 mm and (c) 4.0 mm.

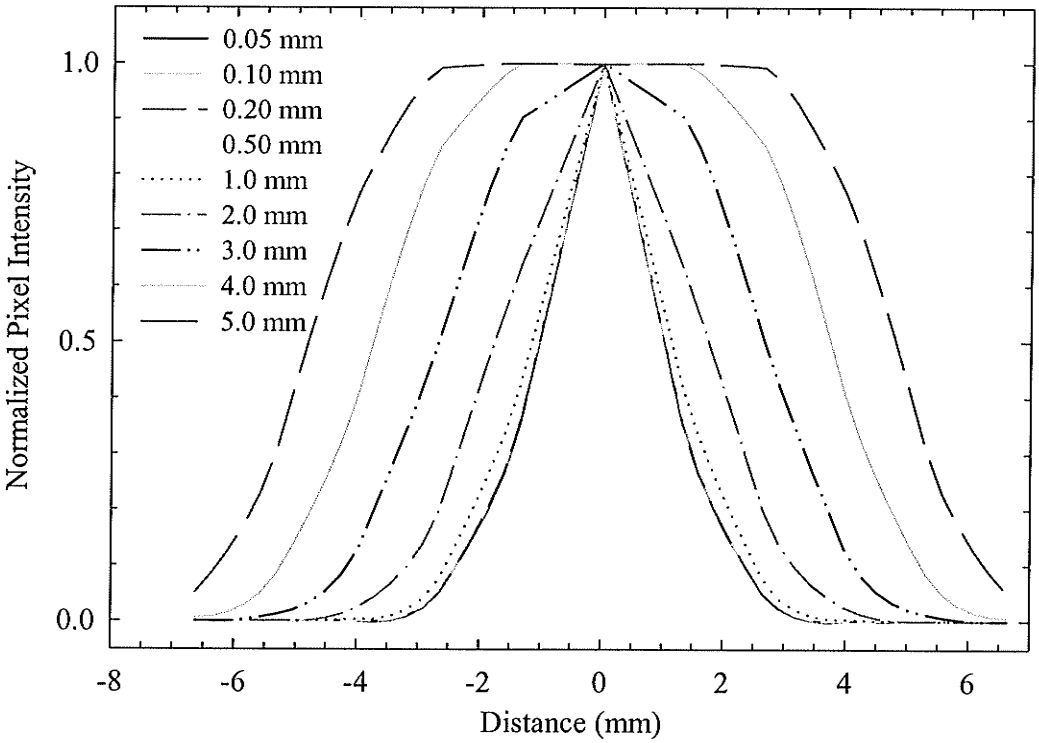

Figure 6.12 Plots of the point spread profiles for the wire radii listed in the legend. Note that the profiles for wires of radius ≤ 0.5 mm are indistinguishable.

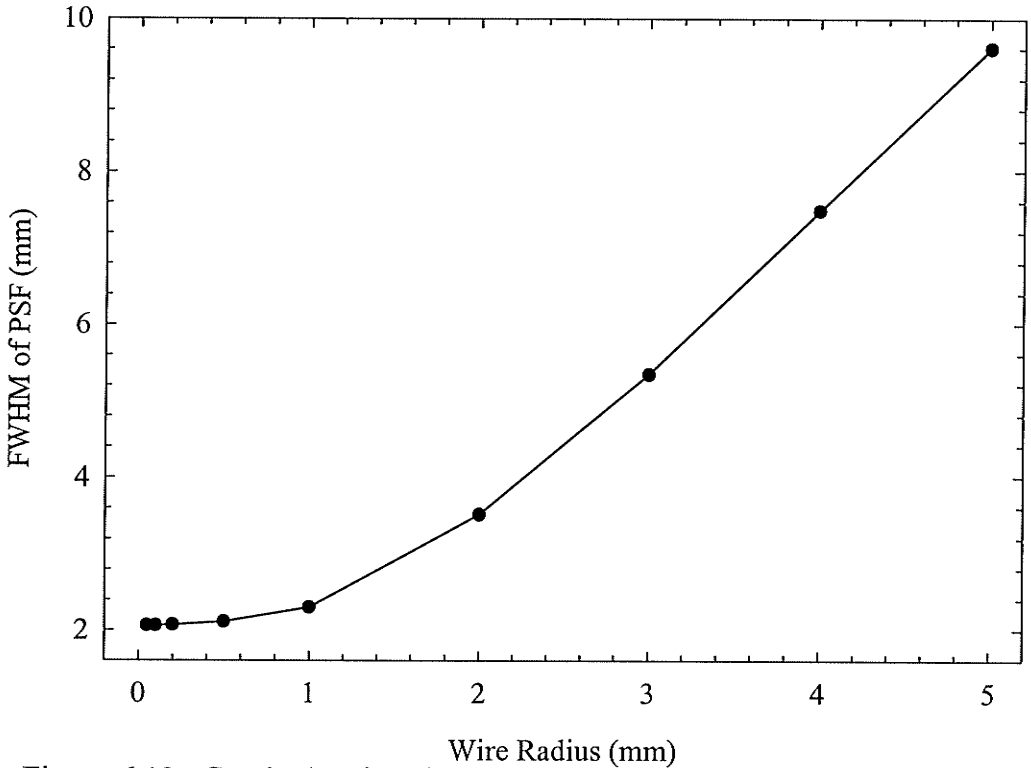

Figure 6.13 Graph showing the FWHM of the PSFs plotted as a function of wire radius.

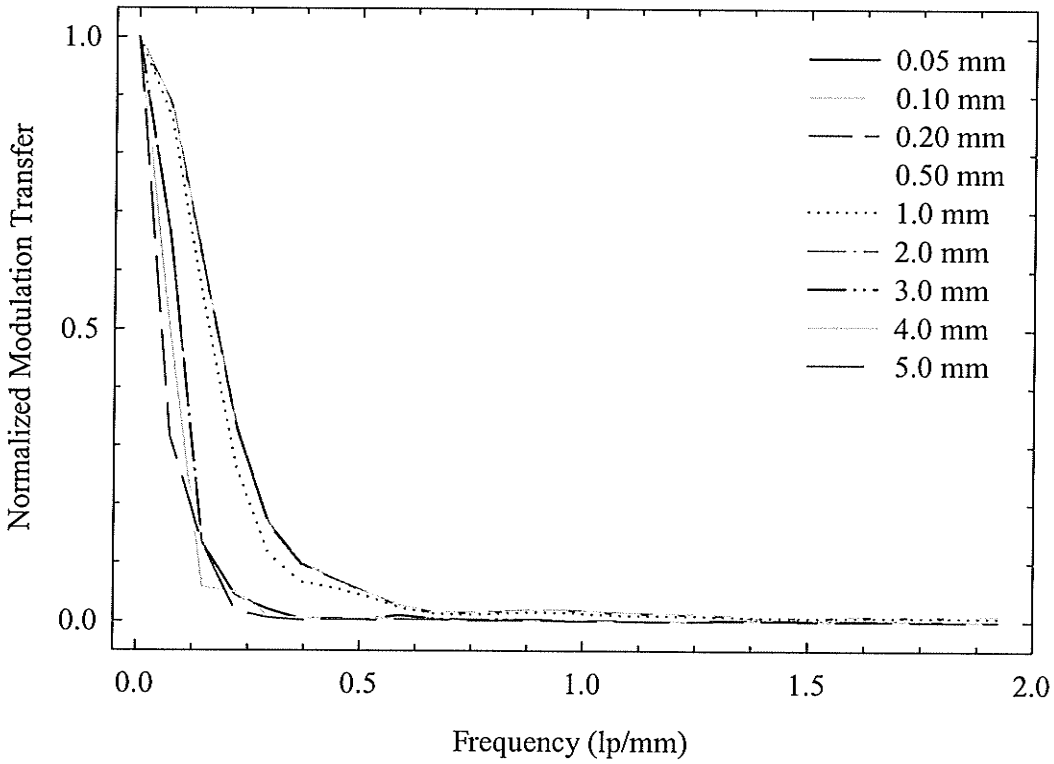

Figure 6.14 Plot of the modulation transfer functions as a function of frequency (line pairs/mm) for the wire radii listed in the legend. Note that the MTFs for wires of radius ≤ 0.50 mm are indistinguishable.

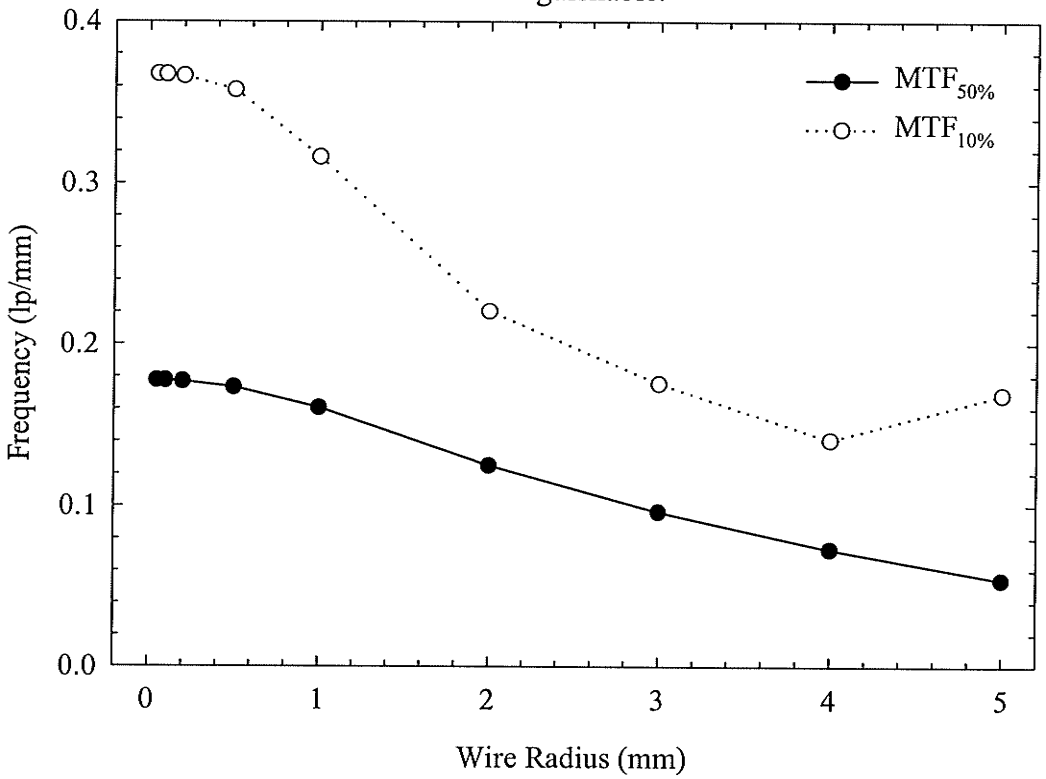

Figure 6.15 Graph showing the 50% and 10% points of the MTFs plotted as a function of wire radius.

6.2.3 Source Size and Spacing

In practice, the HDR BT treatment unit only allows 2.5 mm dwell position spacing, resulting in 864 dwell positions, or 5.0 mm dwell position spacing, resulting in 432 dwell positions. However, in the simulation, any combination of source sizes and dwell positions can be implemented.

6.2.3.1 Method

Projection data were generated using a total of 768 detectors of width d_w = 2.75 mm. The images were reconstructed using a discrete SL filter (f_N = 0.38 lp/mm) as described by (6.15). PSFs were generated using sources 1.0, 1.5, 2.0, 2.5, 3.0, 3.6 and 4.0 mm in length and n_s = 432, 864, and 1728. The FWHM of the PSF was calculated from each image.

Note that the sample spacing $\Delta x_r'$ when rebinning from a fourth generation to a first generation geometry was held constant even though Δx_r (Figure 6.2b) varied as a function of number of source positions n_s. The $\Delta x_r'$ value corresponding to n_s = 864 was used. This was done to eliminate the influence of varying pixel size (recall pixel size $\Delta p = \Delta x_r'/5$ in §6.2) from the analysis. The effect of varying pixel size on the high contrast resolution is a subject for future work.

6.2.3.2 Results

The PSFs obtained using different source lengths and n_s = 864 are plotted in Figure 6.16. The PSF profiles for n_s= 432 and 1728 are similar in appearance. The FWHM of the PSFs are plotted as a function of source size in Figure 6.17. The MTFs corresponding to the PSFs shown in Figure 6.16 are displayed in Figure 6.18. Not shown are the MTFs for n_s= 432 and 1728, which display similar trends to the n_s = 864 MTFs. Figure 6.19 plots the 50% and 10% MTF points as a function of source size for n_s = 432, 864 and 1728. As can be seen, the PSF broadens with increasing source size and decreasing number of source positions. Note that the decrease in FWHM with increasing number of source positions is an artifact of aliasing in the projection data, i.e., the n_s = 432 and 864 images are aliased. Increasing the number of source positions should have a small effect on the PSF after the radial sampling is adequate. The trend displayed in Figure 6.17 suggests

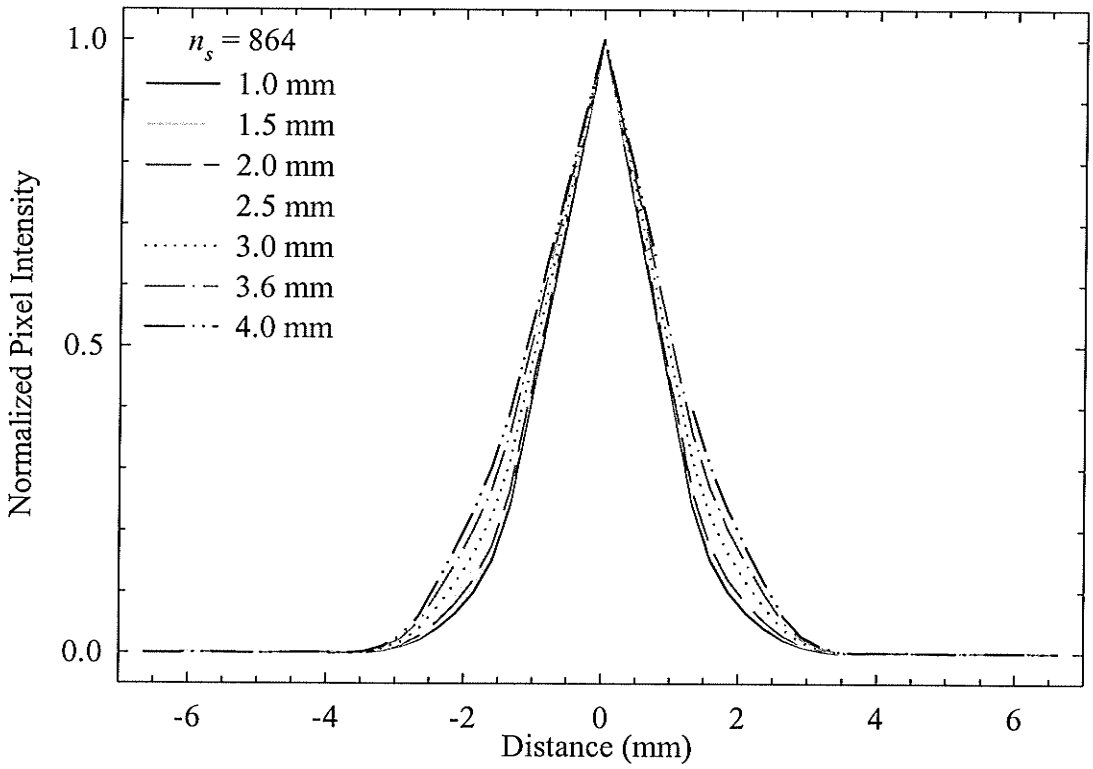

Figure 6.16 Point spread profiles for n_s = 864 and the source lengths listed in the legend.

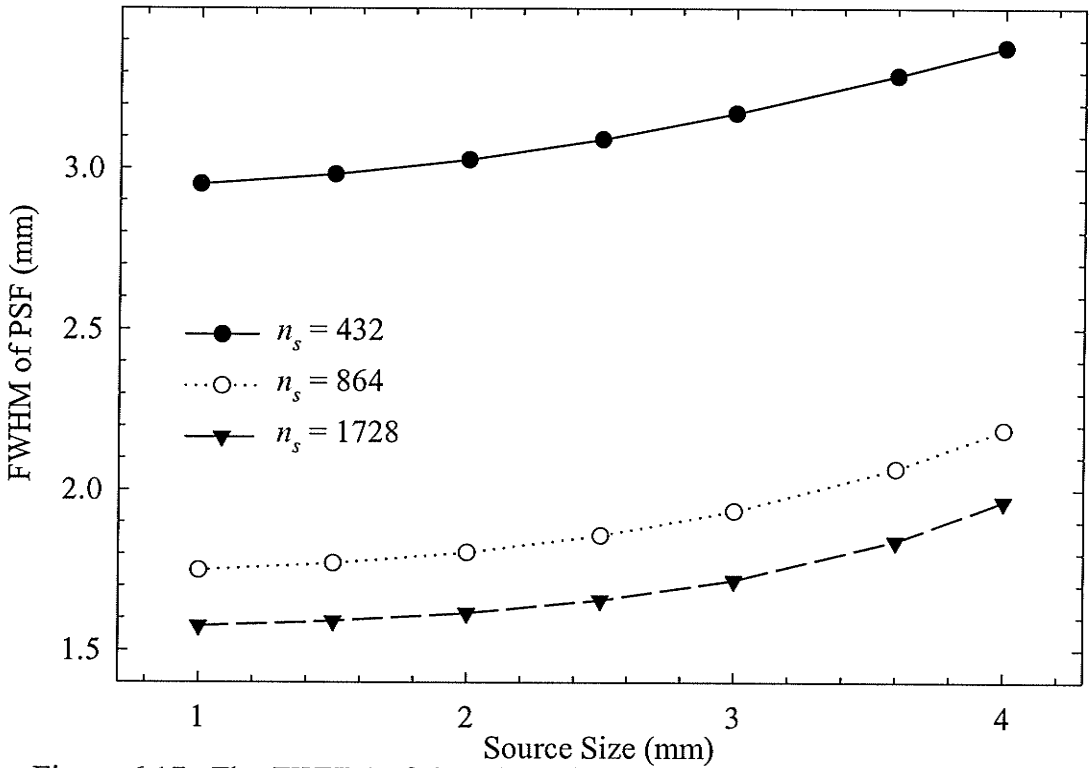

Figure 6.17 The FWHM of the PSFs plotted as a function of source size for number of source positions n_s = 432, 864 and 1728.

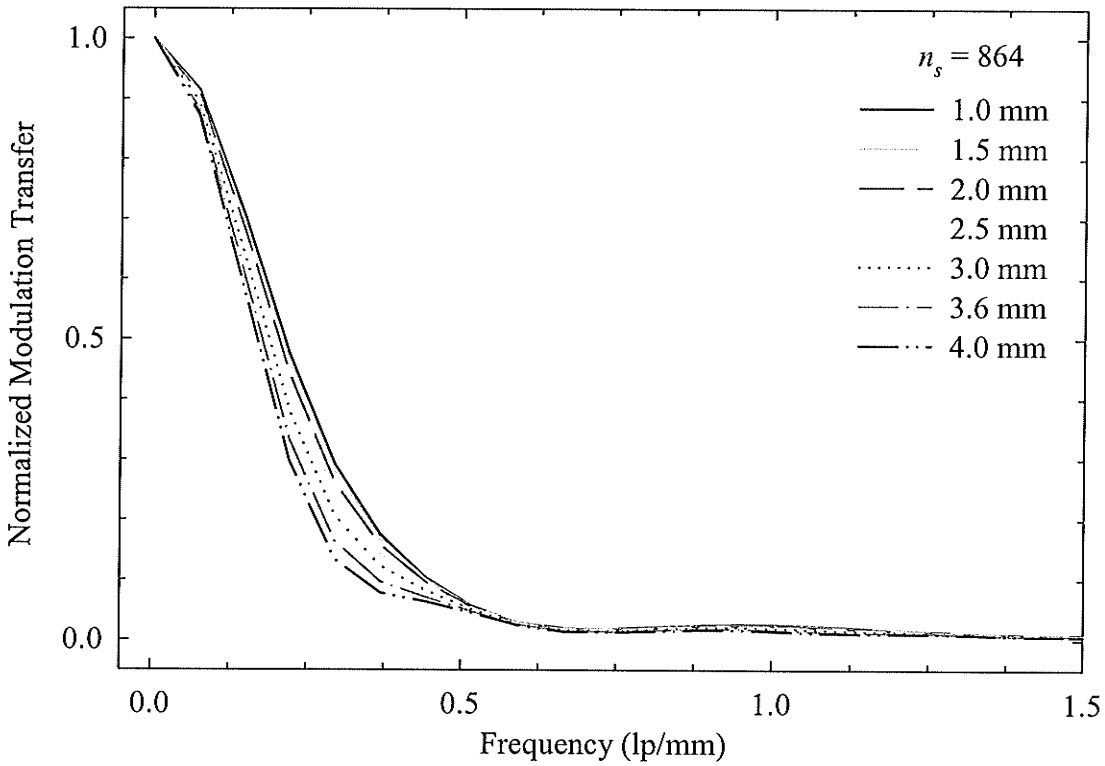

Figure 6.18 Plot of the modulation transfer functions for n_s = 864 and the source lengths listed in the legend.

that the decrease in FWHM with increasing number of source positions becomes less pronounced with a large number of source positions, i.e., the cost-benefit ratio increases with a large number of source positions. Also, a smaller source length becomes more important if the number of source positions is increased.

6.2.4 Detector Size and Spacing

Unlike the source size and spacing, which can be varied independently, the detector size and spacing are linked. Although it is possible to have gaps between the detectors, this would result in wasted photons. It is not possible to have overlapping detectors. Therefore, the number of detectors n_d and detector width d_w are related by $n_d \cdot d_w = 2\pi R_d$, where R_d is the radius of the detector ring, as established in Chapter 5.

6.2.4.1 Method

The width of the PSF was examined as a function of number of detectors and detector size. The images were reconstructed using a discrete SL filter as described by (6.15). PSFs were generated using detectors four active elements (Figure 2.5c) wide (d_w = 5.9

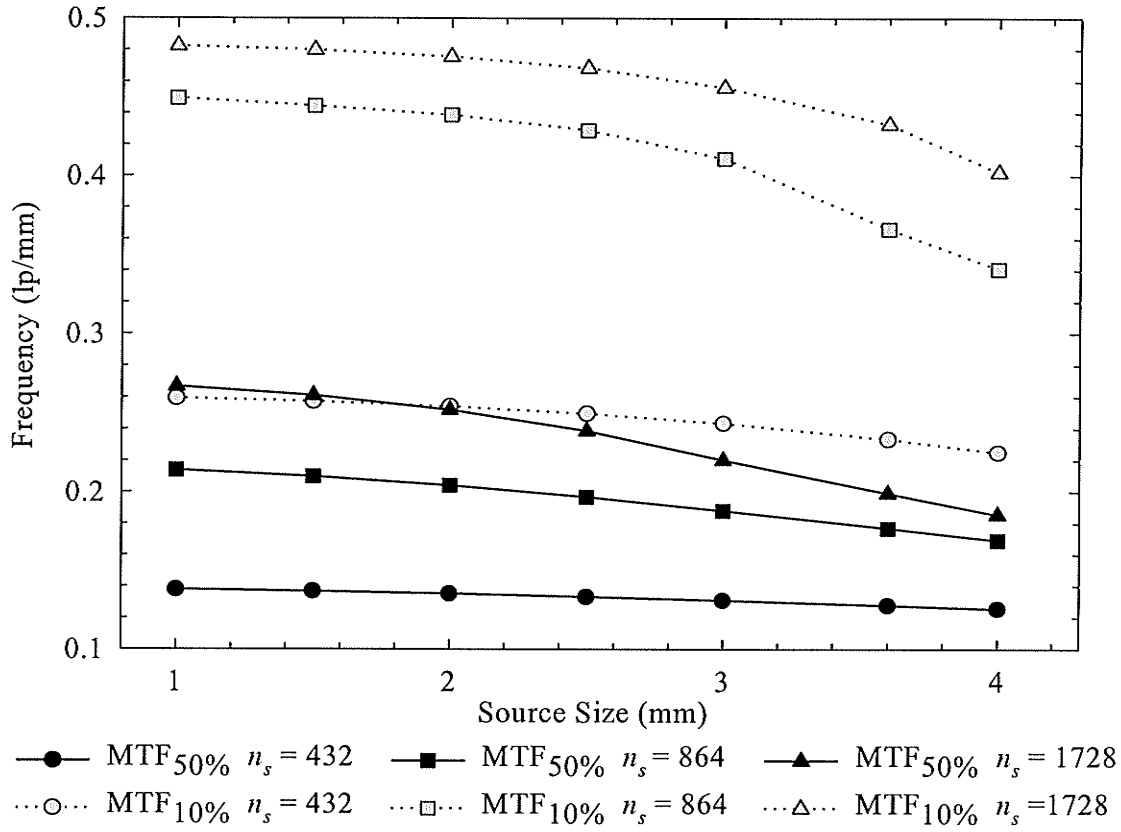

Figure 6.19 Graph showing the 50% and 10% points of the MTFs plotted as a function of source length for number of source positions n_s = 432, 864 and 1728.

mm, n_d = 384), two active elements wide (d_w = 2.75 mm, n_d = 768), and one active element wide (d_w = 1.175 mm, n_d = 1536). Because the ^{192}Ir source length is much greater than the detector width for n_d = 1536, arbitrary source lengths of s_l = 1.8 mm and 1.0 mm were also examined.

6.2.4.2 Results

The PSF profiles obtained by varying the detector size, number of detectors and source length are shown in Figure 6.20. As can be seen, the PSF becomes narrower when increasing the number of detectors from 384 to 768. Increasing the number of detectors to 1536 offers little improvement because the source size of 3.6 mm dominates the FWHM of the beam profile. More specifically, the FWHM of the beam profile at the scanner center is equal to the larger of the scaled source length $s_{l\text{-}sc}$ or detector width $d_{w\text{-}sc}$. However, if the source length is decreased, the width of the PSF decreases with further reduction in detector width. The corresponding MTFs are shown in Figure 6.21.

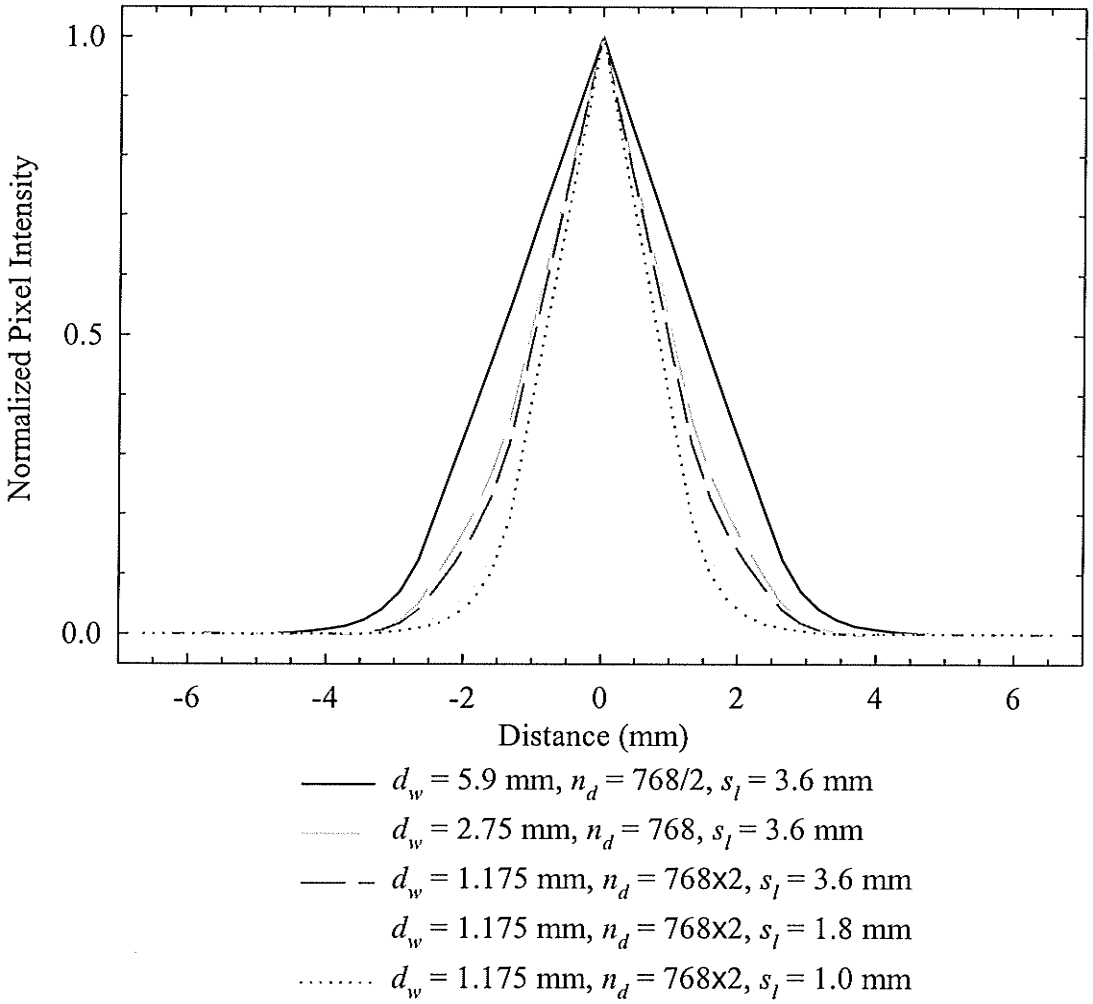

Figure 6.20 Point spread profiles for various source lengths, detector widths and number of detectors. n_s = 864 for all of the plots.

6.2.5 Filter Function

Both the SL and RL filters described above were examined by substituting various values of f_N into (6.12) and (6.13). A smaller f_N value allows a smaller fraction of high frequency information to be reconstructed, resulting in a broader PSF, while a larger value of f_N will sharpen the image. As described above, the SL filter attenuates the high frequency components more effectively than the RL filter. It is therefore expected that the PSF generated using a RL filter will be narrower than that generated using a SL filter.

6.2.5.1 Method

Projection data were generated using 768 detectors and 864 source positions. The unscaled detector width and source length were 2.75 mm and 3.6 mm respectively. A

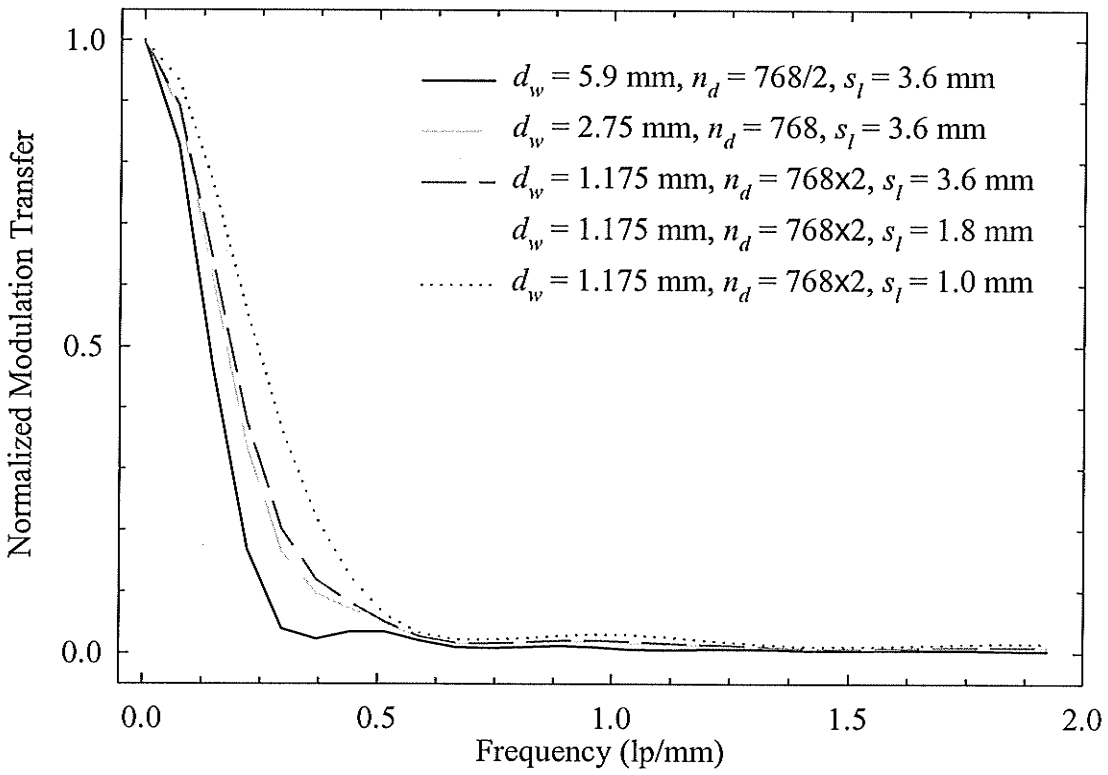

Figure 6.21 Graph of the modulation transfer functions for various source lengths, detector widths and number of detectors. n_s = 864 for all of the plots.

number of different f_N values were investigated for both the SL and RL filters. The value f_N = 0.38 lp/mm corresponds to the Nyquist frequency f_N for the sampling frequency used, i.e., $f_N = 1/2\Delta x = 1/2(1.326\,\text{mm}) = 0.38\,\text{lp/mm}$.

6.2.5.2 Results

The PSFs generated using a SL filter are shown in Figure 6.22. The PSFs generated using a RL filter (not shown) are similar in appearance. The FWHM values of the PSFs generated using both a SL and RL filter are plotted in Figure 6.23 as a function of f_N. As can be seen, the FWHM of the PSFs generated using a SL filter are broader than those generated using a RL filter. In addition, the FWHM increase with decreasing f_N as predicted above. The MTFs corresponding to Figure 6.22 are shown in Figure 6.24. The MTFs found using a RL filter (not shown) are similar to those generated using a SL filter. The frequencies corresponding to 50% and 10% of the maximum MTF values are plotted in Figure 6.25.

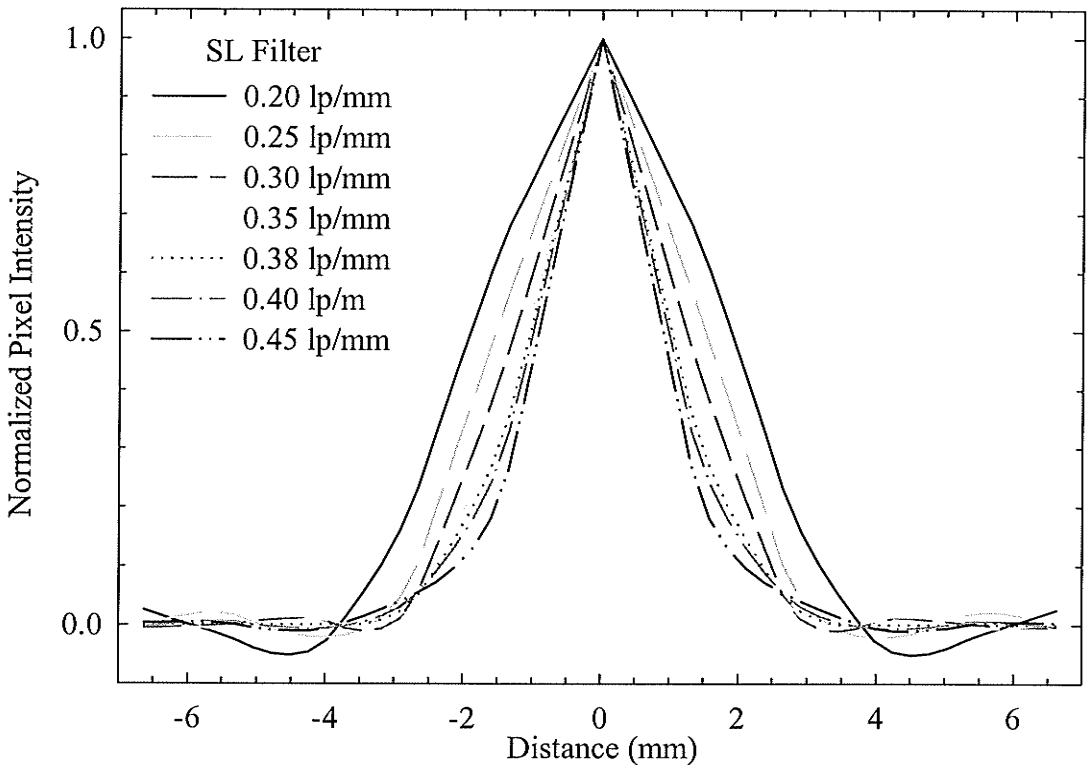

Figure 6.22 Plot of the point spread profiles for the SL filter and the f_N values listed in the legend.

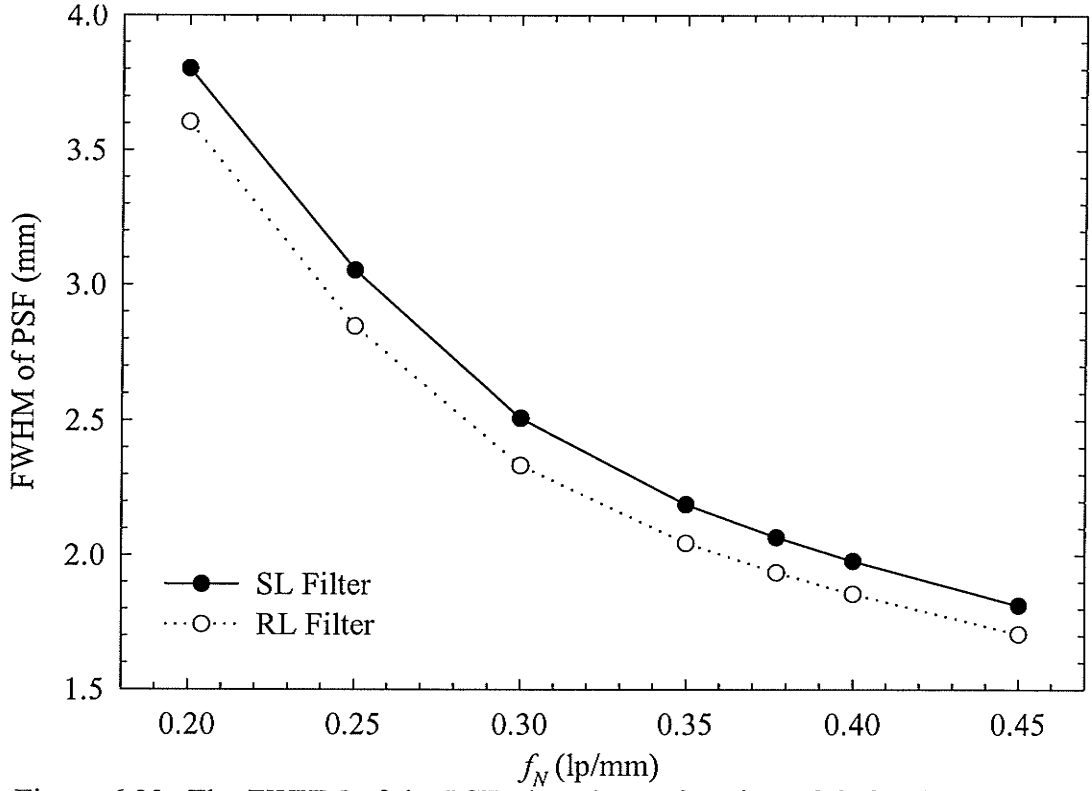

Figure 6.23 The FWHM of the PSF plotted as a function of f_N for the SL and the RL filters.

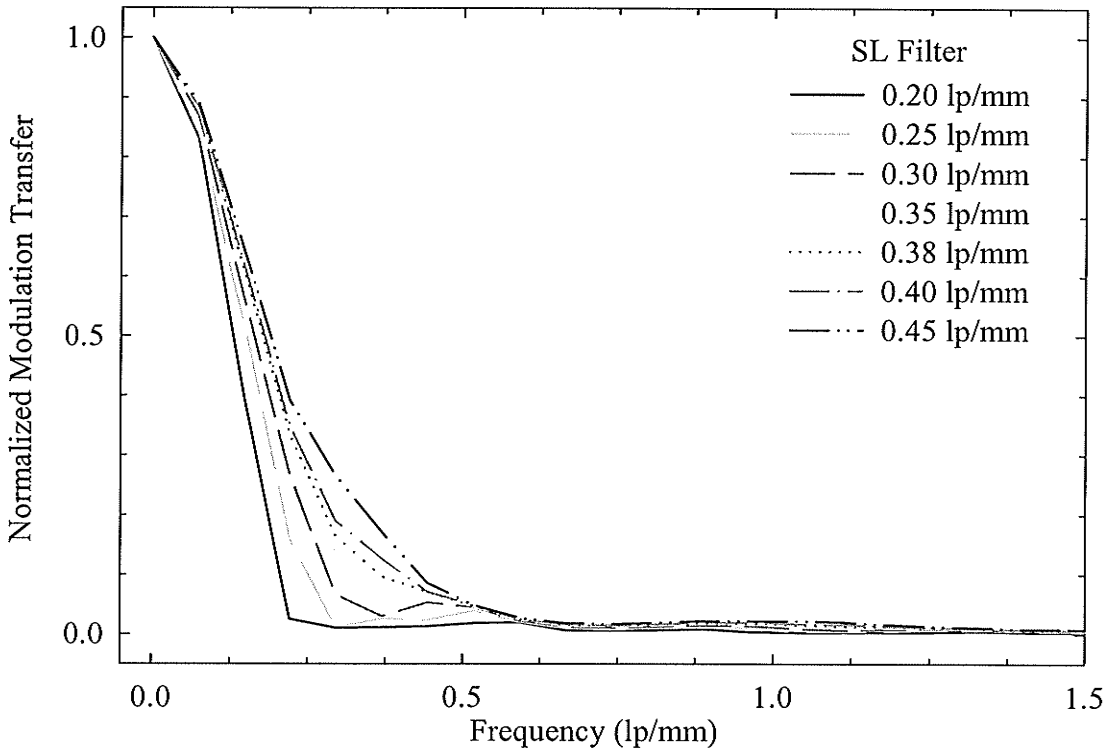

Figure 6.24 Plot of the modulation transfer functions for the SL filter and the f_N values listed in the legend.

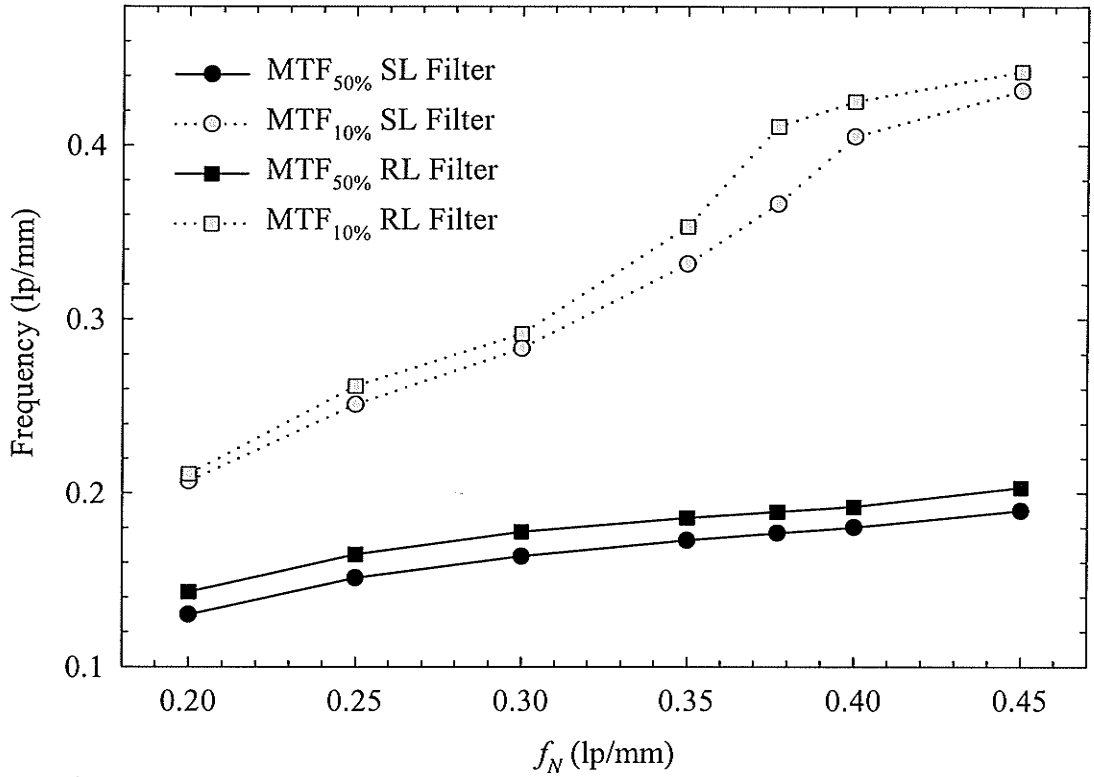

Figure 6.25 Graph showing the 50% and 10% points of the MTFs plotted as a function of f_N for the SL and RL filters.

6.3 Noise

A CT image of an object of uniform composition will contain a distribution of CT numbers due to effects such as beam hardening, artifacts and quantum mottle (Zatz, 1981; Hanson, 1981). Quantum mottle or noise due to the random number of detected photons is of particular interest here. Image noise in CT is affected by the factors that determine the number of photons detected per ray-sum including source strength, source-to-detector distance (diameters of the source and detector rings), sampling interval (scan time), slice thickness (collimator design), detector efficiency and detector size. Image noise in CT is also affected by the shape and cut-off frequency of the convolution filter in the filtered backprojection method of image reconstruction. An analysis of image noise is important, as image noise directly affects the low contrast resolution of a CT scanner (Hanson, 1981), which is the ability to distinguish between regions with small differences in attenuation coefficient (Zatz, 1981).

This section consists of three components. First, three different approaches are presented for incorporating noise into the simulated images. Next, the standard deviation (SD) in the central region of simulated Plexiglas phantom images is determined as a function of source strength, number of projections, sample spacing, filter function and interpolation method. Finally, noise power spectra (NPS) of CT image noise are generated using different filter functions and interpolation methods. (The effect of different numbers of source and detector positions on the NPS will be considered in the future.) Noise analysis was performed using first generation as well as fourth generation scanner geometries because theoretical expressions exist describing the SD and NPS for the first generation geometry. Agreement between the first generation results and the theoretical expressions provides validation of the analysis methods being used.

6.3.1 Generation of Noise Images

Images incorporating quantum mottle were generated by modeling both a first generation and a fourth generation scanner, and employing three approaches to incorporate noise into the projection data. The first approach uses a Gaussian random number generator to add noise to the first generation projection data in the absence of an object. This approach

was implemented solely to validate the computer simulation used in this thesis, more specifically, for comparison with the results produced by Kijewski and Judy (1987), who also used this approach to generate noisy images. The second approach simulates images of a Plexiglas disk object using both first generation and fourth generation scanner geometries. Noise was incorporated in the projection data based on the number of photons transmitted through the Plexiglas disk and assuming Poisson counting statistics. For the final approach, noise was added to the projection data by scaling the noise in experimental data (§3.3), which includes both quantum and electronic noise.

6.3.1.1 First Generation Scanner

Image noise was examined for a first generation scanner before performing any noise analysis on the fourth generation scanner because theoretical expressions exist describing the SD and NPS for the first generation geometry. Agreement between the first generation results and the theoretical expressions provides validation of the analysis methods being used.

The first generation scanner used to generate the noise images is a simplification of the fourth generation scanner described in §6.1. As was the case for the fourth generation scanner, the source and detector positions are known. Their locations with respect to the scanner isocentre can be described in the rotated coordinate system (y-axis parallel to the ray connecting the source and the detector) by

$$x_s(l) = l\Delta x \qquad y_s(l) = R_s \qquad l = 0, 1, 2, \ldots, L \tag{6.26}$$

$$x_d(l) = l\Delta x \qquad y_d(l) = R_d \qquad l = 0, 1, 2, \ldots, L \tag{6.27}$$

where R_s is the distance from the source to the scanner centre, R_d is the distance from the detector to the scanner centre, L is the number of source and detector positions and Δx is the distance the source-detector assembly steps between measurements, i.e., the sample spacing. The projections are denoted by j = 0, 1, 2, . . ., J with angular spacing $\Delta\phi = \pi / J$. Note however that no angular dependence has been incorporated into the above expressions as the object being scanned is circularly symmetrical, and the projections therefore have no angular dependence.

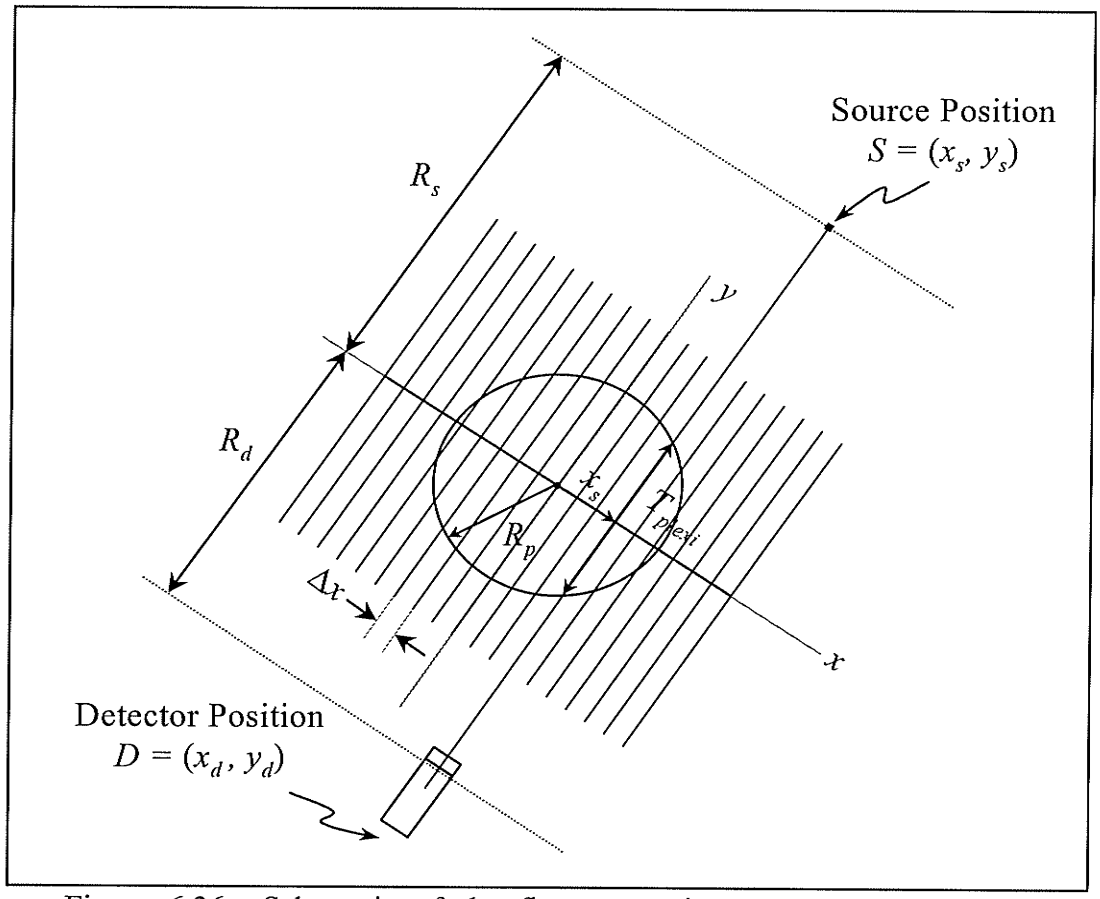

Figure 6.26 Schematic of the first generation scanner showing the geometry used to determine the detector output.

The thickness of Plexiglas T_{plexi} traversed by a particular ray (Figure 6.26) is calculated as follows

$$T_{plexi} = 2\sqrt{R_p^2 - x_s^2} \,. \tag{6.28}$$

where R_p is the radius of the Plexiglas disc object. This thickness is used to determine the detector output for calculating the projection data. A total of J projections were generated for each image. The projections were filtered using Ram-Lak and Shepp-Logan filters as described in §6.1.3 and backprojected onto a Cartesian grid to generate an image.

6.3.1.2 Noise-Only Images

The first set of images incorporating noise are generated using a technique described by Kijewski and Judy (1987), where the object information is subtracted leaving only a noise image. These are referred to as noise-only (NO) images in the subsequent discussion. The

projection data are simply Gaussian random numbers, the justification for which is provided by Riederer et al. (1978) and summarized below.

Projection data including the effect of noise are given by

$$P = -\ln\left(\frac{\overline{N} + n}{\overline{N}_o}\right) \tag{6.29}$$

where $\overline{N}_o$ is the mean number of photons incident on an object, $(\overline{N} + n)$ is the number of transmitted photons with mean $\overline{N}$, and n is a zero-mean random number from a Poisson distribution with a standard deviation $\sigma_{\overline{N}}$ given by

$$\sigma_{\overline{N}} = \sqrt{\overline{N}}\,. \tag{6.30}$$

As the number of incident photons is about one magnitude larger than the number of transmitted photons, the random fluctuations in $\overline{N}_o$ are ignored for the sake of simplicity. In the limit of a large number of photons, Gaussian, rather than Poisson counting statistics can be used. In this case

$$n = R_G\sqrt{\overline{N}} \tag{6.31}$$

where R_G is a zero mean Gaussian random number with unit variance (Riederer et al., 1978). Equation (6.29) can then be rewritten as

$$\begin{aligned} P &= -\ln\left(\frac{\overline{N} + R_G\sqrt{\overline{N}}}{\overline{N}_o}\right) \\ &= -\ln\frac{\overline{N}}{\overline{N}_o}\left(1 + \frac{R_G}{\sqrt{\overline{N}}}\right) \\ &= -\ln\frac{\overline{N}}{\overline{N}_o} - \ln\left(1 + \frac{R_G}{\sqrt{\overline{N}}}\right). \end{aligned} \tag{6.32}$$

For noise calculations, only the noise is of interest. Subtracting the average signal (Riederer et al., 1978), namely,

$$\overline{P} = -\ln\left(\frac{\overline{N}}{\overline{N}_o}\right) \tag{6.33}$$

from (6.32) yields

$$\begin{aligned} P_\Delta &= -\ln(1 + R_G/\sqrt{\overline{N}}) \\ &\approx R_G/\sqrt{\overline{N}} \end{aligned}\,. \tag{6.34}$$

where the last approximation is valid as $R_G << \sqrt{\overline{N}}$. Providing $\sqrt{\overline{N}}$ remains relatively constant over the projection, which can be achieved by using a beam shaping wedge

(Riederer et al., 1978), the $\sqrt{\overline{N}}$ in the bottom line of (6.34) acts as a scaling factor to determine the magnitude of the noise. The approach for incorporating noise into the projection data described here is used only for generating simulated NPS for comparison with the theoretical first generation NPS expression (Kijewski and Judy, 1986), and is not used to assess the noise magnitude. To this end, the $\sqrt{\overline{N}}$ is ignored, as was done by Kijewski and Judy.

Gaussian random numbers R_G were produced by summing K uniformly distributed random numbers R_U (James, 1980) produced using a uniform random number generator (IDL 5.3.1, Research Systems, Inc.) according to

$$R_G = \sum_{i=1}^{K} R_U(i) - K/2 \tag{6.35}$$

where the subtraction of $K/2$ is necessary to ensure a zero mean. A value of $K = 12$ was used (James, 1980).

6.3.1.3 Exponential Attenuation with Poisson Noise (Theoretically-Based Noise)

The second approach for incorporating noise into the simulated images modeled a disk object with theoretically based Poisson noise added to the associated projection data. These images are referred to as theoretical noise (TN) images in the subsequent discussion. The number of photons incident on each detector is calculated assuming monoenergetic photons of energy 355 keV to yield (§3.6)

$$\dot{E}_{incident} = \left(\frac{\Gamma_{^{192}\mathrm{Ir}} A A_c}{d^2} \right) \Bigg/ \left(\frac{\mu_{en}}{\rho} \right)_{355\,\mathrm{keV},air} \left(\frac{e}{\overline{W}} \right)_{air} \frac{\mathrm{J}}{\mathrm{s}} \tag{6.36}$$

where $\dot{E}_{incident}$ is the power incident on the detector, $\Gamma_{^{192}\mathrm{Ir}} = 3.36 \times 10^{-11}\ \mathrm{Gy \cdot m^2/(mCi \cdot s)}$ is the exposure rate constant of ^{192}Ir, $A = 2.2 \times 10^{-5}\ \mathrm{m^2}$ is the detector area, A_c is the source strength in mCi, d is the source to detector distance in m, $(\mu_{en}/\rho)_{355\ \mathrm{keV},air} = 0.002914\ \mathrm{m^2/kg}$ is the mass attenuation coefficient of air at 355 keV and $(e/\overline{W})_{air} = 1/33.97$ C/J. The number of photons $\overline{N}_o$ incident on a detector then can be found using

$$\overline{N}_o = \frac{\dot{E}_{incident}}{E/photon} \Delta T \tag{6.37}$$

where $E/photon = 355\ \mathrm{keV} = 5.68 \times 10^{-14}$ J and $\Delta T = 0.097952$ s is the integration time for data collection using a 10 Hz sampling frequency. Evaluating (6.37) yields

$$\overline{N}_o = 14.9\, A_c / d^2 \tag{6.38}$$

photons incident on each detector in the absence of an attenuator. The mean number of photons transmitted through the Plexiglas object is calculated using

$$\overline{N} = \overline{N}_o e^{-\mu_{plexi} T_{plexi}} \tag{6.39}$$

where $\mu_{plexi} = 0.129$ cm^{-1} is the linear attenuation coefficient of Plexiglas at 355 keV and T_{plexi} is the thickness of Plexiglas traversed, calculated using (6.28) or (6.1), depending upon whether a first or fourth generation geometry is used. Noise is incorporated by adding n as given by (6.31) to $\overline{N}$ and the projection data are then calculated using (6.29).

6.3.1.4 Experimental Detector Output and Noise (Experimentally-Based Noise)

The third approach for incorporating noise into the simulated images modeled a disk object with experimentally measured quantum and electronic noise added to the projection data. The goal is to use existing experimental data to calculate the mean detector output and SD for arbitrary source strength A_c, source-to-detector distance d, and Plexiglas thickness T_{plexi}. Images generated using this approach are referred to as experimental noise (EN) images.

Measurements of the detector output and its associated SD as a function of Plexiglas thickness using collimation similar to that proposed for the final scanner are described in §3.6.2.1 and §3.3.1.1, respectively. A source strength of $A_{c\text{-}meas} = 5.3$ Ci and a source-to-detector distance of $d_{meas} = 0.825$ m were used to collect these data. The experimentally measured detector output voltage V_{meas} described in §3.6.3.1 can be modeled as a function of source strength $A_{c\text{-}meas}$, source-to-detector distance d_{meas} and Plexiglas thickness T_{plexi} using

$$V_{meas}(A_{c-meas}, d_{meas}, T_{plexi}) = v \cdot f(T_{plexi}) \cdot \frac{A_{c-meas}}{d_{meas}^2} \tag{6.40}$$

where $f(T_{plexi})$ is a function accounting for the attenuation and scattering in Plexiglas and v is a proportionality constant, incorporating factors such as $\Gamma_{^{192}Ir}$, the luminous efficiency of $CdWO_4$ and the photosensitivity of the photodiode. It follows that the detector output for an arbitrary source strength A_c and source-to-detector distance d can be calculated using

$$V(A_c, d, T_{plexi}) = v \cdot f(T_{plexi}) \cdot \frac{A_c}{d^2}. \tag{6.41}$$

When combined with (6.40), (6.41) becomes

$$V(A_c, d, T_{plexi}) = V_{meas}(A_{c-meas}, d_{meas}, T_{plexi}) \cdot \frac{d_{meas}^2}{A_{c-meas}} \frac{A_c}{d^2}. \tag{6.42}$$

If the ray from the source to the detector does not intersect the object, (6.42) becomes

$$V(A_c, d, 0) = V_{meas}(5.3\,\text{Ci}, 0.825\,\text{m}, 0) \cdot \frac{(0.825\,\text{m})^2}{5.3\,\text{Ci}} \frac{A_c}{d^2}. \tag{6.43a}$$

where V_{meas}(5.3 Ci, 0.825 m, 0) is the experimentally measured detector output for T_{plexi} = 0 m. If the ray from the source to the detector intersects the Plexiglas disk phantom, the detector output at arbitrary Plexiglas thickness T_{plexi} is found by interpolating the data in Figure 3.39 to find V_{meas}(5.3 Ci, 0.825 m, T_{plexi}), and then scaling this value according to

$$V(A_c, d, T_{plexi}) = V_{meas}(5.3\,\text{Ci}, 0.825\,\text{m}, T_{plexi}) \cdot \frac{(0.825\,\text{m})^2}{5.3\,\text{Ci}} \frac{A_c}{d^2}. \tag{6.43b}$$

The next step is to determine the SD in the detector output as a function of source strength, source-to-detector distance and Plexiglas thickness. The measured SD in the detector output $\sigma_{meas}(A_{c-meas}, d_{meas}, T_{plexi})$ as described in §3.3.1.1, is given by

$$\sigma_{meas}(A_{c-meas}, d_{meas}, T_{plexi}) = \sqrt{\frac{\sum_{i=1}^{N}\left[V_{i-meas}(A_{c-meas}, d_{meas}, T_{plexi}) - \overline{V}_{meas}(A_{c-meas}, d_{meas}, T_{plexi})\right]^2}{N-1}} \tag{6.44}$$

where $\overline{V}_{meas}(A_{c-meas}, d_{meas}, T_{plexi})$ is the mean measured voltage from 250 measurements of $V_{i-meas}(A_{c-meas}, d_{meas}, T_{plexi})$. The SD in the measured detector output $\sigma_{meas}(A_{c-meas}, d_{meas}, T_{plexi})$ is a consequence of quantum noise $\sigma_{q-meas}(A_{c-meas}, d_{meas}, T_{plexi})$ and electronic noise $\sigma_{electronic}$, where the latter is independent of source strength, source-to-detector distance and Plexiglas thickness. The SD in the measured detector output can therefore be written as

$$\sigma_{meas}(A_{c-meas}, d_{meas}, T_{plexi}) = \sqrt{\sigma_{q-meas}^2(A_{c-meas}, d_{meas}, T_{plexi}) + \sigma_{electonic}^2}. \tag{6.45}$$

where $\sigma_{electronic} \approx 115\,\mu\text{V}$ from §3.2. Modeling the quantum noise as

$$\sigma_{q-meas}^2(A_{c-meas}, d_{meas}, T_{plexi}) = k(T_{plexi}) \frac{A_{c-meas}}{d_{meas}^2}, \tag{6.46}$$

the thickness dependent factor $k(T_{plexi})$ can be found from the experimental data using

$$k(T_{plexi}) = \frac{(0.825\,\text{cm})^2}{5.3\,\text{Ci}}\left[\sigma_{meas}^2(5.3\,\text{Ci}, 0.825\,\text{m}, T_{plexi}) - \sigma_{electronic}^2\right]. \tag{6.47}$$

The value of $k(T_{plexi})$ at arbitrary Plexiglas thicknesses is found by interpolating between the $k(T_{plexi})$ values found from the experimental measurements. The quantum noise in the detector output for an arbitrary Plexiglas thickness, source-to-detector distance d and source strength A_c can then be found using

$$\sigma_q^2(A_c, d, T_{plexi}) = k(T_{plexi})\frac{A_c}{d^2} \tag{6.48}$$

to yield a total noise $\sigma(A_c, d, T_{plexi})$ of

$$\sigma(A_c, d, T_{plexi}) = \sqrt{k(T_{plexi})\frac{A_c}{d^2} + \sigma_{electronic}^2}\ . \tag{6.49}$$

Noise is incorporated into the simulation by multiplying the SD found using (6.49) by a random number R_G as given by (6.35). This value is then added to $V(A_c, d, T_{plexi})$ calculated using (6.43a) or (6.43b) and the projection data determined using

$$P = -\ln\left(\frac{V(A_c, d, T_{plexi}) + \sigma(A_c, d, T_{plexi}) \cdot R_G}{V(A_c, d, 0)}\right). \tag{6.50}$$

6.3.1.5 First and Fourth Generation Images

Simulated images were required for the SD and NPS analysis carried out in §6.3.2 and §6.3.3. Figure 6.27 shows a sample first generation image for each of the three approaches used to incorporate noise into the images. No object is visible in the noise-only image (§6.3.1.2), because the detector signal has been subtracted, leaving only noise. The computer generated theoretical noise image (§6.3.1.3) of a disk object appears smooth with no artifacts. The rings appearing in the Plexiglas phantom of the experimental noise image (§6.3.1.4) are present because the data in Figure 3.39 (plot of the detector output as a function of Plexiglas thickness for "scanner collimation" conditions) are not completely smooth. The mottle appearing in Figure 6.27b is considerably less than that appearing in Figure 6.27c because the theoretical noise analysis assumes a larger number of photons incident on the detectors than the experimental noise analysis. This is due to the approximations associated with (6.36), as outlined in §3.6.1. Sample theoretical noise and experimental noise images generated using a fourth generation scanner geometry are shown in Figure 6.28. Note that their

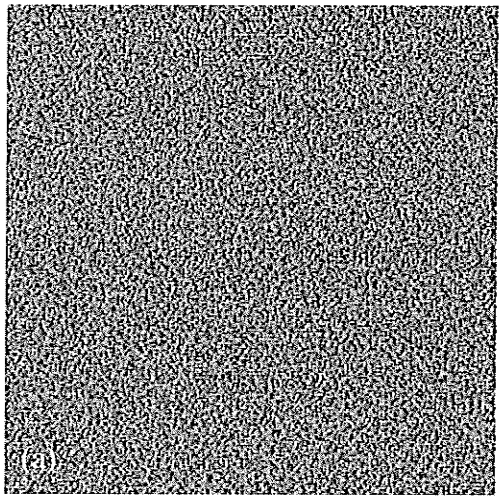

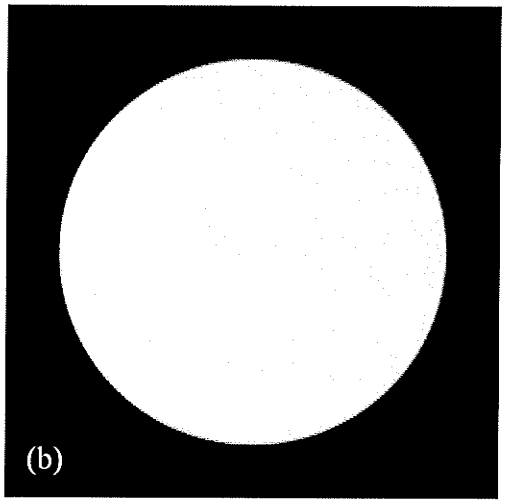

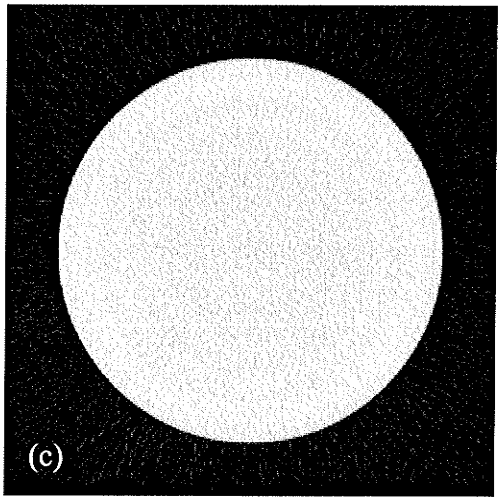

Figure 6.27 First generation scanner images of (a) noise only, a 10.0 cm radius Plexiglas phantom incorporating (b) theoretical noise, and (c) experimentally measured noise. All images were generated using A_c = 7.5 Ci, a Shepp-Logan filter, linear interpolation, J = 350, Δx = 0.1 cm and pixel size Δp = 0.1 cm.

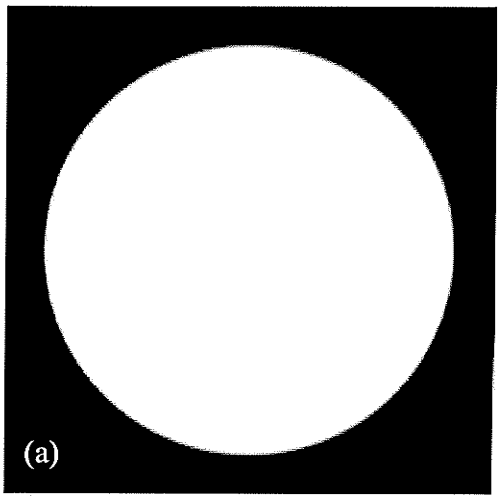

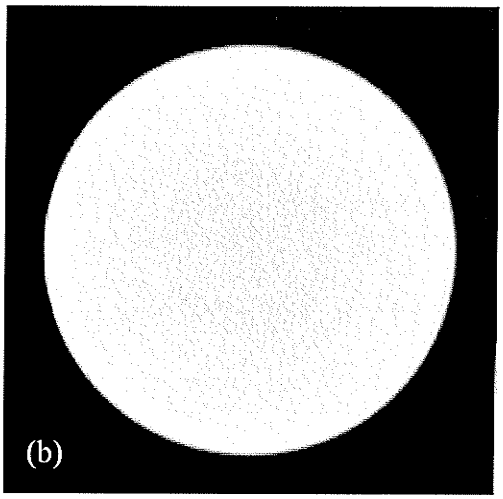

Figure 6.28 Fourth generation scanner images of a 12.5 cm radius Plexiglas phantom incorporating (a) theoretical noise and (b) experimentally measured noise, generated using a Shepp-Logan filter, linear interpolation, A_c = 7.5 Ci, J = 768, Δx = 0.1326 cm and pixel size Δp = 0.1326 cm.

appearance is very similar to the first generation images shown in Figure 6.27. However, there are subtle differences that will be discussed in the next sections. Note that the mottle appearing in Figure 6.28b is of the order expected for actual images generated using the ^{192}Ir source-based scanner.

6.3.2 Standard Deviation Analysis

Calculating the SD provides a quick and easy method of characterizing image noise. In addition, a simple equation can be found that predicts the effect of parameters such as the number of photons, filter function, number of projections and sample spacing on the SD at the center of a uniform disk image for a first generation geometry. This section first compares the predictions of the SD expression to the simulated SD in first generation geometry disk images. After having verified the noise analysis technique for a first generation geometry, this section examines the effect of number of photons, filter function, number of projections, sample spacing and interpolation scheme on the SD at the centre of simulated fourth generation geometry disk images.

6.3.2.1 Theory

Gore and Tofts (1978) and Barrett and Swindell (1981) have described the propagation of noise in the projection data through the filtered backprojection reconstruction method. Using their analysis, the SD can be calculated for each stage of the reconstruction process, as outlined in Appendix A. This derivation yields the following expression describing the variance at the centre of an image

$$\sigma_\mu^2(0,0) = \frac{\Delta\phi^2\,\Delta x^2}{\pi^2}\sum_{j=0}^{J-1}\sum_{l=-\infty}^{\infty}\frac{q^2(l)}{\overline{N}_{lj}}. \qquad (6.51)$$

where $q^2(l)$ is the filter function as described by (6.14) or (6.15), and $\overline{N}_{lj}$ is the number of transmitted photons. For a circular disc object, $\overline{N}_{lj}$ is independent of the projection j, and changes very little with l over the significant non-zero values of $q^2(l)$ because the pathlength through the object is approximately constant near the center of the disk. Therefore $\overline{N}_{lj} \cong \overline{N}_{0j}$ and

$$\sigma_\mu^2(0,0) \cong \frac{\Delta\phi^2\,\Delta x^2}{\pi^2}\frac{1}{\overline{N}_{0j}}\sum_{j=0}^{J-1}\sum_{l=-\infty}^{\infty}q^2(l). \qquad (6.52)$$

Substituting $\Delta\phi = \pi / J$ into (6.52) and carrying out the summation over j yields

$$\sigma_{\mu}^{2}(0,0) \cong \frac{\Delta x^{2}}{J\bar{N}_{0j}} \sum_{l=-\infty}^{\infty} q^{2}(l). \tag{6.53}$$

The summation in (6.53) can be evaluated analytically. As the cut-off frequency of the filter is usually half the sampling frequency, i.e., $f_N = 1/2\Delta x$, it can be shown that for the Ram-Lak (RL) and Shepp-Logan (SL) filters

$$\begin{aligned} \sum_{l=-\infty}^{\infty} |q_{RL}(l)|^{2} &= 0.08333 \frac{\pi^{2}}{\Delta x^{4}} \\ \sum_{l=-\infty}^{\infty} |q_{SL}(l)|^{2} &= 0.05066 \frac{\pi^{2}}{\Delta x^{4}} \end{aligned} \tag{6.54}$$

so that (6.53) becomes

$$\sigma_{\mu_{RL}}^{2}(0,0) = \frac{0.08333\pi^{2}}{J\bar{N}_{0j}\,\Delta x^{2}} \tag{6.55}$$

and

$$\sigma_{\mu_{SL}}^{2}(0,0) = \frac{0.05066\pi^{2}}{J\bar{N}_{0j}\,\Delta x^{2}} \tag{6.56}$$

for the RL and SL filters, respectively.

Equations (6.55) and (6.56) indicate that the SD at the center of a CT disk image decreases with increasing number of photons ($\bar{N}_{0j} \propto A_c \Delta T / d^{2}$; A_c = source activity, ΔT = integration time, d = source-to-detector distance) and correspondingly, increasing dose. This is in contrast to planar radiographs where the SD increases with increasing number of photons[3]. The reason for this is that in CT we are calculating a relative quantity, i.e., projection data. Thus the image brightness does not increase with increasing number of photons, as is the case for a planar radiograph. Equations (6.55) and (6.56) further indicate that the SD decreases with increasing number of projections J. Assuming that the number of photons per ray sum remains constant, an increasing number of projections will also result in an increased dose. Note that the SD *increases* with increasing number of source and detector positions. In this instance, the noise increases with increasing dose. However, this is only due to the effect of the filter

[3] The SD is not to be confused with the SNR, which increases with increasing number of photons for both planar radiographs and CT images.

function on the image. As the sample spacing decreases, the cut-off frequency of the filter increases, resulting in noise at higher spatial frequencies in the filtered projection data. Recall the discussion in §6.2.3 stating that there is minimal improvement in the high-contrast resolution with increasing number of source positions beyond the Nyquist limit. Since a further increase in the number of source positions provides no benefit, the number of source positions should be chosen to avoid aliasing but should not be higher.

6.3.2.2 First Generation Scanner

The goal of this section is to verify that the SD at the centre of the simulated images agrees with the SD predicted by (6.55) and (6.56). This will confirm that the method for simulating noisy images is correct and can be extended to a fourth generation geometry.

Method

Using the technique described in §6.3.1.3, ten 32x32 pixel theoretical noise images, corresponding to the central region of a 10 cm radius Plexiglas disk were generated for all permutations of the following parameters:

(i) Ram-Lak (RL) and Shepp-Logan (SL) filter;

(ii) linear (LI) and nearest neighbor (NN) interpolation.

For each of the above permutations, the source activity A_c (the relationship between the source activity and number of photons is given by (6.38); d = 74 cm), the number of projections J, and the sample spacing $\Delta x_r'$ and were varied follows:

(iii) A_c = 5.0, 6.25, 7.5, 8.75 and 10.0 Ci; J = 350; $\Delta x_r'$ = 0.1 cm;

(iv) A_c = 7.5 Ci; J = 200, 250, 300, 400 and 450; $\Delta x_r'$ = 0.1 cm;

(v) A_c = 7.5 Ci; J = 350; $\Delta x_r'$ = 0.06, 0.08, 0.12 and 0.14 cm.

Note that for a first generation scanner geometry, the sample spacing $\Delta x_r'$ and the number of ray sums per projection L required to encompass the object are related, i.e., increasing $\Delta x_r'$ requires a smaller number of source and detector positions, and vice versa. The number of ray sums per projection was always chosen to be adequate to encompass the entire Plexiglas disk. The reconstruction pixel size Δp was set equal to

$\Delta x_r'$. The effect of varying pixel size on the SD was not examined. The SD of the central 25x25 pixels was found for each of these images.

Results

Figures 6.29, 6.30 and 6.31 show the SD, averaged over ten images, plotted as a function of source strength, number of projections and sample spacing, respectively. The error bars show the SD in the ten SD values. The theoretical SD calculated using (6.55) and (6.56) appears as a solid line in the plots.

The plots of SD versus source strength A_c (Figure 6.29) show that the SD decreases with increasing A_c as expected. The SD of the images generated using LI is smaller than that of the images generated using NN interpolation because LI provides greater smoothing than NN interpolation. Both the NN and LI points agree well with the trend predicted by (6.55) and (6.56). The difference in magnitude between the theoretical and the simulated SD values occurs because the theoretical expressions do not take any of the interpolation required for backprojection into account.

The plots of SD versus number of projections J (Figure 6.30), and SD versus sample spacing $\Delta x_r'$ (Figure 6.31) show similar behavior in that the trends predicted by (6.55) and (6.56) are followed for both the NN and LI points. As discussed in §6.3.2.1, the SD decreases as J and $\Delta x_r'$ increase.

Figures 6.29 to 6.31 demonstrate that the noise incorporated in the first generation images obeys the predictions of (6.55) and (6.56). This confirms the correctness of the noise generation technique, indicating that it can be applied to a fourth generation geometry with confidence.

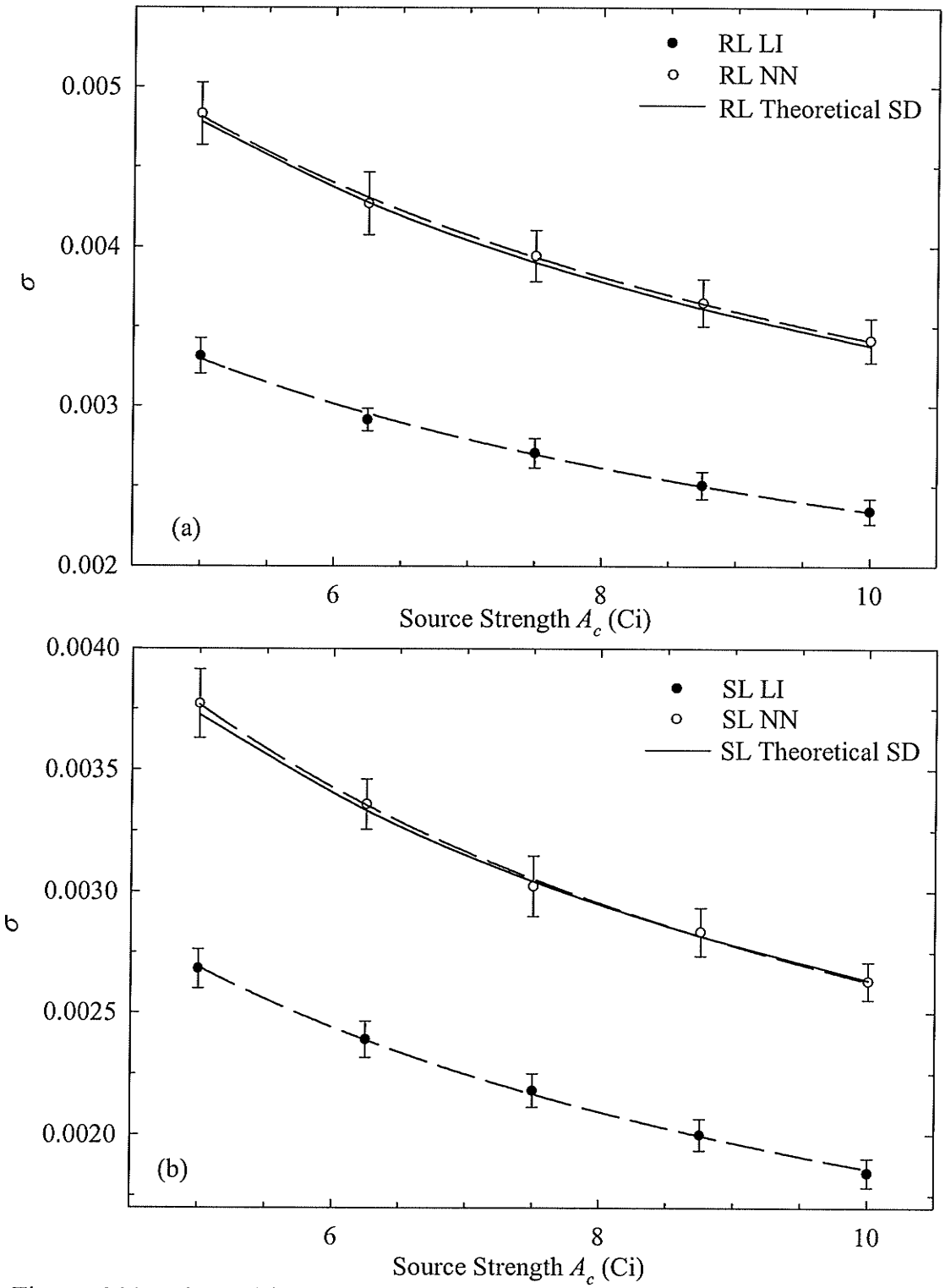

Figure 6.29 Plots of image SD as a function of source strength A_c for a first generation scanner using number of projection $J = 350$, sample spacing $\Delta x_r' = 0.1$ cm, nearest neighbor (NN) or linear interpolation (LI) and a (a) RL and (b) SL filter. The dashed lines represent a power law regression fit through the data, while the solid lines illustrate the predictions of (6.55) and (6.56).

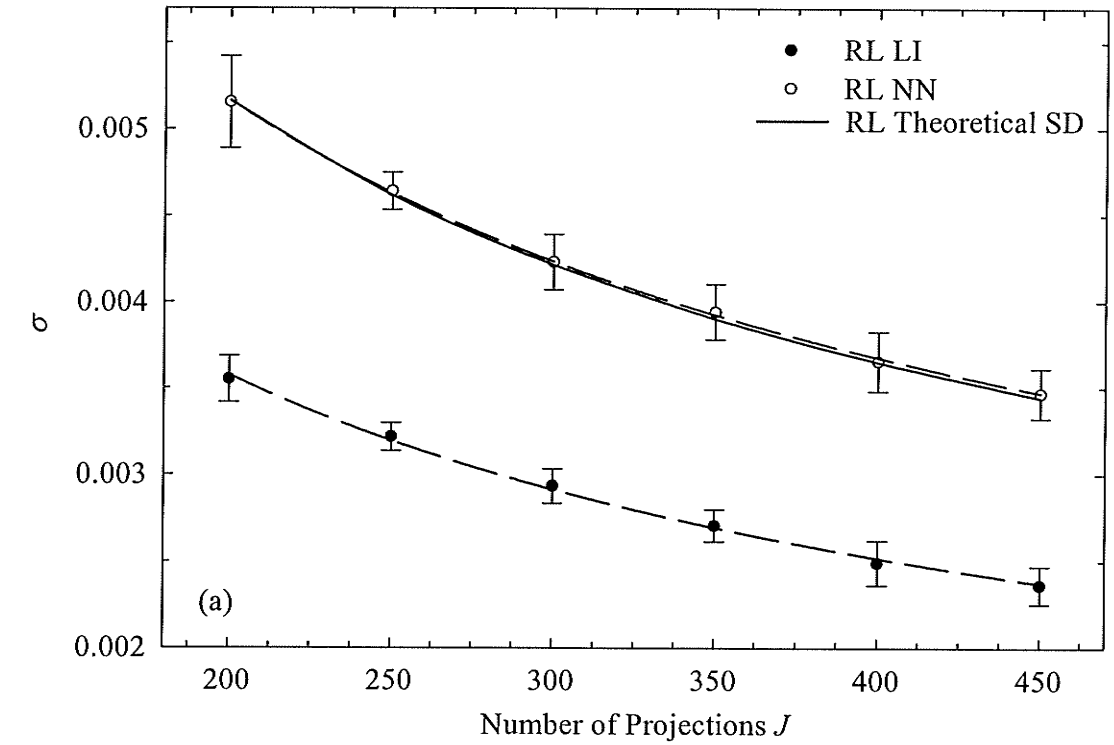

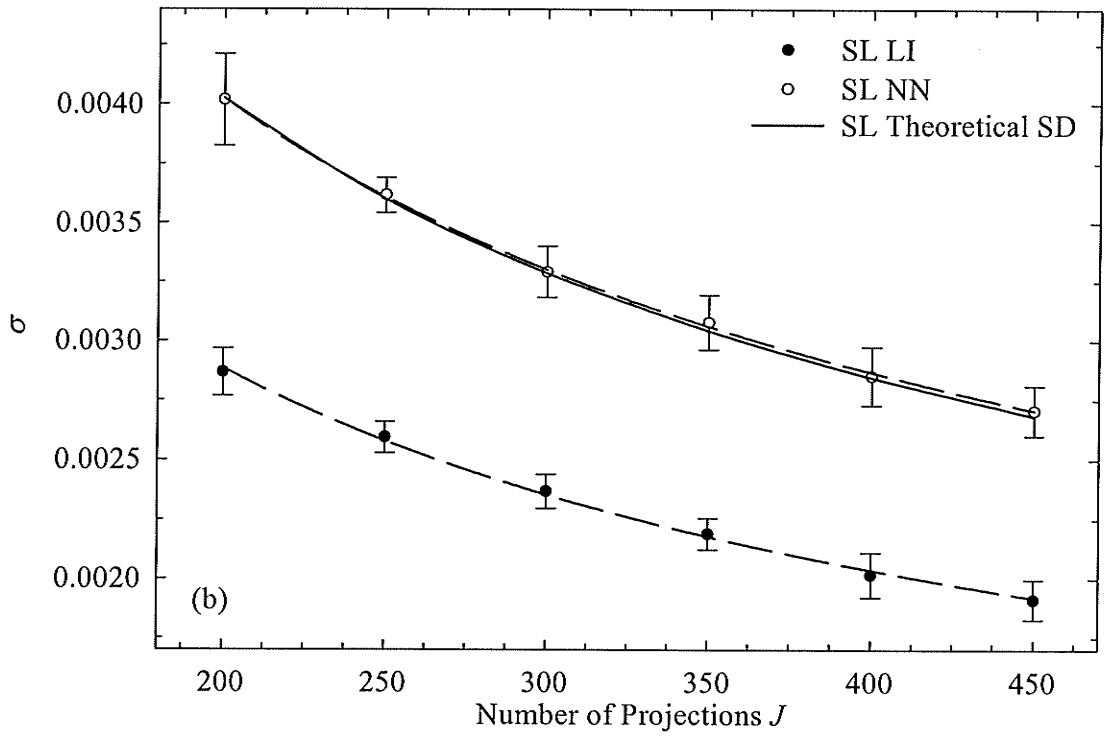

Figure 6.30 Plots of image SD as a function of number of projections J for a first generation scanner using source strength A_c = 7.5 Ci, sample spacing $\Delta x_r'$ = 0.1 cm, nearest neighbor (NN) or linear interpolation (LI) and a (a) RL and (b) SL filter. The dashed lines represent a power law regression fit through the data, while the solid lines illustrate the predictions of (6.55) and (6.56).

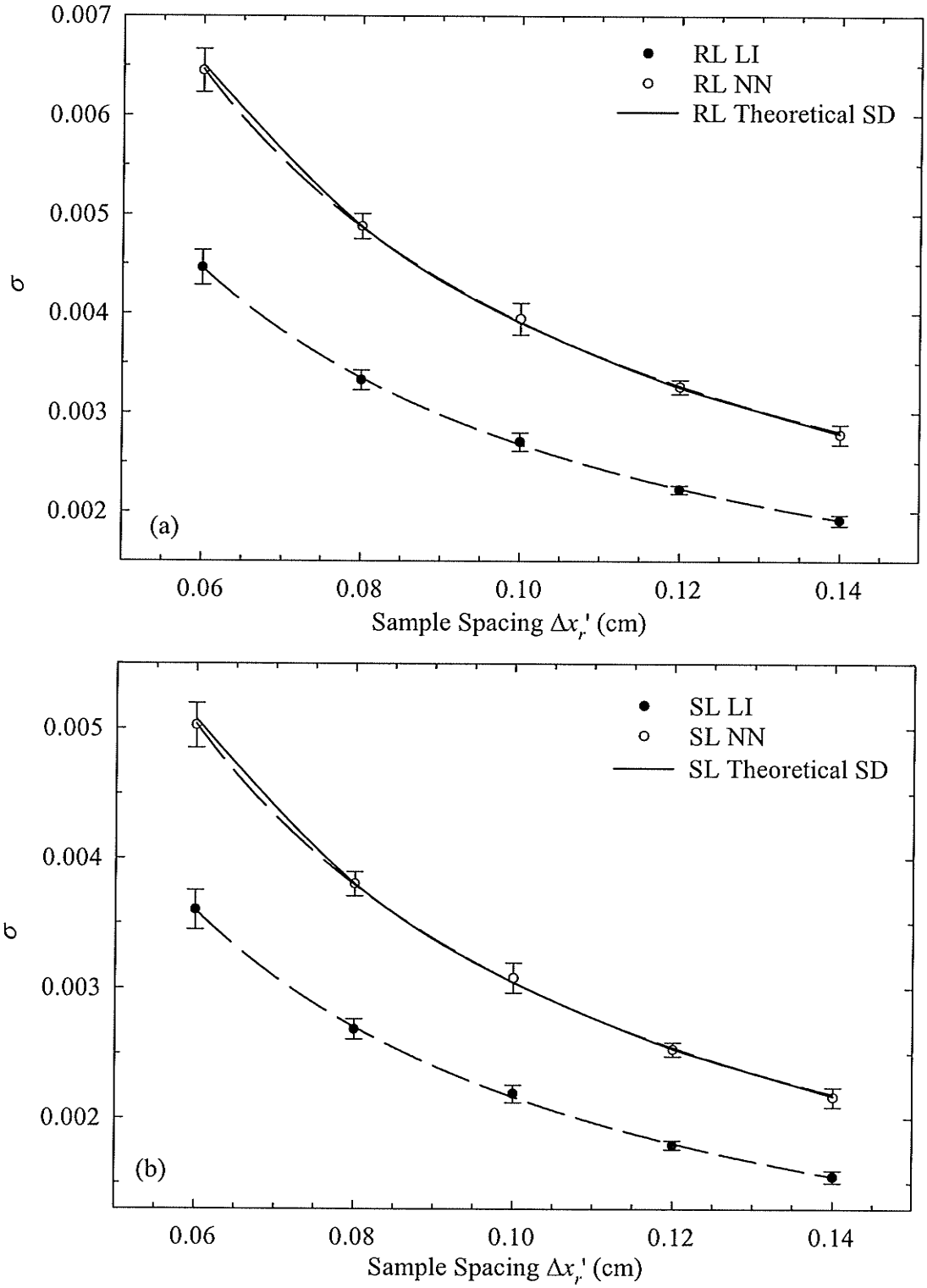

Figure 6.31 Plots of image SD as a function of sample spacing $\Delta x_r'$ for a first generation scanner using source strength A_c = 7.5 Ci, number of projections J = 350, nearest neighbor (NN) or linear interpolation (LI) and a (a) RL and (b) SL filter. The dashed lines represent a power law regression fit through the data, while the solid lines illustrate the predictions of (6.55) and (6.56).

6.3.2.3 Fourth Generation Scanner

The goal of this section is to examine the effect of the source strength, number of projections and sample spacing on the SD at the center of fourth generation Plexiglas images.

Method

Ten 31x31 pixel images[4], corresponding to the central region of a 10 cm radius Plexiglas disk were generated for all permutations of the following parameters:

(i) Ram-Lak (RL) filter and Shepp-Logan (SL) filter;

(ii) linear (LI) and nearest neighbor (NN) interpolation;

(iii) theoretical noise (TN) §6.3.1.3 and experimental noise (EN) §6.3.1.4.

For each of the above permutations, the source strength A_c, the number of projections J, and sample spacing Δx_r and were chosen as follows:

(iv) $A_c = 5.0$, 6.25, 7.5, 8.75 and 10.0 Ci; $J = 768$; $\Delta x_r = 0.1326$ cm;

(v) $A_c = 7.5$ Ci; $J = 568$, 668, 768, 868 and 968; $\Delta x_r = 0.1326$ cm;

(vi) $A_c = 7.5$ Ci; $J = 768$; $\Delta x_r = 0.0884$, 0.1091, 0.1527 and 0.1736 cm.

Note that for the fourth generation geometry, the number of detector positions n_d equals the number of projections J. The sample spacing Δx_r depends upon the spacing between the source positions (Figure 6.2b), which is in turn determined by the number of source positions n_s. The sample spacing Δx_r decreases with increasing number of source positions and vice versa. The number of source positions corresponding to each of the Δx_r values listed above is as follows: Δx_r=0.0884, n_s = 1296; Δx_r=0.1091, n_s = 1050; Δx_r=0.1326, n_s = 864; Δx_r=0.1527, n_s = 750; and, Δx_r=0.1736, n_s = 660. The reconstruction pixel size Δp was chosen to equal Δx_r. The effect of pixel size on the image SD was not examined. The SD of the central 25x25 pixels was found for each of these images. Note that rings appearing in Figure 6.28b occur some distance away from the center of the disk, while the center of the image is quite uniform; the rings are therefore not expected to have an impact on the SD values.

[4] For the fourth-generation scanner, 31x31 images, rather than 32x32 images were generated as the nearest neighbor algorithm was more easily implemented for a 31x31 image.

The images generated in this section deliver a variable dose that depends on the parameters used. In other words, increasing the number of projections or decreasing the sample spacing, which requires a larger number of source positions to be used, will increase the dose, and vice versa. This confuses the interpretation of the results. Thus, an additional series of simulated theoretical noise (§6.3.1.3) images was generated using a constant number of photons per image n_{total} while varying the parameters listed in (v) and (vi). More specifically, $n_{total} = n_s \cdot n_d \cdot \varphi_{n_s n_d}$ was held constant by normalizing the number of photons per ray $\varphi_{n_s n_d}$ according to

$$\varphi_{n_s n_d} = \varphi_{864,768} \cdot \frac{864}{n_s} \cdot \frac{768}{n_d}. \tag{6.57}$$

Results

Figures 6.32, 6.33 and 6.34 show the SD, averaged over ten images, plotted as a function of source strength, number of projections and sample spacing, respectively. The error bars show the SD in the ten SD values.

The SD decreases with increasing source strength A_c as shown in Figure 6.32. This is expected because of the increasing dose with increasing source strength. The noise is smaller for the LI images than the NN images because of the increased filtration associated with the former interpolation technique. Using a SL filter also results in decreased noise compared to the RL filter because of the high frequency roll off associated with the SL filter (Figure 6.5). Note that (6.36) overestimates the actual output of the detector as described in §3.6.1; consequently the noise for the theoretical noise (TN) images is smaller than for the experimental noise (EN) images.

Figure 6.33 plots the SD as a function of the number of projections J. The SD decreases with increasing number of projections because of the increasing dose. Figure 6.34 shows the SD as a function of sample spacing Δx. The SD decreases as the sample spacing increases even though the dose is also decreasing. This is due to the effect of the filter function, i.e., the filter cut-off frequency is decreasing.

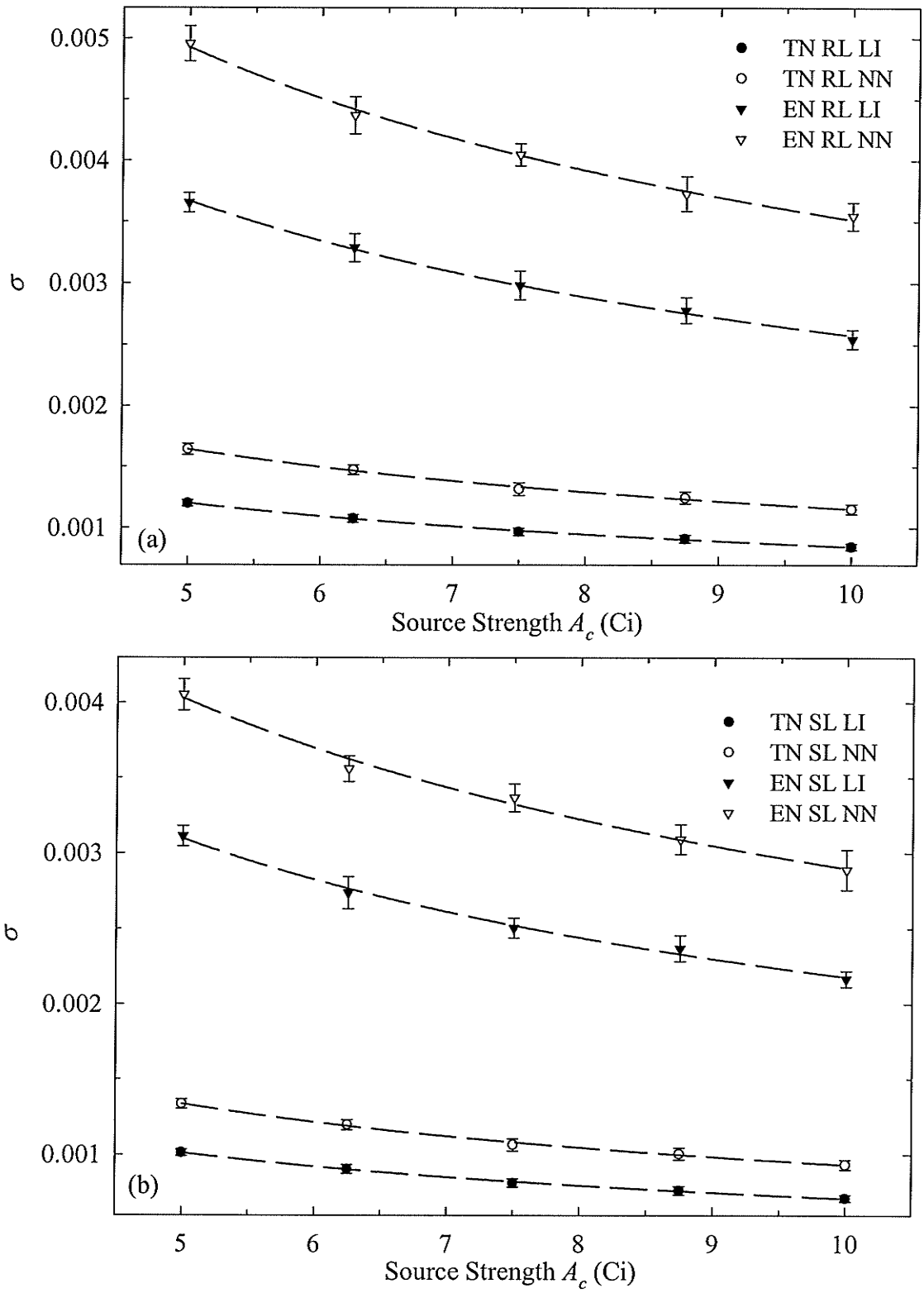

Figure 6.32 Plots of image SD as a function of source strength A_c for a fourth generation scanner using number of projections J = 768, sample spacing Δx_r = 0.1326 cm, nearest neighbor (NN) or linear interpolation (LI) and a (a) RL and (b) SL filter. The dashed lines represent a power law regression fit through the data.

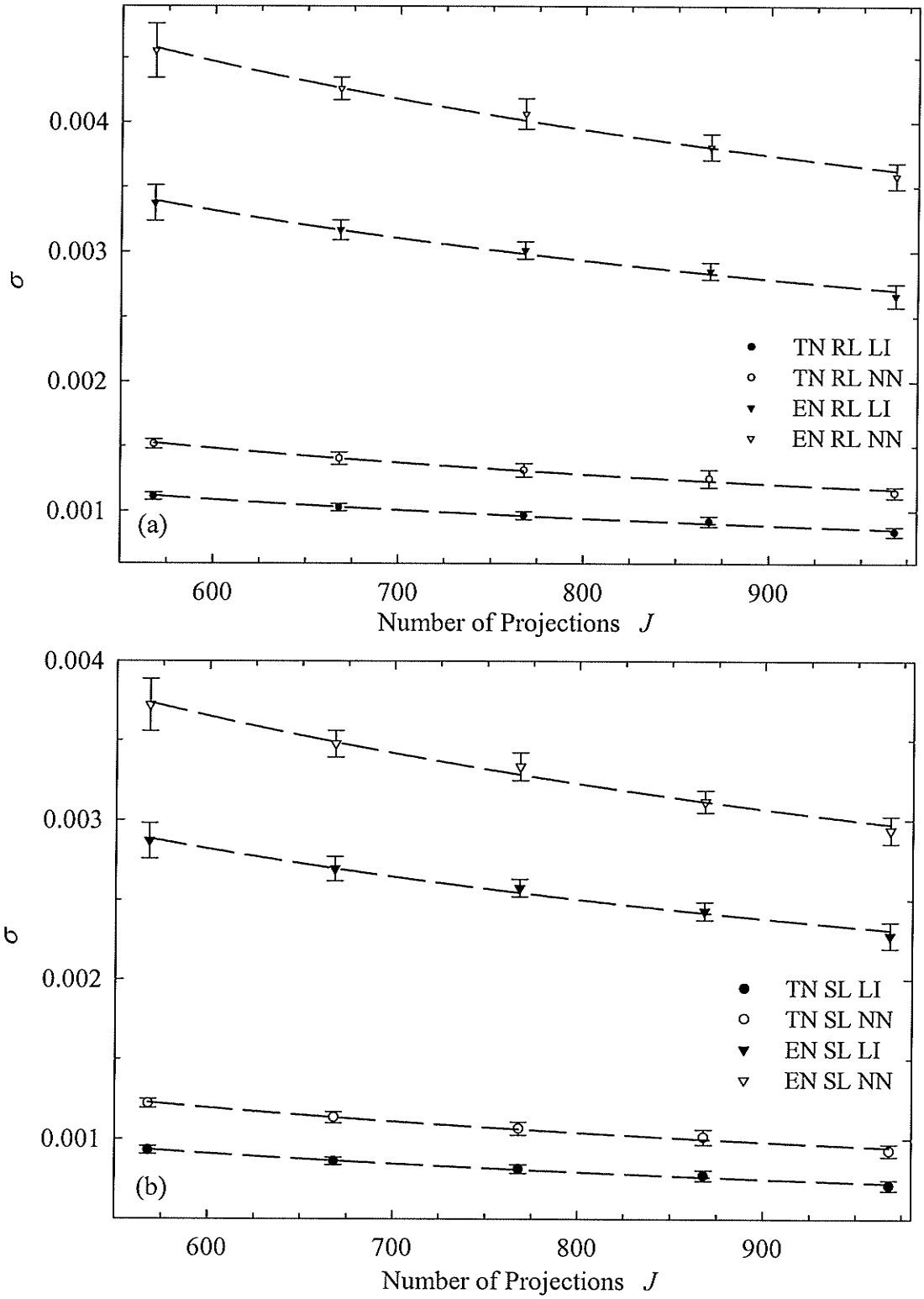

Figure 6.33 Plots of image SD as a function of number of projections J for a fourth generation scanner using source strength $A_c = 7.5$ Ci, sample spacing $\Delta x_r = 0.1326$ cm, nearest neighbor (NN) or linear interpolation (LI) and a (a) RL and (b) SL filter. The dashed lines represent a power law regression fit through the data.

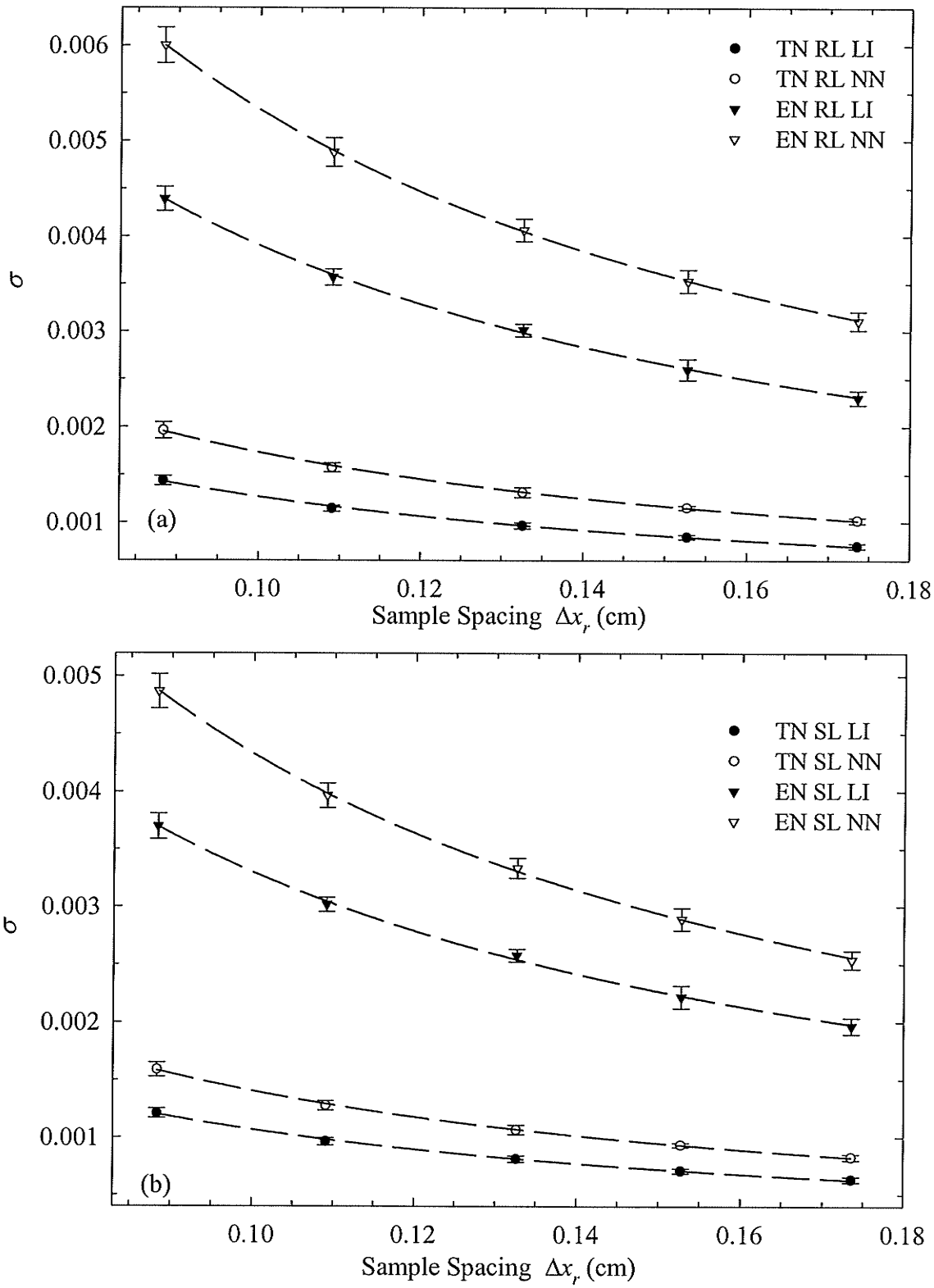

Figure 6.34 Plots of image SD as a function of sample spacing Δx_r for a fourth generation scanner using source strength A_c = 7.5 Ci, number of projections J = 768, nearest neighbor (NN) or linear interpolation (LI) and a (a) RL and (b) SL filter. The dashed lines represent a power law regression fit through the data.

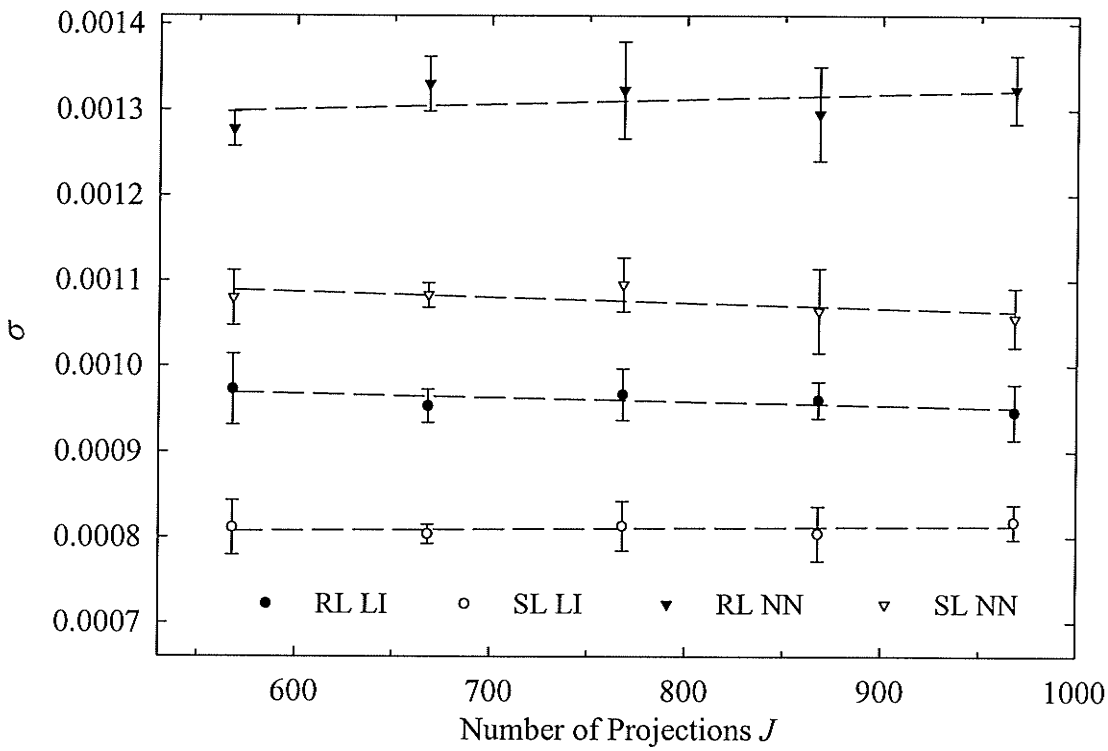

Figure 6.35 Plots of image SD as a function of number of projections J for a fourth generation scanner. Images were generated using a constant n_{total}, A_c = 7.5 Ci, Δx_r = 0.1326 cm, nearest neighbor (NN) or linear interpolation (LI) and theoretical noise incorporated in the detector signal (§6.3.1.3). Regression lines through the data are also shown.

It can be seen in Figure 6.35 that increasing the number of projections while maintaining a constant number of photons n_{total} for each image provides no change in the SD. The decrease in SD with increasing number of projections shown in Figure 6.33 is simply a consequence of the corresponding increase in dose, rather than the increasing number of projections. For a fourth generation scanner geometry, increasing the number of projections (recall that this is equal to the number of detectors n_d) results in an improved high contrast resolution (Figure 6.20). Therefore it may be beneficial to use a larger number of narrower detectors to decrease the beam width and improve the high contrast resolution. However a reduction in detector width should be accompanied by a reduction in the source length.

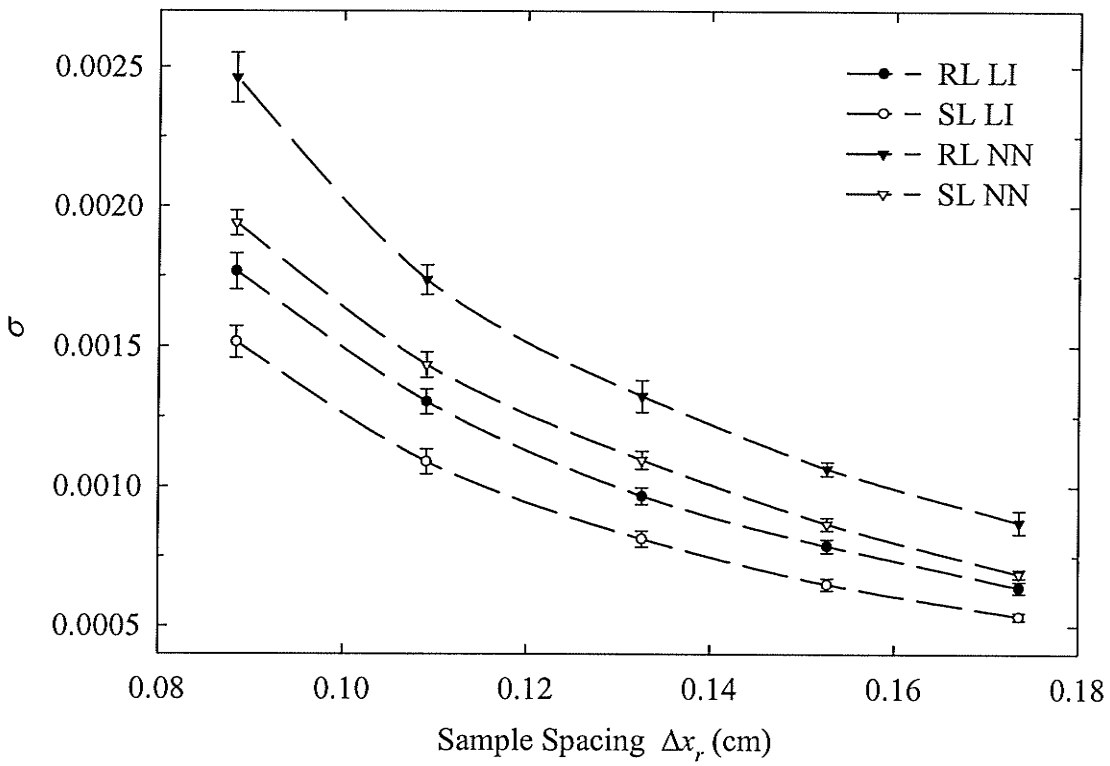

Figure 6.36 Plots of image SD as a function of sample spacing Δx_r for a fourth generation scanner. Images were generated using a constant n_{total}, A_c = 7.5 Ci, number of projections J = 768, nearest neighbor (NN) or linear interpolation (LI) and theoretical noise incorporated in the detector signal (§6.3.1.3).

Figure 6.36 shows an even more dramatic increase in SD with decreasing sample spacing than Figure 6.34. This is because the effect of increasing dose with decreasing sample spacing has now been removed. Figure 6.36 emphasizes the earlier conclusion that decreasing the sample spacing, i.e., increasing the number of source positions beyond that required to satisfy sampling requirements is not desirable. More specifically, if the dose is held constant and the sample spacing is reduced for the purpose of increasing the resolution, the image noise will increase.

6.3.3 Noise Power Spectrum Analysis

A complete characterization of image noise requires generation of a noise power spectrum (NPS). This section first presents the expression used to generate a NPS from the simulated images. To ensure that the simulated NPS are correct, NPS generated using simulated first generation images (§6.3.1.2) are compared to the theoretical first generation NPS equation. Having confirmed the validity of the NPS generation technique, simulated NPS are calculated for a fourth generation scanner geometry using the noise generation approaches presented in §6.3.1.3 and §6.3.1.4, RL and SL filters, and nearest-neighbor and linear interpolation schemes.

6.3.3.1 Theory

NPS using Simulated Images

The noise power spectra $\overline{C}(f_x, f_y)$ of both the first and fourth generation simulated images were found using

$$\overline{C}(f_x, f_y) = \frac{1}{M}\sum_{m=0}^{M-1}\left|\frac{1}{N^2}\sum_{x=0}^{N-1}\sum_{y=0}^{N-1}\Delta S(x,y)e^{-2\pi i\left(\frac{xf_x}{N}+\frac{yf_y}{N}\right)}\right|^2 \qquad (6.58)$$

where M is the number of image pairs and $\Delta S(x,y) = S_{2m}(x,y) - S_{2m+1}(x,y)$ is the difference of two N x N simulated images $S_{2m}(x,y)$ and $S_{2m+1}(x,y)$. The subtraction process generates zero mean data, as required for NPS analysis.

Theoretical First Generation NPS Expression

A theoretical expression predicting the NPS for a fourth generation geometry has not been published. Kijewski and Judy (1987) have however developed an expression for a first generation scanner geometry. In order to verify the above simulation technique for determing NPS, the NPS obtained when applying (6.58) to first generation images were compared to the predictions of Kijewski and Judy's expression. Once the simulation technique has been verified to work correctly for first generation images, it can easily be extended to a fourth generation geometry.

Kijewski and Judy (1987) present a complete NPS analysis for a first generation scanner geometry taking into account the effect of the filter function (RL or SL),

interpolation scheme (LI or NN), backprojection and the effect of displaying the image on a discrete grid. The following discussion summarizes some of the pertinent expressions given in Kijewski and Judy's paper. These are used for validation purposes as described in Appendix B.

The sampled projection data are collected by making statistically independent radiation measurements. The NPS of the projection data is therefore given by

$$\Gamma_P(f) = \frac{\sigma_P^2}{L} \sum_{k=-\infty}^{\infty} \text{rect}(\Delta x_r' f - k) \tag{6.59}$$

where σ_P is the standard deviation in the projection data[5] and L is the number of rays per projection. The rect function and summation over k in (6.59) are due to the sampling of rays with spacing $\Delta x_r'$, which causes shifted replicas of the Fourier transform of the projection data to appear in the frequency domain (Barrett and Swindell, 1981).

When reconstructing the image using the filtered backprojection algorithm, the projection data are first filtered and then backprojected. Filtering is performed by convolving the sampled projection data with a filter function $q(x_r')$. Since convolution in the spatial domain is equivalent to multiplication in the frequency domain, the NPS of the filtered projection data $\Gamma_{\tilde{P}}(f)$ is obtained by multiplying the NPS of the projection data $\Gamma_P(f)$ by the Fourier transform $|Q(f)|$ of the filter function,

$$\Gamma_{\tilde{P}}(f) = \frac{\sigma_P^2}{L} \sum_{k=-\infty}^{\infty} \left| Q\left(f - \frac{k}{\Delta x_r'} \right) \right|^2 \text{rect}(\Delta x_r' f - k). \tag{6.60}$$

Interpolation is then performed on the filtered projection data, as required for backprojection. This is also modeled by a multiplicative factor, namely, $G(f) = \Delta x_r' \text{sinc}(\Delta x_r' f)$ for NN interpolation and $G(f) = \Delta x_r' \text{sinc}^2(\Delta x_r' f)$ for LI. The interpolated projection data is continuous; consequently, its Fourier transform does not consist of the summation of shifted replicas, and the function $G(f)$ is placed outside of the summation. The NPS of the interpolated filtered projections $\Gamma_{\tilde{P}_G}(f)$ is given by

---

[5] Recall that the projection data P is equal to $P = -\ln(N/N_0)$, where N is the mean number of transmitted photons detected by the detector and N_0 is the number of photons detected in the absence of an attenuator. The variance in the projection data is $\sigma_P^2 \cong 1/N$ (see Appendix A). Thus the noise in the projection data decreases with increasing number of photons.

$$\Gamma_{\tilde{P}_G}(f) = \frac{\sigma_P^2}{L}|G(f)|^2 \sum_{k=-\infty}^{\infty}\left|Q\left(f - \frac{k}{\Delta x_r'}\right)\right|^2 \text{rect}(\Delta x_r' f - k). \qquad (6.61)$$

The two-dimensional NPS of the reconstructed image incorporating the effect of summing over all projections and displaying the image on a discrete grid is given by

$$\Gamma(f_x, f_y) = \frac{\pi\sigma_P^2}{JL}\sum_{m=-\infty}^{\infty}\sum_{n=-\infty}^{\infty}\sum_{j=1}^{J}\delta_s|G(f)|^2\sum_{k=-\infty}^{\infty}\left|Q\left(f_a - \frac{k}{\Delta x_r'}\right)\right|^2 \text{rect}(\Delta x_r' f_a - k) \quad (6.62)$$

where J is the number of projections, Δp is the pixel size,

$$\delta_s = \delta\left[\left(f_x - \frac{n}{\Delta p}\right)\sin\left(\frac{\pi j}{J}\right) - \left(f_y - \frac{m}{\Delta p}\right)\cos\left(\frac{\pi j}{J}\right)\right] \qquad (6.63a)$$

and

$$f_a = \left[\left(f_x - \frac{n}{\Delta p}\right)^2 + \left(f_y - \frac{m}{\Delta p}\right)^2\right]^{1/2} \qquad (6.63b)$$

where f_x and f_y are Cartesian frequency space variables. In (6.63a) δ_s is a line in 2D frequency space at the angle of the j^{th} projection with respect to the f_x axis, i.e., it is one spoke in the NPS.

6.3.3.2 Algorithm Validation

Appendix B outlines an extensive evaluation to understand the predictions of (6.59) to (6.62), and to verify their validity for the first generation scanner modeled in the computer. A representative sample of four NPS calculated from first generation images are presented here to demonstrate the agreement between (6.62) and the simulated NPS found using (6.58). Equation (6.58) was applied to the central N x N = 128 x 128 pixels of M = 500 image pairs to generate the NPS shown in Figure 6.37. The first generation images were generated using J = 350, L = 256, Δx = 0.1 cm and Δp = 0.09 cm, with only the central 128 x 128 pixels reconstructed to reduce the simulation time. The noise power shown in Figure 6.37 is reduced at the origin because the projection NPS is multiplied by the filter function (see (6.60)), which decreases with decreasing frequency. The noise power is reduced at high frequencies because the interpolation process causes the NPS of the filtered projection data $\Gamma_{\tilde{P}}(f)$ to be multiplied by $G(f)$, which decreases with increasing frequency near the edges of the NPS $\Gamma(f_x, f_y)$.

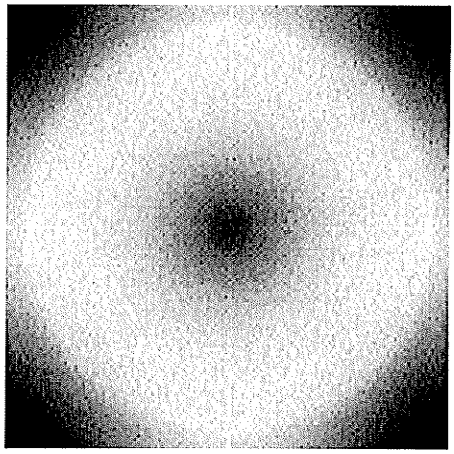

NO RL NN

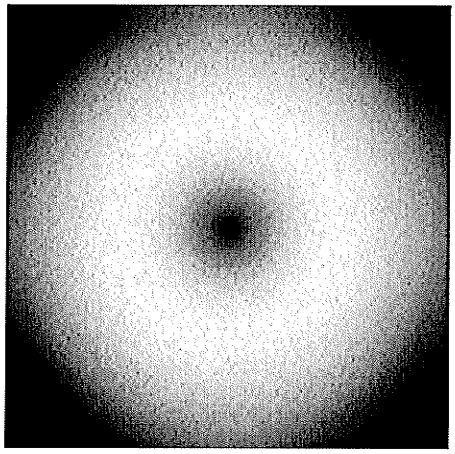

NO RL LI

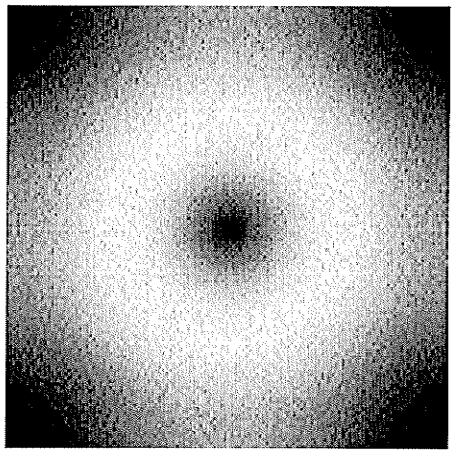

NO SL NN

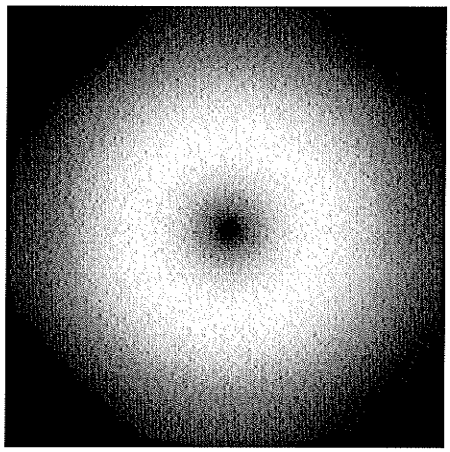

NO SL LI

Figure 6.37 NPS generated from the central 128x128 pixels of 500 first generation image pairs simulated using the noise-only scheme described in §6.3.1.2, $L = 256$, $J = 350$, $\Delta x = 0.1$ cm and $\Delta p = 0.09$ cm.

Profiles along the principal and diagonal axes of the simulated NPS (Figure 6.37) are plotted in Figure 6.38. Also plotted in Figure 6.38 is the theoretical NPS calculated using (6.62). The summations over k, m and n in (6.62) were carried out over –4 to 4 for LI and –8 to 8 for NN interpolation. Summation over a larger range resulted in negligible difference in the theoretical NPS. The theoretical and simulated NPS were normalized to the same total noise power, as described in Appendix B. Agreement between the theoretical and simulated NPS shown in Figure 6.38 is excellent, validating the analysis technique used.

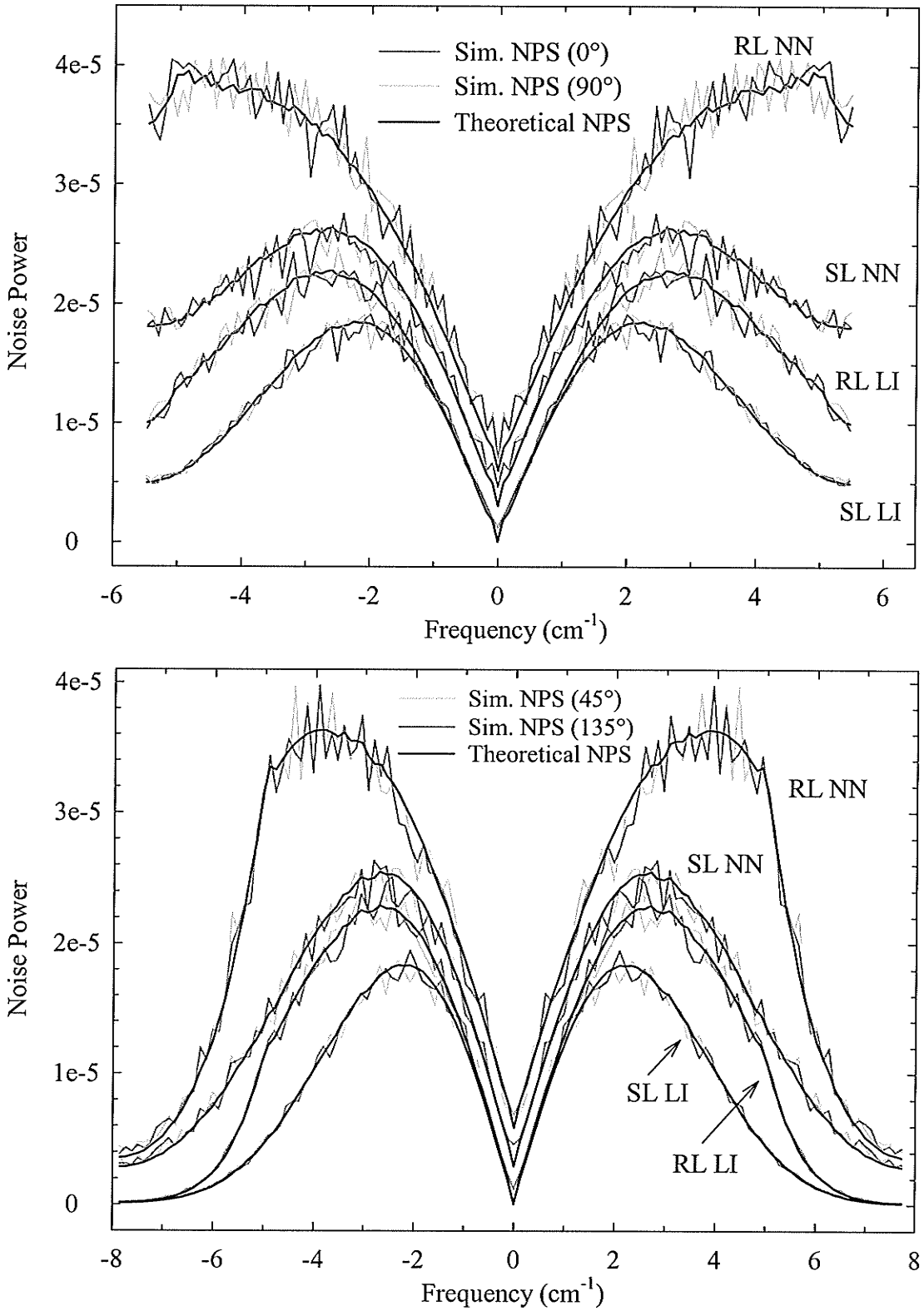

Figure 6.38 Profiles along the principal axes (top) and diagonals (bottom) of the NPS shown in Figure 6.37. Also shown are the theoretical NPS found using (6.62).

The total power under the profiles in Figure 6.38 confirm the results found in §6.3.2 that NN interpolation and the RL filter result in noisier images. Images generated using NN interpolation and a RL filter also display the largest amount of high-frequency noise. Using a SL rather than a RL filter decreases the magnitude and alters the shape of the NPS. This can be understood by considering Figure 6.5, which shows that the SL filter reduces high frequency noise more effectively than the RL filter. Linear interpolation further reduces the image noise, so that LI together with a SL filter results in images with the least noise.

6.3.3.3 Fourth Generation NPS

The simulated fourth generation NPS were generated in a similar manner to the first generation NPS. A total of $M = 500$ image pairs were generated using $n_s = 768$, $n_d = 864$, $\Delta x = 0.1326$ cm and $\Delta p = 0.1193$ cm. Either theoretical noise (§6.3.1.3) or experimental noise (§6.3.1.4) was incorporated into the simulation assuming a 7.5 Ci source.

NPS generated using experimental noise are shown in Figure 6.39. Noise is minimal at zero frequency, i.e. at the centre, and at high frequencies because of the shape of the reconstruction filter and the interpolation required for backprojection. The NPS generated using theoretical noise are not shown since these are similar in shape to those illustrated in Figure 6.39.

Profiles along the principal and diagonal axes of the NPS are plotted in Figures 6.40[6] and 6.41. A comparison with the theoretical NPS was not made since (6.62) is strictly valid only for a first generation geometry because it does not account for the interpolation required to rebin from a fourth to a first generation geometry. The trends displayed by the fourth generation NPS are however similar to those exhibited by the first

[6] Note that the NPS were generated using a slightly different expression than that given in §6.3.1.3. An attenuation coefficient of $\mu_{plexi} = 0.133$ cm^{-1} (linear attenuation coefficient of Plexiglas weighted over the ^{192}Ir spectrum) was used rather than $\mu_{plexi} = 0.129$ cm^{-1} (linear attenuation coefficient of Plexiglas at 355 keV). This difference has a small impact on the number of photons transmitted, and has minimal impact on the NPS. A value of 1.49 A_c/d photons/detector was used rather than 14.9 A_c/d photons/detector, as stated in §6.3.1.3. This means that the magnitude of the NPS are too large by a factor of $\sqrt{10}$, which was corrected for by dividing all of the values in Figure 6.40 by $\sqrt{10}$.

generation NPS in that the RL NN NPS has the largest power, while SL LI images will have the least noise. Comparison of the first and fourth generation NPS shows that the fourth generation NPS display much less high frequency noise. This is due to the smoothing effect of the interpolation required to rebin from a fourth to a first generation geometry.

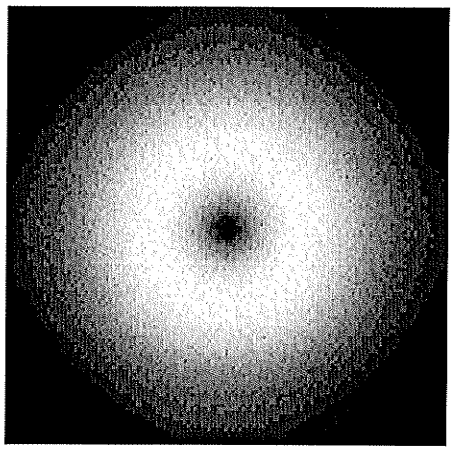

EN RL NN 4

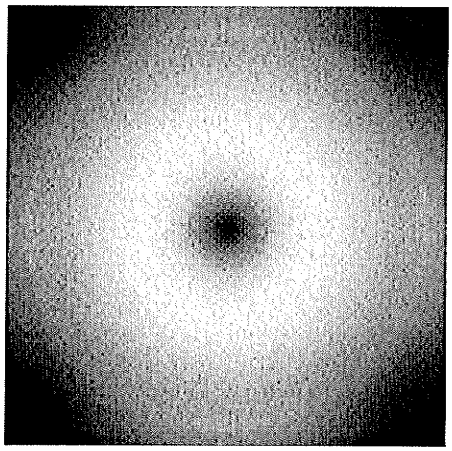

EN RL LI 4

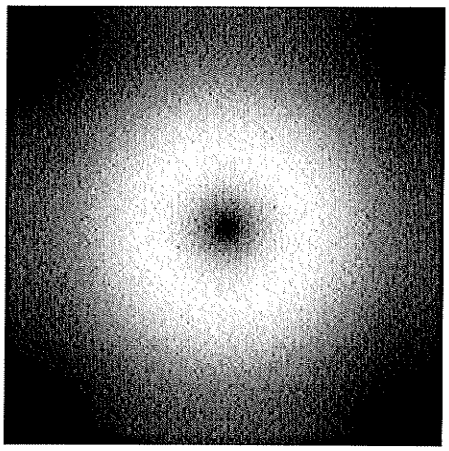

EN SL NN 4

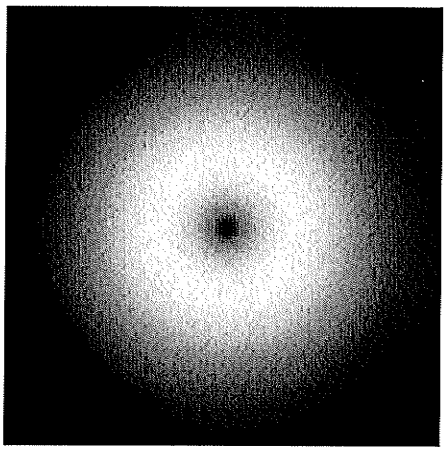

EN SL LI 4

Figure 6.39 NPS generated from the central 128x128 pixels of 500 fourth generation image pairs simulated using experimental noise (§6.3.1.4), n_s = 864, n_d = 768, Δx = 0.1326 cm and Δp = 0.1193 cm.

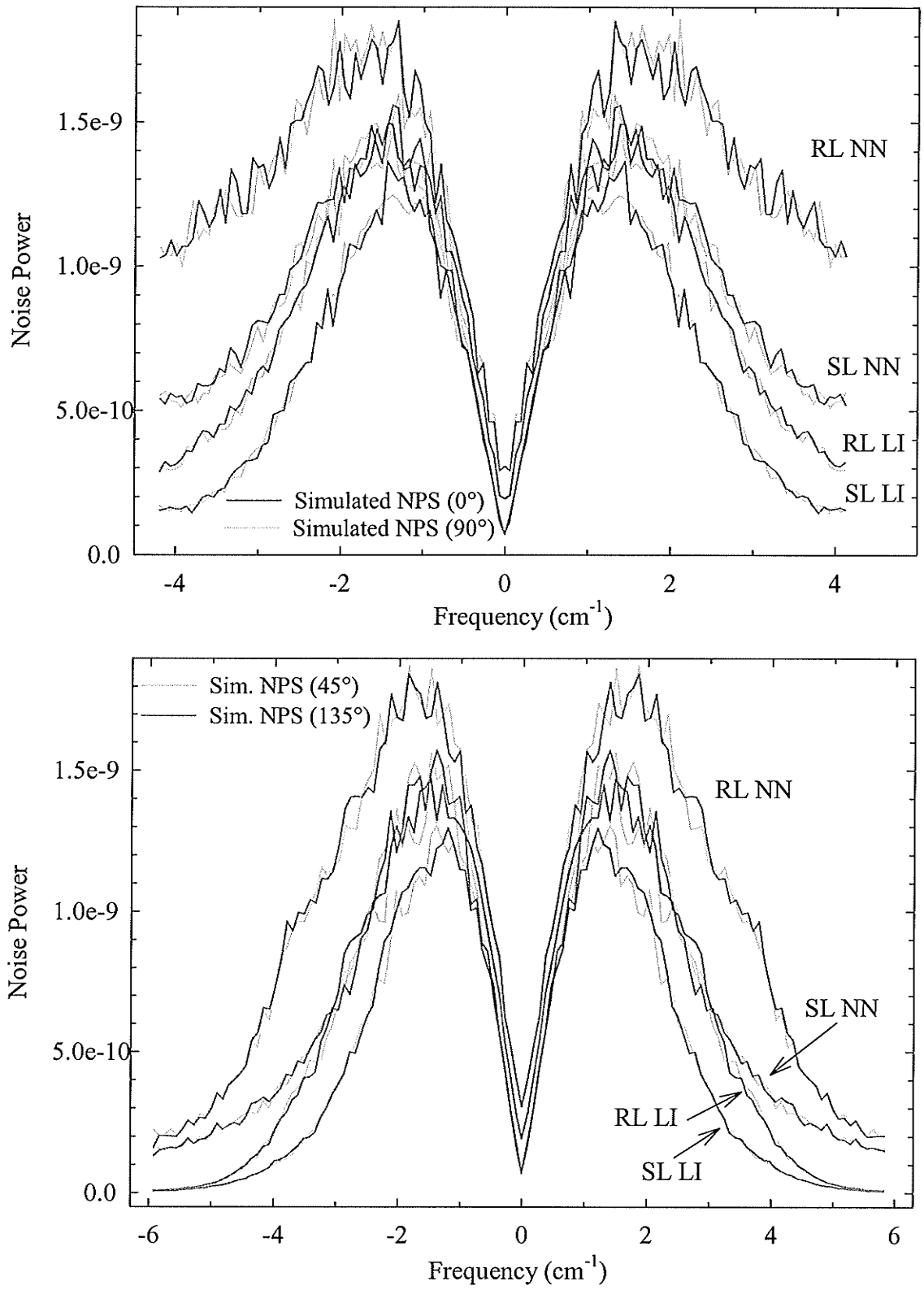

Figure 6.40 NPS along the principal axes (top) and diagonals (bottom) generated using fourth generation theoretical noise images (§6.3.1.3).

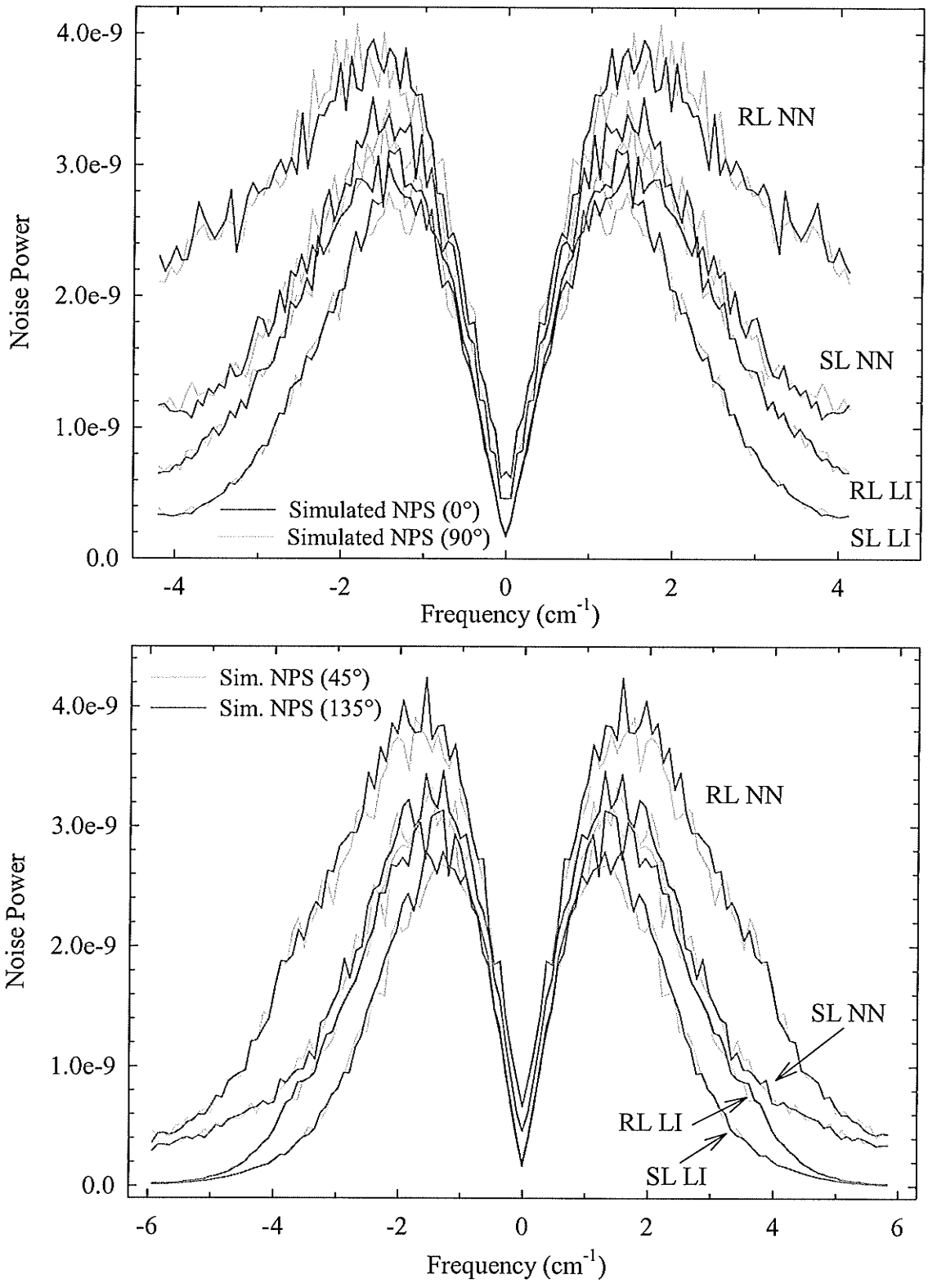

Figure 6.41 NPS along the principal axes (top) and diagonals (bottom) generated using fourth generation experimental noise images (§6.3.1.4).

6.4 Dose

The dose received by a patient is dependent upon a number of factors including source energy, source strength, irradiation time, slice thickness, slice spacing and collimator design (Rothenberg and Pentlow, 1995). In this section, patient dose is measured as a function of the product of source strength A_c and irradiation time. This is achieved by measuring the dose profile perpendicular to the slice direction using an ion chamber array, and then measuring the dose at the centre of a 32 cm diameter Plexiglas body phantom using a CT ion chamber.

6.4.1 Computed Tomography Dose Index

Determination of the dose delivered by a CT scan is complicated by the fact that irradiation at a particular slice location also contributes to the dose at other locations within the patient. This is due to scattered photons and beam divergence (Rothenberg and Pentlow, 1995). The dose received by a particular section of the phantom increases as the number of slices increases. Consequently, considering only the dose delivered by a single slice is inappropriate for a CT examination involving several slices. To account for the fact that CT scans generally consist of multiple slices, the computed tomography dose index (CTDI) was developed by Shope et al. (1981). This is defined as

$$\mathrm{CTDI} = \frac{1}{T}\int_{-\infty}^{\infty} D(z)\,dz \tag{6.64}$$

where T is the nominal slice thickness and $D(z)$ is the single scan dose profile (SSDP), which is the dose for a single slice as a function of position along the long axis (z-axis) of a cylindrical phantom aligned with the rotational axis of the scanner. Because the SSDP drops to small values after about 7 slice thicknesses from the scanner centre, the U.S. Centre for Devices and Radiological Health proposed an alternate definition for the CTDI (Knox and Gagne, 1996; Shope et al., 1981)

$$\mathrm{CTDI} = \frac{1}{T}\int_{-7T}^{7T} D(z)\,dz = \frac{1}{T}\int_{-T/2}^{T/2} D_{14,T}(z)\,dz \tag{6.65}$$

where $D(z)$ is the SSDP and $D_{14,T}(z)$ is the multiple scan dose profile (MSDP), which is the dose for 14 scans as a function of position along the long axis (z-axis) of a cylindrical phantom aligned with the rotational axis of the scanner.

Measurement of the SSDP is a considerable effort (Rothenberg and Pentlow, 1995), requiring film, thermo-luminescent dosimeters (TLDs) or an ion chamber array. Although this may be carried out when commissioning a CT scanner, such a measurement is not practical for routine quality assurance. To this end, the CTDI is normally measured using a 10 cm long ion chamber placed at the centre of a 16 cm diameter cylindrical Plexiglas head phantom or a 32 cm diameter cylindrical Plexiglas body phantom. This effectively provides an integral over the SSDP as required by (6.65). For a slice thickness other than 7 mm, this however does not correspond to integration from $-7T$ to $7T$. Knox and Gagne (1996) have derived a correction factor CF given by

$$CF = \frac{\frac{1}{T}\int_{7T}^{7T} D(z)dz}{\frac{1}{T}\int_{-L/2}^{L/2} D(z)dz} \tag{6.66}$$

where L is the chamber length, to account for the fact that the SSDP is being integrated over more (or less) than $-7T$ to $7T$.

In this thesis, the CTDI is calculated from a single slice ion chamber measurement using the following expression (Rothenberg and Pentlow, 1995)

$$\begin{aligned} \text{CTDI} &= \frac{1}{T}\int_{-7T}^{7T} D(z)\, dz \\ &= \frac{\frac{1}{T}\int_{7T}^{7T} D(z)dz}{\frac{1}{T}\int_{-L/2}^{L/2} D(z)dz}\,\frac{1}{T}\int_{-L/2}^{L/2} D(z)dz \\ &= CF \cdot \frac{C \cdot L \cdot X}{T} \quad \text{[cGy]} \end{aligned} \tag{6.67}$$

where CF is the correction factor given by (6.66), T is the slice thickness, C is the ion chamber calibration factor (cGy/electrometer reading) , L is the ion chamber length, and X is the ion chamber reading. Note that the last equality in (6.67) is valid because the

dose measurement over the ion chamber length integrates the SSDP from $-L/2$ to $L/2$ (Knox and Gagne, 1996).

By definition, the slice thickness T is equal to the slice spacing I when determining the CTDI. Although this is appropriate for diagnostic CT scanners, images collected using the ^{192}Ir source-based CT scanner will utilize a slice spacing greater than the image slice thickness[7]. When $T \neq I$, the patient dose is characterized by the multiple-scan average dose (MSAD) given by (Rothenberg and Pentlow, 1995)

$$\begin{aligned}
\text{MSAD} &= \frac{1}{I}\int_{-I/2}^{I/2} D_{N,I}(z)\,dz \\
&= \frac{\frac{1}{I}\int_{-I/2}^{I/2} D_{N,I}(z)\,dz}{\frac{1}{T}\int_{-L/2}^{L/2} D(z)dz}\,\frac{1}{T}\int_{-L/2}^{L/2} D(z)dz \\
&= \frac{\frac{1}{T}\int_{-I/2}^{I/2} D_{N,I}(z)\,dz}{\frac{1}{T}\int_{-L/2}^{L/2} D(z)dz}\cdot\frac{C\cdot L\cdot X}{I} \\
&= CF'\cdot\frac{C\cdot L\cdot X}{I} \quad [\text{cGy}]
\end{aligned} \tag{6.68}$$

where $D_{N,I}(z)$ is the MSDP for N scans with spacing I.

6.4.2 Method

Two measurements were performed to assess the patient dose. The first measurement using an ion chamber array determines the SSDP as required by (6.66) to calculate the factor CF. The second measurement determines the exposure X for a single slice, from which the CTDI (6.67) or MSAD (6.68) can be determined.

The SSDP was measured using an array of 47 ion chambers (LA48 PTW Freiburg) "sandwiched" between 8.3 cm of Plexiglas attenuation and 3.4 cm of

[7] The image slice thickness of the ^{192}Ir source-based CT scanner is about 0.38 cm (Figure 5.12), while the radiation slice thickness is about 2.66 cm (Table 5.4). The large difference between the image and radiation slice thickness occurs because the source has no additional collimation, as would be the case for the x-ray tube in a conventional CT scanner which has an x-ray beam collimator traveling around the patient along with the x-ray tube. For the fourth generation ^{192}Ir source-based CT scanner, the source has no separate collimator in the interest of design simplicity.

backscatter, to simulate a water phantom. The ion chamber array was positioned perpendicular to the prototype collimators (Figure 5.11b) at a distance of 34.4 cm from the source (Figure 6.42a) to mimic alignment of the ion chamber array with the scanner axis.

The ion chamber array consists of liquid-filled ionization chambers (4 x 4 x 0.5 mm^3) spaced 8 mm apart. To obtain a finer sample spacing for the SSDP measurements, the collimators were moved in 2 mm increments using a translation stage, to yield four profile measurements. These data were interleaved to obtain a single profile, which was used to find the factor *CF* given by (6.66). When measuring the SSDP, the ion chamber array was operated in integrate mode to reduce noise. A total of three trials, each (900 s/position) x (4 positions) = 3600 s in duration were performed. These were averaged and corrected for background.

The SSDP profile measurements made using the ion chamber array do not provide an absolute dose measurement. The latter was found using a 10 cm long ion chamber (MDH 1015C; Radcal 10x5-10.3 CT) placed at the centre of a 32 cm diameter Plexiglas body phantom, aligned 34.4 cm from the source (A_c = 5.6310 Ci). The prototype collimators (Figure 5.11b) were used to collimate the source, as shown in Figure 6.42b. The exposure for three 100 s irradiations was found and corrected for background.

The calibration factor *C* for the 10 cm CT ion chamber at the mean energy of ^{192}Ir (355 keV) was not provided by the manufacturer. The ion chamber was therefore calibrated using an orthovoltage 250 kVp beam (Therapax 3 Series, Theratronics) and a Cobalt radiotherapy machine (Theratron 780C). The orthovoltage measurement was performed in air and the cobalt measurment was carried out using a buildup cap, such that the ion chamber was at the depth of maximum dose d_{max} = 0.5 cm. Both ion chamber measurements were corrected to account for temperature and pressure, field size, and absence of surrounding phantom material (Khan, 1994). In each instance, the ion chamber was irradiated with a known dose and a calibration factor found. The calibration factor *C* for 355 keV photons was then found using linear interpolation.

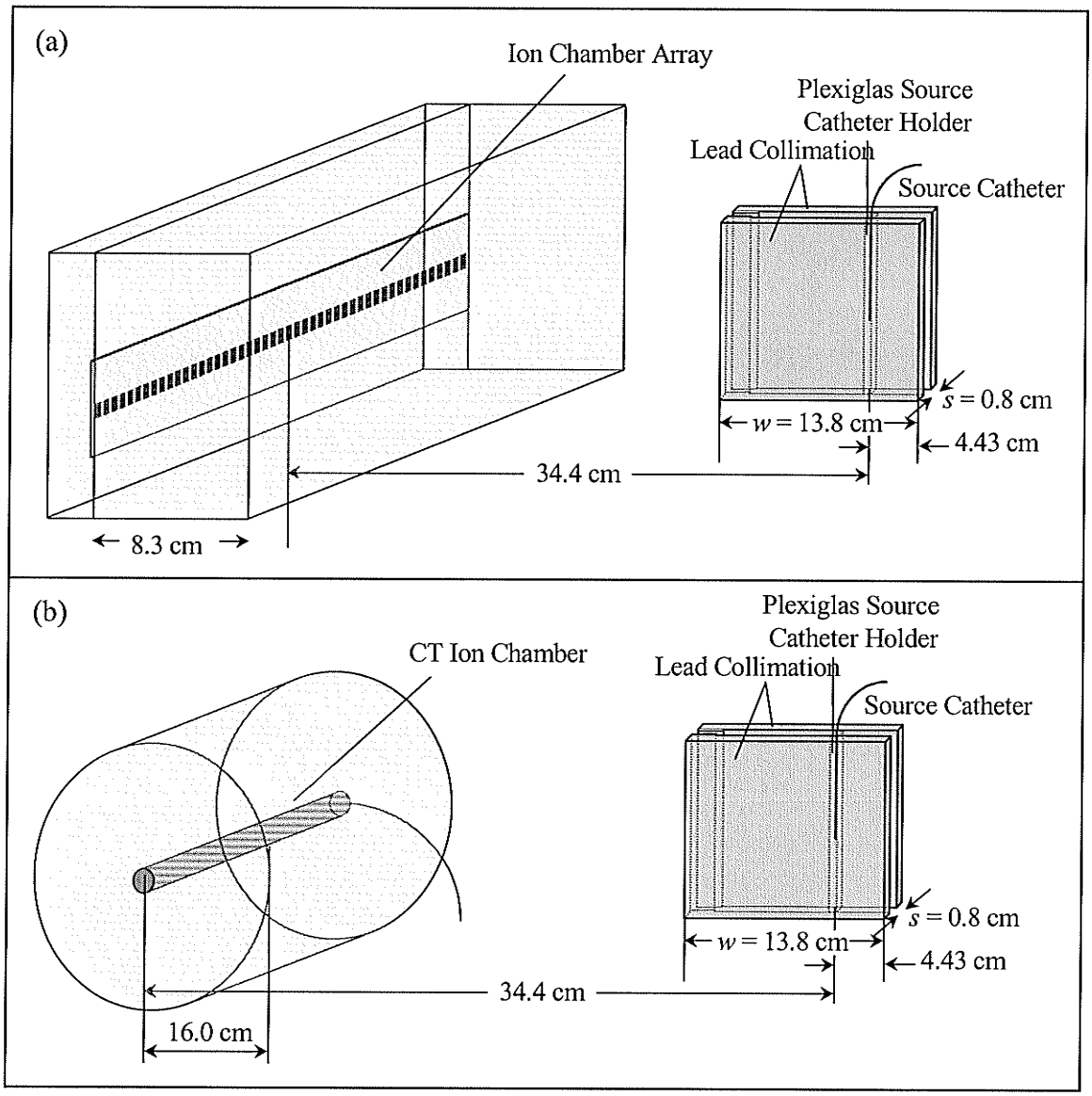

Figure 6.42 Experimental set-up used for (a) the SSDP measurements using the ion chamber array and (b) the CT ion chamber measurements. The goal of the set-up shown is to mimic the irradiation conditions along the axis of the fourth generation ^{192}Ir source-based CT scanner.

6.4.3 Results

The SSDP collected using the ion chamber array is shown in Figure 6.43. The scatter in the data occurs because of the low fluence of the ^{192}Ir source. Ideally, the SSDP would have been measured at the centre of the cylindrical phantom shown in Figure 6.42b. This could have been achieved by placing TLDs inside of the hole reserved for the CT ion chamber (Rothenberg and Pentlow, 1995). However, the low γ-ray fluence of the ^{192}Ir

source would have required prohibitively long irradiation times. Note also that that the thickness of the Plexiglas buildup used for the ion chamber array (8.3 cm) is considerably less than the radius of the Plexiglas body phantom (16 cm) used in Figure 6.42b. (The 8.3 cm of buildup used to measure the SSDP is appropriate for dose measurements made using an 8 cm radius head phantom.) SSDP measurements made using 15 cm of Plexiglas buildup were quite noisy, and are therefore not used. Note that the FWHM of the profiles measured using 8.3 cm and 15 cm of buildup are quite similar, although the relative magnitude of scatter is larger for the profiles measured using 15 cm of buildup. Calculations indicate that this has a small influence on the factor CF calculated using (6.66).

The CTDI was calculated from the CT ion chamber measurements by incorporating the following parameters into (6.67): C = 1.19 cGy/electrometer reading, CF = 0.811 (found using (6.66)), L = 10.0 cm, T = 0.4 cm, and an ion chamber reading X = 59.3 x 10^{-3} electrometer reading (A_c = 5.6310 Ci, 100 s irradiation). Scaling the ion chamber reading X to a 7.5 Ci source ($7.5\,\text{Ci}/5.6\,\text{Ci} \times 59.3$ x 10^{-3} electrometer reading = 79.4 x 10^{-3} electrometer reading) yields CTDI = 1.92 cGy (A_c = 7.5 Ci, 100 s irradiation). The MSAD for a 1.0 cm slice spacing (proposed slice spacing for the final scanner) and 14 scans evaluated using (6.68) and $CF'_{1\text{cm}}$ = 1.14 was found to equal 1.07 cGy (A_c = 7.5 Ci, 100 s irradiation).

The MSDPs for the two slice spacings I = 0.4 cm and I = 1.0 cm are shown in Figure 6.44. The decrease in dose with increasing slice spacing is evident. Increasing the slice spacing to equal the width of the SSDP would further reduce the patient dose, but would provide inadequate resolution in the axial direction.

Note that the dose is proportional to the source strength and the irradiation time. As the source strength decreases, it may be necessary to increase the irradiation time in order to maintain an acceptable low contrast resolution, i.e., for the image dose to remain constant. Similarly, if an improved low contrast resolution is desired for a given source strength, it would also be necessary to increase the irradiation time. However, this would result in an increase in patient dose.

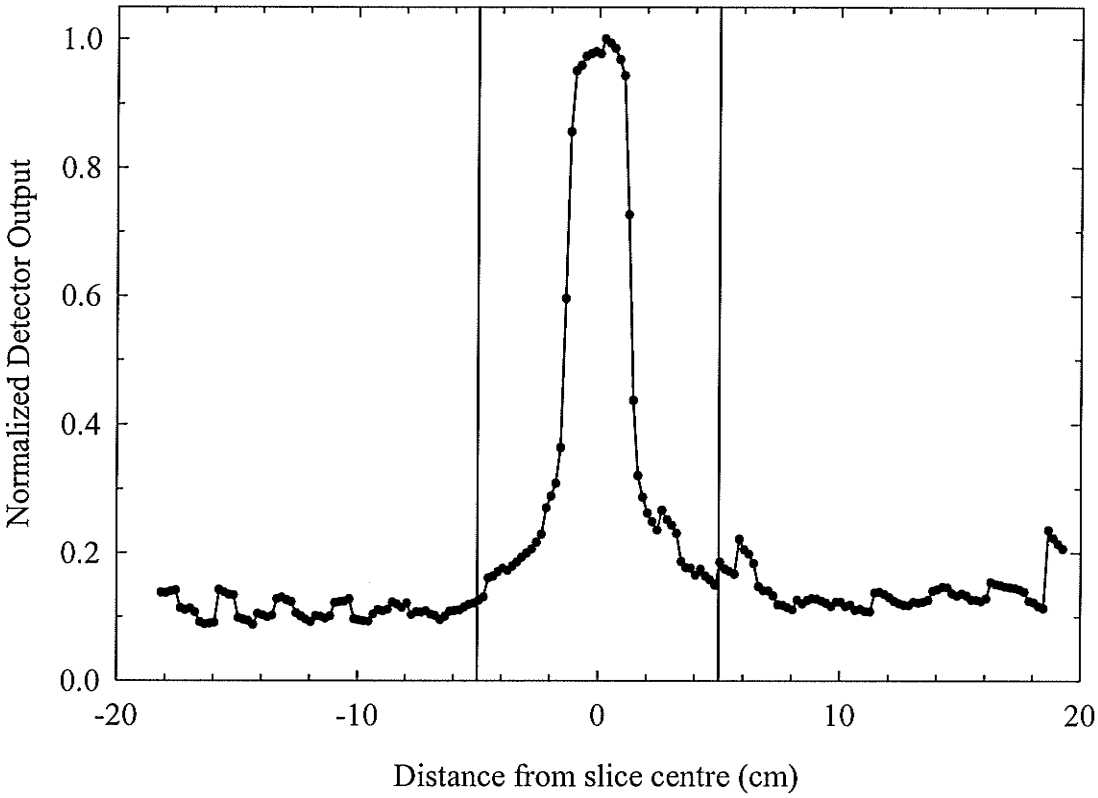

Figure 6.43 SSDP taken using an ion chamber array with 8.3 cm of buildup. The vertical lines at –5 cm and 5 cm represent the extent of the ion chamber used to make the CTDI measurement.

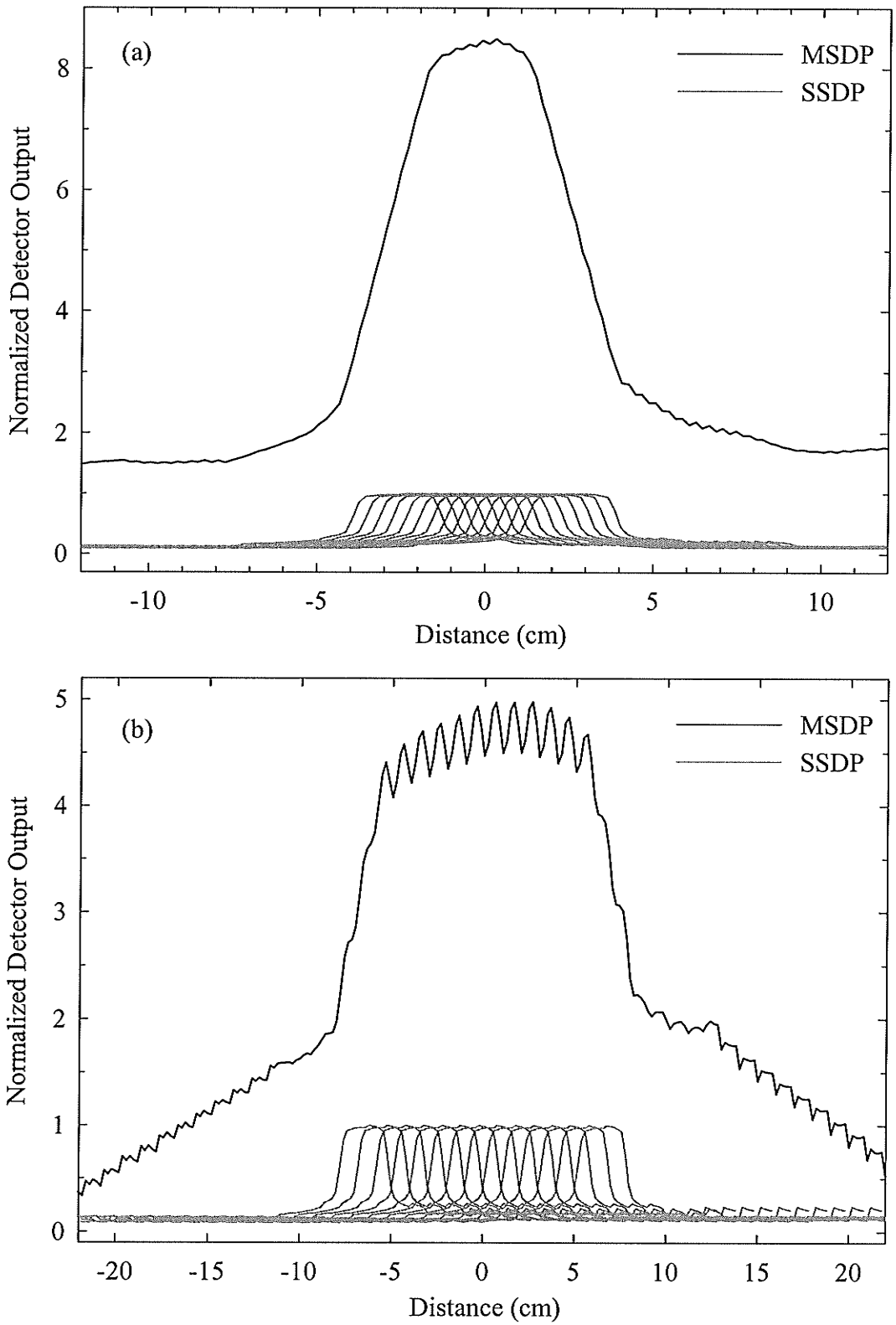

Figure 6.44 MSDPs of 14 scans using slice spacings of (a) 0.4 cm and (b) 1.0 cm.

Chapter 7

Discussion and Conclusion

This thesis describes and characterizes the sub-systems (source, detectors, data acquisition system and collimator) of a prototype fourth generation CT scanner that uses the ^{192}Ir isotope from a commercial HDR brachytherapy treatment unit. The MTF and NPS of the system were studied by using a combination of measurements and computer simulations.

7.1 Instrumentation

Chapter 2 provides a description of the source and the detector electronics, and gives justification for the choice of scintillating crystal material and dimensions used in the scanner.

The scintillator $CdWO_4$ was chosen on the basis of its attenuation coefficient, non-hygroscopic nature, large luminous efficiency and low afterglow. An alternative scintillator, CsI(Tl), possesses a larger luminous efficiency and an optical emission spectrum more closely matched to the photodiode sensitivity, but suffers from 10 times

larger afterglow than that of $CdWO_4$ measured at 100 ms (Grabmeier, 1984). More importantly, CsI(Tl) has a much lower attenuation coefficient than $CdWO_4$. $CdWO_4$ is therefore the more suitable scintillator.

The scintillating crystal dimensions were chosen to be 8.0 x 2.75 x 10.0 mm^3 (length x width x thickness) on the basis of the measurements in §2.5. The crystal width of 2.75 mm is fixed by the spacing of the photodiode array elements. The 8% increase in detector output and 10% increase in SNR observed when increasing the crystal length from 8.0 mm to 12.0 mm (Figure 2.13) is accompanied by an approximate 50% increase in the crystal cost. It was therefore decided to use the 0.8 cm long crystals in the final scanner. A larger crystal thickness of 12.0 mm would have increased the detector output by 3% and increased the SNR by 12%. However, this improvement comes with a 20% increase in crystal cost. Further increasing the crystal thickness results in a decrease in detector output (Figure 2.12). This effect was also observed by Mosleh-Shirazi et al. (1998) when performing Monte Carlo calculations and measurements at 6 MV of the light emission of BGO and CsI(Tl) scintillators as a function of crystal height, and by Vittori et al. (2000) who studied the light emission of YAP:Ce and CsI(Tl) scintillators using Monte Carlo and ^{57}Co. The detector output decreases for crystals beyond a certain thickness because of light losses due to effects such as absorption in the crystal coating material and in the scintillator itself. More importantly, optical photons incident on the crystal surfaces at angles greater than the critical angle are reflected back into the crystal. They then undergo multiple internal reflections and are generally absorbed at the crystal surfaces. Assuming Lambertian reflection, where the angle of reflection may be different from the incident angle (Vittori et al., 2000), the optical photon may eventually impinge on the exit crystal surface at an angle less than the critical angle, at which point it may be detected. However, the taller the crystal, the more likely it will impinge on one of the other crystal walls, resulting in a decreasing light emission with increasing crystal length (Mosleh-Shirazi et al., 1998). Although the crystals and photon energies used by Mosleh-Shirazi et al. and Vittori et al. differ from those used in this study, similar principles apply.

Gelcoat was found to be the most suitable crystal coating material on the basis of (i) detector output, which characterizes the ability of the coating material to reflect optical photons trying to escape the crystal back into the crystal, whereupon they may be detected; (ii) coating material opacity, which determines the ability of the coating material to prevent photons generated in one crystal from reaching the next crystal, influencing the magnitude of the optical cross-talk; and, (iii) appropriateness for crystal array manufacturer, i.e. ease with which crystal arrays can be manufactured. Although Teflon tape resulted in a higher detector output (Figure 2.15), it would be difficult to construct crystal arrays using this material. In addition, the detector response decreased as a function of time because the optical coupling gel permeated the Teflon tape rendering it translucent. Measurements of the effectiveness of array masks (Figure 2.11) found that Bare-Metal Foil (BMF) and 3M 850 tape increased the detector output up to 31% and 22%, respectively, compared to measurements made in the absence of a mask. Gelcoat coated crystal arrays were easily constructed. Note that in the final scanner, 3M 850 tape was used because it was easier to apply.

7.2 System Characterization: Single-Channel Measurements

The behavior of a prototype single-channel detector was characterized in Chapter 3. The electronic noise analysis considered the noise in the detector output voltage. This analysis showed that the electronic noise is less than the γ-ray quantum noise expected when imaging all patients that can be accommodated by the scanner. The measured electronic noise of about 115 μV at a 10 Hz sampling frequency (Table 3.4) results from various electronic noise sources in the gated integrator and gain-and-filter stage. The largest noise source, due to charge injection in the analogue switch described in §3.1.1.3, was eliminated by sampling the output of the gain-and-filter stage twice during the integration cycle, namely, at time T_i to yield voltage V_i and at time T_f to yield V_f, and then subtracting these values to give $\Delta V = V_f - V_i$. Using the detector output data of Figure 3.7 and $n = 128$, $\sigma_{V_f} \approx 190\,\mu$V and $\sigma_{V_i} \approx 180\,\mu$V, while $\sigma_{\Delta V} \approx 115\,\mu$V. This clearly demonstrates the noise reduction provided by the subtraction process. The second largest noise source is due to the combined effect of the photodiode noise current, the op-amp input noise

current and the switch leakage current noise. Of these, the noise contribution of the op-amp dominates. Any efforts to further reduce the electronic noise should focus on reducing the input noise current of the op-amp.

The theoretical estimate of the standard deviation in the detector output (electronic noise only) plotted in Figure 3.2 agrees somewhat with the experimental measurements, considering that the manufacturer's typical values used to calculate the theoretical noise may vary substantially from the noise characteristics of the actual components used. The standard deviation in the detector output decreases with increasing sampling frequency because the noise power decreases. Mathematically, there is a decrease with sampling rate in the area under the product of the integrator transfer function and the gain-and-filter stage transfer function (see Figure 3.1). Because the standard deviation is the integral of the NPS over frequency, a decrease in the area under the NPS results in a decrease in the standard deviation. Note however that this does not provide justification for using an increased sampling frequency since the signal also decreases, with the overall effect being a reduction in the SNR with increasing sampling frequency. That is, the SNR for the data in Figure 3.33 decreases with increasing sampling frequency.

A sampling frequency of 10 Hz is proposed for the final scanner. This corresponds to the minimum dwell time (time the source can be programmed to remain at a particular position) imposed by the HDR BT treatment unit, and allows a scan to be completed in less than 100 seconds. If a higher SNR is required, the dwell times could be increased in multiples of 0.1 s. For instance, doubling the dwell time to 0.2 s would increase the SNR by a factor of $\sqrt{2}$.

The power spectra presented in §3.2 indicate that the detector noise is white, except for power line interference spikes and a low-frequency component due to a long-term drift in the detector output voltage. The contribution of power line interference to the total noise standard deviation is insignificant as the power contained in these peaks is small compared to the total power. Notice that the power line interference spikes are not visible in Figure 3.12 as they have been completely obscured by the quantum noise. The fourth generation scanner will incorporate electro-magnetic shielding to minimize the

electrical interference. The long term drift is also not expected to be a problem because the imaging time is only about 100 s per slice, whereas the 10 Hz data used to generate the power spectra in §3.2 were collected over 5000 s. Typically, the drift in the detector voltage in the absence of light is about 40 μV/minute. Thus over a 100 s scan, the magnitude of the drift is about a factor of two smaller than the electronic noise. Electromagnetic shielding is also expected to reduce the interference contribution to the long term drift (recall Figures 3.7 and 3.9, along with the associated discussion in §3.2.3.3). In addition, the temperature contribution to the long term drift can be corrected for by simply monitoring the detector temperature. The lack of high-frequency roll off in the power spectra plotted in Figures 3.4 to 3.9 can be understood by recognizing that the sampling frequency equals the integrate discharge frequency. In other words, we are sampling at f_N rather than $2f_N$, and thus the power spectrum is inherently aliased. Sampling at frequencies greater than f_N would require decoupling of the integration from the sampling, which is nonsensical for the circuit design presented. The quantum noise power spectra in Figure 3.12 show that the noise power decreases as the source-to-detector distance increases, as expected.

Possibly the most important parameter describing the detector is the SNR. Figure 3.11 shows both the total and the electronic SNR in the presence of a patient as simulated by variable thicknesses of Plexiglas absorber. The SNR resulting from the γ-ray quantum noise is much less than the SNR due to electronic noise at all signal levels, indicating that the detector output is dominated by quantum noise, rather than electronic noise. This indicates that the photon statistics and detector efficiency (strictly DQE) rather than the electronic noise will limit the scanner's SNR and therefore the low contrast resolution.

The detector linearity was evaluated using both optical photons and γ-rays. The measurements made using optical photons found the detector output to be reasonably linear (Figure 3.25; standard error of estimate with respect to the mean = 0.3%) between 8×10^{-11} W/cm^2 and 3×10^{-8} W/cm^2 of incident light power, corresponding to 2.6 orders of magnitude. Note that a light power of 8×10^{-11} W/cm^2 approximately corresponds to the light output of the scintillator in the presence of a 7.5 Ci source placed 74 cm from the detector and attenuated by 42 cm of Plexiglas. Because the scanner can

only accommodate patients up to 50 cm in diameter (inner bore diameter = 50 cm), the detector is linear over a range that is adequate for this application. The response of the detector to narrow-beam collimated γ-rays (Figure 3.40) also agrees well with the expected trend calculated using (3.103) (standard error of estimate with respect to the mean = 3.8%) for Plexiglas thicknesses up to 45.5 cm, which confirms the conclusions drawn from the optical photon measurements.

The fourth generation scanner uses the collimation presented in §5.3 rather than narrow beam collimation, resulting in the detection of more scattered radiation. Figure 3.39 shows the detector output as a function of Plexiglas attenuator thickness using collimation similar to that of the fourth generation scanner. This plot is a more realistic representation of the detector output than Figure 3.40, and shows that the contribution of scatter to the detector output is substantial for large Plexiglas thicknesses. In general, scatter is a problem in fourth generation scanners (Arenson, 1995) because the relative orientation of the source and the detectors is not fixed, hindering incorporation of focussed scatter rejection collimation. The effect of scatter in CT is to produce shading and streak artifacts, and quantitative errors in the CT number (Glover, 1982; Hsieh, 1995; Johns and Yaffe, 1982; Joseph, 1981; Joseph and Spital, 1982; Merritt and Chenery, 1986). These occur because the presence of scatter causes inconsistencies in the projection data, namely, $\log(N_{true}+N_{scatter}) \neq \log(N_{true}) + \log(N_{scatter})$, where N_{true} is the number of primary photons and $N_{scatter}$ is the number of scattered photons (Joseph, 1981). In other words, contrary to planar radiographs where uniform scatter produces a uniform darkening of the image, scatter in CT does not uniformly increase the magnitude of the projection data because of the nonlinear logarithmic operation. Artifacts are most prevalent when the scatter-to-primary ratio (S/P) is large, which is the case for large objects containing high density inhomogeneities (Joseph and Spital, 1982; Glover, 1982). Figure 3.39 indicates that the S/P ratio for a 20 cm Plexiglas thickness is 24%, and at 35 cm, half of the signal is due to scatter. The large percentage of scatter is due to inadequate collimation of the ^{192}Ir photons as confirmed by the S/P expression[1]

[1] The expression of Johns and Yaffe predicts the scatter-to-primary ratio for 120 kVp photons. They further demonstrate that the S/P ratio has little energy dependence between 60 kVp and 140 kVp when using a

developed by Johns and Yaffe (1982). The latter predicts S/P = 12% and 73% for a 20 cm and 35 cm phantom, respectively, for the experimental set-up illustrated in Figure 3.10. In contrast, the S/P ratio for a diagnostic fourth generation scanner with a detector distance R_d = 40 cm (measured from the scanner central axis), irradiated slice thickness t = 6 mm and no post-patient collimation is on the order of 14% for a body scan, i.e., a 30 cm diameter phantom (Johns and Yaffe, 1982). A few studies have corrected for the effects of scatter on CT images in software (Ohnesorge et al., 1999; Joseph and Spital, 1982; Glover, 1982), and diagnostic scanners routinely use proprietary scatter correction algorithms. It is expected that the images produced by our scanner will exhibit artifacts due to scatter, requiring software corrections to be incorporated. Alternatively, the slice thickness could be reduced by using the moving collimator design described in §7.7.

Another effect that produces artifacts similar to those produced by scatter is beam hardening (Joseph, 1981), although in our scanner the impact of this effect is much smaller than that of scatter. Deviation of the detector output predicted by (3.103), which includes the effect of the polychromatic ^{192}Ir spectrum, from a straight line is 4% and 13% for Plexiglas thicknesses of 20 cm and 35 cm, respectively. The detector output prediction incorporating the ^{192}Ir spectrum is greater than that assuming monoenergetic photons because beam hardening causes the attenuation coefficient to decrease with increasing Plexiglas thickness, resulting in an increased transmission. Note however that the beam hardening associated with ^{192}Ir is much less than for a conventional CT scanner. This is confirmed by Figure 3.46a showing a phantom containing metal BT needles (collected using a single detector channel and the ^{192}Ir source), which displays fewer beam hardening streaks than Figure 3.46b[2] (collected using a diagnostic CT scanner). More specifically, the energy dependence of the attenuation coefficient is minimal for Compton interactions. Beam hardening is therefore not of concern in our scanner.

The first generation images shown in §3.8 demonstrate the use of the detector in a CT scanner. As can be seen, the preliminary CT images are free of serious artifacts.

---

rectangular phantom. The energy of ^{192}Ir is clearly much greater than 140 kVp, but the expression of Johns and Yaffe can still be used to obtain an estimate of the expected scatter.

[2] Manufacturer has already incorporated a beam hardening correction.

Although the high average photon energy of ^{192}Ir raised concerns regarding the achievable low contrast resolution, the image contrast is adequate to distinguish between bone, lung and soft-tissue in the non-eviscerated chicken (Figure 3.45). In addition, the high photon energy provides the advantage that metal can be imaged without streak artifacts (Figure 3.46a), which have been reported to obscure structures of interest in diagnostic scans of gynecological implants (Stuecklschweiger et al., 1991). The relatively high energies of the γ-rays however reduce contrast compared to a diagnostic scanner. Artifacts resulting from scatter are not a problem in these images due to the small size of the objects, as predicted by Figure 3.39.

7.3 System Characterization: Eight-Channel Measurements

Chapter 4 characterizes parameters specific to the eight-channel detector. More specifically, measurements of the inter-channel variability and cross-talk for the eight-channel detector are discussed. In our scanner the inter-channel variability is automatically corrected for because the detector signal V is divided by the air scan data V_0 when calculating the projection data $P = -\ln(V/V_0)$. A large inter-channel variability, however, would suggest a problem with the detector design or the presence of a faulty component.

The total variability of the eight channels of a detector assembly (normalized to the channel with the greatest response) was found to be 11.5% for the Al_2O_3 coated array and 4.4% for the gelcoat coated array (Table 4.2). The electronic gain variability, which reflects the variation in the components constituting the gated integrator and the gain-and-filter stage of each detector, was found to be 2.2% (Table 4.1). The crystal and photodiode array variability, which is due to variations in the photodiode array channels, the individual crystals, and the coupling of the crystals to the photodiode array was 9.9% for the Al_2O_3 coated array and 2.6% for the gelcoat coated array (Table 4.3). From these measurements, it is obvious that the gelcoat coated array is a better choice. The higher crystal and photodiode array variability of the Al_2O_3 coated array is due to the light leakage from the outer channels (Figure 4.2a). For the gelcoat coated array, the electronic and crystal array variability are nearly the same.

Cross-talk is an important parameter that affects image quality. Spillover in signal from one detector channel to the neighboring channels results in reduced resolution and inconsistencies in the measured projection data. Two techniques were described for characterizing the cross-talk between channels. The first technique used the cross-covariance and has the advantage that it can measure cross-talk due to the electronic components in the absence of optical photons or γ-rays. A large amount of electronic cross-talk would indicate that the electronic noise between channels is correlated, leading to serious image artifacts (Parker et al., 1982). The second technique used a narrowly collimated γ-ray source to measure the cross-talk between crystals and provided a more intuitive understanding of cross-talk.

Analysis of cross-talk in the absence of optical photons or γ-rays using the cross-covariance technique revealed no measurable cross-talk in the detector electronics. However, the component specifications give cross-talk values for the op-amps, sample-and-hold, switches and the MUX. In the worst case, the cross-talk is –50 dB for the MUX at 3 MHz; it is expected that the cross-talk is much less at the 10 Hz operating frequency of the detector. A plot of the cross-covariance (Figure 4.6) and the corresponding cross-power spectrum (Figure 4.7) in the absence of light shows 60 Hz and 120 Hz interference from electric power lines. However, the power under these peaks is insignificant compared to the total power, and will therefore have no impact on the image quality. The cross-covariance technique revealed a measurable level of cross-talk between adjacent channels when the detector assembly was irradiated with γ-rays. However, the fluctuations in the cross-covariance plots (Figure 4.12) are too great to characterize cross-talk beyond nearest neighbors.

The second technique for measuring cross-talk used a narrowly collimated ^{192}Ir source. The data plotted in Figure 4.15 show that the cross-talk for the Al_2O_3 coated array is significant and extends essentially the entire detector array. The nearest-neighbor cross-talk is about 20% and the next-nearest-neighbor cross-talk is about 7%. The decrease in cross-talk for the gelcoat coated array (Figure 4.17) is evident: the nearest-neighbor cross-talk is about 13% and the next-nearest-neighbor cross-talk is about 2%. This reduction in cross-talk is expected considering that the optical density of gelcoat is

much greater than that of Al_2O_3 (Figure 2.16). The remaining cross-talk shown in Figure 4.17 must therefore be primarily a consequence of radiation cross-talk, i.e., intercrystal scattering of γ-rays. The lack of cross-talk in measurements made using optical photons (Figure 4.18) confirm that the cross-talk visible when using γ-rays (Figures 4.15 and 4.17) is indeed associated with radiation or optical cross-talk in the crystal array as opposed to inadequate collimation of the source (which would have led to more than one crystal being simultaneously irradiated), or cross-talk in the electronics.

Note that the photodiode array manufacturer could have provided photodiode arrays without a protective epoxy layer. Mounting the crystal arrays directly onto the photodiode arrays may have further reduced the cross-talk because the small gap between the crystals and the active elements would then have been reduced (the gap produced by the optical coupling gel would still be present). However, we were cautioned against doing this, as the unprotected photodiode arrays are very fragile.

7.4 Scanner Design

The filtered backprojection reconstruction algorithm used to transform the projection data collected by the scanner into transverse images requires accurate knowledge of the source locations used during data acquisition. Otherwise, large deviations from the source positions used by the algorithm would lead to artifacts in the reconstructed image (Joseph, 1981). The imprecision in the source position was measured to be less than 0.12 mm. Because this is much smaller than the source spacing of 2.5 mm utilized by the scanner, it is not expected to introduce any errors in the image reconstruction.

The length of the ^{192}Ir source is one of the parameters discussed in Chapter 6 that determines the scanner resolution. Although the manufacturer of the HDR BT treatment unit provided source dimensions, an independent verification of source size and uniformity was performed. The measured length of 3.6 mm agrees well with the manufacturer's value of 3.5 mm. The source intensity was uniform to within 0.8% along its length. Although not significant to the scanner design, the source width was also measured and found to agree with the manufacturer's value of 0.6 mm to within 15%.

It is interesting to note that the above results also have an impact on BT treatments (Berndt et al., 2000b). In stepping source BT, it is essential that the source be positioned accurately and reproducibly. In addition, the source length must be accurately known for dose distribution calculations. These results show that the HDR BT treatment unit is not a source of significant errors in clinical treatments.

The current scanner design was based on a decision to locate all possible source dwell positions uniformly around the patient. The largest source ring radius is therefore 34.38 cm.

To obtain the sharpest collimation, the collimator annulus should be as wide as possible while still enabling the patient to fit into the scanner. Clearly, the bore radius must be smaller than the source ring radius (34.38 cm). The minimum bore radius in commercial CT scanners is 22.5 cm (Arenson, 1995). The lateral half-separations of some of the brachytherapy patients approaches this value, providing a lower limit for this parameter. Thus, a slightly larger radius of 25 cm was chosen to accommodate these larger patients and an existing scanner couch. The scanner design does permit the bore radius to be reduced if required.

The trade-offs involved in deciding the detector ring radius are complex, and the radius of 38.81 cm, corresponding to 768 detectors was chosen for a number of reasons. First, the minimum detector ring radius is constrained by the source ring radius, while a larger detector ring radius would reduce the already low photon fluence, and would increase the scanner cost because a larger number of detectors would be required. The number of detectors must also work well with digital electronics. Many electronic components come in eight channels per package. Thus, the number of detector assemblies should be a multiple of eight. The impact of the number of detectors on view sampling requirements was also important and is discussed in detail in §7.5.

7.5 Image Quality

A computer technique for simulating fourth generation CT scanner data collection and image reconstruction is described in Chapter 6. This technique was used to characterize the high contrast spatial resolution and image noise.

The high contrast resolution was examined by finding the PSF and the MTF as a function of source size and spacing, detector size and spacing, and filter function. The beam profile was determined by modeling both the source intensity and detector sensitivity distributions as rect functions. Modeling the source intensity as a rect function is verified by the profile shown in Figure 5.6a. In addition, Figure 4.17 shows the response of the detector array as it is translated past the collimated source and illustrates that the detector sensitivity distribution is well approximated by a rect function.

The FWHM of the scanner PSF depends upon a number of parameters, including the scanner geometry (number of source positions and source size, number of detectors and detector size) and filter function (Blumenfeld and Glover, 1981).

As expected, Figure 6.17 shows how the PSF width decreases with decreasing source length. For example, reducing the source length from 3.6 mm to 2.0 mm for n_s = 864 source positions would result in a 13% decrease in the PSF width. Therefore the smaller the source, the finer the spatial resolution. However, this will increase image noise or scan time unless there is a corresponding increase in specific activity, or an increase in source width, which is undesirable for BT treatments.

The FWHM of the beam profile at the scanner center is determined by the source and detector sizes. In this scanner with n_d = 768 detectors, the source length of 3.6 mm in the slice plane dominates the FWHM of the beam profile, meaning that a smaller detector size would provide only minimal improvement in the PSF. However, reducing the number of detectors by a factor of two, i.e., 5.9 mm wide detectors, causes the detector width to dominate the FWHM of the beam profile (this is the case for n_d 610; when n_d = 610, the scaled source length $s_{l\text{-}sc}$ equals the scaled detector width $d_{w\text{-}sc}$), leading to an increased width for the PSF (Figure 6.20). These results demonstrate that a significant increase in resolution would require a reduction in both source length and detector width.

The inherent resolution of a CT scanner is determined by the FWHM b of the beam profile at the scanner center, which gives a maximum resolvable frequency of $f_{scanner}$ 1/b in the CT images (Schultz and Felix, 1980; Joseph, 1981). The maximum resolvable frequency associated with the radial sample spacing Δx (determined by the number of source positions) is f_{sample} = $1/2\Delta x$. Theoretically, aliasing in the radial

direction does not occur[3] if $f_{sample} \geq f_{scanner}$, or equivalently $b \geq 2\Delta x$. The FWHM of the beam profile at the center of the ^{192}Ir source-based CT scanner is effectively equal to the larger of the scaled source length $s_{l\text{-}sc}$ or the detector width $d_{w\text{-}sc}$. For the present design the FWHM is equal to $s_{l\text{-}sc}$= 1.86 mm, which corresponds to a maximum resolvable frequency $f_{scanner}$ = 0.54 lp/mm. The mean sample spacing for n_s = 864 is Δx = 1.33 mm, resulting in f_{sample} = 0.38 lp/mm. Since $f_{sample} < f_{scanner}$, aliasing induced streak artifacts may be present near sharp discontinuities. The effects of aliasing are evident in Figure 6.17 where the width of the PSF increases for fewer source positions. This is because the images become aliased when n_s is reduced. Of the results shown in Figure 6.17, only images corresponding to n_s = 1728 are free from aliasing artifacts. Aliasing can be prevented if the number of source positions n_s is increased to ≥ 1232. Because the present HDR BT treatment unit software does not allow this, other techniques must be used to prevent aliasing as discussed in §7.7.

The above analysis assumes a rectangular beam profile whereas the actual beam profile is trapezoidal. The frequency representation of the latter is the product of two sinc functions, which has smaller sidelobes than a sinc function. Thus, a trapezoidal beam profile will result in less aliasing than a rectangular beam profile, even though they both have the same FWHM. A more detailed analysis incorporating the effect of the beam profile (Stockham, 1979) is planned for the future.

In the fourth generation scanner the number of detectors n_d is equal to the number of projections. The number of projections, together with the maximum resolvable frequency discussed above determine the presence of view aliasing[4] described by Joseph and Schulz (1980), Joseph (1981), and Snyder and Cox (1977). They showed that an insufficient number of projections results in streaks at a distance from high density

[3] This analysis assumes a rectangular beam profile and negligible response beyond the first zero crossing of the sinc function, which is not entirely valid (Joseph, 1981). Thus some aliasing may still result even if this criterion is satisfied.

[4] The beam width and radial sample spacing determines the presence of aliasing within a projection. Too large of a sample spacing may result in streak artifacts. Digitally filtering the sampled projection data does not alleviate aliasing due to inadequate sample spacing. The number of projections required to prevent view sampling artifacts depends on the maximum frequency present in the projection data and the object size. Digitally filtering the projection data to reduce the maximum frequency reduces the number of projections required to prevent view sampling artifacts. (Joseph, 1981)

objects. Conventionally, projection requirements are based on providing an artifact free scan circle of diameter D for a dense object at the center of the scanner. This criterion requires that the number of projections over 180° be given by $\pi D f_{max}$, where f_{max} is the maximum frequency in the projection data. Therefore, a total of 597 projections over 180° are required to provide an artifact free reproduction of maximum spatial frequency 0.38 lp/mm over a 50 cm diameter scan circle. Since the present detector arrangement provides only 384 projections over 180°, the artifact free circle is 32 cm in diameter. When a Shepp and Logan filter function is used to filter the projections, the artifact free circle diameter increases.

The effect of the filter function on the width of the PSF was demonstrated in §6.2.5. Although this parameter is related to the reconstruction algorithm rather than the scanner design, its impact is still of interest. Figure 6.23 shows that the RL filter results in a narrower PSF than when using a SL filter. This is because the RL filter nearly replicates the ideal $|f|$ function while the SL filter is obtained by sinusoidal apodization in frequency space to reduce the noise at high spatial frequencies.

The width of the PSF is also influenced by the choice of f_N (the filter cut-off frequency). The f_N value of 0.38 mm^{-1} corresponds to the conventional definition of $f_N = 1/2\Delta x$, where Δx is the sample spacing. For f_N values less than this smoothing of the image results, while f_N values close to this sharpen the image. Each of these options has advantages and disadvantages. Although the width of the PSF increases with decreasing f_N, it will also reduce image noise. In our scanner, high contrast resolution is not a primary concern because the objects that must be identified for treatment planning will be readily visible (Figure 3.46). (Planar radiographs must still be taken to identify the x-ray markers.) However, the images generated by the scanner will be somewhat noisy, e.g. Figure 3.47 due to the low fluence rate of the ^{192}Ir source. Thus, use of a SL filter is recommended to improve low contrast resolution. The value $f_N = 1/2\Delta x$ was chosen for the filter cut-off because larger or smaller f_N values result in ringing artifacts. The predicted resolution of the scanner using 768 detectors, 864 source positions, a source width of 3.6 mm, a detector width of 2.75 mm, a SL filter and linear interpolation is 0.37 lp/mm at 10% MTF and 0.51 lp/mm at 5% MTF. The FWHM of the PSF is 2.1 mm.

The effects of various scanner and reconstruction algorithm parameters on image noise were also examined in Chapter 6. The image SD was calculated as a function of filter function, interpolation method (the influence of interpolation method on scanner resolution was not examined), source activity, number of projections and sample spacing. The image SD was smaller for the SL than the RL filter because the SL filter more effectively reduces high frequency noise. NN interpolation resulted in an increased SD over LI because the latter has a smoothing effect on the projection data. Therefore LI will be used when reconstructing images for the scanner. When the number of photons per image was held constant, the image SD showed no dependence upon the number of projections. Interestingly, the image SD increased with decreasing sample spacing when the total number of photons used to generate the image was held constant. This is due to the effect of the filter function. Specifically, the filter cut-off frequency increases with decreasing sample spacing, resulting in noise at higher spatial frequencies in the filtered projection data. Consequently, decreasing the sampling spacing beyond that required to prevent aliasing is not desirable. The predicted noise at the center of a 25 cm diameter Plexiglas phantom generated using a 7.5 Ci source, 768 detectors, 864 source positions, a SL filter and linear interpolation is 23 HU.

The NPS analysis gives the noise power as a function of spatial frequency. In all instances the NPS increased with increasing frequency due to the shapes of the SL and RL filter functions, both of which increase with increasing frequency. Eventually a point was reached where this trend was reversed and the NPS decreased with further increases in frequency due to the interpolation required for filtered backprojection and the nature of the system's MTF. Comparison of the first and fourth generation NPS shown in Figures 6.38 and 6.40 reveal that the peaks in the fourth generation NPS appear at lower frequencies than in their first generation counterparts. This is due to the additional smoothing provided by the rebinning from fourth generation to first generation geometry. The results found by the SD analysis were confirmed by the NPS analysis. A RL filter and NN interpolation resulted in the largest noise, while images generated using a SL filter and LI contain the least noise. As stated above, a SL filter will be used as it results in lower noise in the images.

The dose delivered to a patient during a 100 s scan[5] was measured in Chapter 6. The MSAD for a 1.0 cm slice spacing of 1.07 cGy (100 s irradiation using a 7.5 Ci source) is lower than the CTDI of 2 - 4 cGy for a body scan generated using a 1.0 cm slice spacing on a conventional scanner (Rothenberg and Pentlow, 1995). The CTDI for a 0.4 cm slice spacing is 1.92 cGy (100 s irradiation using a 7.5 Ci source). The lower delivered dose however results in a low-contrast resolution and SNR inferior to that of a diagnostic scanner. Clearly, increasing the dose would increase the SNR. Although the dose is lower, it does not correspond well to the lower SNR, i.e., the SNR is lower than expected for the measured dose, when comparing to the SNR and the dose of a conventional CT scanner. This is because the ^{192}Ir source-based scanner makes poor use of dose due to the lack of additional source collimation (Figure 5.12). If the source were separately collimated as opposed to relying on the detector collimation, a lower patient dose would be incurred. One must, however, keep in mind that patient dose is not an issue with this scanner because most patients undergo external beam radiation therapy prior to their brachytherapy treatments. A typical external beam dose regimen delivers 5000 cGy or about 2500 times that given by our scanner. Even the uncertainty in the linear accelerator (used to deliver external beam treatments) calibration of ±2% is about 50 times higher, e.g. 100 cGy, than the dose given by our scanner.

7.6 The Scanner

The role of CT in planning, performing and assessing BT treatments has been clearly demonstrated. Treatments can be designed with better tumor volume coverage and less dose to the surrounding critical structures. However, conventional diagnostic scanners are not able to provide images cost effectively and reliably (due to patient transport issues). Although a dedicated in-room CT scanner would eliminate these problems, conventional scanners are expensive, large, and images at energies that would cause substantial streaking due to the beam hardening produced by the metal applicators. The ^{192}Ir source-based CT scanner described in this thesis is unique in that it is designed specifically to

[5] Actual irradiation time is (864 source positions) x (0.1 s) = 86.4 s. Note that this does not include the patient exposure incurred while the source is travelling to and from the HDR BT treatment unit.

overcome these limitations associated with imaging BT implants. The novel concepts of (i) using the BT treatment source to both image and treat a patient, and (ii) incorporating the source-transportation mechanism of a commercial HDR BT treatment unit (i.e. transporting the source at the end of a wire, driven by a computer controlled stepper) allows a compact, inexpensive in-room CT scanner to be constructed. In addition, the high energy of the ^{192}Ir source allows streak free images to be generated.

The measurements presented in this thesis show that the detector designed expressly for use in an ^{192}Ir source-based CT scanner has been effectively customized for the low γ-ray fluence and high average γ-ray energy of the ^{192}Ir source (355 keV). More specifically: the scintillating crystal (§2.4), array design (§2.5), and detector gain (§2.3.1.4) were chosen such that the detectors respond linearly to an incident γ-ray fluence for Plexiglas thicknesses up to at least 45.5 cm (§3.6); and, the detector electronics (§2.3.1) have been designed to ensure that the detector noise is dominated by quantum rather than electronic noise (§3.1 and §3.2, §3.3), despite the low source output and high energy of the ^{192}Ir source.

The predicted limiting resolution of the scanner is 0.51 lp/mm based on the 5% MTF while that for a commercial scanner is about 0.8 lp/mm for a pelvis image. The noise at the center of a 25 cm diameter Plexiglas phantom is about 23 HU and the MSAD for a 100 s irradiation and 7.5 Ci source strength, assuming a 1.0 cm slice spacing is 1.07 cGy. The level of noise which can be tolerated depends upon the clinical application and is a topic for future work. The noise in a conventional CT scanner for a CTDI of 2 to 4 cGy ranges from 6 to 15 HU for a body scan (McCollough and Zink, 1995). Thus in our scanner, the noise is higher, but the dose is also lower.

Currently, a prototype scanner is under construction using the detectors, collimators, and geometry described in this thesis. The detectors have been characterized and found to function well. The image quality predicted in Chapter 6 indicates that the scanner will be extremely useful for HDR BT treatment planning. There are however a number of design and implementation considerations that need to be addressed, as discussed in the following section.

7.7 Future Work

The eight-channel detector assembly presented in this thesis has sensitivity and SNR characteristics that are well suited for an ^{192}Ir source-based CT scanner. However, much work remains to be done before a clinically viable scanner exists. The first and foremost task is the construction of the scanner. The scanner support and collimators have been constructed, as shown in Figure 2.1 and the crystal arrays have been completed. The measurements performed in this thesis used Dow Corning Q2-3067 optical coupling gel. This couplant is however unsuitable for the final fourth generation scanner because the couplant must also bond the crystals to the photodiode arrays. To this end, a two part silicon optical coupling compound (Rexon Components, Inc. RX-22P) was used. Future measurements will be performed to test the effectiveness of this coupling material.

Further efforts will be made to resolve the aliasing issue discussed in the previous section. An intuitive solution is to simply collect more samples. This could be achieved by appropriate programming of the HDR BT treatment unit. The most distal source dwell position in a single catheter is determined by a "length" parameter l, which can be set in 1 mm increments. It would be possible to set the length to l, perform a scan with 2.5 mm spacing between the dwell positions, then set the length to $(l + 1)$ mm and repeat the scan. The data from the two scans could then be interleaved to obtain finer sample spacing. This technique has the disadvantage of doubling the image collection time and patient dose. A second technique requires offsetting half of the source positions (for instance, the source positions in the lower half of the scanner ring) a distance of 1.25 mm by physically adjusting the catheter locations. This technique will interleave the data. However, there may be subtle effects on the image that require more research. The computer simulation described in Chapter 6 could easily be used to investigate this sampling scheme. The simulation program could also be used to examine the effect of slight positioning errors in the source catheters, which could result in image artifacts (Joseph, 1981).

Once the scanner is complete, the next step will be to experimentally examine the imaging characteristics predicted in Chapter 6. This would include measurement of the PSF, NPS and dose, as well as calculation of the effective dose equivalent. Other

measurements such as assessment of the low contrast resolution would also be performed. A more detailed comparison of the ^{192}Ir source-based CT scanner with a conventional CT scanner would be of particular interest.

The patient dose could be reduced by motorizing the collimation jaws, so that the source collimation is always smaller than the detector collimation, thereby reducing the irradiated slice thickness. Motorized collimation may be more important for image quality because it would result in reduced scatter.

Although this is not presently possible, some changes could be made to the HDR BT treatment unit to aid its use in CT. Useful modifications would include: continuous source travel at any speed, or a much larger number of dwell positions with a smaller spacing, which would eliminate the projection aliasing discussed above; controlled movement of the source within the catheter along its entire length rather than only along 12 cm (see §5.3.1), which would allow two, rather than 18 catheters to be used; and, hardware changes that would allow direct communication between the HDR BT treatment unit and the ^{192}Ir source-based CT scanner so that the source position is always known by the CT scanner data acquisition control circuit. At present, separate collimated radiation detectors are fixed adjacent to each of the 18 catheters at the location where they enter the collimator ring. These provide a signal to the data acquisition control circuit when the source passes through each of the catheters, which in turn triggers the appropriate acquisition sequence. This is not ideal however as there is a small uncertainty in the position of the source due to the finite width of the detector, and consequently the time at which it arrives at the first dwell position. Direct communication between the HDR BT treatment unit and the ^{192}Ir source-based CT scanner would eliminate this problem.

The final stages of the project would involve scanning more complex phantoms. Ultimately, our goal is to image patients and incorporate the images into the treatment planning process.

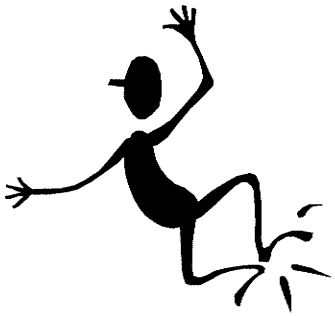

The End!!!

Appendix A
Standard Deviation Analysis

The propagation of noise in the projection data through the filtered backprojection method has been described by Gore and Tofts (1978) and Barrett and Swindell (1981). Using this analysis, the noise can be calculated for (i) the output of each individual detector; (ii) the projection data; (iii) the filtered projection data; and, (iv) the reconstructed image. This provides an understanding of the noise at all stages of the reconstruction process.

Noise in the Detector Output

Photon emissions from a radioactive source and interactions within materials obey Poisson statistics. In addition, the noise ΔN_{lj} in a detector at position l and projection j is independent of the noise $\Delta N_{l'j'}$ in a detector at position l' and projection j'. The variance in the detector output $\langle \Delta N_{lj} \Delta N_{l'j'} \rangle$ is therefore given by (Barrett and Swindell, 1981)

$$\langle \Delta N_{lj} \Delta N_{l'j'} \rangle = \overline{N}_{lj} \delta_{ll'} \delta_{jj'} \qquad \text{(A.1)}$$

where $\overline{N}_{lj}$ is the mean number of photons detected by the detector and δ is a Kronecker delta which equals 1 if the subscripts are equal, i.e., $l = l'$, and is 0 otherwise. The subscript l indexes the detector and source position as described by (6.26) and (6.27), and $j = 0, 1, 2, \ldots, J-1$ indexes the projection angle where J is the number of projections.

Noise in the Projection Data

The next step in the image generation process, after data collection is to calculate the projection data P_{lj} for a detector at position l and projection j,

$$P_{lj} = -\ln\left(\frac{\overline{N}_{lj}}{N_o}\right) \qquad \text{(A.2)}$$

where N_o is the number of detected photons in the absence of an attenuator. It can be shown (Barrett and Swindell, 1981) that the variance in the projection data $\langle \Delta P_{lj} \Delta P_{l'j'} \rangle$ is

$$\left\langle \Delta P_{lj} \Delta P_{l'j'} \right\rangle \cong \frac{\delta_{ll'} \delta_{jj'}}{\overline{N}_{lj}}. \tag{A.3}$$

where ΔP_{lj} is the noise in the projection data at position l and projection j and $\Delta P_{l'j'}$ is the noise in the projection data at position l' and projection j'. To permit easier mathematical manipulation of the filtering and backprojection expressions, discrete functions in (A.3) must be changed to continuous functions, namely,

$$\left\langle \Delta P_{\phi}(x) \Delta P_{\phi'}(x') \right\rangle = \frac{\delta(\phi - \phi')\, \delta(x - x')}{\overline{n}_{\phi}(x)} \tag{A.4}$$

where the Kronecker delta was replaced by a Dirac delta function, $\overline{n}_{\phi}(x)$ is the linear photon density over the detector

$$\overline{n}_{\phi}(x) = \frac{\overline{N}_{lj}}{\Delta\phi\, \Delta x}, \tag{A.5}$$

x and ϕ indicate projection data at position x and angle ϕ, x' and ϕ' indicate projection data at position x' and angle ϕ', Δx is equal to the detector dimension and $\Delta\phi = \pi / J$. The Dirac delta functions $\delta(\phi - \phi')$ and $\delta(x - x')$, indicate that the noise in the projection data is spatially uncorrelated.

Noise in the Filtered Projection Data and Final Image

The reconstructed image is generated by filtering and backprojecting the projection data using the expression

$$\mu(r,\theta) = \frac{1}{\pi} \int_0^{\pi} d\phi \left[P_{\phi}(x) * q(x) \right]_{x = r\cos(\theta - \phi)} \tag{A.6}$$

where the continuous projection data $P_{\phi}(x)$ are convolved with the continuous filter function $q(x)$ given by (6.12) or (6.13), to give the filtered projection data. Angular integration describes backprojection to obtain the reconstructed image. The noise variance in the reconstructed image is related to $\left\langle \Delta P_{\phi}(x) \Delta P_{\phi'}(x') \right\rangle$ as follows (Barrett and Swindell, 1981)

$$\sigma_\mu^2(r,\theta)=\left\langle \frac{1}{\pi^2}\int_0^\pi d\phi \int_0^\pi d\phi' \int_{-\infty}^{\infty} dx \int_{-\infty}^{\infty} dx'\, \Delta P_\phi(x)\, q[r\cos(\theta-\phi)-x]\,\Delta P_{\phi'}(x')\, q[r\cos(\theta-\phi')-x'] \right\rangle$$

$$=\frac{1}{\pi^2}\int_0^\pi d\phi \int_0^\pi d\phi' \int_{-\infty}^{\infty} dx \int_{-\infty}^{\infty} dx'\, q[r\cos(\theta-\phi)-x]\, q[r\cos(\theta-\phi')-x']\left\langle \Delta P_\phi(x)\Delta P_{\phi'}(x')\right\rangle$$

$$=\frac{1}{\pi^2}\int_0^\pi d\phi \int_0^\pi d\phi' \int_{-\infty}^{\infty} dx \int_{-\infty}^{\infty} dx'\, q[r\cos(\theta-\phi)-x]\, q[r\cos(\theta-\phi')-x']\frac{\delta(\phi-\phi')\,\delta(x-x')}{\overline{n}_\phi(x)}$$

$$=\frac{1}{\pi^2}\int_0^\pi d\phi \int_{-\infty}^{\infty} dx \frac{1}{\overline{n}_\phi(x)} q^2(r\cos(\theta-\phi)-x). \qquad \text{(A.7)}$$

The noise variance at the origin $r = 0$ (center of the reconstructed image) is then described by

$$\sigma_\mu^2(0,0)=\frac{1}{\pi^2}\int_0^\pi d\phi \int_{-\infty}^{\infty} dx \frac{1}{\overline{n}_\phi(x)} q^2(x). \qquad \text{(A.8)}$$

In order to compare the results of (A.8) with the simulation data, this expression is discretized using

$$\begin{aligned} \phi &= j\Delta\phi & j &= 0,\ldots,J\text{-}1 \\ x &= l\Delta x & l &= -\infty,\ldots,\text{-}1,0,1,\ldots,\infty \end{aligned} \qquad \text{(A.9)}$$

so that

$$\sigma_\mu^2(0,0)=\frac{\Delta\phi\,\Delta x}{\pi^2}\sum_{j=0}^{J-1}\sum_{l=-\infty}^{\infty}\frac{1}{\overline{n}_\phi(x)} q^2(l). \qquad \text{(A.10)}$$

The $1/\overline{n}_\phi(x)$ term can be replaced by $\Delta\phi\Delta x/\overline{N}_{lj}$ to give

$$\sigma_\mu^2(0,0)=\frac{\Delta\phi^2\,\Delta x^2}{\pi^2}\sum_{j=0}^{J-1}\sum_{l=-\infty}^{\infty}\frac{q^2(l)}{\overline{N}_{lj}}. \qquad \text{(A.11)}$$

Appendix B
NPS Verification

B.1 NPS Generation – Part I

Kijewski and Judy (1987) present a complete NPS analysis for a first generation scanner geometry taking into account the effect of the filter function (RL or SL), interpolation scheme (LI or NN), backprojection and the effect of displaying the image on a discrete grid. The analysis presented here investigates the noise properties at each stage of the image generation process, including the NPS of the projection data, the NPS of the filtered projection data, and the NPS of the interpolated filtered projection data. More specifically, Part I verifies the validity of expressions (6.59) to (6.61) using the first generation scanner geometry modeled in §6.3.1.1 and the noise generation technique described in §6.3.1.2.

The projection NPS $\overline{C}_P(f)$[1] was generated by setting the projection data equal to Gaussian distributed random numbers (recall (6.34)) and using the following expression

$$\overline{C}_P(f) = \frac{1}{M}\sum_{m=0}^{M-1}\left|\frac{1}{L}\sum_{l=0}^{L-1}P_m(l)e^{-2\pi i l f / L}\right|^2 \qquad \text{(B.1)}$$

where $M = 12\,000$ is the number of periodograms, $L = 256$ is the number of detector and source positions and $P_m(l)$ is the projection data used to generated the m^{th} periodogram. The results of this expression for $f_N = 1/2\Delta x = 5$ cm^{-1} are shown in Figure B.1. As can be seen, the power spectrum is flat as expected for white noise. The agreement of (B.1) with (6.59) is excellent. Note that the results of (B.1) are not shifted or normalized.

The projection data generated for (B.1) are filtered in the spatial domain by convolving them with (6.14) or (6.15) for the RL and SL filters, respectively, to yield

[1] The notation introduced in §3.2 will be preserved, i.e., Γ represents the ensemble average of the NPS and C represents the NPS estimate.

filtered projections $\tilde{P}_m(l)$.The latter are used to generate the filtered projection power spectrum $\overline{C}_{\tilde{P}}(f)$

$$\overline{C}_{\tilde{P}}(f)=\frac{1}{M}\sum_{m=0}^{M-1}\left|\frac{1}{L}\sum_{l=0}^{L-1}\tilde{P}_m(l)e^{-2\pi ilf/L}\right|^2. \qquad \text{(B.2)}$$

The agreement of (B.2) with (6.60) is excellent, as can be seen in Figure B.2. Note that the results of (B.2) are not shifted or normalized. Equation (6.60) predicts a NPS equal to the square of the filter function shown in Figure 6.5. This can be clearly seen in Figure B.2.

The interpolated filtered projection power spectrum $\overline{C}_{\tilde{P}_G}(f)$ is found using

$$\overline{C}_{\tilde{P}_G}(f)=\frac{1}{M}\sum_{m=0}^{M-1}\left|\frac{1}{L}\sum_{l=0}^{L-1}\tilde{P}_{Gm}(l)e^{-2\pi ilf/L}\right|^2 \qquad \text{(B.3)}$$

where $\tilde{P}_{Gm}(l)$ is the interpolated filtered projection data. Interpolation was carried out by finding the projection values at increments of $0.096\,\Delta x/4$ for both the RL and SL filters. The result of (B.3), and the expected NPS shape calculated using (6.61) are shown in Figures B.3 and B.4. The interpolated filtered projection NPS for the RL filter using LI (not

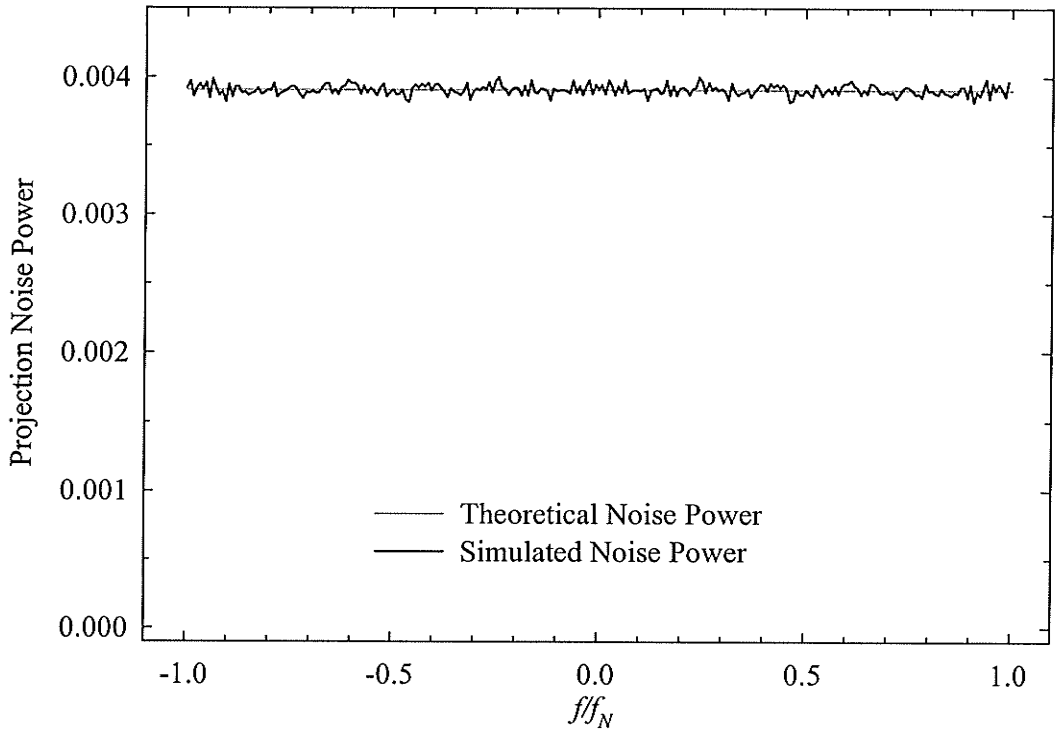

Figure B.1 Plot of the theoretical (6.59) and simulated (B.1) projection noise power as a function of frequency. $f_N = 5$ cm^{-1}.

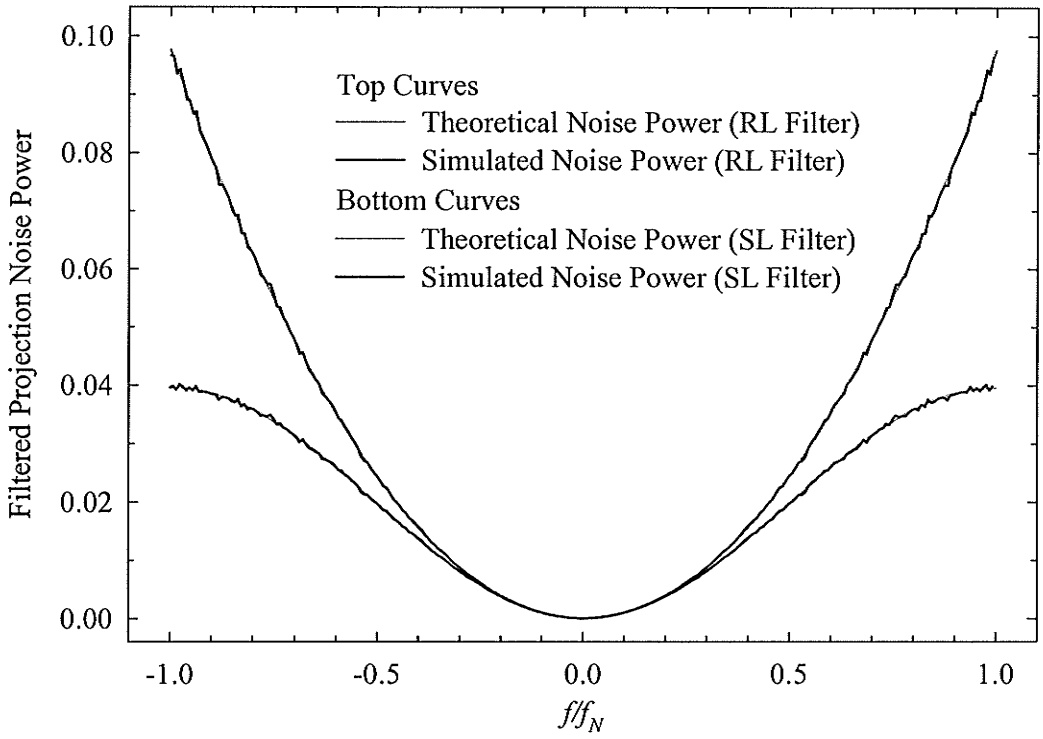

Figure B.2 Plot of the theoretical (6.60) and simulated (B.2) filtered projection noise power as a function of frequency for both the RL and SL filters. $f_N = 5$ cm^{-1}.

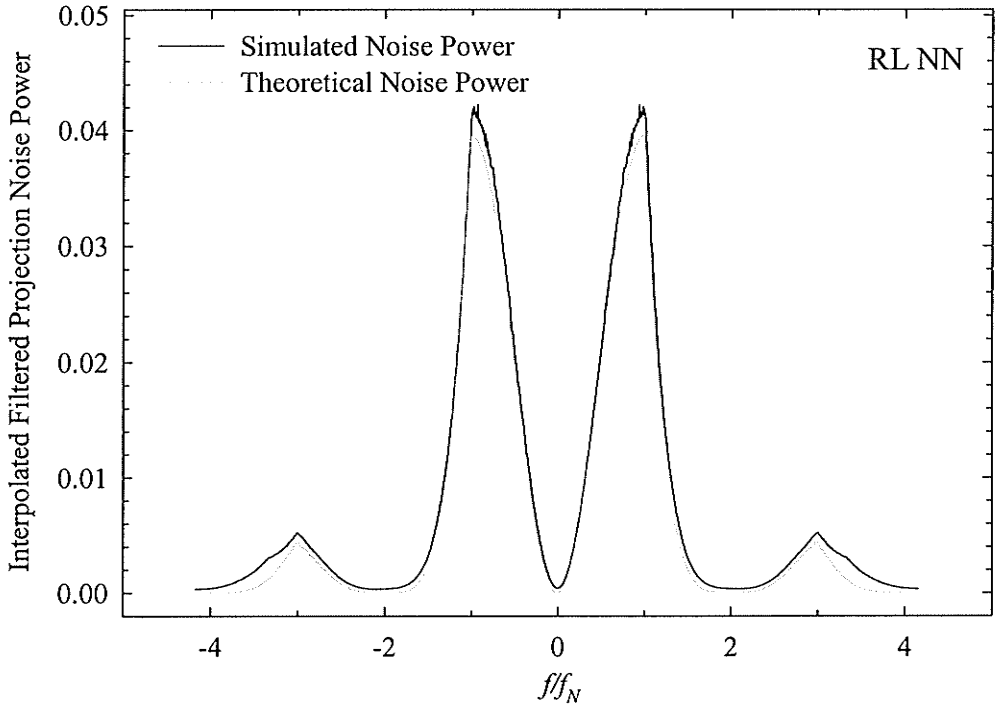

Figure B.3 Plot of the theoretical (6.61) and simulated (B.3) interpolated filtered projection noise power as a function of frequency for the RL filter using NN interpolation. $f_N = 5$ cm^{-1}.

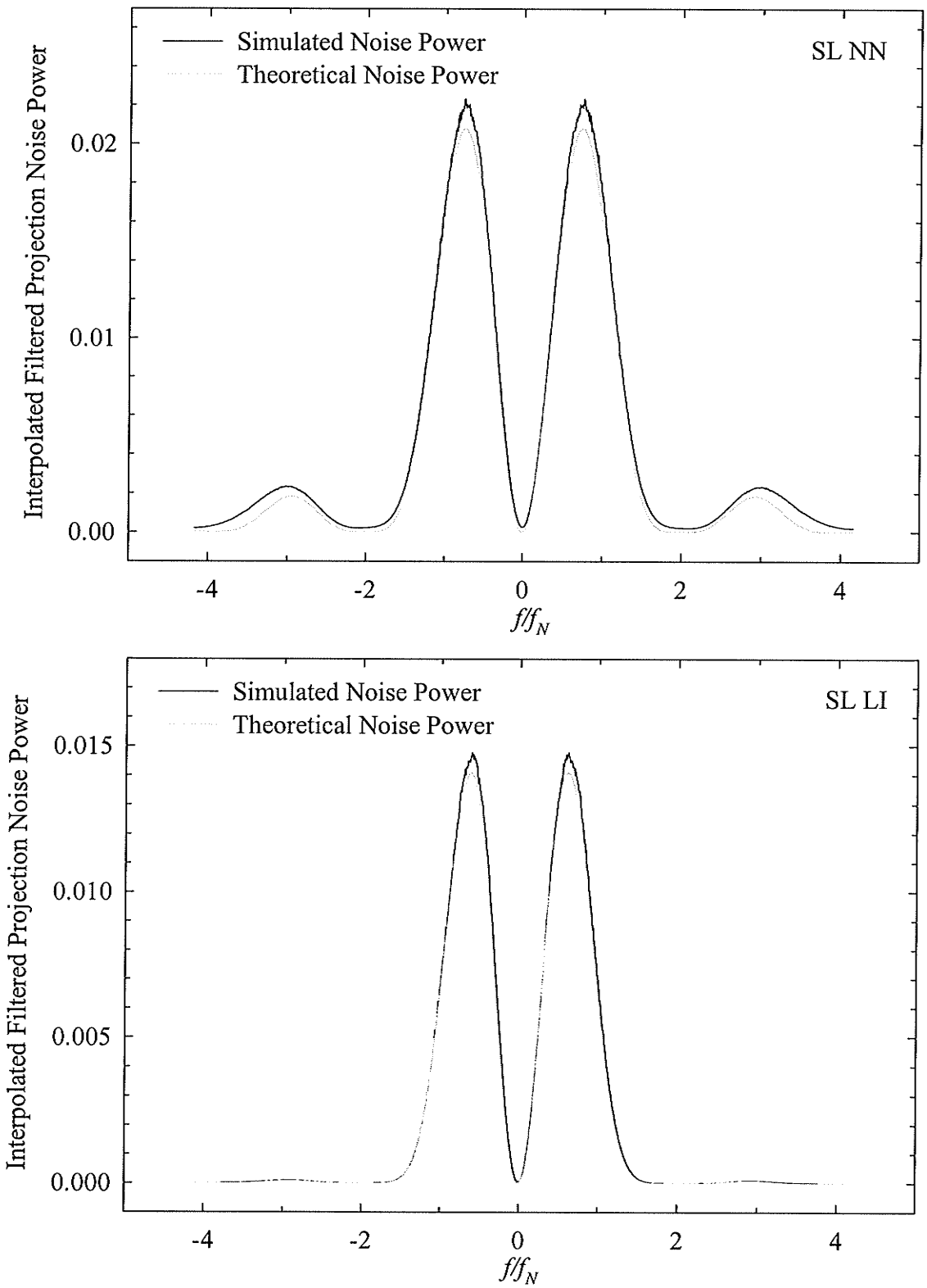

Figure B.4 Plot of the theoretical (6.61) and simulated (B.3) interpolated filtered projection noise power as a function of frequency for the SL filter using NN and LI. $f_N = 5$ cm^{-1}.

shown) is similar in appearance to the SL LI interpolated filtered projection NPS (Figure B.4). The difference between the theoretical and simulated NPS occurs in part because the simulated NPS is aliased (i.e. the effect of frequencies greater than $4f_N$ are folded back onto the NPS), whereas the theoretical power spectrum is not aliased.

B.1 NPS Generation –Part II

In Part I, (6.59) to (6.61) were compared to their simulated counterparts. The purpose of Part II is to consider the influence of the summations in (6.62), to determine the effect of the pixel spacing Δp on power spectrum aliasing, and to examine the effect of the number of projections J on the NPS.

Summing over m and n results in shifted replicas of the power spectrum appearing at intervals of $1/\Delta p$ along the f_x and f_y axes in frequency space (Kijewski and Judy, 1987). A smaller pixel spacing Δp will result in less aliasing of the power spectrum as the shifted replicas will appear at a greater distance from $(f_x, f_y) = (0,0)$, and will consequently have a smaller influence on the power spectrum between $\pm f_N$. The converse is also true.

The effect of aliasing for projections along the principal axes is demonstrated in Figures B.5 to B.7. Figure B.5 shows the NPS for $\Delta p = 0.04$ cm, Figure B.6 uses $\Delta p = 0.075$ cm and Figure B.7 uses $\Delta p = 0.14$ cm. It can be seen that the $n = 1$ and $n = 2$ shifted replicas have an increasing influence on the simulated power spectrum with increasing Δp.

The effect of aliasing for projections along the principal axes is fairly easily understood. The effect of aliasing from projections along some arbitrary angle is however not as straight forward. The aliased portion of the power spectrum generated using a projection at 15° appears as the small hills in Figure B.8. These will contribute to the power spectrum spokes at other angles. Further examples of this effect are shown below.

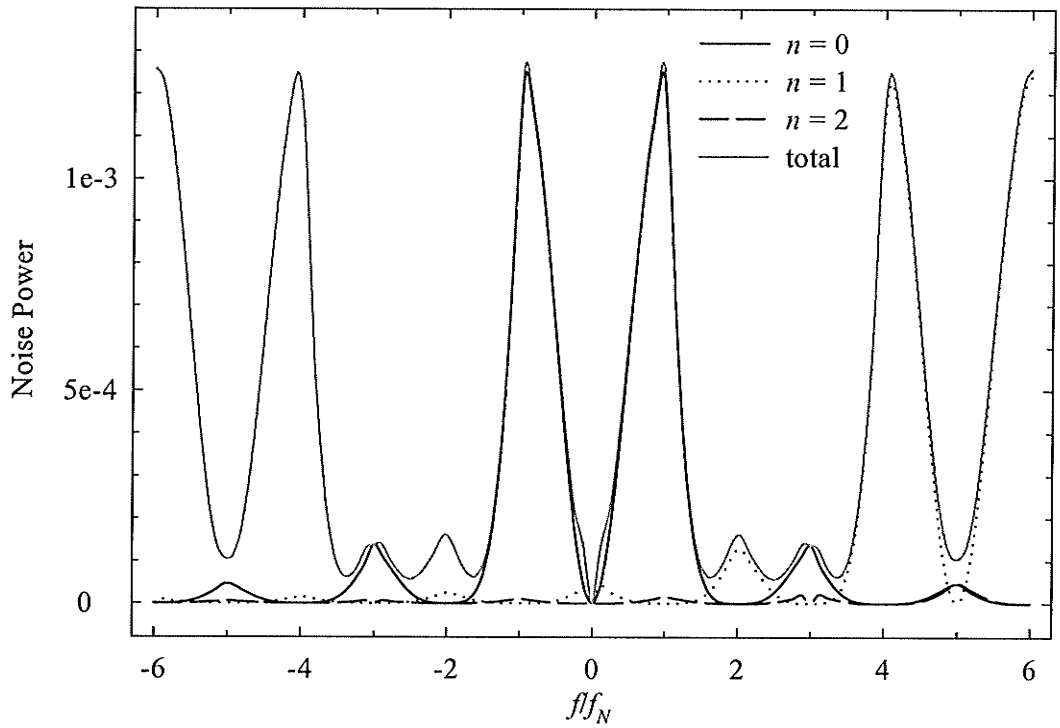

Figure B.5 NPS calculated using (6.62) and a RL filter, NN interpolation, $\sigma_P = 1.0$, $J = 1$ (0°), $L = 256$, $\Delta x = 0.1$ cm, $\Delta p = 0.04$ cm summing over k = -8 to 8, $m = 0$ and n as shown (total n = -8 to 8).

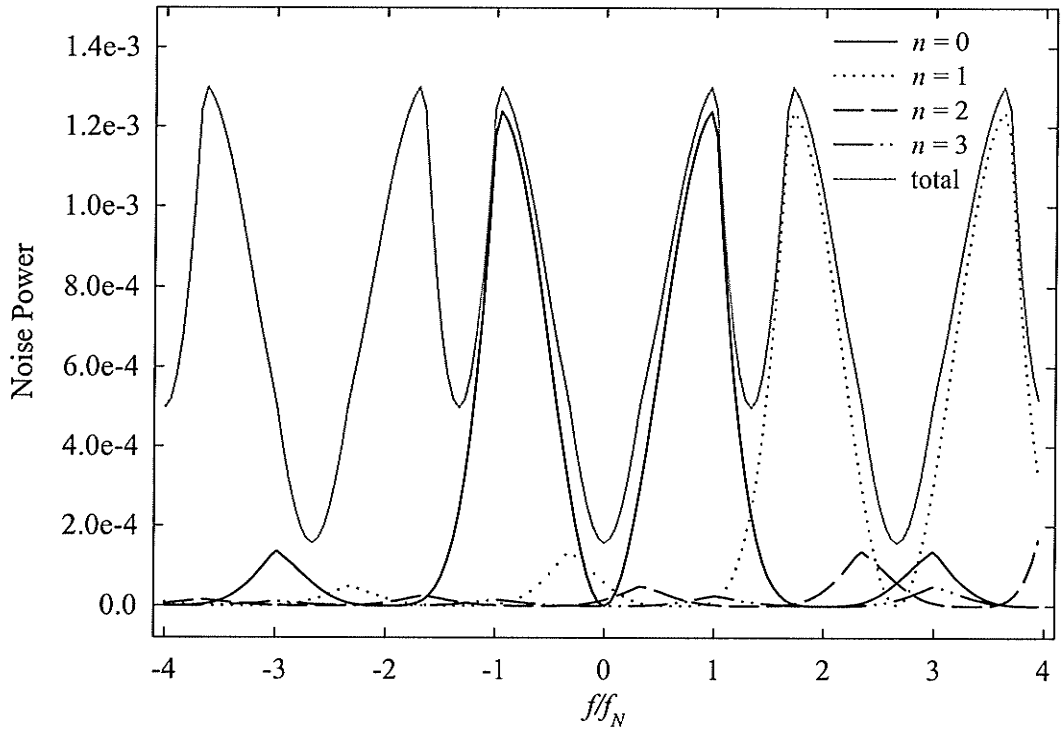

Figure B.6 NPS calculated using (6.62) and a RL filter, NN interpolation, $\sigma_P = 1.0$, $J = 1$ (0°), $L = 256$, $\Delta x = 0.1$ cm, $\Delta p = 0.075$ cm, summing over k = -8 to 8, $m = 0$ and n as shown (total n = -8 to 8).

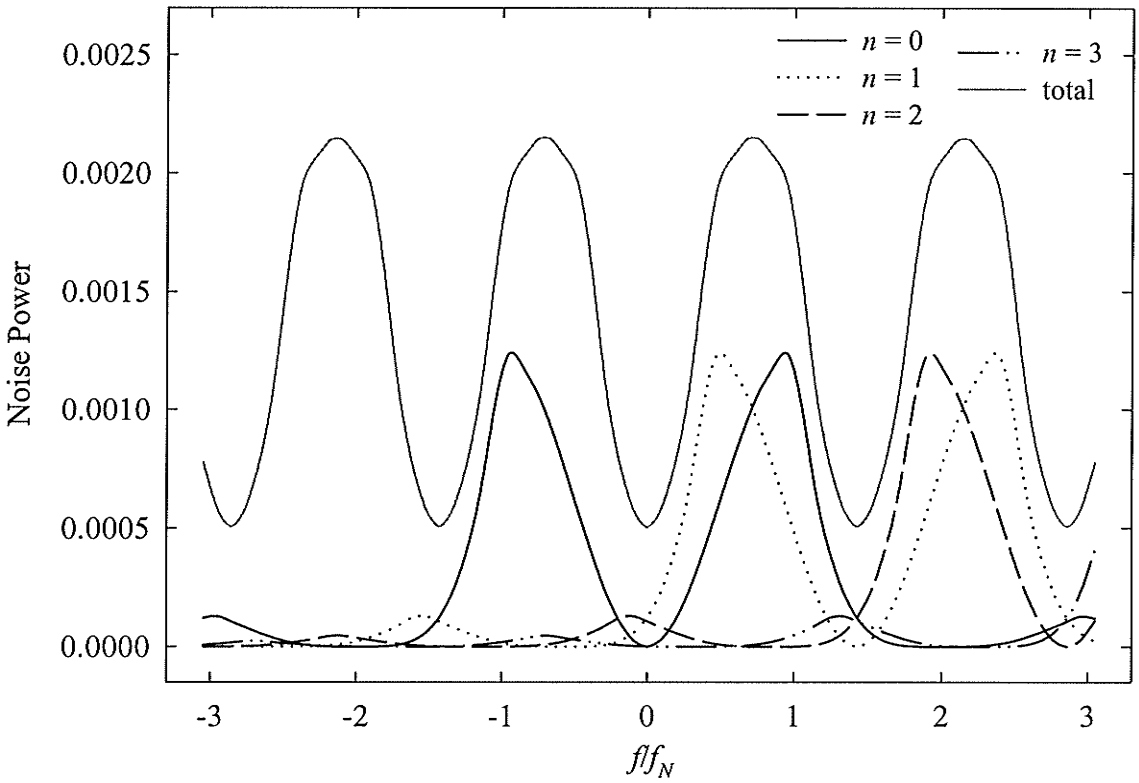

Figure B.7 NPS calculated using (6.62) and a RL filter, NN interpolation, $\sigma_p = 1.0$, $J = 1$ (0°), $L = 256$, $\Delta x = 0.1$ cm, $\Delta p = 0.14$ cm, summing over k = -8 to 8, $m = 0$ and n as shown (total n = -8 to 8).

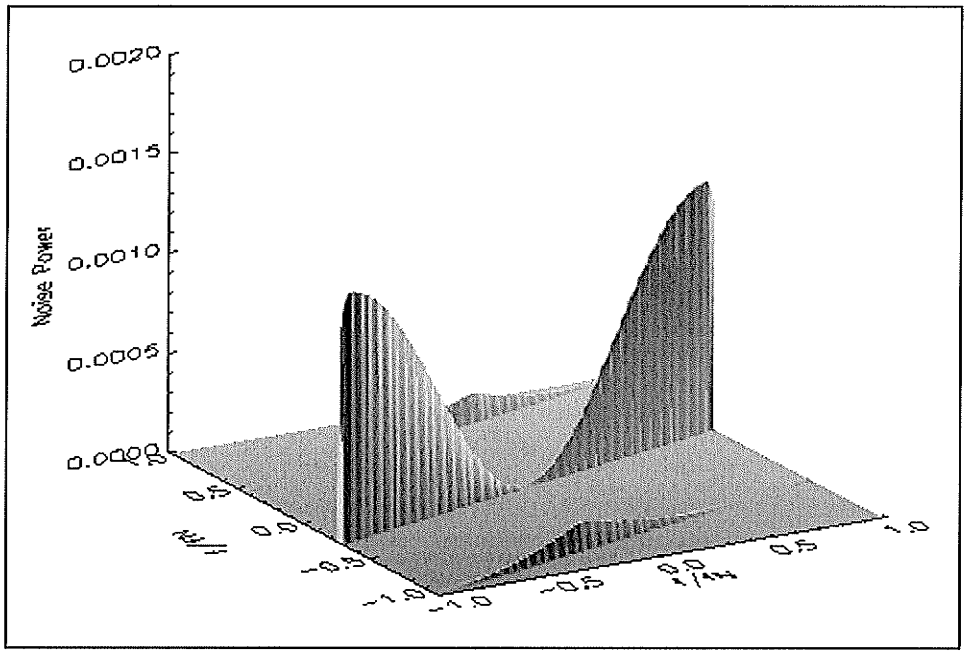

Figure B.8 NPS calculated using (6.62) and $\sigma_p = 1.0$, $J = 1$ (15°), $L = 256$, $\Delta x = 0.1$ cm, $\Delta p = 0.075$ cm, summing over k = -5 to 5, m = -1, 0, 1 and n = -1, 0 1.

As can be seen from Figure B.8, projections at a particular angle result in spokes in frequency space along that direction (Hanson, 1979). The power spectrum of images collected with more than one projection (as would always be the case!) would consist of J equally spaced spokes. The NPS shown in Figure B.9a generated using $J = 16$ clearly shows 16 spokes[2]. Note the small spokes near the edges of the NPS in Figure B.9a. These are due to aliasing, as demonstrated in Figure B.8. Using a larger number of projections ($J = 64$), as shown in Figure B.9b results in spokes that are much more closely spaced. Further increasing the number of projections would result in a smoother distribution.

Generation of the theoretical NPS for large values of J is complicated by the fact that the NPS is the summation of a large number of spokes. For $J = 350$, the spokes in the simulated NPS merge together to form a smooth distribution due to the statistical nature of the NPS. The theoretical NPS however still shows the spoke structure. As a result, the theoretical NPS along a particular axis displays peaks that do not appear in the simulated NPS. The location of the peaks depends upon the size of the grid used to generate the NPS and the width of the δ_s-function in (6.63a). To simulate the smoothing effect experienced by the simulated noise power spectrum, a very large number of projections ($J = 5000$) was used to determine the theoretical NPS along the principal and diagonal axes. Consequently, it was necessary to scale the theoretical NPS. This was achieved by setting the power under the theoretical NPS to equal the power under the simulated NPS.

Figures B.10 and B.11 supplement Figure 6.38 in the main text. They show further examples of first generation noise power spectra generated using theoretical noise (§6.3.1.3) and experimental noise (§6.3.1.4), respectively. The trends displayed by Figures B.10 and B.11 are identical to those of Figure 6.38. The NPS display minima at zero and larger frequencies due to the effects of the reconstruction filter function and the interpolation required for backprojection. As was the case for Figure 6.38, the RL NN NPS contains the most power, and the SL LI NPS contains the least power.

[2] When calculating (6.62), summation was performed over k, m, n = -4 to 4 for LI and k, m, n = -8 to 8 for NN interpolation. Summation over a larger range resulted in negligible difference in the theoretical NPS.

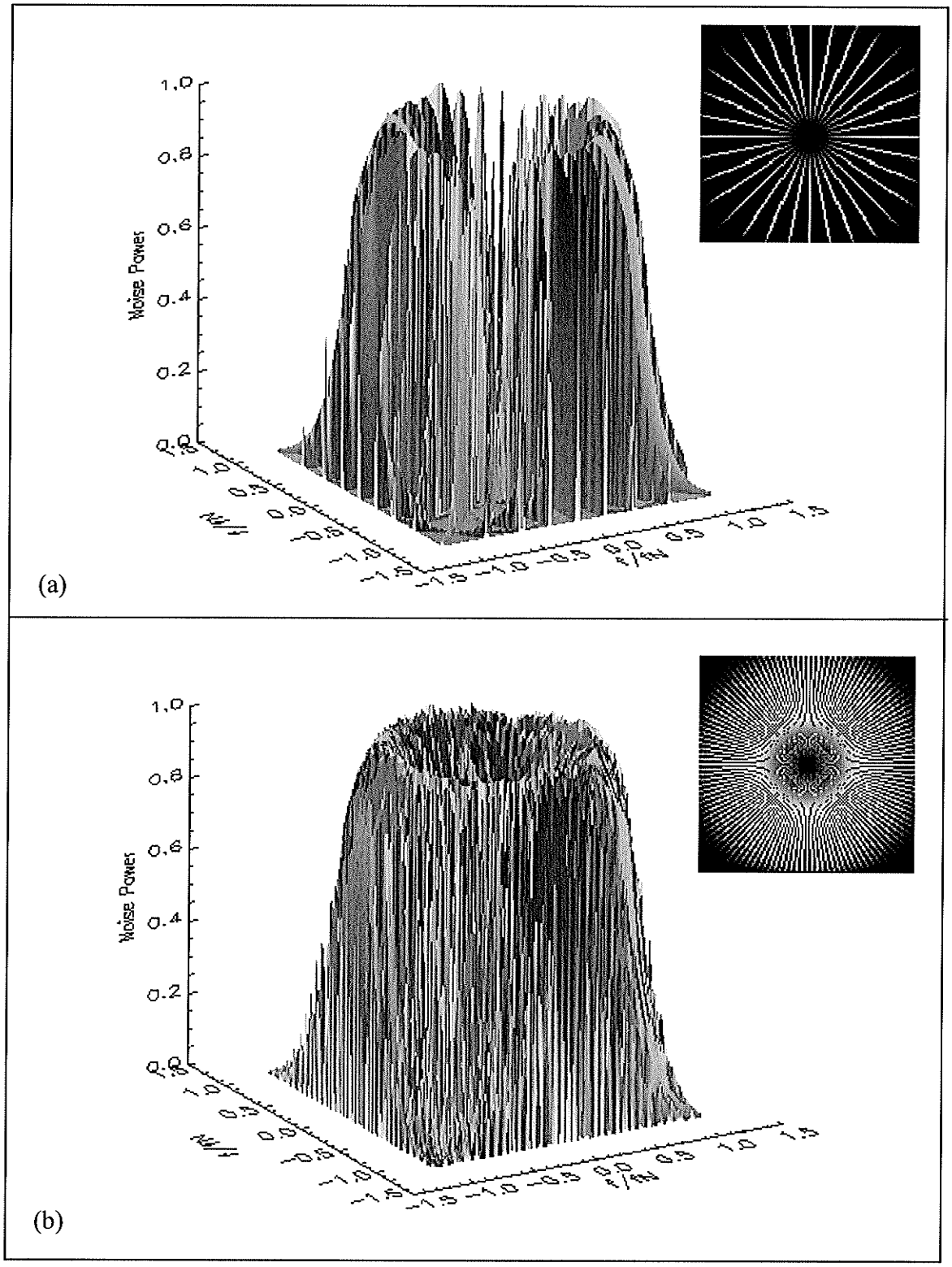

Figure B.9 Normalized theoretical NPS generated using a RL filter, LI, $L = 256$, $\Delta x = 0.1$ cm, $\Delta p = 0.09$ cm and (a) $J = 16$, (b) $J = 64$. The top right-hand images are a greyscale representation of the NPS, showing the spoke pattern described in the text.

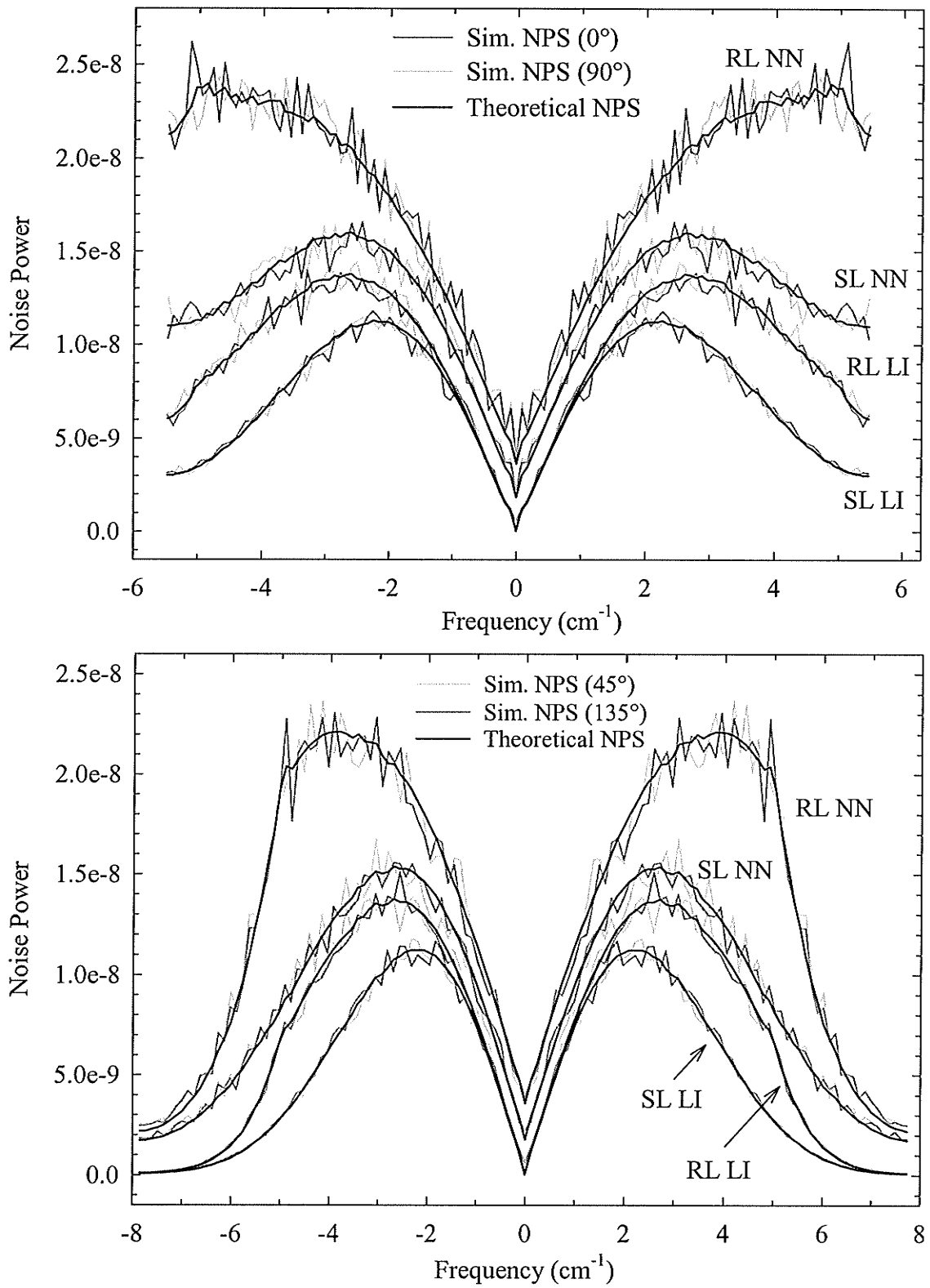

Figure B.10 NPS along the principal axes (top) and diagonals (bottom) generated using first-generation theoretical noise images (§6.3.1.3). Also shown are the theoretical NPS found using (6.62).

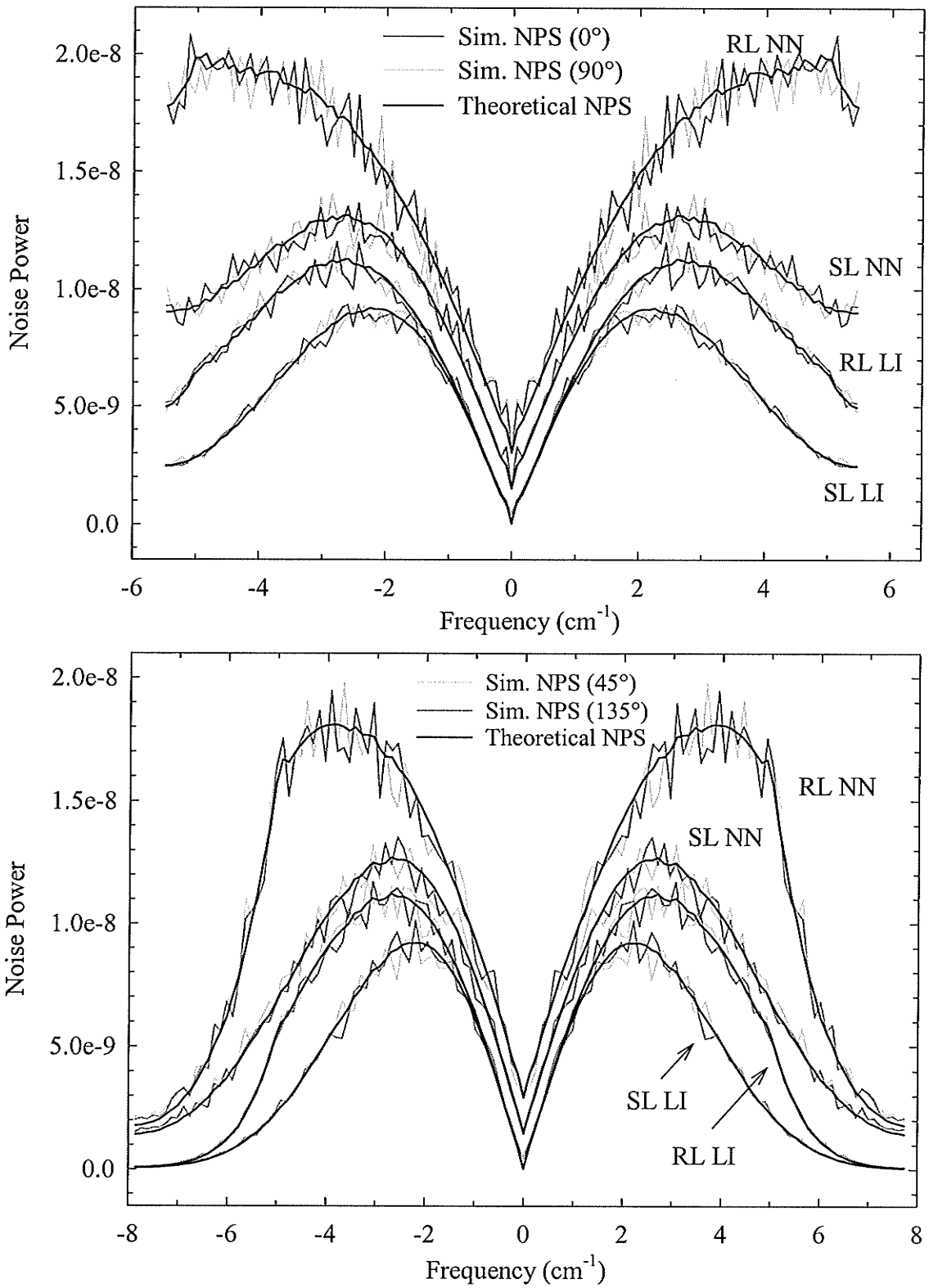

Figure B.11 NPS along the principal axes (top) and diagonals (bottom) generated using first-generation experimental noise images (§6.3.1.4). Also shown are the theoretical NPS found using (6.62).

References

Araujo, L. I., J. M. Jimenez-Hoyuela, J. R. McClellan, E. Lin, J. Viggiano and A. Alavi, Improved Uniformity in Tomographic Myocardial Perfusion Imaging with Attenuation Correction and Enhanced Acquisition and Processing, J. Nucl. Med., 41, 1139-1144, 2000.

Arenson, J., Data Collection Strategies: Gantries and Detectors, Medical CT and Ultrasound: Current Technology and Applications, American Association of Physicists in Medicine, 1995 Summer School, Eds. L. W. Goldman and J. B. Fowlkes, Advanced Medical Publishing, Madison, 1995.

Attix, F. H., Introduction to Radiological Physics and Radiation Dosimetry, John Wiley & Sons, New York, 1986.

Barrett, H. H. and W. Swindell, Radiological Imaging, Academic Press, New York, 1981.

Berndt, A., S. Rathee, D. W. Rickey and J. Bews, An 8-channel Detector for an ^{192}Ir Brachytherapy Source-Based Computed Tomography Scanner, IEEE Trans. Nucl. Sci., 47(3), 1261-1267, 2000a.

Berndt, A., D. W. Rickey, S. Rathee and J. Bews, Size and positioning reproducibility of an ^{192}Ir brachytherapy stepping source, Med. Phys., 26(1), 129-131, 2000b.

Bevington, P. R. and D. K. Robinson, Data Reduction and Error Analysis for the Physical Sciences, McGraw-Hill Inc., New York, 1992.

Bicron Brochure, Saint-Gobain/Norton Industrial Ceramics Corporation, Newbury, Ohio, 1990.

Bielajew, A. F., Lecture notes: Photon Monte Carlo simulation, National Research Council of Canada, Report PIRS-0393.

Blumfield, S. M. and G. Glover, Spatial resolution in computed tomography, Radiology of the skull and brain Volume 5: Technical Aspects of Computed Tomography, Eds. T. H. Newton and D. G. Potts, The C.V. Mosby Company, St. Louis, 1981.

Boyd, D. P., Computerized-Tomography: Isotope Sources, Int. J. Rad. Onc. Biol. Phys., 3, 53-56, 1977.

Boyd, D. P., C. E. Cann, H. K. Genant, R. G. Gould and L. Kaufman, A proposed multisource CT scanner for ultra-accurate tomodensitometry throughout the body, J. Comput. Assist. Tomogr., 3(6), 856, 1979.

Boyd, D. P., Transmission Computed Tomography, Radiology of the skull and brain Volume 5: Technical Aspects of Computed Tomography, Eds. T. H. Newton and D. G. Potts, The C.V. Mosby Company, St. Louis, 1981.

Bracewell, R. N., Strip integration in radio astronomy, Aust. J. Phys., 9, 198-217, 1956.

Bracewell, R. N. and A. C. Riddle, Inversion of fan-beam scans in radio astronomy, Astrophys. J., 150, 427-434, 1967.

Bracewell, R. N., The Fourier Transform and Its Applications, Second Edition, Revised, McGraw-Hill Book Company, New York, 1986.

Brach, B., C. Buhler, M. H. Hayman, L. R. Joyner and S. F. Liprie, Percutaneous Computed Tomography-guided Fine Needle Brachytherapy of Pulmonary Malignancies, Chest, 106, 268-274, 1994.

Brinkmann, D. H. and R. W. Kline, Automated seed localization from CT data sets of the prostate, Med. Phys., 25(9), 1667-1672, 1998.

Brooks, R. A., Comparative Evaluation of CT Scanner Technology, Medical Physics of CT and Ultrasound: Tissue Imaging and Characterization. Eds. G. D. Fullerton and J. A. Zagzebski, AAPM Monograph No. 6, American Institute of Physics, New York, 1980.

Brooks, R. A. and G. DiChiro, Principles of Computer Assisted Tomography (CAT) in Radiographic and Radioisotopic Imaging, Phys. Med. Biol., 21(5), 682-732, 1976.

Bull, J., History of computed tomography, Radiology of the skull and brain Volume 5: Technical Aspects of Computed Tomography, Eds. T. H. Newton and D. G. Potts, The C.V. Mosby Company, St. Louis, 1981.

Burr-Brown Application Bulletin AB-057A, Burr-Brown Corporation, 1993.

Cionini, L., and R. Santoni, Treatment Planning by Computed Tomography in the Curietherapy of Invasive Cervical Cancer, Cervix, 8, 277-289, 1990.

Cormack, A. M., Representation of functions by its line integrals with some radiological application-I, J. Appl. Phys., 34, 2722-2727, 1963.

Cormack, A. M., Representation of functions by its line integrals with some radiological application-II, J. Appl. Phys., 35, 2908-2913, 1964.

Cormack, A. M., Development of the CT Concept, Medical Physics of CT and Ultrasound: Tissue Imaging and Characterization. Eds. G. D. Fullerton and J. A. Zagzebski, AAPM Monograph No. 6, American Institute of Physics, New York, 1980.

Crow, E. L., F. A. Davis and M. W. Maxfield, Statistics Manual, Dover Publications, Inc., New York, 1960.

Dainty, J. C. and R. Shaw, Image Science principles, analysis and evaluation of photographic-type imaging processes, Academic Press, London, 1974.

Derenzo, S. and W. W. Moses, Experimental Efforts and Results in Finding New Heavy Scintillators, Proceedings of the CRYSTAL 2000 International Workshop on Heavy Scintillators for Scientific and Industrial Applications, Chamonix, France, 125-135, 1992.

EG&G Catalogue, EG&G Optoelectronics Canada, 1992.

Farukhi, M. R., Scintillation Detectors for CT Applications An Overview of the History and State-of-the-Art, Technical Paper 100, Rexon Components, Inc., 1978.

Fontanesi, J., R. L. Heideman, M. Muhlbauer, R. Mulhern, R. A. Sanford, E. C. Douglass, E. Kovnar, J. J. Ochs, J. F. Kuttesch, D. Tai and L. E. Kun, High-activity ^{125}I interstitial irradiation in the treatment of pediatric central nervous system tumors: a pilot study, Pediatric Neurosurgery, 22(6), 289-297, 1995.

Garrard, J. L., H. H. Hines and W. K. Braymer, Factors to Consider in the Selection of a Non-Uniform Attenuation Correction System, ADAC Publication.

Giger, M. L., K. Doi and C. E. Metz, Investigation of basic imaging properties in digital radiography. 2. Noise Wiener spectrum, Med. Phys., 11(6), 797-805, 1984.

Glasgow, G. and L. Dillman, Specific γ-ray constant and exposure rate constant of ^{192}Ir, Med. Phys., 6(1), 49-52, 1979.

Glover, G. H., Compton scatter effects in CT reconstructions, Med. Phys., 9(6), 860-867, 1982.

Gonzalez, R. and P. Wintz, Digital Image Processing, Addison-Wesley Publishing Company, London, 1977.

Gore, J. C. and P. S. Tofts, Statistical Limitations in Computed Tomography, Phys. Med. Biol., 23(6), 1176-1182, 1978.

Grabmaier, B. C., Crystal Scintillators, IEEE Trans. Nucl. Sci., 31(1), 372-376, 1984.

Graeme, J. G., Photodiode Amplifiers, McGraw-Hill, New York, 1996.

Griffin, P. C., P. A. Amin, P. Hughes, A. M. Levine, W. W. Sewchand and O. M. Salazer, Pelvic Mass: CT-guided Interstitial Catheter Implantation with High-Dose-Rate Remote Afterloader, Radiology, 191(2), 581-583, 1994.

Grimm, P. D., J. C. Blasko and H. Ragde, Ultrasound-guided transperineal implantation of iodine-125 and palladium-103 for the treatment of early-stage prostate cancer: technical concepts in planning, operative technique, and evaluation, Urol. Clin., N. Amer., 2, 113, 1994.

Grindrod, S. R., The potential resolution of a ^{137}Cs computerized tomographic scanner for radiotherapy planning, Br. Journal of Radiology, 52, 322-324, 1979.

Hamamatsu,16 Element Silicon Photodiode Array S 5668 Series, 1994.

Hamamatsu Catalogue, Hamamatsu Photonics K.K. Solid State Division, Hamamatsu, Japan, 1995.

Hangartner, T. N. and T. R. Overton, Quantitative Measurement of Bone Density Using Gamma-Ray Computed Tomography, J. Comput. Assist. Tomogr., 6(6), 1156-1162, 1982.

Hangartner, T. N., The OsteoQuant: An Isotope-Based CT Scanner for Precise Measurement of Bone Density, J. Comput. Assist. Tomogr., 17(5), 798-805, 1993.

Hanson, K. M., Detectability in computed tomography images, Med. Phys., 441-451, 1979.

Hanson, K. M., Noise and contrast discrimination in computed tomography, Radiology of the skull and brain Volume 5: Technical Aspects of Computed Tomography, Eds. T. H. Newton and D. G. Potts, The C.V. Mosby Company, St. Louis, 1981.

Haque, P. and J. H. Stanley, Basic principles of computed tomography detectors, Radiology of the skull and brain Volume 5: Technical Aspects of Computed Tomography, Eds. T. H. Newton and D. G. Potts, The C.V. Mosby Company, St. Louis, 1981.

Hendee, W. R., History of Computed Tomography, Medical Physics of CT and Ultrasound: Tissue Imaging and Characterization. Eds. G. D. Fullerton and J. A. Zagzebski, AAPM Monograph No. 6, American Institute of Physics, New York, 1980.

Herman, G. T., Advanced principles of reconstruction algorithms. Radiology of the skull and brain Volume 5: Technical Aspects of Computed Tomography, Eds. T. H. Newton and D. G. Potts, The C.V. Mosby Company, St. Louis, 1981.

Holdsworth, D. W., R. K. Gerson and A. Fenster, A time-delay integration charge-coupled device camera for slot-scanned digital radiography, Med. Phys., 17(5), 876-886, 1990.

Holl, I., E. Lorenz and G. Mageras, A Measurement of the Light Yield of Common Inorganic Scintillators, IEEE Trans. Nucl. Sci., 35(1), 105-109, 1988.

Horsman, A., J. Sutcliffe, L. Burkinshaw, P. Wild, J. Skilling and S. Webb, Isotope computed tomography using cone-beam geometry: a comparison of two reconstruction algorithms, Phys. Med. Biol., 32(10), 1221-1235, 1987.

Hounsfield, G. N., Computerized transverse axial scanning (tomography): Part I. Description of system, Br. Journal of Radiology, 46, 1016-1022, 1973.

Hsieh, J., Image Artifacts, Causes and Corrections, Medical CT and Ultrasound: Current Technology and Applications, American Association of Physicists in Medicine, 1995 Summer School, Eds. L. W. Goldman and J. B. Fowlkes, Advanced Medical Publishing, Madison, 1995.

ICRU Report 44, Tissue Substitutes in Radiation Dosimetry and Measurements, Bathesda, Maryland, 1989.

James, F., Monte Carlo theory and practice, Reports on Progress in Physics, 43, 1152-1153, 1980.

Jenkins, G. M. and D. G. Watts, Spectral Analysis and its applications, Holden-Day, San Francisco, 1968.

Johns, P. M. and M. Yaffe, Scattered radiation in fan beam imaging systems, Med. Phys., 9(2), 231-239, 1982.

Joseph, P. M. and R. A. Schulz, View sampling requirements in fan beam computed tomography, Med. Phys., 7(6), 692-702, 1980.

Joseph, P. M., Artifacts in computed tomography, Radiology of the skull and brain Volume 5: Technical Aspects of Computed Tomography, Eds. T. H. Newton and D. G. Potts, The C.V. Mosby Company, St. Louis, 1981.

Joseph, P. M. and R. D. Spital, The effects of scatter in x-ray computed tomography, Med. Phys., 9(4), 464-472, 1982.

Joseph, P. M., Overview of the History and Principles of CT Scanning, Medical CT and Ultrasound: Current Technology and Applications, American Association of Physicists in Medicine, 1995 Summer School, Eds. L. W. Goldman and J. B. Fowlkes, Advanced Medical Publishing, Madison, 1995.

Kalender, W. A., W. Seissler, E. Klotz and P. Vock, Spiral volumetric CT with single-breath-hold technique, continuous transport, and continuous scanner rotation, Radiology, 176, 181-183, 1990.

Kalender, W. A., Principles and Performance of Spiral CT, Medical CT and Ultrasound: Current Technology and Applications, American Association of Physicists in Medicine, 1995 Summer School, Eds. L. W. Goldman and J. B. Fowlkes, Advanced Medical Publishing, Madison, 1995.

Kapp, K. S., G. F. Stuecklschweiger, D. S. Kapp and A. G. Hackl, Dosimetery of intracavitary placements for uterine and cervical carcinoma: results of orthogonal film, TLD and CT-assisted techniques, Radiotherapy and Oncology, 24, 137-146, 1992.

Khan, F., The Physics of Radiation Therapy 2nd Edition, Williams & Wilkins, Baltimore, 1994.

Kijewski, M. F. and P. F. Judy, The noise power spectrum of CT images, Phys. Med. Biol., 32(5), 565-575, 1987.

Kinloch, D. R., W. Novak, P. Raby and I. Toepke, New Developments in Cadmium Tungstate, IEEE Trans. Nucl. Sci., 41(4), 752-754, 1994.

Knox, H. H. and R. M. Gagne, Alternative Methods of Obtaining the Computed Tomography Dose Index, Health Physics, 71(2), 219-224, 1996.

Kocher, D. C., Radioactive Decay Data Tables, Technical Information Center, U.S. Department of Energy, 1981.

Koutrouvelis, P. G., Three-dimensional stereotactic posteriour ischiorectal space computerized tomography guided brachytherapy of prostate cancer: a preliminary report, J. of Urology, 159, 142-145, 1998.

Kuhl, D. E. and R. Q. Edwards, Image Separation Radioisotope Scanning, Radiology, 80, 653-661, 1963.

LaVigne, M. L., S. L. Schoeppel and D. L. McShan, The use of CT-based 3D Anatomical Modeling in the Design of Customized Perineal Templates for Interstitial Gynecologic Implants, Medical Dosimetry, 16, 187-192, 1991.

Leach, M. O., S. Webb and R. E. Bentley, A rotate-translate CT scanner providing cross-sectional data suitable for planning the dosimetry of radiotherapy treatment, Med. Phys., 9(2), 269-275, 1982.

Ling, C. C., M. C. School, K. R. Working, J. Jentzsch, L. Harisiadis, S. Carabell and C. C. Rogers, CT-Assisted Assessment of Bladder and Rectum Dose in Gynecological Implants, Int. J. Rad. Onc. Biol. Phys., 13(10), 1577-1582, 1987.

Macovski, A., Basic concepts of reconstruction algorithms. Radiology of the skull and brain Volume 5: Technical Aspects of Computed Tomography, Eds. T. H. Newton and D. G. Potts, The C.V. Mosby Company, St. Louis, 1981.

McCollough C. H. and F. E. Zink, Quality Control and Acceptance Testing of CT Systems, Medical CT and Ultrasound: Current Technology and Applications, American Association of Physicists in Medicine, 1995 Summer School, Eds. L. W. Goldman and J. B. Fowlkes, Advanced Medical Publishing, Madison, 1995.

McCollough, C. H., Principles and Performance of Electron Beam CT, Medical CT and Ultrasound: Current Technology and Applications, American Association of Physicists in Medicine, 1995 Summer School, Eds. L. W. Goldman and J. B. Fowlkes, Advanced Medical Publishing, Madison, 1995.

Merritt, R. B. and S. G. Chenery, Quantitative CT measurements: the effect of scatter acceptance and filter characteristics on the EMI 7070, Phys. Med. Biol., 31(1), 55-63, 1986.

Monahan, W. G., Computed Tomography using a Cs^{137} Source, IEEE Trans. Nucl. Sci., 24 (1), 567-569, 1977.

Mosleh-Shirazi, M. H., W. Swindell and P. M. Evans, Optimization of the scintillation detector in a combined 3D megavoltage CT scanner and portal imager, Med. Phys., 25(10), 1880-1890, 1998.

Munzenrider, J. E., A. P. Brown, J. C. H. Chu, L. R. Coia, K. P. Doppke, B. Emami, G. J. Jutcher, R. Mohan, J. A. Purdy, B. Shank, J. R. Simpson, L. J. Solin and M. M. Urie, Numerical Scoring of Treatment Plans, Int. J. Rad. Onc. Biol. Phys., 21, 147-163, 1991.

Ohnesorge, B., T. Flohr and K. Klingenbeck-Regn, Efficient object scatter correction algorithm for third and fourth generation CT scanners, Eur. Radiol., 9(3), 563-569, 1999.

Oldendorf, W. H., Isolated Flying Spot Detection of Radiodensity Discontinuities – Displaying the Internal Structural Pattern of a Complex Object, IRE Transactions on Bio-Medical Electronics, BME-8, 68-72, 1961.

Oppenheim, A. V. and R. W. Schafer, Digital Signal Processing, Prentice-Hall, Inc., Englewood Cliffs, NJ, 1975.

Palmer, J., R. Pearcey and H. Lukka, The use of CT for selectron patients, Med. Dosim, 15(4), 193-197, 1990.

Parker, D. L., J. L. Couch, K. R. Peschmann and V. Smith, Structured noise in computed tomography: Effects of periodic error sources, Med. Phys., 9(5), 722-732, 1982.

Peebles, P.Z., Probability, Random Variables, and Random Signal Principles, McGraw-Hill Book Company, New York, 1980.

Percival D. B. and A T. Walden, Spectral Analysis for Physical Applications, Cambridge University Press, Cambridge, 1993.

Perera, F., F. Chisela, J. Engel and V. Venkatesan, Method of Localization and Implantation of the Lumpectomy Site for High Dose Rate Brachytherapy After Conservative Surgery for T1 and T2 Breast Cancer, Int. J. Rad. Onc. Biol. Phys., 31(4), 959-965, 1995.

Pratt, W. K., Digital Image Processing, Wiley, New York, 1984.

Purtill, P., Siemens Service Representative, Private Communication, 2001.

Radon, J., Über die Bestimmung von Funktionen durch ihre Integralwerte längs gewisser Mannigfaltigkeiten, Ber. Verh. Saechs. Akad. Wiss., 69, 262-277, 1917.

Ramachandran, G. N. and A. V. Lakshminarayanan, Three-dimensional reconstruction from radiographs and electron micrographs: Applications of convolutions instead of Fourier transforms, Proc. Natl. Acad. Sci. USA, 68, 2236-2240, 1971.

Rathee, S., Z. J. Koles and T. R. Overton, Image Restoration in Computed Tomography: Estimation of the Spatially Variant Point Spread Function, IEEE Trans. Med. Imaging, 11(4), 539-545, 1992.

Rathee, S., Image Restoration in Computed Tomography (Ph. D. Thesis), Department of Electrical Engineering, Edmonton, AB, 1992.

Riederer, S. J., N. J. Pelc and D. A. Chesler, The Noise Power Spectrum in Computed Tomography, Phys. Med. Biol., 23(3), 446-454, 1978.

Rothenberg, L. N. and K. S. Pentlow, CT Dosimetry and Radiation Safety, Medical CT and Ultrasound: Current Technology and Applications, American Association of Physicists in Medicine, 1995 Summer School, Eds. L. W. Goldman and J. B. Fowlkes, Advanced Medical Publishing, Madison, 1995.

Roy, J. N., K. E. Wallner, S. Chiu-Tsao, L. L. Anderson and C. C. Ling, CT-based optimized planning for transperineal prostate implant with customized template, Int. J. Rad. Onc. Biol. Phys., 21, 483-489, 1991.

Roy, J. N., K. E. Wallner, P. J. Harrington, C. C. Ling and L. L. Anderson, A CT-based evaluation method for permanent implants: application to prostate, Int. J. Radiat. Oncol. Biol. Phys., 26(1), 163-169, 1993.

Rüegsegger, P., U. Elsasser, M. Anliker, H. Gnehm, H. Kind and A. Prader, Quantification of Bone Mineralization Using Computed Tomography, Radiology, 121, 93-97, 1976.

Saleh, B. E. A. and M. C. Teich, Fundamentals of Photonics, John Wiley & Sons, Inc., New York, 1991.

Salomons, G. J., B. Kim, G. Gallet, A. Kerr and L. J. Schreiner, CT Imaging with a prototype Cobalt-60 Tomotherapy Unit, In Proceedings of: 45th Annual Conference of the Canadian Organization of Medical Physics, Sherbrooke, PQ, 187-189, 1999.

Scharfen, C. O., P. K. Sneed, W. M. Wara, D. A. Larson, T. L. Phillips, M. D. Prados, K. A. Weaver, M. Malec, P. Accord, K. R. Lamborn, S. A. Lamb, B. Ham, and P. H. Gutin, High Activity Iodine-125 Interstitial Implant for Gliomas, Int. J. Rad. Onc. Biol. Phys., 24, 583-591, 1992.

Schultz, E. and R. Felix, Fan-Beam Computerized Tomography Systems with Rotating and with Stationary Detector Arrays ('Third' and 'Fourth' Generation), Med. Prog. Technol., 7, 169-181, 1980.

Shepp, L. A. and B. F. Logan, The Fourier reconstruction of a head section, IEEE Trans. Nucl. Sci., 21, 21-43, 1974.

Shope, T. B., R. M. Gagne and G. C. Johnson, A method for describing the doses delivered by transmission x-ray computed tomography, Med. Phys., 8(4), 488-495, 1981.

Simpson, R. E., Introductory Electronics for Scientists and Engineers, Alyn and Bacon, Inc., Boston, 1987.

Snyder, D. and J. Cox, Jr., An Overview of Reconstructive Tomography and Limitations Imposed by a Finite Number of Projections, Reconstruction Tomography in Diagnostic Radiology and Nuclear Medicine, Eds. M. M. Ter-Pogossian, M. E Phelps, G. L. Brownell, J. R. Cox, D. O. David, and R. G. Evens, University Park Press, Baltimore, 3-31, 1977.

Stockham, C. D., A Simulation Study of Aliasing in Computed Tomography, Radiology, 132, 721-726, 1979.

Stuecklschweiger, G. F., K. S. Arian-Schad, E Poier, J. Poschauko and A. Hackl, Bladder and Rectal Dose of Gynecologic High-Dose-Rate Implants: Comparison of Orthogonal Radiographic Measurements with in Vivo and CT-assisted Measurements, Radiology, 181, 889-894, 1991.

Temic Semiconductors, Quad SPST CMOS Analog Switches DG442, Siliconix, 1997.

Teo, P. and D. Chung, An Accurate Method of ^{192}Ir Wire Implantation for Locally Advanced Carcinoma of Breast, Acta Oncologica, 26, 273-276, 1987.

Texas Instruments, TL074C, Low Noise JFET Input Operational Amplifiers, 1996.

Tod, M. and W. J. Meredith, Treatment of cancer of the cervix uteri – a revised Manchester method., Br. Journal of Radiology, 26, 252-257, 1953.

UDT Sensors, Inc. Catalogue, Optoelectronics Components Catalog, Hawthorne, CA.

Vittori, F., F. de Notaristefani, T. Malatesta and D. Puertolas, A study on light collection of small scintillating crystals, Nuclear Instruments and Methods in Physics Research, Section A, 452, 245-251, 2000.

Wagner, R. F., Fast Fourier digital quantum mottle analysis with application to rare earth intensifying screen systems, Med. Phys., 4(2), 157-162, 1977.

Wagner, R. F. and J. M. Sandrik, An Introduction to Digital Noise Analysis, The Physics of Medical Imaging, Ed. A.G. Haus, American Association of Physicists in Medicine, New York, 524-546, 1979.

Wallner, K., S. Chiu-Tsao, J. Roy, V. E. Arterbery, W. Whitmore, S. Jain, B. Minsky , P. Russo and Z. Fuks, An improved method for computerized tomography-planned transperineal ^{125}Iodine prostate implants, J. of Urology, 146, 90-95, 1991.

Wang, X., H. Hines, J. Liebig, Non-Uniform Attenuation Correction, Publication Preprint, 1994.

Webb S. and M. O. Leach, Alternative tomographic systems for radiotherapy planning, Computerized Axial Tomography in Oncology, Eds. J. E. Husband and P. A. Hobday, Churchill Livingstone, Edinburgh, 1981.

Wilson C. R., Quantitative Computed Tomography, Medical Physics of CT and Ultrasound: Tissue Imaging and Characterization. Eds. G. D. Fullerton and J. A. Zagzebski, AAPM Monograph No. 6, American Institute of Physics, New York, 1980.

Zamorano, L., M Dujovny, G. Malik, D. Yakar and B. Mehta, Multiplanar CT-guided stereotaxis and ^{125}I interstitial radiotherapy. Image-guided tumor volume assessment, planning, dosimetric calculations, stereotactic biopsy and implantation of removable catheters, Applied Neurophysiology, 50, 281-286, 1987.

Zatz, L. M., General overview of computed tomography instrumentation, Radiology of the skull and brain Volume 5: Technical Aspects of Computed Tomography, Eds. T. H. Newton and D. G. Potts, The C.V. Mosby Company, St. Louis, 1981.